

Zhengping Zou · Songtao Wang
Huoxing Liu · Weihao Zhang

Axial Turbine Aerodynamics for Aero- engines

Flow Analysis and Aerodynamics Design



上海交通大学出版社
SHANGHAI JIAO TONG UNIVERSITY PRESS



Springer

Axial Turbine Aerodynamics for Aero-engines

Zhengping Zou · Songtao Wang
Huoxing Liu · Weihao Zhang

Axial Turbine Aerodynamics for Aero-engines

Flow Analysis and Aerodynamics Design



Zhengping Zou
Beihang University
Beijing
China

Huoxing Liu
Beihang University
Beijing
China

Songtao Wang
Harbin Institute of Technology
Harbin
China

Weihao Zhang
Beihang University
Beijing
China

ISBN 978-981-10-5749-6 ISBN 978-981-10-5750-2 (eBook)
<https://doi.org/10.1007/978-981-10-5750-2>

Jointly published with Shanghai Jiao Tong University Press, Shanghai, China

The print edition is not for sale in China Mainland. Customers from China Mainland please order the print book from: Shanghai Jiao Tong University Press.

Library of Congress Control Number: 2017946675

© Springer Nature Singapore Pte Ltd. and Shanghai Jiao Tong University Press 2018

This work is subject to copyright. All rights are reserved by the Publishers, whether the whole or part of the material is concerned, specifically the rights of translation, reprinting, reuse of illustrations, recitation, broadcasting, reproduction on microfilms or in any other physical way, and transmission or information storage and retrieval, electronic adaptation, computer software, or by similar or dissimilar methodology now known or hereafter developed.

The use of general descriptive names, registered names, trademarks, service marks, etc. in this publication does not imply, even in the absence of a specific statement, that such names are exempt from the relevant protective laws and regulations and therefore free for general use.

The publishers, the authors and the editors are safe to assume that the advice and information in this book are believed to be true and accurate at the date of publication. Neither the publishers nor the authors or the editors give a warranty, express or implied, with respect to the material contained herein or for any errors or omissions that may have been made. The publishers remains neutral with regard to jurisdictional claims in published maps and institutional affiliations.

Printed on acid-free paper

This Springer imprint is published by Springer Nature

The registered company is Springer Nature Singapore Pte Ltd.

The registered company address is: 152 Beach Road, #21-01/04 Gateway East, Singapore 189721, Singapore

Preface

With the progress of aviation technology, turbine aerodynamic, as one of the major support subjects for the development of aero-gas turbine, has experienced a rapid development in the recent 20 years, with new physical phenomena being discovered and understood constantly, as well as new design methods emerging continuously. Thanks to these achievements, aerodynamic design capability for aero-gas turbines has increased rapidly, and the design level has reached a new stage. It is exactly the application of the latest fine aerodynamics design technologies in aero-gas turbines greatly improves the aerodynamic load and efficiency of turbines in modern aero-engines. In order to timely introduce the latest achievements and provide some reference for fundamental research on turbine aerodynamics and for the development of engineering design methods, the authors carried out a thorough sorting of research progresses on turbine aerodynamics in the recent 20 years, and based on that, wrote this book. This book systematically introduces the research achievements on mechanisms of complex flows in turbines and aerodynamic design methods, and is expected to be able to make some contributions to the theoretical research on aero-gas turbine aerodynamics and development of turbine aerodynamic design technology.

This book has eight chapters. Chapter 1 introduces the basic turbine aerodynamics concepts involved in this book, particularly highlighting some new concepts and supplements and extensions to original concepts, which were proposed recently, such as the Zweifel coefficient, used to represent the blade loading, and efficiency definitions of cooled turbines. Chapter 2 expounds the mechanisms of complex flows in high-pressure turbines, including aerodynamic and geometrical features of high-pressure turbines, complex wave systems with its flow structures and organizations, secondary flows and the relevant influencing factors, and mixing between cooling flow and the main flow. Chapter 3 presents the complex flows in inter-turbine ducts and its influencing factors, and discuss the relevant aerodynamic design methods. Chapter 4 expounds the geometrical and aerothermodynamic features of low-pressure turbines and the development trends, and gives a systematical introduction to the research achievements concerning the current hot issues, such as spatial-temporal evolution of blade boundary layer, interaction

between complex flows in shrouds and the main flow, secondary flows in the endwall regions of high-loading low-pressure turbines, and flows in low pressure turbines at low Reynolds number. Chapter 5 shows the complex flows in turbine rear frame ducts with its influencing factors, and its aerodynamic design methods. Chapter 6 presents the achievements about the aerodynamic design methods for turbines, including loss models, turbine parameters selection in low dimensional design numerical evaluation methods, blade profiling and 3D stacking technology, and refined turbine design technology, which is a research hot spot in recent years. Chapter 7 introduces the application of flow control technologies in turbines, including control of turbine boundary layers, secondary flows and tip leakage flows, and turbine working state adjusting technology, which is also a research hot spot in recent years. Chapter 8 gives a brief introduction to multidisciplinary conjugate problems involved with turbines, including conjugate heat transfer, flow–structure interaction, aero-acoustic conjugate, and multidisciplinary design optimization, which are still hot topics in turbine research.

The authors of this book comes from Beihang University and Harbin Institute of Technology. Chapter 1 was written by Prof. Zhengping Zou and Dr. Weihao Zhang; Chapter 2 was written by Prof. Songtao Wang; Chapter 3 was written by Prof. Huoxing Liu; Chapter 4 was written by Prof. Zhengping Zou and Dr. Weihao Zhang; Chapter 5 was written by Prof. Huoxing Liu; Sections 6.4.1 and 6.4.2 of Chap. 6 were written by Prof. Songtao Wang, and the rest of this chapter was written by Prof. Zhengping Zou; Chapter 7 was written by Prof. Huoxing Liu; Chapter 8 was written by Dr. Weihao Zhang and Prof. Zhengping Zou.

This book can be used as a reference book for teachers engaged in gas turbine teaching, researchers engaged in fundamental and applied research of aerodynamics of aviation, ground, and ship gas turbines, technicians engaged in engineering design of turbines, and graduate students and senior undergraduate students in relevant majors.

Beijing, China
April 2017

Zhengping Zou

Acknowledgements

The authors of this book have been engaged in studies on aero-gas turbine aerodynamics for years, during which they have received concern, support, and help from many professors. We are particularly grateful to Academician Maozhang Chen, Prof. Liping Xu, Prof. Haokang Jiang, and Prof. Ren Fang from Beihang University, and Academician Zhongqi Wang and Prof. Guotai Feng from Harbin Institute of Technology. Through communication and cooperation, experts in this field, including Lei Wang and Yun Chen from AECC Shenyang Aeroengine Research Institute, Wei Li, Jianqiao Luo, Ying Zhou, and Shangneng Pan from AECC Hunan Aviation Powerplant Research Institute, Jun Zeng, Gang Wei, and Kangcai Huang from AECC Sichuan Gas Turbine Establishment, made contributions to some parts of this book and provided great support to the authors. In addition, many predecessors in the academic circle, including Chaoqun Nie and Junqiang Zhu from Institute of Engineering Thermophysics, Chinese Academy of Sciences, Prof. Xin Yuan from Tsinghua University, and Prof. Baoguo Wang from Beijing Institute of Technology, also provided their support and assistance. Sincerely thanks to all of them! Doctoral dissertations of many graduated students including Dr. Lin Yang, Dr. Jian Yang, Dr. Zhengqiu Zhang, Dr. Lei Qi, Dr. Yu Li, Dr. Yang Zhou, Dr. Hongjun Zhang, Dr. Weihao Zhang, Dr. Lei Huo, Dr. Kun Zhou, Dr. Peng Wang, Dr. Fengbo Wen, Dr. ShaoPeng Lu, who were supervised by the authors, are used as references in this book, and their remarkable work enriches this book. In the writing process, many graduate students, including doctoral candidates, Yuge An, Chao Ding, Shining Chan, Wei Jia, Fei Shao, Yun Liang, Chao Fu, Tao Cui, Lei Luo, Longfei Wang, Yufeng Wang, Jinsheng Wang, Xiaojuan He, Lin Huang, and postgraduates, Yanmei Mei, Di Dong, Shaobo Zhang, Huan Li, Yan Zhang, Zhihua Zhou, Bowen Hong, Wei Zhang, offered their help and did a lot of work in data collection and arrangement, formula and picture processing, and proofreading. We are grateful to them. Besides, we would also like to thank Dr. Fangzhen Qian, Zhen Wang, and Jianmei Xu from Shanghai Jiao Tong University Press. This book cannot be published so smoothly without their assistance and highly professional work.

Finally, some research work in this book were funded by the National Natural Science Foundation of China (NSFC, No. 50776003, No. 51176013, No. 51676005, No. 51406003), and the publication of this book was supported by China Book International (CBI) project. They are also acknowledged.

Contents

1	Fundamental Concepts	1
1.1	Introduction to Gas Turbines	1
1.2	Primary Geometrical Parameters	2
1.3	Fundamental Equations of Turbine Aerothermodynamics	4
1.3.1	Continuity Equation	4
1.3.2	Energy Equation	4
1.3.3	Moment of Momentum Equation	6
1.4	Velocity Triangles of Conventional Axial Turbine Stages	7
1.5	Boundary Layer on Blade Surface	9
1.5.1	Boundary Layer Thickness	9
1.5.2	Boundary Layer Transition	10
1.5.3	Boundary Layer Separation	13
1.6	Wakes	14
1.7	Secondary Flows	15
1.8	Tip Leakage Flow	17
1.9	Potential Field	19
1.10	Shock Waves and Expansion Waves	20
1.11	Flow Mixing in Turbines	22
1.12	Blade Loading	25
1.13	Loss and Efficiency	27
1.13.1	Loss and Efficiency of Turbine Cascades	27
1.13.2	Efficiency of Uncooled Turbine	29
1.13.3	Efficiency of Cooled Turbine	31
	References	34
2	Flow Mechanism in High Pressure Turbines	37
2.1	Introduction to High Pressure Turbines	37
2.1.1	Structure and Characteristics of High Pressure Turbines	37

2.1.2	Development Status and Trends of High Pressure Turbines	39
2.1.3	Factors on Efficiency of High Pressure Turbines	42
2.1.4	Further Development of High Pressure Turbines and New Features of Aerodynamic Research	44
2.2	Aerodynamic and Geometrical Features of High Pressure Turbines	44
2.2.1	Aerodynamic Design Features of High Pressure Turbines	44
2.2.2	Blade Profile Features of High Pressure Turbines	45
2.3	Complex Wave System in High-Loaded High-Pressure Turbines	46
2.3.1	Wave Systems in High Pressure Turbines	46
2.3.2	Interaction Between Shock Waves and Boundary Layer	57
2.4	Secondary Flow of High Pressure Turbines and Control Techniques	60
2.4.1	Secondary Flow in High Pressure Turbines	62
2.4.2	Factors of Influencing Secondary Flows in High Pressure Turbines	65
2.5	Leakage Flows of High Pressure Turbines and Control Techniques	67
2.5.1	Geometrical and Aerodynamic Parameters on Tip Leakage Flows in High Pressure Turbines	74
2.5.2	Active Clearance Controls	91
2.6	Influence of Interaction Between Cooling Flow and the Main Flow on Aerodynamic Performance	93
2.6.1	Influence of Film Cooling on Aerodynamic Performance	93
2.6.2	Influence of Endwalls and Sealing Flow on Aerodynamic Performance	99
	References	111
3	Flow Mechanism in Inter Turbine Ducts	115
3.1	Geometrical and Aerodynamic Characteristics of Inter-turbine Duct and Development Trends	115
3.2	Influence of Geometrical Parameters on Flow Structures and Performance	119
3.2.1	Influence of Curvature of Meridian Passage	119
3.2.2	Influence of Area Ratio	122
3.2.3	Influence of Struts	122
3.3	Influence of Aerodynamic Parameters on Flow Structures and Performance	125
3.3.1	Influence of Inlet Mach Number	125

3.3.2	Influence of Turbulence Intensity	126
3.3.3	Influence of Inlet flow Angle	127
3.3.4	Influence of Wakes	129
3.3.5	Influence of Leakage Flows.	130
3.4	Optimal Design of ITDs and Flow Control	135
3.4.1	Optimal Design of ITDs	135
3.4.2	Flow Control in ITDs	138
	References.	141
4	Flow Mechanisms in Low-Pressure Turbines	143
4.1	Geometrical and Aero-Thermal Characteristics of Low-Pressure Turbines and their Development Trends	143
4.1.1	The Geometrical and Aero-Thermal Characteristics of LP Turbines	143
4.1.2	Flow Characteristics and Losses in LP Turbine Passages	144
4.1.3	Development Trends of LP Turbine Design	147
4.2	Boundary Layer Spatial-Temporal Evolution Mechanism in LP Turbines	149
4.2.1	Flat Plate Boundary Layer Evolution and Flow Losses	149
4.2.2	LP Turbine Boundary Layer Spatial-Temporal Evolution Under Steady Uniform Inflow.	160
4.2.3	Single Stage LP Turbine Boundary Layer Spatial-Temporal Evolution Mechanism	165
4.2.4	Unsteady Flow and Boundary Layer Evolution in Multi-stage LP Turbines	184
4.2.5	Boundary Layer Losses and Prediction Models.	190
4.3	Complex Flow in Shroud and Its Interaction with the Main Flow	196
4.3.1	Leakage Flow in the Shroud Cavities	196
4.3.2	Interaction Between Leakage Flow and Main Flow and Its Effects on the Aerodynamic Performance	203
4.3.3	Shroud Leakage Flow Low-Dimensional Models and Multi-dimensional Coupling Simulation	209
4.3.4	Shroud Leakage Flow Control Technology	217
4.4	Secondary Flow in High-Loaded LP Turbine Endwall Region	223
4.4.1	Secondary Flow Structure and Loss Characteristics in LP Turbine Endwall Region	223
4.4.2	Pressure Surface Separation and Its Impacts on Flow in LP Turbine Endwall Region	226
4.4.3	Endwall Boundary Layer Evolution Mechanism and Its Impacts	230
4.4.4	LP Turbine Endwall Flow Under Unsteady Conditions.	235

- 4.5 Low Reynolds Number Effects in LP Turbines 238
 - 4.5.1 Effects of Reynolds Number on the LP Turbine Aerodynamic Performance. 239
 - 4.5.2 LP Turbine Internal Flow Under Low Reynolds Number Conditions 243
- References. 248
- 5 Flow Mechanism in Turbine Rear Frame Ducts. 259**
 - 5.1 Geometrical and Aerodynamic Characteristics of Turbine Rear Frame and Their Development Trends 259
 - 5.2 Influence of Geometrical Parameters on Flow Structures and Performance. 261
 - 5.2.1 Influence of Meridian Profile of Duct 261
 - 5.2.2 Influence of OGVs’ Profile Parameters 262
 - 5.2.3 Influence of Hanging Structure 264
 - 5.2.4 Influence of OGV Surface Deformations. 266
 - 5.3 Influence of Aerodynamic Parameters on Flow Structures and Performance. 268
 - 5.3.1 Influence of Inlet Flow Angle 268
 - 5.3.2 Influence of Turbulence Intensity 270
 - 5.3.3 Influence of Inlet Mach Number 271
 - 5.4 Methods for Designing TRF Ducts with Large Turning-Angle OGVs. 272
 - 5.4.1 Design of Duct Profile. 272
 - 5.4.2 Design of OGV Profile 273
 - 5.4.3 Selection of Axial Length of the Duct. 274
 - References. 275
- 6 Aerodynamic Design Technologies for Turbines. 277**
 - 6.1 Introduction to Aerodynamic Design Process for Turbines. 277
 - 6.2 Aerodynamic Loss Models for Turbines. 279
 - 6.2.1 Deviation Angle Model. 280
 - 6.2.2 Ainley and Mathieson Loss Model 282
 - 6.2.3 AMDC Loss Model. 286
 - 6.2.4 Kacker and Okapuu Loss Model. 288
 - 6.2.5 Traupel Loss Model 292
 - 6.2.6 Craig and Cox Loss Model. 297
 - 6.2.7 Denton Loss Model. 306
 - 6.2.8 Coull and Hodson Profile Loss Model 309
 - 6.2.9 Cooling Flow Mixing Loss Models. 313
 - 6.3 Selection of Geometrical and Aerodynamic Parameters in Low-Dimensional Design Space. 320
 - 6.3.1 Methods for Assessing Aerodynamic Performance of Turbines in Low-Dimensional Design Space. 320

- 6.3.2 Selection and Optimization of Aerodynamic Parameters for Multi-stage LP Turbine in Low-Dimensional Design Space. 333
- 6.3.3 Design of Low-Dimensional Design Parameters for Variable-Speed Power Turbines. 338
- 6.3.4 Selection of Low-Dimensional Design Parameters for Versatile Core-Engine Turbines. 345
- 6.3.5 Selection of Low-Dimensional Design Parameters for Counter-Rotating Turbines. 349
- 6.4 Multi-dimensional Numerical Evaluation System of Turbine Aerodynamic Performance 364
 - 6.4.1 S2 Calculation for Air-Cooled Turbines 364
 - 6.4.2 Error Analysis of Various Factors in CFD-Based Air-Cooled Turbine Calculation. 374
 - 6.4.3 Numerical Simulation Methods with Geometric/ Aerodynamic Uncertainty Being Considered. 388
 - 6.4.4 Numerical Simulation Methods with Multi-dimensional Coupling 392
- 6.5 Blade Profiling Methods. 399
 - 6.5.1 Traditional Blade Profiling Methods 400
 - 6.5.2 Parametric Blade Profiling Methods and Procedures 402
 - 6.5.3 Blade Leading Edge Profiling/Modifying Methods and Applications 410
- 6.6 Influence of 3D Blade Stacking on Turbine Flows and Performance 414
 - 6.6.1 Basic Concept of 3D Profiling. 414
 - 6.6.2 Influence of Blade Curving on Turbine Flows and Performance 416
 - 6.6.3 Influence of Blade Sweeping on Turbine Flows and Performance 424
 - 6.6.4 Influence of Combination Blade Profiling on Turbine Flows and Performance 428
 - 6.6.5 Influence of Blade Stacking Errors 430
- 6.7 Fine Flow Organizing and Design Technologies 433
 - 6.7.1 Basic Concept of Fine Flow Organizing and Design. 433
 - 6.7.2 Applications of Fine Flow Organizing and Design 434
- References. 472
- 7 Flow Control Technologies 485**
 - 7.1 Introduction to Flow Control Technology. 485
 - 7.2 Flow Control Technology for Boundary Layer. 490
 - 7.2.1 Transition Inducing Technology Based on Surface Trip Wires 490
 - 7.2.2 Transition Controlling Technology Based on Rough Surface 492

- 7.2.3 Vortex Generator Technology 493
- 7.2.4 Plasma Boundary Layer Exciting Technology 497
- 7.3 Flow Control Technology for Secondary Flow 499
 - 7.3.1 Control Technology Based on End-Wall Fence 500
 - 7.3.2 Control Technology Based on Vortex Generator 502
- 7.4 Tip Leakage Flow Control Technology 505
 - 7.4.1 Blade Tip Jet Technology 505
 - 7.4.2 Casing Air Injection Control Technology 507
 - 7.4.3 Vortex Generator and Plasma Exciting Control
Technology 509
 - 7.4.4 Shroud Air Curtain Jet Technology 511
- 7.5 Turbine Working State Adjustment Technology 514
 - 7.5.1 Geometric Adjustment Technology for Turbines 515
 - 7.5.2 Aerodynamic Adjustment Technology for Turbines 519
- References 523
- 8 Multidisciplinary Coupling Analysis and Design 527**
 - 8.1 Conjugate Heat Transfer Problems 527
 - 8.1.1 Conjugate Heat Transfer in Turbines 527
 - 8.1.2 Research Methods for Aerodynamic-Heat Transfer
Coupling in Turbines 529
 - 8.1.3 Mechanism of Interaction Between Flow Field
and Temperature Field in Turbines 533
 - 8.2 Flow-Structure Interaction Problems 536
 - 8.2.1 Flow-Structure Interaction Problem in Turbines 536
 - 8.2.2 Forced Response of Turbine Blades 537
 - 8.2.3 Blade Flutter 541
 - 8.3 Aero-acoustic Conjugate Problems 544
 - 8.3.1 Noise and Aero-acoustic Conjugate Problems
in Turbine 544
 - 8.3.2 Noise Reduction in Low-Dimensional Aerodynamic
Design 547
 - 8.3.3 Aero-acoustic Integrated Design Based on Fully
3D-Modeling 549
 - 8.4 Multidisciplinary Design Optimization Technologies 550
 - 8.4.1 General Description of MDO Problem 551
 - 8.4.2 Application of MDO Technology in Turbines 553
 - References 556
- Index 561**

Abstract

This book is a monograph on turbine aerodynamics. It gives a brief introduction to the concepts related to turbine aerodynamics, systematically expounds the mechanisms of flows in axial turbines, inter-turbine ducts, and turbine rear frame ducts, analyzes the numerical evaluation methods in different dimensions, introduces the latest research achievements in the field of gas turbine aerodynamic design and flow control, and explores multidisciplinary conjugate problems involved with turbines.

This book should be helpful for scientific and technical staffs, college teachers, graduate students, and senior college students, who are engaged in design and research of gas turbines.

Chapter 1

Fundamental Concepts

1.1 Introduction to Gas Turbines

A turbine is one kind of rotating machinery that extracts energy from a fluid flow and converts it to mechanical work. It is widely used as one kind of significant component in power and energy equipments such as aircraft gas turbines, industrial gas turbines, steam turbines, hydraulic turbines, wind turbines, turbochargers, etc. and serves as an important component. This book mainly focuses on the turbine in gas turbine engines, which uses gas as the working fluid. The fundamental principles about this turbine can be also applicable to other types of turbines.

A turbine typically consists of at least one stationary part (i.e. stator) and one moving part (i.e. rotor), of which one stage is constituted by a stator row and a rotor row. A gas turbine may have one stage or multiple turbine stages. The stator, in which the gas expands and accelerates in the passage, as well as changes the flow direction, is used for converting enthalpy of gas into kinetic energy and satisfying the requirement of velocity and direction of the downstream rotor blades. The rotor extracts energy from the working fluid and converts it into shaft work. If necessary, it also can be used to adjust axial force of a gas turbine.

There are many ways to classify gas turbines. One kind of classification is to divide gas turbines into axial turbines and radial turbines based on flow direction, as shown in Fig. 1.1. An axial turbine, in which the main flow in the passage is parallel to the shaft, is mainly used in large-sized and medium-sized gas turbines because of large flow rate and high power. A radial turbine, in which the flow is radial to the shaft, is characterized by small flow rate and compact construction, and forasmuch, it is mainly used in various compact power systems. Otherwise, turbines can be also classified into single-stage turbines and multi-stage turbines, single-shaft turbines and multi-shaft turbines, reaction turbines and impulse turbines, subsonic turbines and transonic turbines, as well as gas turbines and power turbines.

Turbines in engines are operating in high-temperature and high-pressure environment. Furthermore, great pressure and temperature gradient in gas turbines as

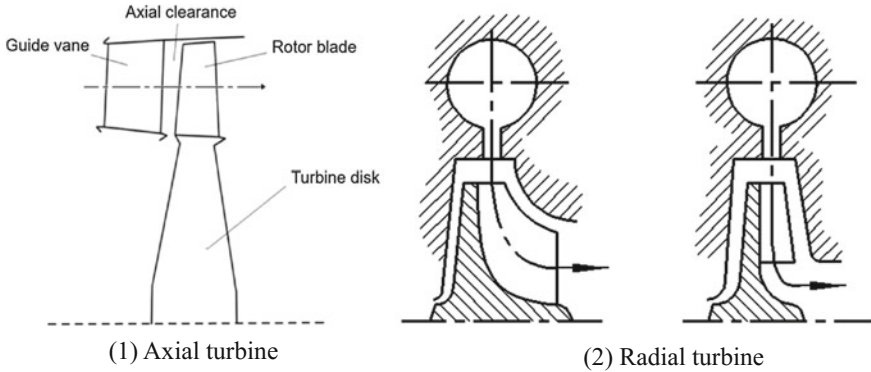


Fig. 1.1 Axial turbine and radial turbine

well as high rotation speed of turbine rotors make internal flows more complicated and lead to various kinds of secondary flows (including passage vortices, tip leakage flows, etc.), unsteady potential affection (including shock waves, expansion waves, etc.), and periodic wakes, of which the flow structures may have intense interactions potentially. In addition, the great pressure and temperature gradient as well as the high rotation speed would also result in great stress on blades, hub, casing, and the disc, and this problem would become more serious in high-temperature environment. Therefore, Aerodynamic protection should be taken for the turbines, such as use of blade cooling airflows and sealing air flows to prevent high temperature gas from entering the disc cavity. However, these actions bring more complex geometry features of turbine passage and blades. Furthermore, these air flows would finally enter into the passage and interact with the main flow intensely, making internal flows more complicated.

To sum up, flows in gas turbines are characterized as highly 3D, unsteady complex flows as well as strong shear, which exist in high-temperature and high-pressure environment with great pressure and temperature gradient. This book is devoted to expounding and discussing the latest research results of mechanisms of complex flows in turbines, as well as exploring the relevant technologies of flow control and aerodynamic design.

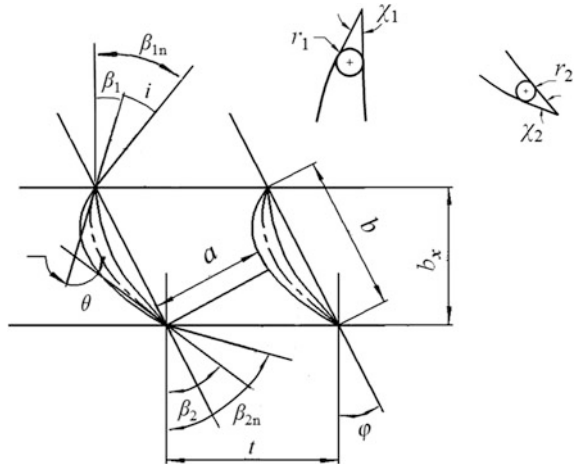
1.2 Primary Geometrical Parameters

Primary geometrical parameters of axial turbine stages mainly include these of describing the meridional passage and the geometry of blades. The parameters for describing the meridional passage mainly include outer radius R_H , inner radius R_B , average radius R_{av} ($R_{av} = \frac{R_H + R_B}{2}$ or $R_{av} = \sqrt{\frac{R_H^2 + R_B^2}{2}}$), axial length L , and hub ratio

\bar{d} ($\bar{d} = \frac{D_B}{D_H}$). As shown in Fig. 1.2, the parameters for describing blade profile geometry mainly include chord length b , stagger angle φ (defined as the included angle between the chord line and the axis), axial chord length b_x , pitch t , solidity τ ($\tau = \frac{b}{t}$ or $\tau = \frac{b_x}{t}$), leading/trailing-edge metal angles β_1/β_2 , leading/trailing edge radiuses r_1/r_2 , and leading/trailing-edge wedge angles χ_1/χ_2 . The above parameters can be used to describe the 2D blade geometry in the surface of revolution, and the 3D geometry can be obtained by combining them with the spanwise parameters, including blade height h_B , aspect ratio ($AR = \frac{h_B}{b}$), and tip clearance δ . For skewed and swept blades, the starting and ending height of skewed/swept section and the corresponding skew/sweep angle should be given additionally. These parameters determine the geometry of a turbine as well as the basic aerothermodynamic processes and flow fields in it. This book will discuss the relations between some key parameters and flow structures as well as aerodynamic performance of turbines in the following chapters.

The above-mentioned geometrical parameters are used for describing traditional turbines. However, with the development of aerodynamic design technologies, turbine geometry becomes more complex and requires more detailed parameters to describe it. For example, when applying the widely used non-axisymmetric endwall technology. Besides maximum convex value, maximum concave value, and their locations as well as other qualitative parameters, designers needs to provide surface equation or set of coordinate points to describe the endwall surface accurately. Other advanced blade profiling technologies, such as 3D profiling of blade leading-edge in endwall regions and 3D blade tip shape, also require complicated parameters to describe the geometry.

Fig. 1.2 Cascade geometry schematic



1.3 Fundamental Equations of Turbine Aerothermodynamics

Aerothermodynamic processes in turbines can be also described by the continuity equation, energy equation, and momentum equation. These equations are expressed in their specific forms when being used to describe internal flows in turbines.

1.3.1 Continuity Equation

The continuity equation between any two sections (namely section 1 and section 2) of a gas turbine is given by

$$\dot{m}_1 = \dot{m}_2 \quad (1.1)$$

In addition, the flow rate at any section of the turbine can be written as

$$\dot{m} = K \frac{P^*}{\sqrt{T^*}} q(\lambda) A \sin \alpha \quad (1.2)$$

where, K is a constant; A ; area of the section α is the angle between the direction of velocity and circumferential direction.

At a certain rotation speed, the flow rate in a turbine would gradually increase with the decrease of backpressure from a high level, hence the turbine would be in the sub-critical state. When backpressure decreases to a certain value, the flow velocity would increase to the speed of sound at one section, and the flow rate in the turbine would become constant and not increase with the decrease of backpressure any longer; at this point, the turbine would be in the critical state. The turbine would be in the super-critical state if backpressure keeps decreasing. The sonic section is called a throat section, which determines the flow capacity of the turbine. In conventional turbines, the throat section is generally located in the guide vane passage of the first stage, while it may exist in the rotor blade passage of the first stage in counter-rotating turbines.

1.3.2 Energy Equation

Energy exchange would occur when the working fluid passes through a gas turbine. Here defines the output work and heat release per unit mass of gas L_u and q_e respectively, then the energy equation in the form of enthalpy in a gas turbine can be written as

$$-L_u - q_e = h_2 - h_1 + \frac{C_2^2 - C_1^2}{2} = h_2^* - h_1^* \quad (1.3)$$

where, the static enthalpy $h = C_p T$, and the total enthalpy $h^* = C_p T^*$. Equation (1.3) is an expression of the energy equation in an absolute coordinate system, which can be used to describe the conversion and transfer of gas energy in the rotor and stator of the gas turbine. For flows in the stator, the work is 0. Assuming the flows are adiabatic, then Eq. (1.3) can be simplified as

$$h_2^* = h_1^* \quad (1.4)$$

Namely, the total enthalpy keeps constant when the gas passes through the stator passage. For flows in the rotor, the work is 0 in the coordinate system rotating together with the rotor. However, the rotating coordinate systems are non-inertial systems, consequently the work done by inertial forces should be considered. The work done by the centrifugal force on unit mass of gas is given by

$$L_{c1} = \int_1^2 [-\vec{\omega} \times (\vec{\omega} \times \vec{r})] \cdot d\vec{s} = \frac{U_2^2 - U_1^2}{2} \quad (1.5)$$

where, ω is the revolution speed of the turbine; $U = \omega r$, representing the peripheral speed at the radius r . It can be proved that the work done by the Coriolis' force on unit mass of gas is zero. So, the energy equation can be then written as

$$\frac{U_2^2 - U_1^2}{2} = h_2 - h_1 + \frac{w_2^2 - w_1^2}{2} \quad (1.6)$$

Define a new quantity called rothalpy given by: $I = h + \frac{w^2}{2} - \frac{U^2}{2}$. Hence, the above equation becomes:

$$I_2 = I_1 \quad (1.7)$$

In the rotating coordinate system, rothalpy is constant at each section of the rotor passage. Assuming rotational velocity keeps constant in the turbine passage, then the work shown in Eq. (1.5) is zero too, and the energy equation can be written as

$$h_{r2}^* = h_{r1}^* \quad (1.8)$$

Namely, the relative total enthalpy h_{r2} keeps constant at each section of the rotor passage under the above assumptions.

1.3.3 Moment of Momentum Equation

The moment of momentum equation for a turbine stage can be obtained by applying the theorem of moment of momentum into the rotor, and is given by

$$M = \dot{m}(C_{2u}r_2 - C_{1u}r_1) \tag{1.9}$$

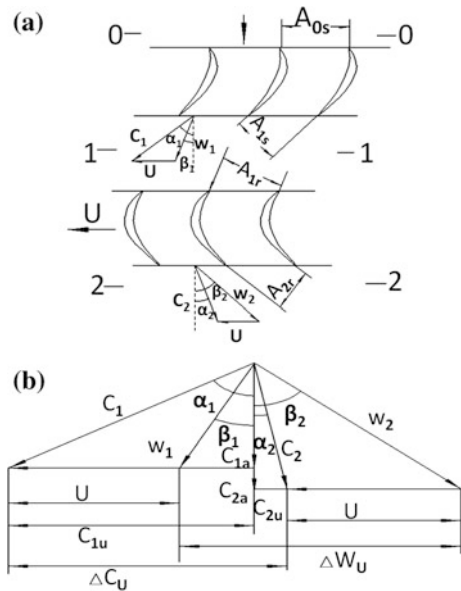
where, M is the moment of surface force of blades on the gas; C_{2u} and C_{1u} are the circumferential components of the absolute velocity at the outlet and inlet of the rotor respectively (see Fig. 1.3). Hence, the output work per unit mass of gas L_u is expressed as

$$L_u = \frac{-M\omega}{\dot{m}} = \omega(C_{1u}r_1 - C_{2u}r_2) \tag{1.10}$$

This is namely the application of the Euler Equation in turbomachinery. When the inlet radius and outlet radius of the rotor are the same, i.e. $r_1 = r_2 = r$, then Eq. (1.10) can be simplified to

$$L_u = \omega r(C_{1u} - C_{2u}) = U\Delta C_u \tag{1.11}$$

Fig. 1.3 Elementary turbine stage and the velocity triangle



1.4 Velocity Triangles of Conventional Axial Turbine Stages

Figure 1.3a shows an elementary stage of a conventional axial turbine. In this figure, the inlet section of the turbine stage, the inlet section of the rotor, and the outlet section of the turbine stage are denoted by section 0, section 1 and section 3; A represents the area, and the subscripts, s and r , represent the stator and rotor respectively. The velocity triangle of the elementary stage consist of using the velocity vectors at the inlet and outlet of the rotor (see Fig. 1.3b). The work in the elementary stage is determined by the velocity triangle, moreover, the shape of the velocity triangle determines the basic aerothermodynamic characteristics of the gas in the elementary stage, such as flow turning angle, expansion degree and its distribution, etc. So, it basically determines the aerodynamic efficiency of turbines, particularly for subsonic turbines. Therefore, the shape of velocity triangles, which is a key point in elementary stage design, is one of the most significant key point in the discussion of this book. It is easy to know that 6 parameters are needed to determine the size and shape of the velocity triangles in Fig. 1.3b. The number of parameters can be reduced to 5 only if the shape of the velocity triangle is considered. The dimensionless parameters used to describe a velocity triangle generally include: loading coefficient H_T , flow coefficient φ , reaction degree Ω , axial velocity ratio K , and inlet to outlet mean diameter ratio D . All parameters, which have definite physical meaning, is the key points of one dimensional aerodynamic design of turbine stage. The former three parameters are mainly discussed in this section because that the inlet to outlet mean diameter ratio D as well as axial velocity ratio K , which change within a narrow range, have limited influence on the aerodynamic performance of turbines.

Loading coefficient H_T is defined as the ratio of work in the elementary turbine stage to the square of revolution speed (see Eq. (1.12)), as well as represents the relative load in the turbine. The high load coefficient, which means large circumferential velocity change as well as large flow turning angle (at a fixed axial velocity), may cause strong secondary flows in endwall regions, hence lead to greater loss. On the other hand, low loading coefficient means large radial dimensions of the turbine or too many turbine stages, which may result in problems of turbine weight and rotor dynamics.

$$H_T = \frac{L_u}{U^2} \approx \frac{\Delta C_u}{U} \quad (1.12)$$

Flow coefficient φ is defined as the ratio of axial velocity to rotational velocity in the elementary stage (see Eq. (1.13)). This parameter represents flow capacity of the cascade. In the process of design, when flow rate and other parameters are fixed, large flow coefficient means large axial flow velocity and small flow area required; thus, the height of the meridional channel is relatively small and the endwall flow

region accounts for a relatively high percentage, which result in a serious influence of secondary flows. On the other hand, small flow coefficient means large height of the meridional channel, namely large blade height, which brings about higher friction area. Meanwhile, small flow coefficient would increase AN^2 and lead to strength problems.

$$\varphi = \frac{C_a}{U} \quad (1.13)$$

Reaction degree Ω is defined as the ratio of isentropic enthalpy drop across the rotor to total isentropic enthalpy drop across the elementary stage, thus it is also called energy reaction degree (see Eq. (1.14)). To correlate reaction degree with aerodynamic parameters and velocity triangles, the concept of kinematics reaction degree is generally used in turbine design, which is defined as the ratio of expansion work in the rotor to rim work in the elementary stage, namely the ratio of actual enthalpy drop across the rotor to total enthalpy drop across the elementary stage (see Eq. (1.15)). Assuming both circumferential velocity and axial velocity at the inlet of the rotor in the elementary stage are same as those at the outlet, namely $U_1 = U_2$, $V_{1a} = V_{2a}$, the kinematics reaction degree can be expressed by velocities (see Eq. (1.16)). As per the definition of reaction degree, reaction degree also represents the ratio of gas expansion work in rotor blades to total expansion work in the elementary stage. Relatively large reaction degree means great expansion in the rotor, which may lead to high tip leakage loss and axial force in the rotor. Inversely, relative small reaction degree may make it difficult to organize flows at the root of rotor blades so far as to may result in a “compressor”-like state at the root region. Because Expansion and acceleration of gas in the elementary stage help inhibit separation and secondary flow development in the passage, reasonable distribution of expansion work (i.e. Ω value determination) is of great significance in reducing aerodynamic loss in turbines.

$$\Omega = \frac{h_1 - h_{2s}}{h_0 - h_{2s}} \quad (1.14)$$

$$\Omega = \frac{h_1 - h_2}{Lu} = \frac{h_1 - h_2}{h_0^* - h_2^*} \quad (1.15)$$

$$\Omega \approx 1 - \frac{V_{1u} - V_{2u}}{2U} \quad (1.16)$$

The above discussion on parameters about velocity triangle is based on conventional axial turbine stages. Nevertheless, Velocity triangles of axial counter-rotating turbines and centripetal turbines have their own characteristics corresponding to their internal flow patterns, which will be discussed in the following chapters.

1.5 Boundary Layer on Blade Surface

The concept of boundary layer was first proposed by Ludwig Prandtl, which refers to the flow region in the immediate vicinity of a solid surface at high Reynolds numbers. Because of viscosity, the flow velocity normal to the wall varies intensely in this region, which means that the velocity increases from zero at the solid wall to that of the freestream in a very small space. Figure 1.4 shows a flat-plate boundary layer. The flows outside of boundary layer could be regarded as non viscous flows, since velocity gradient is small as well as viscous force could be neglected in this region. Meanwhile, According to the comparison of the magnitude of scale and velocity rate of change, the Navier–Stokes equations can be simplified to the boundary layer equation. The concept of boundary layer plays a great role in the development of fluid mechanics hence makes it possible to solve viscosity problems without computer support. With the development and application of computers and computing technologies, 3-D viscosity problems can be solved through various approaches, but the concept of boundary layer still serves as a convenient and powerful tool for investigating physical problems in flow phenomena.

1.5.1 Boundary Layer Thickness

Boundary layer thickness is one of the key points of boundary layers. Boundary layer thickness δ is generally defined as the normal distance from the solid body to the position of a certain percentage of the inviscid flow velocity, as well as the nominal thickness of the boundary layer. For example, $\delta_{0.99}$ is the boundary layer thickness at which the viscous flow velocity is 99% of the inviscid flow velocity. The nominal thickness of a boundary layer is highly arbitrary and cannot reflect the physical essence of the boundary layer. In addition, values at different working conditions are incomparable. Therefore, researchers developed some other

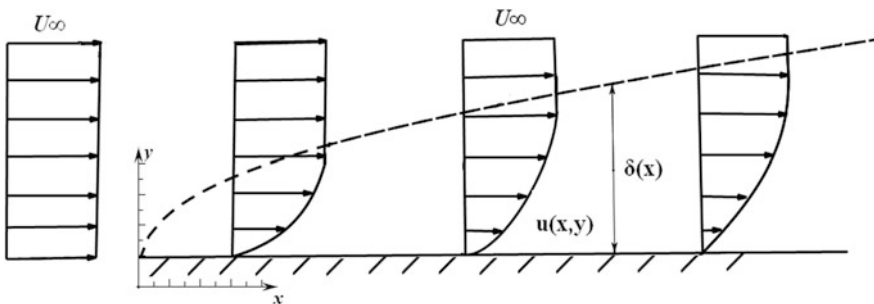


Fig. 1.4 Flat-plate boundary layer

parameters with more clearly physical meaning, such as boundary layer displacement thickness δ^* , which is a fictitious thickness to balance the mass flow reduction caused by the boundary layer.

$$\delta^* = \frac{1}{\rho_e u_e} \int_0^{\delta} (\rho_e u_e - \rho u) dy = \int_0^{\delta} \left(1 - \frac{\rho u}{\rho_e u_e}\right) dy \quad (1.17)$$

Similarly, the thickness corresponding to the momentum loss caused by the boundary layer is called momentum thickness, expressed as θ or δ^{**}

$$\theta = \frac{1}{\rho_e u_e^2} (u_e \int_0^{\delta} \rho u dy - \int_0^{\delta} \rho u^2 dy) = \int_0^{\delta} \frac{\rho u}{\rho_e u_e} \left(1 - \frac{u}{u_e}\right) dy \quad (1.18)$$

Energy thickness (δ_3 or δ^{***}) represents the kinetic energy loss caused by the boundary layer, and is given by

$$\delta_3 = \int_0^{\delta} \frac{\rho u}{\rho_e u_e} \left(1 - \frac{u^2}{u_e^2}\right) dy \quad (1.19)$$

Respectively from the perspectives of mass flow, momentum, and kinetic energy, these dimensionless parameters of boundary layer thickness reflect the size of flow loss caused by the boundary layer. Thus, the dimensionless thickness of the boundary layer at the cascade outlet is often used to represent the total loss of boundary layer flows on the surface of the cascade, as well as to establish quantitative relationships with profile loss obtained by using other definitions.

1.5.2 Boundary Layer Transition

Patterns of boundary layer flows include laminar flow, turbulent flow, and transition—the transient state from laminar flow to turbulent flow. In a laminar flow, fluid particles have orderly movement paths without obvious random motions as well as do not mingle mutually. On the contrary, disorderly and unsystematic motions exist in a turbulent flow. Because the mixing effect of a turbulent flow is relatively strong, the velocity profile of a turbulent boundary layer is plumper than laminar boundary layers. The Reynolds number $\left(\text{Re} = \frac{\rho u L}{\mu}\right)$ is an important parameter which is used to help determine flow patterns in boundary layers, as well as the ratio of inertial forces to viscous forces in the flowing process of a fluid, where ρ is the density of the fluid; u is the velocity of the fluid; L is the characteristic length; μ is

the dynamic viscosity of the fluid. With the increasing of Reynolds number, viscous forces decreases with respect to inertial forces. The transition process would begin as a result of enlarging of disturbances in the flow when Reynolds number exceeds a certain range. The transition process from laminar flow to turbulent flow is always achieved by creation and growth of turbulent spots. The turbulent spots, which is generated from the laminar boundary layer, gradually increase in size, merge with each other, and eventually grow into fully developed turbulent flow in the transport process to the downstream. Transition length is dependent on evolution properties of turbulent spots to a great extent, which mainly include spot creation rate, leading edge and trailing edge propagation velocities of turbulent spots, lateral growth rate, interaction and merging of turbulent spots [1, 2].

In 1951, Emmons [3] firstly found the “separate turbulent areas” and named them turbulent spots. Afterwards, Schubauer and Klebanoff [4] investigated man-made turbulent spots in 1955, and found that turbulent spots are nearly triangular at zero pressure gradient and grow at a steady rate. Their studies showed that, the lateral spreading half-angle of a turbulent spot is about 10° – 11° at low speed, and the half-angle of its leading-edge triangle is 15° . The leading-edge and trailing-edge velocities are approximately $0.88U_e$ and $0.5U_e$ (U_e is the local freestream velocity) respectively, averaging at $0.7U_e$ [5, 6]. There is a nearly rectangular non-turbulent region upstream of the turbulent spot, which is insensitive to disturbances as well as could remain in laminar for a longer time than surrounding fluid, thus it is called calmed region. The leading edge of the calmed region is the trailing edge of the turbulent spot, and the trailing edge propagation velocity is approximately $0.3U_e$. Shear stress in the turbulent spot is at high level with intense pulsation, while shear stress in the contiguous calmed region gradually decreases from the same level as in the turbulent spot to the level in the undisturbed laminar flow. Because the calmed region has plumper velocity profile than laminar flow and is insensitive to external disturbances, it can remain in laminar condition for a longer time than its surrounding fluid and resist transition and separation. In addition, the propagation velocity of the calmed region is relatively low, thus a certain position is controlled by the calmed region for a longer time than the turbulent region. These characteristics of the calmed region are of great significance in aerodynamic design of low-pressure turbines, and will be discussed in detail in the following chapters.

Intermittency factor Γ , which is used to describe the degree of transition of boundary layer, is defined as the probability of turbulent flow at the certain position. The boundary layer transition process from laminar to turbulent corresponds to the changing process from $\Gamma = 0$ to $\Gamma = 1$. Based on studies on creation and growth of multiple turbulent spots, Narasimha [7] worked out the following expression of intermittency factor

$$\Gamma(x) = 1 - \exp\left[-\frac{n\sigma}{U_\infty}(x - x_t)^2\right], \quad (x \geq x_t) \quad (1.20)$$

where, U_∞ is the freestream velocity; n is the creation rate of turbulent spots; σ is the dimensionless transport coefficient of Emmon turbulent spots. By bringing in the Reynolds number $Re_x = U_\infty x / \nu$, Mayle [8] gave the modified version

$$\Gamma(x) = 1 - \exp\left[-\hat{n}\sigma(Re_x - Re_{xt})^2\right], \quad (x \geq x_t) \quad (1.21)$$

where, $\hat{n} = nv^2/U_\infty^3$ is the dimensionless parameter of the creation rate of turbulent spots. As can be seen from the above equation, boundary layer transition mainly depends on the starting position of transition and creation rate of turbulent spots.

Intermittency factors of boundary layers can be obtained accurately through measurement in laboratory as well as reveal the flow of boundary layer precisely. However, it is difficult to realize in the practical engineering. The shape of velocity profile in the boundary layer is preferred to determine flow characteristics of boundary layer in engineering. However, the plumpness of velocity profile in the boundary layer cannot be applied for engineering and comparison between different conditions. So, researchers developed the shape factor H (or H_{12}) to quantify the shape of velocity profile in the boundary layer

$$H = \frac{\delta^*}{\theta} \quad (1.22)$$

Smaller H means plumper velocity profile. $H = 1$, which represents the plumpest velocity profile, means that there is no boundary layer. The shape factor H of typical laminar flat boundary layer is about 2.6, while that of typical turbulent flat boundary layer is within the range of 1.2–1.5.

As mentioned above, the Reynolds number is an important parameter used to determine flow patterns in boundary layers. The characteristic parameters of turbines are axial length of blades, relative outlet velocity as well as density. The self-modeling Reynolds number which is defined by parameters above is about 2×10^5 approximately. If the Reynolds number exceeds the value, the effect on aerodynamic performance of turbines can be neglected. If the Reynolds number is lower than this value, then the influence on boundary layer flows and turbine performance has to be considered. In addition, pressure gradient, surface roughness, background turbulence intensity, as well as external disturbance are influence factors of transition. Under an adverse pressure gradient, the critical Reynolds number would decrease rapidly and the transition process would be done in a shorter distance with advanced starting position. In addition, intensity of external disturbances can be directly changed by background turbulence intensity or surface roughness, so boundary layer transition can be controlled by these approaches as well. These methods for controlling boundary layer transition have been widely used in airfoil profile and turbine blade design with good success. The applications in turbine flow control are expounded in detail in the following chapters.

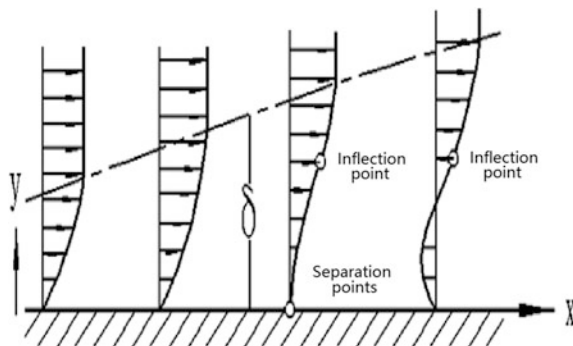
1.5.3 Boundary Layer Separation

Flow separation is one of the most important phenomena of boundary layer in gas turbines. The performance of gas turbines could be evaluated only if the possibility and position of separation, as well as behaviors following separation are forecasted accurately. Boundary layer separation may occur at positions with sharply or violently changing of wall curvature, such as trailing edges of turbine blades and step structures at endwalls between blade rows, where the supply of load has little demand. Although separation at these positions may have some influence on aerodynamic performance of turbines, the influence is generally non disruptive. Boundary layer separation may also occur at positions with slowly changing of wall curvature, such as blade surface and endwalls in blade row passage. Separation at these positions has great influence on loading and aerodynamic performance of turbines, and is mainly discussed in this book.

Viscosity and adverse pressure gradient are necessary conditions of flow separation. With an adverse pressure gradient, velocity of fluid in the boundary layer would decrease gradually with kinetic energy turning into pressure potential energy as well as an inflection point would occur on the velocity profile. In critical cases, kinetic energy of fluid in the boundary layer is not enough to meet the demand for pressure build-up, so the boundary layer flow would stagnate or even backwards, thus result in separation, namely boundary layer separation. As shown in Fig. 1.5, under an adverse pressure gradient, velocity of the fluid closer to the wall drops more violently. As a result, the velocity profile would become “thinner” in the process. As mentioned above, the shape of velocity profile in the boundary layer can be measured by the shape factor H . This provides an approach to determine boundary layer separation and predict its tendency. Typical laminar boundary layer separation would occur when the shape factor is approximately 4, and separation of turbulent boundary layers would occur when the shape factor H reaches 2–3.

In turbines, the great flow loss may exist result from the separation of boundary layer with an adverse pressure gradient near the trailing edge on the suction surface.

Fig. 1.5 Separation of flat plate boundary layer



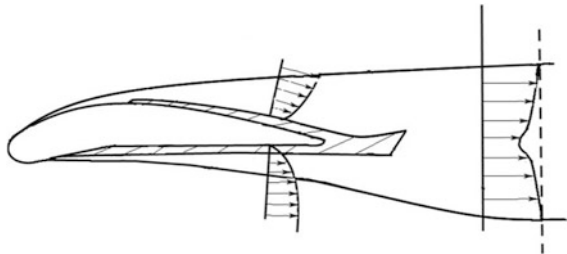
This is particularly true in turbines with highly loaded blades, because the adverse pressure gradient near the trailing edge on the suction surface is generally high and the adverse pressure gradient region is large. Suction surface boundary layers in turbines operating at low Reynolds numbers may remain in laminar condition across a wide range, and thus face a high risk of separation. Therefore, effective control of suction surface boundary layers to inhibit separation is a key technology in developing high-performance highly-loaded turbines at low Reynolds number, and discussed in the following chapters.

1.6 Wakes

As shown in Fig. 1.6, boundary layers of suction surface and pressure surface develop into wakes after leaving the trailing edges of blades. Wakes are mainly characterized by velocity loss, thus wakes can be regarded as jet flows opposite to the main flow, as well as so-called “negative jets” [9]. In turbines, wakes serving as negative jets would pump the fluid from the pressure surface to the suction surface thus impact pressure and velocity distribution on blade surface [10]. On the other hand, if suction-surface and pressure-surface boundary layers on blades are considered as two vortex layers, wakes can be regarded as a result of merging of the two vortex layers in opposite direction. In addition, trailing edges of turbine blades are thick, so there would be obvious features that flow around the bluff body in the wake region after the boundary layer leaves the trailing edge. Unsteady shedding vortices from the trailing edge can be observed as well. These are one of the main sources of unsteady wake flows and turbulent pulsation. Therefore, turbulence intensity is generally high in wakes. In conclusion, key parameters for describing single wakes include width of the wake, maximum velocity loss, and turbulence intensity in the wake.

In a turbine, periodic wakes of upstream flows have a great effect on on boundary layers, leakage flows, and secondary flows in downstream blade rows, and the influence can reach to two or more blade rows downstream. Unsteady effect of upstream wakes has been regarded by many researchers as one of the most

Fig. 1.6 Boundary layer and Wake



important unsteady mechanisms in axial turbines, particularly in low-pressure turbines [11, 12]. Effective control of suction-surface boundary layer transition and separation in low pressure turbines through reasonable selection of parameters of upstream periodic wakes (including single wake characteristics, and reduced frequency and flow coefficient of periodic wakes) is one of the main approaches to improve blade loading of low pressure turbines and lower their weight without impairing their aerodynamic performance, and is also a research focus.

In a multi-stage turbine, wakes may influence many blade rows in the downstream, moreover the maximum turbulence intensity in wakes may increase in a blade passage [13]. Thus, the effect of wakes of far upstream blades may be enhanced. Under the combined effect of multiple rows of blades, unsteady flows in a multi-stage low-pressure turbine would become more and more complicated with the number of turbine stages increases [14, 15].

1.7 Secondary Flows

In the field of turbomachinery, flows which are inconsistent with the main flow are generally called secondary flows. Leakage vortices (discussed in the next section) are one of the main secondary flows in a turbine rotor passage. Besides, there are horseshoe vortices, passage vortices, and corner vortices in a cascade passage, as well as these secondary flow structures are the main source of flow loss near endwalls of a turbine. As a matter of fact, flow loss near endwalls is a major part of aerodynamic loss in turbines with small aspect ratios [16].

When getting close to the leading edge of blades, the incoming endwall boundary layer would bring about a radial pressure gradient, under which the fluid in the boundary layer would move towards the endwall and then roll up after meeting the endwall, thus forming a vortex. The vortex keeps moving downstream around the leading edge and develops into a horseshoe-shaped vortex, called horseshoe vortex. Under the effect of transverse pressure gradient, the pressure-side branch of a horseshoe vortex passes through the passage, moves towards the suction surface of the adjacent blade, then merges with the suction-side leg of its horseshoe vortex. On the other hand, the fluid in the endwall boundary layer is at a low velocity and moves towards the suction side under the effect of transverse pressure gradient, thus forming a vortex in the same rotation direction as the pressure-side leg of a horseshoe vortex. The two vortices finally develop into a passage vortex. Passage vortices are the most important secondary flow near endwalls, which makes flows overturning at endwalls and underturning in the middle of blades. Except for passage vortices and horseshoe vortices, there are other complex vortices near endwalls, of which the strongest is the corner vortices near the suction side of the blade. Corner vortices have opposite rotation direction to passage vortices and are formed in the similar manner as horseshoe vortices. Corner vortices begin to generate when the streamlines reach to the position of the maximum curvature of the blade profile at the suction side. However, they come

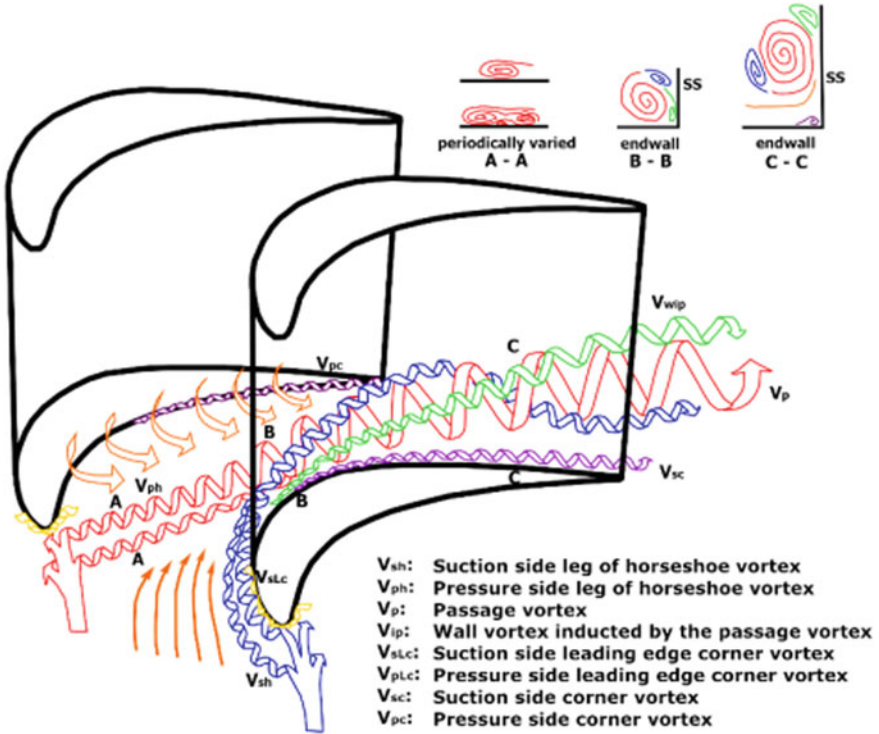


Fig. 1.7 Secondary flow structures near endwalls [20]

into being only if blade loading is large enough to result in intense interaction between passage vortices and flow near the blade surface. Figure 1.7 shows secondary flow structures near the endwall regions. Research has shown that factors influencing the intensity of the above mentioned secondary flows near endwalls include incidence angle, flow turning angle, solidity, aspect ratio, blade loading distribution, and inlet vortex intensity [17–19]. Influence of these factors on secondary flow structures will be discussed in detail in the following chapters.

The above analysis indicates that boundary layers and pressure gradient near the endwalls are the key factors influencing secondary flows and are the keypoints of controlling the secondary flows effectively. From this point, researchers have tried various design methods to control secondary flows near endwalls, including skewed and swept blade profiling, modification to leading-edge near endwalls of blades, and non-axisymmetric endwall profiling. These methods, through local adjustments to geometry around endwalls, are used to optimize the evolution of endwall boundary layers and pressure distribution of the endwalls as well as blade, thus achieve the purpose of restricting secondary flows.

1.8 Tip Leakage Flow

A radial clearance between rotating blade tips and the stationary casing is inevitable in a turbine. Driven by pressure difference across both sides of the clearance, a part of fluid in the main flow goes from the pressure surface to the suction surface through the tip clearance, thus resulting in tip leakage flows. Under the effect of viscosity, the tip leakage flow mixes with the main flow around the suction surface and rolls up, thus forming leakage vortices. Rotor blade tips of low pressure turbines are generally equipped with shrouds, which can effectively reduce the leakage flow and the intensity of leakage vortices. Although the amount of leakage flows from shrouds are relatively small, they can interact with the main stream significantly and may even increase flow loss in some cases as well [21]. Therefore, it is necessary to design a shroud with the aerodynamic-structural integrated method to take full advantage of aerodynamic effect of shroud, instead of only for the purpose of structural strength. High pressure turbines generally use unshrouded blades because of their high-temperature and high-rotation-speed operating conditions. As a result, the tip leakage flows, which serves as an significant secondary flow structure of high pressure turbine, is quite intense, as well as the resulting flow loss is 30%, or even higher, of total loss in the blade row [16]. Influences of tip clearance on aerodynamic performance of turbines are as follows: reducing work done by the fluid at blade tips; resulting in flow blockage in the passage; increasing mixing loss between leakage flows and the main flow; leading to nonuniform distribution of flow inlet angle of the downstream blade row.

Factors influencing tip leakage flows include pressure difference at blade tips between suction side and pressure side (i.e. load distribution), height and geometry of tip clearance, boundary layers on the casing, and relative motion between the casing and blades. With the increasing of clearance height, flow rate of leakage as well as the size and intensity increase, which result in larger loss of the tip leakage flow [22]. In the case of large tip clearance, thickness of the wall boundary layer in the clearance is relatively small, so the effect of viscosity on tip leakage flows can be neglected. When leakage flows pass through the tip clearance, separation bubbles may come into being at blade tips, resulting in a convergent-divergent flow passage near the pressure surface within the clearance. As shown in Fig. 1.8, pattern and size of the separation bubbles depend on the relative size of the clearance. Research has shown that, when blade thickness reaches to 4–6 times as large as the tip clearance height [16, 23], relatively small closed separation bubbles would come into being at the blade tip near the pressure surface, and leakage flows would have been mixed fully in the clearance with increased static pressure and loss; when blade thickness is small enough, separation bubbles would not attach to the blade tip surface and static pressure at the tip could not be restored. Typical structures of tip leakage flows in the above two cases are shown in Fig. 1.8.

Because the direction of motion of the casing relative to blades in a turbine is opposite to that of tip jet flows, the relative motion between the casing and blades would reduce leakage flow, weaken leakage vortices, and thus decrease tip leakage

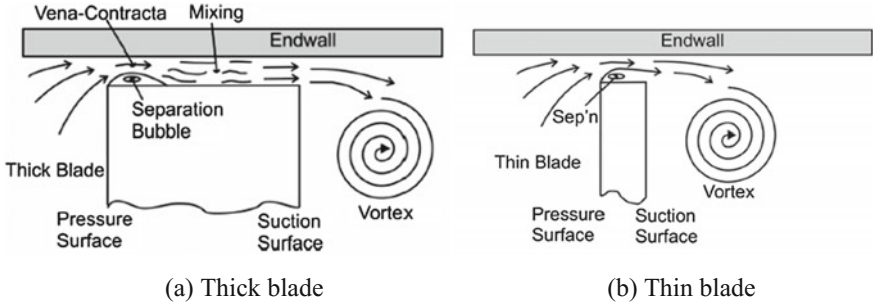
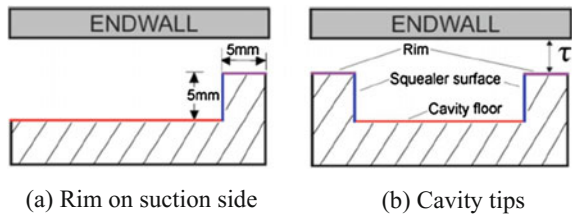


Fig. 1.8 Tip leakage flow in unshrouded turbines [16]

loss. However, the relative motion would enhance casing passage vortices as well as make both the leakage vortices and passage vortices closer to the suction surface of blades. In addition, the relative motion may bring about intense shear between the casing boundary layer and tip outlet jets, thus resulting in scraping vortices that are opposite in rotation direction.

With the further studies, researchers begin to explore 3-D blade tip shapes, such as use of oblique tip sections, addition of rims to blade tips, and addition of winglets to blade tips, as shown in Fig. 1.9. Reasonable use of these shapes can effectively inhibit the generation of leakage flows or leakage vortices and thus improve aerodynamic performance of turbines. However, unreasonable 3-D blade tip shapes may lower down the aerodynamic performance. Therefore, specific analysis and optimization should be carried out in practical application. For high pressure turbines, the heat transfer problem around blade tips is also a research focus. Thus, 3D optimization of blade tip geometry should be aimed not only at improving aerodynamic performance, but also at optimizing heat transfer performance. In addition, cooling air flows are often injected into the main flow from blade tip in high pressure turbines. Problems such as how to reasonably choose the position and style of cooling air injection, how to optimally mix between cooling flows and leakage flows and the main stream, as well as add complexity to optimization of blade tip geometry.

Fig. 1.9 3D modeling of turbine blade tips [24]



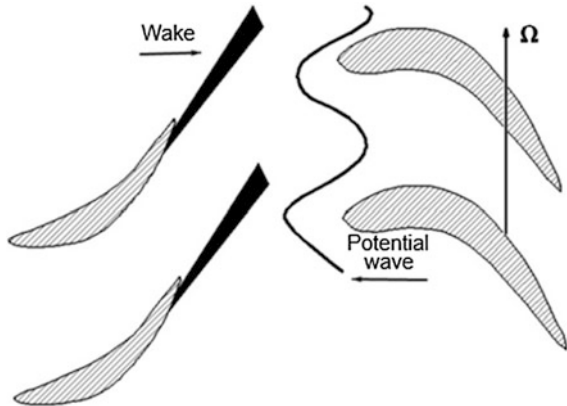
1.9 Potential Field

Broadly speaking, the potential field in a turbine refers to all the interactions in the form of pressure field, such as shock waves, expansion waves, as well as upstream and downstream periodical changing pressure fields, while its narrow meaning only refers to the later, namely the mutual interference caused by circumferentially non-uniform pressure fields of rotor and stator blade rows. This section is devoted to discussing the narrow meaning of potential field see (Fig. 1.10), and shock waves as well as expansion waves will be discussed in the next section.

The strength of the potential field partially depends on the circumferential non-uniformity of pressure fields, which is determined by the pressure difference between the suction surface and pressure surface of turbine blades, i.e. blade loading. In other words, the potential field is generally strong in turbines with highly loaded blades. On the other hand, the strength of the potential field also depends on the attenuation characteristics of pressure fields in the process of spatial transporting. Research has shown that influence of the potential field would decay exponentially with the characteristic distance, and it is worth noting that the characteristic distance depends on pitch, rather than chord length. In a turbine, influences of the potential field on upstream and downstream of adjacent blade rows are generally significant, and the influence on further blade rows can be neglected. The strength of the potential field in a turbine is determined by many factors. Except for the strength of the potential field, flow velocity is another key parameter to determine the influence range of the potential field. Research shows that, at subsonic flow velocity, attenuation of a potential field is in direct proportion to the following equation [25, 26]

$$\exp\left\{-2\pi\sqrt{1 - Ma^2}\frac{x}{t}\right\}, \quad Ma < 1.0 \tag{1.23}$$

Fig. 1.10 Potential field in a turbine



where, x is the axial distance from the blade row; t is the pitch; Ma is the local Mach number. As can be seen from the above equation, when the Mach number approaches to 1, attenuation of the potential field would slow down rapidly, indicating that the potential field at high Mach numbers is stronger than that at low Mach numbers.

The second is the influence range of the potential field. Because the potential field presents as inviscid pressure perturbation, its influence would propagate to the upstream and downstream at the velocities of $1 - Ma$ and $1 + Ma$ respectively. When flow velocity exceeds the sound velocity, the potential field will only propagate to downstream. Therefore, the potential field of a blade row in a subsonic turbine would influence both the upstream and downstream blade rows; however, the potential field of a blade row in a supersonic turbine could not get over the supersonic zone and propagate to upstream; when the axial velocity at the outlet of a blade row exceeds the speed of sound, the blade row would be unaffected by the potential field of downstream blade rows.

To determine the remarkable influence of potential field and upstream wakes, Korakianitis [27] carried out a numerical simulation to compare the two unsteady effects at different stator-to-rotor blade number ratios (R). The results show that when $R \approx 1$, the unsteady effect of stator wakes dominates; yet when $R > 3$, the potential field of stators dominates.; when R is set at an intermediate value, the wakes and potential fields basically have the same level of influence. The unsteady effects of rotors to stators have the same way like above.

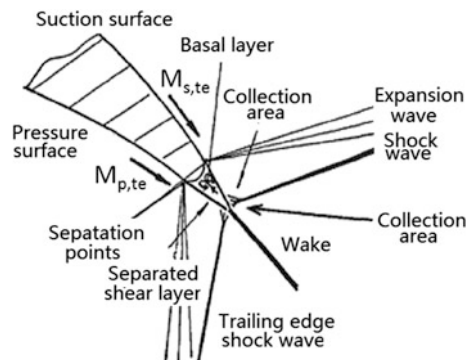
1.10 Shock Waves and Expansion Waves

Gas, which expands in turbine cascades, accelerates stronger with the lower backpressure. When the backpressure decreases to a certain value, there would be a local supersonic zone in the flow field, which is always near the position of the maximum curvature on the suction surface, as well as this zone generally terminates with a normal shock wave. As the backpressure decreases, this zone would increase gradually and the position of the normal shock wave would shift to downstream. If the backpressure further decreases, flows in pressure side and suction side would flow out from the trailing edge at a large enough Mach number, forming two free shear layers that come together in the downstream. There would be a low-pressure and low-velocity “triangle” area between the two free shear layers, which is called the trailing-edge base region. Meanwhile, the two free shear layers would generate a series of expansion waves at their respective separation points (i.e. the positions where they leave the blade), which expand and accelerate to reach the base pressure in the base region. Sometimes, there would be a trailing-edge separation shock following a series of expansion waves, which is a necessary shock wave to pressure the flows because the excessive expansion and deflection result from the geometry of the trailing edge, as well as thus the pressure of flows is lower than base pressure of trailing-edge. The reason for the generation of the shock wave is described as

follows: the flow at the separation point expands and deflects excessively due to the local geometry of the trailing edge, so that the flow. When the flows from the suction surface and pressure surface get together at the end point of the trailing-edge base region, the two flows would be forced to turn to the same flow direction. Shock waves are needed to achieve the deflection of the supersonic flows, so a pair of swallowtail shock waves, which take the convergent point as their vibration source and extend to the downstream, are generated. One of the branches extending within the flow passage is called inner trailing edge shock, as well as the other branch extending outside of the flow passage is called outer trailing edge shock (see Fig. 1.11). If the backpressure continues decreasing, the inner trailing edge shock would meet the normal shock wave following the local supersonic zone on the suction side of the adjacent blade and form a shock wave that runs through the entire passage. At this point, the turbine cascade would enter the blockage state, and the inlet Ma number would not change with the backpressure. As the backpressure decreases further, the inner trailing edge shock may act on the trailing edge of the adjacent blade, with the coincidence of the reflected wave and the outer trailing edge shock, as well as the the last expansion wave of accelerating region and tangential direction of the cascade. Meanwhile, the axial velocity component of the outlet flow reaches to the sound velocity and the expansion capability of the turbine cascade reaches to the maximum. Even though the backpressure keeps decreasing, the flow can only expand outside of the cascade passage, and both pressure distribution on blade surface and aerodynamic forces on turbine blades would stay unchanged.

Flow velocity near the outlet of the turbine cascade may be highly supersonic as required by aerothermodynamic processes. In this case, complex and strong wave structures would be generated at the trailing edge of the blade. Shock waves themselves may result in great flow loss, and meanwhile, would exert great influence on boundary layers, passage vortexes, leakage flows, and other secondary flows. In the environment of turbine stages, the outer trailing edge shock of the upstream cascade may exert unsteady effect on flows at downstream blades. In high-loaded transonic/supersonic turbines, steady and unsteady flow losses caused by the above shock waves are always the major component of the total turbine loss, so reasonable organizing of shock wave systems is of great significance in reducing shock waves and their resulting losses.

Fig. 1.11 Shock wave system at trailing edge [28]



1.11 Flow Mixing in Turbines

The discussing mixing process is that several flows(or fluid elements) in different conditions(such as different pressure, temperature and velocity) mix together thus forming a uniform flow(or fluid elements). Mixing processes due to different velocity are most common as occurring when shear flow exists. Due to the effect of viscosity, flow loss is inevitable in mixing processes. Except for boundary layers, mixing processes caused by intense shear also exist in wake region, separation areas, secondary flow tip leakage vortex. Because the equivalent viscosity of turbulent flows is generally two orders of magnitude higher than that of laminar flows, the mixing processes would lead to greater flow loss in the regions. In cooled turbines, there is also intense shear between the main flow and cooling air flows after they enter the cascade passage. Moreover, cooling air flows generally have different temperature and pressure from the main flow, so heat transfer, expansion, and other thermodynamic processes would occur after they enter the cascade passage, thus making the mixing process very complex. In addition, non-uniform incoming flows such as upstream secondary vortexes, hot streaks, etc. would also lead to mixing processes in the turbine. In a word, mixing processes exist extensively in the turbine passage.

Because mixing processes in a turbine are extremely complex and are generally unsteady, it is difficult to quantify the real-time local losses. However, under some assumptions, the total loss of most mixing processes can be calculated by volume controlled method with momentum conservation equations and energy conservation equations. In this way, we do not need to know the details of flow mixing processes. Thus, high-precision measurement or numerical simulation can be saved, and quantitative estimation of flow losses in mixing processes becomes possible.

A simplest mixing loss model is that . Two flows with different total temperature and total pressure mix together in a long duct with constant cross section, as shown in Fig. 1.12. It is assumed that friction effect of the walls is ignored with all the wall adiabatic, as well as the two flows mix completely at the outlet. Applying the energy equation for the control volume in the figure, the total temperature at the outlet can be written as

$$T_e^* = \frac{\dot{m}_1 T_1^* + \dot{m}_2 T_2^*}{(\dot{m}_1 + \dot{m}_2)} \quad (1.24)$$

Define an impulse function F as

$$F = PA + mv \quad (1.25)$$

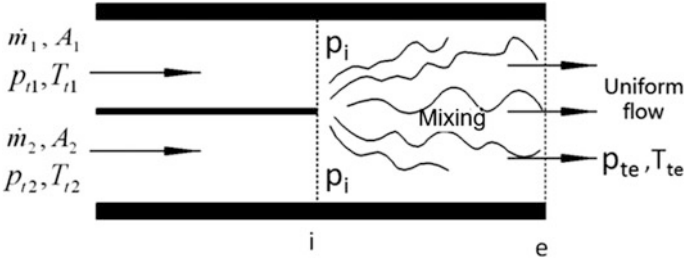


Fig. 1.12 Mixing process in a long duct with constant cross section

Apply the theorem of impulse for the control volume, then

$$F_e = F_1 + F_2 \tag{1.26}$$

Nondimensionalize the impulse function as

$$\tilde{F}_e = \frac{F_e}{(\dot{m}_1 + \dot{m}_2) \sqrt{C_p T_e^*}} \tag{1.27}$$

Thus, the dimensionless impulse function only depends on the Mach number and specific heat ratio

$$\tilde{F}_e = \left(\frac{\sqrt{k-1}}{kMa_e} \right) \frac{1 + kMa_e}{\sqrt{1 + \frac{k-1}{2} Ma_e^2}} \tag{1.28}$$

It is clear that, once the Mach number, total temperature, and passage area are given, all the physical quantities of interest after the mixing could be obtained. It is worth noting that there are generally two Mach numbers (a supersonic Mach number and a subsonic Mach number) that can satisfy Eq. (1.28). If both the two inlet flows are subsonic, then only the subsonic Mach number is the physical solution, however if one or both of the two inflow is supersonic, then both of the subsonic and supersonic Mach number may be the physical solution. The entropy generation coefficient defined by Denton [16] is given as

$$\zeta_s = \frac{\bar{T}^* \Delta s}{\frac{1}{2} \bar{v}^2} \tag{1.29}$$

where, \bar{T}^* and \bar{v} are the average total temperature and average velocity of the two inlet flows respectively. Figure 1.13 shows the entropy generation coefficient distribution at different conditions.

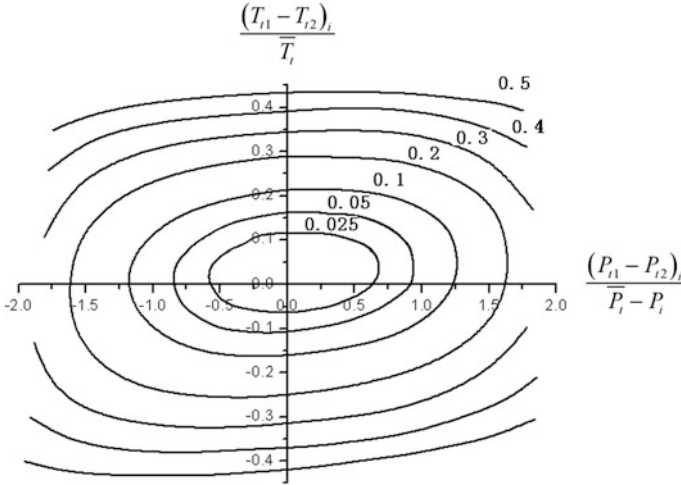


Fig. 1.13 Entropy production coefficient for mixing in a long duct with constant cross section [16]

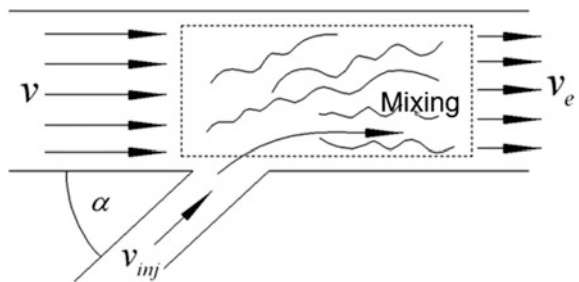
If the mass flow rate is far less than the other flow, the jet flow mixing model can be obtained through simplifying the above discussion. This model better fits the mixing of tip leakage flow and cooling air mixing which is widely used in turbines. This model was first proposed by Shapfro [29] (see Fig. 1.14). After the mixing of two flows which the mass flow rate of the jet flow m_{inj} is far less than that of the main flow m , the entropy production of the main flow can be written as

$$\Delta s = C_p \frac{m_{inj}}{m} \left\{ \left(1 + \frac{k+1}{2} Ma^2 \right) \frac{T_{inj}^* - T^*}{T_{inj}^*} + (k-1) Ma^2 \left(1 - \frac{v_{inj} \cos \alpha}{v} \right) \right\} \tag{1.30}$$

If the jet flow and the main flow have the same total temperature, the loss of the main flow in the mixing process can be expressed as

$$T \cdot \dot{S} = Tm\Delta s = m_{inj}(v^2 - vv_{inj} \cos \alpha) \tag{1.31}$$

Fig. 1.14 Jet flow mixing model



1.12 Blade Loading

Section 1.4 introduces the concept of turbine loading coefficient, which represents the load of a turbine stage. Moreover, the load on a single blade is also a concern of designers. If the load on a single blade is too low, then more blades are needed in a turbine stage, thus increasing the weight of the turbine. On the other hand, if the load on a single blade is too high, losses of blade boundary layer, secondary flow, tip leakage flow, and other flows in the turbine passage may increase. Therefore, for a given design problem, the magnitude of blade loading should be selected reasonably to balance the aerodynamic performance against turbine weight which, should be done on the basis of a reasonable standard for assessing blade loading.

The Zweifel coefficient [30] is a widely used parameter to represent the magnitude of blade loading, and defined as the ratio of actual circumferential force on the blade to an ideal circumferential force, which is obtained under the condition that the static pressure on the pressure surface, as well as suction surface is uniform and equal to the inlet total pressure and outlet static pressure respectively.

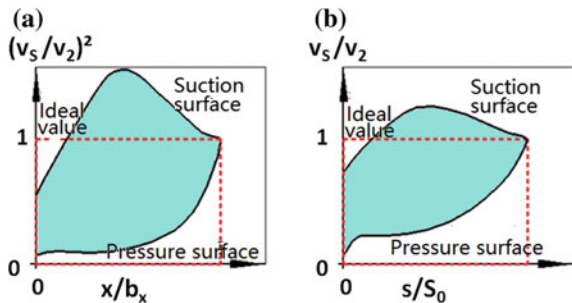
$$Z_w = \frac{F_\theta}{b_x(p_1^* - p_2)} = \frac{\oint p dx}{b_x(p_1^* - p_2)} = \oint \frac{p}{p_1^* - p_2} d\left(\frac{x}{b_x}\right) \tag{1.32}$$

where, the circulation integral should be performed in the direction from leading edge to trailing edge of the pressure surface. The above equation shows that the Zweifel coefficient represents the area enclosed by the dimensionless blade pressure distribution curve as shown in Fig. 1.15a. For incompressible conditions, the above equation can be written as

$$Z_w = \oint \left(\frac{v_s}{v_2}\right)^2 d\left(\frac{x}{b_x}\right) \tag{1.33}$$

It should be noted that the direction of the circulation integral in the above equation is opposite to that in Eq. (1.32), namely from trailing edge to leading edge of the pressure surface. By control volume method, the circumferential force

Fig. 1.15 Dimensionless blade loading distribution



on the blade can be further expressed as a function of inlet and outlet flow parameters

$$Z_w = \frac{\rho v_x t \Delta v_\theta}{b_x \frac{1}{2} \rho v_2^2} = \frac{2t}{b_x} \sin^2 \alpha_2 (\cot \alpha_1 + \cot \alpha_2) \quad (1.34)$$

Namely, the Zweifel coefficient of a low-speed cascade depends on solidity, inlet and outlet flow angle. Equation (1.34) also shows that, at a fixed $\frac{t}{b_x}$, multiple combinations of inlet and outlet flow angles determine a same Z_w value, but when the inlet angle α_1 is given, there are still two outlet flow angles α_2 that may determine a same Z_w value. In other words, at the same incoming flow condition and solidity, two cascades with different blade outlet flow angles may have a same Zweifel coefficient, nevertheless. The two cascades obviously have different aerodynamic loads. The reason for this conflict is that the Zweifel coefficient represents magnitude of relative load and the bases to evaluate the load (outlet pressure or outlet velocity) may change under different operating conditions. It suggests that the Zweifel coefficient should be carefully used for comparing blade loading. High attention should be paid to this point in practical application, or else mistakes may occur.

The circulation coefficient C_o [31] represents the magnitude of blade loading in terms of circulation. It is defined in a similar way of the Zweifel coefficient, and defined as the ratio of actual circulation to an ideal circulation, which is obtained under the condition that the velocity on the suction side is uniform and equal to the outlet flow velocity, the velocity on the pressure side is zero.

$$C_o = \frac{\oint v_s d(s)}{v_2 S_0} = \oint \frac{v_s}{v_2} d\left(\frac{s}{S_0}\right) \quad (1.35)$$

According to the above equation, the coefficient represents the area enclosed by the dimensionless velocity distribution curve as shown in Fig. 1.15b. For incompressible flows, the above equation can be written as

$$C_o = \frac{t}{S_0} \sin \alpha_2 (\cot \alpha_1 + \cot \alpha_2) \quad (1.36)$$

It can be seen that the circulation coefficient C_o and the Zweifel coefficient have similar expressions. The ratio between the two is given by

$$\frac{Z_w}{C_o} = \frac{2S_0 \sin \alpha_2}{b_x} \quad (1.37)$$

Namely, the ratio between the two parameters depends on curvature of the blade. For flat plates, the ratio is 2. For curved blades, the ratio is usually less than 2 because the inlet flow angle is generally greater than the outlet flow angle, but

always greater than 1. The circulation coefficient C_o of a blade is always smaller than the Zweifel coefficient.

As can be seen from the definition, the circulation coefficient C_o represents relative load size as well, as well as depends on blade solidity, and flow angles. When the inlet flow angle α_1 is given, there are two outlet flow angles α_2 that may determine a same C_o value. These characteristics are same as the Zweifel coefficient. Therefore, the circulation coefficient may face the same problem that the Zweifel coefficient faces. However, the circulation coefficient C_o has its own advantages. Coull and Hodson [31] pointed out that, when the maximum speed position and leading edge load are given, the circulation coefficient C_o may determine the diffusion factor of the trailing edge of the blade, thus providing some reference for aerodynamic design of the blade, but the Zweifel coefficient does not have this property.

Except for the above two coefficients, there are some other methods for evaluating the magnitude of blade loading, which are not discussed here. These parameters are defined in different manners and from different perspectives, so they have different physical meanings and are applicable for different conditions. Researchers should gain a deep insight into these parameters and choose suitable parameters for specific applications.

1.13 Loss and Efficiency

Flow loss and aerodynamic efficiency are core parameters to evaluate the aerodynamic performance of turbines. This section is devoted to discussing this topic in three aspects: cascade rows, uncooled turbines and cooled turbines.

1.13.1 Loss and Efficiency of Turbine Cascades

Cascade rows are the basic units of a turbine stage, in which the loss directly determines the aerodynamic performance of the turbine. The total pressure recovery coefficient σ and the total pressure loss coefficient Y reflect flow loss in terms of the drop of total pressure of the flow passing through cascades. The two parameters have definite physical meanings and simple formulas, and have been widely used. For a turbine cascade, they are defined as

$$\sigma = \frac{p_1^*}{p_0^*} \quad (1.38)$$

$$Y = \frac{p_0^* - p_1^*}{p_1^* - p_1} \quad (1.39)$$

where, the subscripts 0 and 1 represent the inlet outlet section of the cascade respectively. Except for total pressure loss, kinetic energy loss can be also used to reflect aerodynamic performance of the cascade. The energy loss coefficient ζ_{cascade} is defined as

$$\zeta_{\text{cascade}} = \frac{h_1 - h_{1,is}}{h_0^* - h_{1,is}} \quad (1.40)$$

where, the numerator represents the difference between the ideal kinetic energy and actual kinetic energy at the outlet of a cascade, and the denominator represents the ideal kinetic energy at the outlet. Thus, the energy loss coefficient ζ_{cascade} represents the ratio of kinetic energy loss to the ideal kinetic energy.

Both the two cascade loss assessing methods are defined and discussed in the inertial system. As a matter of fact, in most cases, when applying these coefficients for rotating blade rows, the above loss coefficient formulas are still available only if replace the total parameters in with relative total parameters. It is worth noting that this may result in errors. It can be proved that the term $(p_{0w}^* - p_{1w}^*)$ contains not only the total pressure loss across the cascade but also the work done by the centrifugal force when circumferential velocities at the inlet and outlet are different. Therefore, the total pressure recovery coefficient σ and total pressure loss coefficient Y cannot be used directly in this case, and the numerator should be revised as $(p_{1w,is}^* - p_{1w}^*)$, where $p_{1w,is}^*$ is the ideal relative total pressure at the outlet, which can truly reflect the relative total pressure loss.

In terms of energy utilization ratio, the cascade efficiency η_{cascade} is defined as the ratio of actual kinetic energy to ideal kinetic energy at the outlet of a turbine cascade

$$\eta_{\text{cascade}} = \frac{C_1^2}{C_{1,is}^2} = \frac{h_0^* - h_1}{h_0^* - h_{1,is}} \quad (1.41)$$

It can be seen that the cascade efficiency η_{cascade} and the energy loss coefficient ζ have the following relation

$$\eta_{\text{cascade}} = 1 - \zeta_{\text{cascade}} \quad (1.42)$$

In addition, the velocity loss coefficient φ_{cascade} is defined as

$$\varphi_{\text{cascade}} = \frac{C_1}{C_{1,is}} = \sqrt{\eta_{\text{cascade}}} \quad (1.43)$$

Similarly, the total inlet parameters should be replaced with ideal relative total parameters at the outlet when applying the above two parameters in rotor cascades.

1.13.2 Efficiency of Uncooled Turbine

Depending on different requirements and objectives, there are many ways to evaluate the aerodynamic efficiency of a turbine stage, in which the commonly used aerodynamic efficiencies include isentropic efficiency η , effective efficiency η_u , adiabatic efficiency η_{ad} , and polytropic efficiency η_n .

The isentropic efficiency η , also called the isentropic total-to-total efficiency, is defined as the ratio of the work done by the gas flowing through the turbine L_u to the isentropic stagnation enthalpy drop of the gas

$$\eta = \frac{L_u}{h_0^* - h_{2,is}^*} \quad (1.44)$$

The work can be expressed by actual enthalpy drop of the gas, so the isentropic efficiency η can be written as

$$\eta = \frac{h_0^* - h_2^*}{h_0^* - h_{2,is}^*} \quad (1.45)$$

In this definition, it is assumed that the kinetic energy corresponding to the residual velocity at the outlet of a turbine stage can be further used in the downstream turbine stages or components, as well as the loss of residual velocity is not considered. Thus, the isentropic stagnation efficiency η is suitable for turbines of turbojet aero-engine, and front stages of multi-stage turbines.

If the specific heat capacity can be regarded as a constant (not changing with temperature), then turbine efficiency is a function of inlet-to-outlet total temperature ratio, expansion ratio, and specific heat ratio, which is given by

$$\eta = \frac{1 - \frac{T_2^*}{T_0^*}}{1 - \left(\frac{p_2^*}{p_0^*}\right)^{\frac{k-1}{k}}} \quad (1.46)$$

The above equation is simple and clear, but may lead to errors when being used in modern gas turbines directly. This is mainly because the temperature difference between the inlet and outlet of gas turbines is large and thus the specific heat capacity cannot be regarded as a constant. To solve this problem, the following methods can be used in actual calculation. The first method is that the temperature range of the turbine is roughly divided into several sections and the specific heat capacity in each section is regarded as a constant to simplify calculation. The second is that the average value of the starting and ending specific heat of the gas passing through a section is regarded as the specific heat in the process. This method is more accurate than the first one. However, the starting and ending temperatures are unknown in most cases and need to be calculated through iteration. The third is a method of variable specific heat, in which the constant-pressure

specific heat and enthalpy are regarded as functions of gas composition and temperature. This method has high precision and can truly reflect the physical essence of the flow process.

In turbines of turbo-prop and turbo-shaft aero-engines, gas turbines, and steam turbines, kinetic energy of residual velocity of exhaust cannot be reused and thus should be regarded as energy loss. In this case, the effective efficiency η_u is suitable for these turbines. The effective efficiency η_u is defined as the ratio of the work L_u to the energy released by the gas passing through the turbine, namely the isentropic enthalpy drop of the fluid expanding from the inlet total pressure p_0^* to the outlet static pressure p_2 .

$$\eta_u = \frac{h_0^* - h_2^*}{h_0^* - h_{2,is}^*} \quad (1.47)$$

It can be seen that, because kinetic energy of residual velocity is regarded as loss in calculating the effective efficiency η_u , the effective efficiency η_u is always less than the isentropic efficiency η for a same turbine stage.

Compared to the above two kinds of efficiency, the adiabatic efficiency η_{ad} of a turbine stage focuses only on changes of static parameters in a turbine stage and involve no kinetic energy of incoming flow and kinetic energy. It is defined as the ratio of actual enthalpy drop to isentropic enthalpy drop, and is given by

$$\eta_{ad} = \frac{h_0 - h_2}{h_0 - h_{2,is}} \quad (1.48)$$

The adiabatic efficiency η_{ad} defined as above is also called the static-to-static efficiency. It can be proved that the adiabatic efficiency η_{ad} of a turbine is equal to its isentropic efficiency η if the inlet velocity is equal to the outlet velocity. The η_{ad} is used to replace η , can be used to replace η in multi-stage turbines because the above condition could be satisfied in multi-stage turbines..

All the above three definitions of efficiency reflect the effective work of a turbine stage based on changes of thermodynamic parameters in an isentropic process. The polytropic efficiency η_n is based on changes of thermodynamic parameters in a polytropic process. Assume the polytropic exponent of a polytropic process, whose starting state and ending state are expressed by the total parameters of inlet and outlet flows respectively, is n , then the polytropic efficiency η_n is defined as

$$\eta_n = \frac{L_u}{\int_0^2 \frac{1}{\rho} dp^*} = \frac{h_0^* - h_2^*}{\int_0^2 \frac{1}{\rho} dp^*} = \frac{\frac{k}{k-1}}{\frac{n}{n-1}} \quad (1.49)$$

Single-stage turbines and multi-stage turbines are not distinguished in the above definitions of turbine efficiency. For multi-stage turbines, the numerator should be taken as the sum of effective work in all the turbine stages, as well as parameters in the denominator should be taken as the corresponding inlet and outlet values. If

only a stage of a multi-stage turbine is considered, the isentropic stagnation efficiency η and the adiabatic efficiency η_{ad} is suitable instead of the effective efficiency η_{gu} , which regards the kinetic energy of residual velocity as loss. Since there is “reheat effect” (namely, the energy loss in the front stage can be reused in the following stages) in multi-stage turbines, the isentropic efficiency η and the adiabatic efficiency η_{ad} of a multi-stage turbine are generally higher than the corresponding efficiency of each stage. The “reheat effect”, which related to expansion ratio of the turbine and efficiency of each stage, means that more obvious “reheat effect” is caused by higher expansion ratio or the lower efficiency of the front stages. It also suggests that it is unreasonable to use the isentropic stagnation efficiency η and the adiabatic efficiency η_{ad} to compare multi-stage turbines with different expansion ratios. As indicated by the definition formula of the polytropic efficiency η_n , it is unrelated to expansion ratio, which means that all the expansion processes along a same polytropic line will have the same efficiency. Therefore, the polytropic efficiency η_n can be used to compare performance of turbines with different expansion ratios.

1.13.3 Efficiency of Cooled Turbine

Researchers have been trying to define the efficiency of cooled turbine for a long time. However, conclusion has not been reached and further discussion is still needed. The primary cause for this difficulty is described as follows. In principle, turbine efficiency is still defined as the ratio of actual output work to ideal work, but there are many unsolved problems due to cooling air flows such as how to calculate actual output work using inlet and outlet aerodynamic parameters, as well as how to define an ideal process and then calculate ideal output work.

The results have shown that different methods for calculating the ideal output work P_{id} have great influence on efficiency value, in which The core problem is how to treat with the mixing process between cooling flows and the main flow. For actual output work P_{ac} , two terms need to be distinguished. The first one is the actual work delivered by the turbine, which is equal to the energy extracted from the gas passing through the turbine. The second one is the shaft work output by the turbine, which is obtained by subtracting windage in turbine disc, bearing loss, etc. from the actual work delivered by the turbine. If the shaft work output by the turbine can be obtained through experimental measurement, it would be reasonable to use the measured value as P_{ac} . If not, or cannot be obtained through numerical simulations, it is difficult to accurately calculate turbine disc windage and bearing loss, and thus the actual work delivered by the turbine can be approximatively regarded as the actual output work P_{ac} . In the case, the key of reasonable calculation of the actual output work P_{ac} is how to deal with the work done by cooling air flows.

The simplest and most classic definition of air-cooled turbines was proposed by Hartsel [32]. He considered that all the cooling flows can do work, and ignored the

mixing loss between cooling flow and the main flow. The actual output work of a turbine is defined as the total enthalpy drop of the main flow and cooling flows between the inlet (including cooling air inlets) and outlet of the turbine stage

$$P_{ac} = m_g(h_0^* - h_2^*) + \sum_{i=1}^n m_{ci}(h_{i,0}^* - h_2^*) \quad (1.50)$$

Correspondingly, the ideal output work of the turbine is given by

$$P_{id} = m_g(h_0^* - h_{2,is}^*) + \sum_{i=1}^n m_{ci}(h_{i,0}^* - h_{i,2,is}^*) \quad (1.51)$$

Hence, the turbine efficiency is written as

$$\eta = \frac{P_{ac}}{P_{id}} = \frac{m_g(h_0^* - h_2^*) + \sum_{i=1}^n m_{ci}(h_{i,0}^* - h_2^*)}{m_g(h_0^* - h_{2,is}^*) + \sum_{i=1}^n m_{ci}(h_{i,0}^* - h_{i,2,is}^*)} \quad (1.52)$$

The efficiency definition has the advantages of clear physical meaning and easy to calculate. However, because it does not consider the actual mixing and expanding process between the main flow and cooling air flows, the efficiency value is generally a bit higher than the real value. Based on this definition, researchers have made some improvements to the method for calculating the actual output work. Kurzke [33, 34] considered that cooling flows in rotor blades do not apply work and thus should be ignored in efficiency calculation, while cooling flows in guide vanes would expand and do work after mixing with the main flow under the pressure of the main flow and entering into the turbine. Hence, the turbine efficiency is defined as the ratio of the actual expansion work of the flow in turbine rotors to ideal expansion work

$$\eta_{FR} = \frac{m_1(h_1^* - h_{2'}^*)}{m_1(h_1^* - h_{2',is}^*)} = \frac{h_1^* - h_{2'}^*}{h_1^* - h_{2',is}^*} \quad (1.53)$$

where, $2'$ represents the flows conditions of which the flows in rotors expand to the pressure as turbine outlet, as well as mix with the cooling flows in rotors. Moreover $h_{2'}^*$ can be obtained using the following equation

$$h_{2'}^* = \frac{(m_1 + \sum_{i=1}^n m_{ci,rotor})h_2^* - \sum_{i=1}^n m_{ci,rotor}h_{0i,rotor}^*}{m_1} \quad (1.54)$$

For multi-stage turbines, the above definition can be directly used to calculate the actual output work of each turbine stage, and based on that, efficiency of each

stage and the entire turbine can be obtained. In addition, according to the above definition, a multi-stage turbine can be regarded as an equivalent single-stage turbine to calculate its total efficiency, and this treatment is suitable for the situation in which only inlet and outlet parameters and cooling air parameters are known. In this case, corresponding the potential ability of work of cooling air flows in each blade row should be given. Thus, it can be assumed that cooling air flows in each blade row are injected at the outlet, and that the percentage of mass flow rate of which applies work is equal to the ratio of the number of rotor blade rows, that it passes through to the total number of rotor blade rows. This method is relatively convenient for calculating the efficiency of multi-stage turbines, but may lead to errors due to the inexact evaluation of potential ability of applying work of cooling air flows. Because this efficiency definition does not consider the influence of cooling air flows in the rotor passage, the value predicted by using this definition in practical applications may be higher than the real value as well as even higher than the value obtained by using Hartsel's method.

To solve this problem, researchers began to consider the influence of the mixing in the calculation of the ideal output work P_{id} . The typical definitions include the "Mainstream-Pressure" method (MP method for short), the "Fully Reversible" method (FR method for short), and the "Weighted-Pressure" method (WP method for short), which were developed by Horlock et al. [35, 36]. These methods assume that cooling air flows and the main flow mix together in different processes and the mixed flow enters into the turbine and does work, thus adding the influence of the mixing to the formula. These methods can be described by the following uniform expression

$$\eta_m = \frac{P_{ac}}{(m_g + \sum_{i=1}^n m_{ci}) (h_{0,m}^* - h_{2,m,is}^*)} \quad (1.55)$$

where, $h_{0,m}^*$ is the total enthalpy after the mixing between the main flow and cooling air flows as well as $h_{2,m,is}^*$ is the ideal total enthalpy when the mixed flow reaches to turbine outlet conditions through expansion. The MP method assumes that cooling air flows mix with the main flow under the pressure condition of the main flow. However, this method cannot reflect the influence of cooling air conditions on turbine efficiency, and the efficiency value obtained by using this method is a little higher than the real value. The FR method assumes the main flow first mixes with all the cooling air flows in an isentropic process, after which the total temperature $T_{0,m}^*$ after the mixing can be obtained, and then get the total pressure $p_{0,m}^*$ after the mixing by a reversible isothermal process. The maximum work delivered by a turbine is given under certain main flow and cooling air conditions by this definition. However, the efficiency value obtained by using the FR method is a little higher than the real value because that the real mixing process is not isentropic. Based on that, the WP method assumes that the main flow and cooling air flows first conduct heat under their own pressure conditions, after which the total temperature

T_{0m} can be obtained, and thus get the total pressure $p_{0,m}^*$ after the mixing by a reversible isothermal process. Comparison of application between these methods shows that the WP method could generally present satisfactory evaluation of turbine efficiency.

References

1. Krishnan, L., & Sandham, N. D. (2006). On the merging of turbulent spots in a supersonic boundary-layer flow. *International Journal of Heat and Fluid Flow*, 27(4), 542–550.
2. Krishnan, L., & Sandham, N. D. (2006). Effect of mach number on the structure of turbulent spots. *Journal of Fluid Mechanics*, 566, 225–234.
3. Emmons, H. W. (1951). The laminar-turbulent transition in a boundary layers, Part 1. *Journal of the Aeronautical Sciences*, 18(7), 490–498.
4. Schubauer, G. B., & Klebanoff, P. S. (1955). Contributions on the mechanics of boundary layer transition. *NACA TN*, 3489.
5. Cousteix, J., & Houdeville, R. A. (1977). Transition d'une couche limite soumise à une oscillation de l'écoulement extérieur. In *Conference Proceedings*.
6. Obremskij, H. J., & Fejer, A. A. (1967). Transition in oscillating boundary layer flows. *Journal of Fluid Mechanics*, 29(01), 93–111.
7. Narasimha, R. (1957). On the distribution of intermittency in the transition region of a boundary layer. *Journal of the Aeronautical Sciences*, 24(9), 711–712.
8. Mayle, R. E. (1991). The role of laminar-turbulent transition in gas turbine engines. *Journal of Turbomachinery*, 113(4), 509–536.
9. Meyer, R. X. (1958). The effect of wakes on the transient pressure and velocity distributions in turbomachines. *Journal of Basic Engineering*, 80(7), 1544–1552.
10. Wu, X., & Durbin, P. A. (2001). Evidence of longitudinal vortices evolved from distorted wakes in a turbine passage. *Journal of Fluid Mechanics*, 446, 199–228.
11. Hodson, H. P., & Howell, R. J. (2005). The role of transition in high-lift low-pressure turbines for aero engines. *Progress in Aerospace Sciences*, 41(6), 419–454.
12. Hodson, H. P., & Howell, R. J. (2005). Bladerow interactions, transition, and high-lift aerofoils in low-pressure turbines. *Annual Review of Fluid Mechanics*, 37, 71–98.
13. Stieger, R. D., & Hodson, H. P. (2005). The unsteady development of a turbulent wake through a downstream low-pressure turbine blade passage. *Journal of Turbomachinery*, 127(2), 388–394.
14. Binder, A., Schroeder, T., & Hourmouziadis, J. (1989). Turbulence measurements in a multistage low-pressure turbine. *Journal of Turbomachinery*, 111(2), 153–161.
15. Schroder, T. (1991). Investigations of blade row interaction and boundary layer transition phenomena in a multistage aeroengine low pressure turbine by measurements with hot-film probes and surface-mounted hot-film gauges. In *Boundarylayers in Turbomachines*, VKI Lecture Series No. 9. Von Karman Institute.
16. Denton, J. D. (1993). Loss mechanisms in turbomachines. *Journal of Turbomachinery*, 115(4), 621–656.
17. Bindon, J. P., & Lecturer, S. (1980). Exit plane and suction surface flows in an annular cascade with a skewed inlet boundary layer. *International Journal of Heat and Fluid Flow*, 2(2), 57–66.
18. Boletis, E., Sieverding, C. H., & Van Hove, W. (1983). *Effects of a skewed inlet end wall boundary layer on the 3-d flow field in an annular turbine cascade*. Belgium: Von Karman Inst For Fluid Dynamics Rhode-Saint-Genese.
19. Walsh, J. A., & Gregory-smith, D. G. (1987). *The effect of inlet skew on the secondary flows and losses in a turbine cascade*. IMechE Paper C275.

20. Wang, H. P., Olson, S. J., Goldstein, R. J., et al. (1997). Flow visualization in a linear turbine cascade of high performance turbine blades. *Journal of Turbomachinery*, 119(1), 1–8.
21. Rosic, B., & Denton, J. D. (2008). Control of shroud leakage loss by reducing circumferential mixing. *Journal of Turbomachinery*, 130, 021010.
22. Tallman, J., & Lakshminarayana, B. (2001). Numerical simulation of tip leakage flows in axial flow turbine, with emphasis on flow physics, Part I: effect of tip clearance height. *Journal of Turbomachinery*, 123(2), 314–323.
23. Heyes, F. J. G., & Hodson, H. P. (1993). The measurement and prediction of the tip clearance flow in linear turbine cascades. *Journal of Turbomachinery*, 115(3), 376–382.
24. Zhou, C., & Hodson, H. (2011). The tip leakage flow of an unshrouded high pressure turbine blade with tip cooling. *Journal of Turbomachinery*, 133, 041028–041039.
25. Opoka, M. M., Thomas, R. L., & Hodson, H. P. (2006). *Boundary layer transition on the high lift T106A LP turbine blade with an oscillating downstream pressure field*. ASME Paper GT2006-91038, 2006.
26. Opoka, M. M., & Hodson, H. P. (2008). Transition on the T106 LP turbine blade in the presence of moving upstream wakes and downstream potential fields. *Journal of Turbomachinery*, 130, 041017.
27. Korakianitis, T. (1993). On the propagation of viscous wakes and potential flow in axial-turbine cascade. *Journal of Turbomachinery*, 115(1), 118–127.
28. Denton, J. D., & Xu, L. (1990). The trailing edge loss of transonic turbine blades. *Journal of Turbomachinery*, 112(2), 277–285.
29. Shapiro, A. H. *The dynamics and thermodynamics of compressible fluid flow*. New York: Ronald Press, pp. 1953–1954.
30. Zweifel, O. (1945). Die frage der optimalen schaufelteilung bei beschauelungen von turbomaschinen, insbesondere bei grober umlenkung in den schaufelreihen. *Brown Boveri Mitteilungen*, 32(2), 436–444.
31. Coull, J. D., & Hodson, H. P. (2012). Blade loading and its application in the mean-line design of low pressure turbines. *Journal of Turbomachinery*, 135, 021032.
32. Hartsel, J. E. (1972). *Prediction of effects of mass-transfer cooling on the blade-row efficiency of turbine airfoils*. AIAA Paper 72–11, 1972.
33. Kurzke, J. (2002). *Performance modeling methodology: Efficiency definitions for cooled single and multistage turbines*. ASME GT-2002-30497, 2002.
34. Kurzke, J. (2007). *GasTurb details 5: An utility for gasturb 11[EB/OL]*. <http://www.gasturb.de/gasturb-details.html>.
35. Young, J. B., & Horlock, J. H. (2006). Defining the efficiency of a cooled turbine. *Journal of Turbomachinery*, 128(4), 658–667.
36. Horlock, J. H., & Torbidoni, L. (2008). Calculations of cooled turbine efficiency. *ASME Journal of Engineering for Gas Turbines and Power*, 130(1), 1–5.

Chapter 2

Flow Mechanism in High Pressure Turbines

2.1 Introduction to High Pressure Turbines

2.1.1 *Structure and Characteristics of High Pressure Turbines*

The study of High pressure turbine (HP turbine, HPT) is dependent on the development of engines. The characteristic parameters of some high pressure turbines, as shown in Table 2.1, were collected from engine manuals and other materials for reference. As can be seen from the table, with the continuous development of the engines, the thrust-to-weight ratio, turbine inlet temperature, and total pressure ratio are reaching higher and higher levels, which means high-pressure turbines will be operating in more severe environment and it becomes more and more challenging to study and design high-performance high-pressure turbines.

Structural diagrams of meridional flow passage of high-pressure turbines in typical aircraft engines are shown in Fig. 2.1, for typical military turbine engines, and Fig. 2.2, for civil turbine engines. High-pressure turbines for military, which generally use one-stage design, pay more attention to high thrust-to-weight ratio instead of turbine efficiency. In this way, higher stage pressure ratio could be obtained, while shock loss and secondary flow loss would be greater. Two-stage high-pressure turbines are typically used for large civil engines, sometimes one-stage turbines are also used. These engines require high efficiency of high-pressure turbine stage. Besides, cooling flow rate of these turbines is greater than that of military turbines under the same turbine inlet condition.

Because the pressure and density of the flow in high pressure turbines are much higher, the hub ratio of the meridional flow passage is generally higher than that of low-pressure turbines, reaching up to around 0.8–0.88. Besides, high-pressure turbines have higher rotating speed, and thus their tangential velocity is relatively high in spite of their small outer diameter. Though the loading coefficient of the

Table 2.1 Parameters of civil and military engines

Engine type	Model	Thrust to weight ratio	Fuel consumption (kg/daN h)	Turbine inlet temp. (K)	Overall pressure ratio	Pressure ratio of high pressure compressor	Number of high pressure turbine stages and expansion ratio	Manufacturer
Civil engines	CF6-50A	6.18	0.6505	1583	32.5	13	2/4.4236	GE
	CF6-80C2	6.8	0.61	1588	30.4–32.7	13	2/	GE
	GE90	6.3	0.56	1703	39.3	23	2/	GE
	JT9D	5.63	0.6903	1585	24.21	10.3	2/3.6225	PW
	PW2000	5.24	0.574	1698	27.6		2	PW
	PW4084	6.0	0.566	1777	34.2		2	PW
	V2500-A5	5.84	0.585	1700	31.4		2	IAE
	CFM56-5C2	5.5	0.577	1635	37.4	11.2	1/3.78	CFM
	Trent884	5.3	0.567	1686	39.88		1 (three-axis)	RR
	F404-402	7.83	0.76	1686	26		1	GE
Military engines	F110-129	9.5	0.7	1728	32		1	GE
	F100-229	7.9	0.66	1672	32		1	PW
	F119	11.6	0.62	1950	35		1	PW
	M88-2	8.8	0.89	1850	25		1	SNECMA
	AL-31F	7.14	0.795	1665	23.8		1	NPO

Fig. 2.1 Structural diagram of meridional flow passage of high-pressure turbines in military turbine engines

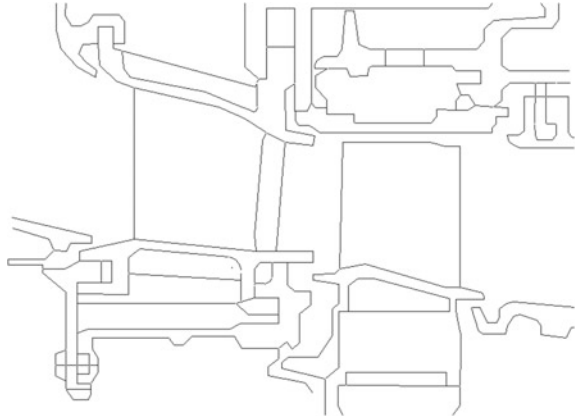
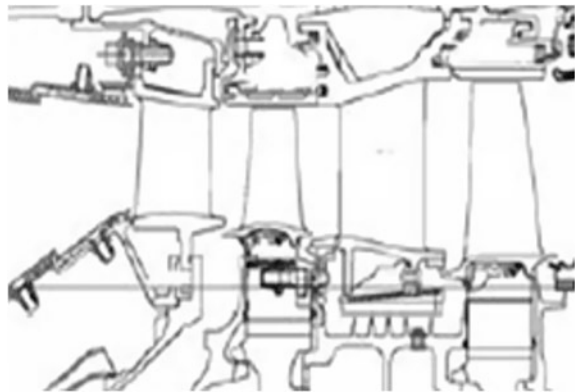


Fig. 2.2 Structural diagram of meridional flow passage of high-pressure turbines in civil turbine engines



high-pressure turbine stage is not high, the centrifugal force on the blades is large. For this reason, the tangential velocity, U , should be limited in aerodynamic design.

2.1.2 Development Status and Trends of High Pressure Turbines

The most important feature of high-pressure turbines is high turbine inlet temperature, which leads to prominent cooling problems and then large cooling flow demand. It's also the requirement of improving turbine engines' thrust-to-weight ratio and reducing fuel consumption. Figure 2.3 shows the development trends of aircraft engines in various countries; Figure 2.4 shows the changing trends of modern aircraft engines' turbine inlet temperature over the years; Figure 2.5 is a diagram of two-stage high-pressure turbines' cooling structure.

Fig. 2.3 Development trends of aircraft engines in various countries

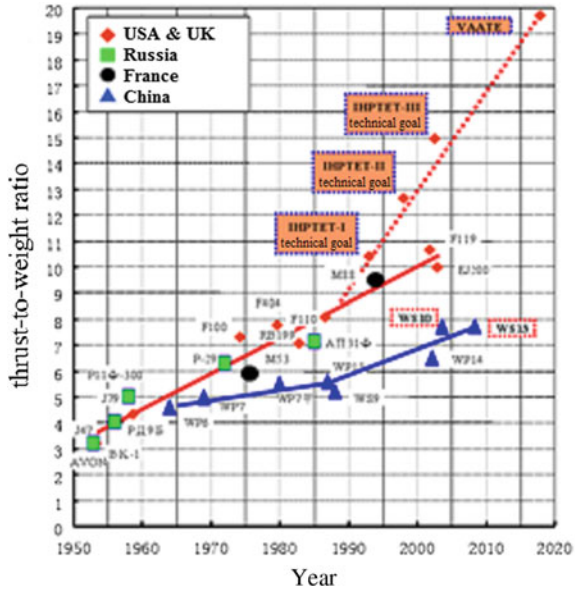
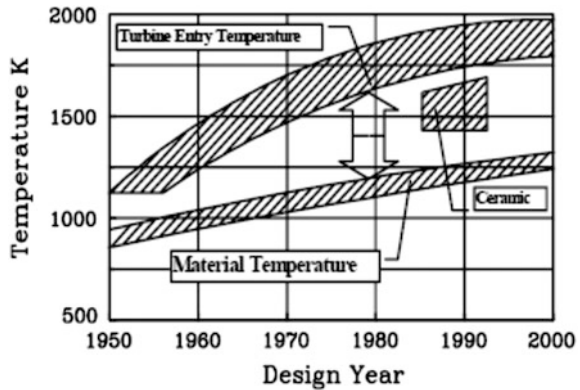


Fig. 2.4 Changing trends of modern aircraft engines' turbine inlet temperature



Generally speaking, military aircraft engines have gone through the following four generations: the typical first-generation engines were turbojet engines, which were widely used in 1950s–1960s with a thrust-to-weight ratio of 3–4 and turbine inlet temperature of 1100–1300 K; the second generation was dominated by afterburning turbojet engines, whose thrust-to-weight ratio and turbine inlet temperature were increased to 5–6 and 1400–1500 K respectively; the third generation was dominated by turbofan engines, whose thrust-to-weight ratio and turbine inlet temperature reached 7–8 and 1600–1750 K respectively, and the typical models include F100, F110, and F404 (the United States), as well as RD-33 and AL-31F (the Soviet Union); the fourth-generation aircraft engines, whose thrust-to-weight

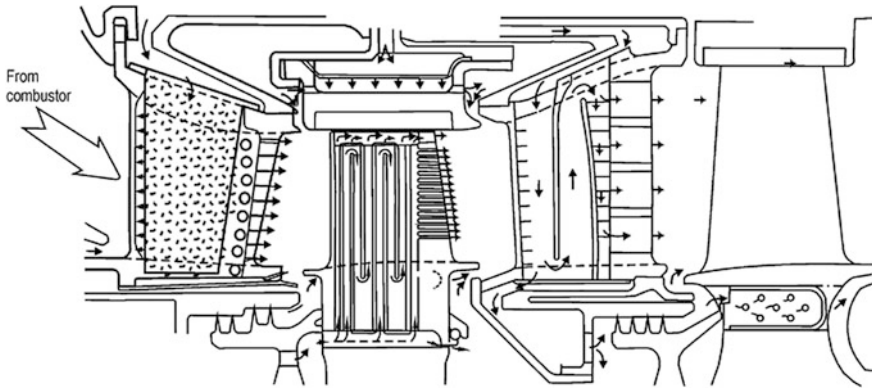


Fig. 2.5 Diagram of two-stage high-pressure turbines' cooling structure

ratio and turbine inlet temperature reached 9–10.5 and 1850–2000 K respectively, have been under development since 1980s, and the typical models include F119, F135 (the United States), EJ200 (Europe), M88-III (France), and AL-41F (Russia).

After completing the IHPTET program successfully, the United States carried out its succeeding program—VAATE in 2006, which is intended to increase the economic affordability of aircraft engines to ten times as much as that of the F119 engine before 2017; the economic affordability refers to the ratio of capacity to life cycle cost, and the capacity is a function of thrust-to-weight ratio and fuel consumption rate. As the program has been in full swing, the aircraft engine with a thrust-to-weight ratio of more than 20 is expected to be developed before 2030. The new engine will be able to reach Mach 3–4.5 at the cruise altitude of 21 km, with its life cycle cost reducing by 64% and economic affordability increasing by about 11.5 times compared to F119. Almost at the same time, Russia implemented a similar program, so did England, Germany, and Italy. The turbine inlet temperature of the fourth-generation engines has reached 1850–2000 K, and achieving the goals of the VAATE program need to increase this temperature to 2300–2400 K.

With respect to civil engines, NASA sponsored the E³ program in the 1980s. This program greatly improved the technologies for developing high-loaded transonic compressors, low-pollution combustors, and high-loaded transonic turbines, and its achievements were directly used in newly-developed aircraft engines, such as CFM56-5, PW2037, PW4000, V2500, etc. Currently, various countries in the world have been pouring enormous energy in developing aircraft engines. The inlet temperature of the PW4084 engine is as high as 1777 K, and the HPT inlet temperature of the civil engines being developed by Rolls-Royce Company will be within the range of 2050–2150 K.

The primary goal of all the above aircraft engine programs is to improve thrust-to-weight ratio and efficiency. According to the thermodynamic cycle of gas

turbines, turbine inlet temperature needs to be further raised to achieve the goal. However, the rise of the temperature would lead to a lot of difficulties in engine design for the reasons below. First, the improvement in heat-resistant materials' performance lags far behind the rise of turbine inlet temperature, as can be seen in Fig. 2.4. Therefore, in order to achieve the aforesaid goal, more effective cooling technologies must be developed to ensure safe and reliable operation of turbine blades in high temperature environment, that is, high-efficiency cooling technologies are crucial in achieving high thrust-to-weight ratio. Second, the rise of turbine inlet temperature would inevitably lead to the increase of cooling flow rate. According to the current cooling technologies and material performance, it is conservatively estimated that the total cooling flow rate will reach more than 25% of core engine flow to achieve the aforesaid goal. The great cooling flow rate and complex physical conditions cause great trouble in aerodynamic design of turbines. For this reason, the design methods, design system, and design philosophy should be further improved.

Figure 2.5 is a diagram of high-pressure turbines' cooling structure. The requirements of blade cooling structure, the influence of film on aerodynamic performance, and the influence of flow field around blades on film's cooling effect should all be considered in aerodynamic design of high-pressure turbines. In addition, the influence of cooled turbines' wall temperature distribution and gas injection on flow pattern should be considered as well. Flow structures are significantly correlated with heat exchange on blades, and their influence on loss should also be considered.

2.1.3 Factors on Efficiency of High Pressure Turbines

The core issue in HPTs aerodynamic design is how to increase high-pressure turbines' aerodynamic efficiency. Figure 2.6 shows the trend line of efficiency of high-pressure turbines over the years. As can be seen from the figure, the efficiency

Fig. 2.6 Changing curve of efficiency of high-pressure turbines over time

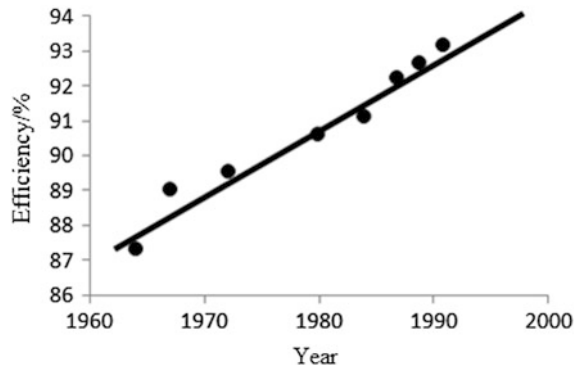
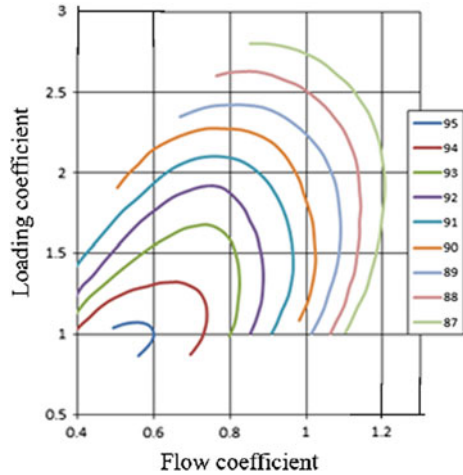


Fig. 2.7 Relation between flow coefficient and loading coefficient



increased by 6% over the 30 years, and some progress has been further made since 1995. The efficiency of civil high-pressure turbines can reach 92–94%, and military high-pressure turbines also experienced a significant increase in efficiency. As turbine inlet temperature and expansion ratio increase continuously, how to improve efficiency of high-pressure turbines still needs to be further studied.

Because the loading coefficient of high pressure turbines is not very large and flow coefficient is relatively high, HPTs are often located in the central section of the loading coefficient figure (see Fig. 2.7). High-pressure turbines’ loading coefficient is mainly restricted by stage expansion ratio, temperature ratio, and rotation speed, and flow coefficient is more related to hub ratio. As can be seen from the loading coefficient figure, efficiency of high-pressure turbines is within 90–93%. Of course, efficiency of high-pressure turbines is determined by many factors, but even a little distance between two points in the loading coefficient figure would cause a difference in efficiency as much as 1–2%.

Because high-pressure turbines, especially those for military use, have relative high pressure ratio, complicated wave system, high hub ratio, and small aspect ratio, they suffer from large shock loss, secondary flow loss, and clearance loss. Thus, many problems still need to be solved to reduce flow loss in high-pressure turbines. High-pressure turbines’ inlet or outlet conditions are correlated with the matching relationship between the high-pressure turbine and combustor or low-pressure turbine. So, in the design process of high pressure turbines enough attention should be paid to some other problems, such as hot spots in inlets of HPTs, inter-turbine duct between the high-pressure turbine and low-pressure turbine, etc.

2.1.4 Further Development of High Pressure Turbines and New Features of Aerodynamic Research

In the field of large civil turbofan engines, GE developed GENx based on GE90; GE and P.W developed GP7000 together; Rolls-Royce Company developed Trent 1000; CFM developed LEAP-X1C. The turbine inlet temperature and overall pressure ratio of the turbines that Rolls-Royce Company is developing are expected to be 2050–2150 K and 50–60 respectively. As for military engines, new engines such as F135 have been developed based on F120 and F119. The goal now is to increase thrust-to-weight ratio to 15–20, turbine inlet temperature to 2300–2400 K, and increase overall pressure ratio to 40. Meanwhile, the sixth-generation variable cycle engines are under development at the same time.

Development of high-pressure turbines is closely related to engine development. For new civil engines and military engines with high thrust-to-weight ratio, turbine inlet temperature and pressure ratio still need to be increased, thus resulting in larger cooling flow consumption and more complicated wave system. Therefore it is necessary to improve aerodynamic design of high-pressure turbines to a new level. In addition, with a further increase in high-pressure turbines' inlet temperature, the complex cooling structure makes flow field, heat transfer, and structure problems interact with each other. Thus parallel design and optimization of high-pressure turbines' aerodynamic, heat-transfer, and structural characteristics will be inevitably placed on the agenda. The calculation methods, mechanism, and design criteria of thermal-flow-elastic coupling are being researched, and a series of achievements have been made. These achievements will be continuously applied to the design of new high-pressure turbines and play a positive role in the development of new high-pressure turbines.

2.2 Aerodynamic and Geometrical Features of High Pressure Turbines

2.2.1 Aerodynamic Design Features of High Pressure Turbines

Aerodynamic design features of high pressure turbines should be fully considered in the design process. Although great progress has been made in turbine design theories and methods (see Fig. 2.8), the effect of cooling flow should be always taken into consideration in each level of aerodynamic design of high-pressure turbines. Because of large cooling flow rate and high carbon content in the high-temperature gas, the influence of film coolant injection and multiple components, thermal radiation, and wall coating should be considered in the 3D numerical simulations of wall heat transfer. Various complex physical processes are involved in the process of gas flow in high-pressure turbines and they should be carefully considered in the simulations.

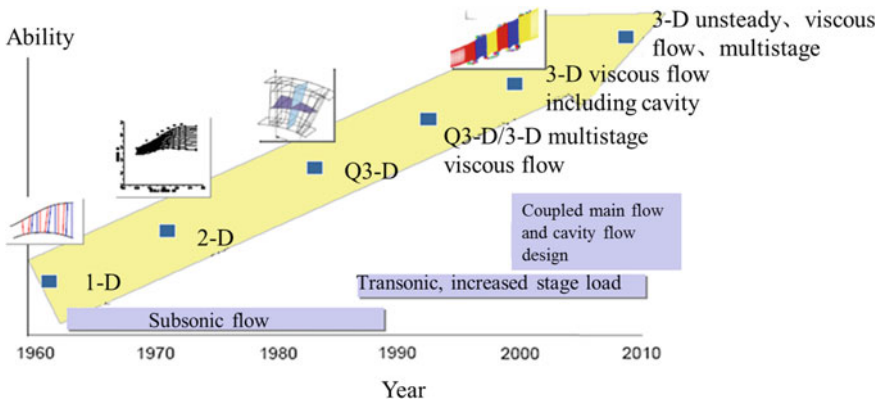


Fig. 2.8 Development of aerodynamic design methods for turbines

2.2.2 Blade Profile Features of High Pressure Turbines

The specific form of high-pressure turbines’ blade profile is mainly determined by high-pressure turbines’ aerodynamic requirements and relevant structural design schemes. The aerodynamic requirements include geometrical parameters of turbine inlet and outlet, radial dimension, contraction and expansion of upper and lower flow passages, etc. Structural design schemes refer to the following characteristics: the existence of cooling flow; structure of blade cavity; ways to connect and fix blades to casing and disk; shroud tip or unshroud tip.

Solidity is suggested to be chosen in the optimal range. However, the optimal solidity may not be used in the design of turbine nozzle due to the restrictions imposed by manufacturing process and structure. Besides, strength should be considered in the design of rotor blades, and for this reason, the optimal solidity of rotor blades’ roots has to be adjusted. Because of the decrease in section area and increase in blade pitch, the optimal solidity for blade tips may be abandoned as well [1].

Convergence of flow passages between blades should be as smooth as possible and local divergence rate should be less than 5%. Besides, the curvature of profile after the throat of suction surface should be determined reasonably according to the Mach number at the throat in actual design. Generally, if the Mach number is less than 1.2, convex shape could be used in profile design. If described by back-sweep angle, the angle should be between 1° and 16°; the larger the Mach number, the smaller the back-sweep angle should be. If the Mach number is greater than 1.2, concave shape could be used in profile design to form a convergence -expansion flow passage.

Trailing edge wedge angle is usually small (less than 6°), and should be chosen according to specific design. It is better to make trailing edge of turbine blade as

thin as possible, because flow loss is in direct proportion to its thickness. However, it has to be made a little thicker in consideration of strength and actual manufacturing process. What's more, manufacturing tolerance should be taken into account to avoid the trailing edge from being too thin after processing. Furthermore, when designing the blade roots of high-pressure turbines, reasonable adjustments in consideration of the design of tenons should be taken into account, so as to avoid the suction surface near the blade roots from being cut off.

The main profile features of high-pressure turbines' stator blades are as follows: leading edge radius is relatively large; the maximum thickness is located in the forepart of the blade; the outlet metal angle is relatively small.

2.3 Complex Wave System in High-Loaded High-Pressure Turbines

In high pressure turbines, the internal flow is complex, especially for high-loaded high-pressure turbines. Shock wave is an important factor causing flow losses. This section mainly discusses the complex wave systems in high-pressure turbines and the interaction between shock waves and boundary layer.

2.3.1 Wave Systems in High Pressure Turbines

The high-pressure turbines with shock waves can be divided into two types: transonic high-pressure turbines and supersonic high-pressure turbines. Flow features of transonic high-pressure turbines are obviously different from those of supersonic high-pressure turbines, and thus there is certain difference in aerodynamic design concept between the two types. In the actual internal flow process, wave structure in the turbine would be in different forms for different Mach numbers at the outlet. Flow conditions in the turbine would become more complicated if interactions between rotor blades and stator blades are taken into account.

This section first introduces the conditions of high Mach number cascade flow, and then further describes the wave systems under the circumstances of rotor-stator interactions.

2.3.1.1 Introduction to Characteristics of Flow in High Pressure Turbine Cascades

For the high-pressure turbines with relatively low outlet Mach number supersonic flow could only be seen in part regions near the suction surface, and there is no shock wave at the trailing edge. With the increase of blade loading and the decrease

of pressure on the suction surface, local supersonic areas arise near the throat of the suction surface as the local Mach number gradually increases and exceeds 1. In some cases, local supersonic areas would also appear behind the leading edge of the suction surface, where profile curvature is relatively high, thus causing additional aerodynamic losses, such as shock loss and wave drag. In addition, the shock waves increase the adverse pressure gradient on the suction surface, which further promotes the tendency of boundary separation and increases the profile loss of high-loaded blades.

In the past few decades, fruitful achievements have been made in the researches of cascade potential flow, and a large number of accurate results about subsonic compressible flows can be used for references. The research on transonic cascade flow, whose complex flowing characteristics are shown in Fig. 2.9, is also remarkable.

The pressure distribution, sonic lines, and shock distribution in the cascade at different Mach numbers are shown in this figure. When outlet Mach number is 0.7, all the points in the flow filed are subsonic. When outlet Mach number rises to 0.9 as backpressure decreases (inlet total pressure and inlet flow angle remain unchanged), blade loading increases gradually as shown in the pressure distribution figure, and a narrow supersonic area can be seen in the range of 35–75% axial chord. This flow characteristic is very typical in most turbines of the current generation. As backpressure further decreases, outlet Mach number would gradually increase and exceed 1, and meanwhile, inlet Mach number would gradually increase to upper limit and then would not change anymore. At the same time, the sonic line would spread to the upstream of the throat, which is one of its limits. At this time, the sonic line is highly curved. The cascade is in a relatively highly-loaded condition, and the area enclosed by pressure curves would increase with the decrease of backpressure. As backpressure further decreases, pressure distribution on the pressure surface and a large part of suction surface would not change anymore, and a shock wave would propagate from near the trailing edge to the suction surface of the adjacent blade and then reflected by the suction surface.

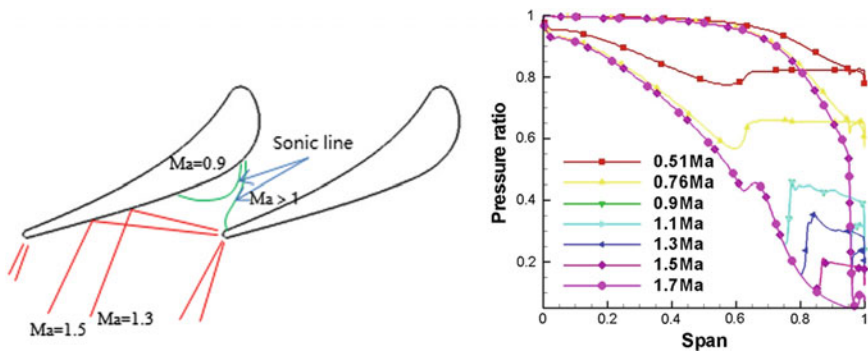


Fig. 2.9 Transonic cascade flow

As Mach number keeps on increasing, the shock wave would gradually deflect to the downstream. When the shock wave finally reaches the trailing edge, we call this condition as “ultimate load state”, in which the axial force on blades reaches its maximum. The concept of ultimate load will be discussed in detail in the following section [2].

A brief introduction to the changing process of operating state of the turbines under different conditions was given above. Characteristics of actual working process in high pressure turbines under different working conditions are summarized as follows.

(1) Determined factors on cascade loss

When the Reynolds number is large enough and outlet Mach number $M_a \geq 0.4 \sim 0.5$, the compressibility of gas will play a leading role and the Mach number will be the main factor influencing cascade energy loss. The relation between profile loss coefficient and the Mach number at cascade outlet (M_a) is shown in Fig. 2.10. As can be seen from the figure, when the Mach number is less than a certain number, M_c , the profile loss coefficient will decrease with the increase of the Mach number, and the number (M_c) is called critical Mach number, which is defined as the Mach number at cascade outlet when the maximum flow velocity on the back of blades reach the local speed of sound.

Under the subsonic condition ($M_a < M_c$) without boundary separation, the pressure gradient would increase with the increase of M_a ; namely, pressure in the convergence zone would drop more rapidly, causing thinner boundary layer, and the initial point of the diffusion area would move to the downstream, leading to reduction of profile loss. As positive pressure gradient in the diffusion area increases, the increase in boundary layer thickness would accelerate boundary layer separation and increase profile loss. The flow on the surface of blades in a turbine cascade is basically under positive pressure gradient, so the pressure distribution on the surface of blades would improve with the increase of M_a , and profile loss would be reduced.

If the Mach number at cascade discharge (M_a) is in high-subsonic range, namely $M_c < M_a < 1$, there would be boundary layer separation on the back of blades. What's more, local supersonic areas would come into being on the back of blades

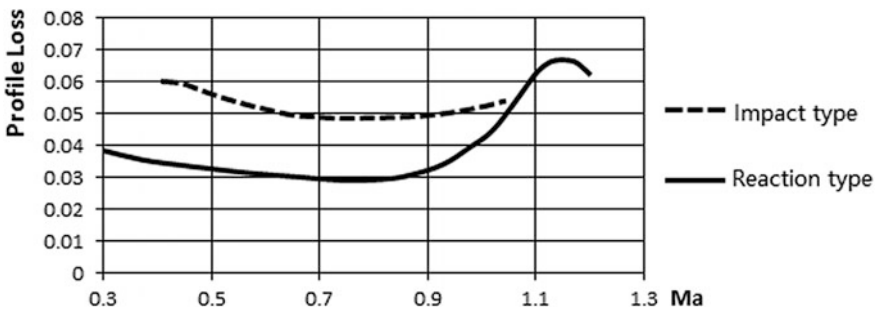


Fig. 2.10 Influence of mach number on profile loss

and closed shock wave system would be generated. In this case, additional shock loss would be caused, and meanwhile, the increase in boundary layer thickness, which is caused by the shock waves, would lead to dramatic increase of profile loss. This condition would get worse with the increase of M_a ; in other words, profile loss would increase rapidly with the increase of M_a .

When the Mach number at cascade outlet, $Ma > 1$, flow blockage would come into being in cascade passage, and the Mach number would not change with the decrease of backpressure. At this time, not only the local wave system on the surface of blades would be enhanced, but also shock waves would be generated at the trailing edge due to the expansion of flow. Then strong wake vortexes appear and Profile loss would increase continuously with the increase of M_a .

When the Mach number at cascade outlet (M_a) is within 1.1–1.3, the location of local wave system on the back of blades would move to the downstream along the flowing direction with the increase of M_a , and the pressure behind the wave system would increase and get close to the backpressure, thus greatly reducing the diffusion area on the backside of blades and decreasing the adverse pressure gradient. In addition, flow blockage would facilitate boundary separation in the diffusion area, so the energy loss would tend to decrease. It is generally accepted that it is feasible not to use the convergent-divergent nozzle when the Mach number at cascade outlet reaches 1.1–1.2 [3].

When the flow in front of the cascade is supersonic, detached shock waves may be generated in front of the cascade. The merging of these shock waves with those from adjacent cascades would lead to great wave drag. To obtain attached shock, the inlet must be made sharp-pointed. As the Mach number increases continuously, the shock waves in front of blades would get into cascade passage. When supersonic air flows pass through the shock wave system, there would be energy loss. Under the influence of shock waves and local separation, great losses may also occur near the outlet section of the flow passage. In addition, due to flow blockage in some cascade passages, there may be strong instabilities that would increase energy loss. In a word, as for supersonic flows, profile loss would increase dramatically with the increase of M_a .

(2) Ultimate load in high pressure turbines

The process of turbine blade loading increasing from low level gradually to high level and eventually to ultimate level during the work process has been described above. Understanding the ultimate load state is helpful to design high-loaded high-pressure turbines.

The flow passage of turbine nozzle consists of two adjacent stator blades, hub and shroud (see Fig. 2.11a). It is used to convert gas' thermal energy to kinetic energy and deflect the gas to a certain direction. Figure 2.11b shows the sectional view of the nozzle at mean radius. As can be seen from the figure, the axis of the nozzle is curved. When the flow leaves the passage of the nozzle, there would be an angle, α_1 , between the direction of the flow and the circumferential direction, u . This is intended to facilitate the conversion of the flow's energy from kinetic energy to mechanical work once the flow enters into the passage formed by rotor blades.

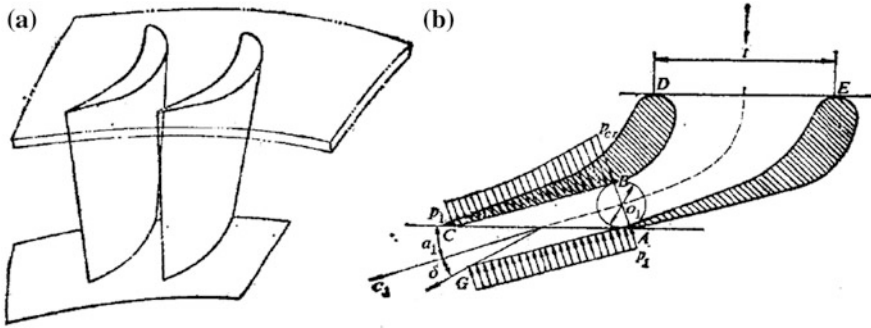


Fig. 2.11 Typical nozzle

As shown in Fig. 2.11b, the flow passage of the nozzle consists of two parts: one is the contraction part, ABDE, where the sectional area of the flow passage decreases gradually along the direction of flow; the other is the scarfed part, ABC.

In actual working condition, gas would lose some energy while flowing through the nozzle passage; namely, it is not an isentropic process. To simplify the analysis, the influence of gas viscosity is neglected. Experiments show that, when flow velocity at the section of nozzle outlet is close to the critical velocity, the flow angle, α_1 , obtained on the premise of isentropy, is quite close to the actual mean flow outlet angle, α_1 ; when the flow is low-subsonic, gas viscosity would exert some influence on the flow angle. When the flow is hypersonic, according to the knowledge of aerodynamics, the influence of gas viscosity is very little, and it is the interactions between shock waves and expansion waves as well as their effects on the boundary layer that influence the outlet flow angle and complicate the flow analysis. Gas expansion in the nozzle is analyzed respectively in the following two different conditions based on the assumption of one-dimensional and isentropic flow.

First condition: when pressure ratio at the section of nozzle outlet is greater than or equal to the critical pressure ratio, flow velocity at the section of nozzle throat (AB) is less than or equal to the speed of sound. The pressure on the section of the throat is equal to the backpressure (p_1) of the nozzle. In this case, gas only expands in the convergence part of the nozzle, and the gas in the scarfed part does not expand. On the section of nozzle outlet (AC), the direction and average velocity of flow are basically the same as those at the throat section.

The average outlet flow angle of the nozzle can be calculated approximatively using the equation below:

$$\alpha_1 = \arcsin \frac{0_1}{t_1} \quad (2.1)$$

where

- o_1 breadth of nozzle throat (the perpendicular distance from Point A to the convexity of the adjacent blade, see Fig. 2.11b);
- t_1 pitch of the nozzle (the circumferential distance between corresponding points on two adjacent blades, see Fig. 2.11b).

Second condition: when pressure ratio at the section of nozzle outlet is less than the critical pressure ratio, flow velocity at the section of nozzle throat (AB) is equal to the critical velocity and pressure is equal to the critical pressure. After passing through the scarfed part located behind the throat section, pressure decreases from the critical pressure at the throat section, p_{cr} , to the pressure at nozzle outlet, p_1 . As shown in Fig. 2.11b, pressure sharply drops from the critical pressure to the pressure at nozzle outlet, p_1 at Point A, which is a disturbing source. A group of expansion waves are generated at Point A, which then reflect off the blade convexity (BC). Flow expands and accelerates when passing through Point A, and is deflected for a certain angle at Point A. Flow near BC passes through two groups of expansion waves (a group of incident waves and a group of reflected waves). After that, overexpansion of the flow occurs, that is to say, the pressure is lower than the backpressure of the nozzle, p_1 , after passing through the reflected waves. Therefore, shock wave will be generated after the reflected waves; after the flow passes through the shock wave, its pressure will be increased to the backpressure of the nozzle, p_1 . Thus it can be seen that flow expansion in the scarfed part of the nozzle is a very complicated process. The flow near trailing edges will be further analyzed hereinafter. In this section, turning angle of flow is calculated approximatively based on one-dimensional flow theory. As shown in Fig. 2.11b, on the assumption of one-dimensional condition, the pressure drops from p_{cr} to p_1 along BC, and is evenly distributed along AG (p_1). So, the resultant force from BC plane on flow is greater than that from AG plane, and thus the flow would be deflected for an angle of δ at Point A.

The turning angle of flow in the scarfed part can be calculated approximatively by using continuity equation. Generally, the throat section of the nozzle is the minimum section of the contraction part. On the assumption of isentropic flow, the critical velocity occurs at the throat section, and the mass flow passing through the throat section of the nozzle can be written:

$$G = F_{\min} \rho_{cr} a_{cr} = l_1 t_1 \sin \alpha_1 \rho_{cr} a_{cr} \quad (2.2)$$

The mass flow passing through the outlet section of the nozzle can be written:

$$G = F_1 \rho_1 a_1 = l'_1 t_1 \sin(\alpha_1 + \delta) \rho_1 c_1 \quad (2.3)$$

For steady cases, the following equation holds:

$$\sin(\alpha_1 + \delta) = \sin\alpha_1 \frac{l_1 \rho_{cr} a_{cr}}{l'_1 \rho_1 c_1} \quad (2.4)$$

where

l_1 height of nozzle throat;
 $l'_1 n$ height of nozzle outlet section.

In general, the height of nozzle throat is approximately equal to the height of nozzle outlet section ($l'_1 \approx l_1$), so Eq. (2.4) can be also written:

$$\sin(\alpha_1 + \delta) = \sin\alpha_1 \frac{\rho_{cr} a_{cr}}{\rho_1 c_1} \quad (2.5)$$

According to the definition of corrected mass flow rate, it can be further written:

$$\sin(\alpha_1 + \delta) = \frac{\sin\alpha_1}{q_1} \quad (2.6)$$

The corrected mass flow rate, q_1 , is only related to gas property (adiabatic exponent, k) and λ number or Ma number of nozzle outlet. So, Eq. (2.6) can be written:

$$\sin(\alpha_1 + \delta) = \sin\alpha_1 \left[\frac{2}{k+1} \left(1 + \frac{k+1}{2} \lambda_1^2 \right) \right]^{\frac{1}{k-1}} \frac{1}{\lambda_1} \quad (2.7)$$

Or

$$\sin(\alpha_1 + \delta) = \sin\alpha_1 \left[\frac{2}{k+1} \left(1 + \frac{k+1}{2} M_1^2 \right) \right]^{\frac{k+1}{2(k-1)}} \frac{1}{M_1} \quad (2.8)$$

where λ_1 and M_{a1} non-dimensional velocity at nozzle outlet. For certain working fluid (air or gas), its M_{a1} number (or λ_1 number) at nozzle outlet corresponds to a certain flow turning angle. This suggests that, when the inflow pressure stays unchanged, the flow turning angle will increase with the decrease of the back-pressure of the nozzle, p_1 . When the pressure, p_1 , reduces to a certain pressure, p_a , at which the last characteristic line of the expansion wave group sent from Point A overlaps with the outlet edge (AC) of the nozzle (see Fig. 2.11), then the expansion capability of the scarfed part of the nozzle will be used up; in other words, when $p_1 < p_a$, gas will be expanded outside of the scarfed part. The working condition, in which $\pi_{1a} = p_a/p_0^*$, is called ultimate condition of the nozzle. Because the last

characteristic line overlaps with AC (see Fig. 2.11) in the ultimate condition, the included angle between the outlet edge (AC) and flow direction, $\alpha_1 + \delta$, is the Mach angle, as shown in the equation below:

$$\sin(\alpha_1 + \delta_a) = \frac{1}{M_a} \quad (2.9)$$

where M_a is Mach number at nozzle outlet in the ultimate condition. By substituting the parameters in the ultimate condition (indicated by the subscript “a”) for the relevant parameters in Eq. (2.5) and defining equation of Mach number, and then substituting them into Eq. (2.9), the following equations can be obtained:

$$\sin\alpha_1 \frac{\rho_{cr} a_{cr}}{\rho_{1a} c_{1a}} = \frac{a_{1a}}{c_{1a}} \quad (2.10)$$

Or

$$\sin\alpha_1 \frac{\rho_{cr}}{\rho_{1a}} = \frac{a_{1a}}{c_{1a}} \quad (2.11)$$

Then, substitute pressure ratio for density ratio by using isentropic process equation,

$$\sin\alpha_1 \left(\frac{\rho_{cr}}{\rho_{1a}} \right)^{\frac{1}{k}} = \frac{\sqrt{k} \frac{p_{1a}}{\rho_{1a}}}{\sqrt{\frac{2k}{k+1} \frac{p_0}{\rho_0}}} \quad (2.12)$$

If $\pi_{1a} = p_{1a}/p_0^*$ and $\pi_{cr} = p_{cr}/p_0^*$, then the above equation can be written:

$$\sin\alpha_1 \left(\frac{\rho_{cr}}{\rho_{1a}} \right)^{\frac{1}{k}} = \sqrt{\frac{k+1}{2}} \pi_{1a}^{1/2} \frac{1}{\pi_{1a}^{1/2k}} \quad (2.13)$$

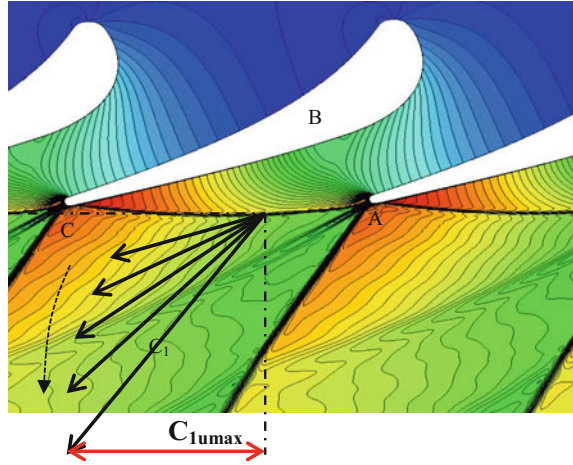
$$\left(\frac{2}{k+1} \right)^{\frac{1}{k-1}} \sin\alpha_1 = \sqrt{\frac{k+1}{2}} \pi_{1a}^{\frac{k+1}{2k}} \quad (2.14)$$

Finally, the pressure ratio of the nozzle in the ultimate condition can be written:

$$\pi_{1a} = \left(\frac{2}{k+1} \right)^{\frac{k}{k-1}} (\sin\alpha_1)^{\frac{2k}{k+1}} \quad (2.15)$$

Figure 2.12 shows the changes of flow velocity in the scarfed part of the nozzle. As can be seen from the figure with the decrease of pressure ratio, π_1 , increment of the circumferential component, $c_1 \cos(\alpha_1 + \delta)$, of flow velocity, c_1 , becomes

Fig. 2.12 Flow turning in the scarfed part of the nozzle



smaller and smaller. When pressure ratio, π_1 , is lower than the ratio in the ultimate condition, π_{1a} , the circumferential component, $c_1 \cos(\alpha_1 + \delta)$, of flow velocity, c_1 , will become constant. This is because, when $\pi_1 < \pi_{1a}$, the flow expansion with pressure ratio dropping from π_{1a} to π_1 occurs outside of the nozzle, and the gas, which expands outside of the nozzle, is only driven by the axial pressure difference ($p_a - p_1$) with no circumferential force on it. For this reason, the pressure distribution on the surface of the nozzle stays unchanged, so does the circumferential component of the resultant force on the surface of the nozzle. Therefore, when carrying out aerodynamic calculations for high-pressure turbine nozzle, its pressure ratio, π_1 , must be greater than the pressure ratio in the ultimate condition, π_{1a} . In addition, due to the change of the outlet flow angle of turbine nozzle, it is necessary to reconsider the design of the inlet metal angle of rotor blades [4].

(3) Analysis of shock waves at trailing edges and wakes in high pressure turbines

From the above content, we can learn that flow condition at trailing edges of blades is complicated, especially when there are shock waves around trailing edges.

General flow characteristics of shock waves around trailing edges are shown in Fig. 2.13. Near the upstream of trailing edges, flow on the suction side is supersonic, and those on the pressure side are transonic. Immediately behind the trailing edge is a region of relatively low velocity fluid at nearly uniform pressure, the base pressure. This base region is roughly triangular in shape at high Mach numbers and is bounded by shear layers in which the velocity rises rapidly from the low value in the base region to the supersonic flow in the free stream. The shear layers start where the flow separates from the blade surfaces close to the start of the trailing edge curvature and the resulting change in direction generates expansion wave which propagate into the main flow. In some cases, the expansion may be immediately followed by a weak shock, the lip shock, which brings the flow to the base pressure while in others the expansion may be directly to the base pressure [5]. The

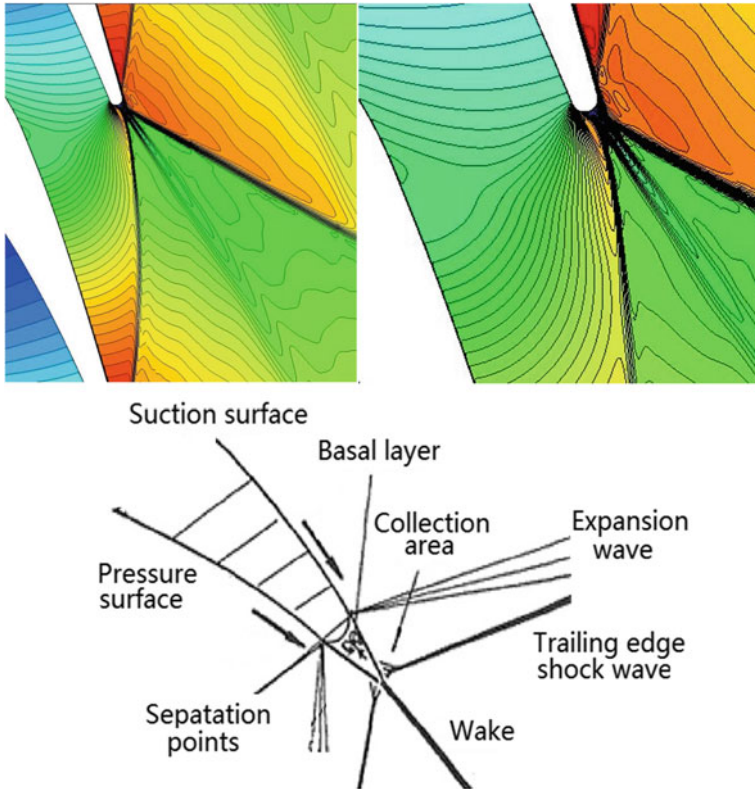


Fig. 2.13 Flow characteristics of supersonic cascade flows near trailing edges

flows from the suction and pressure surfaces must meet downstream of the trailing edge and this occurs in the confluence region at the downstream end of the base region. After meeting, the flows must turn to a common flow direction. In doing so they generate shock waves which again propagate into the flow. One of the shock waves spreads to the suction surface of the adjacent blade, and exerts great influence on the pressure distribution on the suction surface, while the other will run downstream away from blades. Flows in the downstream of the confluence region may be subsonic or supersonic, and a turbulent, unsteady wake could be seen clearly through a schlieren device.

2.3.1.2 Flow Characteristics of Supersonic/Transonic High Pressure Turbines Under Rotor-Stator Interactions

With respect to the actual flow condition at high-pressure turbines rotor blades, unsteady effect is very obvious due to the relative motion between blade rows, and

rotor blades, located behind stator blades, experience circumferential non-uniform flows. In recent years, unsteady flow effect is getting more and more attention in the design of turbomachinery. Unsteady effect could not only result in significant vibration, thus causing blade failure, but also greatly influence aerodynamic performance, heat transfer effectiveness, and noise level.

In the working condition of turbine stages, the unsteady flow between stator and rotor is mainly caused by the following three reasons. First, interactions of potential flows between blade rows, which spreads both to the upstream and downstream. Second, the wakes of stators are continuously cut off and distorted by rotating rotor blades and then travel to the downstream along rotor blade passage. Third, in transonic turbines, interactions of shock waves at trailing edges of stator blades and rotor would also result in complex shock wave structure at rotor inlet.

According to linearized unsteady aerodynamic theory, turbomachines blades could be considered as a barrier which changes the pressure in the original potential field and spreads the changes to the entire flow. According to potential flow theory, when potential field from the upstream flow to the next blade row, pressure on the blade surface would be changed. In subsonic flows, disturbances would be spread to the upstream and downstream of blade rows, and attenuation would be in exponential relation with the distance to the disturbance source. Most of the studies on interactions of potential flow fields between blade rows focus on wake disturbance and potential flow disturbance, and try to compare the magnitude of the two and their respective effects. In flow fields with low Mach number, potential flow disturbance would weaken rapidly with the increase of axial clearance; when axial gap is greater than 30% of blade pitch, the effect of potential flow disturbance can be neglected almostly and wake disturbance would be the main influencing factor. In flow fields with high Mach number, when flow velocity reaches the speed of sound, damping of potential field would become unobvious which can result in significant changes of pressure on the surface of adjacent blades; in this case, the pressure changes caused by interactions between potential flows are an order of magnitude higher than wake disturbance [6].

Wakes are low-energy fluid separated from the main fluid when it goes through trailing edges of blades. They are accompanied by a decrease in impulse which finally acts as frictional loss on the blade surface. The wakes from upstream blade row change the pressure and temperature distribution on the downstream blade surface. The interaction between wakes and downstream blades has an obvious effect on the development of boundary layer on blade surface. Meanwhile, this interaction would also influence noise generation and forced blade vibration.

Compared to subsonic turbines, an additional source of unsteady disturbance in transonic and supersonic turbines is shock wave which generated near trailing edges of stator blades. There may even exist interaction among shock waves when they are reflected by the downstream blade row, complex wave structure would be formed there which could exert significant influence not only on flows in rotor blade passage, but also on pressure distribution on the rotor blade surfaces. The complex shock wave structure could be captured clearly using a schlieren device. Figure 2.14 shows the evolution of shock waves through rotor blade passage, and the graph was developed

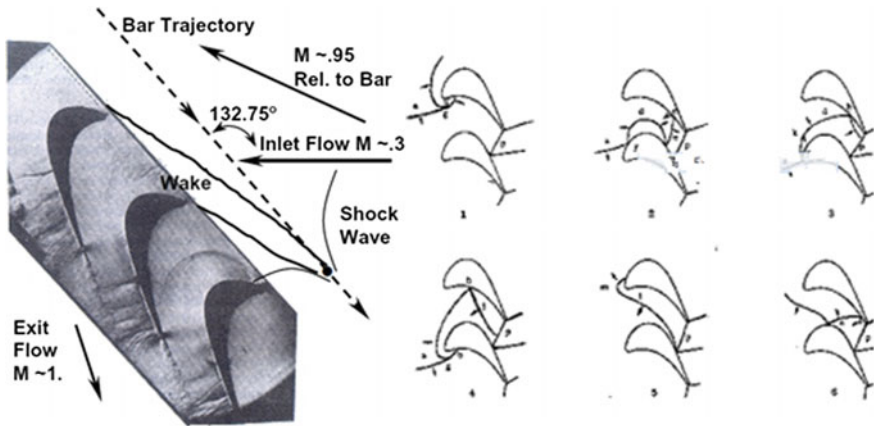


Fig. 2.14 Wave evolution in rotor blade passage [14]

by Doorly (1985) and Johnson (1989). Detailed description can be found in the papers of the two authors [7, 8].

2.3.2 Interaction Between Shock Waves and Boundary Layer

Subsonic, transonic, and supersonic flow conditions of high-pressure turbines has been introduced above, and issues on wakes and shock waves in high-pressure turbines were mainly discussed. On this basis, the following subsection explores another flow problem of particular concern, namely the interaction between shock waves and boundary layer in supersonic flows. Shock waves can be explained by potential flow theory, but boundary layer is more complicated because it involves viscosity. Therefore, it is necessary to take the problem of fluid viscosity into account in the analysis of the interaction between shock waves and boundary layer. The interaction between shock waves and boundary layer is very complex, and the detailed mechanism of the interaction is beyond the scope of this book. Actually the following sections only gives a preliminary qualitative analysis of the problem.

2.3.2.1 Flow Analysis Model for Typical Interaction Between Shock Waves and Boundary Layer

Concerning a supersonic flow on a flat plate, an oblique shock wave impacts on the plate, as shown in Fig. 2.15. The flow assumes to be non-viscous. The incident shock wave impacts on Point B, and radiates a reflected shock wave from the point.

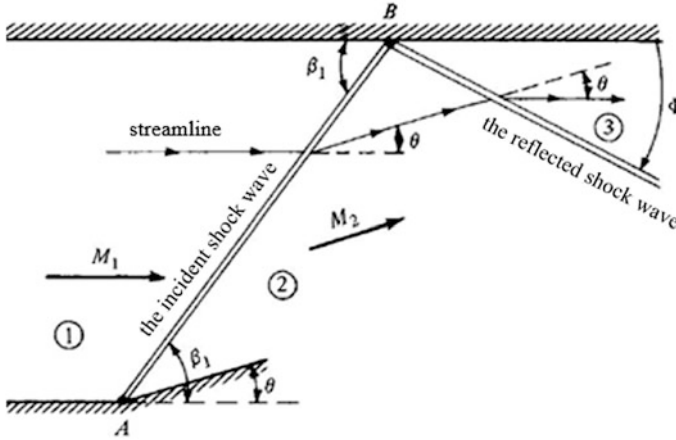


Fig. 2.15 Diagram of shock wave reflection on solid surface

Therefore, a discontinuous pressure rise occurs at Point B, which means the pressure gradient is infinite, and Point B is a singularity.

Suppose that there is a boundary layer on the upper wall surface, then the tremendous adverse pressure gradient, on the point B will lead to boundary layer separation. This is just the basic characteristic of the interaction between shock waves and boundary layer. An incident shock wave would impose a strong adverse pressure gradient on boundary layer, and the boundary separation would further interact with the adjacent shock wave.

This kind of interaction can be further understood from the Fig. 2.16. The boundary layer develops continuously along the flowing direction. Flows in the boundary layer are subsonic, while the main flow is supersonic. When an incident shock wave impacts on the boundary layer the pressure rise behind the shock wave would influence the upstream boundary layer, which makes the actual impact point of the shock wave located in front of the location predicted by inviscid fluid theory. As the thickness of the boundary layer increases, external supersonic flows are disturbed, and thus another shock wave is generated, which is hereinafter referred to as incident separation shock. After that, the separated boundary layer turns to the plate immediately and reattaches to the bottom wall surface. At the moment, the direction of subsequent supersonic flows is towards the wall surface, so the third shock wave, called attached shock, is generated. A series of expansion waves would be formed between the separation shock and attached shock, as shown in the figure. The boundary layer would become thinner at the attachment point where pressure is very high and aerodynamic heating is located. Away from the wall, separation shock and attached shock meet together. In addition, it is necessary to note that the flow condition shown in the figure below is only one of the shock wave-boundary layer interference cases. The interference also depends on the flow pattern of the

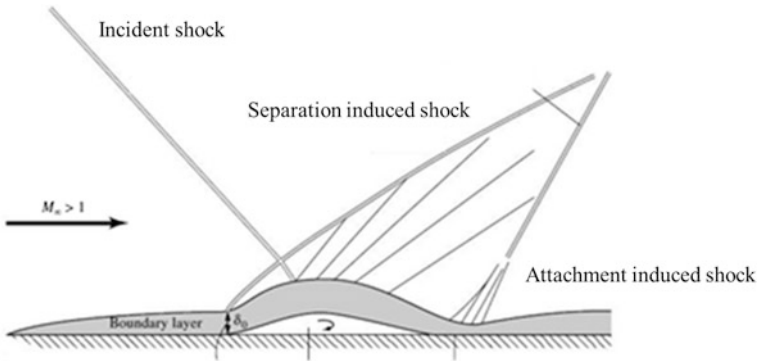


Fig. 2.16 Interaction between shock waves and boundary layer

boundary layer—laminar or turbulent. Laminar boundary layer is more likely to separate compared to turbulent boundary layer.

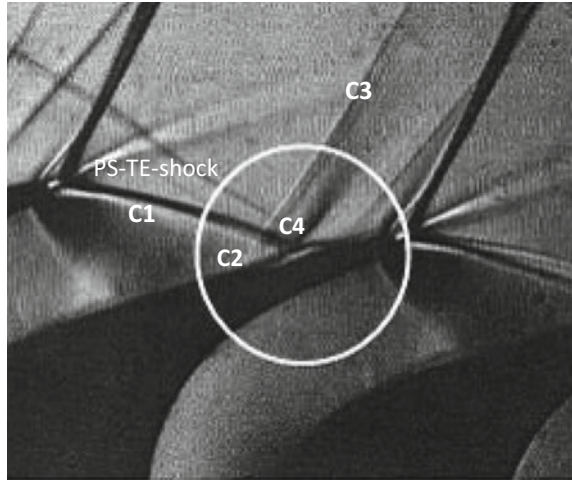
The interaction between shock waves and boundary layer has a great impact on wall pressure, wall shear force, and heat transfer. Generally boundary layer separation will inevitable lead to total pressure loss , so it is necessary to avoid the interaction as much as possible. This it is not easy in actual projects. From another point of view, latest innovative thinking reminds us that the interaction between shock waves and boundary layer also can be used in off-design conditions or some specific controlled flows [9].

2.3.2.2 Interaction Between Shock Waves and Boundary Layer in High Pressure Turbines

We can have a basic understanding of the interaction between shock waves and boundary layer through the above simple model. In high pressure turbines, the interaction between shock waves and boundary layer would generally lead to the generation of a boundary-layer separation bubble below a weak shock wave, and additional dissipation may occur in the downstream of the separation bubble. If the boundary layer is laminar, then transition may happen due to the effect of the shock wave on the boundary layer.

Actually, analyses of the interaction between shock waves and boundary layer are more common in the design of airfoil profile, such as aircraft wings and compressor blades. That's because both separation and wave drag caused by the interaction between shock waves and boundary layer are extremely unfavorable. The flow passages in high-pressure turbines are convergence and flows in the turbines are dominated by positive pressure gradient. For these reasons, influence of the interaction between shock waves and boundary layer on the turbines is not as remarkable as that on the above-mentioned objects. However, for some blades, the interaction between shock waves and boundary layer may be very significant in

Fig. 2.17 Separation bubbles caused by interaction between shock waves and boundary layer in a high pressure turbine



certain working conditions, and obvious separation bubbles could even be generated.

Figure 2.17 is a diagram of shock wave structure in a high-loaded high-pressure turbine, which was obtained by Wako Research Center (Japan) and German Aerospace Center (Germany) using schlieren devices at the time when the isentropic Mach number at turbine outlet reached 1.2 [10]. It can be seen from the figure that a shock wave on the suction side impacts on the suction surface of the prior adjacent blade, and the interaction between the incident shock wave and the boundary layer results in the separation as well as separation bubble. In addition, the wave system structure is similar to that in Fig. 2.16, both containing the separation-inducing shock wave and reattached shock wave. Detailed flow structures of the interaction between shock waves and boundary layer is shown in Fig. 2.18.

2.4 Secondary Flow of High Pressure Turbines and Control Techniques

Aerodynamic problems in turbines are very complicated, and there remains lots of problems to be studied. Because flow passages in turbines involve various geometric forms, such as blades' bending, blade tip clearance, cooling flow holes, changes of upper and lower end-walls, etc., the internal flows present complex 3-D patterns. Generally, the flows can be divided into the following types: boundary layer and secondary flows caused by pressure gradient in blade passage, such as horseshoe vortex, leakage vortex, corner vortex, as shown in Fig. 2.19. Beyond that, centrifugal effect, interaction between shock waves and boundary layer, and rotor-stator interaction make flows in high pressure turbines more complicated.

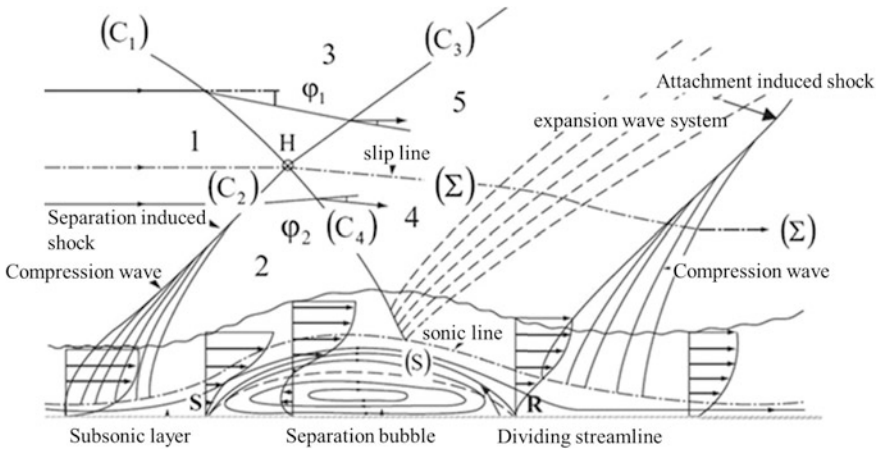
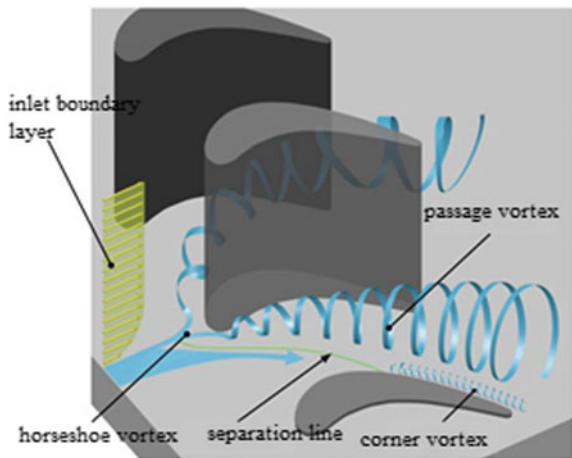


Fig. 2.18 Flow structures of interaction between shock waves and boundary layer in a turbine

Fig. 2.19 Diagram of typical secondary flows in high pressure turbines



Secondary flows are mainly discussed in this section. At half blade height, 2-D cascade analysis methods can be used to analyze the flow in cascade passages. However, flows around the end-walls show complex 3-D characteristics, and there are obvious interactions among the flows. Actually there are significant connections between flows around end-wall areas and the main flow, thus it is nonsense to study the end-wall flow separately without considering the whole flow field.

Due to the large turning angle in the high pressure turbines' rotor blades, vortices and transverse flows in the rotor blades are more intensive than those in stator blades. In the high-pressure turbines with low aspect ratio, secondary flow loss accounts for a great part of the total loss (35–40%), so turbine designers should pay enough attention to it in the design process.

2.4.1 Secondary Flow in High Pressure Turbines

This subsection mainly explores the structure and development of 3-D vortexes in flow passages, which are illustrated in flow field diagrams visualizing flow lines, pressure loss, vortexes, turbulence intensity, and flow turning angle, and introduces induced vortexes at the end.

(1) Horseshoe vortex at the leading edge

Horseshoe vortex at the leading edge are generated at the interface between the endwall and leading edge of the blade. When the fluid come to the stagnation line of the leading edge, the static pressure is equal to the total pressure. Because the velocity of the main flow is higher than that in boundary layer the static pressure in the main flow increases to a higher level than that in boundary layer. The radial pressure gradient at the leading edge would lead to the generation of a vortex, which is called horseshoe vortex. Usually the horseshoe vortex is confined in the region which is thinner than the boundary layer. The adverse flow caused by the horseshoe vortex and incoming flow near the endwall converge at what is called the stagnation point. Generally the stagnation point is near the place where the incident angle of the flow is zero. The horseshoe vortex is typically located between the stagnation point and the leading edge. A study suggests that the exact locations of the stagnation point and horseshoe vortex center are dependent on the radius of curvature of the leading edge and the boundary layer thickness of the incoming flow [11].

Figure 2.20 shows the horseshoe vortexes near the leading edge in a linear cascade flow field. The vortexes rotate anticlockwise, and a number of horseshoe vortexes, which have the same size and rotation direction are generated periodically. In addition, a relatively small counter-rotating induced vortex is generated in the corner of the leading edge.

(2) Suction side leg and pressure side leg of the horseshoe vortex

As shown in Fig. 2.21, horseshoe vortexes flow along the separation line under the effect of pressure gradient and transverse flows near the end-wall region. A horseshoe vortex separates into two legs at the endwall, which are suction side leg and pressure side leg. With the development of the flow, the pressure side leg of the horseshoe vortex gradually flows to the suction surface and the two legs gradually merge into a separate counter-rotating vortex structure. It should be note that the pressure side leg of the horseshoe vortex is larger and stronger than the suction side leg. The vortex structure at this moment is still close to the endwall and suction surface.

(3) Passage vortex and induced vortex

Passage vortex is actually the product of the merging of the suction side leg and pressure side leg of a horseshoe vortex. Because the pressure side leg of the horseshoe vortex is larger and stronger than the suction side leg, the rotation effect

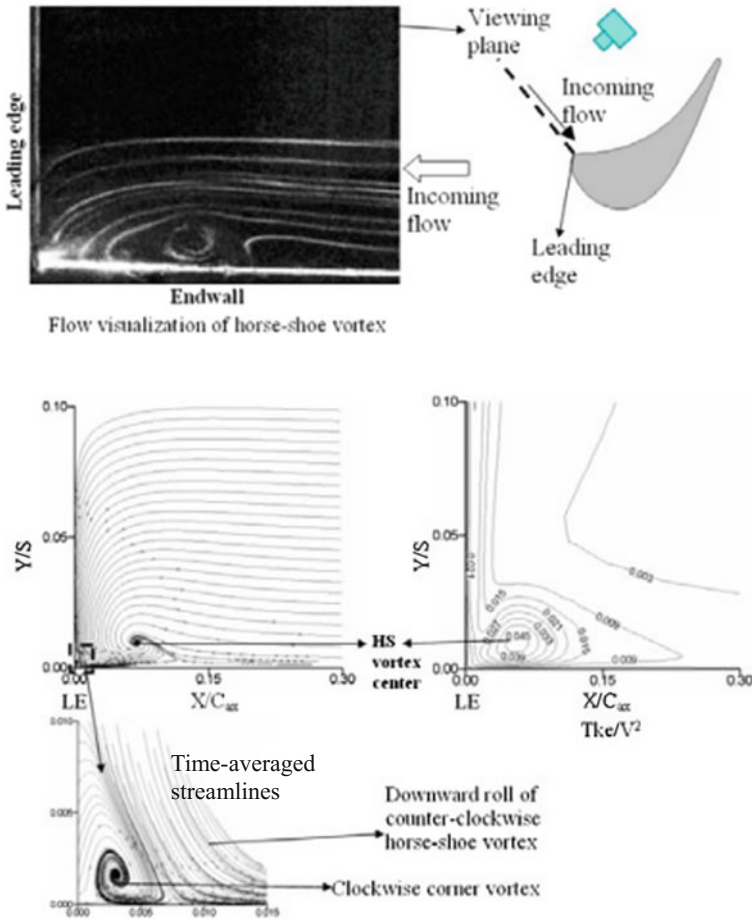


Fig. 2.20 Typical horseshoe vortex near the leading edge and corner vortex; *HS* horseshoe, *LE* leading edge, *Tke* turbulence kinetic energy [12]

of the passage vortex is actually the same as the pressure-side leg of horseshoe vortex. As the passage vortex entrains the main flow and endwall boundary layer, it grows in size and gradually gets closer to the suction surface along the flowing direction. Development of the passage vortex towards the middle of blade span is partly caused by the radial pressure gradient in the boundary layer of the suction surface. Because of this characteristic of the passage vortex and distortion of boundary layer on the endwall, the boundary layer of the suction surface is also distorted and becomes thicker and thicker, and the passage vortex flows to the downstream with the suction side leg of the horseshoe vortex surrounding it.

Figure 2.22 shows the new model of vortex structure in turbomachinery, proposed by Wang Haiping. Actually, a series of vortex structure models had been

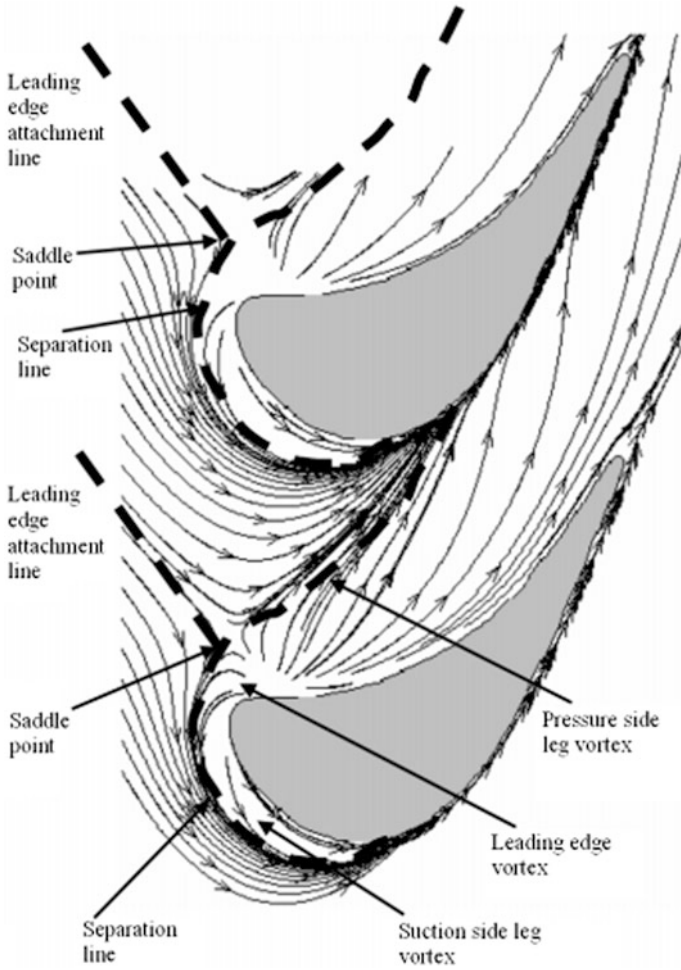


Fig. 2.21 Near-wall separation line of linear cascades [13]

proposed before Wang Haiping's model. As shown in Fig. 2.22, there is a small and clockwise vortex, V_{wip} , which is attached to the suction surface and located above the passage vortex. This vortex is called wall vortex, which is induced by the passage vortex and generated at the initial point of the passage vortex, and the vortex moves to the downstream with the development of the passage vortex. In addition, as described above, an induced vortex would also be generated in the corner of the leading edge with the generation of a horseshoe vortex. Similarly, induced corner vortices would be generated by transverse motion at the corner region between the endwall and the suction surface as well as that between endwall and pressure surface. In fact, corners may be made into fillets in turbine machining,

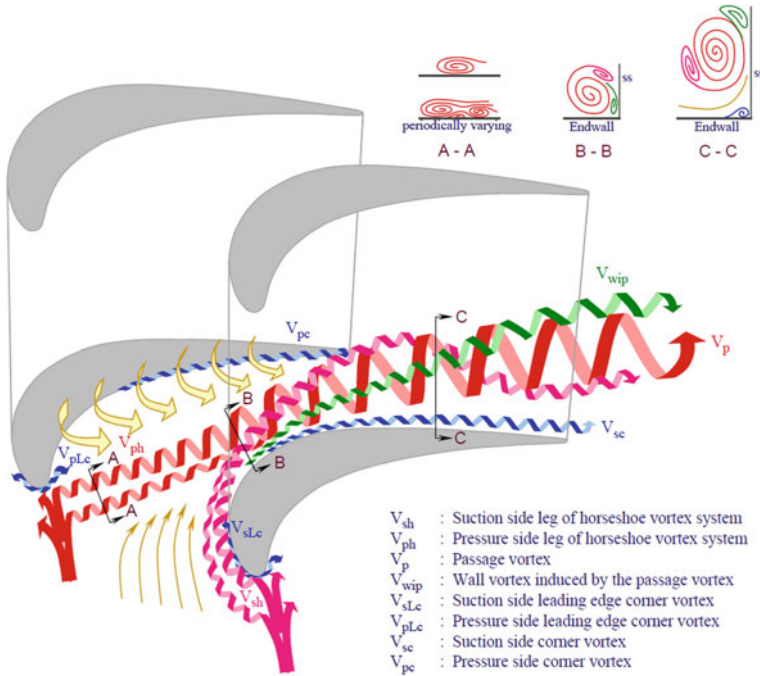


Fig. 2.22 New vortex structure model proposed by Haiping [14]

so the corner vortices may not develop in this way. But the model proposed by Wang Haiping can still provide a reference for vortex analysis.

In general, secondary flows would lead to unsteadiness of cascade outlet parameters, which would further increase noise level, secondary flow loss, and blade loading fluctuation. Secondary flow is a very important phenomenon in high pressure turbines, and designers should give careful consideration to this phenomenon.

2.4.2 Factors of Influencing Secondary Flows in High Pressure Turbines

A large number of studies have been carried out on how to reduce secondary flows as well as the losses by revising geometric structures in turbines. This subsection mainly introduces the factors influencing secondary flows based on these studies.

Actually, in exploring the factors influencing secondary flows, large amounts of experimental data should be regarded as the basis for determining research directions. Mathematical statistics methods should be then used to work out loss model

equations based on the data, which describe secondary flows and other relevant aerodynamic problems. These equations can be used to analyze the factors influencing secondary flows. In addition, some turbine loss models are described in Chap. 6 of this book. Although the loss models are different from each other in loss structure (mainly because researchers used different research strategies, the models are different from each other in both loss classification and extraction method), relevant influencing factors can be found by using corresponding equations. This problem exists not only for secondary flow loss, but also for other losses.

The first factor to mention is aspect ratio of a turbine. Compared to blades with relatively large aspect ratio, the influence of secondary flows in the passages of blades with small aspect ratio could cover the entire blade-span area, and secondary flow loss accounts for a higher proportion of the total loss.

Figure 2.23 [15] suggests that loss coefficient increases rapidly with the decrease of aspect ratio. The data shown in the figure consists of results of two experiments and Soderberg's equation, which describes the relation of loss coefficient with turning angle and Reynolds number. As can be seen from the figure, at the same turning angle, secondary flows will occupy more area on the blade surface with the decrease of aspect ratio, and thus the loss coefficient will increase. For a given flow passage with fixed blade height, the loss coefficient can be reduced only by reducing blade chord length. To maintain the blade loading, the blade pitch should be shortened. However, the wake loss at the trailing edge will rise up. Therefore, designers have to face these contradictions in the design. There are also other constraining factors needed to be taken into consideration in the design progress, such as stress and vibration of blades (blades with high aspect ratio have to bear higher stress at the root and their natural vibration frequency is lower), and so on.

As can be seen from Fig. 2.23, turning angle is another determined factor of secondary flows. When aspect ratio stays unchanged, the loss coefficient at a turning angle of 115° is 3–4 times as much as that at a turning angle of 76° – 80° , suggesting larger turning angle would result in stronger secondary flows. The flow deflects in the blade passage, causing transverse pressure gradient in the process, drives the endwall boundary layer to form a passage vortex. The larger the turning angle, the higher the transverse pressure gradient will be, and the stronger the passage vortex will be.

In 1970, Dunham disposed a large amount of proposed secondary flow loss coefficients, and made some revisions based on the models organized by Ainely and Mathieson. After that, Kacker and Okapuu made further modifications based on the work of Dunham, and the modified models have been widely used till now. These loss models as well as relevant equations can be found in the appendix. Lift coefficient (Zweifel coefficient) is another influencing factor. This coefficient is used to evaluate blade loading, and secondary flow loss is in direct proportion to the square of lift coefficient. The increase of blade loading would also result in the increase of secondary flow loss. In addition, Zweifel coefficient can be used to calculate the optimal blade solidity. Generally, 0.8 is regarded as the optimal lift coefficient.

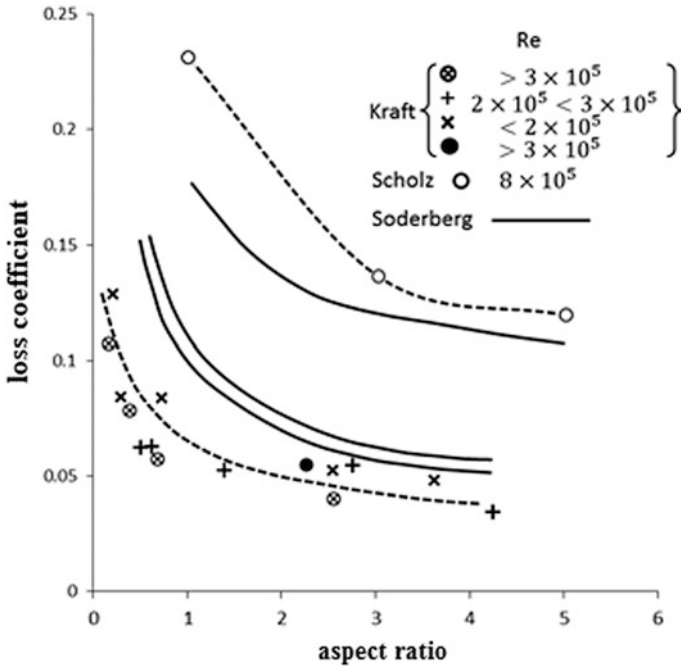


Fig. 2.23 Relation of loss coefficient with aspect ratio and Reynolds number

Compressibility of fluid is another influencing factor, which mainly works in the acceleration of endwall flows, and it would influence boundary-layer flows at the endwall. In subsonic flows, correction can be done by directly multiplying the original loss coefficient and an appropriate coefficient. In supersonic turbines, the high Mach number flows at the leading edge would also influence secondary flow loss, and appropriate correction should be made to the loss coefficient, so as to estimate secondary flow loss more accurately.

2.5 Leakage Flows of High Pressure Turbines and Control Techniques

Side flows [16] are a kind of inevitable flows in turbomachinery, generated at the clearances between rotating components and stationary components of turbomachinery. Side flows include leakage flows over the unshrouded rotor blade tips and stator blade roots, labyrinth flows over shrouded rotor blades and sealed stator roots, windage flows at the rotor disk, and discharge flows through the balance holes of the rotor disk. Clearances structure and Leakage flow of the shrouded

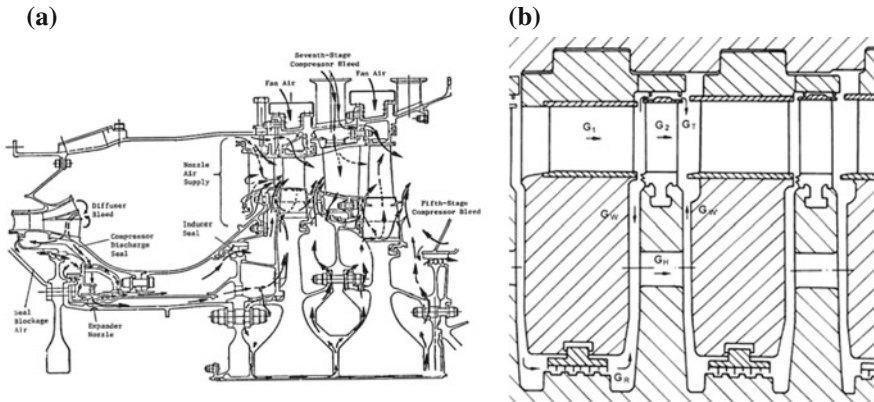


Fig. 2.24 Diagrams of turbine flow passages (G_1 , G_2 —main flow rates in stator and rotor passages; G_T , G_R —leakage flow rates over the rotor blade tip and stator blade root; G_w , G_w' —windage flow rates; G_H —flow rate through the discharge holes of the rotor disk), **a** geometry of high pressure turbine of a modern gas turbine engine [17], **b** impulse turbine geometry [16]

high-pressure stage of a gas turbine engine and an impulse steam turbine are shown in Fig. 2.24.

Since the end of 1960s, blade tip clearance and inter-stage seal have taken an important role in aircraft engine design. With the development of gas turbine engines, blade tip seal has become a challenging problem for gas turbines in both ground and aircraft engines resulting from blade tips and the casing continuous variation under the action of thermal stress and centrifugal stress of rotating and stationary components. This problem is more significant for the aircraft engine because of its operating conditions constantly changing in the flying process.

Figure 2.25 shows the relation between time and the size of clearance, which is acted upon by centrifugal force, thermal stress, and internal pressure, in different operating conditions. The operating conditions include taking off from the ground, cruising, slowing down, ground idle, and reaccelerating. The axisymmetric clearance of large commercial engines experiences a change of over 0.76 mm from accelerating to reaccelerating. Military engines' high requirement on accelerating ability makes the change of the clearance even larger. During cold starting, the clearance size drops dramatically to the minimum point because of the centrifugal force, resulting from takeoff acceleration, the rapid rise of blade temperature, and slow response of the casing to temperature. After that, the clearance becomes larger as the casing expands with heat. Then, the blades expands with heat, which reduces the clearance. In the cruising condition, the casing and the rotor reach a thermal balance, and the clearance size stays at a constant basically. In the cruising condition, throttle status would change with flight height, and the clearance size would change as well. Therefore, it is necessary to keep an appropriate clearance size during cruising to avoid scratches between blades and the casing. In the

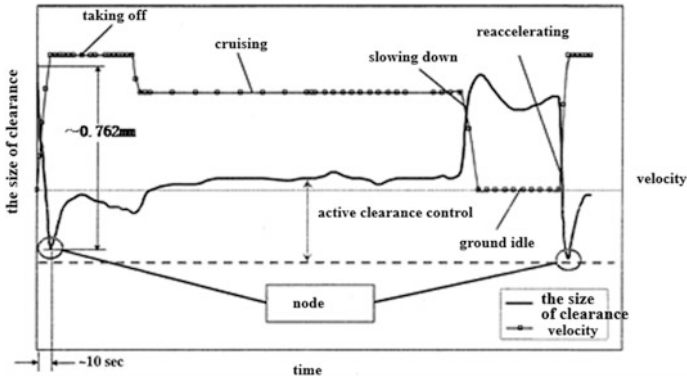


Fig. 2.25 Changes of blade tip clearance with time in different operating conditions [37]

slowing-down condition, the clearance size increases rapidly to the second peak point because of the unloading of the rotor and blades, and the cooling delay of the casing [18].

For unshrouded blades, tip leakage flows are caused by the pressure difference between the suction surface and pressure surface of blades. Under the action of the adverse pressure gradient and wall underflow, tip leakage flows move downwards after flowing out of the tip gap and form tip leakage vortices, thus resulting in reduced work, blockage and additional loss, and making flows near the blade tip extremely complex. The tip leakage flows, which exist in the blade passage in the form of various vortices, would interact with boundary layer of blades and passage vortices, generate complex flows, and increase losses. Meanwhile, the tip leakage flows would influence radial distribution of blade loading, thus reduce blade loading, increase unsteadiness of downstream flows, and make blade heat transfer more complicated, etc. Figure 2.26 shows tip leakage flows at two different kinds of blades with different thickness.

Han and Huang [20] made a detailed analysis of the flow topology and vortex structure in a turbine cascade flow field with a blade tip gap. Because the transverse

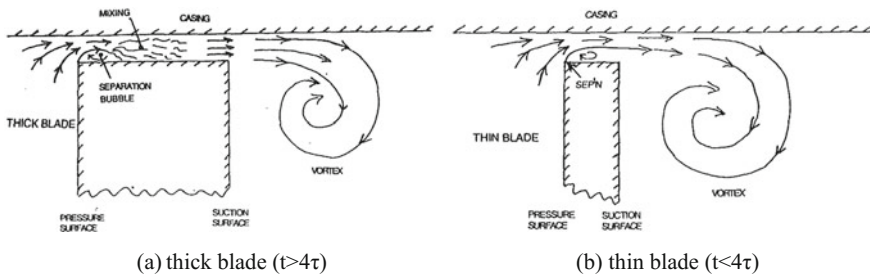


Fig. 2.26 Tip leakage flows at thick and thin blades [19]

pressure gradients near the blade tip region and in the flow passage area are in opposite directions, the endwall boundary layer would separate at the highest pressure point near the pressure edge of the blade tip, and would gather at the lowest pressure point near the suction edge; as a result, a reattachment line (L_r) and a separation line (L_s) are respectively generated near the pressure edge and suction edge of the blade tip, and the flow patterns of double saddle points (Sh , Sl) and double nodal points (Nh , Nl) are generated when the incoming flow boundary layer of the endwall flows around the cylindrical leading edge of the blade tip. At the blade surface and lower endwall, four reattachment lines are sent from the attachment node (N_{im}) at the leading edge respectively to the suction surface and pressure surface, upwards and downwards along the blade span. The reattachment line, which extends upwards along the blade span, passes through the surface of the blade tip and brings about a saddle point (Sc) on the suction edge from which two separation line branches are sent. One of the branches extends to the downstream along the suction edge of the blade tip and ends at the separation node (N_t) on the outlet edge, which is the convergence line of the limiting streamline at the blade tip and the limiting streamline at the top of the suction surface, and also the separation line of the secondary flow whose rotating direction is opposite to that of the leakage vortex. The other branch obliquely extends to the downside of the blade tip on the suction surface and approaches to the separation node (N_u) of the outlet edge at a specific blade span, which is the separation line of the upper passage vortex. The reattachment line starting from N_c , the attachment node generated slightly downstream of Sc , extends to the downstream along the suction surface, and brings into being a saddle point (S_u) between N_t and N_u .

Similarly, there is a reattachment line starting from N_{im} on the suction surface at the middle of the cascade span, which extends from the leading edge to the trailing edge, ends at the saddle point (S_{ms}) on the outlet edge, and merges with the separation line of the lower passage vortex at the trailing edge. On the lower endwall and lower-span suction surface, the incoming flow boundary layer of the endwall separates at the leading edge saddle point (S_a) on the inlet edge, and generates the pressure side leg and suction side leg of the horseshoe vortex. The pressure side leg passes through the flow passage, and merges with the suction side leg of the adjacent blade at an axial position, thus the separation line of the upper and lower passage vortices is generated at the merging point, and the line obliquely extends from this point to the upside along the suction surface, and ends at the separation node (N_{sl}) on the outlet edge. The reattachment line, generated on the suction surface at the middle of the blade span, starts from N_{im} and ends at the saddle point (S_{mp}) on the outlet edge.

In the section next to the outlet located behind the saddle point (S_c), the anti-clockwise upper passage vortex and secondary vortex are generated in the linear cascade and increase in both strength and scale while flowing. The upper passage vortex, whose strength and scale are smaller than those of the lower passage vortex, is rapidly pushed to the middle of the flow passage by the leakage vortex. The secondary vortex is a small-size vortex located near the suction edge of the blade

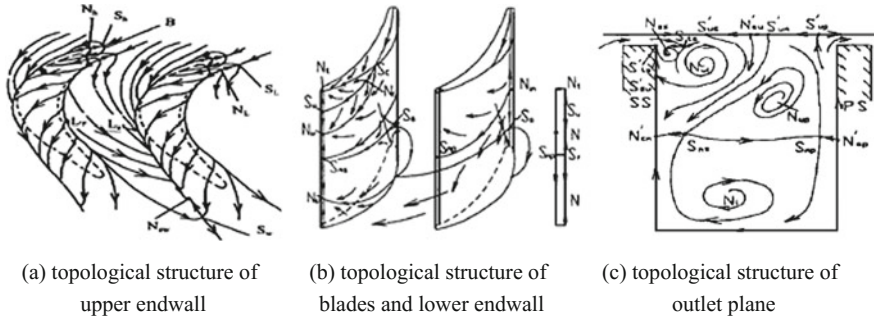


Fig. 2.27 Topological structure of planar cascade [20]

tip, and it interacts with the leakage vortex and brings into being the saddle point (S_{ts}). The vorticity of the three concentrated vortex systems: leakage vortex, upper passage vortex, and secondary vortex is respectively from the upper endwall, the upper blade surface, and blade tip, so six kinds of semi-singularities in different forms are generated on these surfaces (see Fig. 2.27).

Lee et al. [21] further studied the high-turning cascade flows in detail. Two significant phenomena, that is, tip gap vortices and separation/reattachment of blade tip flow, were found in flat tip gaps with different size. The oil-flow diagram suggests that there is rolling flow separation at the leading edge of the tip surface, and the flow is converted into a pair of counter-rotating vortexes along the dot-dash line, which are called tip gap vortexes. The separating flows are not only affected by the flow condition of the main flow near the tip along the blade surface, but also the pressure gradient down the dot-dash line; both of the factors contribute to the separation of the fluid from the blade surface. When the ratio of the gap size to the chord length is $\tau/c = 3\%$, there is a reattachment line along the dot-dash line, as shown in the oil-flow diagram of the middle tip chord. Driven by the pressure difference, most of the fluid in reattachment line flows to the suction surface, and the remaining flows towards the pressure surface to the separation bubble. A separation bubble is generated in the ellipse enclosed by a dotted line in the diagram. Studies on different gap sizes suggest that flow separation at the leading edge is not obvious in small gap size, and the reattachment line in the leading edge area is also unobvious; as the gap increases, the scope of the separation area at the leading edge increases as well, the initial position of the reattachment line gradually gets away from the leading edge, and the separation bubble becomes more complex consequently (see Fig. 2.28).

Two tip flow models respectively for two gap sizes were proposed based on the oil-flow visualization and tip Sherwood number measured. In the circumstance of $\tau/c = 1\%$, the incoming flow gets into the tip gap and separates on the edge of the tip plane at the inlet, and then rapidly attaches to the tip surface. Therefore, the attachment line is very close to the inlet of leakage flow in the tip. Tip gap flows in

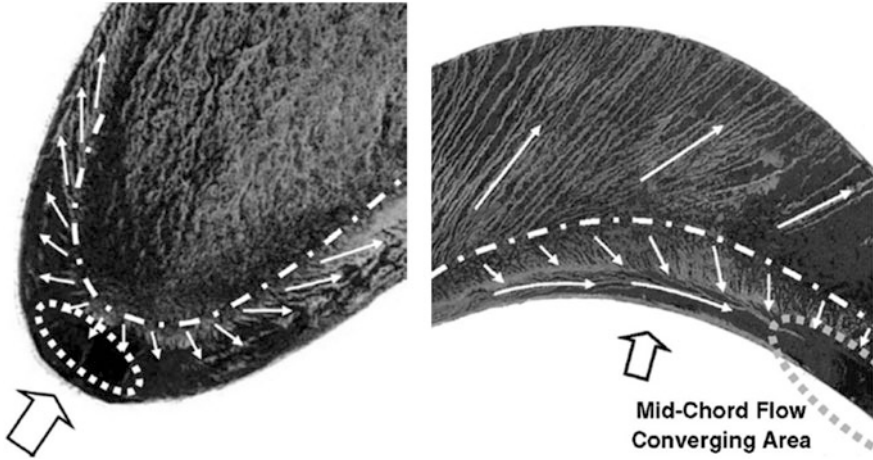


Fig. 2.28 Oil-flow visualization of leading edge and middle chord of blade tip [21]

the other place develop as the development of boundary layer, and have no much complex three-dimensional flow structure such as tip gap vortices, flow separation, separation bubble, etc. While in the case of $\tau/c = 4\%$, the gap flows present complex 3-D flowing characteristics. To be specific, Tip gap vortices come into being and develop; strong separation-reattachment flows occur; the incoming flow evolves into a pair of tip gap vortices at the leading edge; then the suction side leg of the gap vortices leaves the tip soon and flows towards the suction surface of the blade. The pressure side leg of the gap vortices develops in parallel to the pressure edge of the tip, and both its strength and area occupied are larger than those of the suction side leg. This branch gets across the tip gap through the middle of the chord. Its separation line is far away from the leading edge, and the fluid in the separation bubble, next to the wall, moves to the converging area at the middle of the chord from both the leading edge and trailing edge (see Fig. 2.29).

The models thoroughly explored the gap flows for different gap sizes under the condition of a high-turning cascade, and measured heat transfer. However, they did not describe the flow separation conditions in the endwall region and the interaction between tip leakage flow and the main flow.

Losses caused by tip leakage flow of unshrouded blades mainly consist of the following three parts [19]. (1) Gap secondary flow loss and endwall loss: the endwall loss is caused by the frictional drag of leakage flow passing end-walls, while the secondary flow loss includes all the frictional losses except for that from the profile. (2) Shear loss within the gap, caused by the relative movement between the casing and the tip wall and by viscous friction between the leakage flow and layers of the separation flow in the gap. (3) Mixing loss of the leakage flow and the main flow near the suction surface. Because the two flows are greatly different in velocity and direction, vortex layers would be generated at their interface, finally

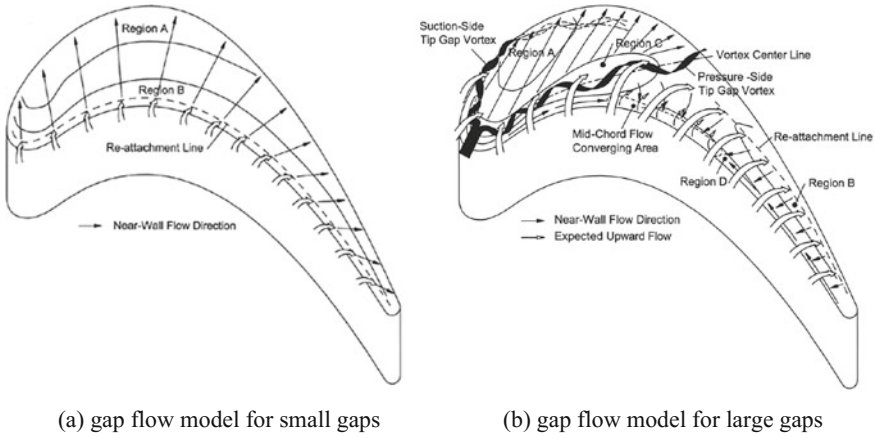
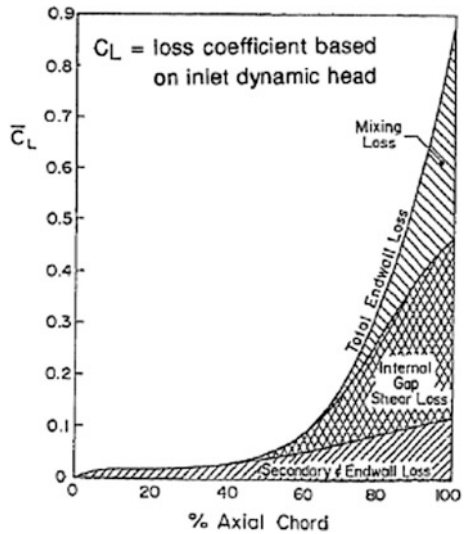


Fig. 2.29 Tip gap flow models for different gap sizes [21]

Fig. 2.30 Development of tip leakage losses in turbine passage [19]



leading to the tip leakage vortex through rolling. Figure 2.30 shows the development of endwall loss of unshrouded blades.

There are two main techniques to control tip leakage flows, which are Active Clearance Controls (ACC) and Passive Clearance Controls (PCC). They can be further divided into the following five kinds according to specific protective measures: Active Thermal Clearance Controls, Active Mechanical Clearance Controls, Active Pneumatic Clearance Controls, Passive Thermal Clearance Controls, and Passive Pneumatic Clearance Controls [18].

Active Thermal Clearance Controls: air from compressors or fans is used to heat (expansion) or cool (contraction) the sealing components on the upper endwall so as to change the size of the clearance. This technique is widely used in modern gas turbine engines for turbine clearance control. One of its disadvantages is its slow thermal response, which limits its application range.

Active Mechanical Clearance Controls: this technique adopts linkage units and excitations (such as hydraulic, electromechanical, and electromagnetic devices, etc.) to change the gap radius of rotor blade tip and thus change the clearance size. A typical example of this system is described as follows: divide the upper endwall into several sections all of which are connected to a ring with the same curvature as the endwall; Through radial rods (spokes) used as the linkage unit, when the ring rotates in a direction or the other direction, the endwall components will move inwards or outwards in a radial manner. This system needs an excitation source that can operate in high-temperature environments. Therefore, its choke point is the absence of exciters and sensors operating in the circumstance of high temperature.

Active Pneumatic Clearance Controls: This technique is aimed to achieve load shift by using a valve to adjust turbine internal pressure and external pressure. The clearance can be changed in a radial manner through sealing upper endwall components or setting up some air boxes. This system is vulnerable to high cycle fatigue (HCF) and very sensitive to pressure balance.

Passive Thermal Clearance Controls: the expansion and contraction processes of rotor blades and the stationary casing are matched dependent on material performance and engine temperature. Though this system is very accurate and reliable, it can only guarantee the optimal clearance for one operating condition. Thus, it is usually used in taking off.

Passive Pneumatic Clearance Controls: based on the driving caused by the gas pressure or power generated by engines, Wardle proposed the idea of floating endwall components. This system requires considerably high accuracy of position, and is very complex generally and vulnerable to high cycle fatigue (HCF). The control effect of cooling air ejected from blade tip in the system falls into the category of using aerodynamic effects.

2.5.1 Geometrical and Aerodynamic Parameters on Tip Leakage Flows in High Pressure Turbines

2.5.1.1 Geometrical and Aerodynamic Parameters on Tip Leakage Flows in Unshrouded Turbines

Tip leakage flows in high-pressure turbines are influenced by the comprehensive effects of many geometrical and aerodynamic parameters, and present a complex three-dimensionality. To explore the influencing factors to tip leakage flows, different leakage flow loss models are used here in unshrouded high-pressure turbines.

Flow losses in the cascade passage can be divided into profile loss, secondary flow loss, and leakage flow loss:

$$\zeta_t = \zeta_{\text{profile}} + \zeta_{\text{secondary}} + \zeta_{\text{tip}} \quad (2.16)$$

The tip leakage loss can be obtained by subtracting the no-clearance loss from the total loss:

$$\zeta_{\text{tip},\tau} = \zeta_t - \zeta_{t,\tau=0} \quad (2.17)$$

In Traupel's model [22], the efficiency reduction, caused by tip leakage flows, is a function of tip gap size, blade height, chord length, tip radius, and mean diameter:

$$\Delta\eta = K_\delta \frac{(\tau - 0.002C)R_{\text{tip}}}{HR_{\text{mean}}} \quad (2.18)$$

where, K_δ is related to the turning angle of cascade flow, C is the chord length of the blade.

Ainley and Mathieson's model [23] assumes that the total pressure loss coefficient is independent of Mach number, and the outlet flow angle is independent of incidence angle at the inlet. In this model, the leakage flow loss is a function of the loading coefficient of the blade, with the ratio of clearance size to blade height as a supplement:

$$\zeta_{\text{tip},\tau} = B \left(\frac{\tau}{H}\right) \left(\frac{C}{s}\right)^2 C_L^2 \left(\frac{\cos^2 \alpha_2}{\cos^3 \alpha_m}\right) \quad (2.19)$$

where, α_m is the average flow angle, $\tan \alpha_m = 0.5 \times (\tan \alpha_1 + \tan \alpha_2)$, α_1 represents the inlet flow angle, α_2 represents the outlet flow angle of the rotor blade, C_L represents the lift coefficient, $C_L = (C/s) \times 2(\tan \alpha_1 - \tan \alpha_2) \cos \alpha_m$, B is a constant, which is taken as 0.5 for radial clearance, and 0.25 for the structure with shrouded seal.

In Dunham and Came's model [24], the tip leakage loss is a function of blade loading and the ratio of tip clearance to blade height. Different from Ainley and Mathieson's model in which tip leakage loss is regarded as a linear function of the tip gap size, Dunham and Came believed the tip loss is a power function of the tip gap size:

$$\zeta_{\text{tip},\tau} = 0.47 \left(\frac{C}{H}\right) \left(\frac{\tau}{C}\right)^{0.87} \left(\frac{C}{s}\right)^2 C_L^2 \left(\frac{\cos^2 \alpha_2}{\cos^3 \alpha_m}\right) \quad (2.20)$$

Kacker and Okapuu's model [25] sets out two computing methods of tip leakage loss respectively for shrouded blades and unshrouded blades. The loss calculation expression for unshrouded blades was obtained based on a large quantity of

experimental data. This model does not provide a method for directly calculating the loss coefficient which is obtained by deducing the changes of turbine stage efficiency and tip gap:

$$\frac{\Delta\eta}{\eta_{\tau=0}} = 0.93 \left(\frac{\tau}{H}\right) \frac{1}{\cos \alpha_2} \frac{R_{tip}}{R_{mean}} \quad (2.21)$$

where, $\eta_{\tau=0}$ represents the efficiency when the tip gap is 0; $\Delta\eta$ represents the change of stage efficiency, which is determined by η , τ , tip radius R_{tip} , mean radius R_{mean} , and α_2 .

In Craig and Cox' model [26], the tip leakage loss is obtained by solving the Eq. (2.21), where the turbine efficiency change caused by leakage flows is a function of leakage coefficient, tip gap area, and throat area of the blade:

$$\frac{\Delta\eta}{\eta_{\tau=0}} = F_k \frac{A_k}{A_t} \quad (2.22)$$

The leakage coefficient, F_k , is a function of speed ratio of tip gap inlet to outlet. When the speed ratio is small, flow acceleration in the cascade passage will result in a large pressure drop in the tip gap, thus leading to the increase of leakage flow rate as well as leakage loss; while the speed ratio is much large, the flow acceleration will be lower, so will the leakage flow loss.

Denton's model [27] was established by using boundary layer theory, basic thermodynamic equations, the mass-conservation equation, the momentum equation and energy equation under specific loss conditions:

$$\zeta = \frac{2C_d\tau C}{Hs \cos \alpha_2} \int_0^1 \left(\frac{V_S}{V_2}\right)^3 \left(1 - \frac{V_P}{V_S}\right) \sqrt{\left(1 - \left(\frac{V_P}{V_S}\right)^2\right)} \frac{dz}{C} \quad (2.23)$$

As to unshrouded blades, the leakage flow loss coefficient is a function of tip gap size τ , chord length C , blade height H , pitch s , relative velocity at the outlet V_2 , velocity on the pressure surface of the blade V_P , and velocity on the suction surface of the blade V_S .

The leakage flow loss model for unshrouded blades, established by Denton, is shown in Fig. 2.31. If assume that the chordwise velocity component of the leakage flow, when passing through the tip gap, stays unchanged, and is equal to the component of the tip velocity along the direction of the pressure surface, V_P , the local leakage flow rate will be dependent on static pressure different between the suction and pressure side of the blade and C_d obtained by using the flow coefficient; the flow coefficient can be obtained through either two-dimensional flow calculation or experience. Therefore, when the leakage flow reaches the suction surface, there is a velocity component V_P in streamwise direction which becomes V_S after mixing with the surrounding flow soon, however. The cooling jet model is used for the mixing, without stagnation temperature difference.

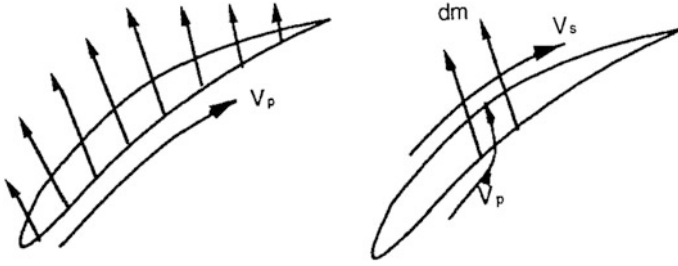


Fig. 2.31 Leakage flow loss model [27]

When the leakage flow passes through a differential part along the direction of the chord, there is

$$\Delta s_{irrev} = C_p(\gamma - 1)M^2\left(1 - \frac{V_p}{V_s}\right)\frac{dm}{m_m} \quad (2.24)$$

where, dm is the mass flow rate of the leakage flow; m_m is the mass flow rate of the main flow; the Mach number of main flow at the suction surface is taken as the Mach number at the merging place; thus, the equation above can be turned into:

$$T\Delta s_{irrev} = V_s^2\left(1 - \frac{V_p}{V_s}\right)\frac{dm}{m_m} \quad (2.25)$$

To obtain the total entropy generation, integrate the equation above along the axial direction of the blade, and one can be obtained:

$$T\Delta s_{tot} = \frac{1}{m_m} \int V_s^2\left(1 - \frac{V_p}{V_s}\right)dm \quad (2.26)$$

The above equation has been proven to be applicable for compressible flows with small temperature change.

On the assumption of two-dimensional flows, the local leakage flow can be obtained through solving the momentum equation in the direction perpendicular to the chord of the blade. The method is simple for incompressible flows and also applicable for compressible fluid as far as numerical calculation. For incompressible fluid, the leakage flow rate along the chord C of the blade is:

$$dm = C_d\tau\sqrt{2\Delta P}\rho dz \quad (2.27)$$

where, τ is the clearance size; C_d is the flow coefficient; ΔP is the pressure difference between the suction surface and pressure surface; C_d is often taken between 0.7 and 0.8. Substituting the equation above into Eq. (2.26), one can be obtained:

$$T\Delta s_{tot} = \frac{C_d \tau C}{m_m} \int_0^1 V_s^2 \left(1 - \frac{V_p}{V_s}\right) \sqrt{2\Delta P \rho} \frac{dz}{C} \quad (2.28)$$

Because the fluid is assumed to be incompressible, the velocity on the blade surface can be obtained through the following equation:

$$\Delta P = 0.5\rho(V_s^2 - V_p^2) \quad (2.29)$$

The total flow rate at a blade passage can be written:

$$m_m = \rho V_2 h s \cos \alpha_2 \quad (2.30)$$

Substitute it in Eq. (2.28),

$$T\Delta s_{tot} = \frac{C_d \tau C}{V_2 h s \cos \alpha_2} \int_0^1 V_s^3 \left(1 - \frac{V_p}{V_s}\right) \sqrt{1 - \left(\frac{V_s}{V_p}\right)^2} \frac{dz}{C} \quad (2.31)$$

Convert the total entropy increase to loss coefficient through $0.5 V_2^2$:

$$\zeta = \frac{2C_d \tau C}{h s \cos \alpha_2} \int_0^1 \left(\frac{V_s}{V_2}\right)^3 \left(1 - \frac{V_p}{V_s}\right) \sqrt{1 - \left(\frac{V_s}{V_p}\right)^2} \frac{dz}{C} \quad (2.32)$$

When the velocity on the blade surface is given, the above integral can be obtained. For turbine blades, V_s/V_2 is taken as one unit, and then V_p/V_2 is 0.3 in general, so the integral value is 0.65 roughly. When C_d is taken as 0.8, the loss coefficient is proportionate to leakage area τC , throat area of the blade $h s$, and $\cos \alpha_2$. Sometimes, this proportion can be used to reflect the tip leakage loss.

The above equation contains the term $\left(\frac{V_s}{V_2}\right)^3$, suggesting that high velocity on the suction surface of the high-loaded blade would result in great leakage loss, which is due to boundary layer loss.

The theory above on turbine is also applicable for compressor blades. By changing the subscript “2” in Eq. (2.32) to “1”, the equation turns to express the loss coefficient of the compressor based on the kinetic energy at the inlet. The coefficient is dependent on the area of the inlet, and the loss will increase with the increase of blade loading.

If the velocity on the blade surface is unknown, the velocity V_s , obtained on the assumption of evenly distributed blade loading, is very close to V_p , which can be described as follow.

$$V_s - V_p = \frac{S}{C} V_x (\tan \alpha_2 - \tan \alpha_1) \quad (2.33)$$

When the blade thickness is small, the following equation can be obtained according to the continuity:

$$V_s + V_p = \frac{2V_x}{\cos \alpha} \quad (2.34)$$

Local $\cos \alpha$ can be obtained by assuming a linear relation between $\tan \alpha$ and x . After knowing Eq. (2.33) and Eq. (2.34), are known, the loss coefficients of the turbine or compressor can be obtained by solving Eq. (2.32).

Baljí and Binsley [28] proposed a loss model, in which the loss coefficient is a function of inlet metal angle of the blade, blade height, blade pitch, thickness of the trailing edge, and tip clearance.

$$\zeta = 0.0696 \tanh(13 \frac{\tau}{C}) \frac{C D}{D H} \sin \alpha m (\cot \lambda_2 - \cot \lambda_1) \quad (2.35)$$

where, $\lambda_1 = \beta'_1 - 90^\circ$, $\lambda_2 = 90^\circ - \beta'_2$.

Yaras and Sjolander's loss model [29] was established on the basis of the energy method. It divides the clearance flow loss into loss in the clearance Y_{gap} and mixing loss that occurs after it flows out of the clearance and mixes with the main flow Y_{mix} .

$$Y_{gap} = 0.007 K_G \left(\frac{C}{s}\right) \left(\frac{C}{H}\right) C_D C_L^{0.5} \left(\frac{1}{\cos \alpha_m}\right) \quad (2.36)$$

where, K_E and K_G are the data related to blade loading distribution; when the blade is front-loaded, $K_E = 0.566$ and $K_G = 0.943$; when the blade is aft-loaded, $K_E = 0.5$ and $K_G = 1$.

$$Y_{mix} = 2 \times K_E C_D \left(\frac{\tau}{H}\right) \left(\frac{C}{s}\right) C_L^{1.5} \left(\frac{\cos^2 \alpha_2}{\cos^3 \alpha_m}\right) \quad (2.37)$$

All the above leakage flow loss model were established without taking into account the influence of tip cooling flow injection on the flow coefficient, so they would result in a major error in predicting the leakage flow loss under the conditions with tip cooling flow injection.

Hamik and Willinger [30] studied the leakage flow loss under the operating condition of tip air injection by using the finite volume method. Assumptions of the model include: (1) incompressible flows; (2) no consideration of relative rotation between blades and the casing; (3) no energy loss occurs when the flow passes through the clearance to the largest contraction surface; (4) on the largest contraction surface, velocity and static pressure are evenly distributed along the

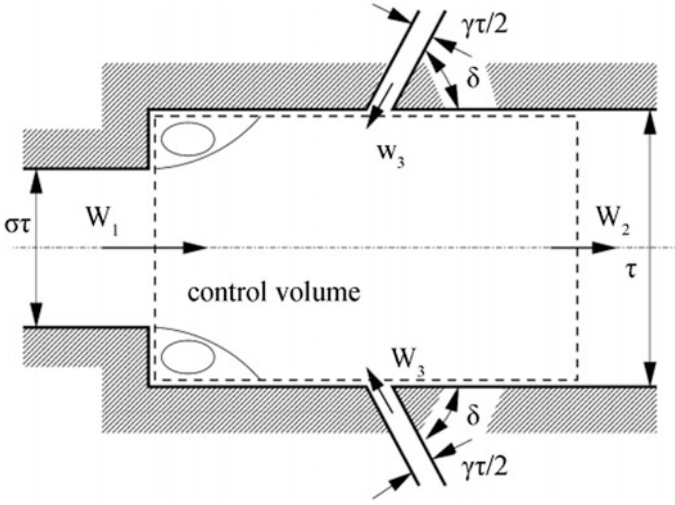


Fig. 2.32 Control volume used in Hamik and Willinger’s model [30]

direction of clearance height; (5) at the clearance outlet on the suction surface, the flow has been thoroughly mixed in the clearance, and velocity and static pressure are evenly distributed along the direction of clearance height.

Figure 2.32 shows the model of the control volume, which is in axially symmetrical distribution centered on the middle plane of the clearance. The left boundary of the control volume is the largest contraction surface in the clearance, and the right boundary is the outlet of the clearance. The length of the control volume in the direction perpendicular to the paper is equal to the chord of the blade. The flow coefficient in the condition of tip air injection can be written as follow:

$$C_D = \left[\left(2 + \frac{0.5\lambda t}{\tau} \right) (1 + \gamma\psi)^2 + \frac{1}{\sigma^2} - \frac{2}{\sigma} + 2\gamma\psi^2 \cos \alpha \right]^{-0.5} \quad (2.38)$$

where λ , is the friction coefficient of the air injection hole, $\lambda = 0.266/\text{Re}_T^{0.25}$ (applicable when $1160 \leq \text{Re}_T \leq 50,000$).

The contraction coefficient $\sigma = \pi/(\pi + 2) \approx 0.611$; the injection speed ratio $\psi = V_{inj}/\sigma V_{in}$; γ is the area ratio between air injection hole and clearance inlet, $\gamma = 0.25\pi r^2/\tau C$; after obtaining the expression of the flow coefficient, the leakage flow loss model for the condition of tip air injection can be established by using anyone of the leakage flow loss models containing flow coefficient.

Ainley and Mathieson, Dunhama and Came, and Kaeker and Okapuu respectively proposed the models for calculating tip leakage flow loss by simulating clearance vortexes and their induced vortexes, and all the models assume that flows are non-viscous and incompressible. Ainley and Mathieson are the first to consider the

influence of tip clearance in calculating secondary flow loss, and they believed that the tip leakage loss coefficient is a function of inlet and outlet flow angles and the ratio of clearance size to blade height. Based on experimental data about the cascade, Dunham & Came believed that the relation between the tip leakage loss and the ratio of the clearance size to blade height is not a simple linear relation, and they modified the model by introducing exponential relation. Taking Dunham and Came's model as the basis, Kaeker and Okapuor revised the leakage loss model for unshrouded tips based on experimental data. Craig and Cox believed the cascade efficiency reduction caused by leakage flows is a function of leakage coefficient, and the ratio of clearance area to throat area of the blade, and the leakage coefficient is a function of the speed ratio of clearance inlet to outlet. This model was established also based on experimental data on turbines.

Denton developed a simple leakage loss model based on the methods for analyzing clearance flows. In the model, the loss coefficient is a function of flow angle, clearance size, the ratio of blade height to chord length, flow velocity, and the flow rate ratio of the clearance flow to the main flow.

Baljé and Binsley's clearance loss model was established based on experimental data. In this model, the loss coefficient is a function of loading coefficient of the blade, the ratio of tip clearance size to blade height, and cascade solidity. It is very similar to Ainley and Mathieson's model.

Yaras and Sjolander's model was established based on the energy method. It divides the clearance flow loss into loss in the clearance and mixing loss that occurs after leakage flow flowing out of the clearance and mixing with the main flow.

Hamik and Willinger's model, based on Yaras and Sjolander's model, is a clearance flow loss model for the condition with tip cooling flow injection.

From the above-described models, it can be seen that geometrical parameters influencing the tip leakage flows in high pressure turbines include clearance height, metal angle of the inlet and outlet, blade spacing, chord length, blade height, tip diameter, mean diameter, flow turning angle, flow passage area, air injection position, etc. The aerodynamic parameters include inlet flow angle, outlet flow angle, lift coefficient, loading coefficient, flow rate, and so on.

2.5.1.2 Geometrical and Aerodynamic Parameters on Tip Leakage Flows in Shrouded Turbines

Egli [31] assumed that the kinetic energy of the leakage flow is zero when approaching to the first labyrinth seal. After a series of throttling actions, the leakage flow would obtain certain kinetic energy when it gets to the last labyrinth seal. It is also assumed that the leakage flow is subject to the Fanno line when it passes through the labyrinth seals, and it has no heat exchange with the surrounding environment. The flow rate of the leakage flow can be written as follow:

$$\dot{m}_L = A_{fin} C_c \psi_{th} \sqrt{p_{02} \rho_{02}} \quad (2.39)$$

where, ψ_{th} is the theoretical expansion factor, defined as:

$$\dot{m}_L = A_{fin} C_c \psi_{th} \sqrt{p_{02} \rho_{02}} \quad (2.40)$$

Using a large amount of experimental data obtained on an impulse test rig, Traupel worked out a loss relation model to estimate the leakage flow rate. In this model, the leakage flow rate is written:

$$m_L = A_{fin} \varepsilon \sqrt{p_2 \rho_2} \quad (2.41)$$

where, ε is a flow rate characteristic parameter of different labyrinth seals.

Egli's model is only applicable for adiabatic flows, and Traupel's empirical correlation coefficient is related to actual geometry and limited by parameters, including the relation between heat transfer and speed approaching to nonzero.

In Denton's leakage loss model for shrouded blades, it is assumed that the entropy generation of the tip leakage flow is mainly from the mixing between the leakage flow and the main flow. As for the shrouded blade, the leakage fluid would contract to a jet flow when passing through the labyrinth seal, and the contraction coefficient is often taken as 0.6. When there is no great drag in the upstream of the labyrinth seal, the process of the fluid reaching the throat of the jet flow can be regarded as a isentropic one. The leakage flow rate is dependent on the size of the sealed clearance, contraction coefficient, meridional velocity-based stagnation pressure, and static pressure of the jet flow. The static pressure of the jet flow would be influenced by the mode of the leakage flow joining into the main flow. If there is no significant flow drag below the labyrinth seal, the static pressure of the jet flow will be close to the pressure of the main flow (see Fig. 2.33).

The leakage flow mixes with the main flow outside of the clearance, mixing which is an irreversible entropy increasing process. In most actual cases, the clearance of shroud is much larger than that of leakage jet flow, so all the kinetic energy of the jet flow relating to the velocity on the meridian plan dissipates. In this process, Denton and Johnson (1976) believed the circumferential velocity of the leakage flow is not much different from the velocity when it approaches to the blade [64].

When the leakage fluid rejoins into the main flow, the difference between the meridional velocity and circumferential velocity of the two flows would result in additional mixing loss, and the entropy production is as follows:

$$\Delta s = C_p \frac{m_c}{m_m} \left[\left(1 + \frac{\gamma - 1}{2} M_m^2 \right) \frac{T_{oc} - T_{om}}{T_{om}} + (\gamma - 1) M_m^2 \left(1 - \frac{V_c \cos \alpha}{V_m} \right) \right] \quad (2.42)$$

When the temperature of the two flows is same, the entropy generation rate can be written:

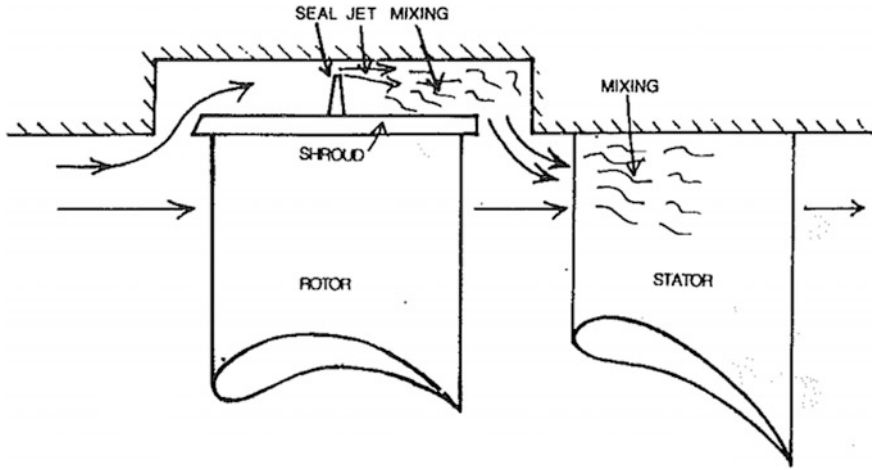


Fig. 2.33 Labyrinth seal structure of shrouded turbine

$$Tm_m \Delta s = T\dot{S} = m_c (V_m^2 - V_m V_c \cos \alpha) \tag{2.43}$$

The entropy generation Eq. (2.42) suggests that it should reduce the injection angle of the leakage flow into the main flow in the meridian plane as well as velocity difference between the two flows as far as possible. However, in many cases, the difference of circumferential velocity dominates, and it is independent on the direction of the jet flow. If the circumferential velocity of the leakage flow in the clearance does not change much, the difference of circumferential velocity will be the same as that when it passes through the blade. Based on the assumption above, a model, referred as shrouded turbine leakage loss theory, was proposed by Denton. As shown in Fig. 2.35, it is assumed that there is no loss and tangential action when the leakage flow reaches the throttling throat; so, the tangential velocity stays unchanged before interacting with the main flow. It is also assumed that, except for the location of labyrinth seals, there is no large drag at the rest of the clearance. Therefore, the static pressure of the leakage flow in the clearance downstream of the labyrinth seals is the same as that at the outlet of the blade. The leakage flow is observed in a relative coordinate system. If radius change is neglected, the leakage flow and the main flow will have the same relative stagnation enthalpy, which is a constant (see Fig. 2.34).

For simplicity, it is assumed that the leakage fluid is incompressible, and this assumption can be expressed by other complex equation. At the throat, this assumption can be described as follows:

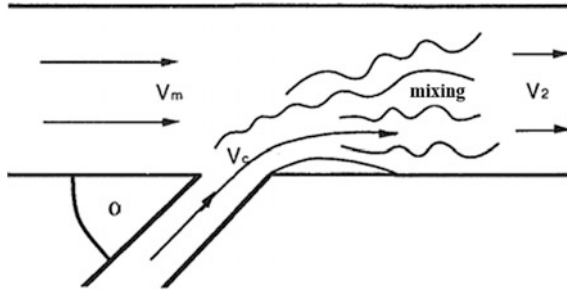


Fig. 2.34 Mixing loss of two flows with different velocity and temperature

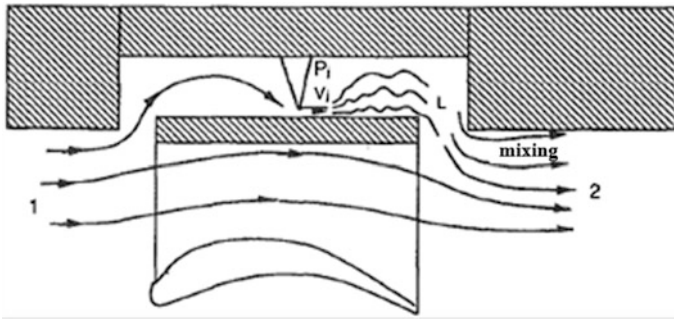


Fig. 2.35 Flows through shrouded seal structure

$$p_0 = p_{01} = p_j + 0.5\rho V_j^2 + 0.5\rho V_{\theta 1}^2 = p_2 + 0.5\rho V_2^2 \tag{2.44}$$

where, V_j is the axial velocity of the jet flow.

Assume $p_j = p_2$, and then one can be obtained:

$$V_j = \sqrt{V_2^2 - V_{\theta 1}^2} \tag{2.45}$$

The flow rate of the leakage flow is:

$$m_L = \rho g C_c \sqrt{V_2^2 - V_{\theta 1}^2} \tag{2.46}$$

where, C_c is the contraction coefficient of the jet flow; the proportion of the leakage flow is:

$$\frac{m_L}{m_m} = \frac{gC_c \sqrt{V_2^2 - V_{\theta 1}^2}}{hV_2 \cos \alpha_2} \quad (2.47)$$

where, h is the blade height. If V_x stays constant when the leakage flow passes through the blade, then the equation above can be written as a function of flow angles:

$$\frac{m_L}{m_m} = \frac{gC_c}{h} \sqrt{\sec^2 \alpha_2 - \tan^2 \alpha_1} \quad (2.48)$$

Entropy increase of the main flow only occurs during the mixing with the leakage flow. If the axial velocity and tangential velocity of the leakage flow are respectively V_{xL} and V_L when it joins into the main flow, then the conservation equation can be used to describe the vortex caused by the tangential jet flow, and the losses caused by the axial flow and tangential flow can be analyzed separately:

$$T\Delta s = \frac{m_L}{m_m} \left[V_{\theta 2}^2 \left(1 - \frac{V_{\theta L}}{V_{\theta 2}} \right) + V_{x2}^2 \left(1 - \frac{V_{xL}}{V_{x2}} \right) \right] \quad (2.49)$$

The method is also applicable for compressible flows. If the geometrical size of the gap where the leakage flow rejoins into the main flow is unknown, V_{xL} cannot be obtained. However, it can be neglected in most cases, because the gap is wide and the leakage flow joins the main flow basically in radial direction. Therefore, the influence of V_{xL} is neglected, and then one can be gotten:

$$T\Delta s = \frac{m_L}{m_m} V_2^2 \left(1 - \frac{V_{\theta L}}{V_{\theta 2}} \sin^2 \alpha_2 \right) \quad (2.50)$$

Assume that the axial velocity of the leakage flow when passing through the blade is a constant, and the equation above becomes simpler:

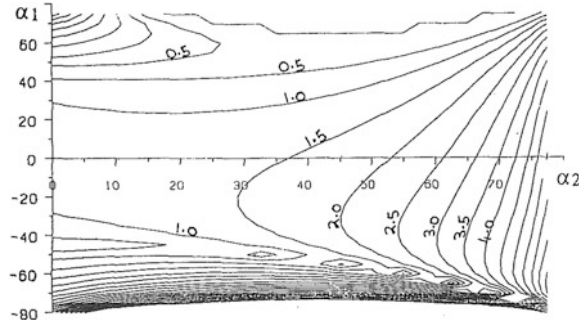
$$\frac{T\Delta s}{0.5V_2^2} = 2 \frac{m_L}{m_m} \left(1 - \frac{\tan \alpha_1}{\tan \alpha_2} \sin^2 \alpha_2 \right) \quad (2.51)$$

When m_L/m_m is appropriately calculated, the above equation is also applicable for compressible flows. Loss prediction by the model is shown in Fig. 2.36.

Denton's model does not take into account the number of seals, and the temperature difference between the leakage flow and the main flow is neglected when calculating the mixing loss of the two. Thus, the entropy generation in the entire mixing process is underestimated by 20%.

Dosoky et al. [32] established a mixing loss model for steady tip leakage flows. They used flow parameters actually measured to analyze the influence of the

Fig. 2.36 Tip clearance leakage loss of shrouded turbine, Percentage contour of kinetic energy at the outlet corresponding to each 1% of the clearance size



leakage flow on the performance of shrouded turbine stage. The model performs well in predicting the flow coefficient of the leakage flow, tip leakage flow, and mixing loss. By introducing the interaction between the leakage flow and the main flow, the model analyzes the generation of negative incidence. The loss will increase with the increase of angle of leakage flow injection. The model also describes the geometry parameters of the labyrinth seals related to leakage loss and turbine efficiency, such as clearance width, number of labyrinth seals, etc. The comparison with the baseline data shows the model has good consistency between qualitative and quantitative analysis. Increasing the number of labyrinth seals can increase the drag of the labyrinth passage, and thus increase the flow rate of the leakage flow. However, when the number of labyrinth is more than 3, this effect attenuates. The size of the sealed clearance is in direct proportion to the flow rate of the leakage flow, tip leakage loss coefficient, and total mixing loss coefficient. When the leakage flow mixes with the main flow, the loss caused by the traditional mixing in 90° is 28% higher than the loss caused by the mixing in which the leakage flow is parallel with the main flow.

In the downstream of the trailing edge of the rotor blade, the leakage flow above the shroud rejoins into the main flow. Because the two flows have different speeds, the mixing of the two results in entropy increase. It is assumed that the leakage flow is adiabatic when it passes through the labyrinth seals, and its pressure is the same as that of the main flow in the downstream of the rotor blade when mixing with the main flow. Namely, except for the labyrinth seals, the drag of the rest clearance is rather small. The pressure drop caused by each labyrinth seal is approximately equal to that obtained by using Denton's model. When the leakage flow mixes with the downstream main flow, the secondary flow effect of the main flow, especially in the high-pressure turbines with low aspect ratio, is particularly obvious (see Fig. 2.37).

The quantitative model includes two parts. The first part is intended to predict the flow conditions at both the trailing edge of the rotor blade and the outlet of the labyrinth seal, as indicated by 3 and L in Fig. 2.38. The target zone of the second

Fig. 2.37 Simple geometry of typical shrouded high-pressure turbine with labyrinth seals [32]

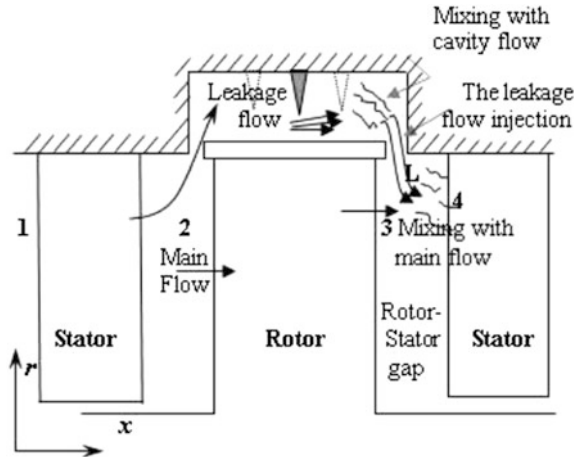
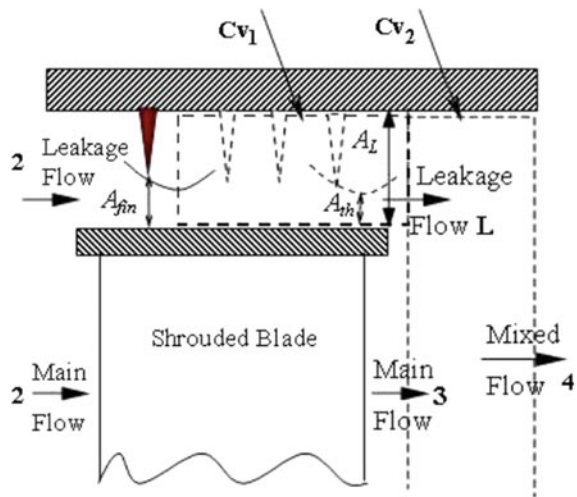


Fig. 2.38 Control volume model of shrouded turbine stage, meridian plan (x, r)



part extends to the junction of rotor and stator blades in the downstream, and it is intended to predict the mass-average mixing entropy loss coefficient.

When the inlet total temperature T_{01} , inlet total pressure p_{01} , flow coefficient ϕ , rotating speed, and outlet flow angle of the stator are given, the tangential velocity in state 2 can be obtained by calculating the circumferential velocity and the velocity of the main flow. The temperature in state 2 also can be obtained according to the first law of thermodynamics. The stagnation pressure at the inlet of the rotor blade can be obtained by substituting the total pressure of the stator and the total pressure loss coefficient Y_{IN} in the equation below:

$$p_{02} = p_{01} \left[Y_{tN} \left(1 - \frac{p_2}{p_{02}} \right) + 1 \right] \quad (2.52)$$

Using the distribution of turbine stage reaction Λ , the static temperature distribution can be obtained:

$$\Lambda = \frac{T_2 - T_3}{T_1 - T_3} \quad (2.53)$$

The relation between the work done by the turbine and the stagnation temperature at the outlet of the rotor can be written as follow:

$$W = U \Delta V_\theta = C_p (T_{01} - T_{03}) \quad (2.54)$$

where, ΔV_θ is the variation of tangential component of the rotor's absolute velocity; C_p is the specific heat at constant pressure.

$$C_p T_{03} = C_p T_3 + \frac{V_{\theta 3}^2 + V_{x3}^2}{2} \quad (2.55)$$

By solving the Eq. (2.54) and Eq. (2.55), the components, $V_{\theta 3}$ and V_{x3} , of the absolute velocity can be obtained. As for the control volume C_{V1} enclosed by a dotted line in Fig. 2.38, assuming that there is no significant reduction of the tangential component before the flow reaching the throat area, the following equation can be obtained according to the mass-conservation equation, momentum equation, and energy equation:

$$p_{th} + \frac{\dot{m}_L}{A_L} V_{thx} = p_L + \frac{\dot{m}_L}{A_L} V_{Lx} \quad (2.56)$$

The subscripts *th* and *L* in Eq. (2.56) represent the shroud throat and outlet respectively. V_{thx} and V_{Lx} represent the axial velocity of the leakage flow at the throat and outlet respectively. The pressure p_L of the leakage fluid after it passes through the last labyrinth seal is:

$$p_L = p_3 \quad (2.57)$$

The pressure drop at each labyrinth seal is approximately equal to the result of dividing the total pressure drop across the blade by the number of the labyrinth seals:

$$p_{th} = p_2 (T_{th}/T_2)^{\frac{\gamma}{\gamma-1}} \quad (2.58)$$

By solving the simultaneous Eq. (2.56) and Eq. (2.58), the pressure and temperature at the throat can be obtained. Then, the density at the throat can be obtained. The actual flow rate of the leakage flow can be obtained by using the following equation:

$$\dot{m}_L = C_d(\rho AV)_{th} \quad (2.59)$$

where, C_d is the flow coefficient of the leakage flow; A_L is the annular area above the shroud; ρ is the density of the fluid; γ is the specific heat ratio. The Eq. (2.59) can be turned into the follow one:

$$\dot{m}_L = C_d \rho_{th} A_{th} \sqrt{2 \frac{\gamma}{\gamma - 1} \frac{p_{02}}{\rho_{02}} r^{\frac{2}{\gamma}} \left(1 - r^{\frac{\gamma-1}{\gamma}}\right)} \quad (2.60)$$

Because the pressure ratio of each labyrinth seal is above 0.5, the flow coefficient C_d can be obtained by using Uerner equation:

$$C_d = \sqrt{\frac{C_c^2(1 - \beta^4)}{1 - C_c^2\beta^4}} \quad (2.61)$$

where, the diameter ratio is:

$$\beta = \sqrt{A_{fin}A_L} \quad (2.62)$$

$$C_c = \left(1 + \sqrt{\frac{1 - \beta^2}{2}}\right)^{-1} \quad (2.63)$$

$$C_c = A_{th}/A_{fin} \quad (2.64)$$

where, A_{fin} , A_L , and A_{th} present respectively the area of the ring between the top of the labyrinth seals and the shroud, the area of the ring between the shroud and the casing, and the area of the ring at the throat. The flow parameters at the outlet section of the rotor blade (position 3) and at the outlet of the clearance (position L) can be obtained by solving the Eq. (2.62) and Eq. (2.64).

The second part of the model is targeted at the control volume C_{V2} enclosed by a dotted line in Fig. 2.39. In this control volume, the leakage fluid mixes with the main flow. The equation of continuity can be written as follow:

$$\rho_4 V_4 \cos \alpha_4 A_4 = \rho_L V_L \cos \alpha_L A_L + \rho_3 V_3 \cos \alpha_3 A_3 \quad (2.65)$$

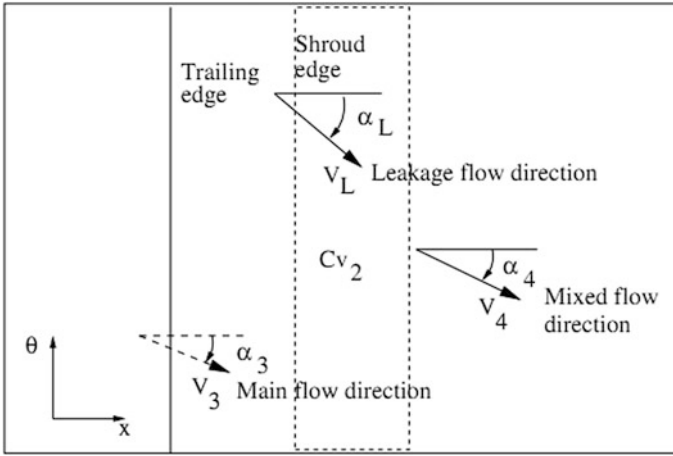


Fig. 2.39 Control volume C_{V2}

The momentum equation in circumferential direction can be written:

$$\rho_4 V_4^2 \cos \alpha_4 \sin \alpha_4 A_4 = \rho_L V_L^2 \cos \alpha_L \sin \alpha_L A_L + \rho_3 V_3^2 \cos \alpha_3 \sin \alpha_3 A_3 \quad (2.66)$$

The momentum equation in axial direction can be written:

$$(\rho_4 V_4^2 \cos^2 \alpha_4 + p_4) A_4 = (\rho_L V_L^2 \cos \alpha_L + p_L) A_L + (\rho_3 V_3^2 \cos \alpha_3 + p_3) A_3 \quad (2.67)$$

The energy equation for the control volume C_{V2} can be written:

$$\dot{m}_4 h_{04} = \dot{m}_L h_{0L} + \dot{m}_3 h_{03} \quad (2.68)$$

where

$$h_0 = C_p T + \frac{V^2}{2} \quad (2.69)$$

The entropy S is a function of temperature and pressure in the circumstance of ideal gas in the baseline S_{ref} . Assume that the gas passing through the turbine is ideal, and then the entropy increase equation of the mixing process can be written as follows:

$$s - s_{ref} = C_p \ln \frac{T}{T_{ref}} - R \ln \frac{p}{p_{ref}} \quad (2.70)$$

Or

$$s - s_{ref} = C_v \ln \frac{T}{T_{ref}} - R \ln \frac{\rho}{\rho_{ref}} \quad (2.71)$$

The subscript “ref” represents reference conditions, which are generally presented as the inlet conditions of the turbine stage. The entropy generation in the mixing process is described according to the second law of thermodynamics. The entropy generation in the control volume is equal to the static entropy flow in C_{V2} :

$$\Delta \dot{S}_{mix} = \dot{m}_4 S_4 - (\dot{m}_3 S_3 + \dot{m}_L S_L) \quad (2.72)$$

Thus, mass-average mixing entropy loss coefficient is equal to:

$$\left(\frac{T_4 \Delta \dot{S}}{0.5 \dot{m}_4 V_2^2} \right)_{mix} \quad (2.73)$$

The gas, which passes through the blade tip of typical shrouded turbines, has the characteristics of high temperature, high vorticity, and low axial momentum, which result in the wall loss and mixing loss between the shroud and casing.

2.5.2 Active Clearance Controls

Due to Working in a wide range of rotor rotating speed and temperature of aircraft engines rotor, its radial clearance at the tip may change a lot. In flying process, a wide change of engine power would result in relative mechanical movement between blade tip and the casing as well as thermal expansion of the components. In addition, excessive flight load on the engine and engine vibration could bring about additional deformations to the parts. The problem becomes more complex when considering the normal manufacturing tolerances of many engine parts that work together, especially for those that would influence the concentricity of the rotor. In conclusion, it is extremely difficult to maintain a close operation clearance during all the flying conditions.

By taking into consideration the random changes of flight load, engine vibration, and tolerances, the minimum radial clearance can be obtained. Generally, it can be proved that the radial clearance in the taking-off condition is greater than in the cruising condition. After determining the factors influencing the minimum operation clearance, the influence of fast-changing engine power on the clearance size must be then determined. The influence of these transitional states on the clearance may be greater than the total influence of all the other factors. Figure 2.25 shows the changes of the clearance in the entire flying process.

The efficiency of all the components, must be kept at a high level during the design of aircraft engine. Taking E3, a high-performance engine, as an example in studies to find out the key factors in some components that potentially influence the performance, the results showed that the blade clearance would exert significant influence on the performance of the compressor, high-pressure turbine, and low-pressure turbine. No matter how small the clearance is set in assembly, if there is not an independent control method in all the operating conditions, the clearance cannot always stay at the minimum level and the size of the tip clearance of the rotor blade would be influenced by various kinds of factors.

(1) Transient heat and mechanical expansion

In the period from ground idle to takeoff at the maximum power, which takes about 10–20 s, the blades extension due to rotor rotation and heat is faster than the expansion of the casing due to heat, so the tip clearance would become smaller, which may even cause friction.

(2) Engine bending

The thrust generated in the engine has to be transferred to the airframe through the engine mount, and engine bending occurs in this process. The thrust required in a takeoff from static state at sea level is about 6 times as much as that required in the cruising condition. Large taking-off thrust would result in deformation of the engine casing, friction at one part of the turbine nozzle, and excessive clearance at the other part. After that the thrust decreases, the casing would return to be round and the clearance at the position where the friction occurred would naturally become larger. Aircrafts' maneuver load also would result in bending of the rotor that bears a large load in a short time, and the bending would cause friction between the rotor blades and the outer ring, and thus result in unrecoverable increase of the clearance (if no other measures are taken).

(3) Rotor and nozzle vibration

In the working process of the engine, the rotor would be affected by various vibrations of different degrees which is dependent on the rotor's natural frequency and excitation frequency that may be generated in the working process of the engine. When the excitation frequency is close to the rotor's natural frequency, the vibration would get worse. In this case, the casing and guiding parts would also vibrate, and thus the possibility of friction on the rotor blade would be higher.

2.6 Influence of Interaction Between Cooling Flow and the Main Flow on Aerodynamic Performance

2.6.1 Influence of Film Cooling on Aerodynamic Performance

Film cooling refers to the practice of injecting secondary flows (cooling flow or jet flow) from one or more discrete holes on the high-temperature surface so as to protect the surfaces in the jet region and downstream region [33]. The cooling flow is injected to different positions through the discrete holes on blades. Compared to the internal cooling method that takes away heat from the inner surface, the cooling flow can directly protect the blade surface. In addition, film cooling can also remove heat from the blade surface within the film holes. The thermal protection can lower the thermal load on the blade surface. However, the injection of cooling flow would inevitably bring some effects on the aerodynamic design of turbine.

The purpose of cooling structure design is to improve the cycle efficiency of the overall unit as far as possible on the premise of guaranteeing the service life. Therefore, an efficient cooling process is required in all cooling parts of turbine. Because cooling flow does not participate in the working cycle, the cooling process is a kind of loss. So, it is necessary to reduce the total cooling flow rate, such as optimizing the cooling structure and improving heat transfer. For the thermally high-loaded turbine blades, both film cooling and internal convection cooling are generally used to ensure that the wall temperature is below the maximum tolerable temperature of the metal.

NASA sets out the following influence of the cooling flow on the blade's aerodynamic force and heat transfer [34]. (1) The aerodynamic loss of the jet flow varies greatly with the location of jet holes on the blade. Only 10–50% of the ideal kinetic energy of the cooling flow, which is jetted from the middle and rear part of the blade back, can be used, while this proportion rises up to 80% for the cooling flow jetted from the leading edge of the suction side and the entire pressure side (except for some areas in the trailing edge). (2) The flow rate and loss of the cooling flow jetted through multi-row film holes neither increase nor decrease, and simple superposition is applicable. (3) The jet angle of cooling flow can influence both cooling effect and aerodynamic loss. Therefore, in the high-speed zone of the profile, a compromise between cooling and aerodynamic performance should be made. Cooling flow jetting with large chordwise velocity and small spanwise velocity could achieve desirable cooling effect and surface coverage and small aerodynamic loss as well. While the jet angle of the cooling flow, which is jetted from the leading edge and pressure side, has little effect on aerodynamic performance. (4) Full-coverage film cooling would badly influence the thermal efficiency of advanced high-temperature turbines. (5) With respect to the stator or rotor blades, equipped with internal convection cooling, film cooling would bring about negative effects in some cases (generally referring to the cases of the ratio of cooling flow and gas flow less than 0.01). (6) Proper combinations of

film cooling and internal convection cooling can achieve lower mean blade temperature than that obtained by separating use of the two methods. (7) The results of the cooling efficiency study on flat show that, when the blowing ratio is 0.5, injecting the cooling flow into the main flow at a small angle (35°) can reach relatively high film cooling efficiency, and the efficiency gradually decreases with the distance increase.

2.6.1.1 Leading Edge Cooling

The leading edge of the blade is confronting very high gas temperature, intensive incoming flow turbulence and strong unsteady effect. So, it is a challenge for designers to design cooling structure for the area. Leading edge film cooling has been typically used in this area. In the past, a lot of experiments and numerical studies were carried out to understand the physical phenomenon of leading edge flows and obtain film cooling efficiency and heat transfer coefficient [35]. Considering the changes of the stagnation line in radial direction and the influence of secondary flows, the film holes should be provided with a radial angle, so as to increase the convective heat transfer coefficient in the holes and film coverage. In fact, the stagnation line is an imaginary line, and its location is unsteady in turbine. Generally, more film cooling holes should be placed on both sides of the line to balance the unsteady effect (see Fig. 2.40 and Fig. 2.41).

2.6.1.2 Trailing Edge Cooling

It is another challenge to cool down the trailing edge of the blade, which is mainly due to the geometry limit by aerodynamic design. From the perspective of aerodynamics, thinner trailing edge is always the better. However, this conflicts with cooling design and structural integrity. The one-side slot on the pressure side is

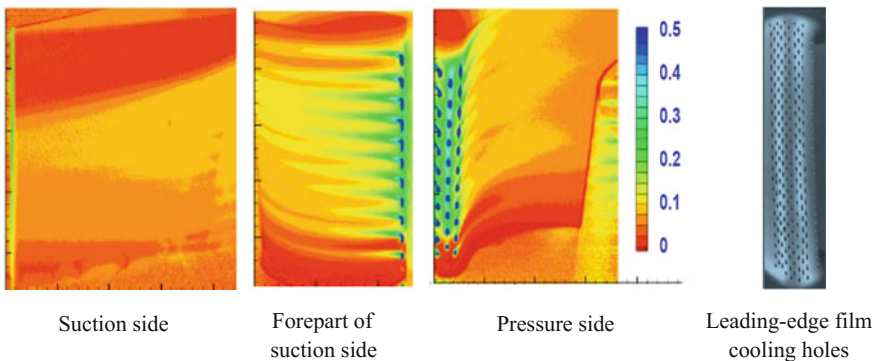
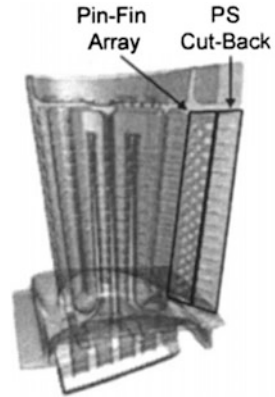


Fig. 2.40 Leading-edge film holes and their coverage [35]

Fig. 2.41 Trailing edge of typical turbine structure [36]



generally used in cooling structure design for stator blades, namely, the trailing edge area on the pressure side is shorter than that on the suction side, in which the cooling flow is injected passing through the one-side slot. To guarantee the structural strength in the trailing edge area, arrays of rib turbulators or pin fins should be placed on the cooling passage between the pressure side and suction side, so as to increase turbulence intensity to improve the internal convection heat transfer coefficients, and meanwhile control the cooling flow rate on the blades.

The film cooling formed by the slot is a complex 3-D structure, especially when the turbulators are placed near the jet slot. Mixing of two kinds of flows occurs near the trailing edge, which is caused by not only different momentums, but also physical dimensions and outlet shape of the slot. Uzol [37, 38] studied the outflow phenomenon at the trailing edge slot for blades with different one-side slot length. Changes of total pressure in the wake region suggest that one-side slot would incur smaller aerodynamic loss compared to both-side slot (see Fig. 2.42).

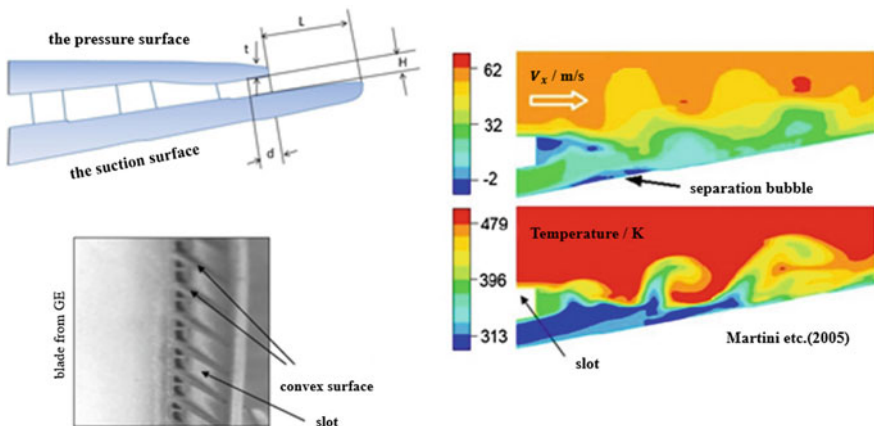


Fig. 2.42 Structures and flow field in trailing edge [36–38]

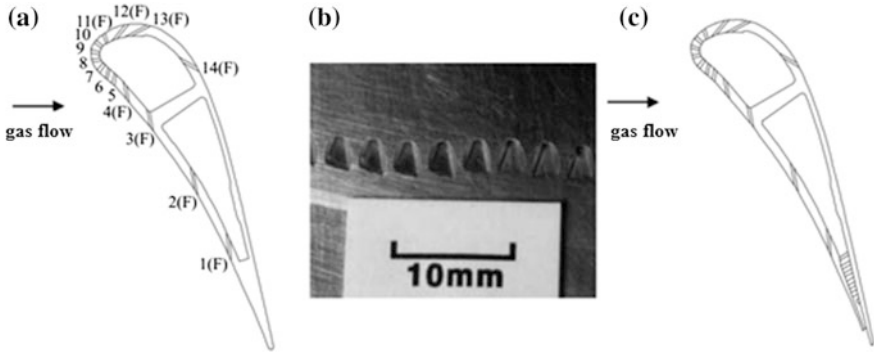


Fig. 2.43 Fan-shaped stator blades in Day's study [39]

Day et al. [39] published their measurements of effectiveness of the stator blade models with different forms of film cooling holes, used by Day et al. in 1999. Their experiment was carried out in an annular transient percussive cascade located in a Cold Heat Transfer Tunnel (CHTT), and flows injected from round holes and fan-shaped holes were compared. Figure 2.43 shows the fan-shaped stator blades used by Day et al.

Figure 2.44 shows the contour of regularized stagnation pressure relative to the upstream stagnation pressure on the measured surface. The subfigures respectively represent different cooling structures: (a) without cooling jet flows, (b) with round-hole cooling structure, (c) with fan-shaped cooling structure, (d) with trailing-edge jet flow, (e) with trailing-edge jet flow plus round-hole cooling structure. The cooling structures (a) and (c), which had no trailing-edge jet flow, had the same wake shape. The deepest sinking point of the wake flow was located on the diameter of the stator blade pitch circle. The wake flow became narrower and shallower along the direction towards the endwall. Basically, the cooling jet flows could not widen the wake flow, and the fan-shaped cooling structure brought the widest wake flow. Thus it can be seen that ejecting of cooling flow would result in greater aerodynamic loss. The wake flow became narrower and more curved after the trailing-edge jet flow entering the flow passage. The jet flow makes the wake flow more sunk, but no changes to the shape of it. It can be seen clearly from the above results that the shape of wake flow and the loss are mainly dependent on the form and location of the cooling jet flows.

By virtue of the CFD method, Kubo et al. [40] studied the changes of stagnation pressure loss of linear stator cascade, which was caused by the film jet flow. Figure 2.45 shows the structures of stator blades and cooling holes. They compared their results with what Otomo et al. [41] obtained by using a low-speed wind tunnel apparatus. The stagnation pressure loss coefficient c_{pt} between the inlet and outlet of the nozzle cascade was determined by the Equation: $c_{pt} = (P_{t1} - P_{t2}) / (P_{t1} - P_{s2})$, where P_{t1} , P_{t2} , and P_{s2} respectively represent the stagnation pressure at the inlet and outlet of the cascade, and the static pressure at the outlet.

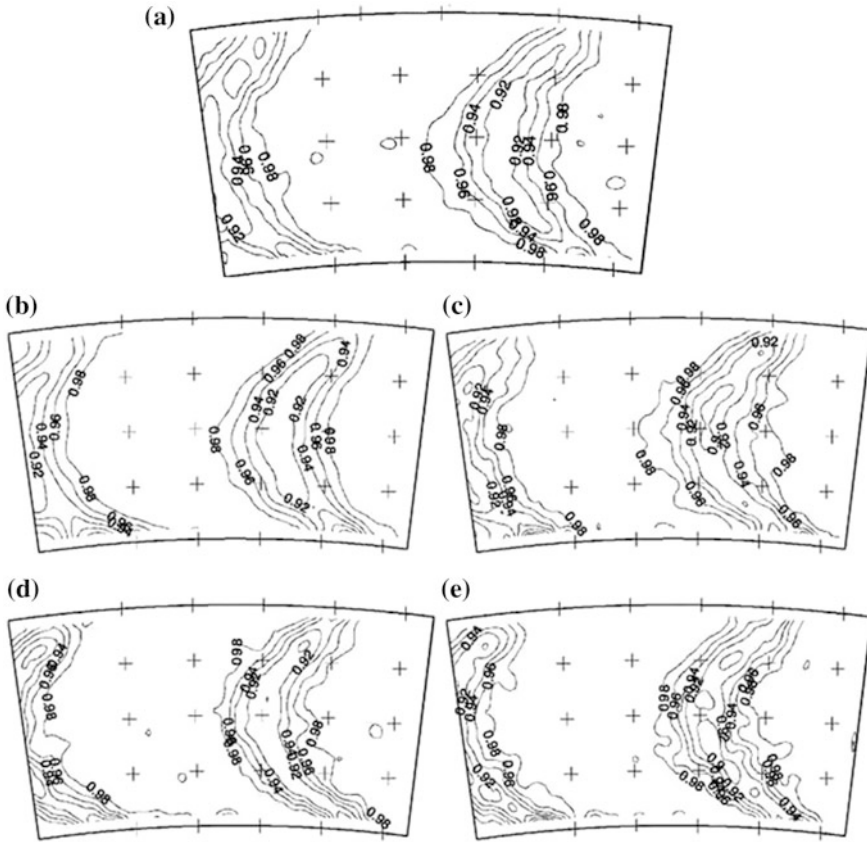


Fig. 2.44 Contour of stagnation pressure [39]

Figure 2.46 shows the loss coefficient curve, which was obtained through experiments under the condition of complete rows of jet flows. This means flows were injected from each row of film holes. The ratio of the mass flow rate of each row of jet flows to the total mass flow rate was respectively 8.4% (SH), 14.4% (S1), 22.6% (S2), 11.3% (P1), 10.9% (P2), and 32.4% (TE), and the ratio was independent of the mass flow rate ratio of the total cooling flow to the gas (G_c/G_g). The results showed that the wake flow loss curve had a deflection at the suction side slope (throat), where the loss peak got to the maximum. Similarly, the wake flow in the cases with cooling jet flows was wider than that without cooling jet flows. The results also show the jet flow losses in different forms of jet flows. The loss ratios of the rows P1 and P2 were high when G_c/G_g was at the lowest, and decreased with the increase of G_c/G_g . The loss caused by the trailing-edge jet flow reached to the maximum in the case of high G_c/G_g .

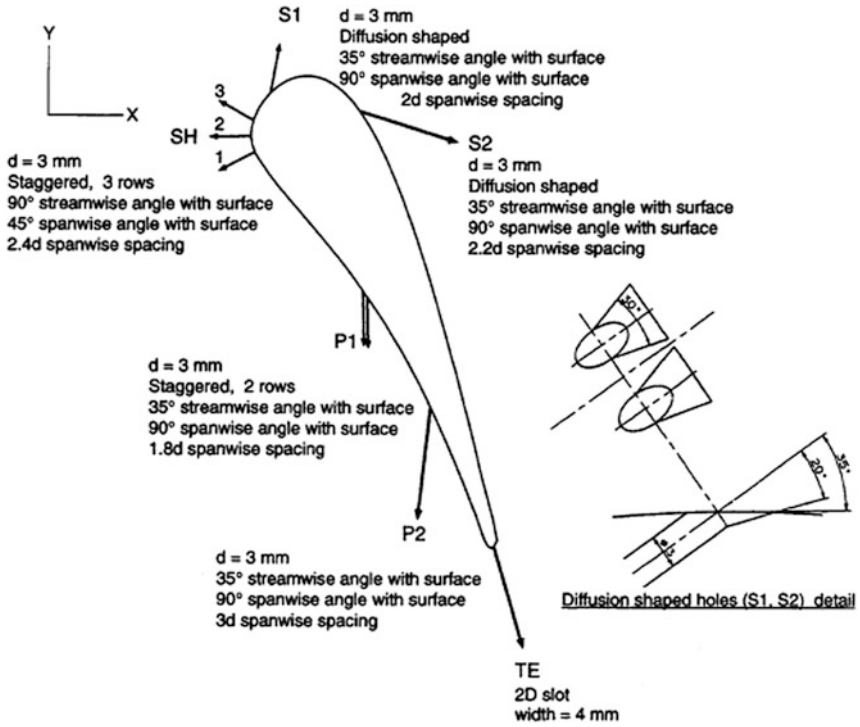
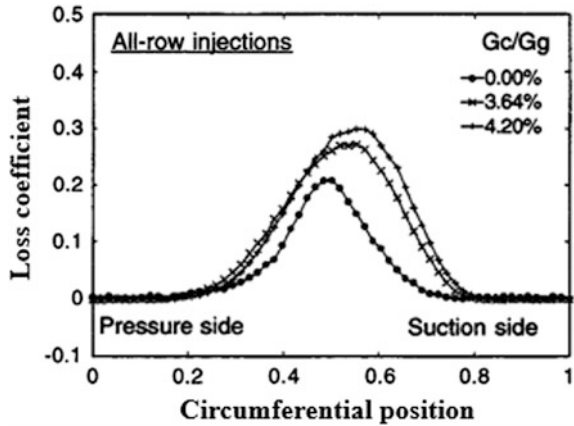


Fig. 2.45 Structures of stator blades and cooling holes used by Kubo [40]

Fig. 2.46 Loss coefficient distribution obtained through experiments [40]



In engineering applications, the cooling flow jet can be assumed as a one-dimension constant pressure mixing process. The approximate expression of the total pressure loss can be written as follows [42]:

$$\frac{\nabla P_t}{P_{tg}} = -\frac{k}{2} M_g^2 \frac{dW_c}{W} \left(1 + \frac{T_c^*}{T_g^*} - 2 \frac{V_c}{V_g} \cos \varphi_c \right)$$

where

- ∇P_t Total pressure drop of the cooling flow
- M_g Mach number of the main flow
- V_g Velocity of the main flow
- T_c^* Total temperature of the cooling flow
- T_g^* Total temperature of the main flow
- V_c Velocity of the cooling flow
- V_g Velocity of the main flow
- φ_c Included angle between the cooling flow and the main flow

It can be seen from the above equation that M_g and dW_c/W are the significant parameters influencing the loss. Obviously, arranging film cooling at high Mach number positions of the blade would cause greater loss, so it should be tried to avoid arranging film holes on the middle and rear of the suction surface.

2.6.2 Influence of Endwalls and Sealing Flow on Aerodynamic Performance

In modern designs with low aspect ratio and low solidity, endwalls account for a large part of total cooling area. With the increase of turbine inlet temperature and pressure, endwall cooling becomes more and more important. In addition, there are both gas leakage in circumferential and axial direction, which makes flows very complex. The endwall area is regarded as a complex area for it contains a wide range of 3-D secondary flows. York et al. [43] pointed out that the basic follow characteristics of the endwall. (1) The secondary flows in the blade passage caused by the pressure and temperature gradient of the inlet flow. (2) Separated horseshoe vortexes generated in the boundary layer near the leading edge of each blade and then joining into the passage. (3) High transverse pressure gradient resulting in the endwall 3-D boundary layer with great transverse velocity component. (4) Influence of the suction surface and horseshoe vortexes in endwall corners.

With respect to turbine endwall cooling, the mode of cooling flow distribution should be different for different turbine inlet temperature [44], as described as follows. (1) 1300–1500 K, simple convection cooling, in which heat-transfer calculation is unnecessary in the design, and only the cooling flow rate needs to be calculated. (2) 1500–1650 K, impingement and convection cooling structures, in

which there are low cooling flow consumption, hardly any additional mixing loss and aerodynamic loss which are caused by margin plate cooling. (3) 1650–1800 K, compound cooling structures, which integrate impingement cooling, convection cooling, and film cooling. The structures have good cooling effect, but consume large amount of cooling flow. The cooling flow rate for the inside and outside margin plates may be up to 1–2% of the inlet flow of a high pressure compressor. In addition, the mixing of the air-film jet flows with the main flow results in mixing loss, deteriorates endwall flow field, and reduces turbine efficiency. To avoid the aerodynamic performance reduction caused by film cooling, the outlets of the film holes should be set in low Mach number zone to the greatest extent, and the influence of the location and direction of air-film jet flows on endwall secondary flows should be taken into account as well.

2.6.2.1 Film Cooling for the Endwall

Flows near the endwall region will be influenced greatly if film cooling flows exist on the endwall surfaces. Secondary flows would make turbine endwall cooling even more complex, mainly because of passage vortexes and endwall transverse flows. The pressure gradient from the pressure surface of the endwall to the suction surface is the main reason for the generation of endwall transverse flows. Meanwhile, the transverse secondary flow would get involved in and increase the pressure side branch of the horseshoe vortex, and then develop into the passage vortex. Though film cooling can cool down the endwall effectively, but it would result in great aerodynamic loss. To reduce the loss and thus increase turbine efficiency, many institutes have carried out a series of studies on film cooling injection to the front of leading edge of the endwall for turbine blades.

Cooling flow would be absorbed by secondary flows and dissipate. To further study the process of film injection, researchers have carried out a wide range of studies on aerodynamic characteristics and heat transfer effect near the endwall. Takeishi et al. [45], Granser and Schulenberg [46], and Harasgama and Burton et al. [47, 48] conducted film cooling experiments at different positions of the endwall and also carried out numerical simulations. They found that endwall secondary flows had negative effects on endwall cooling, particularly for the cooling ejection at the front half of the endwall surface, where transverse flows are most active and passage vortexes are generated. In recent years, film cooling with high cooling flow rate ratio and momentum are used at the leading edge of the endwall to actively control secondary flows in experiments and numerical simulations. Effort in this field includes the studies by Georgiou [49], Burd [50], Liu [51], and others. Their studies reveal that the cooling flow with high momentum can decrease secondary flows, serve as a good thermal protection, and improve aerodynamic performance of the cascade passage in the meanwhile.

Zhang used pressure sensitive paints to study the film cooling for turbine guide vanes (see Fig. 2.47) [52], and found that: at low flow ratio, both holes and slots could not change the situation that endwall secondary flows dominated the endwall

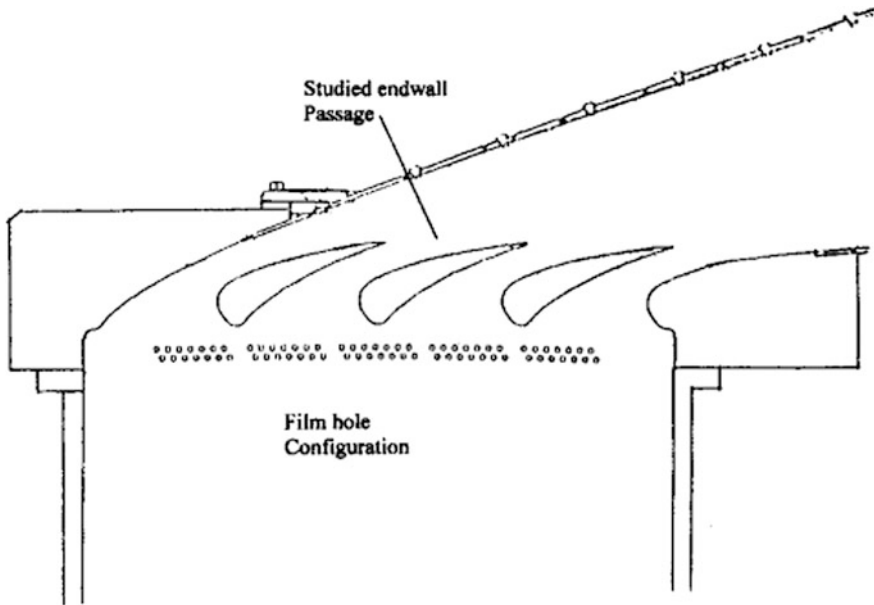


Fig. 2.47 Experimental facilities used by Zhang [52]

flow field, and that cooling flow flows were absorbed rapidly and dissipated; at high flow ratio (about 2.0%), cooling flow flows with high momentum dominated the flow field around the endwall, inhibited the secondary flows, was driven to the pressure side, and consequently resulted in a high cooling efficiency at the trailing edge region.

Friedrich et al. [53] studied the influence of film cooling on flow near end walls in transonic turbines. Figure 2.48 shows the structure of its test object. Studies were carried out with and without considering cooling flow injection at the upstream, middle and downstream of the blade row flow field respectively. Due to great influence of cooling flow injection on the main flow, stagnation pressure losses and secondary flow structures of the endwall with and without cooling were given respectively. When the injection ratio increased, passage vortices got closer to the endwall and their core moved down obviously. Because of the blocking effect, the cooling jet flows locally influenced the pressure fields around the holes. Because of the interaction with flows in the passage, the cooling jet flows also influenced the overall pressure field in the passage. The following figures show the ink marks in the conditions with and without cooling flow injection respectively (see Fig. 2.49 and Fig. 2.50).

Barigozzi [54] studied the influence of fan-shaped holes on aerothermodynamics of turbine. Through this study, aero-thermodynamic analysis could be done for the area near the endwall. Two hole patterns (cylinder-shaped and fan-shaped holes) were studied in the study, and the results showed that: (1) cylinder-shaped and fan-shaped holes had no difference in their influence on endwall secondary flows;

Fig. 2.48 Cooling structure in stator blades [53]

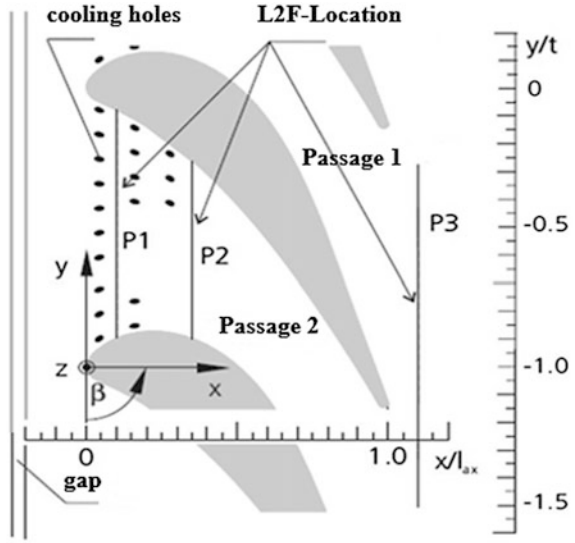
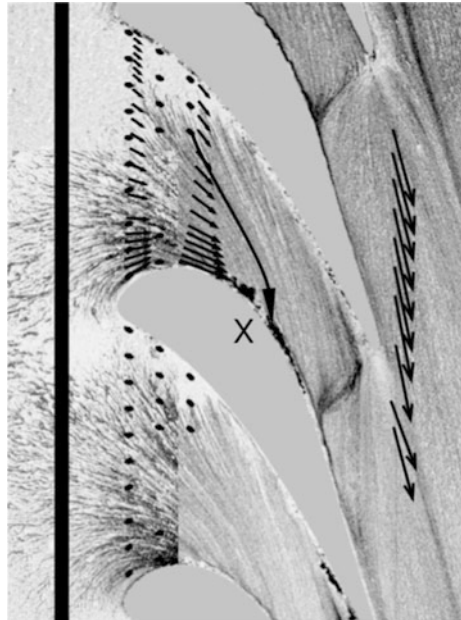
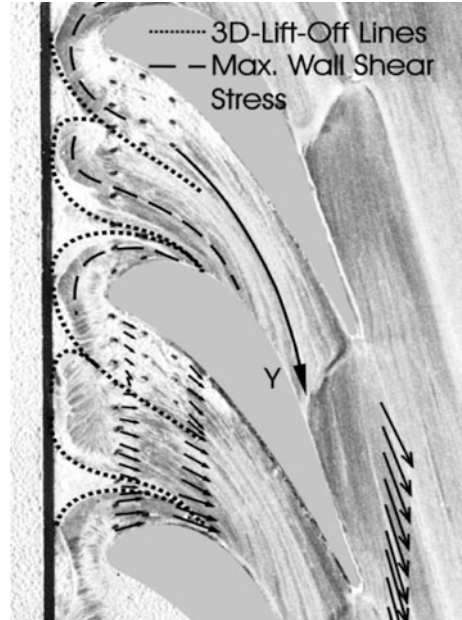


Fig. 2.49 End wall ink marks without cooling flow injection [53]



(2) at the same flow ratio, fan-shaped holes would lead to greater thermodynamic loss; (3) for cylinder-shaped holes, the flow ratio was 1% when minimum loss was achieved, while the ratio was 0.75% for fan-shaped holes; as the flow rate increased, secondary vortices and secondary flows would decrease dramatically, thus resulting in approximately 2-D flow field characteristics (see Fig. 2.51).

Fig. 2.50 End wall ink marks with cooling flow from both slots and holes [53]



The main conclusions about endwall cooling are as follows. (1) Endwall secondary flows and the resulting passage vortices would be weakened by cooling flow injection either in the form of holes or slots. (2) If cooling flow is jetted from slots, horseshoe vortices would be enhanced significantly. That's because the cooling flow slots are set near the saddle points at the leading edge of the blade. To prevent the enhancement to horseshoe vortices, it is best to set the slots far away from the leading edge of the blade. (3) Cooling flow injection from holes or slots would increase turbulence intensity and thus promote heat transfer. (4) Some holes have excessively high blowing ratio, especially for those near the pressure side, which is the reason why much cooling flow separate on the endwall surface. (5) Strong horseshoe vortices are an important reason for the cooling flow being transported from the endwall to the main flow. (6) From the perspective of thermodynamics, the schemes with cooling flow injection would result in higher loss.

2.6.2.2 Sealing Flow Near the Endwall

Due to the rotation of turbine disk, the inherent friction pump effect would continuously pump out air from the cavity and reduce the flow pressure of the cavity. In the case of no cooling flow, the high-temperature gas would flow backward into the cavity. Although with cooling flow, gas would also flow back to the cavity on the action of friction pump effect in the circumstance of the flow rate pumped out greater than that supplied. Thus, except for guaranteeing sufficient cooling effect for the

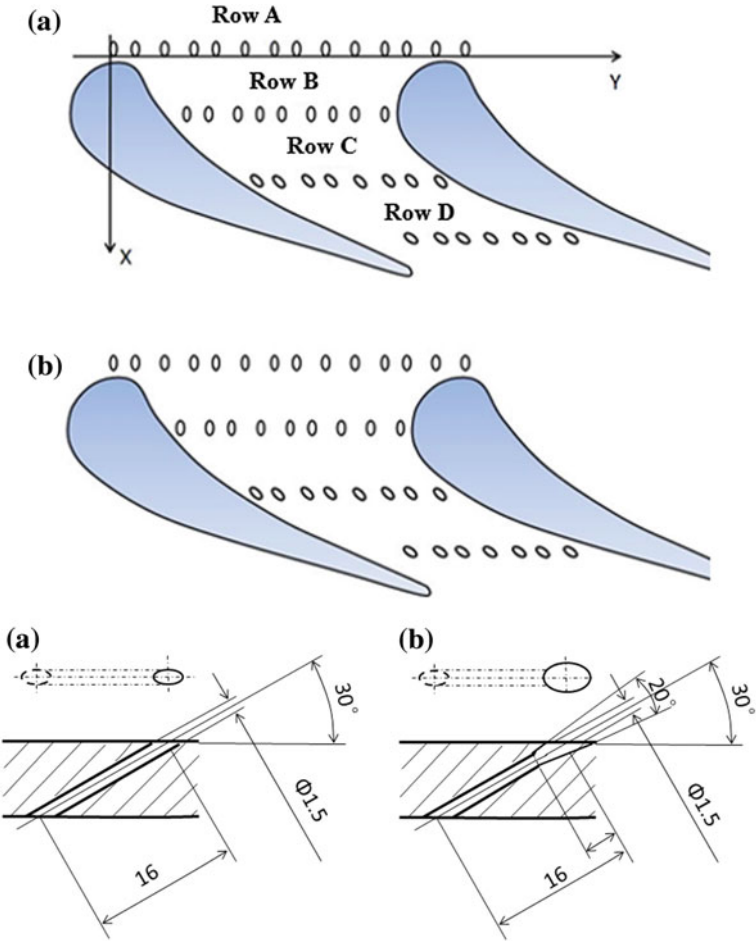


Fig. 2.51 Geometries of cylinder-shaped and fan-shaped holes studied by Barigozzi [54]

turbine disk, the cooling flow should be larger than the minimum flow of keeping gas from intrusion. Figure 2.52 shows a typical structure of a sealing cavity.

The seal leakage flow, which generally flows out of the narrow gap between rotor blades and stator blades, would largely reduce the aerodynamic efficiency. The study by Wang et al. [55] suggested that reducing the seal leakage flow rate by 50% could increase the aerodynamic efficiency by 0.5%. The flow rate of the seal leakage flow shall be high enough to inhibit the indraft of high-temperature gas and cool down the disk in the meantime. Most of the early efforts on seal leakage flow mainly focused on simple structures, gas intrusion prediction, and delicate heat transfer at the disk. McClean et al. [56] took the lead in studying the interaction between leakage flows and the main flow. They compared the geometric

characteristics of three kinds of leakage flows and their influence on turbine stage efficiency and downstream flow field. The results showed that these flows were likely to cause great aerodynamic loss in spite of their low flow rate. Afterwards, a lot of studies were carried out on the influence of leakage flows with different leakage flow ratio and vorticity on the efficiency.

Higher leakage flow ratio (ratio of the leakage flow rate to the flow rate of the main flow) would result in higher cooling flow rate, reduce the strength of passage vortexes, and thus lead to more even cooling flow distribution at the endwall. Burd [57] reached a similar viewpoint. Dénos and Paniagua [58] found that leakage flows would reduce the heat flux at the leading edge of the high-speed turbine rotor blade and front of its suction surface. Wright [59] studied the influence of the jet flow in front of the rotor blade on aerodynamic performance. He used a simple seal structure with an angle of 30° and a slot in front of the rotor blade. He found that: at low leakage flow ratio, the endwall platform of the rotor blade got the maximum cooling protection, while the area behind the endwall could only be protected at high jet flow ratio (2%). Only in the latter case, the influence of secondary flows on cooling flow distribution could be weakened. Meanwhile, the cooling flow absorbed by passage vortexes tended to be separated from the endwall, so their cooling effect on the suction side of the blade was limited. However, so much cooling leakage flow would cause great aerodynamic loss, so it is necessary to study the influence of the interaction between leakage flows and the main flow on thermodynamic effects.

Popović [61] studied seal leakage flow at the rotor blade of high-loaded high-pressure turbines. The study found that the cooling effect of the leakage flow on the endwall in front of the rotor blade was very limited. Higher leakage flow rate would bring about higher cooling capacity, but increase aerodynamic loss. At low leakage flow rate (0.5–1.0% of the main flow), the outlet relative velocity would not exert significant influence on cooling flow coverage. At high leakage flow ratio

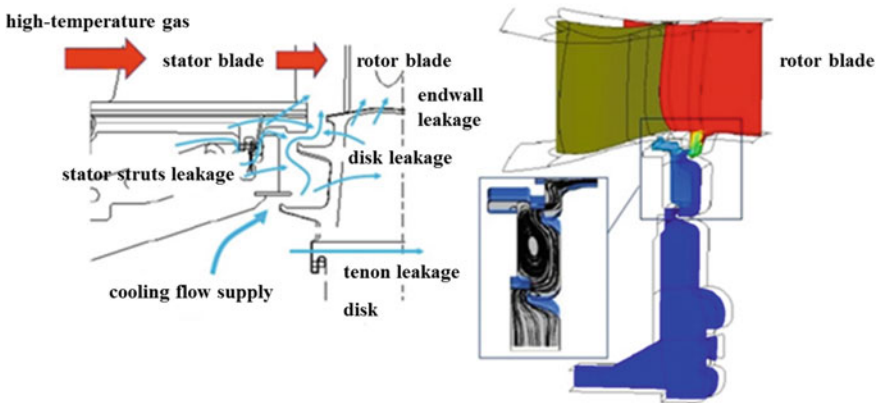


Fig. 2.52 Typical sealed cavity [60]

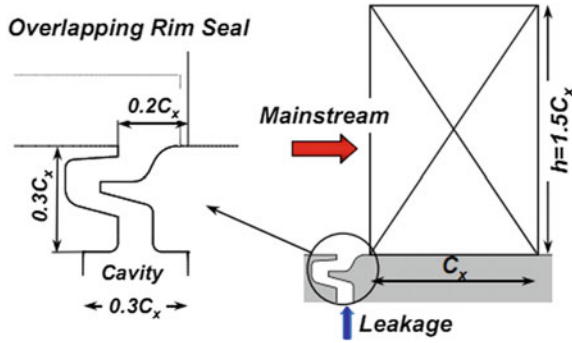


Fig. 2.53 Testing sample [61]

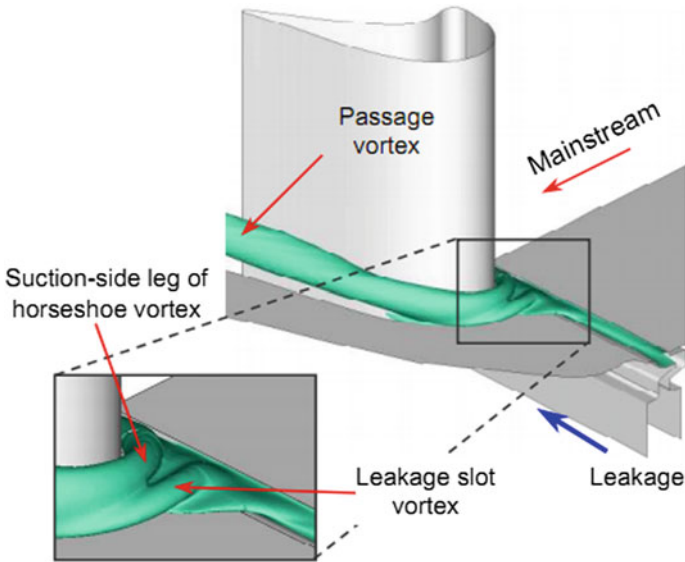


Fig. 2.54 Temperature contour [61]

(1.5%), cooling flow coverage could be increased dramatically by increasing the tangential speed of leakage flow; in this case, the cooling flow joined into the two branches of the horseshoe vortex respectively near the leading edge, thus greatly increasing aerodynamic loss. Compared to the prototype, the area effectively cooled by the leakage flow had higher heat transfer coefficient. However, the study also indicated that the total thermal load in the root endwall area did not change obviously with cooling flow, and the leakage flow only resulted in a redistribution of heat flux in the area (see Fig. 2.53, Fig. 2.54 and Fig. 2.55).

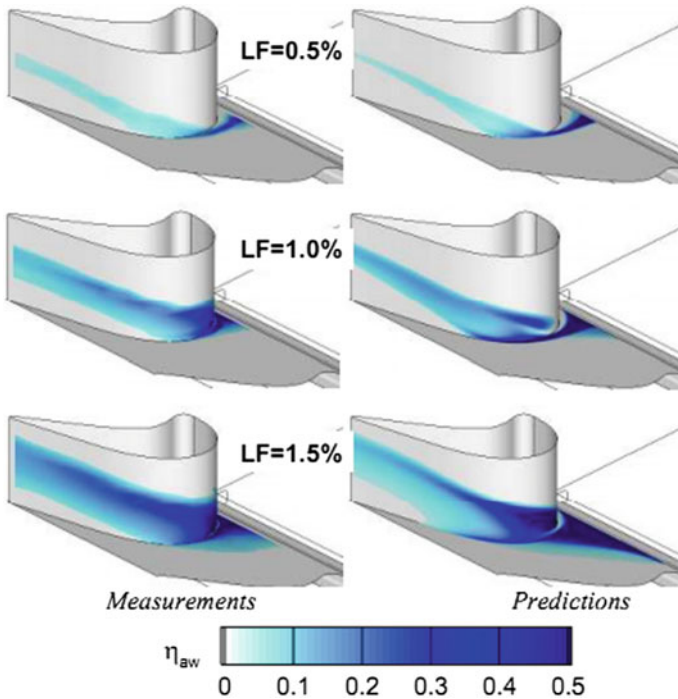


Fig. 2.55 Changes of cooling efficiency with leakage flow rate (LF) [61]

Loss and secondary flow strength would increase with the increase of leakage flow. At low leakage flow rate, the loss would change with relative velocity, but changes of the velocity could indeed improve sealing effectiveness by reducing the circumferential unevenness of leakage air. However, at high leakage flow rate, because of transverse secondary flows enhancement by the velocity relative to the cavity enhances, changing the velocity may increase loss, and thus increases the loss.

Erickson carried [62] out an experimental study on the leakage flow in the disk cavity of a linear rotor cascade, in which two different endwall forms were used for meridional endwalls, and the leakage flow was injected from a simulated rotor-stator cavity. Leakage flow ratio could be measured in the study, and was set at 0.5, 1.0, and 1.5% of the main flow respectively. The typical engine Reynolds number (4.3×10^5), and relatively high freestream turbulence intensity (14%) were adopted in the wind tunnel. The results showed that: in the area close to the leading edge of the blade, more curved the endwalled was, a stronger thermal performance was got. Large curvature radius would make the cavity leakage flow closer to the endwall, and thus increase thermal efficiency (see Fig. 2.56 and Fig. 2.57).

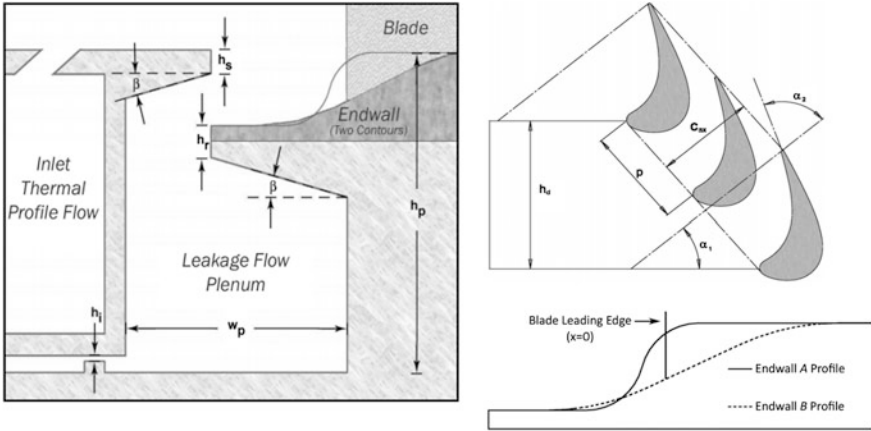


Fig. 2.56 Testing program [63]

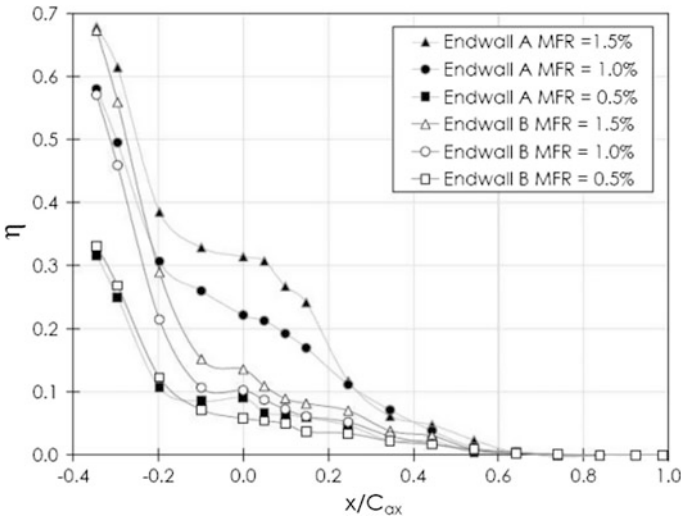


Fig. 2.57 Pitchwise averaged cooling efficiency [63]

Popović [63] tried to improve turbine stage efficiency and sealing effectiveness by modifying seal geometry. A series of engine seal geometries from simple to complex were studied. The test sample was a large-size liner cascade, equipped with a secondary air system, which could provide both different flow ratios and different leakage flow speeds. Meanwhile, the results were supplemented by the CFD results to make the physical analysis as detailed as possible (see Fig. 2.58 and Fig. 2.59).

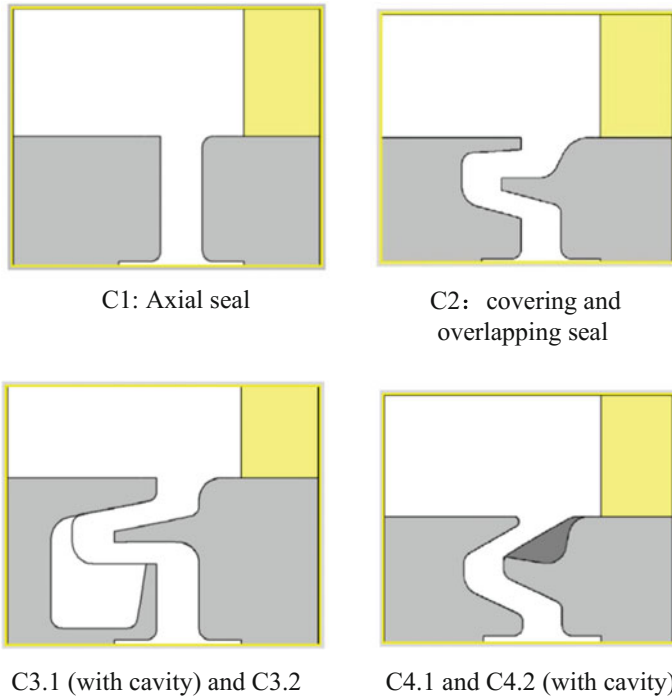


Fig. 2.58 Typical seal geometries

The study found that the key parameters influencing the total loss of the seal and the sealing effectiveness are the location and size of the backflow area. The designers should realize good sealing effectiveness and meanwhile reduce the adverse impact on the main flow passage. However, the two objectives above are contradictory. The backflow area generally exists near the rotor blade where sealing effectiveness is improved by reducing the influence of nonuniform pressure distribution along the circumferential direction. However, the backflow area would increase losses. The best method is to make both the outside part of the seal and the interface between the seal and the rotor blade endwall smooth, so as to reduce spoiling losses. The backflow area should be enclosed in the seal to guarantee acceptable sealing efficiency. I. Popović proposed a new method to solve this problem. The linear cascade experiment revealed that the loss caused by the interaction between the newly designed seal and the main flow were reduced by 33% compared to traditional data. The result was further confirmed in unsteady flow calculation for the turbine stage, which showed a 0.2% rise in stage efficiency (see Fig. 2.60 and Fig. 2.61).

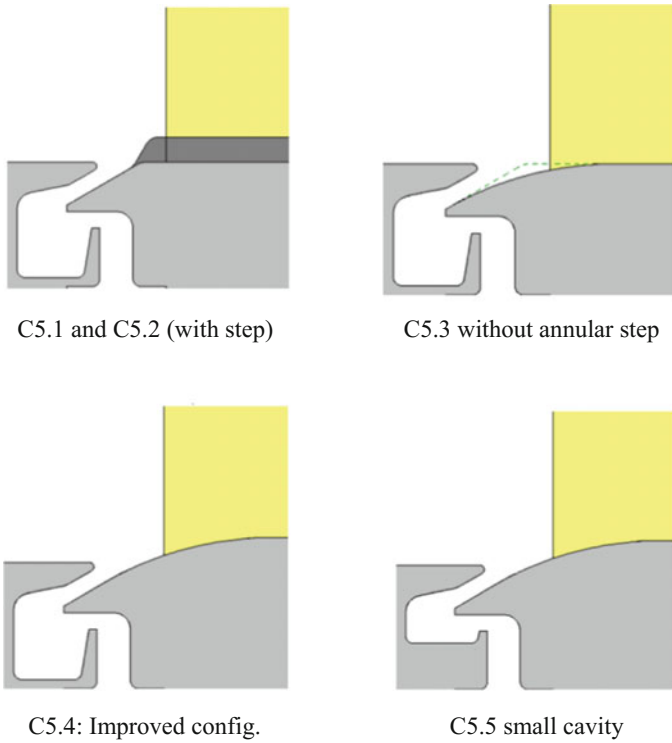


Fig. 2.59 New geometries developed in the study [63]

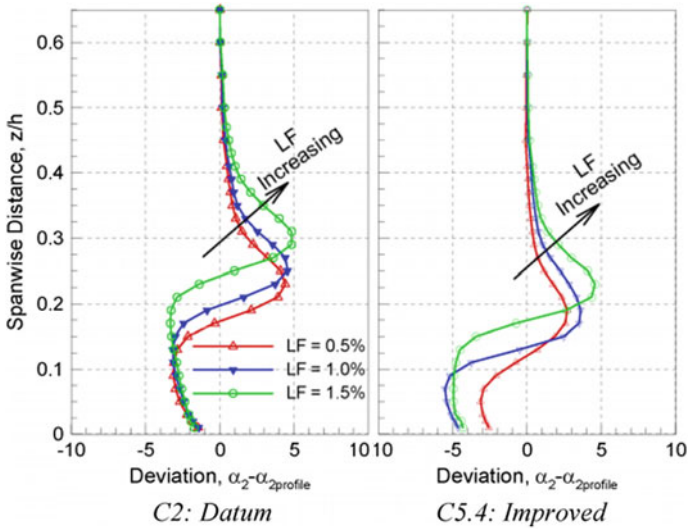
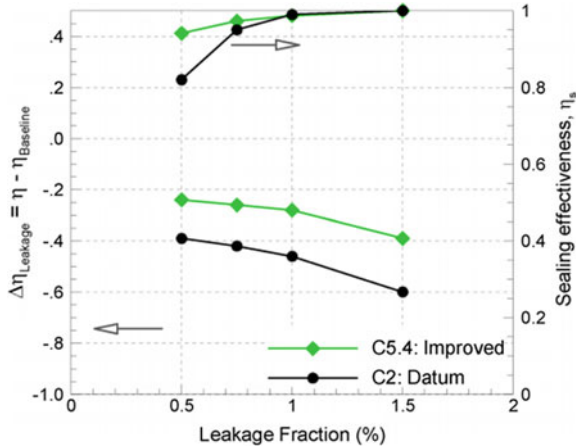


Fig. 2.60 Pitchwise averaged yaw angles at the plane 50% Cx downstream of the blade row [63]

Fig. 2.61 Numerical validation using the unsteady full-stage calculations: time-averaged sealing effectiveness and efficiency drop relative to the baseline [63]



References

1. Ke Do Lev, T. (1978). *Aero engine turbine calculation [M]*. Beijing: National Defense Industry Press, the First edition, 06, 1978.
2. Oates, G. C., et al. (1985). *Aerothermodynamics of aircraft engine components [M]*. AIAA.
3. Liu, S. (1990). *Principle of turbines for vessels [M]*. Harbin: Harbin Institution of Technology Press.
4. Wang, Z., & Qin, R. (1988). *Principle of turbomachinery [M]*. Beijing: China Machine Press.
5. Denton, J. D., & Xu, L. (1990). The trailing edge loss of transonic turbine blades [J]. *Journal of Turbomachinery*, 112(2), 277–285.
6. Laumert, B. (2002). Investigation of unsteady aerodynamic blade excitation mechanisms in a transonic turbine stage—Part I: phenomenological identification and classification [J]. *Journal of Turbomachinery*, 124(3), 410–418.
7. Doorly, D. J., & Oldfield, M. L. G. (1985). Simulation of the effects of shock wave passing on a turbine rotor blade [J]. *Journal of Engineering for Gas Turbines and Power*, 107(4), 998–1006.
8. Johnson, A. B., Rigby, M. J., & Oldfield, M. L. G. (1989). *Unsteady aerodynamic phenomena in a simulated wake and shock wave passing experiment [M]*. Rolls-Royce PLC.
9. Anderson, J. D., Jr. (1985). *Fundamentals of aerodynamics [M]*. Tata McGraw-Hill Education.
10. Sonoda, T., Arima, T., Olhofer, M., et al. (2006). A study of advanced high-loaded transonic turbine airfoils [J]. *Journal of Turbomachinery*, 128(4), 650–657.
11. Acharya, S. (2005). *Endwall cooling with endwall contouring and leading edge fillet [R]*. Annual Reports Submitted to UTSR.
12. Mahmood, G. I., Gustafson, R., & Acharya, S. (2005). Experimental investigation of flow structure and Nusselt number in slow speed linear blade passage with and without leading edge fillets [J]. *Journal of Heat Transfer*, 127(5), 499–512.
13. Smith, L., Karim, H., & Etemad, S., et al. (2006). *The gas turbine handbook [M/OL]*. <http://www.netl.doe.gov/research/coal/energy-systems/turbines/publications/handbook>
14. Wang, H. P., Olson, S. J., Goldstein, R. J., et al. (1997). Flow visualization in a linear turbine cascade of high performance turbine blades [J]. *Journal of Turbomachinery*, 119(1), 1–8.
15. Moustapha, H., Zelesky, M. F., & Baines, N. C., et al. (2003). *Axial and radial turbines [M]*. Wilder, VT: Concepts NREC.
16. Lampart, P. (2007). Tip leakage flows in turbines [J]. *Task Quarterly*, 10(2), 139–140.

17. Halila, E. E., Lenahan, D. T., & Thomas, T. T. (1982). *Energy efficient engine high pressure turbine test hardware detailed design report [R]*. NASA CR-167955.
18. Lattime, S. B., & Steinetz, B. M. (2004). High-pressure-turbine clearance control systems: current practices and future directions [J]. *Journal of Propulsion and Power*, 20(2), 302–311.
19. Denton, J. D. (2004). *Axial turbine aerodynamic design [J]*. Cambridge: Cambridge Turbomachinery Course, p. 22.
20. Han, W., Zhong, J., Huang, H., et al. (1999). Topological and vortex structure the flow field of the positively curved cascade with the tip clearance [J]. *Acta Aerodynamica Sinica*, 17(2), 141–149.
21. Lee, S. W., Moon, H. S., & Lee, S. E. (2009). Tip gap height effects on flow structure and heat/mass transfer over plane tip of a high-turning turbine rotor blade [J]. *International Journal of Heat and Fluid Flow*, 30(2), 198–210.
22. Traupel W. (1977). *Thermische Turbomaschinen Zweiter Band Geländerte Betriebsbedingungen, Regelung, Mechanische Problem, Temperature problem [M]*. Berlin, New York: Springer-Verlag.
23. Ainley, D. G., & Mathieson, G. (1951). *A method of performance estimation for axial-flow turbines [M]*. Defense Technical Information Center.
24. Dunham, J., & Came, P. M. (1970). Improvements to the Ainley-Mathieson method of turbine performance prediction [J]. *Journal for Engineering for Power*, 92(3), 252–256.
25. Kacker, S. C., & Okapuu, U. (1982). A mean line prediction method for axial flow turbine efficiency [J]. *Journal for Engineering for Power*, 104(1), 111–119.
26. Craig, H., & Cox, H. (1970). Performance estimation of axial flow turbines [J]. *Proceedings of the Institution of Mechanical Engineers*, 185(1), 407–424.
27. Denton, J. D. (1993). Loss mechanisms in turbomachines [J]. *Journal of Turbomachinery*, 115(4), 621–656.
28. Baljé, O. E., & Binsley, R. L. (1968). Axial turbine performance evaluation. Part B—optimization with and without constraints [J]. *Journal for Engineering for Power*, 90(4), 349–359.
29. Yaras, M. I., & Sjolander, S. A. (1992). Prediction of tip-leakage losses in axial turbines [J]. *Journal of Turbomachinery*, 114(1), 204–210.
30. Hamik, M., & Willinger, R. (2007). An innovative passive tip-leakage control method for axial turbines: basic concept and performance potential [J]. *Journal of Thermal Science*, 16(3), 215–222.
31. Egli, A. (1935). The leakage of steam through labyrinth seals [J]. *Transactions of the ASME*, 57(3):115–122.
32. El-Dosoky, M. F., Rona, A., & Gostelow, J. P. (2007). *An analytical model for over-shroud leakage losses in a shrouded turbine stage [R]*. ASME Paper GT2007-27786.
33. Goldstein, R. J. (1971). *Film cooling [J]*. *Advances in Heat Transfer*, 7(1):321–379.
34. Moffitt, T. P., Stepka, F. S., & Rohlik, H. E. (1976). *Summary of NASA aerodynamic and heat transfer studies in turbine vanes and blades [R]*. NASA TM-X-73518.
35. Zhang, L., & Moon, H. K. (2006). *Turbine blade film cooling study—The effects of showerhead geometry [R]*. ASME Paper GT2006-90367.
36. Martini, P., Schulz, A., & Bauer, H. J. (2005). *Film cooling effectiveness and heat transfer on the trailing edge cut-back of turbine airfoils with various internal cooling designs [R]*. ASME Paper GT2005-68083.
37. Uzol, O., Camci, C., & Glezer, B. (2001). Aerodynamic loss characteristics of a turbine blade with trailing edge coolant ejection: Part 1—Effect of cut-back length, spanwise rib spacing, free-stream Reynolds number, and chordwise rib length on discharge coefficients [J]. *Journal of Turbomachinery*, 123(2), 238–248.
38. Uzol, O., & Camci, C. (2001). Aerodynamic loss characteristics of a turbine blade with trailing edge coolant ejection: Part 2—External aerodynamics, total pressure losses, and predictions [J]. *Journal of Turbomachinery*, 123(2), 249–257.

39. Day, C. R. B., Lock, G. D., & Oldfield, M. L. G., et al. (1998). *Efficiency measurements of an annular nozzle guide vane cascade with different film cooling geometries [R]*. ASME Paper 98-GT-538.
40. Kubo, R., Otomo, E., & Fukuyama, Y., et al. (1998). *Aerodynamic loss increase due to individual film cooling injection from gas turbine nozzle surface [R]*. ASME Paper 98-GT-497.
41. Otomo, E., Nakatani, Y., Kubo, R., et al. (1997). Pressure loss characteristics of gas turbine nozzle blade row with individual film cooling injection rows [C]. In *Proceeding of 25th Annual Gas Turbine Conference, JSME*.
42. Aero Engine Design Handbook editorial board, & Huang, Q., et al. (2001). *Aero engine design handbook, volume 10, turbine [M]*. Beijing: Aviation Industry Press.
43. York, R. E. (1984). HyltonLD, MihelcMS. An experimental investigation of endwall heat transfer and aerodynamics in a linear vane cascade [J]. *Journal of Engineering for Gas Turbines and Power*, 106(1), 159–167.
44. Aero Engine Design Handbook editorial board, & Wang H., et al. (2001). *Aero engine design handbook, volume 16, Air system and heat transfer analysis [M]*. Beijing: Aviation Industry Press.
45. Takeishi, K., Matsuura, M., Aoki, T., et al. (1990). An experimental study of heat transfer and film cooling on low aspect ratio turbine nozzles [J]. *Journal of Turbomachinery*, 112(3), 488–496.
46. Granser, D., & Schulenberg T. (1990). *Prediction and measurement of film cooling effectiveness for a first-stage turbine vane shroud [R]*. ASME 90-GT-95.
47. Harasgama, S. P., & Burton, C. D. (1991). *Film cooling research on the endwall of a turbine nozzle guide vane in a short duration cascade Part 1: Experimental technique and results [R]*. ASME91-GT-252.
48. Harasgama, S. P., & Burton, C. D. (1991). *Film cooling research on the endwall of a turbine nozzle guide vane in a short duration cascade Part 2: Analysis and correlation of results [R]*. ASME91-GT-253.
49. Georgiou, D. P., Papavasiliopoulos, V. A., & Alevisos, M. (1996). *Experimental contribution on the significance and the control by transverse injection of the horseshoe vortex [R]*. ASME 96-GT-255.
50. Burd, S. W., Simon, T. W. (2000). *Effects of slot bleed injection over a contoured endwall on nozzle guide vane cooling performance: Part I—Flow field measurements [R]*. ASME 2000-GT-199.
51. Liu, S., Liu, G., & Xu, D., et al. (1999). *Aerodynamic investigation of endwall film-cooling in an axial turbine cascade Part I: experimental investigation [R]*. AIAA ISABE99-7080.
52. Zhang, L. J., & Jaiswal, R. S. (2001). *Turbine nozzle endwall film cooling study using pressure sensitive paint [R]*. ASME2001-GT-0147.
53. Friedrich, K., & Martin, N. (2001). *Film-cooled turbine endwall in a transonic flow field: Part I- aerodynamic measurements [R]*. ASME 2001-GT-0145.
54. Barigozzi, G., Benzoni, G., & Franchini, G., et al. (2005). *Fan-shaped hole effects on the aero-thermal performance of a film cooled endwall [R]*. ASMEGT2005-68544.
55. Wang, C. Z., de J. F., & Johnson, B. V., et al. (2007). *Comparison of flow characteristics in axial-gap seals for close and wide-spaced turbine stages [R]*. ASMEGT2007-27909.
56. McLean, C., Camci, C., & Glezer, B. (2001). Mainstream aerodynamic effects due to wheel space coolant injection in a high-pressure turbine stage: Part I—Aerodynamic measurements in the stationary frame [J]. *Journal of Turbomachinery*, 123(4), 687–696.
57. Burd, S. W., Satterness, C. J., & Simon T. W. (2000). *Effects of slot bleed injection over a contoured endwall on nozzle guide vane cooling performance: Part II—thermal measurements [R]*. ASME Paper 2000-GT-200.
58. Denos, P. (2002). *Influence of the hub endwall cavity flow on the time-averaged and time-resolved aero-thermodynamics of axial HP turbine stage [R]*. ASME GT-2002-30185.

59. Wright, L. M., Gao, Z., Yang, H., et al. (2008). Film cooling effectiveness distribution on a gas turbineblade platform with inclined slot leakage and discrete filmhole flows [J]. *Journal of Heat Transfer*, 130, 071702.
60. Bunker, R., Ledezma, G. A., & Laskowski, G. M. (2011). *An investigation of turbine rim sealflow interactions with a transonic hot gas path [R]*. ISABE-2011-1834.
61. Popović, I., & Hodson, H. P. (2010). *Aerothermal impact of the interaction between hubleakage and mainstream flows in highly-loaded HP turbineblades [R]*. ASMEGT2010-22311.
62. Ryan, D., Erickson, T. W., & Simon, L., et al. (2011). *Experimental investigation of discacity leakage flow and hubendwall contouring in a linear rotor cascade [R]*. ASMEGT2011-46760.
63. Popović, I., & Hodson, H. P. (2013). Improving turbine stage efficiency and sealing effectiveness through modifications of the rim seal geometry [J]. *Journal of Turbomachinery*, 135, 061016.
64. Denton, J.D., & Johnson, C.G. (1976). *An experimental study of the tip leakage flow around shrouded turbine blades[R]*. CEGB Report No R/M/N848, Marchwood Engineering Laboratories.

Chapter 3

Flow Mechanism in Inter Turbine Ducts

3.1 Geometrical and Aerodynamic Characteristics of Inter-turbine Duct and Development Trends

In the main flow passage of aero gas turbines, the channel connecting the high-pressure turbine stage and low-pressure turbine stage is generally called inter-turbine duct (ITD). The inter-turbine duct mainly serves as a flow passage, which is formed by the casing and hub, and in some situations, the duct, together with struts, also serves as a supporter and pathway of accessory pipelines. From the perspective of the geometry, the inter-turbine duct is an annular pipe with its two ports having different diameters; the ports connecting to the high-pressure turbine is its inlet, and the other ports, which connects to the low-pressure turbine, is its outlet. Figure 3.1 shows the meridional plane of the inter-turbine duct, as well as its main geometrical parameters except for contour parameters of the ITD hub and casing, where subscript “1” represents the parameters of the inlet section, and subscript “2” represents the parameters of the outlet section.

By nondimensionalizing the above parameters, we can obtain area ratio of inlet to outlet (AR), length to height ratio (Lx/h_1), and radial difference to length ratio ($\Delta R/Lx$), which are the three most important parameters in ITD design. AR represents the pressure difference between inlet and outlet of ITD; Lx/h_1 represents the dimensionless length of ITD; $\Delta R/Lx$ represents the size of the climbing angle of ITD.

According to the fundamental principles of aero gas turbines, high-pressure turbines have high rotational speed and small outer diameter, while low-pressure turbines have low rotational speed and large outer diameter. Meanwhile, as required by the density decrease caused by flow expansion, low pressure turbines should increase its flow area. As a result, the average radius of the outlet surface of ITD (R_2) is larger than that of the inlet surface (R_1), and the height of the outlet ring surface of ITD (h_2) is greater than that of the inlet ring surface (h_1). So, it is obvious that the outlet area is bigger than the inlet area.

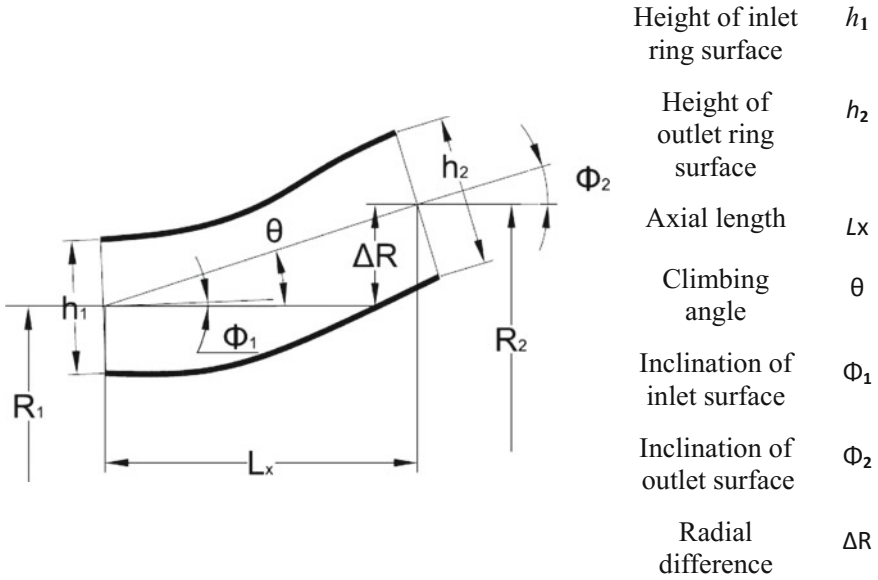


Fig. 3.1 Geometric descriptions of inter-turbine duct

As determined by the geometrical characteristics of ITD, the flows in ITD is essentially characterized by the diffusion. Outlet flows of high-pressure turbines are subsonic in axial direction and no work and mass exchanges between the flows and external environment occur in the process of their passing through ITD. Besides, heat exchange can be neglected due to the short flowing-through time. For the reasons above, the flow area difference between the inlet and the outlet is the driving factor of flow parameter changes. According to aerodynamic principles, flows in ITD are diffuser flows, featuring reduced the velocity of the flow and increased pressure. Because of gas viscosity as well as the adverse pressure gradient that flows in ITD are subject to in the diffusion process, the flows are mainly characterized by boundary layer development and evolution, and separation that maybe exists on hub and casing. Thus, parameters that can be used to describe the changes during the flows passing through ITD as well as ITD performance include:

Static pressure rise coefficient, C_p :

$$C_p = \frac{p_2 - p_1}{\frac{1}{2} \rho V_1^2} \quad (3.1)$$

Ideal static pressure rise coefficient, $C_{p_{ideal}}$:

$$C_{p_{ideal}} = 1 - \left(\frac{A_1}{A_2} \right)^2 \quad (3.2)$$

Diffusion efficiency coefficient, ε :

$$\varepsilon = \frac{C_p}{C_{p_{ideal}}} \quad (3.3)$$

Total pressure loss coefficient, C_{pt} :

$$C_{pt} = \frac{pt_1 - pt_2}{\frac{1}{2}\rho V_1^2} \quad (3.4)$$

Total pressure recovery coefficient, σ :

$$\sigma = \frac{pt_2}{pt_1} \quad (3.5)$$

where, p is the static pressure; pt is the total pressure; V is the velocity; ρ is the density; A is the area.

The parameters above mainly reflect the changes in diffusion degree and power capacity of gas flows along the flowing direction, and are generally taken as the mean values on the investigated section. The uniformity of the flow parameters on the outlet section of ITD has great influence on flow conditions in the low-pressure turbine, which follows the inter-turbine duct, so the parameters that reflect the uniformity are usually used to assess the performance of ITD.

The basic aerothermodynamic characteristics of ITD flows are described as above. However, analysis of the flows will become much more complex if flow structure is taken into account. The inter-turbine duct is located behind the high-pressure turbine, and the outlet flows of the high-pressure turbine are highly complex strong three-dimensional flows with flow parameters varying greatly in the radial direction; for example, the outlet flow angle changes for above 10° from the hub to the casing. In addition, secondary flow vortices, rotor wakes, and tip leakage flows, which have great influence on flow conditions in the downstream ITD and are the main sources of aerodynamic losses.

With the continuous development of aeronautic technologies, the geometry and flow structure of ITD changes as well, especially for high-bypass-ratio civil turbofan engines. As international oil prices rising continuously and the emission standards for aircraft industry set by CAEP (the committee on Aviation Environment Protection) becoming stricter, the US, Europe, and Russia are all taking economy and environmental protection as the primary technical objectives for their next-generation high-bypass-ratio turbofan engines, such as PW1000G, RB282, LEAP, etc. Lower specific fuel consumption, noise, and environmental pollution have become the development trends of future civil turbofan engines. The LEAP-X plan targets issued by CFM company in 2008 include decreasing specific fuel consumption by 16% compared to CFM56, noise by 10–15 dB compared to the phase-IV noise level, NO_x emission by more than 60%, and keeping reliability and maintenance cost basically at the same level as those of CFM56 [1].

In order to reduce turbofan engines' unit thrust specific fuel consumption, it is necessary to increase their cycle thermal efficiency and propulsion efficiency. Cycle thermal efficiency could be improved by increasing overall pressure ratio and maximum cycle temperature, but this would be limited by material and cooling technologies. So, the common practice is to increase component efficiency. Propulsion efficiency is increased mainly by the decreasing speed of the flow of the bypass exhaust, and thus increasing bypass ratio is a powerful method for reducing turbofan engines' specific fuel consumption. GE90's bypass ratio has been increased up to 9 [2], and the ratio will become higher in future engines. Bypass ratio is increased mainly the increasing of fan diameter and the reducing of core engine diameter. These efforts can be seen in the technical schemes of the next-generation engines: LEAP-X and PW1000G, both of which have the geometrical characteristics of smaller core engine size and more compact construction [3].

For the inter-turbine duct that connects the high-pressure turbine to low-pressure turbine, the radial difference between its high-pressure turbine outlet and low-pressure turbine inlet would increase as bypass ratio increases either by increasing fan diameter or reducing core engine size. For weight reduction, the axial length of ITD should be shortened as much as possible. Therefore, to realize the economic and environmental targets of civil engine design, the inter-turbine duct should be shorter with larger radial difference between the inlet and outlet, namely with a larger divergence angle. Meanwhile, low flow loss should be achieved, and an uniform inlet flow field should be provided for the low-pressure turbine. Figure 3.2 indicates the aggressive S-shaped ITD, which is used in modern high-bypass-ratio turbofan engines. As can be seen in the figure, the ITD has larger radius difference between the inlet and outlet and shorter length, and looks like an "S". Generally speaking, the geometrical parameters of ITD of modern aero-engines is quite different from those in 1960s and 1970s. In the early days, the climbing angle of ITD hub was no more than 5° , which modern aggressive ITD has been over 30° typically. Table 3.1 shows ITD parameters of some engines and testing rigs. It can be seen in the table that the development trends of ITDs include larger climbing angle (more than 35° in general, 38° for GE90), larger area ratio, and shorter dimensionless length; in other words, they are becoming closer.

ITD has become a more significant factor influencing the performance of the turbine or even the engine than it was in previous years. Flows in aggressive S-shaped ITD are more complex for the following reasons. First, under the influence of blade wakes and tip leakage flows at the outlet of high-pressure and high-speed rotor, the flow near the inlet of ITD is mainly characterized by unsteady, high turbulence intensity, and strong secondary flows. Second, the great curvature change in the axial direction as well as the high adverse pressure gradient in the flow direction make the endwall boundary layer easier to separate, thus increasing flow losses in the flow passage. Finally, the struts in the flow passage, as required by engine design, would also influence the flows and result in some losses.

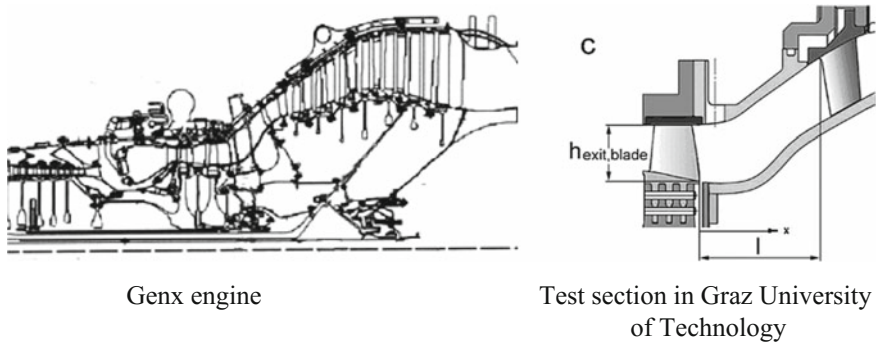


Fig. 3.2 Modern aggressive S-shaped ITD

Table 3.1 ITD parameters of engines and testing rigs

Engine	AR	Lx/h_1	θ/deg
CF6-50	1.35	3.47	30
GE90	1.25	2.67	38
PW6000	1.27	2.05	35
Chalmers (AIDA C1)	1.30	2.03	30
Chalmers (AITEB-2)	1.30	2.03	30
Graz (AIDA C4)	1.50	2.02	32
Graz (AIDA C5)	1.50	1.67	40

Mechanism of complex flows in ITD is explored in the following from the point of geometrical and aerodynamic parameters' influence on ITD flows and performance, and based on that, design methods of aggressive S-shaped ITDs are then discussed.

3.2 Influence of Geometrical Parameters on Flow Structures and Performance

3.2.1 Influence of Curvature of Meridian Passage

Understanding of flows performance in ITD begins with ordinary ITDs in the early days. Compared to S-shaped ITDs, ordinary ITDs have simpler geometrical parameters. Generally, a simple annular inter-turbine diffuser would be first designed based on the fact that diffusion flows dominate in ITD, so as to analyze the influence of geometrical and aerodynamic parameters and performance of the flows in the diffuser inlet, and then the method of the design for the diffuser would be made up. Kline [4] divided diffusers into four types according to separation types: no separation, little separation, large separation, and super-large separation, who

also pointed out that the diffusers with lower diffusion ratio and axial pressure gradient would cause relatively less loss. The separation state of diffusers is determined by static pressure distribution on the endwall surface; the higher the adverse pressure gradient on the endwall, the larger the possibility of separation would be. For annular ducts, the best dimensionless length (the ratio of duct length to inlet height) is within 25–30, and the best endwall coning angle is 14° .

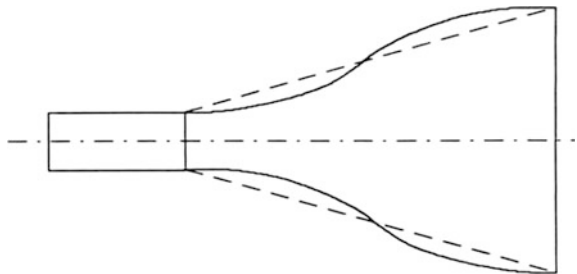
According to the streamline curvature method, concave curvature would lead to decrease in velocity and increase in static pressure of the flow, while convex curvature would lead to increase in velocity and decrease in pressure. Therefore, curvature of meridian plan is an important factor influencing diffuser separation. Different from linear diffusers, the diffuser, shown in Fig. 3.3

There is the concave curvature in front of the figure, while the curvature is in latter of that. Thus, flows in the front are in the condition of adverse pressure gradient, while those in the latter are in the condition of positive pressure gradient. In the front the boundary layer develops slowly and does not separate easily due to the adverse pressure gradient. In the latter the positive pressure gradient has an effect of inhibiting separation. In the whole, this kind on contour can help control separation, and is actually the basic contour form of the commonly used S-shaped ITD casing nowadays.

The change of the curvature is one of the factors determining the pressure distribution in S-shaped ITD. Curvature change can influence not only streamline, but also the development of the boundary layer. At the first turning of the S-shaped ITD, flows would turn from axial direction to radial direction. According to radial equilibrium, a pressure gradient from the casing (low pressure) to the hub (high pressure) would come into being, and the pressure gradient would overlap with the adverse pressure gradient caused by the increase in flow area. So, the pressure gradient can be controlled by optimizing wall curvature. At the position near the ITD outlet, flows would turn back to axial direction, which would also result in a pressure gradient from the casing (high pressure) to the hub (low pressure). Pressure distribution would directly influence the properties of the boundary layer; particularly, high adverse pressure gradient caused by large curvature would easily lead to boundary layer separation. Figure 3.1 indicates the pressure distribution on the casing and hub of an S-shaped ITD.

As can be seen from Fig. 3.4, the adverse pressure gradient generated after the acceleration of the fluid at the first turning of the S-shaped ITD would greatly

Fig. 3.3 Curve change of the diffuser



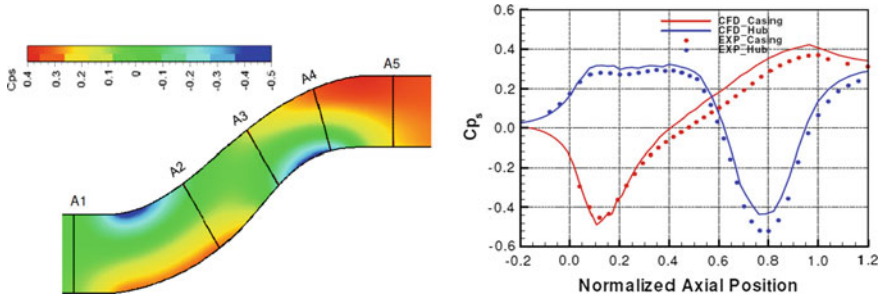
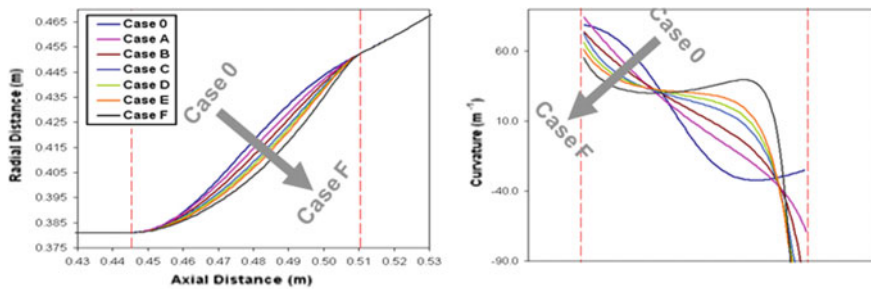


Fig. 3.4 Wall curvature change and pressure distribution in an S-shaped ITD [5]



Case Name	Flow Status	Recurve-Location	Cp	ξ
Case 0	Seperated	48%	-0.0840	0.0873
Case A	Not-Seperated	57%	0.1933	0.0620
Case B	Not-Seperated	67%	0.2074	0.0562
Case C	Not-Seperated	76%	0.1916	0.0545
Case D	Not-Seperated	78%	0.1800	0.0540
Case E	Not-Seperated	80%	0.1663	0.0540
Case F	Not-Seperated	87%	0.1152	0.0540

Fig. 3.5 Performance improvement by optimizing casing wall curvature [6]

increase the risk of the flow separation around the case. Therefore, local loss could be reduced by changing or optimizing the curvature distribution of the adverse pressure gradient zone to minimize the adverse pressure gradient at the first turning. This has been proved by the work of Kuchana et al. [6]. Their numerical study on inter-turbine ducts with variable curvature distribution found that the separation could be reduced or eliminated by moving downstream the first point of inflection on the wall of the casing. This conclusion was verified by two cases, in which the ratios of length to radial difference were 1.28 and 1.08 respectively (see Fig. 3.5).

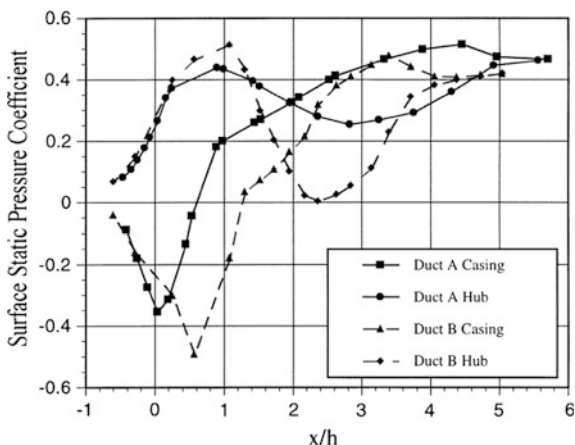
3.2.2 Influence of Area Ratio

The pressure distribution in the S-shaped ITD is influenced not only by wall curvature distribution, but also by flow area variation. Actually, flow area is determined by wall curvature of the casing and hub as well as local radius. The experiments, which were carried out on the testing rig of Durham University, and corresponding numerical analyses revealed the influence of area ratio [7]. The objects of study were two ITDs with same area rate but different axial length. ITD B was 30% shorter than ITD A, and they had different wall curvature and diffusion rate. As can be seen from the pressure distribution shown in Fig. 3.6, the flow on the surface of the casing in the shorter ITD B had larger acceleration and diffusion rate at the first turning, and caused greater loss in the low-pressure zone around the casing. Thicker boundary layer reduced the effective flow area of the ITD, and resulted in smaller static pressure recovery coefficient. The diffusion efficiency of ITD A was 83.5%, and that of ITD B was 75.6%. Based on the details of C_p distribution, it can be concluded that diffusion rate has important influence on the development of secondary vortexes in inter-turbine ducts.

3.2.3 Influence of Struts

Struts are needed in ITD for structural reasons. For multi-spool engines, it is necessary to install struts in ITD to support the bearings or provide pathways for cool gas, lubricating oil, etc. Obviously, the ratio of strut thickness to chord is relatively high due to the requirement of minimum strut section and the restriction of ITD length, and the parameter of modern engines is generally from 0.2 to 0.3. Thus, these struts would inevitably have significant influence on both the flow field and pressure distribution in ITD. First of all, the struts would result in resistance and

Fig. 3.6 Surface static pressure distribution of ITD A and B [7]



frictional loss. In order to reduce the loss, the struts have to be designed to low-resistance shapes, such as airfoil profile. Considering the geometrical sizes of the struts, which are required by the structural design, both their length and thickness are large enough to exert a significant influence on flows in ITD, and flow velocity would increase between the struts. Secondly, the flow direction at the inlet of ITD is not consistent with the axial direction; as it were, there is a flow angle at the leading edge of the struts. In addition, the wakes of turbine blades would also influence flows when sweeping across the struts.

The performance of the wakes on flows which can attribute to the result in the strut passage can be measured and analyzed by arranging pressure ports on the surface of the struts. There is an unsteady separation bubble around the first turning of the casing of the ITD without struts in early research. The distribution of the static pressure on the surface of the struts after put up the struts with the ITD. The blocking effect of the struts resulted in increasing on flow velocity, and the recovery coefficient of the total pressure dropped from 42% to 30%. Furthermore, the main loss of the pressure occurred at the position of the struts in the ITD. The overall loss of the pressure in the ITD with struts nearly doubles the loss of that with no struts (see Fig. 3.7). Separation, which was possibly caused by both the strut expansion and ITD expansion, occurred at the junction between the struts and the casing.

Using CFD, Norris analyzed the interaction between the performance of wakes and whether set up the struts or not [9], and the results showed that there was no direct interaction between them. On the side where the strut was closer to the wake region, the secondary flow caused by the wakes diminished the thickness of boundary layer, which inhibited separation and backflow. Meanwhile, separation and backflow occurred on the other side of the strut. A high-loss region was formed after the trailing edge of the strut and could be observed even at the ITD outlet. The separation bubble in the ITD without struts is periodic, and the performance of the flows around the casing of the ITD are even more stable after considering the influence of the wakes.

Fig. 3.7 Relation between total pressure loss and struts [8]

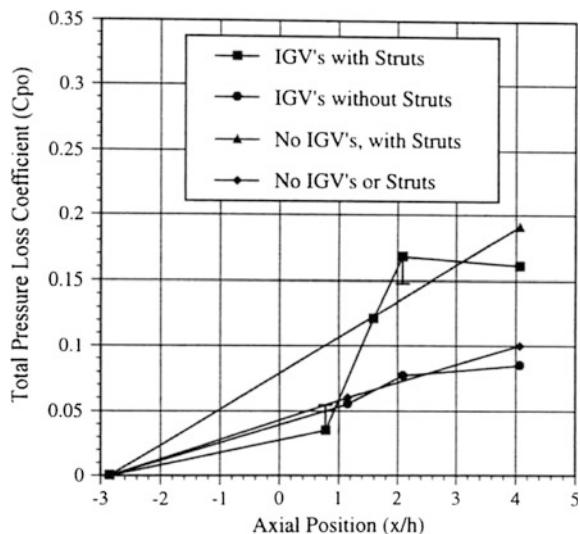
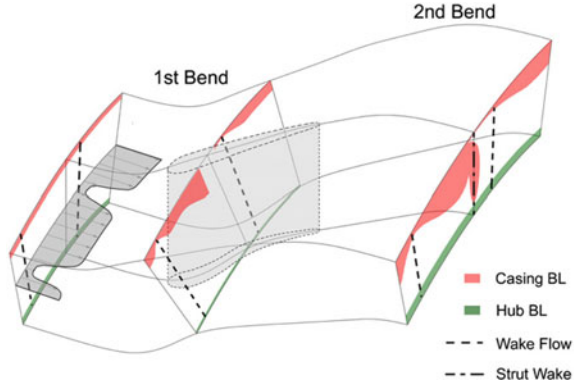


Fig. 3.8 High-loss flow distribution under the influence of wakes and struts [9]



The blocking effect of the strut needs to be taken into account when designing the structure of the ITDs with struts, and the flow area decrease caused by the struts could be compensated by adjusting flow passage profile. This method can reduce the negative effects made by the struts. The secondary flows in the ITD with struts are quite different from those with ordinary guide vanes. The flow structure in the ITD is determined by several factors, including the aspect ratio of the struts wall curvature of the S-shaped ITD, diffusion along the flow direction, influence of the performance of the upstream rotor, and so on (see Fig. 3.8).

Dimensionless parameters of S-shaped ducts without struts mainly include area ratio of inlet to outlet (AR), ratio of radius difference to length (AR/Lx), and ratio of length to height (Lx/h_1). Increasing the first two parameters and decreasing the last parameter would lead to load increase and make the fluid tend to separate. For ducts with struts, one more dimensionless parameter should be considered: t/c (dimensionless maximum thickness), which is related to the separatae diffusion in the strut hub region that makes the flow separate easier. Figure 3.9 shows the relation between the length of duct and losses with struts when $AR = 1$, $Lx/h_1 = 3.3$, and

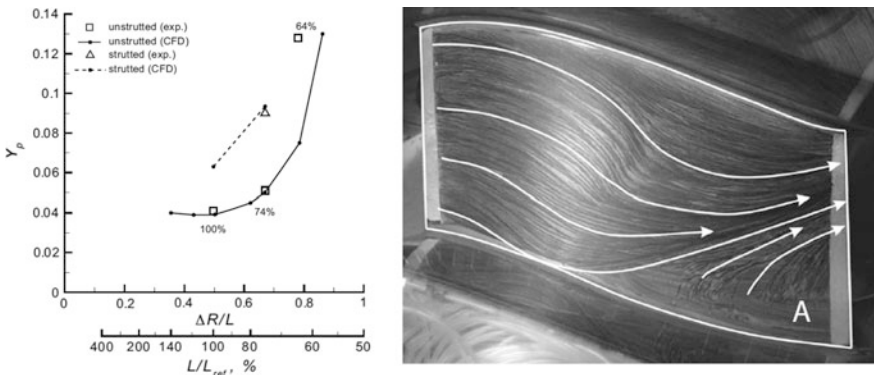


Fig. 3.9 Influence of duct length and struts on losses [10]

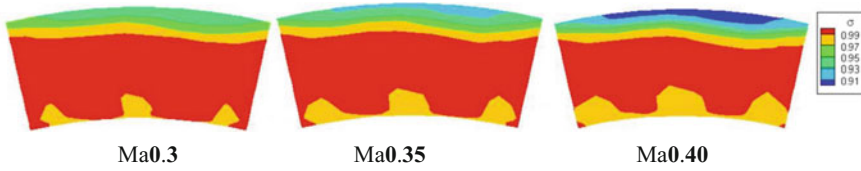


Fig. 3.10 Influence of inlet Mach number on ITD flows [11]

$\Delta R/Lx = 0.5$. It can be deduced from the figure that, the loss had little change when the length decreased from 1 to 74% with the ducts without struts, and then increased rapidly when the length decreased to 64%. For the ducts with struts ($t/c = 0.271$), the loss increased by 50% at the length of 100%, and increased by 88% when the length decreased to 74%. At the length of 100%, there were small separation bubbles in the junction area between the hub and struts, and the bubbles became larger obviously when the length decreased to 74%. These results were obtained in the study of compressor ducts, but they are also applicable in the impact analysis of the struts in inter-turbine ducts (see Fig. 3.10).

3.3 Influence of Aerodynamic Parameters on Flow Structures and Performance

ITD performance depends not only on geometry of it, but also on the condition of incoming flow. In fact, there are various aspects that have different relationships with the performance of the downstream flows involved in the conditions of incoming flow. Non-uniform distribution of flows in the radial direction would directly influence the radial pressure gradient in ITDs, as well as the generation and development of the boundary layer. The wakes of upstream rotor would result in the periodical change of inlet flow angle. The secondary flows and tip leakage flows of the outlet would significantly influence the boundary layer and interact with the high-energy fluid on the casing. The swirl angle, departing from the axis, would result in great change in the flows direction. The influences of some of these parameters are described as follows.

3.3.1 Influence of Inlet Mach Number

The variation of the inlet Mach number in a certain range has little impact on the flow structure in ITDs, but has some impact on the performance, that with the increase of the Mach number, the frictional loss would increase and the total pressure recovery coefficient would decrease. With the practical tangible that the inlet Mach number of the ITD is generally less than 0.5, it is considered that the decreased direction of the changing of the Mach number. One of the major

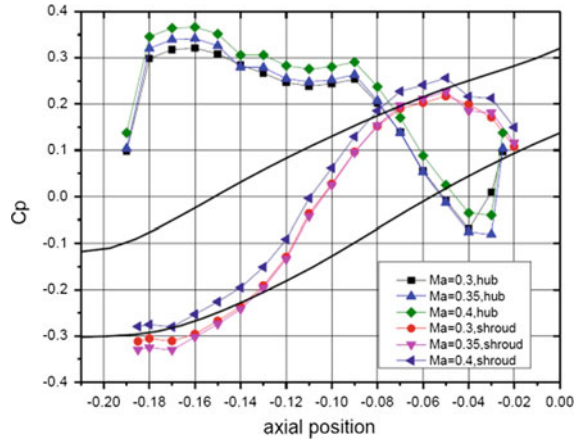
considerations is whether the gas is compressible or not, and larger static pressure rise in ITD would be obtained in the compressible range.

Figure 3.11 shows the ITD flow field distribution at different inlet Mach numbers, which was obtained by Beihang University through detailed experimental measurements of flow field in ITD [11]. The relation between the Mach number and the distribution of the total pressure recovery coefficient at the section located 50% from the inlet can be seen from the figure. The loss at the casing increased obviously with the increase of the Mach number. Figure 3.11 shows the wall pressure distribution and loss in ITD at different inlet Mach numbers. At the casing, the flow was subject to a high adverse pressure gradient, which would cause flow separation easily. There was a positive pressure gradient flow in the second half of the casing. On the surface of the hub, the flow first passed through an adverse pressure gradient region and then a long weak positive pressure gradient region, then entered a sharp positive pressure gradient region at the second turning, and finally changed back to adverse pressure gradient flow. In this process, the adverse pressure gradient regions at the ends would cause separation easily. The pressure at the casing was lower at the front of the ITD, while the pressure at the hub was lower at the rear part. That's because the radial pressure difference caused by curvature variation of the endwall contour would result in radial flow. At different Mach numbers, pressure distribution at the upper and lower endwalls of the ITD was basically the same. Gottlich studied the flow conditions at two different Mach numbers. He found that the ITD had similar flow characteristics at different Mach numbers, except the major difference observed at the outlet [12].

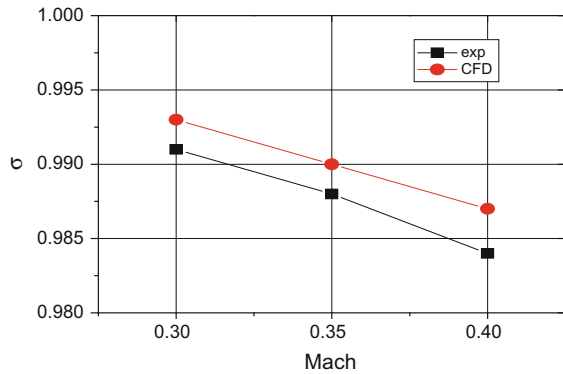
3.3.2 *Influence of Turbulence Intensity*

Turbulence intensity also has great influence on the performance of flows in ITD. As the turbulence intensity increases in a certain range, the boundary layer will resist the flow separation easier. In other words, if there isn't any separation, the turbulence intensity will influence the static pressure coefficient for it has influence on the velocity profile of the boundary layer. Early diffuser studies results is consistent with the statement above. The gas turbine laboratory of NRC-IAR carried out a series of studies in a large scale, low speed, axial turbine facility [13], including an experimental study on the influence of turbulence intensity on the flow field in an ITD. The turbulence intensity was increased by setting up a turbulence grid on the upstream side to the low loaded ITD without struts. Flows in two cases, Case D, high turbulence intensity (2.3%) and Case D-1, low turbulence intensity (0.3%), were studied. Figure 3.12 shows the radial distribution of the total pressure coefficient at positions A1 (inlet) and A5 (outlet) respectively in the two cases. At the position of A1, the thickness of the boundary layer was thin at both the hub and the casing for the low development speed of the boundary caused by the high turbulence intensity. At the position of A5, the thickness of the boundary layers of the hub in two cases are nearly the same. It suggests that high turbulence intensity can enhance the mixing of

Fig. 3.11 Influence of inlet Mach number on ITD performance and flows [11].



(a) Pressure distribution obcasing and hub endwalls



(b) Total pressure recovery coefficient

low-energy fluid and weaken the three-dimensional separation at the hub outlet. Based on the discussion on different turbulence intensity, it can be concluded that high turbulence intensity can slow down the development of boundary layer, which attribute to the delay of the endwall separation and reducing the loss caused by boundary layer separation.

3.3.3 Influence of Inlet flow Angle

Inlet flow angle is one of most important factors among the inlet flow condition parameters. The three key parameters related to the static pressure field in ITD are wall curvature of ITD, axial diffusion rate (area ratio), and inlet swirl angle. Axial

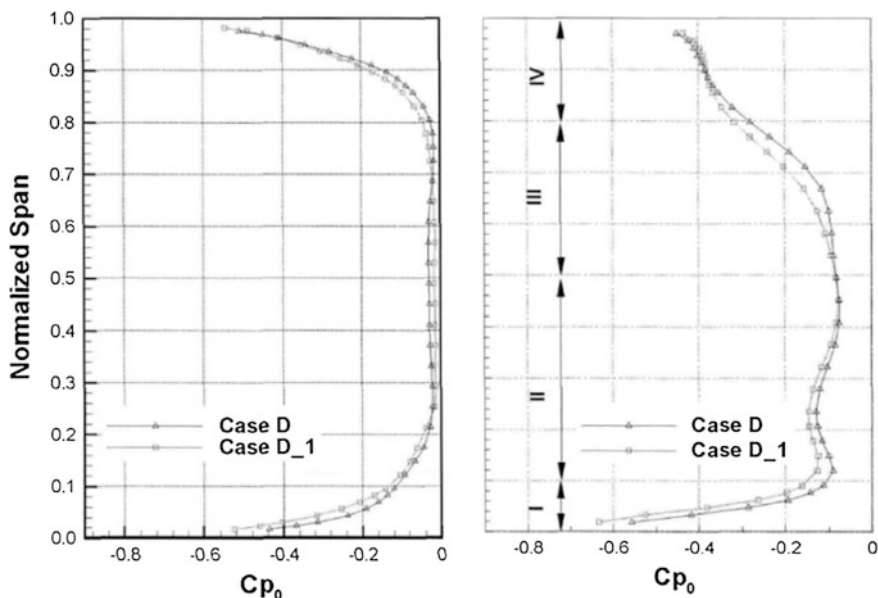


Fig. 3.12 Radial distribution of the total pressure coefficient [13] (left A1 section; right A5 section)

diffusion would result in adverse pressure gradient. Radial pressure gradient is related to the curvature of ITD (local climbing angle). The curvature would counteract or enhance the influence of the swirl angle. The swirl angle would force the fluid to make a turn so that the velocity of the flow would increase, the pressure gradient in axial direction would improve and the centrifugal force on the fluid would change. Because of radial equilibrium, the pressure at the casing would increase, and the pressure at the hub is in the opposite way.

According to the conservation of angular momentum, with the increase of radius, the circumferential speed would decrease which resulting in pressure rise. Thus, it can reduce the effect of streamline curvature as well as the radial pressure gradient, and meanwhile increase frictional loss.

Researches show that the radial pressure gradient would result in the increase of turbulent kinetic energy at the casing and the decrease of turbulent kinetic energy at the hub, which cause the hub and casing have different boundary layer development rate and separation-resisting capability [14]. Therefore, the flow angle would make the boundary layer of the casing more stable, instead of the boundary layer of the hub. On the whole, the flow angle can reduce effective curvature so that the diffusion rate would decrease and the pressure gradient would adverse which would reduce the loss of the boundary layer and increase the loss of the frictional.

The influence of inlet flow angle has been explored or included in quite a lot of studies. Dominy and Kirkham studied the influence of the flow angle with non-rotating wakes, and the inlet flow had thicker wake region and secondary flows

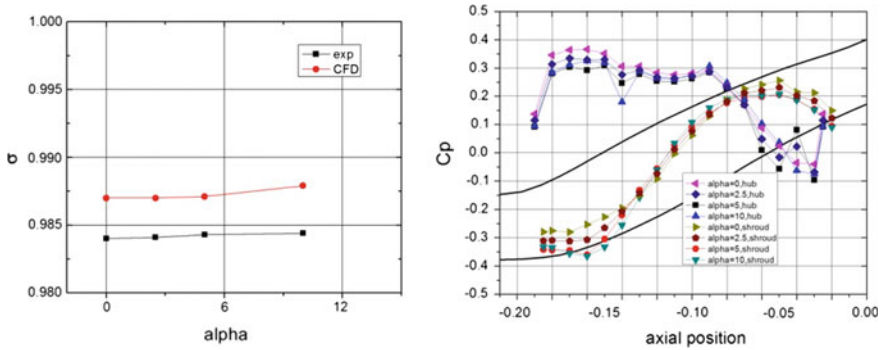


Fig. 3.13 Influence of inflow angle on ITD performance [11]

[15]. Figure 3.13 shows the pressure distribution at both upper and lower endwalls under different inlet flow angle conditions in the same figure. It can be seen clearly that the basic distribution characteristics under different conditions were similar with difference only in value. The data used for drawing was measured by the pressure port at the circumferential position between two struts. When inlet flow angle exist, the pressure on one side of the passage would increase, and the pressure on the other side decrease. This also can be seen from the pressure distribution on the surface of the strut. Therefore, the position of the pressure maximum moved to one side of the strut, and the pressure at the middle position of the strut finally changed.

3.3.4 Influence of Wakes

The influence of wakes is also a major point in ITD research. Dominy and Kirkham [16] studied the influence of two-dimensional wakes on ITDs. They used plates to simulate the wakes of high-pressure blades. The area ratio and hub ratio of the experimental ITD were 1.5 and 0.7 respectively. The Reynolds number based on the inlet passage height was 3.9×10^5 . The study found that the pressure gradient in the passage would drive wake flows from the hub to the casing. The radial velocity in the wake region was the maximum. The wakes maintained their two-dimensional feature in the ITD and only influenced the thickness of the boundary layer near them. The boundary layer thickness of the hub stayed the same in the circumferential direction, while the boundary layer thickness of the casing was not uniform in the circumferential direction due to the effect of the wakes. Vortex pairs come into being on both sides of the wakes, and has little impact at the position of secondary turning because of the positive pressure gradient. There were vortex pairs, which smaller than those at the casing, at the hub outlet of the ITD. The induced deflection angle of the secondary vortex was $\pm 4^\circ$. The high-loss area was located in the place between two wakes, where the boundary layer reached to

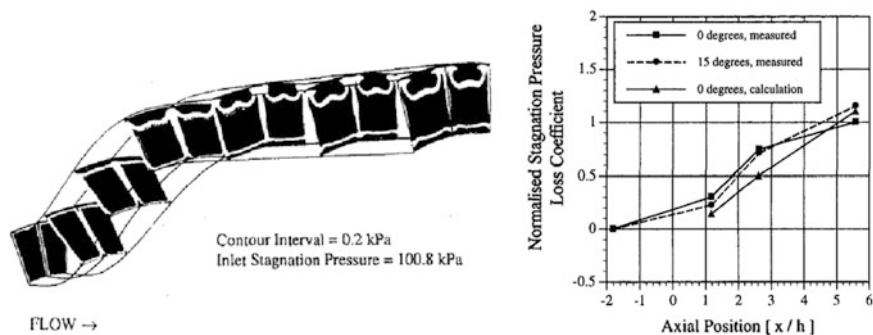


Fig. 3.14 Development of total pressure and loss in ITD along flow direction [16]

the thickest. Another important conclusion is that small changes in inlet condition would have a great impact on the outlet condition because of the radial movement of the wakes in S-shaped ITDs. The secondary flows induced by the wakes had little influence on the overall performance of ITDs, and the influence of the wakes on the pressure distribution on the surface of the hub and the casing was insignificant. This means the loss was redistributed, but not new loss generated. In the meantime, Wendt from Lewis Research Center of NASA also explored the flows in ITDs. By carrying out a large number of detailed experiments, they studied the influence of vortex structure on the flow field in aggressive ITDs [17].

The radial movement of the upstream wakes has influence on the boundary layer of the casing and the hub, and more importantly, the strong secondary flows would result in total pressure distortion. As can be seen from Fig. 3.14, the slight total pressure distortion caused by the wakes at the ITD inlet has great influence on the flow field of the outlet. Changes of flow losses in ITDs at different inflow angles show that, when there is an attack angle, losses would be redistributed, but not new generated.

3.3.5 Influence of Leakage Flows

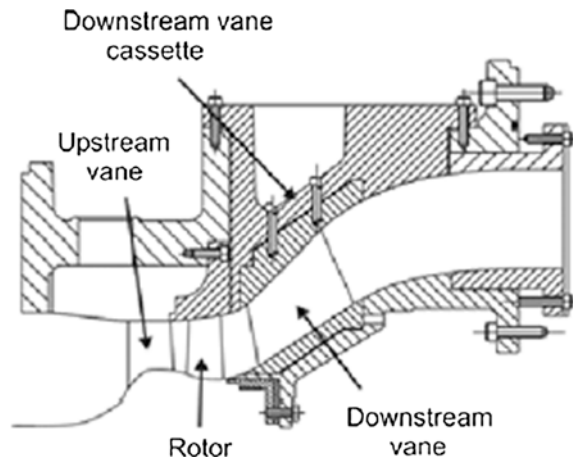
Along with further deep understanding of aggressive ITDs, the influence of upstream rotor on the flow field in ITDs has gradually become a research hotspot. In 2003, Miller et al. studied the influence of upstream rotor on the flow field in an ITD by numerical simulations and experiments [18]. Their experimental facilities included upstream high-pressure turbine stator and rotor, and a downstream low-pressure turbine stator, as shown in Fig. 3.15. The inlet Mach number of the upstream turbine was 0.45. To better study the influence of upstream rotor on downstream flows, the rotor tip clearance was increased to 2.25% of the blade height. The geometrical parameters of the test section were particularly designed for

meeting the requirements of modern aero-engines, so the study is of great significance as a reference. As can be seen from Fig. 3.16, in the condition with tip clearance, three separation lines could be observed on the blade surface due to the influence of tip leakage flows, and this was different from effect without tip clearance. Due to the leakage flow mixing effect, the performance of the region between the trailing edge of the rotor and the leading edge of the downstream stator dropped dramatically. According to the simulation results, the rotor tip leakage flows would increase profile loss by 6% approximately.

In 2004, as a part of EU's AIDA program, MTU Company (Germany) and Graz University of Technology (Austria) built a large-scale transonic aggressive ITD testing rig dedicated for carrying out studies on aggressive ITDs [19]. The gas sources of the testing rig included two centrifugal compressors and two mixed flow compressors, which could provide various inlet conditions. The design power of the test rig was 2800 kW; the design mass flow rate could reach up to 22 kg/s; the design speed of low-pressure turbine was about 11,500 rpm; the turbine inlet temperature changed between 40 and 185 °C; the test rig was equipped with a complete air cooling system (see Fig. 3.17). In the same year, the Aviation Department of Volvo Company (Sweden) also built a large-scale low-speed ITD testing rig in Chalmers University of Technology (Sweden). Its design power was 110 kW; the design mass flow rate was 10 kg/s; the design speed of low-pressure turbine was 1060 rpm; the outlet/inlet area ratio of the test section of the ITD was 1.3, and the outlet geometry was adjustable (see Fig. 3.18) [20, 21].

In 2007, Marn et al. carried out a detailed study on the influence of upstream rotor tip clearance on the flow field of ITD by using the large-scale transonic aggressive ITD testing rig [22]. They used a five-hole probe to perform data measurement. 7 measuring stations were set up along the streamwise direction successively at C (inlet of the ITD), C1, C3, C5, D (the four positions were within the ITD), E (trailing edge of the low-pressure turbine stator), and F (outlet of the ITD). Tip clearance was taken as a variable, which was set at 1.5% and 2.4% of the

Fig. 3.15 Miller's test section



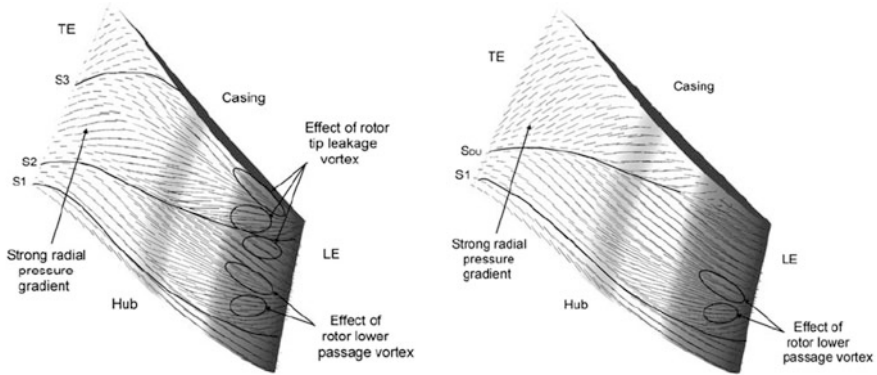


Fig. 3.16 Comparison of flows on suction surface between conditions with and without tip clearance [18]

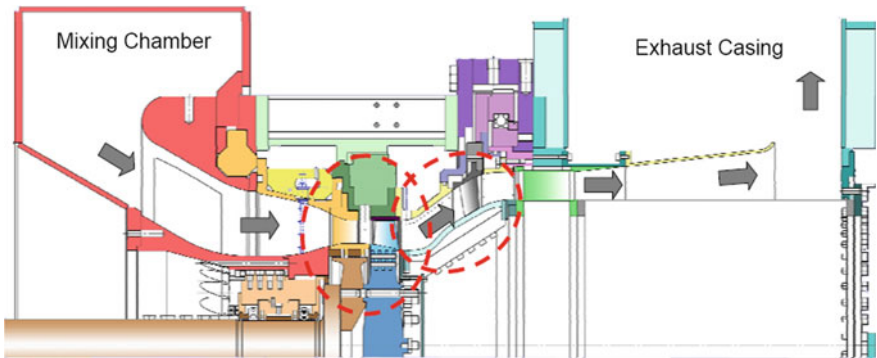


Fig. 3.17 Large-scale transonic aggressive ITD testing rig of Graz University of Technology [19]

rotor blade height respectively. As can be seen from Fig. 3.19, when the tip clearance was larger, high Mach number could be observed at the area above about 80% of the blade height at the inlet of the ITD. Trend could be seen in Fig. 3.20 as well; larger tip clearance result in higher total pressure in the area near the blade tip. By comparing the Mach number distribution with the total pressure diagram, It can be seen that tip clearance had little influence on the Mach number distribution and total pressure distribution at the lower part. Figure 3.20 shows the changes of total pressure loss along the streamwise direction. As can be seen from the figure, the region where the loss has a maximum increase is placed from C to C1. It also can be seen clearly from the figure that larger tip clearance led to higher total pressure loss. Thus, we could draw a finally conclusion that the influence of tip clearance size on the flow field was different at different measuring stations, and the influence would spread to the entire flow field. Therefore, the entire system

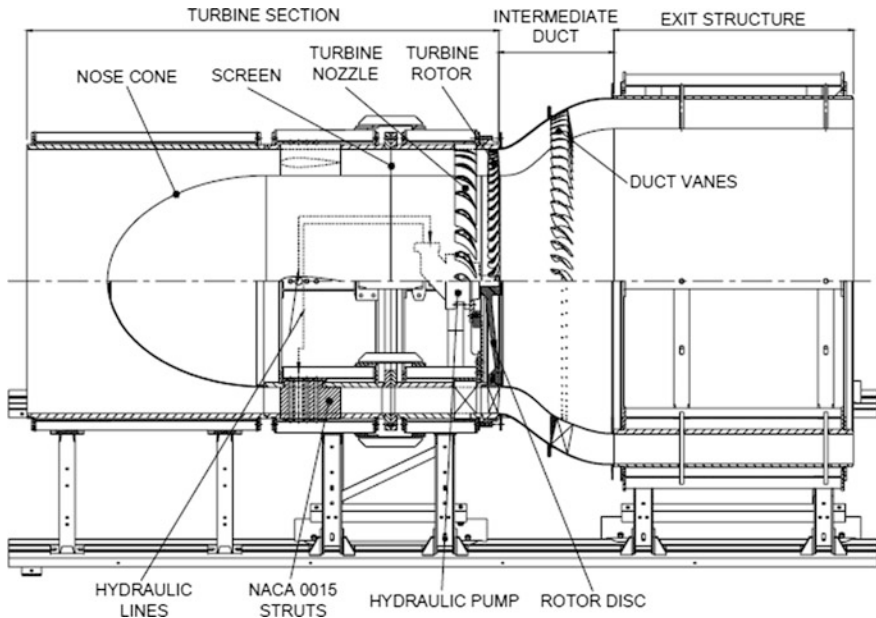


Fig. 3.18 Large-scale low-speed ITD testing rig of Chalmers University of Technology [20]

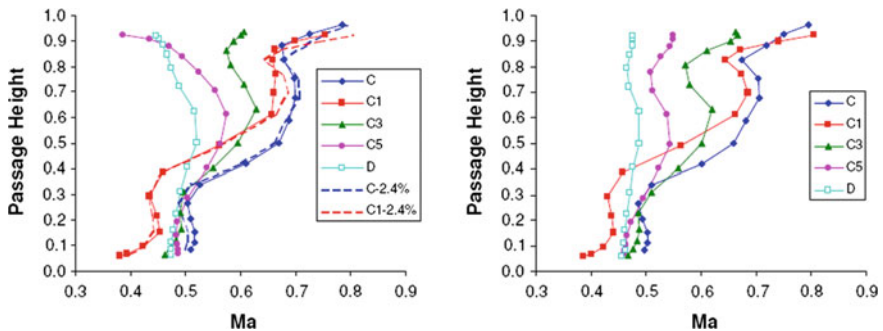


Fig. 3.19 Distribution of Mach number along passage height [22] (left small clearance; right large clearance)

consisting of turbine and inter turbine duct and following parts has to be taken into account during the design process of inter turbine ducts.

Sanz et al. [23] numerically investigated the effect of upstream tip leakage flow on the flow field in an ITD. They studied the effect with three different tip clearance sizes: 0, 0.8, and 1.3 mm. Figure 3.21 compares the vorticity distribution along the streamwise direction at the ITD inlet, which was obtained by numerical simulation. A conclusion could be drawn that leakage vortices caused by upstream rotor tip

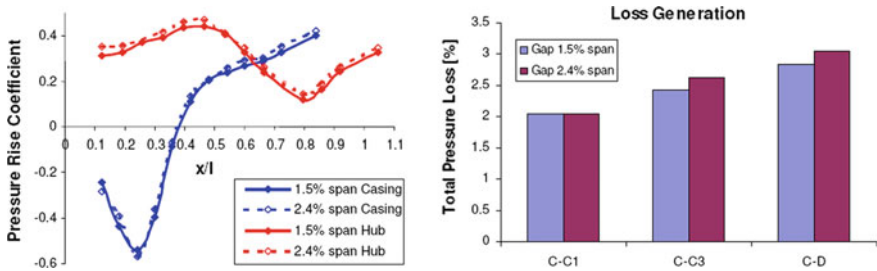


Fig. 3.20 Pressure rise coefficient along the flow direction and comparison of total pressure loss [22]

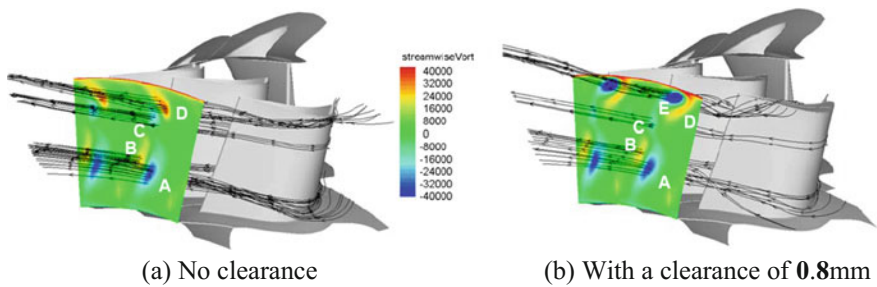


Fig. 3.21 Vorticity distribution at the ITD inlet [23].

clearance could be seen in the diagrams. Figure 3.22 shows the velocity distribution on the meridian plane with different clearance sizes. In the case of no clearance, the high-speed zone at the inlet was smaller compared to the cases with clearance, and there was a low-speed zone near the casing. That's because part of the flow in the tip region did work in the rotor and lost some energy. As a result, the outer duct region is taken by stagnant fluid, so that the effective increase in flow area is smaller than designed and the main flow is less decelerated. When tip clearance existed, the tip leakage flow energizes the outer flow so that it can follow the strong curvature. Thus it can be concluded that upstream rotor tip clearance is a vitally important factor in ITD design process.

Marn further studied the influence of tip clearance size on the flow field in ITDs by a series of experiments, and concluded that tip clearance size would influence the development of separated flow, and that vortex structure in the flow field could not be predicted accurately without considering the boundary condition caused by upstream rotor. As can be seen from the Fig. 3.23, tip clearance size could influence the size of separation points in the endwall region, which further verifies the significance of upstream rotor on ITDs [24].

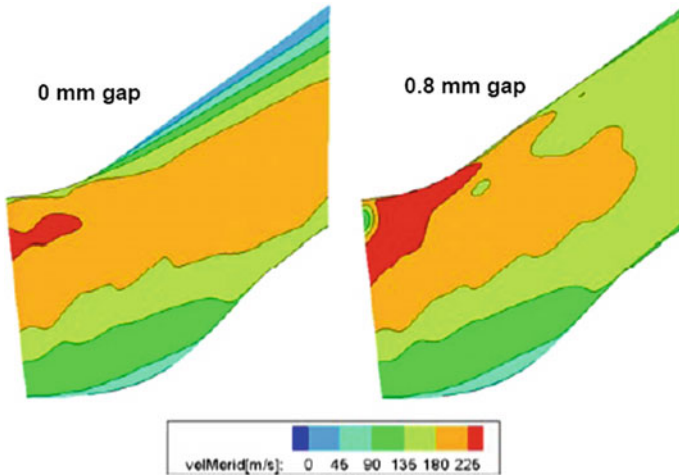


Fig. 3.22 Velocity distribution on meridian plan of the ITD [23]

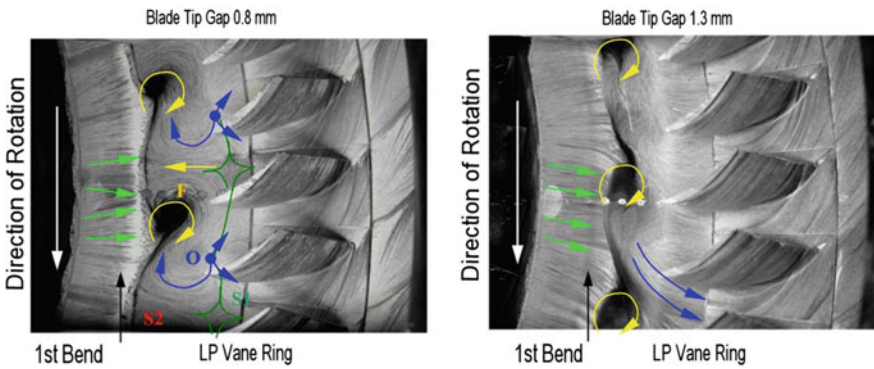


Fig. 3.23 Results of oil visualisation for the upper endwall [24]

3.4 Optimal Design of ITDs and Flow Control

3.4.1 Optimal Design of ITDs

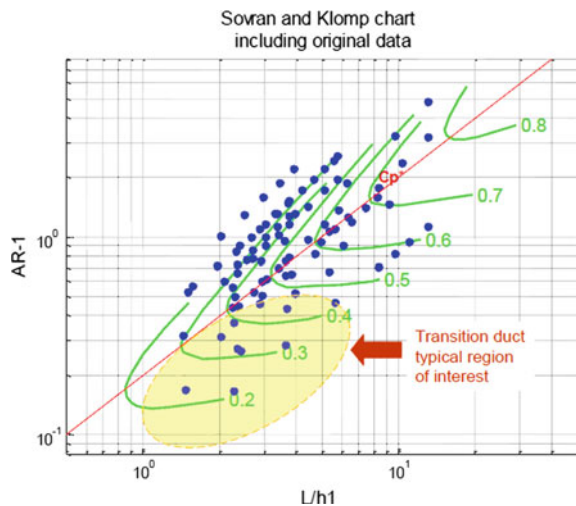
In 1967, Sovran and Klomp experimentally studied three types of rectilinear diffusers, and provided structural drawings of the three types of diffusers, which serve as the reference samples with engineering significance for preliminary design of modern ITDs. After that, they carried out experimental studies on ten cases with different geometrical parameters ($AR-1$ and Lx/h_1), and worked out the diffuser performance curve according to the experimental results, as shown in Fig. 3.24

(generally called S&K chart) [25], in which the blue points represent the original experimental data points. The results suggested that, without considering the influence of climbing angle on ITD performance, both large area ratio and length-to-height ratio could help increase the total pressure recovery coefficient in ITDs.

In earlier days, S&K chart was the major tool in ITD design. However, the influence of flow angle and struts had not been taken into account in performance diagram. Generally, the inlet flow angle of ITDs is non-uniform because ITDs are located downstream of the high-pressure turbine, and thus the total pressure loss in ITDs is related to the losses caused by the flow angle and struts. Couey et al. numerically studied 63 ITD cases, which had different area ratios, length-to-height ratios, and climbing angles, and made some improvements to Sovran and Klomp's diffuser performance diagram (see Fig. 3.24) by considering the influence of climbing angle (see Fig. 3.25) [26].

In recent years, researchers have done a great deal of work in optimal design of aggressive ITDs. First, based on the ITD performance influenced by factors and the influence characteristics, they proposed some significant geometrical parameters in optimal design of ITDs, such as area ratio, hub/casing profile, etc. Taking the total pressure loss coefficient as the objective function, Hu et al. [27, 28] carried out geometric optimization of ITDs by changing area distribution along the streamwise direction as well as curvature of the hub and casing. They concluded that the area at the first turning should be enlarged rapidly so as to minimize the total pressure loss in ITDs; that's because, despite of the rapid increase in thickness of the boundary layer, the velocity at the ITD inlet is high enough to avoid separation even under a strong adverse pressure gradient. Similarly, the area at the ITD outlet should be enlarged rapidly as well, which can be achieved by adjusting local curvature (see Fig. 3.26).

Fig. 3.24 Diffuser performance curve proposed by Sovran and Klomp (S&K chart) [25]



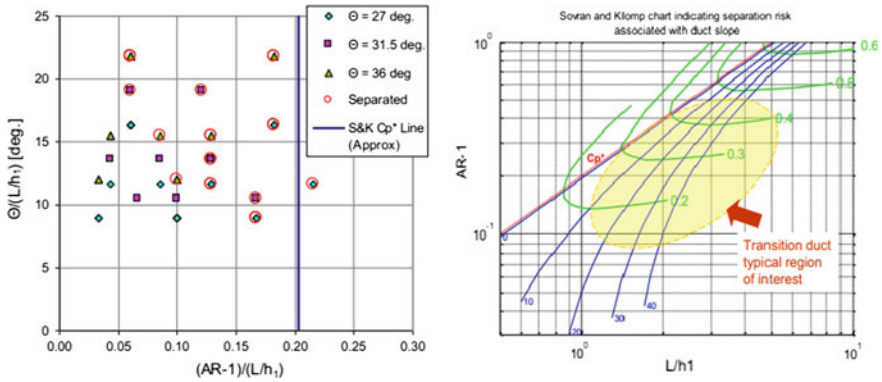


Fig. 3.25 Improved relation between geometrical parameters and ITD performance [26]

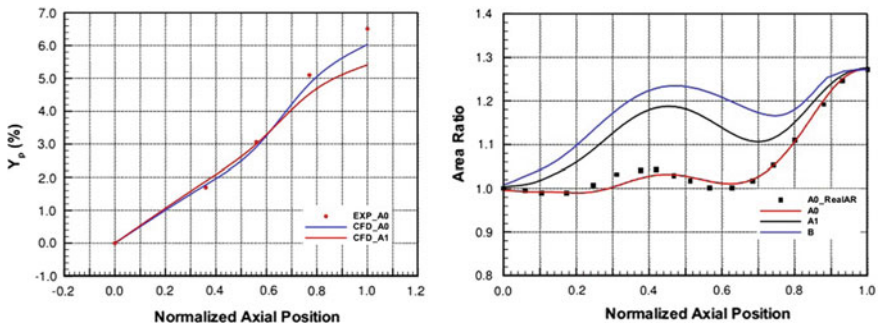


Fig. 3.26 Loss in ITD and area distribution along the streamwise direction [28]

The aerodynamic design method for ITDs used currently is a process of repeated iteration and optimization, which includes four steps: selection of overall geometrical parameters, design of meridional passage contour, strut blade profiling, and verification of aerodynamic performance.

1. Selection of overall geometrical parameters: First, according to the dimensional requirements of the overall plan for the ITD, including the requirements of inlet size and inclination (referring to aerodynamic design of the high-pressure turbine) and the requirements of outlet size and inclination (referring to aerodynamic design of the low-pressure turbine), the inlet-to-outlet area ratio (AR) of the ITD can be calculated. The maximum axial length can be then determined according to the axial length requirements for both the low-pressure turbine and turbine rear frame. The length-to-height ratio, Lx/h_1 , could be then calculated. In addition, the climbing angle of the ITD can be roughly obtained. Thus, all the overall geometrical parameters are determined. After that, it need to be checked

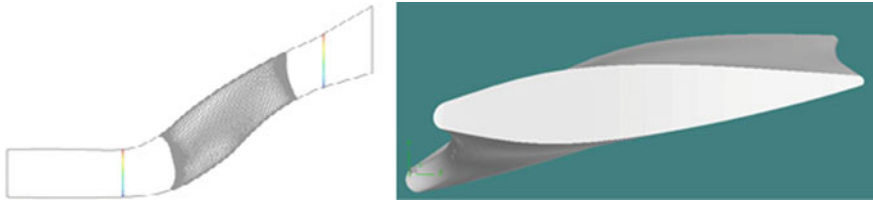


Fig. 3.27 Profile (*left*) and strut (*right*) of ITD [29]

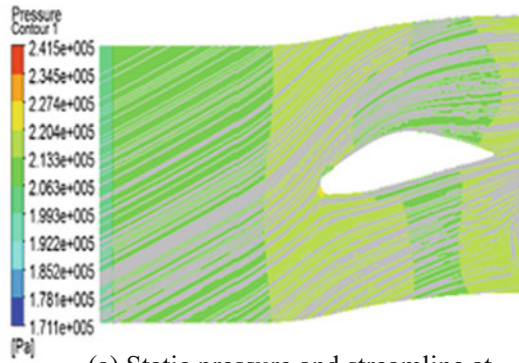
if the flow separation generates according to the relation between geometrical parameters and flow separation (see Fig. 3.25).

2. Design of meridional passage contour: Designers should carry out preliminary design of reasonable contour of the meridional passage according to the parameters determined in the above step, connect the inlet and outlet of the ITD with smooth curves, and ensure the inclinations of the inlet and outlet meet the requirements of the design scheme.
3. Strut blade profiling: In this step, designers should choose a reasonable blade profile according to the principles, such as achieving a proper ratio of the maximum thickness to chord length, minimizing profile loss, and so on, then work out a proper chord length of the strut, its leading edge and trailing edge lines, as well as a reasonable stack mode, and finally produce the profile of the strut by using the profiles of several sections at different blade height (see Fig. 3.27).
4. Verification of aerodynamic performance: The aerodynamic performance of the ITD should be verified by using CFD software. Aerodynamic performance requirements include flow loss requirements for the ITD and matching requirements with the downstream low-pressure turbine. If these requirements cannot be met, the meridional passage contour should be readjusted, and the strut profile with its verification should be performed again. This process of repeated iteration and optimization should be carried on until all the requirements are met. Figure 3.28 and Figure 3.29 show the results of numerical verification for an ITD design scheme.

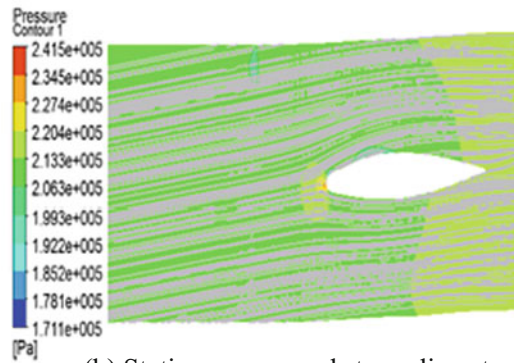
3.4.2 Flow Control in ITDs

Flow control technologies have also been applied in ITDs, so as to further improve the aerodynamic performance of ITDs. Besides, a series of studies about flow control have been carried out. In 2000, the Pratt & Whitney Company (USA) and United Tech Research Center proposed the idea of applying flow control technologies in aggressive ITDs to delay or even eliminate boundary layer separation, thus improving ITDs' aerodynamic performance. Then, they carried out numerical simulation to investigate the control of boundary layer separation in ITDs by using

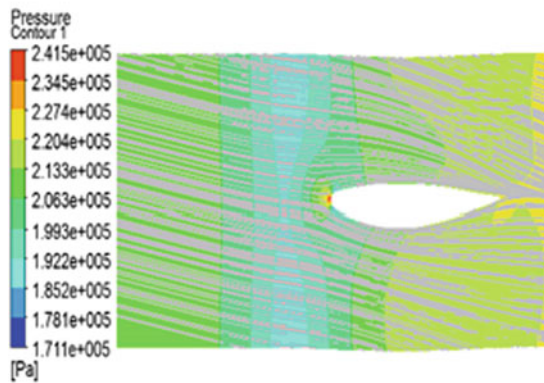
Fig. 3.28 Results of numerical verification for an ITD design scheme [29].



(a) Static pressure and streamline at 10% of blade height



(b) Static pressure and streamline at 50% of blade height



(c) Static pressure and streamline at 90% of blade height

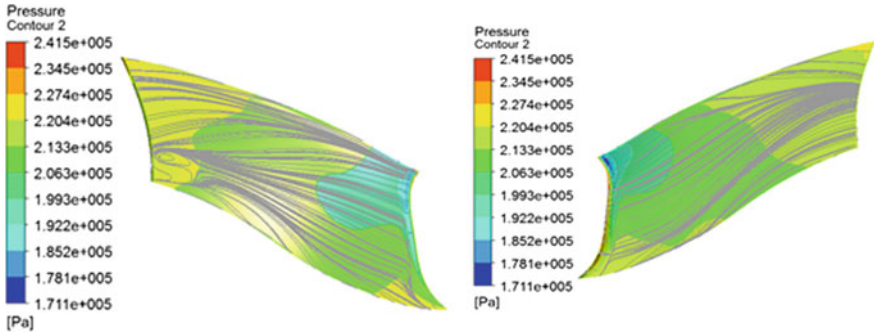


Fig. 3.29 Static pressure on strut surface and limiting streamline [29]

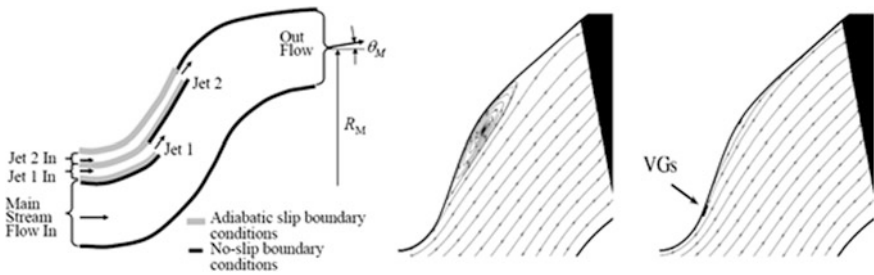


Fig. 3.30 Flow control for aggressive ITDs [30, 31] (left jet type control; right vortex generator)

jets, as shown in Fig. 3.30. Florea et al. studied the flow control technologies for ITDs by numerical simulation [30], and the results showed that flow control technologies, together with advanced ITD endwall design, could effectively improve the flow field, eliminate boundary layer separation, and significantly improve ITDs' aerodynamic performance. The flow-control-enabled ITD and low-pressure turbine brought about a 0.6% rise in fuel efficiency.

Wallin et al. from Chalmers University of Technology used vortex generators to control the flows in aggressive ITDs, and designed flow-control-enabled aggressive ITDs [20]. They concluded that the flow control enabled by vortex generator would increase the loss in ITDs, but if arranged appropriately, the loss caused by the generator might be less than the loss reduced from restraining boundary layer separation. As can be seen from Fig. 3.30, the flow-control-enabled ITD with vortex generators had obviously reduced separation area near the casing on the meridian plane, reduced loss in the flow passage, and improved the flow conditions in the inlet of the guide vanes of the low pressure turbine.

The results of an experimental study on flow control in an aggressive ITD using vortex generators [31] showed that the vortex generators could effectively restrain boundary layer separation in the aggressive ITD with relatively great separation

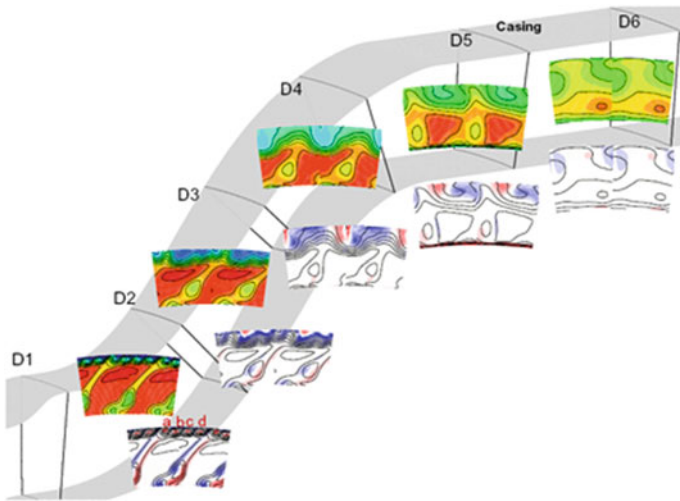


Fig. 3.31 Influence of flow control on total pressure and velocity [31]

(see Fig. 3.31). In ITDs, struts are mainly used for supporting and only few struts exist, so their flow control effect is limited and the flow would rapidly deteriorate in the case with large variation of inflow angle [32].

References

1. Aviation Industry Corporation of China. (2010). *Advanced technology analysis of LEAP-X engine [R]*. Beijing: China Aviation Industry Development Research Center.
2. GE90[DB/OL]. <http://zh.wikipedia.org/wiki/GE90>.
3. Pratt & Whitney PW1000G. (2008). *Jane's aero engine [M]*.
4. Kline, S. J., Abbott, D. E., & Fox, R. W. (1958). *Optimum design of straight walled diffusers [M]*. Stanford: Department of Mechanical Engineering, Stanford University.
5. Zhang, X. F., Hu, S., & Benner, M., et al. (2010). *Experimental and numerical study on an inter-turbine duct [R]*. ASME Paper IMECE2010-37322.
6. Kuchana, V., Guntu, S., & Srinivasan, B., et al. (2013). *Numerical study on inter-turbine ducts with variable curvature distribution [R]*. AIAA Paper 2013-3686.
7. Norris, G., & Dominy, R. G. (1997). Diffusion rate influences on inter-turbine diffusers [J]. *Journal of Power and Energy*, 211(3), 235–242.
8. Norris, G. (1998). *Flows through S-shaped annular, inter-turbine diffusers [D]*. Durham University.
9. Norris, G., Dominy, R. G., & Smith, A. D., et al. (1999). *Flow stability within a diffusing, annular s-shaped duct [M]*. Rolls-Royce PLC.
10. Naylor, E. M. J., Dueñas, C. O., Miller, R. J., et al. (2010). Optimization of nonaxisymmetric endwalls in compressor S-shaped ducts[J]. *Journal of Turbomachinery*, 132, 011011.
11. Huoxing, L. (2012). *Experimental study on aggressive inter-turbine duct with strut fairings [R]*. Beijing: Beihang University.
12. Göttlich, E., Marn, A., & Malzacher, F. J., et al. (2007). Experimental investigation of the flow through an aggressive intermediate turbine duct downstream of a transonic turbine stage

- [C]. In *Proceedings of 7th European Conference on Turbomachinery Fluid Dynamics and Thermodynamics*, 2007.
13. Shuzhen, Hu. (2012). *Flow mechanism and flow control investigation within inter-turbine duct [D]*. Beijing: Graduate School of Chinese Academy of Sciences (Engineering Thermophysics).
 14. Bradshaw, P. (1973). *Effects of streamline curvature on turbulent flow [R]*. Paris (France): Advisory Group for Aerospace Research and Development.
 15. Dominy, R. G., & Kirkham, D. A. (1995). *The influence of swirl on the performance of inter-turbine diffusers [J]*. Rolls Royce PLC-Report-PNR.
 16. Dominy, R. G., & Kirkham, D. A. (1996). The influence of blade wakes on the performance of inter-turbine diffusers [J]. *Journal of Turbomachinery*, 118(2), 347–352.
 17. Wendt, B. J., & Reichert, B. A. (1996). Vortex ingestion in a diffusing S-duct inlet [J]. *Journal of Aircraft*, 33(1), 149–154.
 18. Miller, R. J., Moss, R. W., & Ainsworth, R. W., et al. (2003). *The development of turbine exit flow in a swan-necked inter-stage diffuser [R]*. ASME Paper GT2003-38174.
 19. Göttlich, E., Marn, A., Pecnik, R., & Malzacher, F. J., et al. (2007). *The influence of blade tip gap variation on the flow through an aggressive S-shaped intermediate turbine duct downstream of a transonic turbine stage—Part II: time-averaged results and surface flow [R]*. ASME Paper GT2007-28069.
 20. Wallin, F., & Eriksson, L. E. (2006). *Response surface-based transition duct shape optimization [R]*. ASME Paper GT2006-90978.
 21. Axelsson, L. U., Osso, C. A., & Cadrecha, D., et al. (2007). *Design, performance evaluation and endwall flow structure investigation of an S-shaped intermediate turbine duct [R]*. ASME Paper GT2007-27650.
 22. Marn, A., Göttlich, E., & Pecnik, R., et al. (2007). *The influence of blade tip gap variation on the flow through an aggressive S-shaped intermediate turbine duct downstream a transonic turbine stage: Part I—time-averaged results [R]*. ASME Paper GT2007-27405.
 23. Sanz, W., Kelterer, M., & Pecnik, R., et al. (2009). *Numerical investigation of the effect of tip leakage flow on an aggressive S-shaped intermediate turbine duct [R]*. ASME Paper GT2009-59535.
 24. Marn, A. (2008). *On the aerodynamics of aggressive intermediate turbine ducts for competitive and environmentally friendly jet engines [M]*. NA.
 25. Sovran, G., & Klomp, E. D. (1967). Experimentally determined optimum geometries for rectilinear diffusers with rectangular, conical or annular cross-section [J]. *Fluid Mechanics of Internal Flow*, 270–319.
 26. Couey, P. T., McKeever, C. W., & Malak, M. F., et al. (2010). *Computational study of geometric parameter influence on aggressive inter-turbine duct performance [R]*. ASME Paper GT2010-23604.
 27. Zhang, X. F., Hu, S., & Benner, M., et al. (2010). *Experimental and numerical study on an inter-turbine duct [R]*. ASME Paper IMECE 2010-37322.
 28. Hu, S., Zhang, X. F., Benner, M., et al. (2010). *Geometric optimization of aggressive inter-turbine ducts [R]*. ASME Paper IMECE 2010-37323.
 29. Zou, Z. (2011). *Aerodynamic design for low pressure turbine of a turbofan engine [R]*. Beijing: Beihang University.
 30. Florea, R., Bertuccioli, L., & Tillman, G. (2007). Flow-control-enabled aggressive turbine transition ducts and engine system analysis [J]. *Journal of Propulsion and Power*, 23(4), 797–803.
 31. Zhang, Y., Hu, S., & Zhang, X. F., et al. (2012). *Flow control in an aggressive inter-turbine duct using low profile vortex generators [R]*. ASME Paper GT2012-69951.
 32. Du, Q., Wang, P., Gong, J. B., et al. (2012). Design performance evaluation and vortex structure investigation of different S-shaped intermediate turbine ducts [J]. *Science China Technological Sciences*, 55(12), 3510–3520.

Chapter 4

Flow Mechanisms in Low-Pressure Turbines

4.1 Geometrical and Aero-Thermal Characteristics of Low-Pressure Turbines and their Development Trends

4.1.1 *The Geometrical and Aero-Thermal Characteristics of LP Turbines*

In aircraft engine, the main task for low-pressure turbine (LP turbine, LPT) is to drive rotational components, for example the fan or booster stages. It also can be used as direct power output apparatus, which provides shaft power to drive a propeller, fan, or other lift or thrust equipment. In turboprop and turboshaft engine, LP turbine is also known as power turbine or free turbine. For the spatial position in the flow path, LP turbine locates behind the high-pressure turbine (HP turbine, HPT). Between the HP turbine and LP turbine, in high bypass ratio(BPR) turbofan engines, there usually arranges the bearing framework known as the inter-turbine duct. And the LP turbine is connected with outlet nozzle using the turbine rear frame (TRF).

The mission of the aircraft and its operating environment determine that LP turbine has its own characteristic geometrical and aero-thermal parameters. Comparing with the HP turbine geometry, due to the lower rotational speed and different aero-thermo parameters, LP turbine is with larger size, more stages, and heavier weight. Take the LP turbine that directly drives the fan in high BPR turbofan engine as an example. Since the LP turbine and the fan are connected via the same shaft, they must be in the same rotational speed. Considering the fan performance and noise restrictions, tip velocity of fan can be generally established. With increasing the fan diameter, it results in a low level rotational speed of the LP shaft, which limits single-stage LP turbine power capability. Also because the LP turbine has relatively low inlet temperature and pressure, it further limits the work capability of units mass flow rate. Additionally, though the gas mass flow rate through the LP turbine is less than that through the fan, the power output from LPT

should not be low. Eventually it leads to the design of LP turbine has larger outer diameter and more stages to avoid lack of power capacity. For the LP turbine that drives BPR turbofan, it can be 5–7 stages and contributes 25–30% of the whole engine weight. In addition, since the hot gas already expands in the HP turbine, the gas density reduced significantly, which leads to increased volume flow rate. Meanwhile, due to the Mach number limitation at LP turbine outlet to be in the range of 0.4–0.6, it ultimately leads to an increasing cross section area of the flow passage. Therefore, geometrically LP turbine has longer blade with larger aspect ratio and smaller hub diameter. A typical LP turbine blade aspect ratio is between 3:1 and 7:1. In high-loaded low pressure turbine cascade, the flow turning angle is large, typically 100° – 110° or even higher, so the cascade has a relatively smaller convergence. To summary, the main geometric characteristics of the LP turbine cascade are, low hub-to-tip ratio, high aspect ratio, large turning angle and small convergence passage.

In terms of velocity triangle, the low shaft speed means a lower tangential speed. Generally, it results in significantly larger flow coefficients and blade loading factors when compared to the HP turbine, and thus is not conducive to improving the aerodynamic performance of LP turbines [1].

In the aspect of aero-thermal process, since the LP turbine locates after the HP turbine or ITD, it faces the upstream blade wake, leakage flow, secondary passage vortices, and also the existing of strong shock wave near high loaded HP turbine trailing edge. All these lead to a complicated inflow condition for LP turbine, and aggravate the uneven distribution of the inflow aero-thermal parameters. It means that design should consider the matching between LP and HP turbine within all operating points. In addition, the LP turbine outlet normally requires axial out flow. With small convergence of the blade passage, it is not easy to achieve in the final stage of a LPT. However, if the outlet guide vane in the turbine rear frame (TRF) is designed with aero-loading, the LP turbine outlet flow angle may deviate from the axial for 20° – 30° . This is beneficial to reduce the number of LP turbine rows. Meanwhile, the LP turbine passage has the lowest hot gas density and the lowest Reynolds number level [2] in the engine. As shown in Fig. 4.1, during high altitude cruise, the LP turbine Reynolds number can be as low as 3×10^4 to 5×10^4 [3], especially for the final stage. In this case, low Reynolds number effect is one of the key factors on LP turbine aerodynamics performance, for example the efficiency and flow capacity, which must be considered specific [4]. To summarize, for conventional LP turbine, the main aero-thermo characteristics include low Mach number, low Reynolds number, high loaded, and complex inflow boundary conditions.

4.1.2 Flow Characteristics and Losses in LP Turbine Passages

Figure 4.2 shows the typical flow visualization results on a LP turbine blade [5]. As shown in the figure that the flow field near blade tip and hub has been strongly

Fig. 4.1 Reynolds number levels of components in a mid-size engine [2]

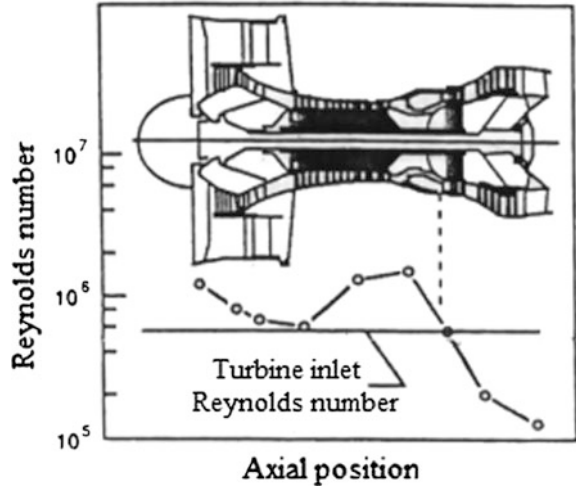
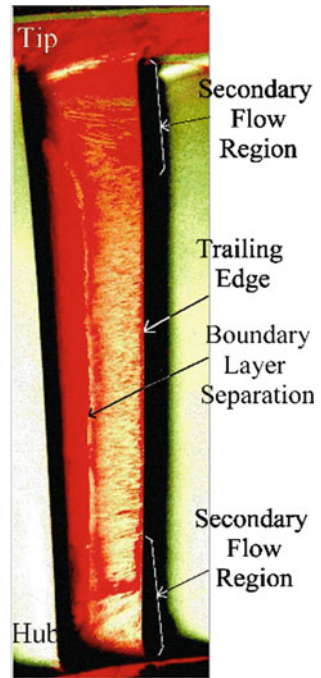
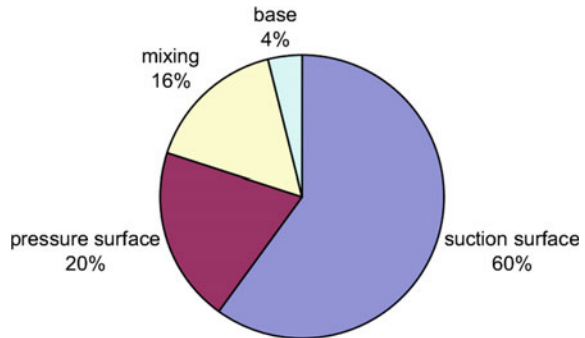


Fig. 4.2 Flow visualization on a LP turbine blade [5]



impacted by the secondary flow with three dimensional characteristics. Secondary flow loss also dominates these regions. However, due to the large aspect ratio of the blade, the region impacted by the secondary flow is limited, thus its loss contributes small portion of the overall losses. In most of the blade span, flow shows

Fig. 4.3 Estimated loss breakdown for datum blade [7]



quasi-two-dimensional characteristics that boundary layer associated profile loss dominates. Since the LP turbine rotor blade normally has shroud, the tip leakage flow is relatively weak and its loss is not significant. So in general, the profile loss is the most important source of aero-loss, the main factor which affects the performance, and also the major point should be considered in the design.

The profile loss is mainly determined by the status of the boundary layer development on the blade, base region formed due to boundary layer shedding at the trailing edge, and mixing between wake flow and main flow [6], etc. As shown in Fig. 4.3, due to the small radius of the trailing edge, the base region loss and mixing loss is less. Relatively, the flow condition of boundary layer contributes the major portion of aero loss, which directly affects the friction loss and separation loss, etc. Here, the blade surface friction loss is proportional to the cubic of hot gas velocity. Due to the velocity difference between pressure side and suction side, the pressure side friction loss is significant less comparing to that on suction side. In addition, due to the adverse pressure gradient near the trailing edge, flow separation often happens on the suction side, which causes more serious damage [5], resulting in a sharp increase of loss. Studies showed that the suction side total loss raised about 60% while about 20% on the pressure side. Mixing loss caused by wake is about 16% and the rest is base region loss, which accounting for about 4% [7]. Therefore, effective control of the boundary layer state, especially on suction side, is particularly important for LP turbine profile design.

Although the secondary flow loss contributes small proportion of the overall loss, it cannot be simply ignored in detail design process. The shrouded LP turbine blades can suppress leakage flow and vortices, but the flow in the shroud region is complicated. If the shroud is not designed properly, leakage flow will interact with main flow and leads to the influence that may not smaller than the unshrouded blades [8]. In addition with ultra-high-lift LP turbine profile, the corresponding secondary flow changes significantly. With the interaction between secondary flow and separation bubble near the leading edge of the pressure side, it enhances secondary flow intensity and further distorts the boundary layer [9], the secondary flow loss increases. Therefore, secondary flow loss cannot easily be ignored in high performance and high-loaded LP turbine design.

4.1.3 Development Trends of LP Turbine Design

In the past two decades, research of fluid mechanism and high-performance high-loaded LP turbine aero-design has seek significant attention from engine companies and universities. With the support from many research programs, the understanding of flow mechanism and the capability of component design have been improved rapidly. The new technologies are more and more used in aero-engine design, which effectively improves its performance. Technically, some major trends are:

1. Through the careful study of aerodynamics in real geometry and thermo environment, establish the mathematical-physical model; develop detail design methods, explore the potential of improving efficiency, provide support to enhance performance.

In aero-engine, different components have different impacts on the specific fuel consumption (SFC). Table 4.1 shows the components performance exchange to SFC for a civil aircraft cruise at 0.8 Mach number in 10,000 m altitude. It shows that LP turbine efficiency has significant impact on SFC [10] that 1% efficiency change in LP turbine causes 0.9% or even more SFC change. With the incense of bypass ratio (BPR) in civil turbofan engine, this sensitivity would be even larger. Thus, to increase LP turbine efficiency is important for reducing the cost of the engine or even the operation. But with matures of design technology, the development of individual technology has difficulty to significantly enhance the LP turbine efficiency. So, people gradually turned their attentions to some design details which had been overlooked in the past, such as shroud, hub seal plate, blade leading edge shape, blade-hub junction shape, endwall non-axisymmetric surfaces, and so on. More detailed design methods and guidelines are developed accordingly [11]. Although each individual technology has limited contribution to enhance performance, their integration is very impressive, so that the LP turbine performance still rose considerably.

2. Deep understand the unsteady flow mechanism, investigate the ways to apply unsteady effects within design purpose and develop corresponding design method, increase loading with similar or improved efficiency in order to reduce weight, also reduce the production and maintenance cost by reducing parts.

Table 4.1 Fuel consumption sensitives with components efficiency in one civil aviation turbofan [10]

1% change in efficiency of	Fan (%)	LP compressor (%)	HP compressor (%)	HP turbine (%)	LP turbine (%)
Percent change in specific fuel consumption (SFC)	0.62	0.22	0.66	0.82	0.96

The weight of LP turbine accounts for a large proportion of the whole engine weight, which can be up to one-third. And the huge amount of LP turbine blades, which can be even thousands, increases the cost of manufacturing and maintenance. Survey data shows that with 17% engine weight reduction, the operation cost can reduce by 1%, which means cost deduction \$200,000 per year [12]. Thus another important LP turbine technology trend is to increase load with current or improved performance, which means to reduce number of blades and turbine weight. The most successful example is the “calmed” effect application. This technology improved the LP turbine loading by 30–40%, and has already been applied to the UK Rolls-Royce BR71 * series, TRENT series, Engine Alliance’s GP7000 series and other high bypass ratio (BPR) turbofan engine [13–15].

3. Based on high-performance high-loaded design methods, further investigate the influences of small geometric deviations and assembly errors, perform parameter optimization, thus to develop robust aero design techniques, and reduce production and maintenance costs.

In modern aero engine technology, manufacturing is crucial to engine performance and reliability. There are defective events occurred due to manufacturing and assembly errors. Due to the complicated flow field in turbomachinery, subtle changes in the key parameters would directly affect detailed flow field and components matching, which would eventually leads to significant change in performance. Study from Cambridge University shows that the change of geometry or surface roughness at the leading edge of the compressor blade will significantly affect the flow separation near compressor hub. Study from MIT indicates that the typical manufacture errors can cause efficiency decreased by 1% in multiple stages compressor [16, 17]. It also happens to turbine. Study from Beihang University (BUAA) shows that subtle changes on profile can lead to local flow deterioration, which would be amplified in whole engine environment and reduce performance significantly [18, 19]. Although there is not much publication in this area, it is an inevitable trend to investigate geometric error or assembling error for robust design.

4. Considering LP turbine component-matching in full operation range, study the factors and mechanisms that impact performance degradation after long-operation time in real work environment, it is possible to abstract low-order coupled model, develop multi-disciplinary integrated design technologies for LP turbine so as to significantly improve the performance and reduce its life-cycle cost.

With the increased requirements for aero engine, efficiency at design point is no longer the only performance indicator. Instead, the LP turbine performance in each mission and even in the full lifetime is used for judgment. It means that an good LP turbine should provide good performance over wide operating range, like takeoff, climb, cruise, decent, landing and so on. The performance reduction should be less over time. Also, a longer life time with reliable mechanical integration, less requirement to manufacturing and material, and easy maintenance are also demanded. It means that not only the aero-parameters need to be considered during

design, but also the listed above factors. Eventually to develop the integrated design technology with multidisciplinary coupling can fulfill the performance requirements and full-life time cost.

4.2 Boundary Layer Spatial-Temporal Evolution Mechanism in LP Turbines

The boundary layer and its evolution have significant impact on LP turbine loss. The key phenomena to determine the boundary layer characteristics are flow separation, transition, etc. Therefore, fully understanding mechanisms of separation and transition has significant importance for further organizing and controlling the boundary layer flow, which is essential to reduce LP turbine profile loss.

4.2.1 Flat Plate Boundary Layer Evolution and Flow Losses

4.2.1.1 Flat Plate Boundary Layer Evolution and Flow Loss with Zero Pressure Gradient

To discuss boundary layer evolution in cascade, it is essential to first understand laminar boundary layer transition mechanism on a flat plate in steady flow condition without pressure gradient. The laminar flow falls to different transition paths with different flow disturbances. For this, there are two classic transition modes: If the external disturbances are weak, and the plate wall is smooth, the natural transition happens; if the external disturbances are strong, the bypass transition happens. Recent studies show a more detailed transition road map. In Fig. 4.4, Morkovin shows transition modes with a variety external disturbances [20, 21]. According to this classification, between the natural and bypass transition modes, there also exists “transient growth” mode. Under this mode, different disturbances level corresponds to different transition paths (B–D, see Fig. 4.4) with not exactly the same mechanism.

There are substantial studies on natural transition. Figure 4.5 shows the classic description of flat plate boundary layer natural transition [22]. Laminar boundary layer begins to form at the plate leading edge and develops downstream. Meanwhile it “feels” flow disturbances [23, 24]. When the boundary layer Reynolds number exceed critical value, laminar boundary layer becomes unstable with Tollmien-Schlichting waves (T-S waves) showing inside it. The amplitude of the waves enlarges gradually during propagation. With the secondary instability, λ vortices appear. The λ vortices further develop and deform due to nonlinear impacts, and form three-dimensional hair-pin vortices. The rapid growth of hair-pin vortices eventually leads to the breakdown of the laminar flow and form local turbulent spots. Turbulent spots, which are from different originations, convect and

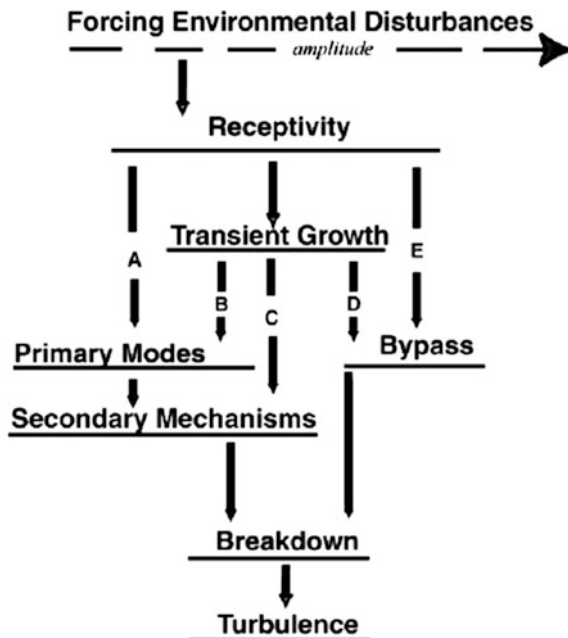


Fig. 4.4 Boundary layer transition roadmap [20]

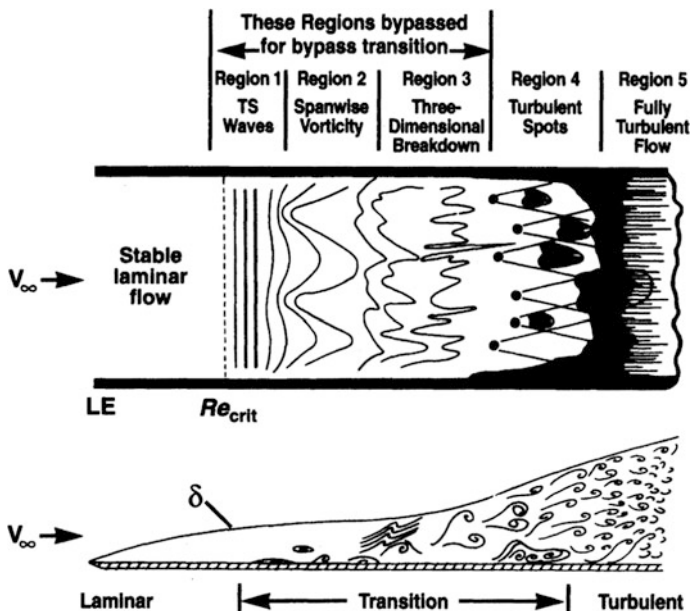
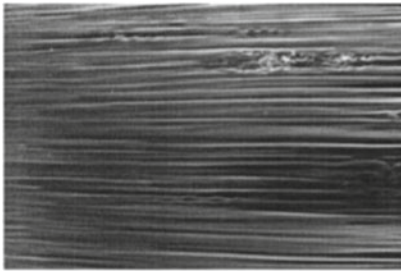


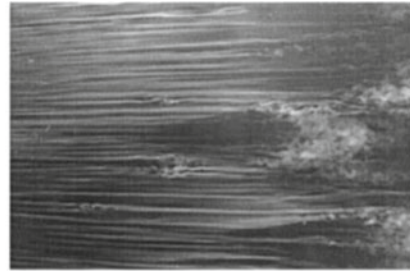
Fig. 4.5 Natural transition of a flat plate boundary layer [22]

diffuse with main flow, eventually combine with each other, and form a fully turbulent boundary layer. This is typical natural transition.

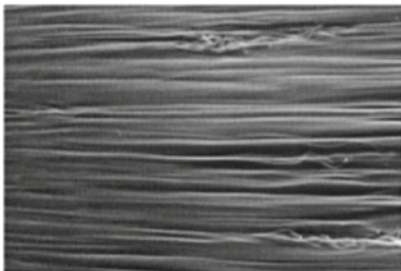
However, when there are strong flow disturbances, such as high level freestream turbulence, surface roughness, noise, vibration or other disturbances in tubomachinery, the first three stages in the natural transition mode may be skipped. Disturbances will penetrate through boundary layer and directly induce turbulent spots, thereby lead the transition process. This is the so-called bypass transition mode. The T-S waves cannot be observed in this mode. Without those three unstable stages, the bypass transition process become faster and its length become shorter. From the flow structure perspective view, the main characteristic of bypass transition is the appearance of streamwise streaks. Studies have shown that those streaks, which develop from the leading edge of plate, are related with low frequency disturbances. Though those disturbances have large scale in streamwise direction, their length scales in spanwise and vertical direction are in the same order with the boundary layer [25]. Figure 4.6 shows the bypass transition sketch with different freestream turbulence intensity (FSTI) and freestream velocity [26]. The results show the streaky structures in four conditions. With streaks developing along streamwise direction, they twist and swing, and ultimately become turbulence. Under low FSTI, the streaky structures last longer, while turbulent spots may



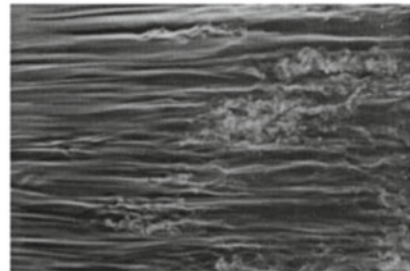
(a) Turbulence intensity 2.2%, $U_\infty = 6\text{ m/s}$



(b) Turbulence intensity 2.2%, $U_\infty = 8\text{ m/s}$



(c) Turbulence intensity 6.6%, $U_\infty = 2\text{ m/s}$



(d) Turbulence intensity 6.6%, $U_\infty = 3\text{ m/s}$

Fig. 4.6 Streamwise velocity streaks in by-pass transition [26]

appear randomly between them. Under high FSTI, these streaky structures are relatively more chaotic mainly due to the turbulent spots appear earlier. In addition, the turbulence spots show larger length scale in spanwise under the above two corresponding conditions. This is, on the one hand, because the turbulence length scales in those two conditions are larger, and on the other hand, due to the flow speed reduction and the resulting incensement of boundary layer thickness.

Although the hydrodynamic stability theory gives some explanations of the streaks, until the end of last century, it was still unclear with the mechanism for the bypass transition, in particular the formation of turbulent spots. Regarding the issue, researchers from Center of Turbulence Research (CTR) in Stanford University using direct numerical simulation (DNS) as the main research tool together with theoretical analysis, had carried out a series of studies and provided comprehensive explanations on the mechanism of bypass transition [27–30]. They believe that due to the shear sheltering effect in laminar boundary layer, shear layer acts similar as a low-pass filter, which means low frequency components from disturbances can enter the boundary layer, while the high-frequency component of the disturbance will be suppressed. Those low-frequency disturbances will then be enlarged and stretched due to shear flow along the streamwise direction and eventually form the streamwise velocity streaky structures. And just those streaks form the forward jet and reverse jet in the disturbance velocity field. As shown in Fig. 4.7, when the reverse jet is being lifted to the edge of the boundary layer, shear sheltering no longer exists. Instead, the Kelvin-Helmholtz instability (K-H instability) in the reverse jet flow velocity profile is triggered by small scale (high frequency band) turbulence. It causes flow instability, and creates random turbulent fragments, which gradually grow into turbulent spots while transporting. The basic form and transport properties of a single turbulent spot have been introduced in the first chapter. Besides, the structural characteristics of the turbulent spots [31] and its evolutionary mechanisms under different environments [32–34] and the regulation of interaction [35–37] have also been the central topics in the community, while they are out of the scope of this book.

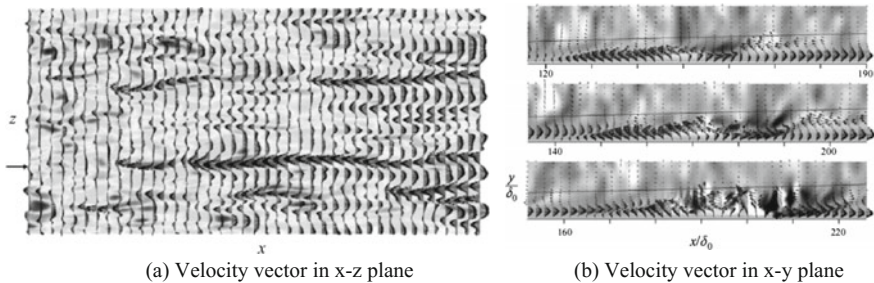


Fig. 4.7 Reverse jet flow in bypass transition [27]

4.2.1.2 Flat Plate Laminar Boundary Layer Separation with Adverse Pressure Gradient

When varying pressure gradient, the temporal evolutions of the boundary layer on turbine blade will be not the same. The adverse pressure gradient after turbine throat will induce boundary layer separation and the resulting load distribution (corresponding to the change in pressure gradient) will play important role in the internal flow field. With the fact that the research on flat plate boundary layer evolution not only can capture the key factor like pressure gradient, but also has the advantages for easy experimental tests and numerical simulations, it becomes important development for the boundary layer in turbomachinery and raised many researchers in this area.

LP turbine, may well encounter laminar boundary layer separation which impacts seriously on aerodynamic performance. First, Laminar boundary layer is gradually decelerating under the influence of adverse pressure gradient, separation may eventually occur. The shear layer after separation will be very sensitive to disturbances due to the inflection point in the velocity profile. It triggers instability and then transition begins. A detailed discussion on this point will be given in the next section. Large scale vortices form in the separated shear layer during transition process. These vortices can entrainment main flow into the boundary layer, which will finally result in the shear layer to reattach and gradually form the turbulent boundary layer. The flow structure formed above is the so-called “laminar separation bubble”. Typical separation bubble structure was first given by the Horton [38] as shown in Fig. 4.8. The streamline which passed the separation point lifts away from wall, then starts to drop to the wall again at the back part of separation

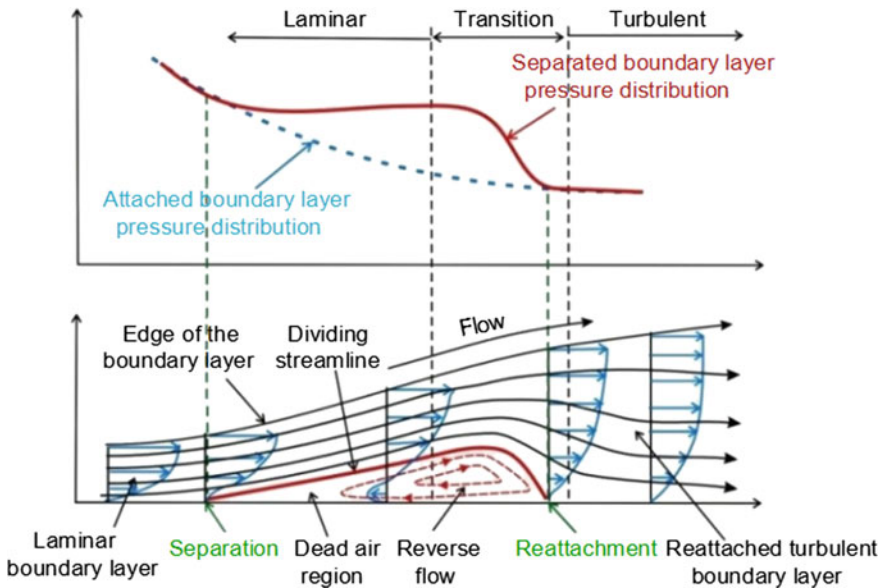


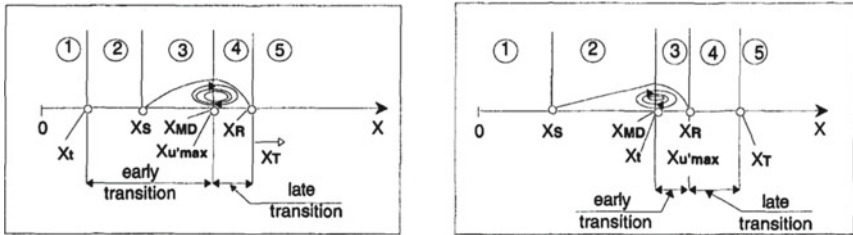
Fig. 4.8 Typical structure of laminar separation bubble

bubble and finally reattaches to wall at the reattachment point. This streamline is called the “dividing streamline”. That is, outside this streamline is the main flow, while the inside wedge-shaped region is the separation bubble. The flow velocity is small after the separation point. Just because the flow here almost stagnates and maintains laminar flow condition, this region is named the “dead-air zone”. Displacement of wedge separation bubble can influence main flow by deflecting the flow and, as a result, causing the pressure gradient in this area to change. Figure 4.8 shows that from the separation point till somewhere upstream of the reattachment point, wall pressure remains unchanged, namely the so-called “pressure plateau”. Near the reattachment point, the pressure recovers to the corresponding re-attached boundary layer level. In this region there is strong reverse flow, whose velocity can reach about 20% of the main flow [2].

As shown in Fig. 4.8, one of the most significant characteristics of separation bubble is the change of the boundary layer pressure distribution, means the existing of plateau. This is a common criterion to determine whether separation happens and its location. Comparing to the physical length of separation bubble, the wall pressure distribution is a more suitable parameter to sort out its type. Accordingly, the separation bubble can be divided into two categories [39]: short bubbles and long bubbles. Short bubbles have weak displacement effect, thus it has limited impact on main stream. It can only influence local pressure distribution and thus less impact on loss. On the contrary, the displacement effect of long separation bubbles is strong, which can affect the distribution of wall pressure in a wide range. Such separation bubble will cause serious profile loss. Besides, it will significantly reduce the flow turning angle and the blade loading. Therefore, long separation bubble must be avoided in the LP turbine blade designs.

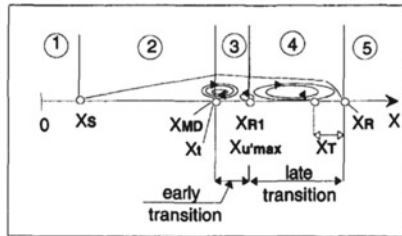
Apart from the above classification method which is based on pressure distribution, there is another common classification, which is based on the flow condition at separation point. It divides separation bubbles into three categories [40]: If the Reynolds number based on momentum thickness at the separation point is $Re_{\theta_s} > 320$, then the transition point prior to the separation, and the separation form as transition separation mode. With decreasing Reynolds number the transition location moves after the separation point. If $240 < Re_{\theta_s} < 320$ with moderate adverse pressure gradient in the flow, this is laminar boundary layer short bubble separation mode. If the Reynolds number continues decrease, and the flow has a strong adverse pressure gradient, then forms the laminar boundary layer long bubble separation mode. Three kinds of separation modes are shown in Fig. 4.9.

Shear layer transition is one of the most important behaviors of separation bubbles. This process is directly related to the separation bubble type and it impacts the entire flow field. Researchers carried out series studies on separated shear layer transition under steady state, and discussed the influences of Reynolds number, turbulence, pressure distribution and other factors. Though the separated shear layer is, in some ways, similar to the free shear layer, it will inevitably be affected by wall that closes to. Thus its transition process may show combined characteristics of free shear layer transition and attached boundary layer transition. In the experiments on flat plate separated boundary layer shear layer evolution, researchers observed similar instabilities as in the free shear layer, such as spanwise vortex roll, etc. But



(a) Transitional separation mode

(b) Laminar separation short bubble mode



(c) Laminar separation long bubble mode

Fig. 4.9 Separation bubble modes in laminar boundary layer [40]

A vortex structure is also observed, which proved that both inviscid and viscous instability mechanisms may exist in the separated shear layer transition process [41]. In addition, other researchers also observed in the experimental studies that the large scale spanwise vortex shading in the transition process has the same dominant frequency as the amplified main frequency in T-S wave [42]. This should be due to the interaction between K-H inviscid instability and T-S viscous instability. Based on these observations, to clarify that which mechanism dominates under which condition, has become the key to further understand separated shear layer transition. Linear stability analysis on reverse velocity profiles shows that the separated shear layer above the bubble has inviscid instability, while inside the bubble there is mainly viscous instability. The strength of the two instabilities depends on the separated shear layer thickness and its distance to wall [43]. Therefore, the bubble thickness can be used to initially determine the dominant transition mechanism. For instance, if the separation bubble has smaller thickness, the wall would have great influence on the shear layer, T-S viscosity instability will dominate. In the contrary, the separation bubble transition will be subject to K-H instability.

Although experiments can capture the main transition process of the shear layer, the detailed information of the flow field provided by them is usually limited as the experiments are always limited by factors such as measurement instruments. Recent years, with the rapid development of computers, direct numerical simulation (DNS), large eddy simulation (LES) and other high-precision numerical simulations are

widely used and played important role in research of the vortices evolution, which is the key to further investigate separated shear layer transition. DNS results [44] of flat plate boundary layer short bubble showed that flow separation in the transition zone is highly three-dimensional. Transition area is controlled by a series of staggered vortices, which pump the near wall fluid outside to form shear layer on top of the vortex. As shown in Fig. 4.10, Λ vortices can also be observed inside the separated shear layer and then break near the reattachment point, then further develop to turbulence. This also shows that the entire transition process of short separation bubble can be described as the production, development and breakdown of Λ vortex structure. Specifically, each characteristic of the short bubble can be presented as following: in the dead-air region and separated shear layer region, Λ coherent structures and Λ vortices are observed. Near the reattachment point, the dominated flow structure is hairpin vortex. While in the reconstructed turbulent boundary layer, besides hairpin vortices, the quasi-streamwise vortices which show as streamwise streaks are also observed.

The vortex structures in separated shear layers vary with inflow conditions. This causes different transition paths. Yaras et al. from Canada Carleton systematically studied laminar flow separation under different conditions using experiments and numerical methods [45–47]. They believed that at low FSTI, the transition of separated shear layer is through K-H instabilities. At high FSTI, the receptivity which leads the roll-up of the shear layer is skipped, while instead are the streamwise streaks which are transported via shear layer. Then the strong shear related to the streaks leads to the secondary instability and eventually produces turbulent spots. Different from the turbulent spots inside the attached flow, the turbulent spots inside shear layer show a series of vortex loops. Figure 4.11 shows the velocity fluctuation contour plot at $\bar{U} \approx 1/2\bar{U}_e$ section under a high FSTI flat plate boundary layer. Here, streamwise streaks can be observed clearly. And turbulent spots which are formed by a series of vortex loops can be seen from contour plots of streamwise and normal velocity fluctuation. In addition, worldwide researchers have continued

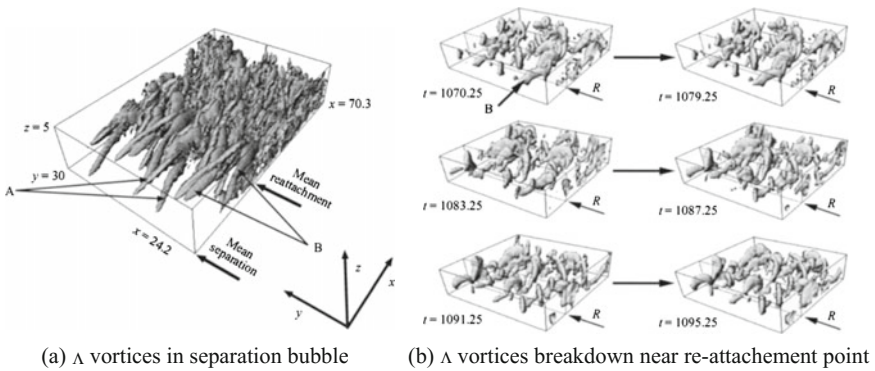
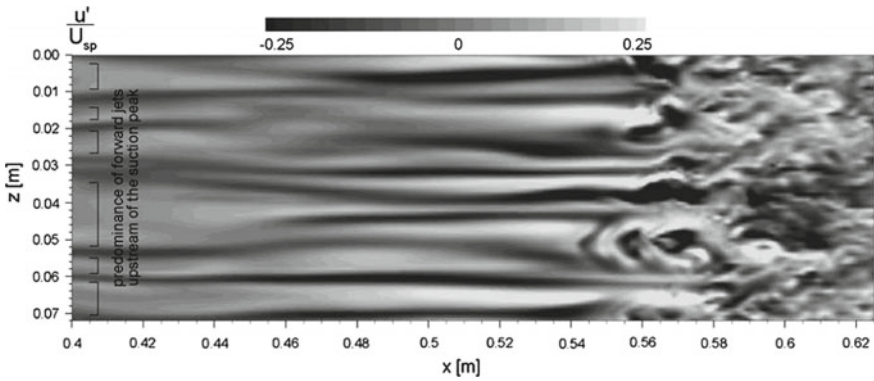
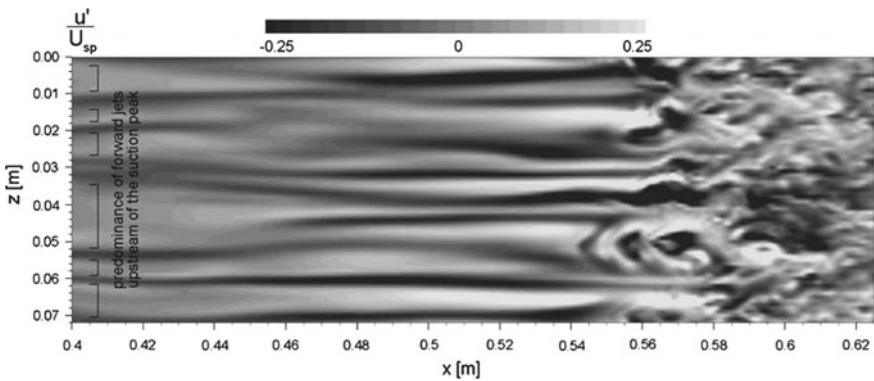


Fig. 4.10 Λ vortices in the separation bubble and its breakdown process [44]



(a) Fluctuation of streamwise velocity



(b) Fluctuation of normal velocity

Fig. 4.11 Separation bubble transition under high inlet turbulence, at $\bar{U} \approx 1/2\bar{U}_e$ plane [47]

further investigation using numerical simulations [48–50] and provided more complete picture of the transition process. However, there has been no unified conclusion yet, and still requires further under different disturbed environment.

4.2.1.3 Separated Shear Layer Transition Mechanism Under Adverse Pressure Gradient and Unsteady Conditions

Basis on steady flow study, researchers turn attention to the boundary layer under unsteady condition, such as the periodic upstream wakes, which is typical inflow boundary condition that turbine should face in real environment. Using the periodic passing cylinders to simulate unsteady wake is commonly used in experiments. Zhong et al. [51] used liquid crystal to re-produce the bypass transition to turbulent spots which are induced by passing wakes. Figure 4.12 shows experiment set-up

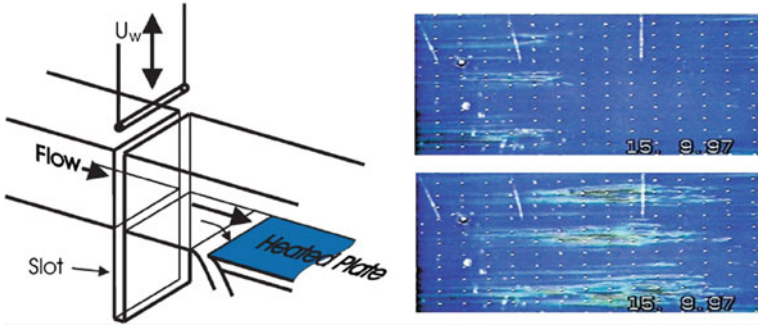


Fig. 4.12 Liquid crystal visualization of wake induced transition [51]

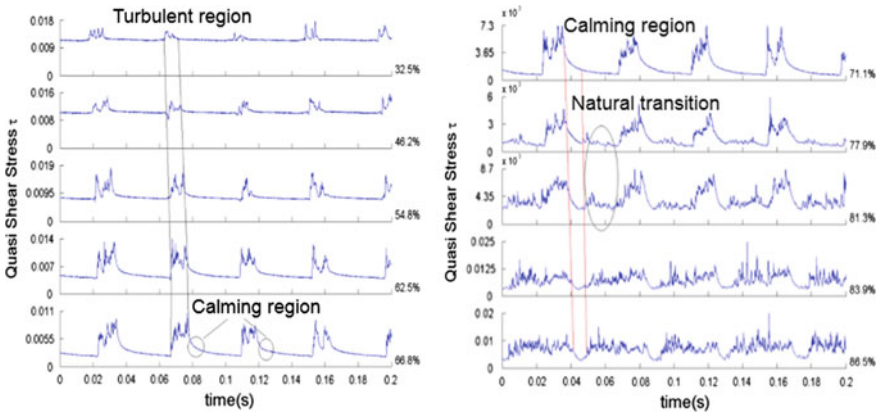


Fig. 4.13 Typical hot-film signal, with unsteady wakes, $Re = 2.1 \times 10^5$ [52]

and the liquid crystal displayed flow structures. There are three clearly visible turbulent spots induced by wake. The measurements showed that their generation and propagation speed are the same as conventional Emmons turbulent spots. When the turbulent spots transport downstream, their length and width grow, turbulence intensity increases, gradually forms spanwise turbulent strips, between adjacent strips, transition is in natural transition mode.

In order to investigate the boundary layer development under different loads and loading nt loads and loading distributions, Zou Zheng Ping, Liang Yun et al. from Beihang University developed adjustable flexible wall plates rig [52], which achieved to simulate different loading on a flat surface and detailed measured boundary layer under different loading and different inflow conditions. Figure 4.13 shows hot-film signal of typical load distribution on suction face in turbine cascade suction surface under wake effect in $Re = 2.1 \times 10^5$. Under the wakes, unsteady turbulent region form near plate leading edge and gradually become larger when transporting downstream, in the meantime the random fluctuation increases. From

66.6% chord, hot-film signal shows typical calmed region characteristics. Measurements show that these calmed regions will continue until the plate trailing edge. Furthermore, the natural transition may also occur between wakes under this condition. Comparing different loading distributions, the uniform loaded boundary condition is less sensitivity to Reynolds number changing in steady states. The loss due to low Reynolds number impact is also less, and therefore more suitable for working at low Reynolds number conditions. However, the situation is different with unsteady wakes, the long pressure gradient region in the front part of the aft-loaded profile can prevent boundary layer transition, together with this, if the adverse pressure gradient induced trailing edge separation could be inhibited by wakes, it will leave a smaller loss than the fore-loaded and uniform loaded profile.

DNS simulation under the unsteady wake shows that the transition of attached boundary layer occurs first in the isolated turbulent spots. With the increase size of turbulent spots transporting downstream, spots gradually join and eventually form a fully developed turbulent boundary layer [53] as shown in Fig. 4.14. Instantaneous flow field shows that prior to the formation of turbulent spots, the reverse jet appears in fluctuating flow velocity field. These reverse jet, which are near the top of boundary layer, ultimately become turbulent spots under the joint effects of K-H instability and small-scale perturbations in the wake. This process is similar to the mechanism described before of attached boundary layer bypass transition to spots under high FSTI.

Compared to velocity stripe and turbulence spots in attached boundary layer, there are more vortex structures in separated shear layer transition process under wakes. Figure 4.15 shows the time series pictures of vortex evolution under interaction between separation bubble and wakes under low Reynolds number using LES [54]. As can be seen, there are a lot of vortices including streamwise vortices, spanwise vortex, hairpin vortex, etc. When the wake just entering the

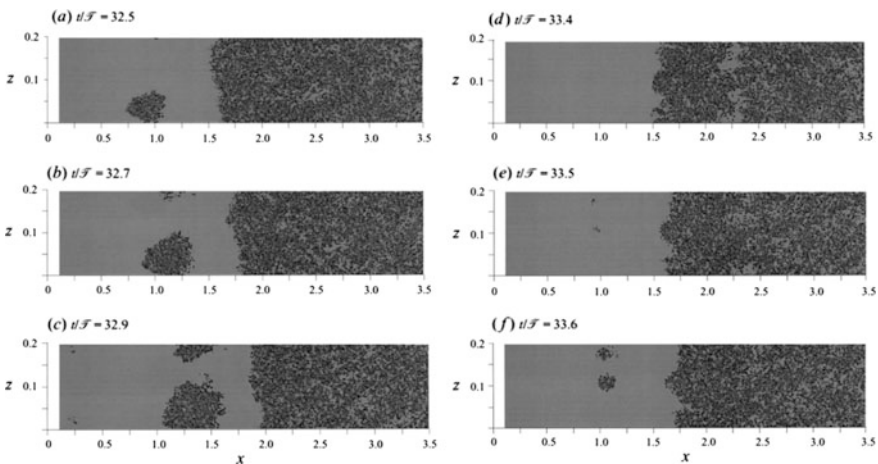


Fig. 4.14 Boundary layer transition and turbulent spots growth under unsteady wakes [53]

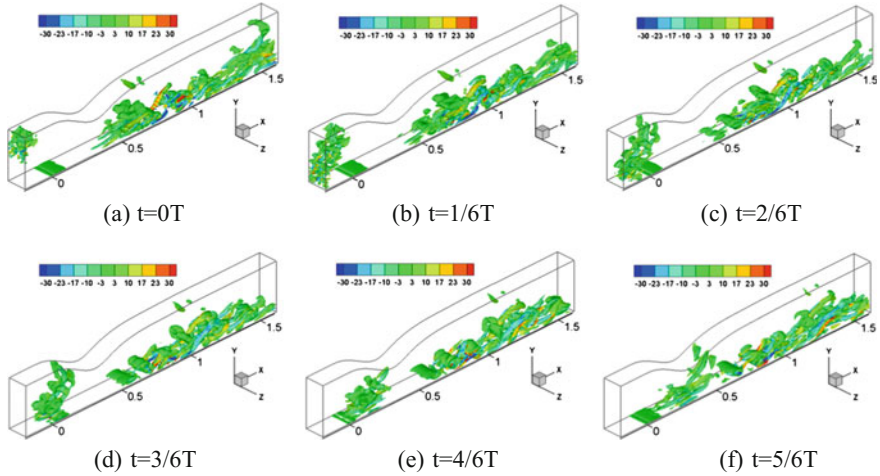


Fig. 4.15 Flow structures and their evolution with interaction between wakes and separation bubbles [54]

computational domain, there exist positive and negative directions streamwise vortices with random distribution. When transporting downstream, the absolute value of the streamwise vorticity is reducing while the size of vortex is increasing and become more structured. Through shrinking channel, stretched by the main flow, there they become more obvious streamwise vortices. After throat, due to the velocity difference across boundary layer, stretching becomes even stronger. Near the wall there generate a lot of streamwise vortex, as shown in Fig. 4.15(f). Vortices continue moving downstream, and interact with separated boundary layer inducing unstable, rapidly developing spanwise vortices, as shown in Fig. 4.15a. With the development of spanwise vortex, flow finally breakdown to turbulence.

4.2.2 LP Turbine Boundary Layer Spatial-Temporal Evolution Under Steady Uniform Inflow

Though flat plate is easy to implement and also to consider most influences of turbine unsteady conditions, the turbine blade has curved surface, which also has an impact on the development of the boundary layer. Therefore, it is necessary to study the LP turbine blade boundary layer evolution based on the understanding of the one for flat plate. This section will discuss suction surface boundary layer evolution in a turbine cascade under steady flow condition.

To discuss the turbine cascade boundary layer development, it is necessary to know the exact condition of boundary layer. Due to the large curvature of cascade, conventional probes may be difficult to implement. Since the hot-film technology

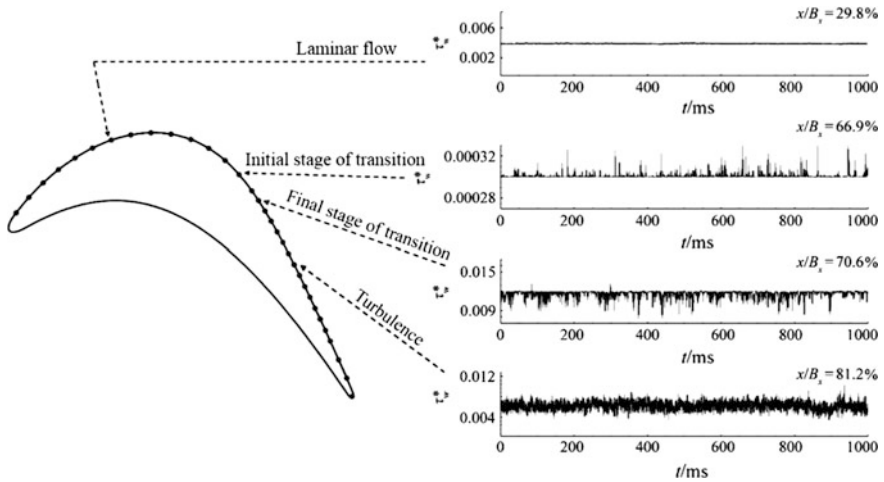


Fig. 4.16 Hot-film signals of a LP turbine suction side boundary layer in the transition process [55]

can capture high frequency quasi shear stress signals near the wall to characterize the state of the boundary layer, it has become an important method for boundary layer method. Figure 4.16 shows Li Wei, Zhu Junqiang et al. measured surface hot film signals in the transition process of LP turbine cascade suction side boundary layer [55]. The figure shows that: In the laminar flow region, flow and heat exchange is relatively stable, and thus hot-film signal fluctuations are small. After the transition begins, turbulent spots began to appear randomly on internal boundary layer, which leads to the increasing heat exchange and the hot-film signal appears with corresponding peaks. In later transition phase, there is mainly turbulence inside boundary layer with occasional laminar region. So hot-film signal exhibits a higher average value and occasional lower peaks. After transition is complete, signals show high-frequency characteristics in the fully developed turbulent region.

Reynolds number and incoming turbulence are important factors which impact the development of turbine cascade boundary layer under steady flow condition. A necessary condition to trigger the transition is sufficient disturbance, which in turn depends on the strength of the initial perturbation in the boundary layer and its growth trends. The initial perturbations in the boundary layer generally come from the main stream disturbances, such as wakes, background turbulence, and perturbations from wall surfaces such as roughness. The growth rate of these perturbations is determined largely by the Reynolds number. Therefore, incoming turbulence and the Reynolds number are the key factors that influence the starting position of the transition. With this understanding, researchers developed a mathematical model to predict the transition of separation bubble within a range of Reynolds number and incoming turbulence intensity, based on the measurement of

the growth trend of disturbances in the separated shear layer [56]. In addition to the transition initial position, the incoming turbulence may also affect the transition mode of the separated shear layer. It has been pointed out earlier that at high inlet turbulence, the streamwise streaks will appear in the separated shear layer of the plate boundary layer, which also occurs in the turbine cascade. Due to these streaks, turbulent energy of the boundary layer increases rapidly, so the initial position of the transition shifts upstream comparing to inlet low turbulent level. Those streaks may induce vortex roll-up through K-H instability and eventually form a turbulent spot. If the flow turbulence is high enough, both the T-S instability mechanism and the K-H instability mechanism may be skipped during the transition process. Instead, turbulent spots directly appear in the separated shear layer [57]. However, it is also found that the detected dominant frequency in the separated shear layer transition zone may be consistent with the maximum frequency of the T-S wave even with the inflow turbulence is 9% [58]. The above results show that although inflow turbulence is one of the key factors that affect the transition, the transition process is restricted by many factors. To accurately understand the mechanism and the transition path, we should not only consider the impact from turbulence intensity.

The above studies are focusing on the separation bubbles on blade suction side, while with increasing blade loading or reducing Reynolds number, the open separation might happen. Figure 4.17 shows a comparison of flow field for a turbine cascade ($Z_w = 1.23$) with a Reynolds number of 1.0×10^5 for different inflow turbulence intensity [59, 60]. The experimental measurements and numerical simulations show that with high turbulence intensity (4.0%), there is small size separation bubble on suction side boundary layer. However, with low turbulence intensity (0.8%), open separation happens and the corresponding profile load reduce about 20%, and the stagnation pressure loss increased significantly.

When the separation bubble on the suction surface evolves into an open separation, the aerodynamic performance of the LP turbine will be affected. The

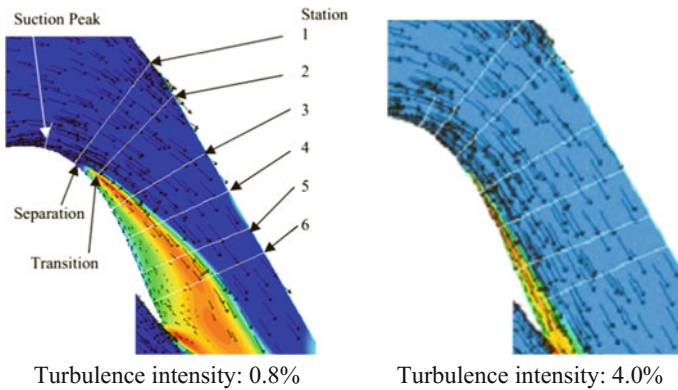
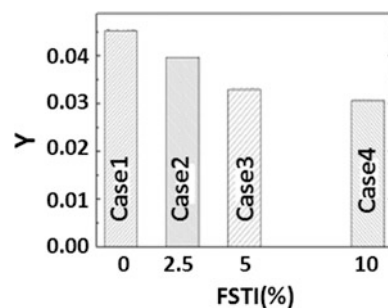


Fig. 4.17 Flow Structures of High-Loaded Turbine Cascades under Different Operating Conditions [59, 60]

transition mechanism on the suction surface, the flow structures and their evolution during the transition process will also be different. Regarding this, many researchers use large eddy simulation to investigate. As the T106D-EIZ low-pressure turbine cascade, which has detailed database available for validation [61, 62], is an ideal research object. Ye Jian, Zhang Weihao, Zou Zhengping et al. from Beihang University studied the evolution of the vortex structure in the open separation of the T106D-EIZ low pressure turbine cascade ($Re = 6.0 \times 10^4$) under constant flow conditions [50, 63–66] and discussed the impact of inflow turbulence on separated shear layer transition. In terms of time-averaged flow, the comparison of the mean stagnation pressure loss coefficients under different incoming turbulence conditions is given in Fig. 4.18. Where the Y-axis is the stagnation pressure loss and the abscissa is the turbulence intensity. It shows that for a cascade with a separating boundary layer on suction side, the stagnation pressure loss coefficient reduces when increasing turbulence comparing to the case of no turbulence. When the FSTI is in range 0–5.0%, it has strong impact on cascade aerodynamic performance. While the freestream turbulence intensity above 5.0%, the influence of turbulence is not obvious.

Regarding the evolution of the shear layer vortex structure, Figure 4.19 shows the coherence structure in the separated shear layer in different turbulence conditions by using iso-surface of $Q = 800$ vorticity identification and dyed with spanwise vorticity ω_z . Apparently spanwise vortices can be observed in the separated shear layer without turbulent flow. As the spanwise vortexes show bending during transport process, two-dimensional flow turns to three-dimensional. Then there will be adjacent spanwise vortexes interact each other and develop in pairs. In the process, the streamwise vortexes developed rapidly then gradually dominant in the downstream of separated shear layer. Due to the inflow turbulence, the shapes of spanwise vortexes are no longer clear, while the corresponding iso-surfaces of Q are no longer smooth, and they cannot occupy the whole blade height. It means that the three-dimensional disturbances appear earlier and stronger in the free shear layer. This also results in the streamwise vortex appear earlier. The rolled up spanwise vortex become unstable and they breakdown much faster, so that there are almost no two parallel spanwise vortexes, and there will be no vortex pairing occurs.

Fig. 4.18 Cascade aerodynamic performance influenced by free stream turbulence intensity [63]



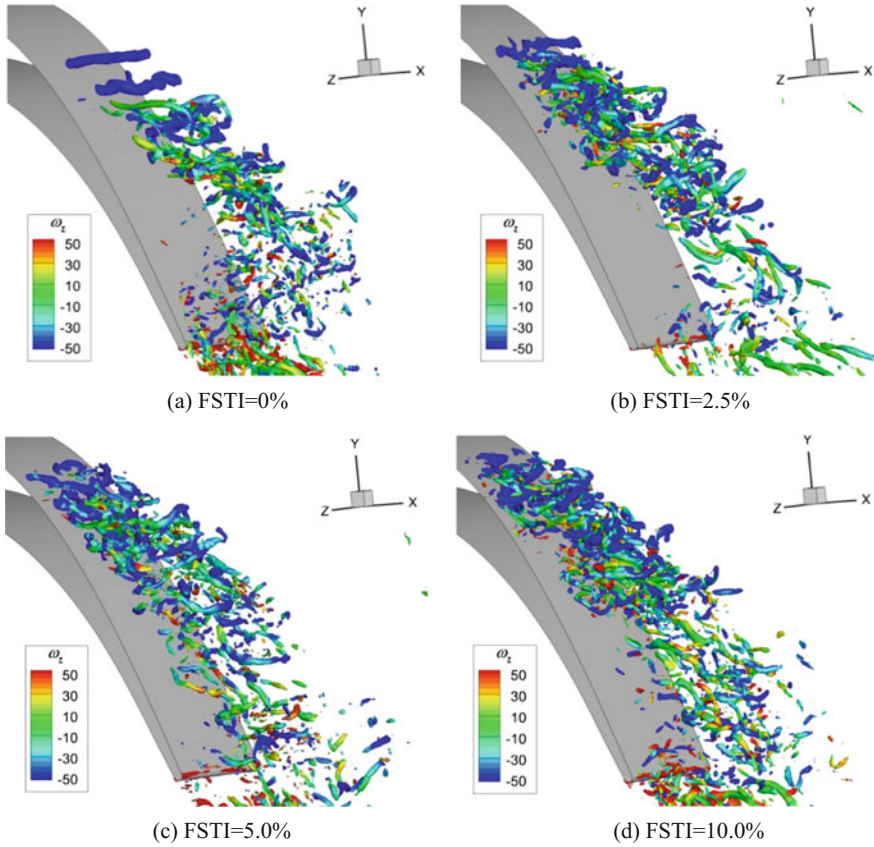


Fig. 4.19 Coherent structure in separated shear layer, iso-surface of $Q = 800$, colored by ω_z [63]

As mentioned above, the separated shear layer transition process may be affected by both the viscous instability mechanism (T-S instability) and the inviscid instability mechanism (K-H instability). For the conditions discussed here, since the open separation is far from the wall, the effect of viscous instability is comparable weak and the transition process should be dominated by the inviscid instability mechanism. This is confirmed by the roll up of spanwise vortex as shown in instantaneous flow field in Fig. 4.19. In addition, the fastest-growing unstable frequency in the free shear layer under K-H instability can be represented by the dimensionless Strouhal number (Sr_θ , based on momentum thickness in shear layer and velocity difference),

$$Sr_\theta = \frac{f\theta_s}{U_{es}} \quad (4.1)$$

Table 4.2 Sr_{θ_s} number in studies

Ref.	Sr_{θ_s}
[67]	0.016
[47]	0.011
[68]	0.008–0.016
[69]	0.005–0.008
[49]	0.005–0.011
[70]	0.010–0.014
[71]	0.0115–0.0128
[63]	0.0113–0.0146

Here, f is the fastest increasing unstable frequency (hereinafter referred to as the most unstable frequency), that is, the vortex rolling up frequency. θ_s and U_{es} are of the boundary layer momentum thickness and boundary layer outer boundary velocity at the separation point, respectively. Study from Ho and Huerre shows that the typical Sr_{θ} value for the plane free shear layer is 0.016 [67]. Many studies have shown that the separated shear layer Strouhal number Sr_{θ_s} is also roughly in this order. Nevertheless, since the separated shear layer is still affected by the wall somehow, this value may be slightly smaller than the value in the free shear layer. Table 4.2 shows Sr_{θ_s} value from the relevant studies. In addition, the discussion on the influence of inflow turbulence shows there is a significant impact from Sr_{θ_s} , which is that the Sr_{θ_s} increases with the increase of turbulence [63].

4.2.3 *Single Stage LP Turbine Boundary Layer Spatial-Temporal Evolution Mechanism*

In real turbine stage environment, turbine internal flow has strong unsteady phenomena. In the LP turbine, upstream wakes sweeping is one of the critical unsteady disturbances for downstream cascades, which has significant impact on the transition and separation of the boundary layer.

4.2.3.1 **Wake Transport Characteristics in LP Turbine Passages**

One of the main characteristics of the incoming wake is the defect of velocity profile, which can be seen as a jet of reverse velocity relative to the main flow, the so-called “negative-jet” [72]. As shown in Fig. 4.20, as the wake enters to next blade row, it is cut by the blade leading edge and becomes independent. Each wake segment can be regarded as a negative-jet. These negative-jets pump fluid from the pressure side to the suction side and affect the profile distributions of pressure and velocity.

The phenomenon of wake transport in the cascade can be summarized as the behavior of cutting, bending, stretching and deformation of the wake [73].

Fig. 4.20 Interactions between wake and turbine cascade boundary layer [12]

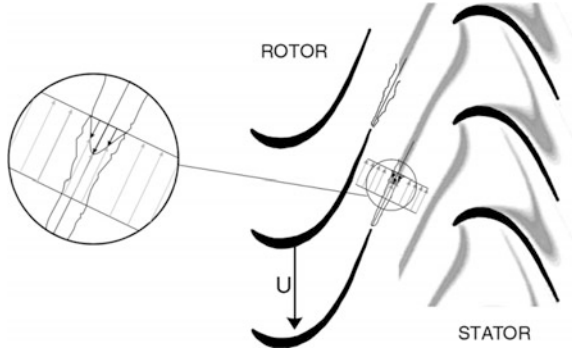


Figure 4.21 shows a group of wakes transport in T106 LP turbine cascade measured by LDV [74]. The showing phase-averaged kinetic energy distribution and time-series of the perturbed velocity, clearly describes the transport process: near the cascade inlet plane, the wake is cut by blade leading edge. Due to the high velocity in the middle of the cascade while small velocity near the blade leading

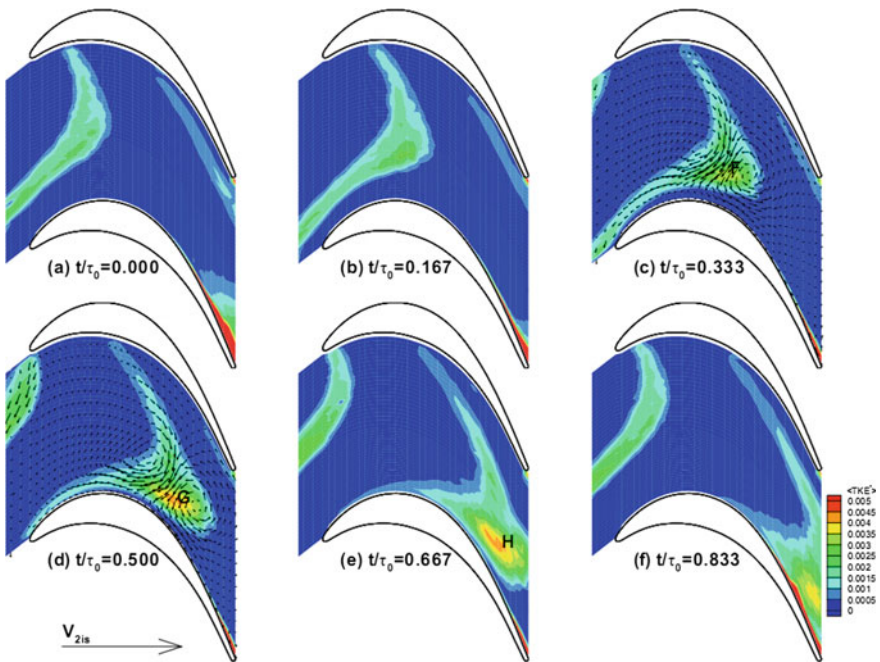


Fig. 4.21 The transport of wake in blade passage, phase-averaged mean turbulent kinetic energy, disturbed velocity [74]

edge, the wake, which is transported by the local velocity, forms an arc, which is the so-called “wake bending”. When the bending wake enters bladerows, it transport faster near the suction surface due to there is higher velocity on suction side. It leads to a slow rotation of the wake-axis, and finally become almost parallel to the pressure surface, which is the process of “wake reorientation”. Due to the same reason, the wake is stretched longer along flow direction. In addition, the negative-jet causes the wake near the pressure side to flow towards suction side. And in the vicinity of the suction side, the width of the wake will increase due to the accumulation of fluid. At the same time, the perturbation of the negative jet also accelerates the flow near the suction side wake center and decelerates upstream surface to form a counter-rotating vortices pair. In fact, the wake propagates quickly which means that there is no flow from the pressure side pumped to the suction side during the wake flowing through the bladerow. In addition, as shown in Fig. 4.21, though most of the wake segments has lower the turbulent kinetic energy, there is a region near the suction side appears increased turbulence, which has profound influence on suction side boundary layer development.

In addition to the velocity profile loss, the incoming wake can also be seen as low-energy fluid shedding from upstream blade boundary layer. The transport of wakes in the bladerow also affects the evolution of these vortices. Figure 4.22 shows the evolution of the vortex structure in the wake of LP turbine cascade under the typical operating conditions obtained by LES [63]. It shows the Q method identified vortex structure in the neighboring phase within same wake cycle and dyed by streamwise velocity u_1 . It shows that before entering the bladerow, the wake mainly contains small-scale vortex structures. After entering, under the acceleration by the main stream, the large eddies in streamwise gradually dominate the wake region. Due to the negative-jet, those eddies accumulate on the suction

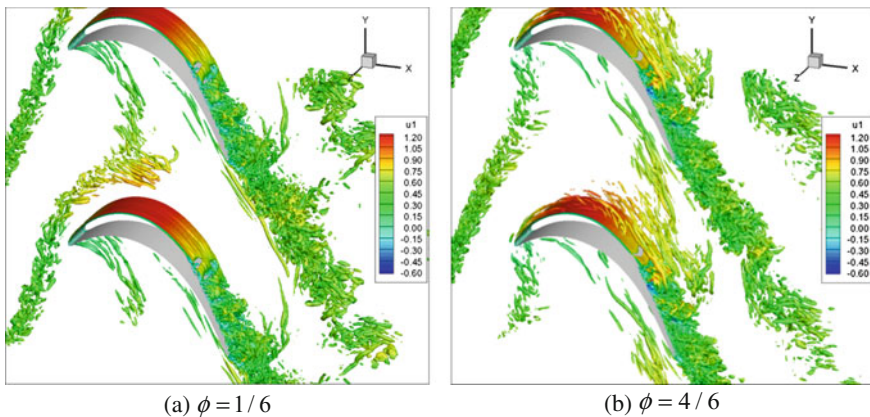


Fig. 4.22 Wake transport in LPT passages, iso-surface of $Q = 20$, colored by axial velocity u_1 [63]

side. Since the flow acceleration on suction side is more obvious, these eddies are almost parallel there. It can be seen that, in addition to the negative-jet, wake-induced vortex pair and some other related mechanisms, those large scale streamwise vortices also have strong impacts on suction side boundary layer.

4.2.3.2 Wake-Induced Boundary Layer Transition Modes

In general, the flow near normal loaded blade pressure side has pressure gradient that keeps boundary layer in a laminar flow state and does not face severe separation problems. Therefore, more attention is paid to the incoming unsteady wake on the development of the suction side boundary layer. Hodson et al. from Whittle Laboratory in University of Cambridge had most representative of the study [3, 12]. Their results show that wake-induced suction side boundary layer transition will occur through one of the following three pathways:

- (1) When the Reynolds number is high enough, the unsteadiness of the wake causes the laminar boundary layer quickly transit to the turbulent. If the adverse pressure gradient near the trailing edge suction side is not large, the wake prevent separation occurs. Alternatively, if the local adverse pressure gradient is sufficiently weak, the laminar flow boundary layer under will not separate under steady state, but the wake induce boundary layer transition. In this case, the turbulence or other disturbances induced transition will occur at a certain distance downstream of the wake, while there is still no flow separation on the suction side boundary layer as shown in Fig. 4.23a.
- (2) With the decrease of Reynolds number or the increase of the adverse pressure gradient at the suction side trailing edge, the laminar boundary layer under the steady condition will separate. Under unsteady condition, though wake can still induce boundary layer transition, if the wake passing frequency is not high enough, the laminar boundary layer will still separate during the gap between passing wakes. In this case, periodic separation bubbles appear in suction surface boundary layer, and transition may be alternated by wake-induced boundary layer transition and laminar flow separation bubble transition, as shown in Fig. 4.23b.
- (3) If the Reynolds number further reduce or the adverse pressure gradient at the trailing edge is large, the laminar boundary layer separation happens very early and the wake induced transition will occur in the free shear layer of the separation zone, as shown in Fig. 4.23c. In serious condition, wake will not induce re-attachment.

4.2.3.3 Flow Structures in Wake-Induced Boundary Layer Transition

Wake-induced boundary layer transition is common in LP turbines with convention load or those operating under a high Reynolds number. Halstead and Wisler et al.

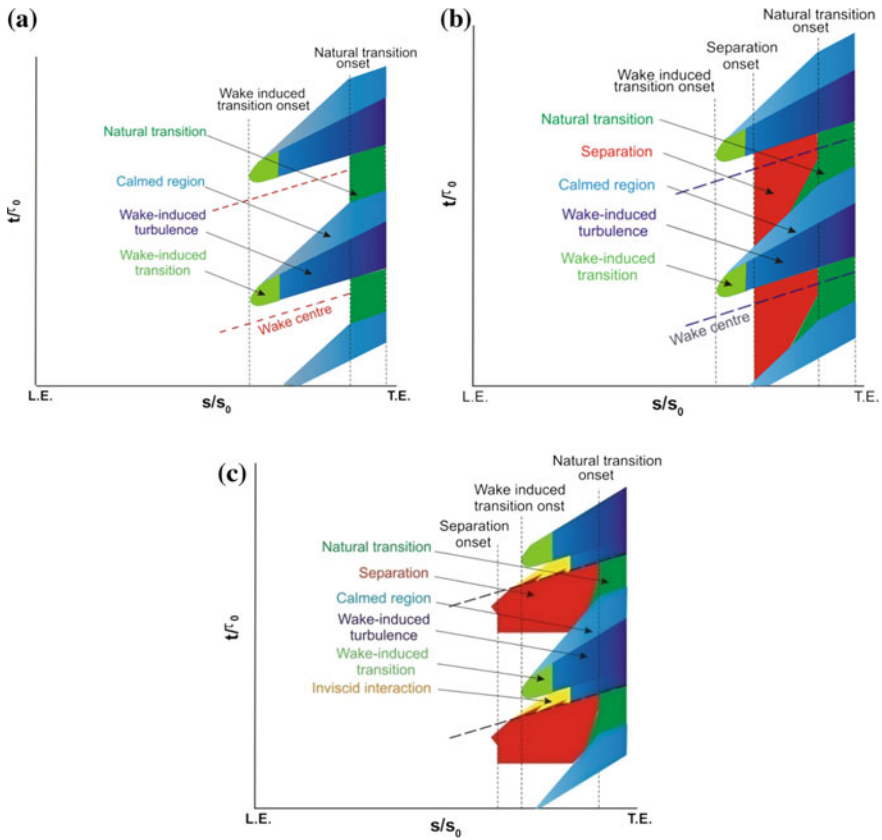
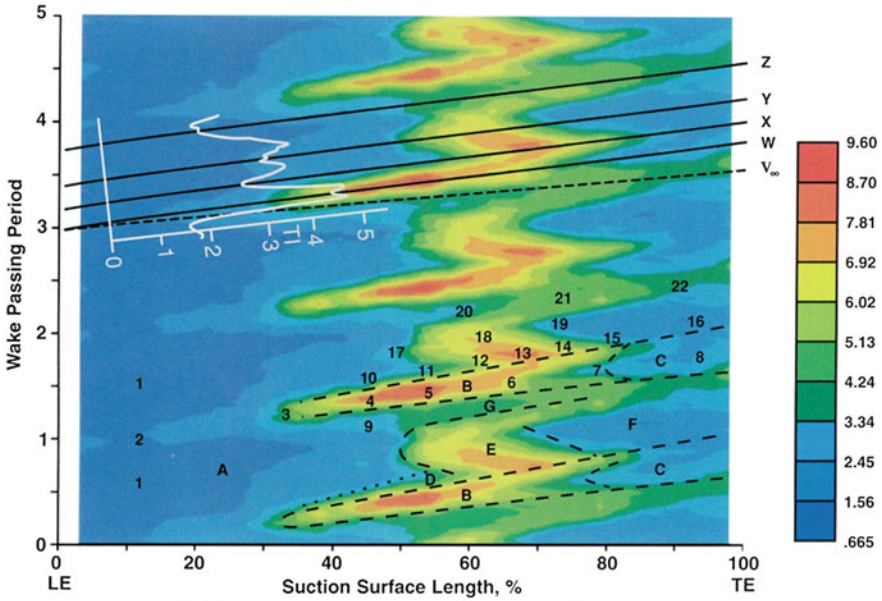
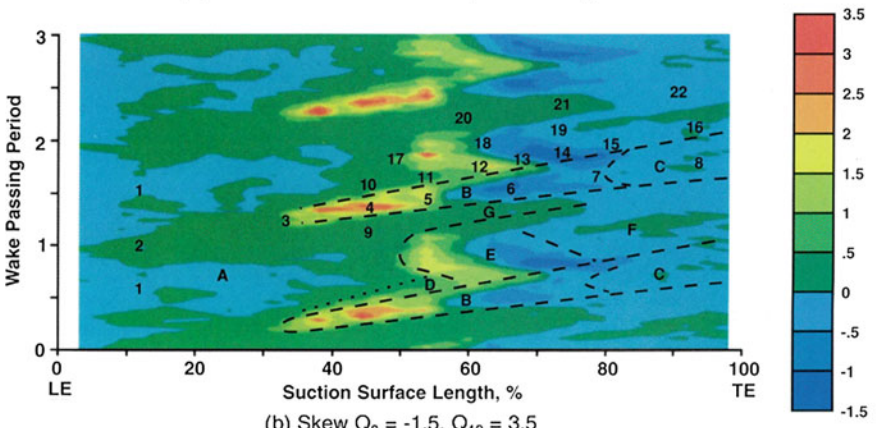


Fig. 4.23 Modes of interaction of wake and separated boundary layer [12, 75–77]

systematically studied the evolution of the attached boundary layer under incoming wakes, and provide the picture of wake-induced transition on suction side [78–81]. Figure 4.24 shows the spatial-temporal distribution of shear stress fluctuation and the skewness factor in a LP turbine test rig. The region A as shown in the figure is the laminar flow region near the leading edge. Starting from 30% suction surface length, the wake-induced transition zone appears periodically, which is labeled as B. Till around 80% suction surface length, the wake-induced boundary layer transition completes and becomes fully developed turbulence, which is the wake-induced turbulent boundary layer (C region). Between wakes, bypass transition happens near around 50% suction surface length under external disturbances, which is marked as E. The transition process completes near about 65–80% suction surface length, and the downstream F region is the turbulent boundary layer between passing wakes. Upstream of the wake-induced transition zone (B) is a region with relatively weak fluctuation, which is the so-called “calmed region(D)”. (D) which observed weak random fluctuation. It is shown that the presence of this region causes the starting position of bypass transition move



(a) Random Unsteadiness $Q_0 = 0.67$, $Q_{10} = 9.60$



(b) Skew $Q_0 = -1.5$, $Q_{10} = 3.5$

Fig. 4.24 Spatial-temporal map of wake-induced boundary layer transition [78]

significantly downstream. Although it is only measurement of one cascade, the main coherent structures and their evolution can qualitatively characterize the evolution of the attached boundary layer under wakes in typical LP turbine.

Similar as flat plate measurements, Figure 4.25 shows the hot-film measured results of the suction surface boundary layer under incoming wakes on a high-loaded LP turbine blade [82]. The increased wall shear stress with strong random fluctuations represent the wake-induced turbulent spots. A calmed region upstream of the turbulence spot is also observed. In this region, the wall shear stress

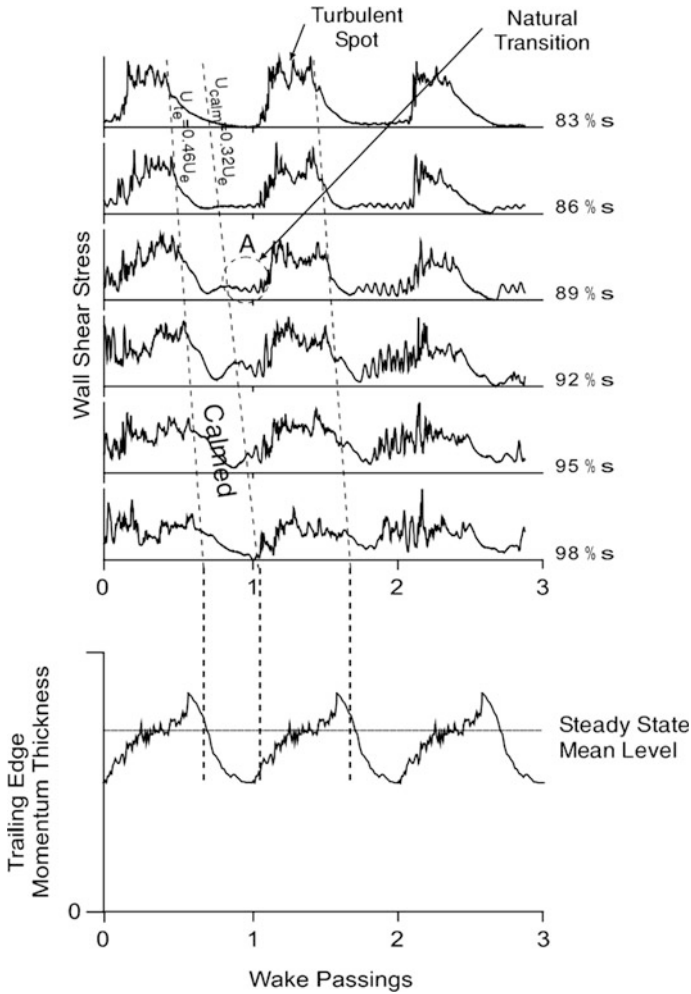


Fig. 4.25 Wall shear stress and suction side loss distribution under unsteady wakes [82]

transits from the turbulent state to the laminar state. Comparing to local laminar boundary layer, the calmed region has more full velocity profile, which can effectively suppress the boundary layer separation [83]. Figure 4.25 also shows the variation of the momentum thickness at the trailing edge of suction side with time, and the loss comparison with steady inflow. This profile has a big separation bubble on suction side under steady inflow. It can be seen that profile loss increases with wake passing by, while decreases in the calmed region after wake. Overall, the presence of wakes makes profile loss on suction side become lower.

It is generally believed that in conventional loaded LP turbine cascade, the transition induced by wakes occurs when the momentum thickness Reynolds number exceeds 90–150 [84]. This is in agreement with the laminar flow boundary

layer behavior at high inlet turbulence intensity. However, the situation is different for high and ultra-high loaded cascades. According to Howell's study, the critical momentum thickness Reynolds number may reach 225, and this difference is considered to be caused by the loading distribution [5]. It should be noted that the acceleration region in the front half of the blade suction side discussed by Howell is longer.

For the situation that separation bubbles show between passing wakes, studies show that the wake can still effectively reduce the profile loss. Figure 4.26 shows the spatial-temporal distribution of the shape factor and dissipation factor of the boundary layer under wakes in turbine blade cascade [85]. There is separation bubble under steady state inflow. As shown in the figure, region between lines B and D represent the wake induced turbulent region, while the immediate following region which between lines D and E is the calmed region. The whole interaction between wake and boundary layer can be described as follows: via bypass transition mode, wakes induce turbulent spots before separation point. The turbulence spots grow and merge into the turbulent patch. Turbulent patch moves into the separation zone, which restraining the separation bubble which is formed after the last wake passing by. Followed by the turbulent zone is the calmed region, full velocity profile can still resist separation. After the calmed region passes, local laminar boundary layer shows inflection point under adverse pressure gradient, and the separation occurs again. Separation indicates an increase in loss. Comparing to Fig. 4.26b, it shows that the region which has higher shape factor region in Fig. 4.26a, has only laminar-like flow energy dissipation, which indicates that this region is just undergoing the initial stage of the formation of the separation bubble. To sum up, the results show that the highly dissipative separation bubbles under adverse pressure gradient in steady flow are replaced by the calmed region and the initial phase of separation flow, which both have low dissipation characteristic.

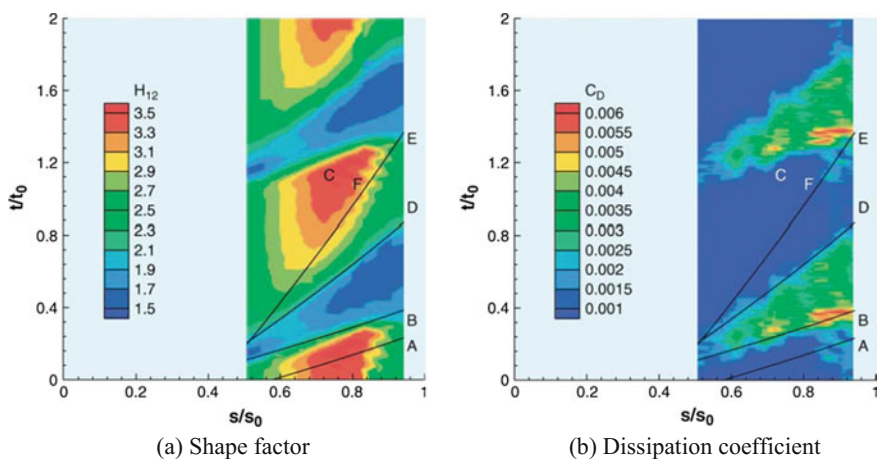


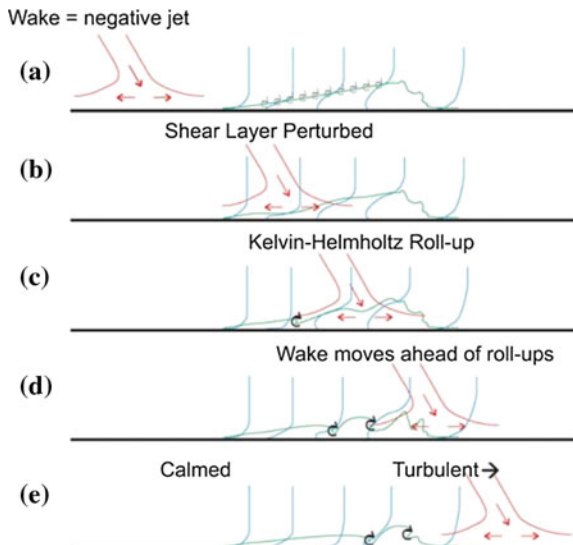
Fig. 4.26 Spatial temporal diagram of boundary layer shape factor and dissipation coefficient [85]

Therefore, under current circumstance, although the wake-induced turbulent zone has a high loss, the time-averaged loss is reduced due to the presence of the calmed zone and the initial stage of separation [86].

If the Reynolds number is low enough or the suction side adverse pressure gradient is very strong, the wake-induced transition cannot occur before the separation point, the wake and laminar separation bubbles will have a very complex interaction, which is facing by suction side boundary layer in most of the LP turbines which operate under low Reynolds number condition. Figure 4.27 shows the interaction between typical wakes with separation bubble [87]. The wall boundary flow downstream of wake center is accelerated by negative-jet, while the upstream flow is decelerated. When the wake reaches the separation zone, the outer region of the boundary layer is accelerated while the inner part, due to viscosity, responds slowly to external disturbances. Therefore, the shear is enhanced in the separation zone. The wake is transported downstream on the outer part of the separation bubble, and the normal component of the negative-jet deforms the shear layer, and makes velocity profile of the separated shear layer unstable. Vortices are rolled-up under the disturbance of wakes. Because of the low transport speed of the roll-up vortices, which is about half of the main flow [88], wakes move downstream of them and continue to disturb the downstream shear layer and create vortices. Finally, the roll-up vortices rapidly break up into turbulence, leading to boundary layer transition. After the roll-up vortices and turbulence boundary layer pass through, the calmed region appears. After the influence of the calmed region disappears, the boundary layer separates again until the next wake comes.

The wake-induced unsteady evolution of the separation bubbles causes unsteady pressure fluctuation on the wall. Figure 4.28 shows wake-induced unsteady pressure fluctuation in the separation region of T106 LP turbine cascade [85, 88]. It can be seen that the pressure fluctuations first appear upstream of the pressure plateau

Fig. 4.27 Sketch of laminar boundary layer roll-up under incoming wakes [87]



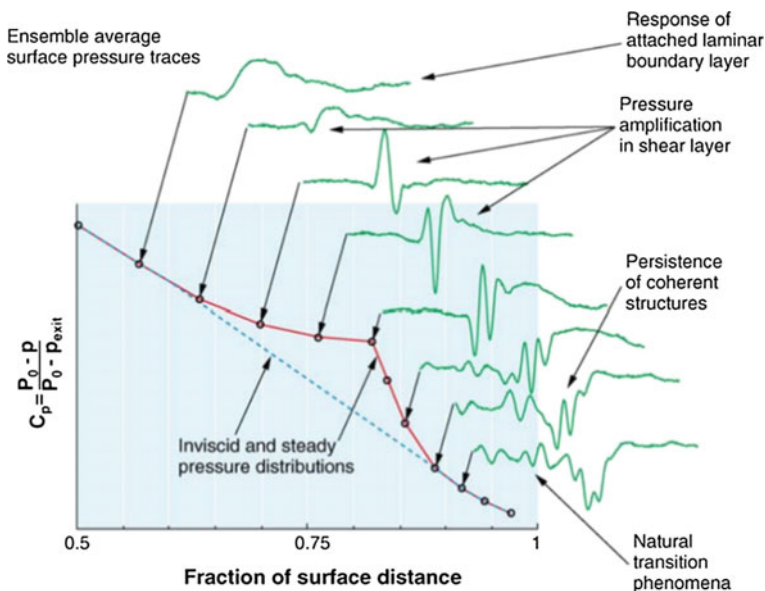
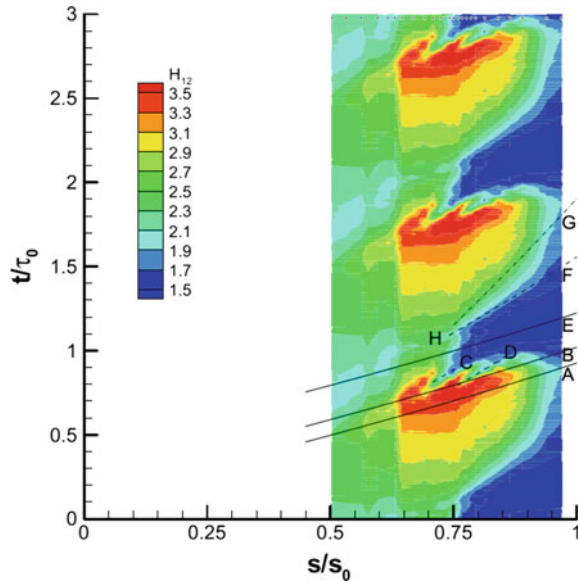


Fig. 4.28 Wake induced pressure fluctuation in the separation boundary layer [88]

and then enhance with the development of the flow. When arriving at the upstream part of the time-averaged plateau, the fluctuation reaches its maximum with the amplitude being 30% of the outlet dynamic pressure. Then it maintains this level. The results show that these pressure fluctuations propagate at velocity that is half of the main flow and have the same phase as the influence of the wakes on this region. So it can be deduced that these pressure pulsations are caused by the rolled-up vortices in the shear layer. Other researchers have observed similar pressure fluctuation in their work [89–91].

For the case of wake-induced shear-layer transition, Figure 4.29 shows the spatial-temporal evolution of the suction side boundary layer shape factor near the trailing edge of the T106 blade [87]. Here, the increasing shape factor indicates the separation bubbles periodically appearing in the boundary layer, and the trajectory of the wake is located between the lines A and E. Line A represents the trajectory of the maximum velocity at boundary outer layer induced by upstream wake. Due to viscosity, the inner region of the boundary layer situated in this trajectory has not achieve the same level acceleration, therefore the shape factor here is larger than the surroundings. Two wedge-shaped regions (C and D) appear at about 70 and 77% suction surface length on B, with propagation velocity which is about half of the main flow. These are the the wall-induced roll-up vortices in the separated shear layer and the resulting turbulent boundary layer after the vortices break down. The results also show that, although there are separated bubbles in the boundary layer, the wake induced attached boundary layer transition structure can be found upstream of the trajectory of wake trailing edge (E). The trajectories F and G in the figure are for the trailing edges of the wake-induced turbulence region and the

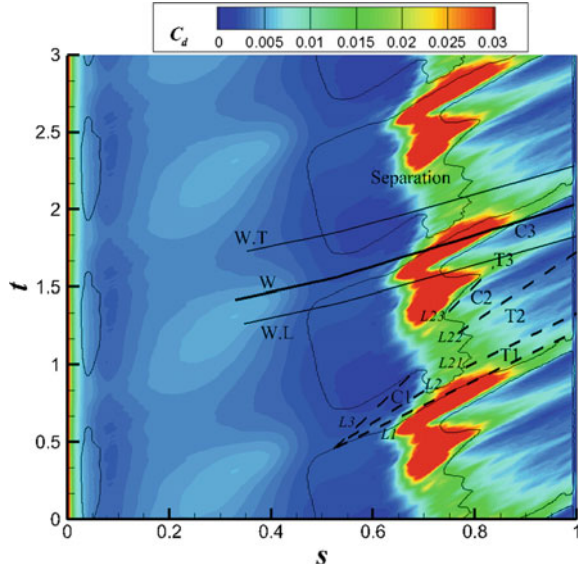
Fig. 4.29 Wake-induced separation bubble transition [87]



calmed region, respectively. Stieger and Hodson explained this phenomenon as a result of boundary layer bypass transition induced by turbulent diffusion [87]. The above results show that if the wake does not induce the boundary layer transition before the separation, the unsteady disturbance of the wake may cause the shear layer unstable via inviscid effect, and then roll up vortex and eventually induce transition. In this case, it is still possible to observe a obvious calmed region in the attached boundary layer in downstream part of trailing edge.

Similar results have also been obtained from LES of the higher loaded T106D-EIZ turbine cascade with typical wake effects [63, 92]. Though there is open separation on the cascade suction surface under steady condition, this open separation is replaced by periodical small separation bubble under wake condition and thus significantly improve its aerodynamic performance. This, again, proved the potential of using unsteady wake to enhance turbine aerodynamic performance. Figure 4.30 shows the spatial-temporal distribution of the dissipation factor in T106D-EIZ turbine cascade boundary layer. The W, WL and WT represent the trajectories of the wake center, leading and trailing edge, respectively, while the black lines represent the spatial-temporal evolution of the separation region. In contrast to Ref. [87], the separation bubbles in the wake passing region is obviously inhibited, which could be the co-effect of the inviscid negative-jet and wake-induced attached boundary layer transition. In the vicinity of the separation bubble reattachment region (70–80% of the suction surface length), two regions with wake-induced roll-up vortices and their induced transition are observed: T2 and T3. The corresponding calmed regions are labeled C2 and C3. The formation mechanism of these regions may be due to the turbulent diffusion induced boundary layer bypass transition mechanism as described in [87]. As for the location of these flow structures are different, it should due to difference of blade loading and the wake conditions.

Fig. 4.30 Spatial-temporal distribution of T106D-EIZ cascade suction surface dissipation coefficient under the unsteady wake condition [63]



4.2.3.4 Effects of Wake Characteristics on Boundary Layer Evolution

Previous section described the typical mechanism of unsteady wake effect on boundary layer development. There are many parameters of wake can influence the boundary layer, including its width, velocity defect, turbulence intensity, passing frequency and flow coefficient, etc. Till now the studies on influence of wake width, velocity defect and turbulence intensity are not very systematic, while the impacts of the wake passing frequency and flow coefficient have been discussed detailedly by many researchers.

The wake frequency can be measured in terms of the reduced frequency, which has similar physical meaning as Strouhal number, defined as the ratio of the time required for passing through the cascade to the time interval between wakes:

$$f_r = \frac{f_b b}{V_{2,is}} = \frac{U_b b}{t_b V_{2,is}} \tag{4.2}$$

Figure 4.31 shows the T106D-EIZ LP turbine cascade suction side shear stress τ_{wall} distribution with different unsteady wake conditions [63]. In which the wake flow coefficient is fixed to 0.83, and the reduced frequency is $f_r = 0.67, 0.335, 1.005, 1.34, 1.675$ respectively. The region where wall shear stress is negative occurred the flow separation. The results show that the size of leading edge separation bubbles decreases with the increase of reduced frequency, and after the reduced frequency f_r exceeds 1.005, those separation bubbles disappear. Regarding the separation point of the trailing edge separation bubble, the change of wake reduced frequency has a relatively small effect on changing its location, and there

Fig. 4.31 Wall shear stress distributions on the suction side at different wake reduced frequencies [63]

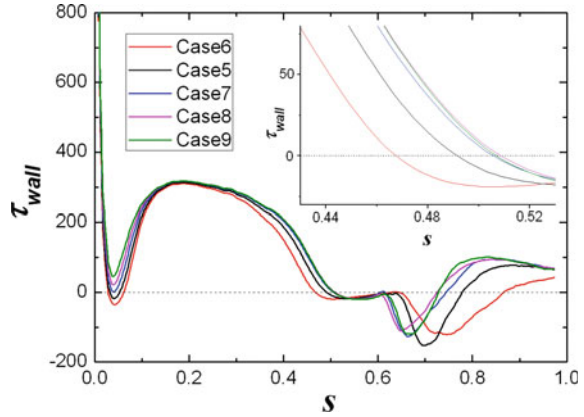
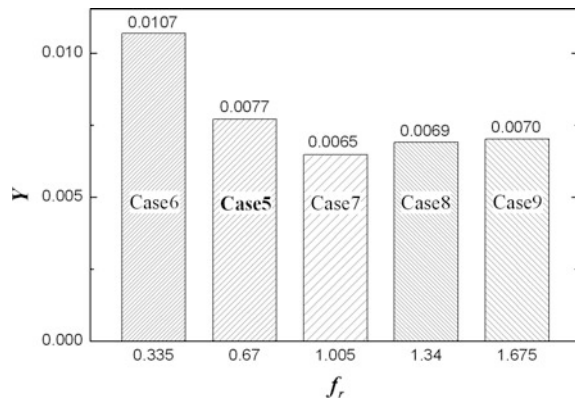


Fig. 4.32 Stagnation pressure loss coefficients with different wake reduced frequencies [63]



are three conditions that the separation point will not change with f_r when f_r is above 1.005. Wake reducing frequency has more impact on reattachment location comparing to separation point. With the increase of f_r , reattachment moves upstream. Above influence caused the axial length of separation bubble under $f_r = 0.335$ condition increase by 38% when compared to baseline condition. While the other three conditions, the length of separated bubbles were reduced by 15, 24 and 23%. In addition, after the wake reduced frequency exceeds 1.34, the position of the separation point and reattachment point will not move with the change of reduced frequency. This is because the wakes will almost join on affecting the suction side boundary layer when the reduced frequency reaches 1.34. Therefore, there is no significantly changes if further increase the reduced frequency [63]. Figure 4.32 compares the total pressure loss coefficients with the corresponding reduced frequencies. When $f_r < 1.005$, the average total pressure loss coefficient decreases with increasing f_r . However, when f_r further increasing to 1.34 and 1.675,

the average stagnation pressure loss coefficient increases, indicating that for the specific turbine cascade, there is optimal reduced frequency.

In case of boundary layer, figure 4.33 shows the flow structures on suction side in one wake phase under five conditions as mentioned above. The figure shows clearly the instantaneous position of wake location and the shape on cross section $z = 0$, which is dyed using spanwise vorticity w_z . In the same time, it shows the contour plot of axial velocity $u1 = 0.1$. It is dyed by pitch velocity $u2$, which can identify boundary layer flow structures, and can also give the approximate location of the separated shear layer in the streamwise direction and the normal direction. The Figure also shows the pitch velocity Vt distribution on the first-layer mesh and the contours of $Vt = 0$ to accurately identify the separation area within the boundary layer. The contour plot are placed side by side with the iso-surface of the axial velocity $u1 = 0.1$. these contours clearly show the relations between the wake, the coherent structure in the boundary layer and the instantaneous location of the separated bubbles.

Researches on the effect of reduced frequency f_r on the development of boundary layer flow structure can be summarized as follows [63]: The transport characteristics of a single wake in the cascade do not change with f_r . Within certain range of f_r , a calmed region can be observed in the boundary layer between wakes, which appears earlier but with a shorter duration when increasing f_r . Too large or too small of f_r will reduce the unsteadiness of the flow inside boundary layer. Correspondingly, the calmed regions in the gap between wakes will disappear. Too large f_r will enlarge turbulent boundary layer area, while too small f_r will enlarge separation area, which both cause profile loss increases. In addition, the wake itself also increases the dissipation in the main flow. The combined effect of the above effects makes it possible to optimize f_r for the aerodynamic performance under certain operating condition. This optimal value is approximately 1 for the T106D-EIZ cascade [63]. Other turbine cascades experiments verify the existence of the optimal reduced frequency [93]. However, the values of the optimal wake frequency may vary due to the blade loading and operating conditions.

Liang Yun and Zou Zhengping et al. did detailed experimental studies [94] on their designed $Zw = 1.33$ high-lift LP turbine blade with Reynolds number of 1.1×10^5 and inflow turbulence intensity of 1%. Their results as well show that the wake frequency has a great effect on the boundary layer separation control, which is mainly displayed by different action times of turbulent spots or calmed regions and different size of the separation region under different wake frequency. Figure 4.34 shows a spatial-temporal plot of the quasi shear stress on the suction side surface with different wake reduced frequencies. The black dot in the figure represents the measurement location of hot-film probe on the suction surface. In the first half of the blade, the flow is laminar, and the shearing stress is low with less fluctuation. Only when the fluid with high turbulence intensity in the wake sweeps through the blade surface will the shear stress increase. Thus it can identify the leading edge of the wake (WL). its slope in the figure can determine the wake propagation velocity. After the wake passes at about 60% of suction surface, calmed region (C) appears,

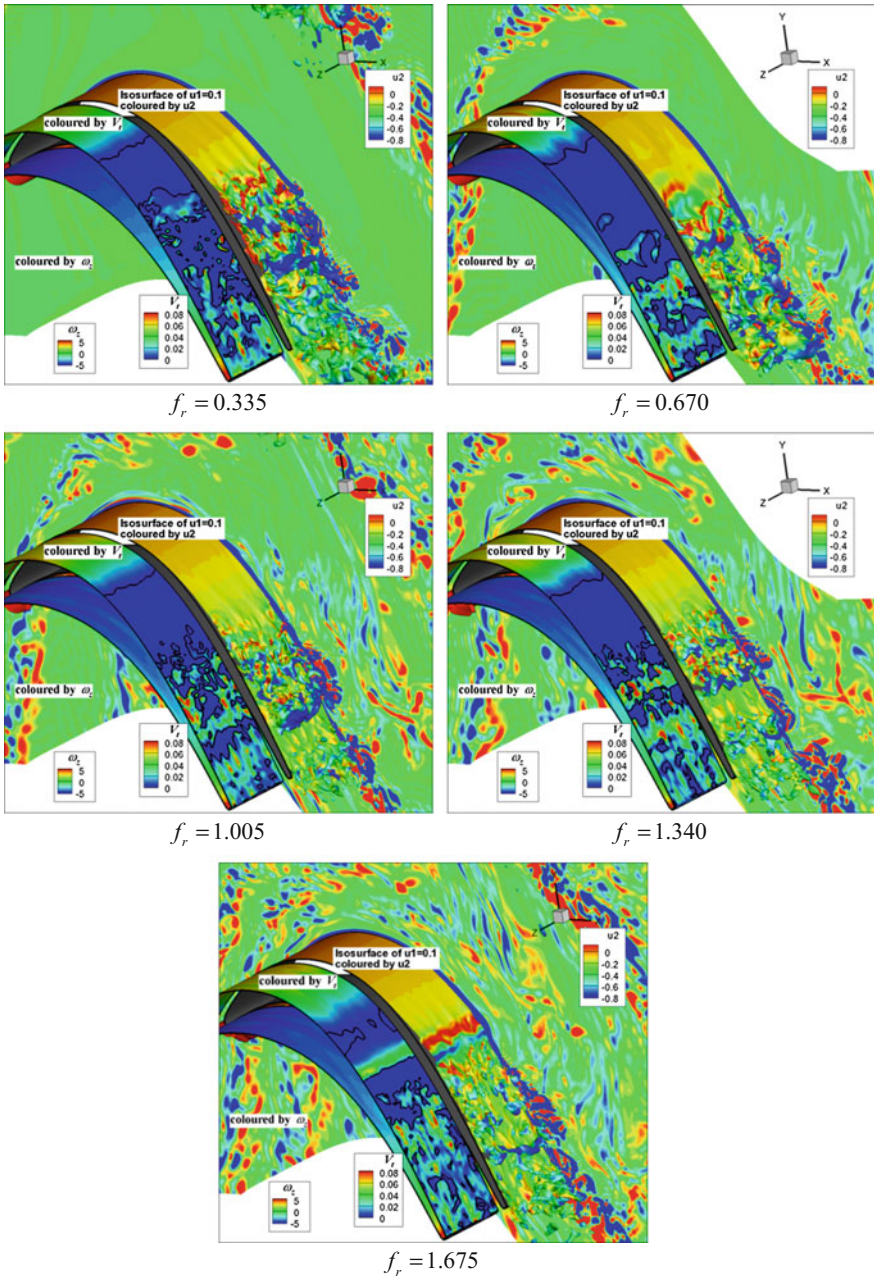


Fig. 4.33 Suction side boundary layer flow structures with different wake reduced frequencies [63]

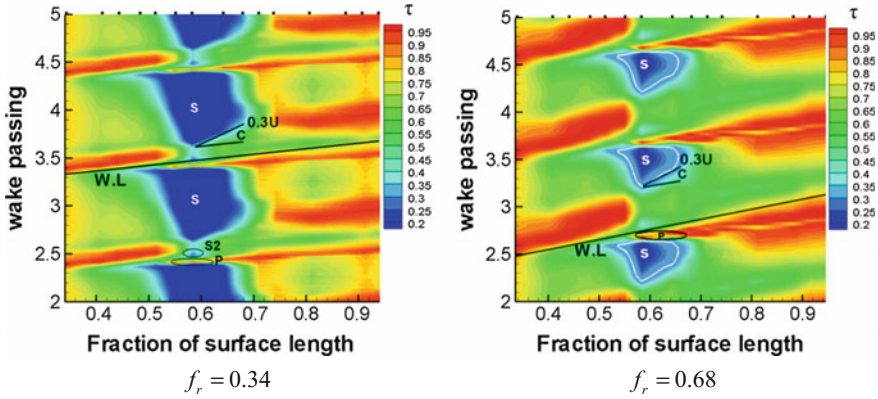


Fig. 4.34 Spatial-temporal diagram of shear stress on suction side with different wake reduced frequencies [94]

identified based on shear stress value. The trailing edge of the calmed region has a propagation velocity of 0.3 times the main flow speed. After the calmed region passes, the boundary layer separates again. Before wake arrives, there already appears high shear stress region (P) from the 52% of suction surface. This is because the negative-jet model in the beginning of wake has certain acceleration effect on the downstream flow. This accelerating effect disturbs the shear layer of the separation bubble, prompting its rapid transition to turbulence, resulting in high shear zone. This also indicates that under this condition, the wake-induced boundary layer transition occurs in the separated shear layer. When wake interacts with separation bubbles, the wake negative-jet will form a series of complex vortex structures with the separated shear layer. Stieger [27] verified this point via PIV. On the shear stress spatial-temporal diagram, the low-shear zone (S2) inside the wake-through region also proves the presence of wake induced complex vortices. This phenomenon is more obvious when the wake frequency is low. It can be seen that the separation is not completely inhibited under two wake frequencies, that is in the gap between wakes, there occurs boundary layer separation again. However, when the wake reduced frequency increases from 0.34 to 0.68, the separation region diminishes obviously with the duration decreases as well.

Wake can control boundary layer separation. Different wake passing frequencies have different control impact. The most direct expression is the change of the boundary layer loss. By analyzing the trailing edge boundary layer momentum thickness at different frequencies, it can be found that the boundary layer loss is greatest when there is no wake, and it decreases rapidly after adding the wake. With the increase of wake frequency, the boundary layer loss decreases. Further research is needed on how the wake reduces loss, and whether there will always be monotonically correlation on wake frequency and loss.

Liang and Zou [94] show the boundary layer momentum thickness at the suction side trailing edge under different conditions (see Table 4.3). It can be seen that the

boundary layer loss decreases monotonically with the increase of wake reduced-frequency, which is consistent with other researchers. Furthermore, Liang and Zou [94] divided the suction surface boundary layer loss into three parts: laminar loss before separation, separation loss and turbulent friction loss. They also provided (see Table 4.4) quantitative analysis on the change of each loss with different wake frequencies. It can be seen that the profile separation loss in the steady state is relatively large in the total loss, so introducing the unsteady effect of wake will inhibit separation and thus can significantly reduce the total loss. In the meantime, the proportion of laminar loss and turbulent friction loss increases, especially the later one. Under this condition, when the reduced wake frequency is 0.68, the ratio of separation loss decreases to 7.04% and the main loss is turbulence friction loss, which indicates that the wake reduced frequency is close to the optimum value.

Similar influence of wake reduced frequency has been shown from even lower Reynolds number experiments [95]. Figure 4.35 shows the spatial-temporal distribution of boundary layer momentum thickness for a turbine cascade with Reynolds number of 2.5×10^4 and inflow turbulence intensity of 0.6%. The solid lines in the figure represent the trajectories of the leading edge of wakes, while the two dotted lines represent the trajectories of the trailing edge of the wakes and the calmed region. When the wake has low passing frequency, the separation bubble will appear near the trailing edge of the profile in the gap between wakes. It should be noted that the definition of the wake reduced frequency ($F = fL_{j-te}/U_{ave}$) is different here, where f is the wake passing frequency, L_{j-te} is the length of the adverse pressure gradient region in the suction side boundary layer, and U_{ave} is the main flow averaged velocity. For the same research object, the specific values of F and f_r are different, but the represented physical concepts and their trends are consistent. The results show that the increase of wake reduced frequency can effectively reduce boundary layer momentum thickness at the trailing edge and reduce the profile loss. The discussion on the influence of Reynolds number shows that when Reynolds number is 2.5×10^4 , there will not be significantly suppressed separation until F reaches around 0.5. When the Reynolds number is 5.0×10^4 , the similar effect can be achieved when $F = 0.3$. This also confirms that the optimum reduced frequency will depend on the cascade specific operating conditions.

Table 4.3 Boundary layer momentum thickness near trailing edge

Wake reduced frequency	0	0.34	0.68
Momentum thickness (mm)	1.93	1.5	1.28

Table 4.4 Profile loss under different reduced frequencies

Wake reduced frequency	Laminar loss (%)	Separation loss (%)	Friction loss (%)
0	8.45	43.1	48.45
0.34	10.68	26.34	62.98
0.68	13.23	7.04	79.73

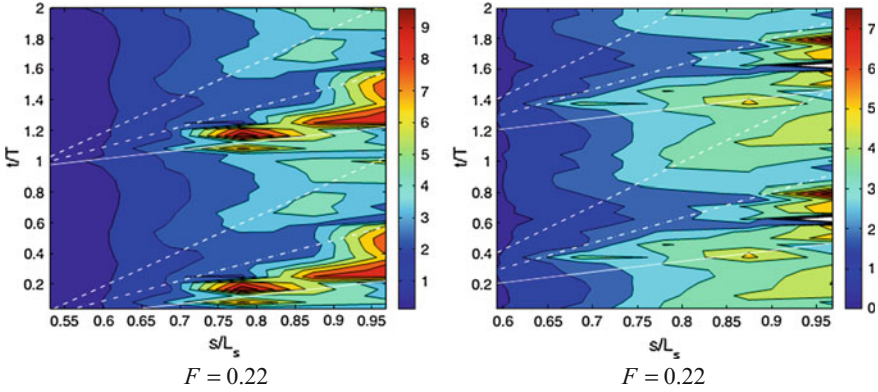


Fig. 4.35 Spatial-temporal distribution of suction side boundary layer momentum thickness under different reduced wake frequencies [95], inlet turbulent intensity 0.6%, $Re = 25000$, $\varphi = 0.7$

In addition to reduced frequency, flow coefficient is also an important parameter to represent incoming wake characteristic, which is defined as the ratio of cascade axial velocity to the wake pitch velocity:

$$\varphi = \frac{V_{x1}}{U_b} \quad (4.3)$$

With other parameters remain constant, the wake flow coefficient φ has obvious influence on wake transport characteristics. The wake entrance angle, width, and relative velocity defect will all change with it [63]. Under same reduced frequency f_r , the influence of φ on the change of time-averaged inlet flow angle is complicated. On one hand, the relative flow angle of the individual wake will increase as ϕ increases, the negative incidence will be improved. On the other hand, the relative wake width increases with ϕ , its impact range is even larger, so that the relative averaged flow angle decreases, negative incidence increases. For a given operating condition, the time-averaged relative flow angle either increased or decreased needs to discuss specifically.

The LES results of T106D-EIZ turbine cascade under different wake flow coefficients show that [63]: In general, the size of the time-averaged separated bubble decreased with the increase of the flow coefficient, but this effect was much weaker compared to reduced frequency. In terms of flow loss, the increase of the flow coefficient makes it impossible to roll up the vortex in the separated shear layer, and thus to reduce the suction side boundary layer flow loss. However, this in turn increases the average disturbance level in the main flow, increasing the main flow loss. The increase of flow coefficient makes the wake act to the boundary layer of the suction surface in a nearly parallel way, thus increasing the influence time of the individual wake to the boundary layer. But the effect of the negative-jet is

weakened, which finally increases the ambient turbulence intensity of the boundary layer and reduces the unsteadiness of the wake. This eventually leads the calmed region not to appear under the large flow coefficient condition. On the contrary, the calmed region is more obvious in the small flow coefficient φ condition. It can be seen that with constant wake reduced frequency f_r , flow coefficient φ has multiple influences on the turbine cascade performance. For the T106D-EIZ turbine cascade, the total aerodynamic losses of the cascade can be reduced at very large or very low flow coefficient conditions. Figure 4.36 shows the suction side boundary layer flow structures of a phase in wake period under different flow coefficients.

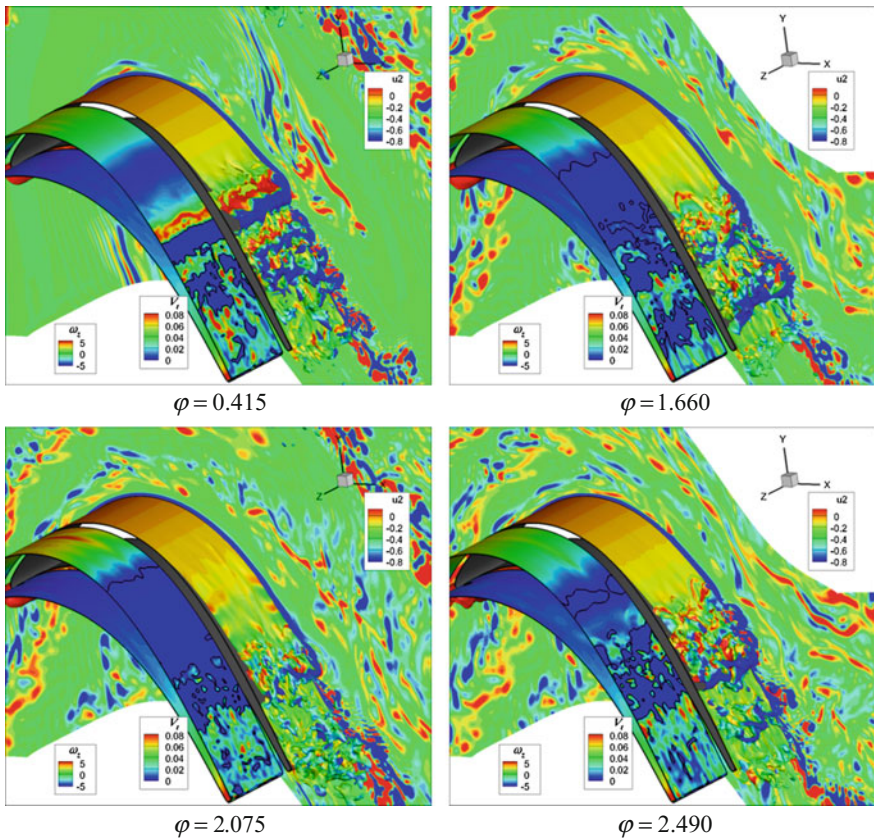


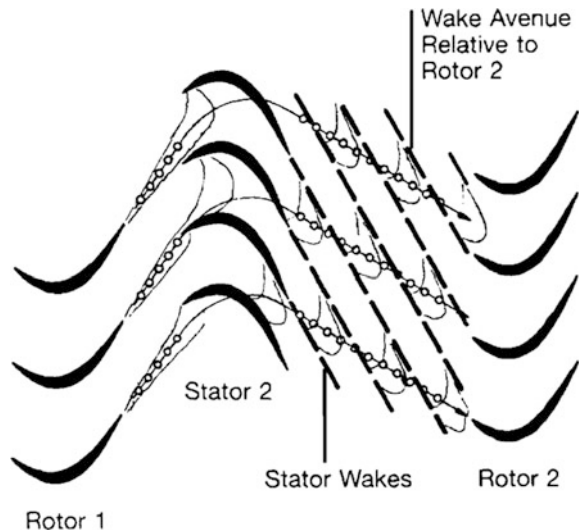
Fig. 4.36 Suction side boundary layer flow with different wake flow coefficients [63]

4.2.4 Unsteady Flow and Boundary Layer Evolution in Multi-stage LP Turbines

LP turbines are generally multiple stages, may reach 5–7 stages, or even more. Though it has been recognized for long that the unsteady nature in multi-stage turbines and their effects may have deeper influences, it is difficult to carry out detailed measurement on the multi-stage turbine test rig, and the cost is very high. The unsteady calculation of the multi-stage turbine also needs a large budget, which has caused some obstacles for research. Thus the research and understanding of unsteady flow phenomena in multi-stage turbines develops slow. With the development of computer hardware and computing technology since 1990s and the improvement of experiment capability, more and more researchers begun to pay attention to the unsteady flow inside multistage turbine, and obtained many important results, which effectively improved the understanding of the relevant issues.

As shown already, potential flow decays fast in space and its influence is generally confined to the adjacent bladerows and the potential field interaction between rows is weak. However, the effective length of wakes is long, which will affect the downstream bladerows. And the maximum turbulence inside the wake may be increased in the blade passages, which may cause the wakes from multiple upstream rows to have a significant effect on the downstream cascade flow, which mainly due to interaction between blades in multi-stages. Figure 4.37 shows the main characteristics of the wake propagation in a multi-stage turbine [96]. It can be seen that the wake from the first-stage rotor (Rotor 1) is cut into segments by the Stator 2. At the same time, wake is distorted in the later channel and the propagation direction is changed. Downstream of Stator 2, the wake from the same first-stage (Stator 1 and

Fig. 4.37 Transport process and morphology of wakes in multi-stage LP turbines [96]



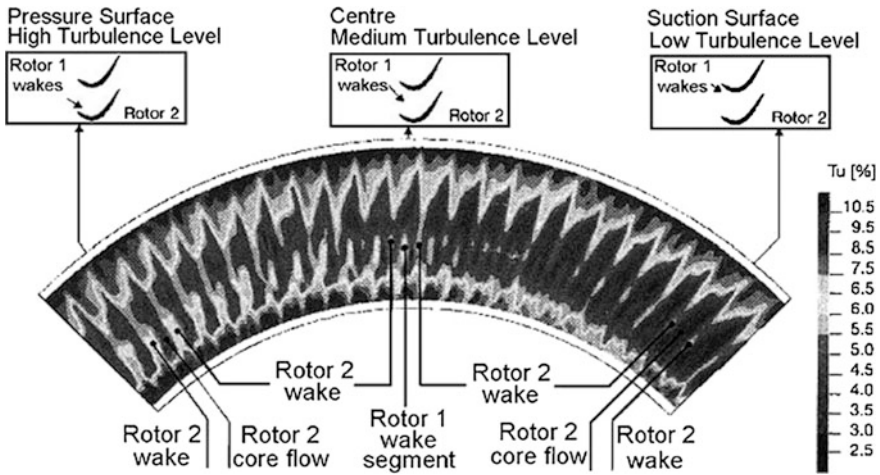


Fig. 4.38 Turbulence intensity distribution at multi-stage turbine outlet [98]

Rotor 1) is no longer continuous, but becomes segments which are divided by the Stator 2 wakes, and they transported downstream together. Normally, the blade numbers of two rotor stages are different, which leads the wakes from Rotor 1 enter the Rotor 2 passage from different circumferential positions and eventually cause the non-uniformity in Rotor 2 wakes circumferentially, that is, the so-called “Beating effect” [97, 98]. Figure 4.38 shows the turbulence intensity distribution at third-stage outlet in a multi-stage LP turbine [99]. This figure clearly shows the wake strength in the axial direction due to the different rotor blade numbers from the first two stages. It can be seen that the unsteady flow inside the multistage LP turbine is more complicated with the increase of the turbine stages due to the interaction between wakes from multiple stages.

The wake propagation mechanism described above results in different unsteady flow fields observed at different downstream positions. Figure 4.39 shows the wake trajectories near the first rotor outlet of a three-stage LP turbine and the variation in turbulence intensity over the trajectories obtained from probes at different axial position [78]. It can be seen that the turbulence intensity in the wake of the first stage rotor is about 5%, the turbulence in the wake of the first stator is in the order of 3.5%, while in the gap between wakes, the turbulence intensity drop to 1.5%. The difference in the turbulence intensity may be about 1% for different circumferential positions of the observed results. In addition, the results also show that the turbulence intensity has changed twice in one cycle at both measurement positions, apparently because of the presence of wakes of two rows of blades upstream. A similar phenomenon was observed at the third stage. These phenomena indicate that, although the upstream vanes may be still relatively, their wakes are cut and subsequently deformed by the relative rotation of the cascade passages, and the wake from those comparable still bladerows also has an unsteady effect on the downstream vane.

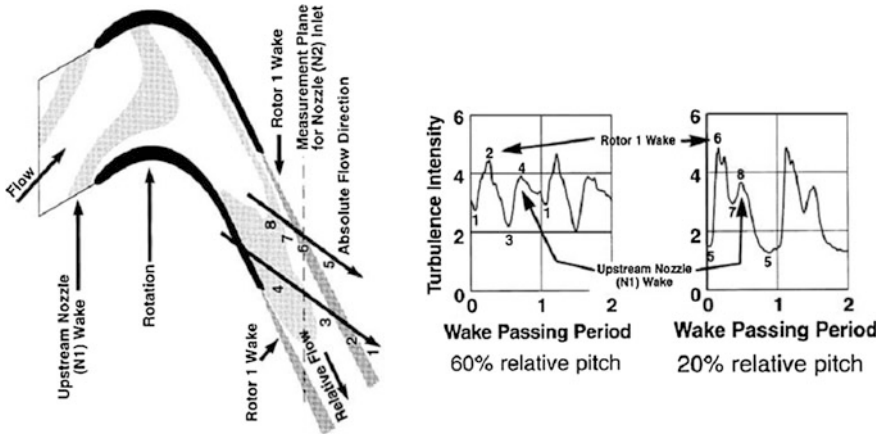
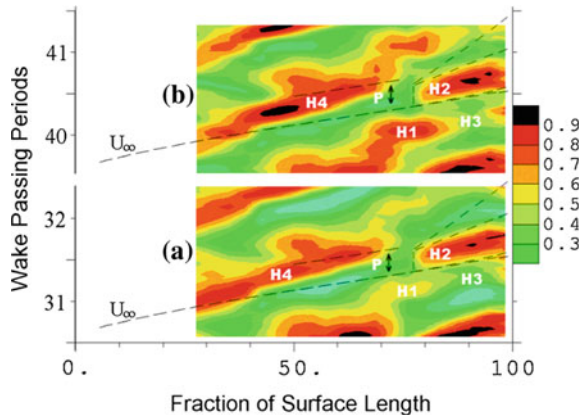


Fig. 4.39 Circumferential non-uniformity of unsteady fluctuation in multi-stage turbine [78]

The development of suction surface boundary layer in the multi-stage turbine still draws research attention. Hudson and Howell et al. measured the suction side boundary layer in a multistage LP turbine using surface hot-film technology [13, 100]. Figure 4.40 shows the non-dimensional quasi-wall shear stress spatial-temporal distribution on the third-stage suction surface boundary layer in LP turbine of the BR715 engine. Figure 4.40a, b show the results for different positions of second-stage rotor, with vertical axis being the passing period of second-stage rotor blade. It should be noted that the region of high shear stress indicated by H4 is not a turbulent region but only a result of the absence of adhesion between wake and laminar boundary layer. In fact, the transition induced by the upstream second-stage moving blade wake starts at H2 which is about 75% of the camberline. In addition to H2 and H4, another region of high shear stress, H1, which is the transition region induced by second stage wakes, is clearly visible in Fig. 4.40b,

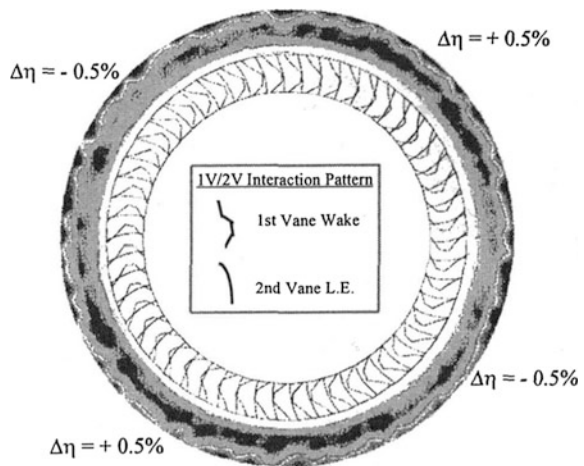
Fig. 4.40 Spatial-temporal distribution of the quasi-wall shear stress on third-stage guide vane suction surface in BR 715 LP turbine [13]



confirming that the upstream bladerows' wakes may also affect the development of the downstream boundary layer. This also clarifies the importance of investigation of wake influences in multi-stage turbine. In addition, transition zone H1 is not evident in Fig. 4.40a, which is caused by circumferential unevenness of wake strength from the upstream row.

It is envisioned that the unsteady effects inside the multi-stage turbine may have a significant effect on the downstream flow. Previous studies pointed out that the relative positional relation of the relative stationary blade row will determine the phase of the upstream wake into the downstream channel, which will affect the downstream flow in the multi-stage turbine and eventually affect the aerodynamic performance of the multi-stage turbine which is so called "clocking effects". Many researches show that the variation range of the aerodynamic efficiency of the multi-stage turbine blades may reach about 0.5% when the relative pitch position of the turbine blades is changed. Generally the highest efficiency occurs when the wake of the upstream blade row passes over the leading edge of the downstream blade while the lowest efficiency occurs when the wake of the upstream blade passes from the center of the downstream blade channel. Experiments and numerical simulations of 2.5-stage turbine with the same number of blades at different working conditions show that [101, 102] the stator clocking effect varies turbine efficiency by 0.3% in both design and off-design conditions. In design condition, the efficiency may vary in the order of 0.5% (see Fig. 4.41) at different pitch locations, while the highest efficiency change at different radial positions can reach 1%. Accordingly, the researchers believed that if we can efficiently use the time series effect between the bladerows, it is definitely possible to improve aerodynamic performance by 0.8%. Similar results have been reported by other researchers on different multi-stage turbines [103–107].

Fig. 4.41 Circumferential efficiency change in a 2.5-stage turbine [101]



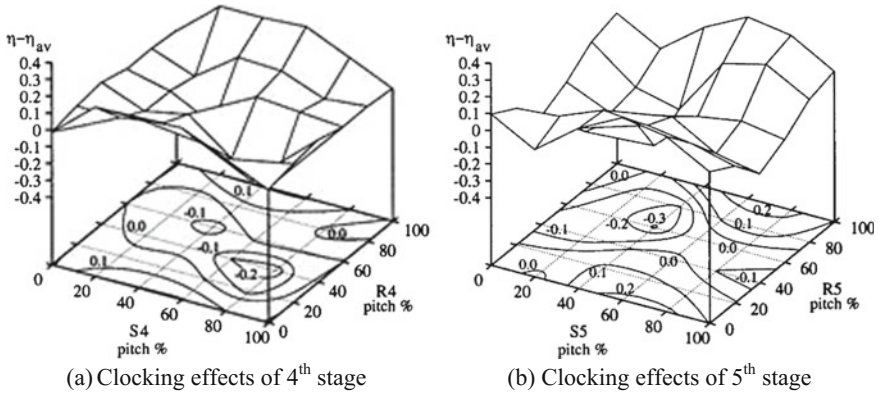


Fig. 4.42 Clocking effects on efficiency in a multi-stage turbine [108]

For the multi-row clocking, Figure 4.42 shows the clocking effect of a three-stage (third, fourth, and fifth stage) of a LP turbine component [108]. The efficiency of the turbine components obtained by separately adjusting the circumferential positions of the fourth and fifth stage blades of the turbine are given separately. The adjustment of the circumferential position of the fourth-stage turbine blades results in a variation of the turbine efficiency of 0.5 and 0.6% by adjusting fifth-stage turbine. The figure shows that, no matter the fourth or fifth stage, there is a strong interaction between rotor/stator circumferential positions. This suggests that it is not sufficient to consider only the clocking effect between stationary blades or rotating blades in a multi-stage turbine. In addition, the results in Fig. 4.42 show that the benefits obtained by individually adjusting the circumferential position of a stage turbine blade are of the same order of magnitude. While the efficiency can change 6.8% [108] by adjusting the axial position of the fourth and fifth stage turbine blades simultaneously, indicating that clocking effect in the multistage turbine is not simply superposition. At present, the researches on the interaction of the stator/rotor clocking effect, the clocking between the relative stationary bladerows, and the interaction between the relatively moving bladerows, are neither deep enough nor systematic. The understanding of the above problems has yet to be further improved.

In addition to the overall performance of turbine components, clocking effect on the evolution of boundary layer structure in multi-stage turbine is also one research topic and many works have been done in recent years [109–111]. Figure 4.43 shows the temporal and spatial distribution of the quasi wall shear stress and the total skewness factor of the shear stress at suction side boundary layer of the second stage in a 1.5-stage turbine [112, 113]. In Fig. 4.43a, b, the first-stage stator locates at different circumferential positions, which correspond to the best and worst aerodynamic performances. The circumferential blade positions in these two conditions differs by about 45% of the first stator pitch. In the figure, the solid line FS is the main stream trajectory, S represents the wake trajectory from first stage stator,

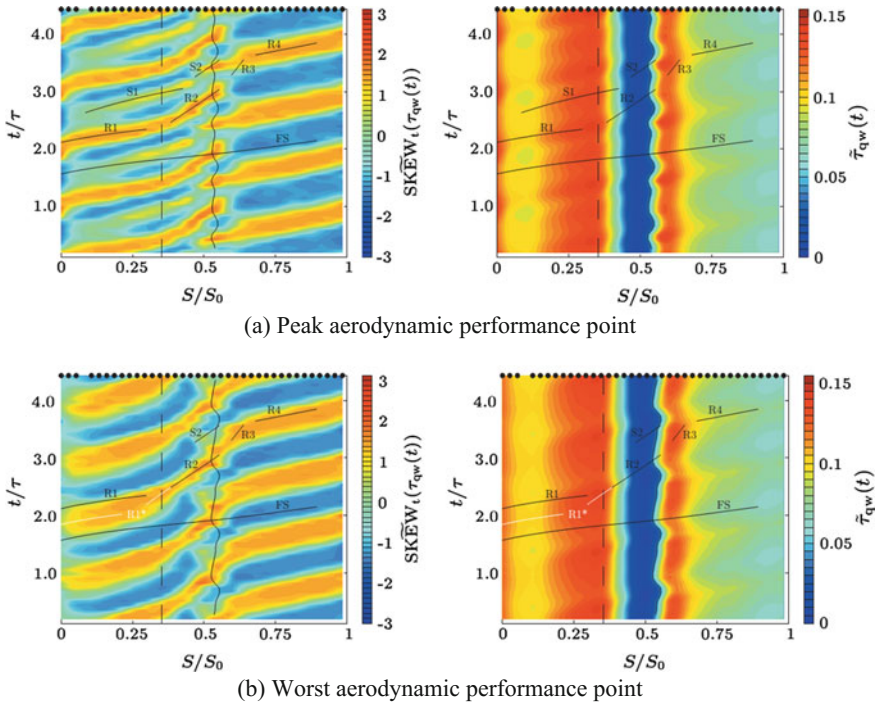


Fig. 4.43 Clocking effects on suction side boundary layer evolution of the second vane in a 1.5-stage turbine [112]

and R represents the wake trajectory of the first stage rotor. Before about 50% of the camber line, the wake trajectories from upstream two were observed simultaneously. While the trajectories of the first stage vane were more pronounced in Fig. 4.43a, this is one of the main differences of boundary layer structure between these two conditions. In addition, the phase of the upstream rotor wake induced structure appears very different under both conditions, especially near the leading edge. It should be noted that the upstream rotor is in the same phase, and the difference of the wake trajectory is caused by the unsteady evolution mechanism of second stage guide vanes inlet flow angle, which is due to stator clocking. The figures also show that the presence of the first stage stator wake in Fig. 4.43a can lead to the transition happen earlier, thus effectively reducing the length of the separation bubble, which is also the main reason to obtain the optimal aerodynamic performance. Based on the study of the two-dimensional clocking effect, many researchers have studied the three-dimensional clocking effects by numerical simulation or experimental measurement [114–116]. Their results show the clocking effect also has significant impact on the intensity and evolution of blade tip leakage flow and end wall secondary flow. This is also an important revenue source for multi-stage turbine timing effect.

4.2.5 Boundary Layer Losses and Prediction Models

4.2.5.1 Attached Boundary Layer Flow Losses

Since the profile loss is a key contribution for flow loss, the assessment and prediction of the flow loss in the boundary layer is also an important topic of studying the evolution of LP turbine boundary layer. Denton pointed out that the entropy production per unit area of the two-dimensional boundary layer can be expressed as [6]:

$$\dot{S}_a = \frac{d}{dx} \int_0^\delta \rho V_x (S - S_\delta) dy = \int_T^\delta \frac{1}{T} \tau_{xy} dv_x \quad (4.4)$$

where, S and S_δ , represent the local entropy and the entropy at outer edge of boundary layer in the same reference condition, respectively. τ_{xy} is the local shear stress. Further, the entropy production yield per unit volume of the two-dimensional boundary layer can be expressed as:

$$\dot{S}_v = \frac{1}{T} \tau_{xy} \frac{dv_x}{dy} \quad (4.5)$$

For most of the boundary layer, the velocity changes strongly near the wall, so most of the entropy production is concentrated there. Especially in the turbulent boundary layer, the entropy production mainly exists in viscosity sub-layer layer and the log-law layer. Quantitative studies show that about 90% of the entropy production of boundary layer occurs in the inner layer [117].

To make simple comparison and application, researchers defined the dimensionless dissipation factor to measure the local loss in boundary layer:

$$C_d = \frac{T \dot{S}_a}{\rho V_\delta^3} \quad (4.6)$$

where V_δ is the velocity at and outer edge of the boundary layer. Clearly, to calculate boundary layer dissipation factor, it is necessary to know the boundary layer flow details, which is obviously not conducive to the application of dissipation factor. Fortunately, researchers have given the ideal solution to this problem. Schlichting pointed out that for turbulent boundary layer, the value of the loss coefficient is relatively less influenced by the details of the boundary layer flow. He gave the approximate formula for the dissipation factor in turbulent boundary layer with the shape factor $1.2 < H < 2.0$, Reynolds number based on momentum thickness $10^3 < Re_\theta < 10^5$ [118]:

$$C_d = 0.0056Re_\theta^{-1/6} \tag{4.7}$$

For most LP turbine blades, the Reynolds number based on turbulent momentum thickness is generally in the order of 10^3 . Denton and Cumpsty further pointed out that in this case, the turbulent boundary dissipation factor can be approximated by a value of 0.002 [119].

For the laminar boundary layer, Truckenbrodt gave the following formula for calculating the dissipation factor [120]:

$$C_d = \beta Re_\theta^{-1} \tag{4.8}$$

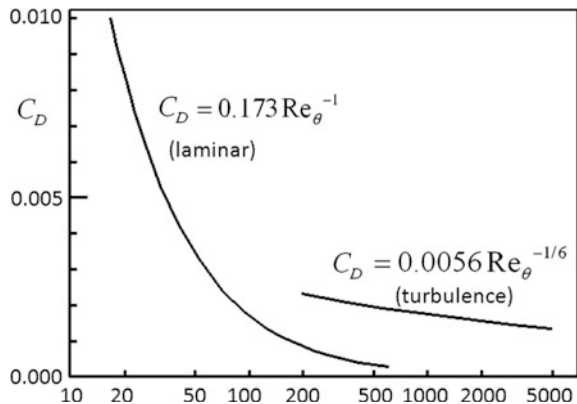
where coefficient β will be affected by the boundary layer shape factor. Truckenbrodt also gave an analytical result for the laminar boundary layer at zero pressure gradient: $\beta = 0.173$. Figure 4.44 shows the variation of the dissipation factor with Reynolds number given by (4.7) and (4.8). It is worth noting that in Reynolds number range where both laminar and the turbulent boundary layer can exist $300 < Re_\theta < 1000$, the typical dissipation factor in the laminar flow boundary layer is significantly smaller than the one in turbulent boundary layer. This also clarifies the importance to control the turbine blade boundary layer transition.

Base on the local loss, the total loss of the boundary layer is also easy to obtain. The boundary layer total entropy production can be calculated by

$$\dot{S} = \int_0^{S_0} \frac{C_d \rho V_\delta^3}{T} ds \tag{4.9}$$

Similar to above, we define the dimensionless boundary layer entropy loss coefficient to measure the total loss in boundary layer:

Fig. 4.44 Boundary layer dissipation coefficient changes with Reynolds number



$$\zeta_s = \frac{T\dot{S}}{\dot{m} \frac{V_{ref}^2}{2}} \quad (4.10)$$

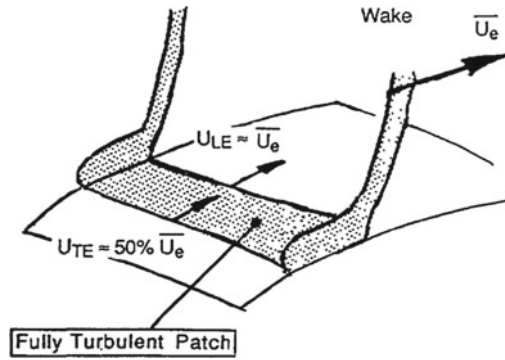
here, V_{ref} is the reference speed. For turbine, it is the general outlet speed. The total entropy loss coefficient in LP turbine boundary layer can be calculated using the following formula:

$$\zeta_s = 2 \sum \frac{S_0}{t \cos \alpha_2} \int_0^1 C_d \left(\frac{V_\delta}{V_2}\right)^3 d\left(\frac{s}{S_0}\right) \quad (4.11)$$

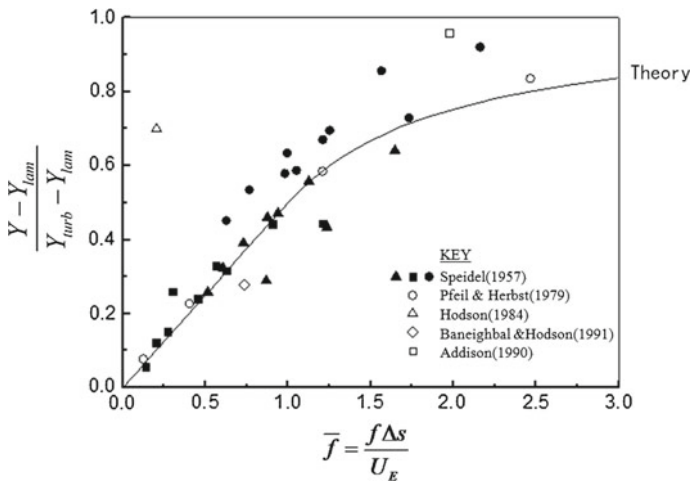
semble in the expression represents the summation of boundary layer at the suction side and the pressure side. If the blade surface velocity distribution and dissipation factor C_d are known, then Eq. (4.9) can be used to estimate the blade boundary layer loss coefficient. Equation (4.11) also shows that this boundary layer loss is proportional to the cube of the velocity, as the dissipation factor C_d does not change much (as previously described, the turbulent boundary layer in the turbine blade basically satisfies this premise). The region with higher velocity will have a greater loss, which also explains that on the same turbine blade, boundary layer loss on the suction surface is generally greater than that on pressure surface.

4.2.5.2 Prediction Models for Interaction Between Unsteady Wake and Boundary Layer

It is also one of the primary goals for researchers to establish physical models that accurately predict the interaction between wake and boundary layers. Thus, many researchers have made detailed investigation on the turbulence spots in the course of wake-induced boundary layer transition [121–123]. These results indicate that the propagation velocity of the trailing edge of the turbulent spots, which are induced by unsteady wakes, is about half of the main flow velocity, while the leading edge of them has a propagation velocity almost equal to the velocity of the main flow, which is different from the steady state. Furthermore, Addison and Hodson assumed that the wake will induce a fully developed turbulence patch even distributing in spanwise on suction side boundary layer. The patch is assumed to originate from somewhere downstream of the leading edge, the propagation velocities of the leading edge and trailing edge are 1 time and 0.5 time of the main flow velocity, respectively. The model is represented in Fig. 4.45a [124]. Based on the above assumptions, local (downstream of the transition position) boundary layer intermittency can be expressed as the ratio of the time that the turbulent patch passing through this place to the passing period of the turbulence patch. The former is determined by the distance from current location to the turbulent spot, while the



(a) Schematic of wake effects



(b) Validation

Fig. 4.45 A simple wake and boundary layer interaction model [124]

latter is determined by the wake passing period. Accordingly, Addison and Hodson gave the prediction of the boundary layer intermittency factor:

$$\Gamma(s) = \frac{\Delta t}{T} = f \int_{s_r}^s \left(\frac{1}{U_{te}} - \frac{1}{U_{le}} \right) ds, \quad (s_r \leq s \leq \begin{cases} s_l \\ s_m \end{cases}) \quad (4.12)$$

Here T and f represent the wake passing frequency ($\frac{1}{T} = f$), Δt represents the duration of boundary layer being turbulence, U_{le} and U_{te} represent the turbulence patch propagation velocity at leading edge and trailing edge, respectively. s_r , s_l and s_m represent the initiation transition location induced by wake, steady boundary layer transition position and transition process completion location induced by

wake. Furthermore, if we assume that the velocity of the main flow in the cascade is constant, and the convective velocity at the leading edge and the trailing edge of the turbulence patch are respectively the main velocity and half of it, the above equation can be simplified as

$$\Gamma(s) = f \frac{s - s_t}{U}, (s_t \leq s \leq \begin{cases} s_l \\ s_m \end{cases}) \quad (4.13)$$

here U is the main flow velocity.

The boundary layer loss can then be predicted base on the intermittency, and Hodson et al. gave the prediction:

$$\frac{Y - Y_l}{Y_t - Y_l} = \begin{cases} 1 - \frac{1}{2\bar{f}}, & \bar{f} \geq 1 \\ \frac{1}{2\bar{f}}, & \bar{f} \leq 1 \end{cases} \quad (4.14)$$

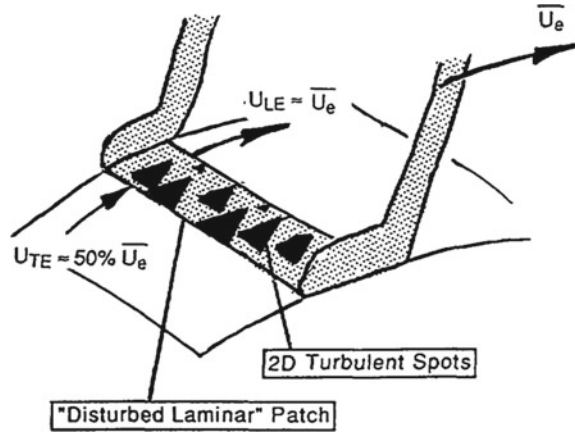
where, Y_l and Y_t represent the boundary layer losses with transition starting at position s_l and s_t , respectively. \bar{f} is calculated using the following equation

$$\bar{f} = f \int_{s_t}^{s_l} \left(\frac{1}{U_{te}} - \frac{1}{U_{le}} \right) ds \approx f \frac{s_l - s_t}{U} \quad (4.15)$$

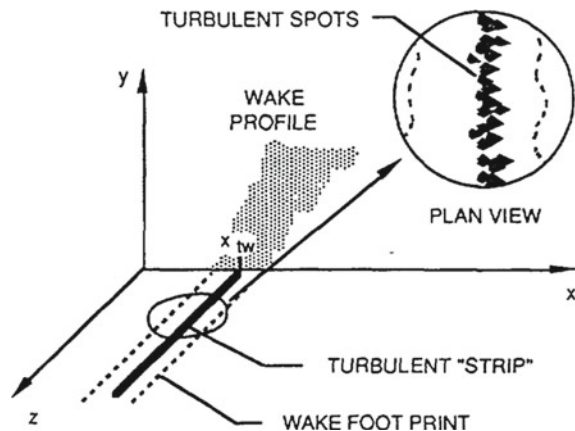
Addison and Hodson used this model to compare with some measurements [125, 126]. The data given in Fig. 4.45b show the good agreement between the model predicted results and the measured data, especially when the wake passing frequency is low.

Although the above model can obtain good prediction under certain conditions, in fact, what the wake induced is not a fully turbulent patch. Instead, they are random appeared independent turbulence events in the wake active region, whose properties are similar as the traditional turbulence spots. Based on this, Hodson et al. [127, 128] modified their former model and proposed that the turbulent spots would be evenly generated along the spanwise direction at a certain rate in the wake active zone, while this zone would propagate downstream along with the wake, as shown in Fig. 4.46a. However, in his model, Hodson used the formula given by Narasimha [129] in 1985 to predict local turbulent spots production rate but did not use the predictive one given by Gostelow and Dey in 1991 [130] which has taken adverse pressure gradient into consideration. This may lead certain errors. Corresponding to the above model, Mayle and Dullenkopf proposed another model based on the turbulence rate [131, 132]. This model no longer considers the wake induced region will move along with the wake, but rather assumes that the wake induced turbulence spot appears at a fixed streamwise location, similar to the approach of Narasimha [133] in studying the transitions of the steady boundary layer. Mayle and Dullenkopf also believed that the wake will induce uniformly distributed turbulent spots in this position, while the transport process of wake on the suction side only impact the production rate of these

Fig. 4.46 Two models on interaction between unsteady wakes and boundary layer based on turbulence spots



(a) Moving turbulent spot source model^[127]



(b) Stationary turbulent spot source model^[131, 132]

turbulent spots. Compared to the experimental data, it is shown that these model can all relatively well predict the wake effect on boundary layer without separation bubble under the condition that the transition initial position and the turbulent spots production rate are reasonable estimated. However, there are still no models to predict the wake influence on boundary layer development with the presence of separation bubbles.

4.3 Complex Flow in Shroud and Its Interaction with the Main Flow

In order to reduce leakage in the gap between rotor blade and stationary casing and reduce the drawback of tip leakage on the aerodynamic performance, many turbine implement shroud seal structures, which are more common in LP turbines. From aerodynamic aspect of view, the shroud not only can effectively reduce the leakage near the gap, but also can enhance the load near the gap, thereby improving the turbine work. From mechanical integrate point of view, although the shroud increases the weight of the rotor blade tip which is not preferred by stress, the blade vibration energy can be absorbed by the friction of adjacent blades shrouds. When the adjacent blades are tightened, the twisting and bending deformation of the blade can be reduced, the rigidity of the blade can be enhanced, and the natural frequency of the blade can be improved.

Although the shroud structure has already widely implemented in gas turbine and steam turbine industry, the research mainly focus on the related structural design and strength calculation. But only in the last decade have the mechanism of shroud leakage flow and its interaction with the main flow gradually become one of the hot topics in turbomachinery field. Shroud generally has labyrinth seal, which, however, cannot completely eliminate the gap. Moreover, the predictable and unpredictable factors, such as axial movement and vibration of the rotor, can cause clearance changes in labyrinth seal. To prevent a serious scratch between the rotational and stationary components, the gap between the tooth and casing is designed to have sufficient margin for safety reasons. In addition, as varying operating conditions is generally required for turbomachinery, the deformation of rotational and stationary parts will change with operating conditions. Consequently, the gap between the tooth and casing and the sizes of inlet and outlet cavities as well will change. Therefore, the flow in the shroud region, including the internal flow inside cavity, the leakage flow of the shroud and its interaction with the main flow will be very complex, which is an important source of flow loss. The shroud tip loss may be greater than that of the non-shrouded blade. The study of the flow pattern and the loss mechanism is important for the aerodynamic design of the shrouded turbine.

4.3.1 Leakage Flow in the Shroud Cavities

Turbine labyrinth seal usually constructed by a series of alternating teeth and cavities, inhibiting fluid flow from the high pressure region to the low pressure region. Labyrinth-teeth is an important part of the shroud, which is also a key factor to determine the shroud internal flow. The main aero-thermo characteristics of air flow through the shroud labyrinth seal are similar to those of the general seal structure, but not identical. Shrouded turbine tip flow has its own characteristics and mechanisms, such as inlet and outlet flow from cavity and the interaction with main flow, etc. Denton also briefly described shrouded turbines flow and loss

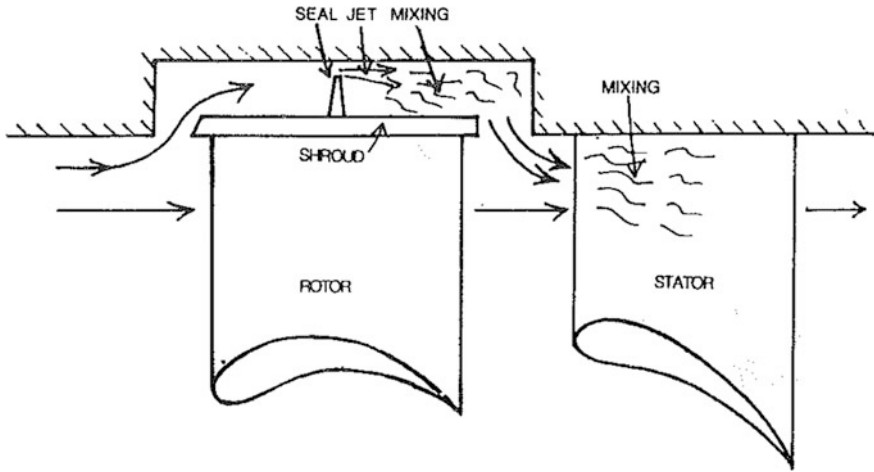


Fig. 4.47 Model of a shrouded blade with single labyrinth tooth [6]

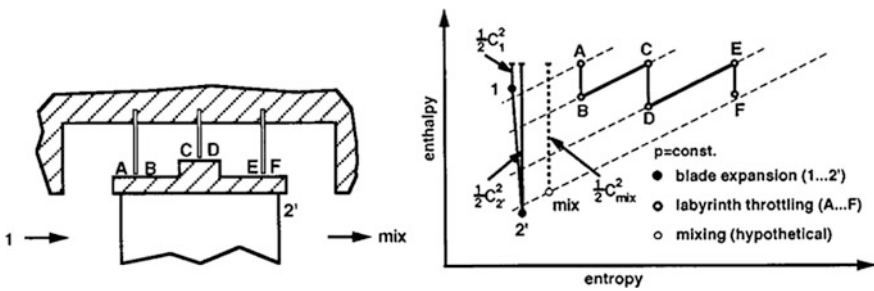


Fig. 4.48 Shroud flow enthalpy-entropy diagram [135]

mechanisms when discussing the turbomachinery loss mechanism [6, 119]. Figure 4.47 shows mechanical model and flow diagram of single labyrinth tooth. In this model, the flow area decreases when the leakage flow passes through the tooth tip which forms a jet flow. If there is no significant restriction upstream of the tooth, the flow till the tooth throat can be approximately considered to be isentropic. Based on this assumption, the leakage flow can be considered to be mainly determined by the size of the labyrinth tooth gap, the shrinkage coefficient, the total pressure based on the meridian velocity upstream of tooth, and the static pressure at the exit of the jet. Here, the outlet static pressure is influenced by the leakage flow which entrances the main flow. However, if there is no significant flow restrictor downstream of the tooth, there is no significant difference between this pressure and the corresponding static pressure in the main flow. When the leakage flow entre into the shroud cavity through the tooth tip they will mix, which leads to entropy increase. In most cases, the cavity outlet space is large enough comparing to the

leakage jet, so it is possible to approximate that the kinetic energy based on the meridional velocity largely dissipate in the outlet chamber, but this is not always the case in reality. Experimental measurements by Denton and Johnson show that the circumferential velocity of the leak flow is not significantly altered during the mixing process in the outlet chamber [134].

In real shrouded turbine design, multi-tooth labyrinth seal structure is more common. Figure 4.48 shows the flow enthalpy-entropy diagram of three-tooth labyrinth seal [135]. Three labyrinth teeth separate the shroud into four cavities. The airflow isentropically expands in the gap of each tooth (A-B, C-D, E-F). The fluid accelerates and passes from the gap into the adjacent low-pressure cavity. Major kinetic energy will be dissipated in the cavities (B-C, D-E) as the fluid undergoes isobaric mixing in cavities. When flow passes from inlet chamber (A) to the outlet chamber (F), it changes the state from rotor inlet to the rotor outlet flow, followed by the leakage flow into the turbine and mixing with the main flow. It can be seen that the flow near the shroud tip can be seen as consisting of two main parts: one is the shroud and teeth cavity flow, the other one is leakage flow which interact with main flow later. The former determines the shroud leakage flow, which is the seal capability, while the later one determines the flow loss caused by shroud. But of course, these two are inseparable, mutual influencing.

To study the flow structure and the evolution mechanism of the shroud flow is the basis for estimating the seal ability and predicting their aerodynamic losses, which is also the theoretical basis to design high performance labyrinth seal. For a typical multi-tooth shroud, the internal flow pattern is also very complex due to the geometrical complexity, including various scales eddies which interacting with each other. Figure 4.49 shows a schematic representation of the flow structure in a typical shroud [136]. Due to the presence of the labyrinth teeth, the most leakage flows through the gap in a jet type flow and flows near the stationary wall of the cavity. At the same time, a series multi-scale eddies are induced by the labyrinth cavity and inlet/outlet cavities. In general, the flow in the inlet and outlet cavities of the shroud is the most complex, especially in the exit cavity, which may have main flow locally ingress and strong unsteadiness.

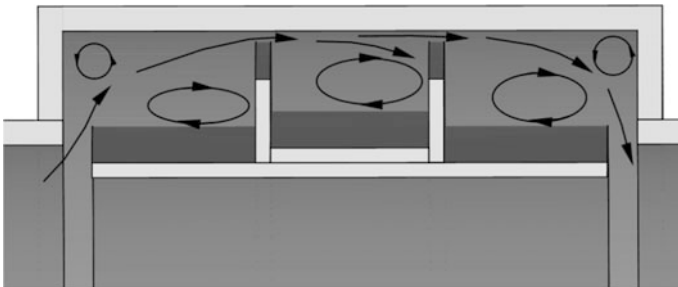


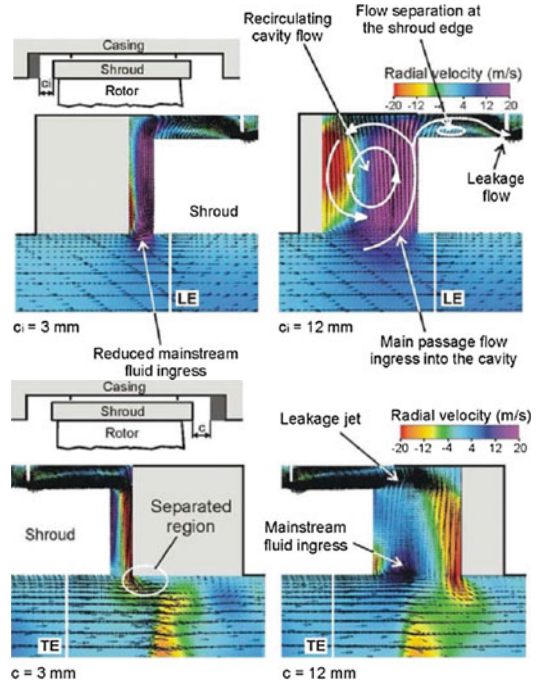
Fig. 4.49 Internal flow structures of the shroud [136]

Because the flow structure in the shroud is affected by its geometry, the corresponding performance parameters such as leakage flow and flow loss will change with the geometry. For the shroud design, it is necessary to understand the geometrical influences and corresponding mechanism. Although there are many researches on general labyrinth parameters design, it is necessary to investigate flow in shroud due to its uniqueness. Rosic et al. [137] carried out detailed experiments and numerical simulations. Their results show that the decrease of the axial length of the inlet and outlet cavities has a very positive effect on the decrease of flow loss inside the shroud. This is mainly due to geometrical changes weaken the main flow ingress and inhibit the generation of complex vortex structures in the two cavities, thereby reducing the mixing loss as shown Fig. 4.50a. In aspect of shroud length, the increase of the inlet plate can weaken the influence of the leading edge potential field and inhibit the high pressure main flow from penetrating into the shroud, which is beneficial for performance. The influence of exit cavity edge length has two sides. On one hand, the increase of the length will increase the leakage velocity, which leads to the increase of mixing loss. On the other hand, it will help to limit the ingress from main flow. The combined effect makes the overall effect of the length of the outlet plate has relatively weak impact on flow loss. The flow structure inside the shroud is not affected by its thickness, but by the size and location of the vortex in the inlet cavity and the position of the leakage jet in the outlet cavity. They will eventually change the shroud thickness, and turbine performance, see Fig. 4.50b. The depth of the shroud cavity is also one of the key factors affecting the shroud internal flow. The decrease of the cavity depth can effectively control the mixing loss inside the inlet cavity and can improve the main flow field to a certain extent. For the outlet cavity, the internal mixing loss also decreases as the cavity depth decreases. However, the velocity of the leakage jet will increase, which may harm to downstream flow field. The effect of different cavity depths on the internal flow structure of the shroud is shown in Fig. 4.50c. Since these results are based on specific blades and shroud, there is no guarantee for a strong generalizability. However, the geometry influences as revealed by those studies provided the guideline on the general shroud design.

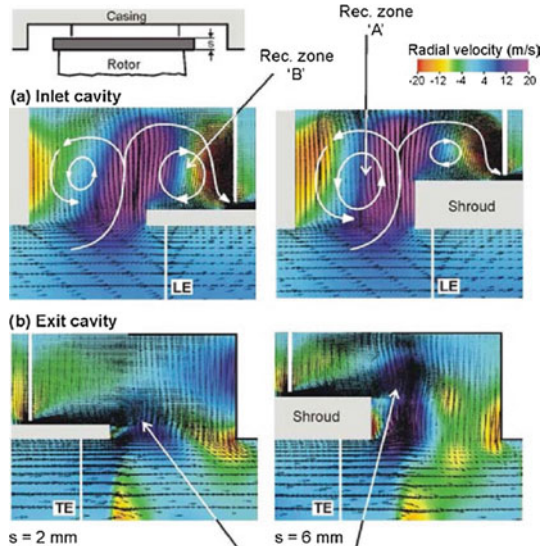
In addition to the geometric parameters, the local aerodynamic parameters also influence the flow structure of the shrouds to a great extent. Such as the difference of flow state between the blade suction side and pressure side, which leads to the circumferential inhomogeneity of the aerodynamic parameter, and also determines the non-uniform of the shroud flow in the circumferential direction. This is another important feature of the shroud leakage flow, which is different from the general labyrinth flow. Both experiments and numerical simulations show that this circumferential inhomogeneity is more pronounced in the vicinity of the inlet and outlet cavities [138, 139].

Figure 4.51 shows the cavity exit radial velocity distribution at different circumferential positions of a shroud [140]. It can be seen that the outlet flow is significantly affected by the circumferential pressure gradient distribution. In the vicinity of the blade pressure side, due to the pressure of the main flow area is higher, the main flow ingress is also very obvious. And it mixes with leakage

Fig. 4.50 Influence of shroud geometries on internal flow structures [137]



(a) Influence of axial length of the cavity



(b) Influence of thickness of shroud thicknesses

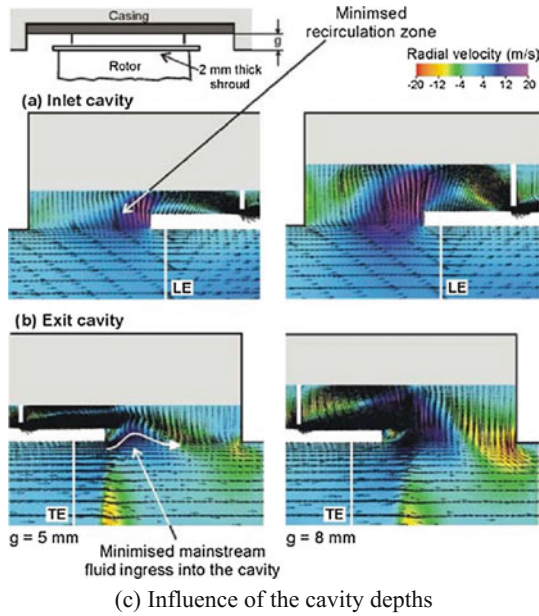


Fig. 4.50 (continued)

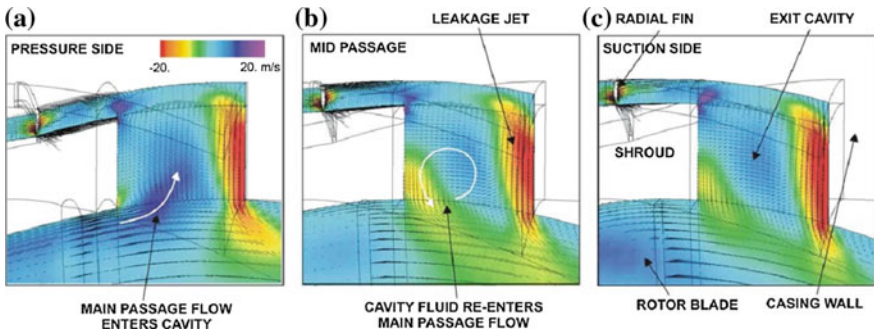
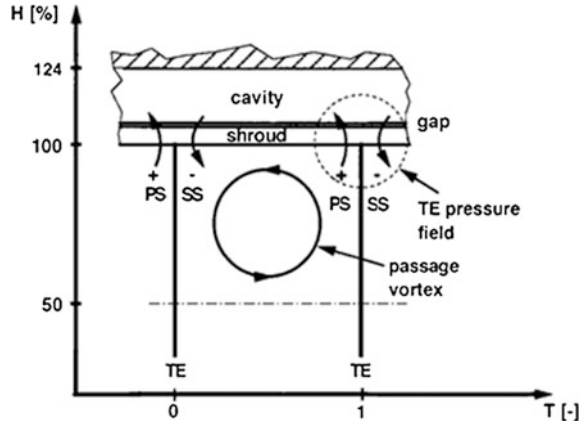


Fig. 4.51 Radial velocity distribution at shroud outlet cavity on different circumferential sections [140]

and forms an eddy filling the major space of the outlet cavity. Then the leakage flow can only be emitted from the position close to the bottom surface of the cavity wall. While in the vicinity of the middle passage and blade suction surface, the fluid penetrating into the outlet cavity again enters the cascade passage from the position close to upper wall of the outlet cavity due to a decrease in main flow pressure. And the formed eddy can still occupy most of cavity volume. In addition, it is shown that the secondary flow structures near the blade tip of the main channel, such as the passage vortex strength and position, also affect the flow structure in the shroud

Fig. 4.52 Sketch of driving mechanisms of flow circumferential nonuniformity in shroud outlet cavity [135]



outlet cavity [141, 142] as shown in Fig. 4.52. In multi-stage turbine, the unsteady potential field and wake from upstream and downstream bladerow all cause the fluctuating flow in the shroud. In fact, in both the steady and unsteady conditions, the internal flow structure in the shroud is the result of passage flow, including the cascade secondary flow and the interaction from upstream and downstream bladerows. It can be seen that the flow structure inside the shroud and the flow in the turbine channel are tightly coupled, and the understanding of their interaction mechanism is the basis for their accurate prediction.

In addition to the strong three-dimensional nature of the leakage flow, it also has a strong unsteadiness. Pfau used a fast-response probe to measure in detail the inlet cavity of a two-stage turbine rotor shroud. The unsteady evolution of the annular vortex in the inlet cavity and its driving mechanism were described in detail [138]. Figure 4.53 shows the tangential vorticity time series at $Z = 0.5$ between the second stage rotor and stator. The dotted lines represent the leading edge position and the blade tip position (i.e. $R = 1$), respectively. The results show that the position, range and strength of the loss core are constantly changing with time. The annular vortex rotates in the inlet cavity with high circumferential speed. The relative rotation between the upstream vane trailing edge and the downstream vane leading edge is the main driving force of the unsteady flow of the inlet cavity. On the basis of the experimental results, Pfau established a simplified flow model. Porreca used experimental and numerical methods to study the unsteady properties of some shroud structures. The mechanism of unsteady loss was discussed in detail. And it is suggested to carry out unsteady analysis when designing shrouded turbine in order to optimize the performance [143].

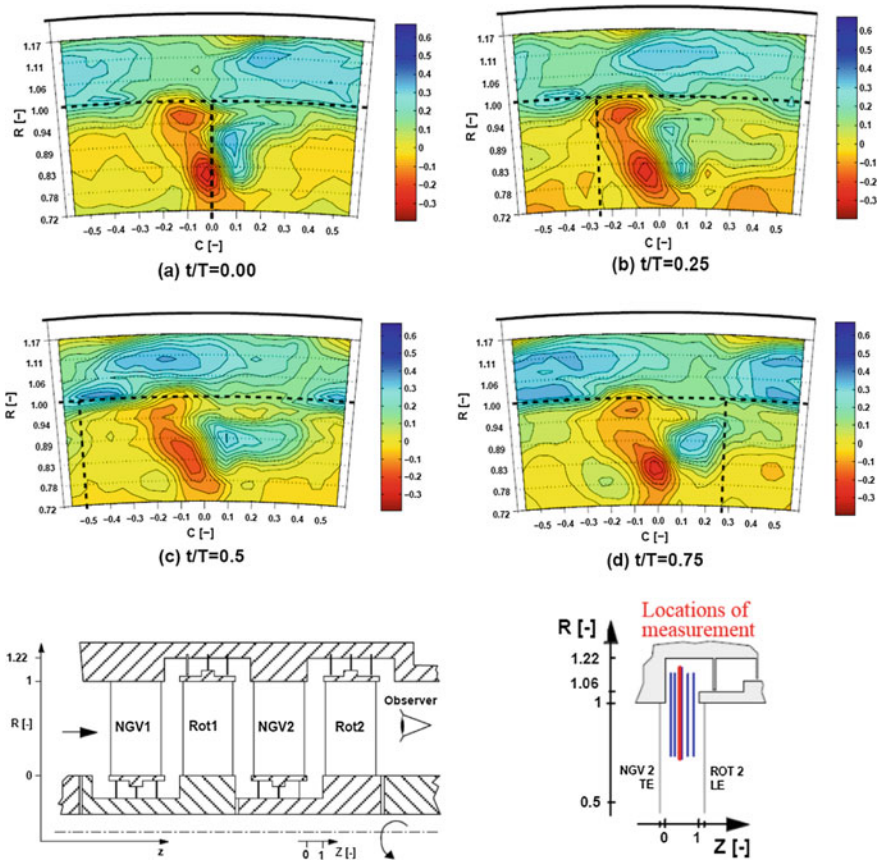


Fig. 4.53 Contours of tangential vortices and corresponding measuring location [138]

4.3.2 Interaction Between Leakage Flow and Main Flow and Its Effects on the Aerodynamic Performance

Leakage flow injected from the shroud outlet cavity will mix with turbine channel flow with complex process. An accurate understanding of this physical process will provide an important theoretical basis for rational organizing of the flow near the tip and reduce the corresponding flow loss. At shroud inlet, the leakage flow is designed to have basically the same velocity triangle as the main stream. However, since there is no blade to turn the flow in the shroud cavity, the leakage flow circumferential velocity has similar flow condition as mainflow at blade tip. At the same time, the leakage axial velocity is complicatedly changed due to the labyrinth teeth action and the obstruction from cavity wall, and thus there is complicated exchange between axial velocity and radial velocity. These factors eventually lead to the velocity triangles of the leakage flow and the main flow no longer match

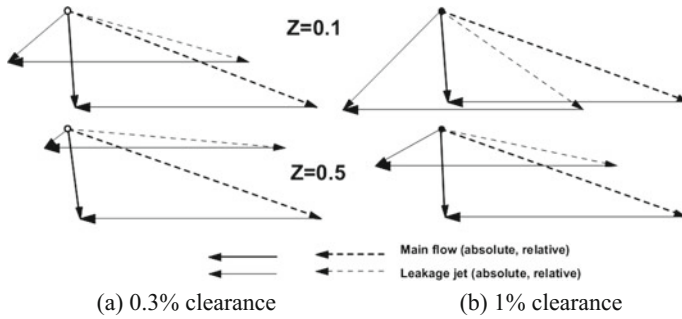


Fig. 4.54 Circumferential mass averaged velocity triangle near shroud outlet cavity [139]

when the leakage re-enters into the turbine channel. It means that the leakage flow relative to the main flow occurs over or under turning phenomena, and then mixing, resulting in flow losses. Mixing causes the leakage flow velocity triangle constantly changing in the flow direction near the end wall. In contrast, the mainflow velocity triangle does not change significantly [139], as shown in Fig. 4.54. The difference between the endwall velocity triangle and the designed velocity triangle also causes the downstream bladerow to have actual larger or smaller incidence than the design one and thereby affect the aerodynamic performance of the downstream bladerow. It should be mentioned that there is no general law governing the relative velocity relation between the leakage flow and the main flow, which includes both the axial velocity and its magnitude. They all depend on turbine aerodynamic environment and the geometrical structure of the shroud.

Due to the uneven circumferential aerodynamic condition in the turbine channel, the leakage flow entering the main flow is not a uniform air curtain, but has a certain distribution along the circumference. The actual distribution pattern is related to the main flow flow field and the shroud structure. In extreme condition, the leakage flow may not be able to flow from the vicinity of the pressure side but only from the vicinity of the suction side that forming a circumferentially distributed jet structure. In addition, under the effects from the secondary flow near the tip and the unsteady condition of upstream and downstream, the shroud leakage flow near blade tip can also show a strong unsteady condition [144, 145]. Leaving from the shroud, leakage flow may also induce a small size but strong streamwise vortex near the blade suction side. The shape of this vortex is similar to the leakage vortex near the tip of the non-shrouded turbine. It will not only accelerate the mixing between the leakage flow and the main flow, its corresponding steady and unsteady effects are likely to show up in the downstream bladerow flow field.

In terms of loss caused by shroud leakage flow, Wallis and Denton et al. first analyzed it in detail [146], which including the following contributions: Leakage fluid does not participate in turbine work and results in loss of turbine work; Mixing loss in the inlet cavity, and drag loss along the shroud; Mixing loss in the outlet cavity; Loss due to mixing between the leakage flow and the main flow, and the

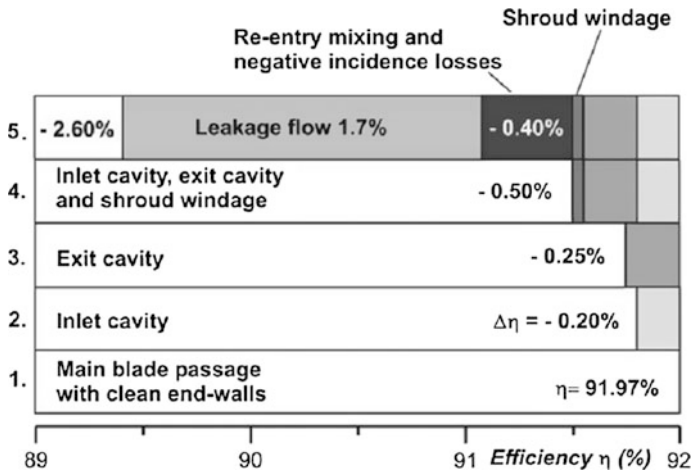


Fig. 4.55 Loss decomposition of shroud leakage flow [8]

corresponding loss caused by the change of the downstream bladerow velocity triangle. Base on those, Rosic and Denton further analyzed the flow loss caused by the shroud using low-speed turbine test rig and numerical simulation method [8]. With different design variants, they gave a quantitative comparison as shown in Fig. 4.55. It can be seen that the total efficiency reduction due to the shroud flow is 2.6%; within it, the efficiency reduction due to mixing in the shroud inlet and outlet cavities was 0.2 and 0.25%, respectively. The decrease of aerodynamic efficiency caused by drag loss of the shroud is the least, about 0.05%. In this study, the leakage flow rate was 1.7%, and it was considered that the resulting turbine work loss and the corresponding decrease in the aerodynamic efficiency were also the same value. The remaining 0.4% decrease in the aerodynamic efficiency is caused by the mixing of the leakage flow with the main stream and the change in the row angle of the downstream blade. The above results indicate that the reduction of turbine performance due to the shroud flow needs to be controlled. In addition to minimizing leakage flow rate, emphasis should be on reducing interactions when leakage flow re-enter into main flow.

Regarding if shrouds are required for turbine rotor or not, it is generally believed that the shrouded turbine has certain aerodynamic performance advantage over the unshrouded turbine with same amount of clearance (labyrinth teeth clearance for the shrouded one). And with the reduction of tip clearance, the aerodynamic performance of the shrouded turbine will decrease gradually and become the same once the clearance reaches to 0. However, it has been found in studies that shrouded turbines and unshrouded turbines may have the same aerodynamic efficiency when the tip clearance decreases to a certain non-zero critical value, which is referred as “Break-even clearance”. Further reducing the clearance, the aerodynamic efficiency of the shrouded turbine will be lower than that of the non-shrouded turbine, and the difference of the efficiency when the gap is 0 is called “offset loss” as shown in

Fig. 4.56 Efficiency trends of turbine with and without shroud [147]

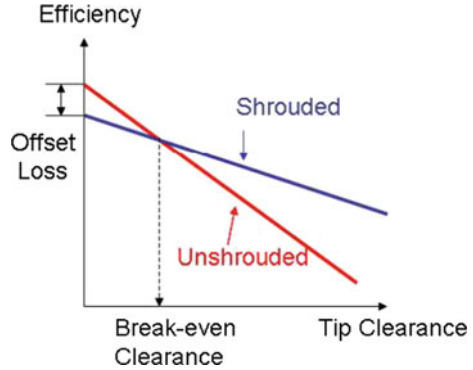


Fig. 4.56. The loss is mainly caused by the mixing in upstream and downstream of the shroud, the drag loss in the cavity and the shroud induced secondary flow loss in the channel. Yoon et al. [147] verified the existence of “break-even clearance” in their experiments. The results show that the values of “break-even clearance” and “compensation loss” of different turbines may be around 0.5%. As the turbine reaction degree decreases, both quantities are reduced. The significance of the existence of the “break-even clearance” is to provide a basis for the choice of whether to use shrouded turbine or not. If turbine tip clearance can be controlled to a smaller level, for example close to or even smaller than the “break-even clearance”, and if factors such as flutter or blade deformation are not taken into account, then turbine without shroud is preferred. Because at this time, aerodynamic performance of un-shrouded turbine will not show significant disadvantages or even better, but it benefit in structural stress and weight.

As shown in the previous section that the geometrical parameters of the shroud directly affect the internal flow structure. This will definitely affect the associated flow loss, and thus affect turbine aerodynamic performance and corresponding parameters. In this area there has already been lots of publications [148–150]. Rosic and Denton et al. further discussed the influence of the main geometrical parameters of the shroud on the leakage flow and the corresponding flow loss based on the discussion of the flow structure [137]. It can be seen from Fig. 4.57 that leakage flow shows a monotonically increasing tendency with the increase of the axial length of inlet and outlet cavity in a wide range. Only when the axial length of inlet cavity is reduced to a certain value or the axial length of outlet cavity is increased to a certain value, the variation range of the leakage flow is gradually reduced, that is, the variation trend is nonlinear. The specific variation amplitude is related to the specific shroud structure selected in the study. Due to the decrease of the leakage flow and the decrease of the mixing loss of the leakage flow in the inlet and outlet

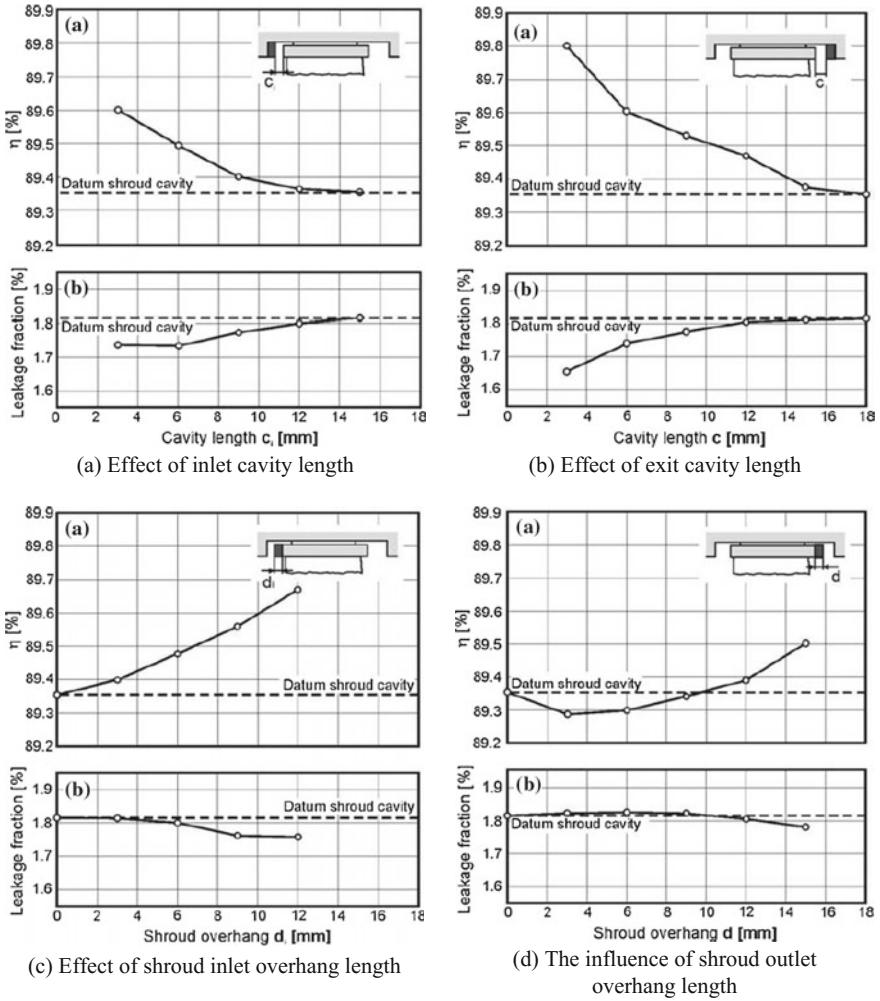


Fig. 4.57 Effects of geometrical parameters of the shroud on turbine efficiency [137]

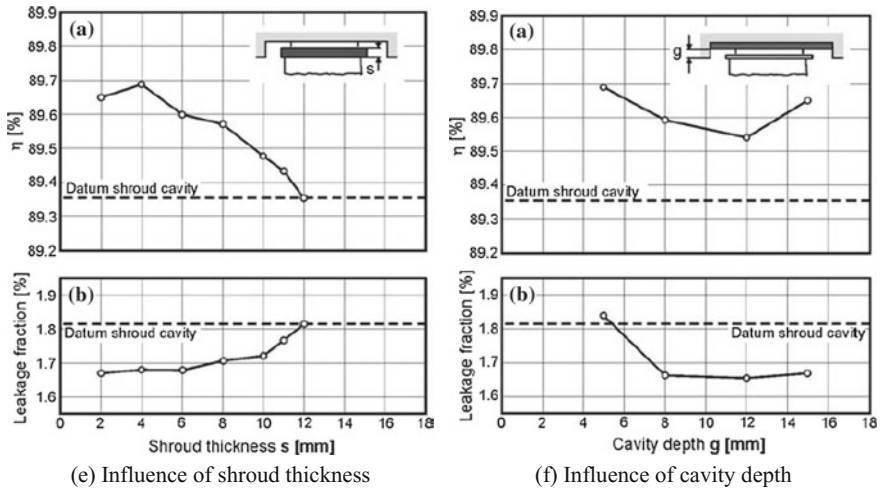


Fig. 4.57 (continued)

cavities, the turbine aerodynamic efficiency decreases monotonically with the increase of cavity axial length. And when the axial length of the cavity is in a certain range with smaller value, the aerodynamic efficiency change is more severe. In terms of the influence of the shroud inlet plate, the leakage flow rate generally decreases with the increase of the length of the edge plate, which is mainly because that the elongation of the inlet edge can keep the inlet cavity away from high pressure region near the blade leading edge. At the same time, it can be seen that the change in leakage flow rate is not very pronounced when the edge plate is very long or very short. While the aerodynamic efficiency of the turbine shows a different trend, which increases linearly with the elongation of the inlet edge plate. The influence of the outlet plate length on the leakage flow rate is small. With the elongation of the outlet edge, the leakage flow rate first increases slightly and then decreases slightly. Correspondingly, the efficiency of the turbine is also decrease and then increase. The change amplitude is smaller than the change due to inlet edge. Increasing the thickness of the shroud edge causes a greater axial velocity of the leakage flow in the vicinity of the first labyrinth tooth, resulting in increased leakage flow rate, which is against the turbine efficiency. On the other hand, an increase in the thickness of the edge plate can also reduce the cavity volume, which is possible to reduce the dissipation of its internal flow. Under the combined influences of these two factors, the aerodynamic efficiency of the turbine increases and then decreases with the increases of the plate thickness. The influence of the shroud cavity height also showed two sides. Increasing the cavity height enhanced the mixing in the cavity, which increases the kinetic loss. But on the other hand, it also reduces the leakage flow rate. Therefore, the turbine efficiency shows a trend of first decrease and then increase.

4.3.3 Shroud Leakage Flow Low-Dimensional Models and Multi-dimensional Coupling Simulation

The function of the shroud is sealing, which determines that it has generally more complex structure and narrow geometric space. It indeed makes the detailed measurement of the flow field of the shroud area difficult to achieve. Numerical simulation has become one of the important investigation methods. Although the numerical simulation can provide detailed flow field, this requires meshing for the complex shroud geometry, which increases the difficulty of pre-processing and time consumption. Moreover, the complicated calculation also increases the difficulty of convergence and accuracy, and puts forward the strict requirements for the selection of the boundary conditions, initial conditions, as well as the turbulence model and the transition model. Even if the above issues can be properly resolved, the increased amount of cells will also greatly increase the computational cost. Therefore, the full three-dimensional numerical simulation which considers the actual geometry of the shroud is still mainly used in the study of the flow mechanism. Regarding the performance evaluation and flow diagnosis for industrial purpose, a more practical method which can take into account both the calculation accuracy and efficiency is needed. The multi-dimensional correlation is a very effective method, which is to establish a low-order mathematical-physical model for the flow in the shroud and its interaction with the main flow, and then couple it with the three-dimensional calculation of the main flow and finally achieve effective results. This is an important research area with shrouded turbines.

The prerequisite for the evaluation of shroud flow field is the precise prediction of the leakage flow, which mainly depends on labyrinth characteristic. So far, there are many studies on the mathematical model of the labyrinth flow, especially the modeling of the labyrinth leakage. Ideally, the flow through the labyrinth seal structure can be calculated according to the isentropic flow theory [151]:

$$\dot{m}_{ideal} = \begin{cases} \frac{p_0 A}{\sqrt{kRT_0}} \sqrt{\frac{2k^2}{k-1} \left(\frac{p_n}{p_0}\right)^{2/k} \left[1 - \left(\frac{p_n}{p_0}\right)^{\frac{k-1}{k}}\right]} & \frac{p_n}{p_0} > \left(\frac{2}{k+1}\right)^{\frac{k}{k-1}} \\ \sqrt{\frac{k}{RT_0}} p_0 A \left(\frac{k+1}{2}\right)^{\frac{k+1}{2(k-1)}} & \frac{p_n}{p_0} \leq \left(\frac{2}{k+1}\right)^{\frac{k}{k-1}} \end{cases} \quad (4.16)$$

where A is the clearance cross-sectional area at tooth tip, the subscripts “0” and “n” represent the corresponding inlet and outlet cross-sections, respectively. In general, the flow through the throttling element results in an actual flow rate smaller than the theoretical flow rate due to inlet loss, friction loss, and outlet sudden expansion losses. Normally flow rate coefficient C_D is introduced for labyrinth seal, which is defined as the ratio of the actual mass flow rate \dot{m}_{real} and the ideal mass flow rate \dot{m}_{ideal} :

$$C_D = \frac{\dot{m}_{real}}{\dot{m}_{ideal}} \quad (4.17)$$

This is a key parameter to evaluate the efficiency of labyrinth seal. This parameter can reflect the contraction effect of gas flow through the gap and the friction influence on the velocity which leads the outlet mass flow rate less than the theoretical value. Its value depends on many labyrinth seal factors such as tooth geometry, gap, number of teeth, inlet and outlet pressure, and other parameters.

In engineering applications, Martin gave the formula to calculate seal leakage in 1908 [152], as shown in Eq. (4.18). Based on adiabatic flow assumption, this method assumes each labyrinth is a series of nozzles and assumes the flow is isothermal. Each element which is formed by a tooth and the followed cavity has the same flow resistance, and the kinetic energy in each chamber is completely converted to heat. Stodola used Bernoulli equation and continuity equation for each section of the tooth, and integrates it along the seal length under the assumption that the pressure difference is not large and then obtained the approximation formula for calculating the leakage of the labyrinth seal [153], as shown in Eq. (4.19). The formula also believes that it is ideal throttling process, no ventilation effect. The formula is only validated for sub-critical condition and the number of teeth is greater than 4.

$$\dot{m} = C_{DA} \frac{p_0}{(RT_0)^{1/2}} \left[\frac{1 - (p_n/p_0)^2}{N - \ln(p_n/p_0)} \right]^{1/2} \quad (4.18)$$

$$\dot{m} = C_{DA} \left(\frac{p_0^2 - p_n^2}{NRT_0} \right)^{1/2} \quad (4.19)$$

The above two methods are relatively simple, but with large errors. Thus they are difficult to meet engineering requirement. Later researchers revised the formula using analytical method and experimental data and gave a relatively high accuracy calculation method. For example, Vermes modified the non-adiabatic condition based on the Martin formula and deduced the correction coefficient of permeability effect. The ratio of the tooth tip width and tooth cavity width to the tip clearance height was taken into account [154]. The resulting formula is shown below:

$$\dot{m} = C_{DA} \frac{p_0}{(RT_0)^{1/2}} \left[\frac{1 - (p_n/p_0)^2}{N - \ln(p_n/p_0)} \right]^{1/2} (1 - \alpha')^{-1/2} \quad (4.20)$$

where term $(1 - \alpha')^{-1/2}$ is the ventilation effect correction term, α' is kinetic energy residual factor, which is related with the shroud cavity geometry. Although the ventilation effect is revised here, the wall effect is still not considered. Thus the accuracy is still needed to be improved [155, 156].

Denton theoretically analyzed the shroud leakage in single labyrinth and assumed the flow does not deflect in the shroud. The leakage flow rate is therefore calculated as below:

$$\frac{\dot{m}}{\dot{m}_{mainflow}} = C_D \left(\frac{g}{h}\right) \sqrt{\sec^2 \beta_2 - \tan^2 \beta_1} \quad (4.21)$$

Here h is the height of the blade. Regarding the shroud loss, early prediction model generally believe that the change in efficiency is proportional to the leakage flow. Based on this understanding, Denton and Johnson presented a very simple model to estimate the turbine shroud loss [134], suggesting that the change in efficiency is proportional to the relative height γ of the gap:

$$\Delta\eta = k\gamma \quad (4.22)$$

where γ is defined as the ratio of the shroud clearance to the blade height, and the proportionality factor k is determined by the actual geometrical parameters of blade and shroud, and the aerodynamic condition of the turbine. Obviously, this simple proportional correlation is too rough, and the proportion coefficient k is also mainly dependent on experience. So this type of prediction models has difficulty to provide satisfactory results for turbine aerodynamic design and optimization process. Later, based on the prediction of the shroud leakage mass flow rate, Denton proposed a mathematical model for single tooth labyrinth shroud to calculate the mixing loss coefficient ζ of the shroud-leakage flow and the main-flow [119]:

$$\zeta = \frac{T\Delta s}{0.5V_2^2} = 2 \frac{\dot{m}}{\dot{m}_{mainflow}} \left(1 - \frac{V_t}{V_{t2,mainflow}} \sin^2 \beta_2\right) \quad (4.23)$$

where V_t and $V_{t2,mainflow}$ are the circumferential velocity of the leak flow and the turbine main flow, respectively. This equation shows that the difference in circumferential velocity is the main source of loss due to leakage and main flow mixing at shroud outlet. In order to reduce this loss, the designer needs to make the circumferential velocity of the leak flow as consistent as possible with the main flow.

Base on above model, Yoon et al. further gave an aerodynamic efficiency correlation to evaluate turbine stage aerodynamic efficiency influenced by shroud [147]:

$$\Delta\eta = \frac{T\Delta s}{\Delta h_{stage}^*} = \frac{\zeta}{2H_T} \left(\frac{W_2}{U}\right)^2 \quad (4.24)$$

This formula shows that the quantitative relationship between the turbine-stage aerodynamic efficiency and the loss caused by shroud flow is determined by turbine load factor H_T , outlet relative velocity W_2 and turbine circumferential velocity U . Further, the change of turbine work can also be primary predicted:

$$\frac{\Delta P_T}{P_{T,noleak}} / \frac{\Delta \eta}{\eta_{noleak}} \approx \frac{\varphi(\tan \alpha_1 - 2 \tan \beta_2) - 1}{\varphi(\tan \alpha_1 - \tan \beta_2) - 1} \quad (4.25)$$

The results predicted by above formula show good agreement with experiments. For a conventional turbine layout, the relative change in the turbine output power, which is affected by the shroud obtained from (4.25), is generally 1.5–2 times of the relative change in efficiency. Based on above analysis, Yoon et al. pointed out that the leakage-caused decrease of aerodynamic performance is more reasonable attributed to dissipation of the relative kinetic energy rather than an increase in leakage flow or associated loss factor. At the same time, Yoon et al.'s results show that the stage reaction rate is also one of the key factors affecting the shroud. For high reaction rate turbine, its aerodynamic efficiency and power are more affected by shroud loss, which is due to the high relative velocity at stage outlet under high reaction rate, i.e., higher relative kinetic energy [147].

Along with deeper studies, researchers expect to obtain more accurate prediction of the influence of the shroud and the flow field in the main channel in order for further accurate investigation and evaluation. It cannot be achieved by only one-dimensional mathematical model. As a compromise between a simple one-dimensional mathematical model and a full three-dimensional numerical simulation, it is an ideal choice to couple the low-order mathematical model with the main flow 3D simulation, which is to add an additional source term in three-dimensional numerical simulation. When the parameters such as the shroud geometry, position, and the flow conditions at inlet and outlet cavities are determined, using one-dimensional model to evaluate the parameters such as the leakage flow rate, the temperature rise and the momentum change, and then apply the corresponding flow parameters at cavity inlet and outlet. Because this method can consider the influence of the leakage flow in the three-dimensional passage flow without increasing computational cost, thus has attracted more attention. At present, this kind of multi-dimensional coupling numerical method has become a new development direction, which plays an important role in the field of shrouded turbine, air system and so on.

Rosic and Denton et al. [157] applied this method to the numerical simulation of one three-stage shrouded turbine test rig. The implementation of the shroud model in the simulation is given in Fig. 4.58. The comparison between experimental results and numerical simulations with/without shroud structure shows that the coupling method is better than the numerical simulation which does not consider the shroud in terms of capturing turbine inner flow structures. But there is still gap comparing to the simulation which fully considering the shroud. Gier et al. have developed a similar coupling method for shrouded turbine. They studied one shrouded turbine, focusing on the influence of the leakage flow on the main flow [158]. Figure 4.59 shows the numerical results comparison between the multi-dimensional coupling method and the full shroud geometry simulation. It shows that the coupling method can effectively analyze the influence of the shroud leakage flow on the main flow except variation of circumferential parameters. The

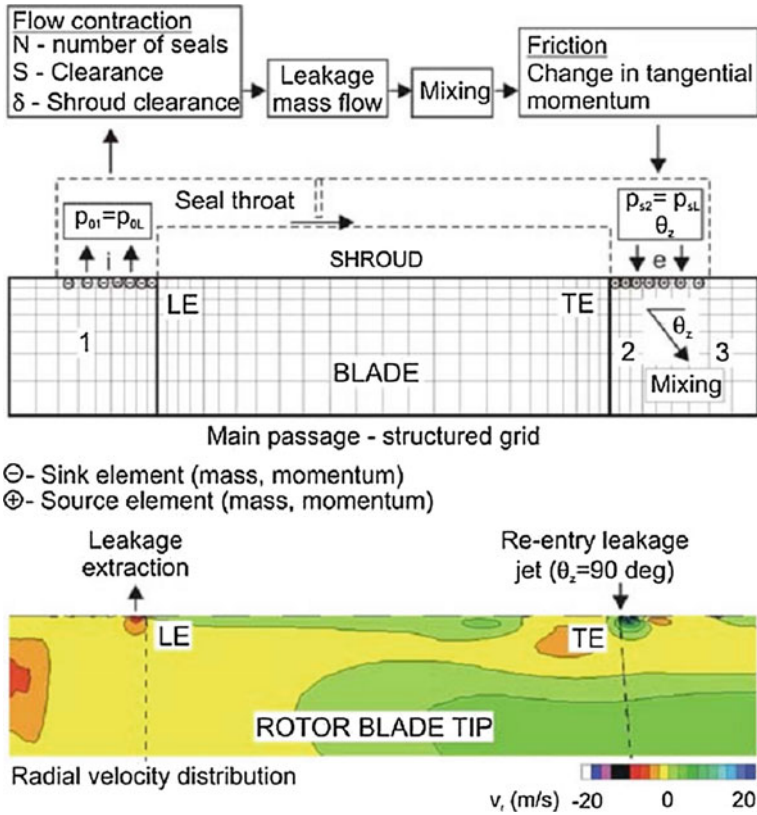


Fig. 4.58 Rosic’s shroud model coupled with the main flow [157]

main disadvantage of using the one-dimensional shroud model is that the circumferential parameters variation of the leakage flow cannot be considered. For this, Hunter analyzed the results of three-dimensional full simulation, extracted the relevant distribution characteristics, focusing on the non-uniform distribution of the flow parameters at the interface between the shroud flow and the main flow on the multi-dimensional coupling calculation [159]. Comparing to experimental results, due to the consideration of 2D characteristics on the interface, this research provided more accurate prediction on shrouded leakage flow and channel endwall secondary flow than traditional one dimensional shroud model. These multidimensional studies have already achieved some useful results. However, the factors considered are not comprehensive and detailed, such as the one-dimensional model did not take specific shroud inlet cavity into consideration, even this local flow field has important impact on shrouded flow. Also, the two dimensional character of the leakage is still need to be modeled and applied in engineering.

Based on the research of Rosic et al., Wang Peng and Zou Zhengping from Beihang University carried out further research on shrouded turbine multidimensional coupling

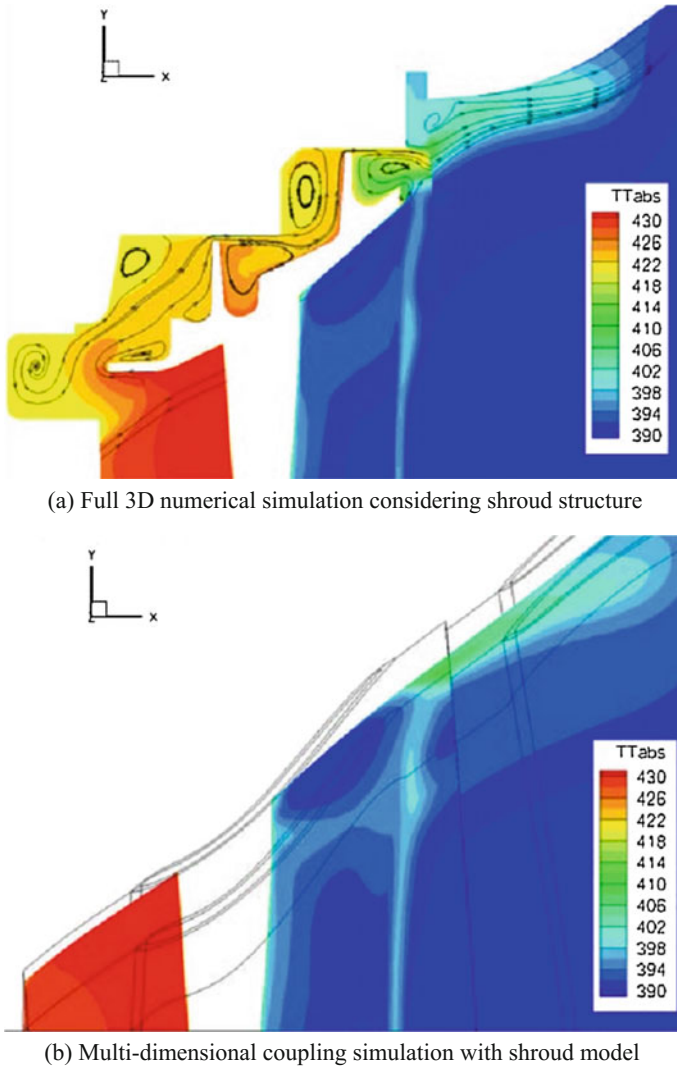


Fig. 4.59 Comparison of shrouded turbine passage flow between different methods [158]

method CFD [160, 161]. Since the prediction accuracy of the low-dimensional shroud leakage flow model is critical to the success of the multidimensional coupling calculation, Wang et al. established a new shrouded leakage flow model. The model can take into account the shroud inlet cavity flow and the key features such as mass/momentum/energy of the leakage flow and predict the two-dimensional distribution of the leakage flow [160]. Details are as follows: In the aspect of the leakage flow rate, according to the jet characteristic of the leakage flow, reasonable modeling is carried out based on classical jet theory to represent the residual kinetic energy in each

part of the shroud. Respectively based on the wall jet and free jet, residual-energy factors of the flow between the labyrinth tooth are evaluated and correlated based on virtual jet theory and then coupled together. The inlet cavities are also modeled and its flow is equivalent to the flow pass several labyrinths. The virtual labyrinth tooth number is used to consider the residual kinetic energy in the inlet cavity when predicting the leakage flow rate. On the basis of the leakage flow rate model, the momentum and energy characteristics of the leakage flow, the effective width of the leakage flow at the interface and the temperature correction of the outlet cavity are modeled respectively based on the angular momentum theorem and the non-isothermal jet theory. The turbulence characteristics of the leakage flow are taken into account. The following is the expression for the number of virtual tooth on the shroud in this leakage model:

$$N^* = N_e + (1 - \alpha_1) + (N_{seal} - 1)(1 - \alpha_2) \quad (4.26)$$

Here the inlet cavity equivalent tooth number and the residual-energy factor of the flow between tooth are:

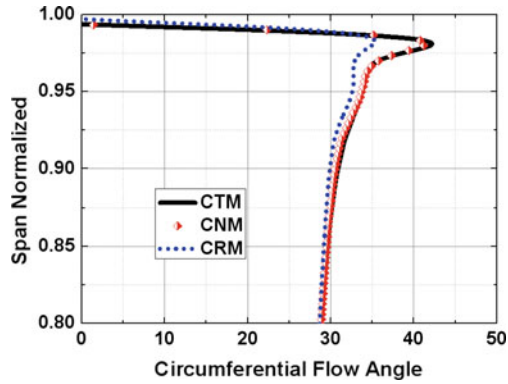
$$N_e = \frac{p_0^2 - p_1^2}{p_1^2 - p_N^2} \left[N_{seal} - \ln\left(\frac{p_N}{p_1}\right) \right] + \ln\left(\frac{p_1}{p_0}\right) \quad (4.27)$$

$$\alpha_1 = \frac{10.390b_0\sqrt{N_e}}{(3.382L01 + L02)} \quad \alpha_2 = \frac{2.009b_0}{0.296L1 + L2} \quad (4.28)$$

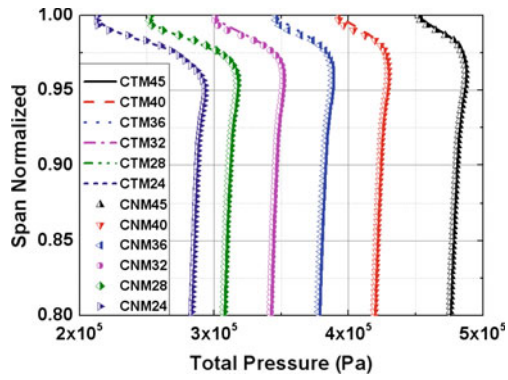
The size parameters like L1 and L2 characterize the key geometrical features of the shroud cavity. Regarding the two-dimensional characteristics of the leakage flow, an approximate relation is given on account of the circumference inhomogeneity at the interface. That is, the shifting correlation between the circumferential distribution of the main flow pressure in the vicinity of the outlet cavity and the circumferential distribution of the leakage jet strength. After shifting downstream by an axial scale along wake trace, the circumferential distribution of the strength characteristic of pressure shows negative correlation with that of the leakage flow strength. Considering the rationality and veracity of multi-dimensional scaling in multi-dimensional coupling computation, a mathematical description of the two-dimensional circumferential characteristics of the outlet cavity is established based on this correspondence relationship. Taking the flow flux as an example, assuming that the circumferential coordinate at the interface is x : Let $F_{\dot{m}}(x)$ be the flow flux at x , and $\bar{F}_{\dot{m}}$ be the circumferential averaged flow flux of the leakage jet at the interface, we can get:

$$F_{\dot{m}}(x) = C_{\dot{m}}\bar{F}_{\dot{m}}\frac{\bar{P}}{P\left(x - \frac{H}{\tan\theta}\right)} - (C_{\dot{m}} - 1)\bar{F}_{\dot{m}} \quad (4.29)$$

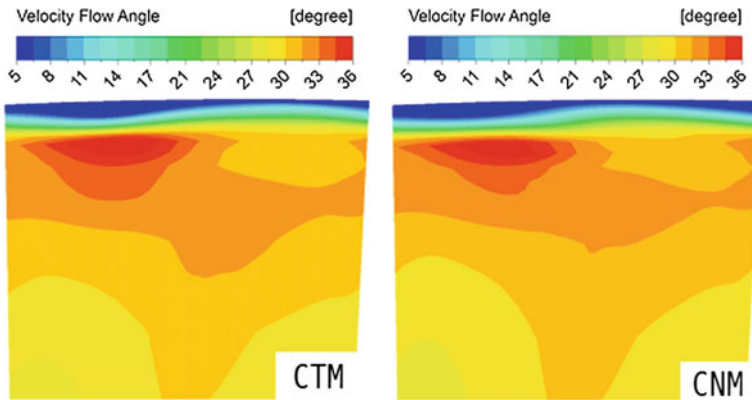
where $P(x)$ is the upstream pressure at circumferential coordinates x of the interface, \bar{P} is the corresponding average pressure, θ is the trailing edge angle of the rotor blade, H is the axial size of the interface, $C_{\dot{m}}$ is the correction factor. At the same time, in terms of the axial direction, there is also no uniform value at the



(a) Radial distribution of flow angle



(b) Radial distribution of total pressure



(c) Contour plot of flow angle downstream of the leakage flow

Fig. 4.60 Multi-dimension coupling simulation results in a shrouded turbine [160]

interface. Therefore, the detailed axial characteristics within the leakage flow are also considered when expanding the models to 2D distributions using the multi-dimensional scaling method. The specific modeling method for the axial distribution is still based on the jet theory.

Based on this new shroud leakage flow, numerical simulations of flow in shrouded turbine based on multi-dimensional coupling method achieve higher accuracy. Figure 4.60a compares the results of different methods for predicting flow angle downstream of the leakage flow. Figure 4.60b compares the radial distribution of total pressure downstream of the leakage flow under variable operating conditions (different backpressures). In the figure, CNM represents multi-dimensional coupling calculation, and CTM represents the result of full 3D shroud calculation. The figures shows that the results predicted by multi-dimensional coupling method agree well with the full three-dimensional shroud results, no matter for the design or off-design conditions. It shows the accuracy of the shroud leakage model and the implement potential of the multi-dimensional coupling method. Figure 4.60c shows that this method also achieves a more accurate prediction in the specific leakage flow region and its downstream flow fields.

4.3.4 Shroud Leakage Flow Control Technology

Since turbine flow loss due to leakage flow cannot be ignored, how to effectively suppress the loss and improve the aerodynamic performance of the shrouded turbine becomes an important research topic. A lot of works have been carried out and some effective flow control methods have been obtained.

As Denton pointed out that the significant difference between the circumferential velocity of the leak flow and the main flow is one of the main sources of mixing loss [119]. This will not only bring a strong mixing near the cavity outlet, but also influences the incidence of the downstream blade row, which in turn affects its flow loss. Studies have shown that various losses caused by the different circumferential velocity would account for 60% of the total loss due to leakage flow [162]. Therefore, effective control the outflow angle of shroud leakage flow may reduce the flow loss. Wallis and Denton et al. [146] first attempted this approach by mounting a series of small vanes on the shroud where concentrated by leakage flow and reversing the leakage. Due to the mechanical constraints of equipment and other reasons, this method did not achieve the desired results, even on the contrary, the turbine efficiency decreased. However, using plates instead of small vanes to turn the leakage flow into axial direction achieved better results. It effectively reduced the rotor outlet circumferential velocity near casing and reduced the downstream stator secondary flow region, thereby increased the efficiency of entire turbine. They pointed out that using diversion devices to control shroud leakage losses is feasible. But it needs deep understanding of the unsteadiness and three-dimensional flow structures near the shroud in order to develop good control method. Based on these observations, Rosic and Denton further investigated this

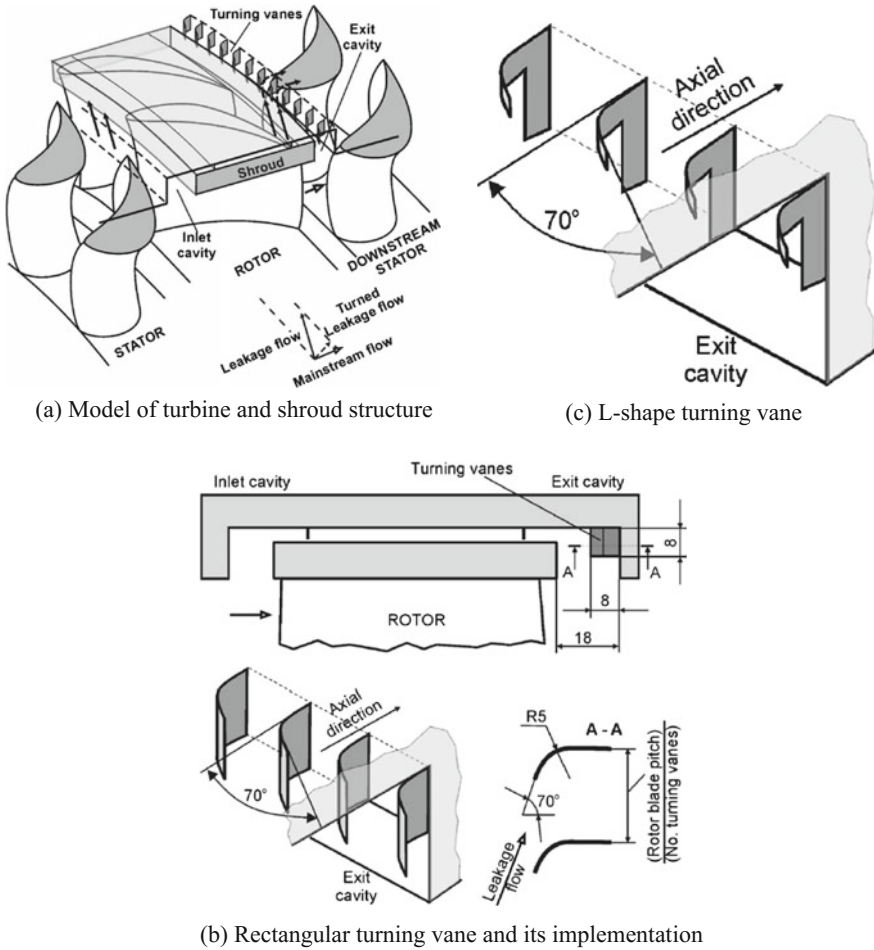


Fig. 4.61 Implementation of turning vane at shroud outlet cavity [8]

idea [8] by mounting with different turning vanes on the casing at rotor outlet as shown in Fig. 4.61. The experimental results show that current control methodology can effectively reduce the loss of flow and improve the aerodynamic performance of the shrouded turbine. This effect depends on the geometrical parameters of the turning vanes and their circumferential distance. Setting eight vanes for each blade channel obviously reduced the loss and improved situations of incidence for the downstream stator blades, resulting 0.4% increase in the turbine brake efficiency. In addition, the experimental study also shows that if change the rectangular vanes to the smaller L-shaped vanes; it is possible to obtain better aerodynamic efficiency and can also effectively avoid axial scratching. Unlike Rosic and Denton, Gao et al. carried out numerical simulations using a row of turning vanes inside the

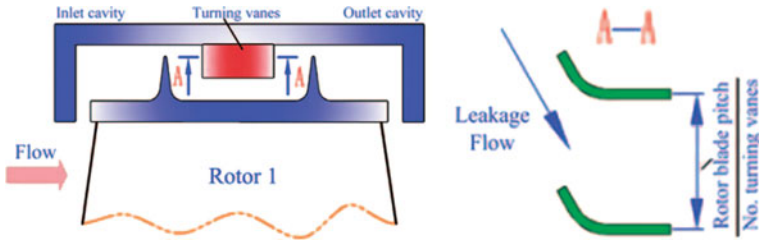


Fig. 4.62 Implementation of turning vane inside shroud cavity [8, 163]

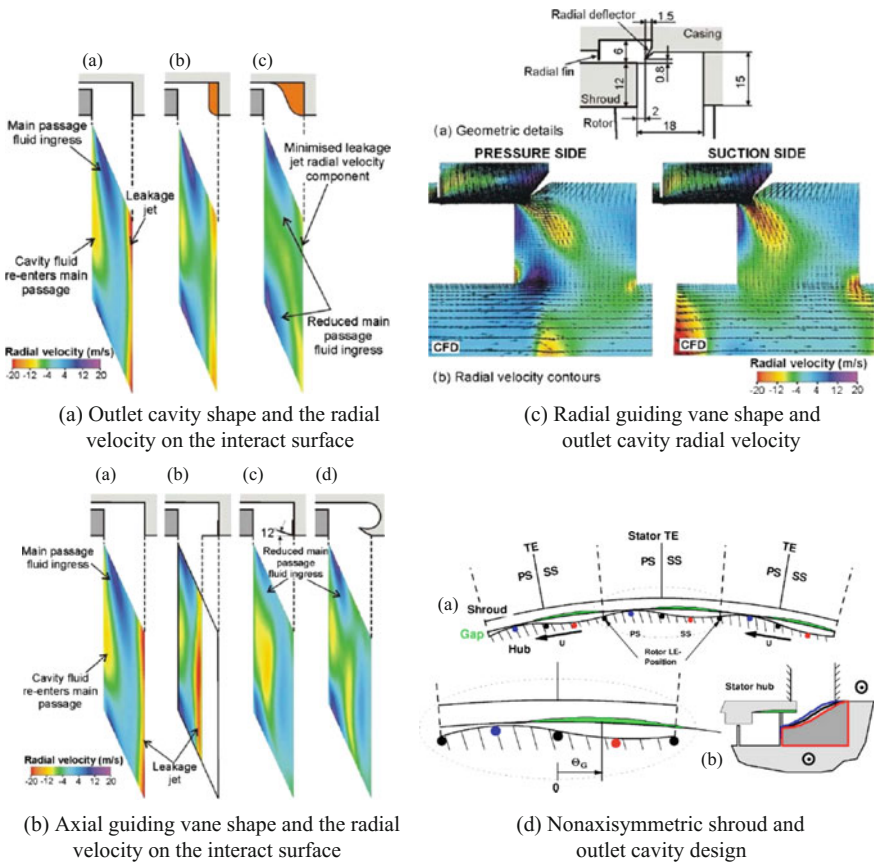


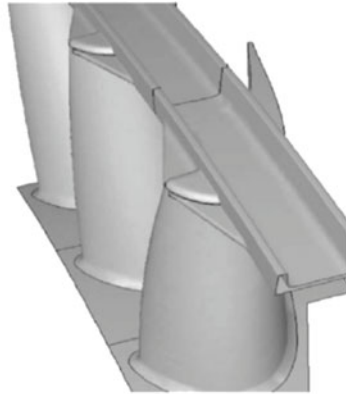
Fig. 4.63 Flow control based on outlet cavity modelling [8, 164, 167]

cavity, say between the two teeth (Fig. 4.62), to turn the leakage flow and consequently achieved certain control effects [163].

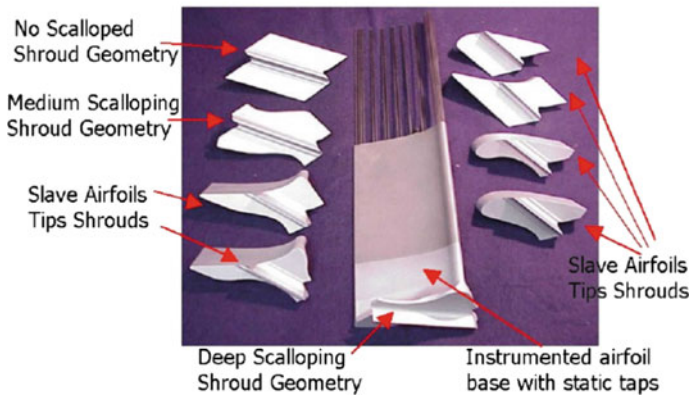
In addition of using turning vanes, the exit geometry of the shroud cavity is one of the important parameter to control leakage influence. Rosic and Denton et al.

[164] made systematic studies on three manufacture methods for exit shape by experiments and numerical simulations. The first method is using proper curvature surface downstream of cavity, such as chamfering as shown in Fig. 4.63a. This method can suppress backflow from main stream, and can reduce corner separation and loss at cavity outlet by controlling radial velocity of the leakage flow, and further reduce the secondary flow intensity. Other researchers also investigated this method and received benefits [165, 166]. The second method is to mount annular axial turning plates at the interface between the outlet cavity and the main channel as shown in Fig. 4.63b. This ring-shaped baffle structure can move the location where leakage flow into mainflow towards upstream, thereby suppressing the penetration of the main flow. This can effectively reduce the associated mixing loss and improve downstream flow conditions. Experiment results also show that the length of plate is the main factor that determines the effectiveness of this method, while the appropriate slope of the plate may lead to better results. Both of the above-mentioned methods increase the rotor axial movement which may cause a risk of scratching. But the plate of the latter method may be of a modular design, which means it can be replaced after damage. Thus it has better engineering applicability. Based on these two methods, Rosic and Denton et al. also developed a method of arranging ring-shaped radial deflectors in the outlet cavity [164] as shown in Fig. 4.63c. The method has the advantages of the former two methods, can effectively reduce the leakage flow mass flow rate, its radial velocity, and shift the location where leakage flow penetrate into main flow to move forward. Thus it can achieve better control results, and also avoid the rotor axial movement which may lead the scratching problem. Experimental results also show that this method is less affected by the location of the deflector/plate, which lead to a strong engineering practicality. And thus it is recommended by researchers. In addition, the effectiveness of the above control methods is enhanced with the increase of the leakage mass flow rate, which is very favorable for turbine component performance under off-design condition and the performance maintenance of wearing labyrinth teeth after long working time. Pfau et al. [167] also proposed a new idea in the shape of the shroud-outlet cavity, which used the idea of non-axisymmetric end-wall. They designed circumferential uneven shroud structure and corresponding cavity outlet based on the circumferential inhomogeneity flow induced by the interaction between the leak flow and the main flow, as shown in Fig. 4.63d. The application of this method on a two-stage turbine test rig showed that this method can effectively adjust the circumferential distribution of leakage flow and improve its interaction with the main flow, and finally achieve the purpose of reducing flow loss and improving aerodynamic performance.

The design of the shroud inlet cavity would also affect the flow field and the loss with a certain impact. Many researchers studied the size of the inlet cavity, the shape of the leading plate, the arrangement of the guiding plates in the inlet cavity, etc. [134, 167, 168]. These methods can benefit in terms of reducing leakage mass flow rate and improving flow field in the main passage. Based on the above work,



(a) Typical partial shroud geometry^[143]



(b) Different partial shroud shapes^[169]

Fig. 4.64 Partial labyrinth shroud geometries

Rosic and Denton et al. optimized the shrouds of a shrouded turbine. They optimized the inlet and outlet cavity geometries with the leakage flow rates of 1.48% and 1.78%, respectively. The turbine aerodynamic efficiency gained 0.60% and 0.75% [164].

The above described shroud flow control methods are carried out under full shroud conditions. Correspondingly, there is also partial shroud, as shown in Fig. 4.64. The main purpose of using partial shroud design is to reduce the shroud's weight and thus reduce stress of blades and discs, and further to ensure the reliability of turbine components. Although the introduction of partial shroud can make the flow field near the shroud more complicated, which often leads to an increase in

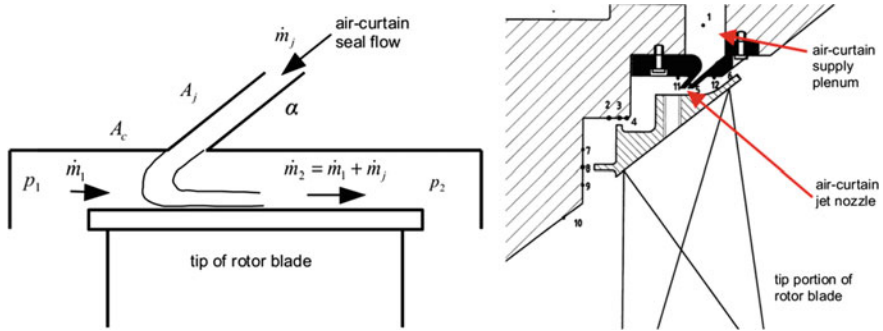


Fig. 4.65 An Air curtain in a turbine blade shroud [173]

flow loss. However, if the structure/geometry of partial shroud can be optimized to achieve reasonable flow field and also reasonably use of some particular characteristics of shroud flow, it may reduce the loss of component aerodynamic efficiency and maintain it in an acceptable range. Its multi-disciplinary performance may be better than the fully shroud design. It may increase aerodynamic efficiency while reducing weight. Although a number of studies have been carried out on partial shrouds [143, 167, 169] and gained certain understanding of the flow characteristics for some typical labyrinth shrouds and their effects on aerodynamic performance, until now, the research on the flow control of partial shroud has still been limited, and lack of universal applicable conclusions and methods.

Apart from using labyrinth shroud geometry modification, aerodynamic method also plays an important role in shroud flow control. Comparing with the conventional labyrinth seal structure, the pneumatic sealing method has certain advantages in structure and aerodynamics. It will not be limited by the mechanical restriction of scratching between rotational and stationary components, and it is not sensitive to the displacement between those two components either. Also, by adjusting the labyrinth seal inject speed and angle can balance the pressure difference, which drives leakage flow, between pressure side and suction side and thus no need to reduce reaction rate of the blade tip region. The thought of using aerodynamic way to seal this direction has existed for long, both for the un-shroud [170] and the shrouded cases [171]. In addition to the direct using injection to weaken the leakage, it is also generate “air curtain” to reduce cross section area thus to reduce leakage [172]. Curtis and Denton et al. [173] verified the aerodynamic seal method on a turbine test rig. The set-up is shown in Fig. 4.65. In this set-up, the air curtain injects towards leakage flow direction and forms 45° angle with the axial direction. Numerical simulation and experimental study on the mass flow rate of different air curtains show that increasing jet flow rate can generally achieve the goal of eliminate leakage. However, at this time the turbine aerodynamic efficiency decreases significantly comparing to non-injection condition. The optimal efficiency occurs when the jet flow rate is $1/3$ of the leakage flow rate without labyrinth seal. Curtis and Denton et al. proposed two predictive models based on the momentum

conservation and the streamline curvature of the injection. Predicted results show good agreement with the experimental results [173]. The use of air curtain in the labyrinth seal has its limitations. On one hand, it is difficult to control the circumferential distribution so do the results. On the other hand, whether it is advantages or disadvantages to the overall turbine performance depends on the source of the air curtain, which means the “extraction” may harm to performance. Besides, using air curtain flow may not only reduce certain amount of leakage flow, but also reduce the originally cooling air amount in this region. Therefore, final results depend on the balance of many factors.

4.4 Secondary Flow in High-Loaded LP Turbine Endwall Region

Because the aspect ratio of LP turbine blades is relatively large, the secondary flow loss in the endwall region is relatively small, so it did not attracted much attention. But with the increasing load and requirements of LP turbine, the influence of secondary flow in endwall region has attracted more and more attention in recent years. The evolution mechanism of the secondary flow and the control of its loss in the endwall region of the high load/ultrahigh load LP turbine are important for the development of the high efficiency and high load LP turbine aerodynamic design method.

4.4.1 *Secondary Flow Structure and Loss Characteristics in LP Turbine Endwall Region*

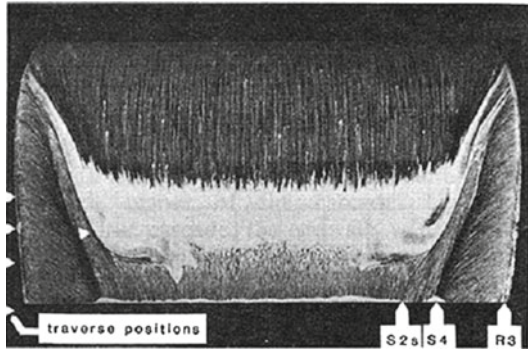
The secondary flow structure and its evolution of the LP turbine endwall are similar to that of the high-pressure turbine. However, comparing to the HP turbine, in addition to the geometric characteristics like high aspect ratio, the LP turbine blade passage generally has more aerodynamic characteristics like high flow turning angle, low Reynolds number, large traverse pressure gradient, adverse pressure gradient near trailing edge, etc. These characteristics determine that the secondary flow structure and the loss configuration of the LP turbine are different from those in HP turbine.

Hodson and Dominy studied the secondary flow structure in a LP turbine cascade [174]. The main characteristics that distinguish the endwall flow in LP turbines from the one in HP turbines are the evolution mechanisms of passage vortices and horseshoe vortices, the formation of corner vortices, the influence of trailing edge shedding vortices and the effects of separation bubble on the blade suction side. Figure 4.66 shows typical secondary flow structures in turbine endwall region. Figure 4.66a, b are the oil visualization results of secondary flow structures on the endwall region and suction surface, respectively. Figure 4.66c shows topology

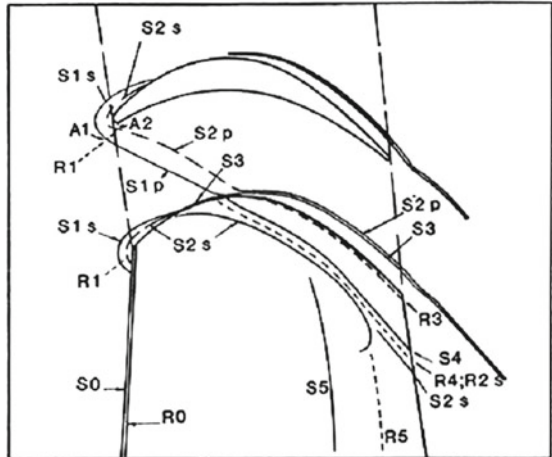
Fig. 4.66 Typical LP turbine endwall region secondary flow structures [174], Endwall flow visualization, blade suction surface flow visualization, flow structures



(a) Endwall flow visualization



(b) Blade suction surface flow visualization



(c) Flow structures

schematic of secondary flow structures. In the figure, “S” and “R” represent the separation and reattachment lines of various separation flow structures. “0” and “5” respectively correspond to the leading edge separation bubble and the trailing edge separation bubble on the suction surface, “1” and “2” represent the incoming boundary layer separation corresponded to the rolled-up horseshoe vortexes (“s” and “p” denote suction side branch and pressure side branch, respectively). “3” represents corner vortex induced separation. “4” represents the separation caused by the passage vortex. The results show that the suction side leg of the horseshoe vortex is not eaten by the passage vortex in the LP turbine, and its trajectory has not been significantly affected by the passage vortex. Basically it locates close to the suction surface of the blade and develops till trailing edge, which may be due to the strong transverse pressure gradient in LP turbine. In addition, the fluid in the suction side of the horseshoe vortex is not drawn into the separation bubble at the trailing edge, yet its strength is weakened by the separation bubble. The appearance of the corner vortex in the LP turbine channel may also be different from that in HP turbine. Observation shows that the corner vortex of this cascade is formed in a position where the suction side leg of the horseshoe vortex hit the suction surface of the blade, which may be closer to the upstream comparing to HP turbine. Since the transverse pressure gradient near the leading edge of the blade determines the position where the suction side leg of the horseshoe vortex hits the suction surface, the blade loading and its distribution, as well as the incidence will directly affect the formation position of the corner vortex. In terms of the evolution of the passage vortex, the LP turbine passage vortex may still be very close to the suction side near the exit of the cascade channel, rather than in a HP turbine that would propagate to a location near the middle of the passage, which would also be due to the greater transverse pressure gradient. Just because the passage vortex of the LP turbine is closer to the blade, its interaction with the trailing edge shedding vortex is more significant. Those trailing edge shedding vortexes will evolve into the counter rotating streamwise vortexes, and eventually may result in flow after leaving the passage shows more serious underturning, which is not seen in HP turbine.

The flow losses in the LP turbine endwall region can generally be divided into endwall boundary layer losses and secondary flow mixing losses, with the later losses dominating, especially for high-loaded LP turbines. There not only exists a variety of large scale vortex structures in the endwall region, but also be lots of turbulences due to the breakdown of vortexes. Therefore, the study of the secondary flow loss in endwall more focus on the evolution of the secondary kinetic energy (SKE) dissipation and turbulent dissipation. Based on the analysis of measurements on three cross sections downstream of one turbine casescade, Moore and Adhere believed that flow losses downstream of the cascade mainly come from the reduction of SKE [175]. However, MacIsaac and other researchers concluded different from another cascade. Their results show that the contribution of SKE reduction to the total loss is only about half [176]. Note that the two researches have different aspect ratios, flow conditions, load and so on, which may be the reason that cause different conclusions. It also indicates that the geometrical aerodynamic characteristics of cascades need to be taken into account when measuring the SKE

loss. In terms of the contribution of turbulence dissipation, results from Gregory-Smith et al. show that although turbulent kinetic energy (TKE) in the cascade may increase tenfold, it can only account for about 25% of the total pressure loss [177]. A similar result was given by MacIsaac et al. [176], in which the total pressure loss of the turbine cascade is present, but the TKE measured at three cross sections downstream of turbine cascade does not increase at all. These results show that there is no clear correlation between the increase of TKE and the increase of flow loss, and therefore the TKE cannot be simply used to measure the flow loss. When measuring the Reynolds stress in the mixing process downstream of cascades, Moore and others found that the production term of turbulence shows good agreement with the total pressure loss. And they believed that the production of turbulence plays a key role in the secondary flow mixing in turbine [178]. This conclusion is also supported by MacIsaac et al. [176] and Lyall et al. [179]. In the meantime Lyall et al. pointed out that after being divided into the secondary flow dissipation and the turbulence dissipation, the Secondary flow loss inside the turbine can be further divided into the reversible term and irreversible term. They also gave expressions for each term through the theoretical derivation.

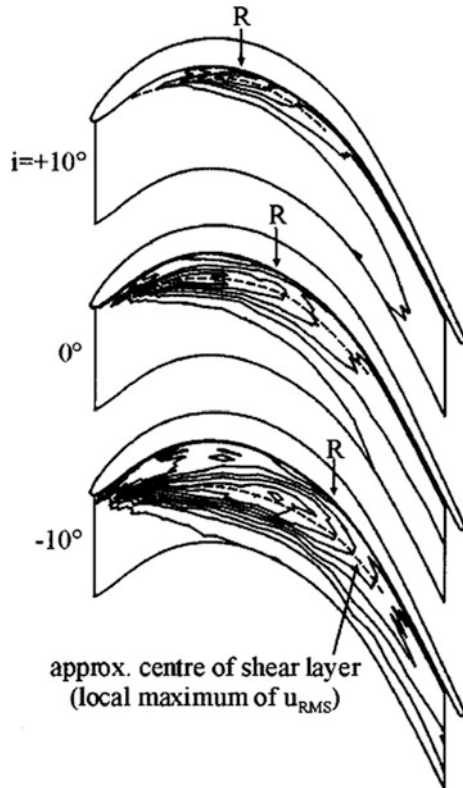
4.4.2 Pressure Surface Separation and Its Impacts on Flow in LP Turbine Endwall Region

It is difficult to avoid the existence of strong adverse pressure gradient in the trailing edge of the suction face due to the increasing load of the blade. This will cause the suction surface boundary layer to thicken rapidly and increase the risk of boundary layer separation. The influence mechanism of the boundary layer thickening and even separation on the endwall secondary flow region is basically the same as that of the HP turbine. For high-loaded low-weight LP turbines, the effect of increasing blade loading is not limited to the suction side, but may also change the pressure surface flow field, resulting in significant change of endwall losses.

There are two options to reduce LP turbine weight: hollow thick blades or solid thin blades. Since the latter have obvious advantages in the processing, manufacturing and maintenance, they are widely used. But with the increasing load, there may be adverse pressure gradient near the leading edge of pressure surface on the solid thin LP turbine blade. As the boundary layer is still in laminar condition at this time, it is easy to form separation bubbles in the design state, that is, pressure side separation. Therefore, it is important to control the separation of the pressure side of the high load/ultrahigh load LP turbine and its effect on the endwall secondary flow.

Although this pressure side separation phenomenon only occur at large negative incidence in conventional turbines or in high load turbines with thick blades, preliminary discussions have been made [180–182]. These studies mainly focus on the impact of the incidence. As Yamamoto found in the study, only the incidence is larger than a certain threshold, the conclusion that the reduction of incidence will

Fig. 4.67 Pressure surface separation in high-loaded LP turbine [184]



inhibit the strength of secondary flow was established. When the incidence is less than this threshold, the decrease of the incidence causes the secondary flow to intensify. The reason is that the pressure surface is separated [183]. However, as the load distribution of the blade changes significantly at negative incidence, these results could not provide satisfactory description to the possibility of a pressure-surface separation bubble and corresponding impact to endwall flow in the high-loaded LP turbine with a thin blade design.

Brear and Hodson tested a cascade of high load LP turbines with a solid thin blade design. Their results show that the pressure surface separation bubble is still evident at $+10^\circ$ incidence, while under the negative incidence the separation bubble can occupy about 65% of the chord length [184], as shown in Fig. 4.67. To discuss the effect of the bubble on the endwall region, Brear and Hodson compared and analyzed the endwall flow of blade (blade A) and the other three blades which have same load and same suction side shape but different pressure surfaces (blade B, C and D) [184]. The geometry of those four blades is shown in Fig. 4.68a. Blade D, like blade A, is uniform in spanwise, while the change of profile is the pressure surface which is a significant thickening of the blade, i.e., a thick blade design. Blade B and C are non-uniform in spanwise, but has the same profile as blade A at

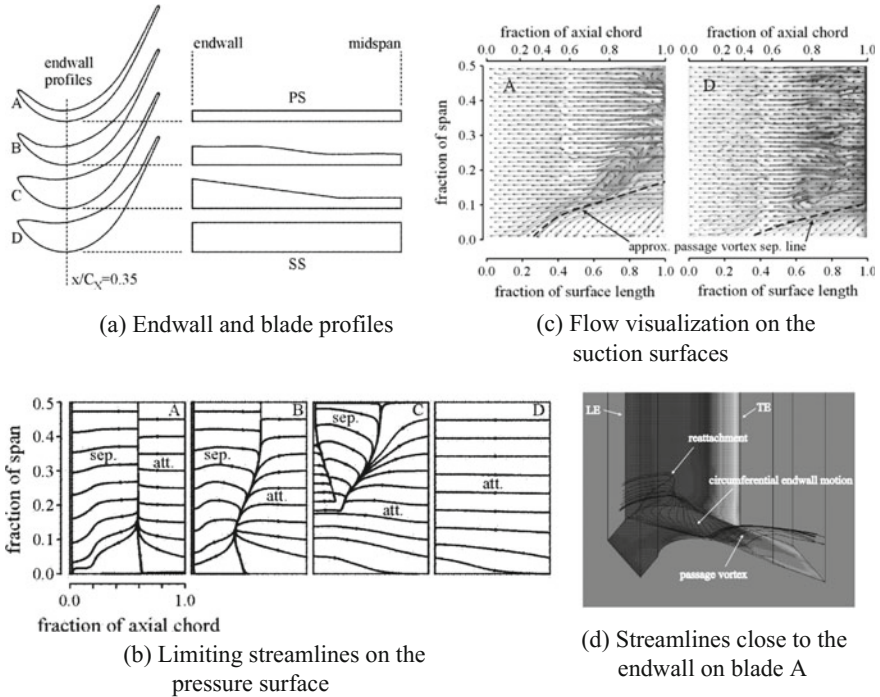


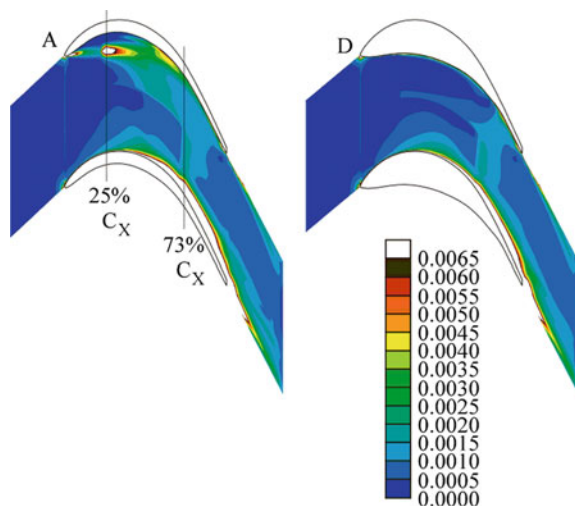
Fig. 4.68 LP turbine blades and flow structures at different pressure surfaces [184]

midspan location. Blade C is the same as blade D at the root while blade B is slightly thinner comparing to blade D at the root. The limiting streamlines on the pressure side of the four blades are given in Fig. 4.68b. It can be seen that the blade D removes the separation bubble from the pressure surface side of entire height, while the blade C can eliminate separation in the endwall, but the separation is still present in the middle of the blade. Blade B cannot eliminate the separation bubble from root, but only to a certain extent, weaken the separation. In terms of the secondary flow, the flow visualization results on the suction surface of the blade A and the blade D are given in Fig. 4.68c. The results show that the formation of the passage vortex in blade D endwall region moves to about 10% of the arc length downstream when compared to blade A, and its spanwise spread near the trailing edge is also significantly reduced. These differences are mostly due to the decreasing of the separation bubble on the pressure surface of blade D when compared with blade A. For blade D, the passage vortex is formed mainly by the fluid coming from the endwall boundary layer and the boundary layer attached to the pressure surface, which is the same as HP turbine. The formation of passage vortex will be affected by the presence of separation bubble on blade A pressure surface. Figure 4.68d shows the three-dimensional streamlines near the endwall on blade A. Due to the pressure surface flow separation, the low-energy fluid in the separation bubble cannot resist the transverse pressure gradient in the passage,

causing the fluid transport toward the suction side. The results in Fig. 4.68d show that the fluid within the separation bubble flows upstream and mix into the boundary layer near the endwall after leaving the pressure surface from near the reattachment point, which is due to the interaction between streamwise adverse pressure gradient in main flow near pressure surface and the pressure side leg of the horseshoe vortex. Those fluids which are from the vicinity of the pressure surface will eventually reach near the suction face and get rolled into passage vortex. Since the momentum of the fluid in the separation bubble is much lower than that in the boundary layer but contains much more fluid than the boundary layer, the vortex in the endwall region will be significantly enhanced once the pressure surface is separating. It can be seen that the key to determine the structure and strength of the secondary flow near the endwall region is the low energy containt fluid and the pressure gradient, and the most direct negative effect of pressure surface separation is the provision of a large number of low energy fluids.

Obviously, Brear and Hodson’s work is about the cascade. The actual pressure gradient inside turbine is more complicated due to bending and other three-dimensional shape of the blade, so the impact of pressure surface separation bubble will be more complex. In addition, the pressure gradients in the radial direction may also be the key factor that influences pressure surface separation bubbles in the rotor blade row. Yamamoto found that the low-energy fluid in the pressure-surface separation bubble would transport towards the blade tip due to radial pressure gradient, and finally leak into the suction side through the gap, which affects the leakage flow near the tip, the passage vortex and other secondary flow structures [183]. This is obviously another way for the pressure-surface separation flow to interact with the endwall secondary flow structure. However, the research on the evolution of pressure surface separation and its interaction with secondary flow in complex pressure gradient environment is still insufficient, and the understanding of this phenomenon needs to be further improved.

Fig. 4.69 Comparison of flow loss near endwall regions in a high loaded LP turbine [184]



In terms of the endwall flow loss, Figure 4.69 shows the distribution of the dissipation coefficient at endwall to 10% span of blade A and D in Fig. 4.68a [184]. Blade A has a large loss in the shear zone of the pressure-separated bubble with the maximum loss appears near the 25% axial chord position, which is the transition position of the separating shear layer. In the blade D, since the pressure-surface separation bubble completely disappears, the corresponding loss does not exist. When focusing on the vicinity of the suction surface, it can be seen that the high loss regions of blade D are obviously reduced and the position is closer to the downstream, which is consistent with the evolution characteristics of passage vortex. The quantitative analysis of the four blades indicated that the flow loss near blade endwall can be reduced by 15% by eliminating the separation bubble on the pressure surface, and the reduction in the flow loss near the pressure and the suction sides can contribute about 80%. This is due to the disappearance of the separation bubble on the pressure side and the weakening of passage vortex in the vicinity of suction surface.

4.4.3 Endwall Boundary Layer Evolution Mechanism and Its Impacts

The development of LP turbine endwall boundary layer is also a key factor to determine the flow structure in endwall region. It has been shown that near the turbine endwall mainly exist the boundary layer of upstream flow and the newly formed boundary layer in the passage. These boundary layers are generally dominated by laminar flow or the boundary layers in the transition process [185, 186]. For LP turbines, Vera et al. [187] measured the flow structure and evolution of the endwall boundary layer in a LP turbine cascade and the second and fourth stage

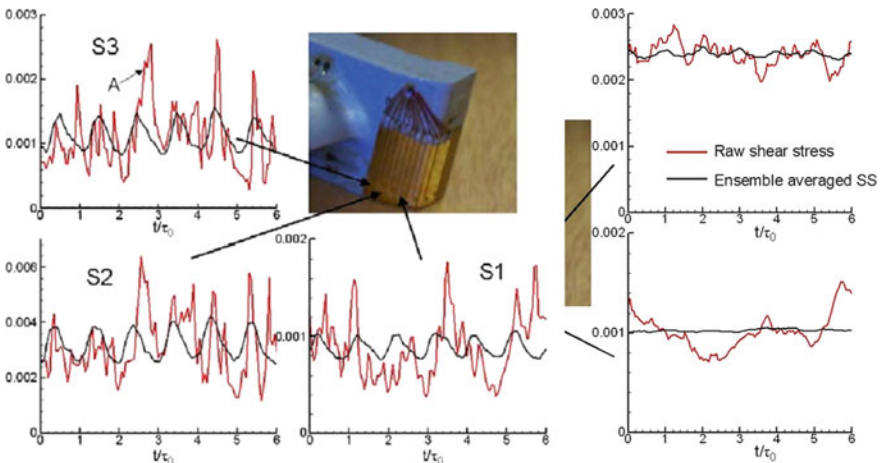


Fig. 4.70 Development of LPT inlet endwall boundary layer [187]

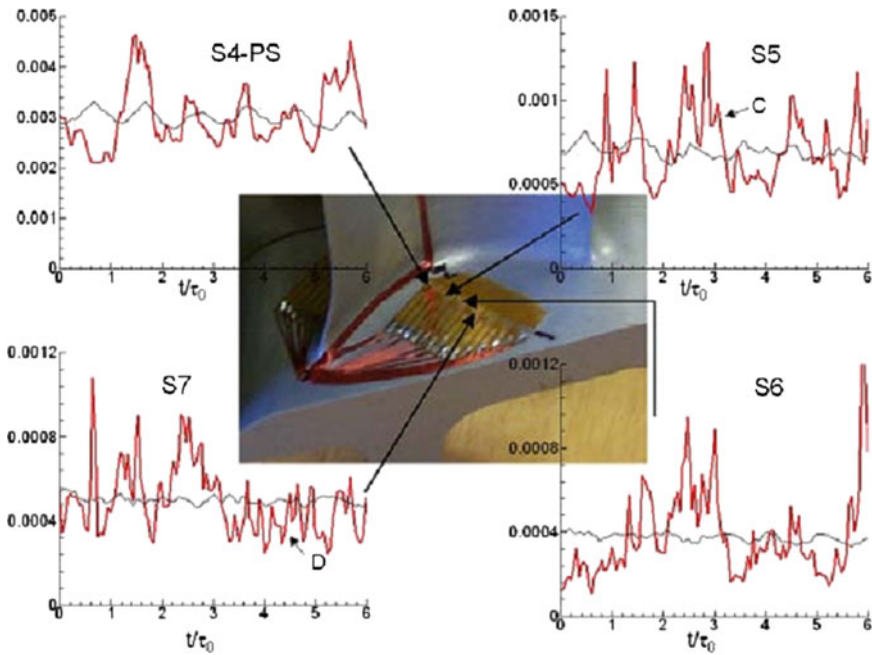


Fig. 4.71 Development of the boundary layer on the pressure side endwall [187]

stator cascade in one four-stage LP turbine using hot-film. Figure 4.70 shows the arrangement of the hot-film measuring points on the endwall near the leading edge of the fourth stage guide vane and the corresponding results. The experimental results show that the Reynolds number is 8.6×10^4 based on measurement condition and axial chord. The original signal and the ensemble-averaged results of the wall shear stress are shown in the figure. Here, measurement points S00 and S01 are located in the sealed cavity. The amplitude of the averaged signal is small and not periodic, which indicates that the development of the boundary layer is dominated by the sealing flow, which has less impact from upstream flow. The measuring points S1, S2 and S3 are located on the endwall of the turbine channel, and the ensemble-averaged results of these three points show obvious periodicity due to the periodic passing upstream rotor row. The pulse of the instantaneous signal at the measuring point S1 is not symmetrical about the ensemble average signal, but exhibits an occasional spike. These spikes correspond to turbulent burst in the boundary layer, indicating that the boundary layer is at the beginning of the transition process. Comparing the signals S1, S2 and S3, it can be found that the large-scale pulsations gradually evolve into high-frequency and low-intensity pulsations, which is typical of the boundary layer transition process. It should be noted out that, S3 still measures significant pulsation, which indicates the transition process of the boundary layer has not been completed, where the boundary layer is still not completely turbulent state.

Figure 4.71 shows the hot-film measurement results of pressure side endwall boundary layer [187]. It should be noted that the measurement results shows no presence of separation bubbles on the pressure side. The pressure surface branch of the horseshoe vortex rolls up the boundary layer of the endwall during its transportation towards to suction surface, causes it to lift away the wall surface, then re-establishes new boundary layer downstream of the endwall. The newly formed boundary layer will re-evolve under the streamwise and transverse pressure gradient. Measurement points S4-S7 located downstream of horseshoe vortex pressure surface branch, which is the interior of the new boundary layer. Results show that the newly developed boundary layer exhibits obvious laminar flow characteristics near the pressure surface, and its evolution to the suction surface side is accompanied by flow transition. In addition, in the region close to the pressure surface. The passing frequency of the upstream rotor was found obvious in the ensemble average results, which indicates that the flow will be affected stongly by the upstream blade row. With the development of the flow, the passing frequency of the upstream blade is weakened in the boundary layer, and disappear in the middle of the passage. This phenomenon is as well the results of strengthen of the horseshoe vortex pressure surface branch which causes the lifting of the fluid near endwall, thus makes the impact of the inflow away from the endwall. For the suction side, the inflow boundary layer near the leading edge is affected by the suction side leg of the horseshoe vortex. If the inflow boundary layer is laminar, it may induce the boundary layer to transit. The boundary layer near the trailing edge, however, is mainly from the new formed boundary layer which was caused by the pressure side leg of the horseshoe vortex and has developed from upstream and the pressure surface. This part of boundary layer usually shows the similar characteristics to fully developed turbulence.

Because the state and thickness of the endwall boundary layer near the leading edge of the blade are largely dependent on the incoming boundary layer, while the endwall boundary layer of the leading edge endwall determines the rolling position and strength of the horseshoe vortex, so the endwall inflow boundary layer will have a significant impact on the flow of the turbine endwall. De la Rosa Blanco and Hodson studied the flow structures and losses of the LPT cascade under different endwall incoming boundary layer conditions [188]. The research subjects are two blades, one of which is thick while the other is thin. Three kinds of inflow boundary layers are given, including a “laminar boundary layer” with shape factor of 2.18, a “turbulent boundary layer” with shape factor of 1.64 and a “thick turbulent boundary layer” with shape factor of 1.44. Similar to the results given in Ref. [184], there is no separation bubble on the pressure surface of the thick blade, whereas there is a wide range of pressure surface separation in the thin blade. In addition, when the endwall inflow boundary layer is turbulent, the pressure surface separation bubble transports apparently towards the endwall, and the root cause of which is the interaction between the pressure side branch of the horseshoe vortex and the separation bubble. When the inflow boundary layer is laminar, the radial transportation phenomenon does not occur because the rolling position and the evolution trajectory of the pressure surface branch of the horseshoe vortex are more deviated from the pressure surface. Figure 4.72 shows cascade endwall flow visualization results

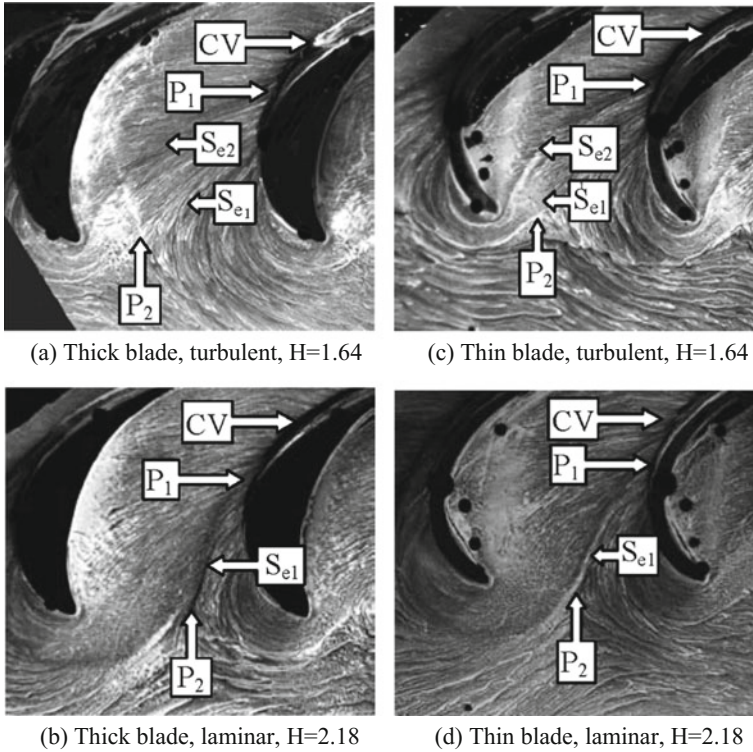


Fig. 4.72 Flow visualization of LPT endwalls with different inlet endwall boundary conditions [188]

under different conditions. In the figure, the main flow structures such as the saddle point P_2 caused by the rolling up of the horseshoe vortex, the pressure surface branch of the horseshoe vortex S_{e1} , the position P_1 where the horseshoe vortex pressure surface striking the suction surface, and the corner vortex CV near the trailing edge of the suction surface are shown. It can be seen that the saddle point P_2 is closer to the suction surface under the condition that the endwall incoming boundary layer is laminar, regardless of whether it is a thick blade or a thin blade. Correspondingly, the position of the horseshoe vortex pressure surface branch S_{e1} is closer to the suction surface and away from the pressure surface, which results that there is no direct interaction between the pressure surface branching S_{e1} of the horseshoe vortices and the pressure surface separation. In addition, flow visualization results also show that in the case the endwall incoming boundary layer is turbulent, another separation line S_{e2} can be observed near the pressure side. In the thin blade cascade, this separation line is more obvious due to the interaction between the pressure surface branch of the horseshoe vortex and the pressure side separation bubble. In the case of corner vortex, its evolution trajectory also shows a significant correlation with the endwall incoming boundary layer flow. No matter the thick

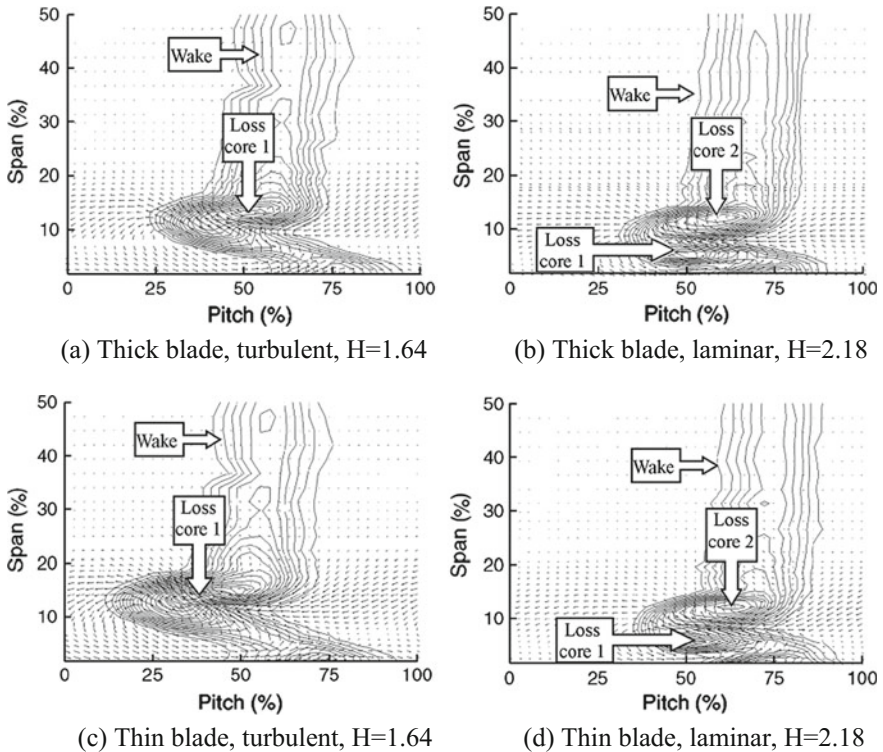


Fig. 4.73 Total pressure loss distributions at the cascade outlet [188]

blade or the thin blade, the corner vortex under the turbulent boundary layer is more obvious.

In terms of flow losses, Fig. 4.73 compares total pressure loss coefficient distribution for the 50% axial chord length section downstream of the cascade. The results show that the influence of the state of endwall incoming boundary layer on the total pressure loss distribution is more obvious, while the influence due to blade thickness is relatively small. When the inflow boundary layer is turbulent, there is a loss kernel/core in the turbine endwall region, and the maximum total pressure loss locates in the center of the core. When the incoming boundary layer is laminar, there are two loss cores appear in the endwall region, but the maximum value of the total pressure loss is less and its position is radially close to endwall. The difference on loss distribution characteristics is caused by the difference on secondary flow evolution mechanisms, which, at the root, is due to the different states of endwall incoming boundary layers. For laminar boundary layer, the passage vortex near endwall region is relatively weak. Then the mixing with the trailing edge shedding vortex after leaving the cascade passage is also weak. Therefore, two vortices can be observed at the 50% axial chord length downstream of the cascade, corresponding to two loss cores. For the incoming turbulent boundary layer, since the

passage vortex is very strong, it has strong mixing process with trailing edge shedding vortex. The trailing edge shedding vortex is not observed after mixing, so there is only one vortex downstream of cascade, but with more obvious loss. Through the analysis of the total flow loss of the cascade, the flow loss increases with the endwall incoming turbulent boundary layer when compared to laminar one, no matter thick or thin blades. And with increased turbulent boundary layer thickness, this loss increases more obvious. Comparing the effects due to blade thickness, under the incoming turbulent boundary layer, the aerodynamic performance of the thin blade significantly decreases. When compared to the thick blade this is mainly due to the interaction between the pressure side branch of the horseshoe vortex and the pressure side separation, so that more low-energy fluid is involved in the passage vortex, so that the passage vortex becomes strong and the loss increases. However, under the incoming laminar boundary layer, the aerodynamic characteristics of the thin blade have no obvious change compared to the thick blade. This is because there is no strong interaction between the branch of the horseshoe vortex and the pressure side separation of the thin blades.

For the development of LPT blade boundary layer, Reynolds number has a very important effect. Results show that Reynolds number is also important for the secondary flow near endwall region. With Reynolds number increases, the blockage effect due to the secondary flow in the endwall region decreases [189], which is the reason why turbine aerodynamic performance increases with Reynolds number. If there is boundary layer separation near the blade endwall, the change of the Reynolds number may change the characteristics of these separated flows, leading to obvious change of the secondary flow near blade endwall [190]. If there is no boundary layer separation, the transition process is affected with changing of the Reynolds number, but the boundary layer flow structure is not affected by that. At high Reynolds number, the transition process accelerates no matter for the incoming boundary layer near the leading edge or the new formed boundary layer in the passage. Therefore, the boundary layer near the leading edge and near the suction surface is closer to the turbulent state. Then, since the state and thickness of the inflow boundary layer will directly influence the position and strength of the horseshoe vortex while the new formed boundary layer affects the amount of fluid entrained in the passage vortex, and intensity of the whole secondary flow in the endwall region will be affected. This is the main influence mechanism of Reynolds number on flow near the endwall region in this circumstance.

4.4.4 LP Turbine Endwall Flow Under Unsteady Conditions

The LP turbine stage is working in the unsteady flow conditions. The upstream periodic wake and other unsteady effects will not be only limited to the blade boundary layer, but will also affect the evolution of the endwall flow structure. Although the current understanding of unsteady flow conditions on the HP turbine endwall region is relatively comprehensive, the research on the unsteady evolution mechanism of flow structures in LP turbine endwall region is less and the

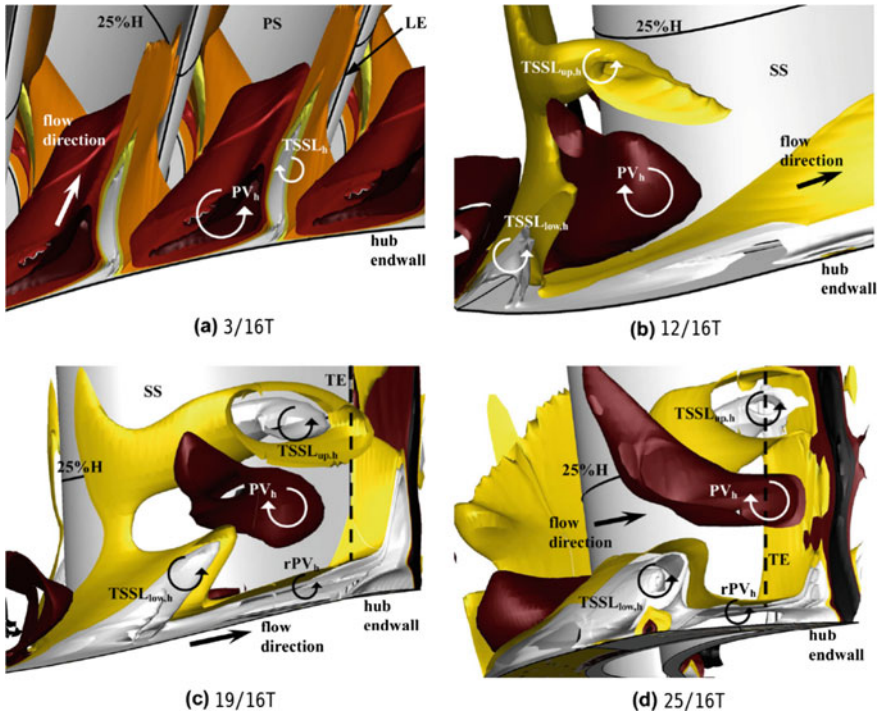


Fig. 4.74 Endwall flow structure of a LPT with unsteady wakes [191]

understanding is not comprehensive enough. It is gratifying that in recent years this problem has aroused the concerns by more researchers with corresponding works.

Schneider from ILA cooperated with MTU made experimental measurements and numerical simulation to investigate the endwall secondary flow in a two-stage LP turbine. This two-stage turbine test rig was used to simulate the third and fourth stages of typical LPT, and the Mach number and Reynolds number were consistent with the actual components [191]. Figure 4.74 shows the flow structure near the endwall in the first-stage rotor under two different phases in a cycle. Here uses contour plot of streamwise vorticity to identify the vortex. The results show that the passage vortex and the wake from upstream guide vanes will have strong unsteady interaction after entering into the downstream blade rows. The main process can be summarized as two stages. Firstly, the shear layer from the upstream wake become unstable in the downstream channel and is cut into independent segments in the spanwise direction. These segments are then rolled up in the channel and gradually formed into streamwise vortex structure. In the diagram, two streamwise vortices, which rolled up by upstream wake shear layer, are respectively identified as $TSSL_{up,h}$ for the one further to the endwall and $TSSL_{low,h}$ for the closer one. Between these two streamwise vortices are the passage vortex PV_h from upstream blade rows. This PV_h plays an important role in the instability and the subsequent

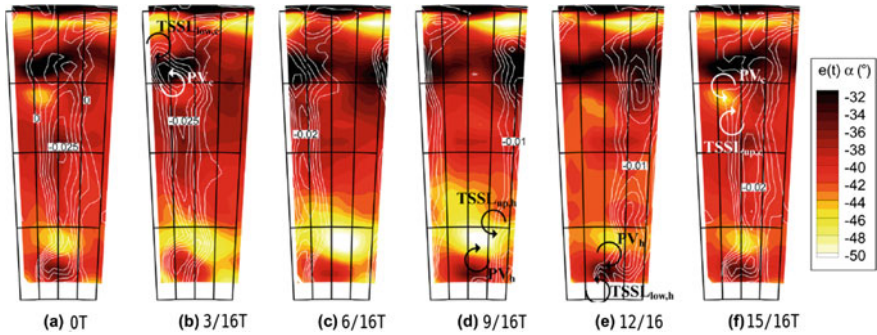


Fig. 4.75 Ensemble average of circumferential absolute flow angle time series [191]

evolution of the upstream wake shear layer. Just because the blockage of the PV_h , the part of the upstream wake shear layer which is near the endwall will not to transport towards blade suction side but is stretched and eventually cut there. On the other hand, the induction of PV_h is also an important reason for the upstream shear layer to roll up and evolve the streamwise vortices. At 25/16T, the passage vortex rPV_h in the rotor blade passage is observed near the trailing edge in the endwall region. The direction of rotation is the same as that of $TSSl_{low, h}$, which is rolled up by the upstream wake shear layer near the endwall, and the two vortices appear very close to each other, so they are possible to merge in the evolution process and enhance the strength. Note that the passage vortex rPV_h cannot be clearly identified at 12/16T, while at the same time the upstream wake is acting near the trailing edge of the suction surface. That is to say, the passage vortex rPV_h is likely to merge with the streamwise vortex $TSSl_{low, h}$, which indicates that the generation and evolution of passage vortex under the unsteady condition will be significantly affected by the unsteady upstream flow condition. Figure 4.75 shows the measured circumferential absolute flow angle changing over time with a dual-filament hot-film. The data are processed using the ensemble average method. It can be seen that the vortices causes the rotor outlet flow angle showing significant over and under turning near the endwall region (corresponding to the white and black areas, respectively). The main vortex pair also results in a large fluctuation of the rotor outlet flow angle with fluctuation amplitude can be as high as $\pm 10^\circ$. These unsteady fluctuations affect not only the local blade row but also cause the incidence loss downstream blade rows undergoing obvious fluctuation.

It can be seen that the LPT endwall flow under the turbine stage environment is significantly different from that under steady flow condition. The vortices generated from the upstream flow field are still strong in the blade passage, while the passage vortex of the blade itself is weakened under the influence of the inflow vortex structures. Similar results have been obtained from unsteady experiments and numerical simulations of the T106 turbine cascade [192]. The discussion of the wake passing frequency on the T106 turbine cascade shows that the intensity of the secondary vortices in the endwall region decreases with the wake frequency increasing. Correspondingly, the radial distribution of the outlet flow angle of the

cascade is also more uniform. It should be noted, however, that the flow coefficient and reduced frequency of the wake in this study are different from those of typical LP turbines, which may affect the propagation characteristics of the wake in the cascade and may affect its interaction with the flow structures near endwall.

Due to the significant changes in the flow structures in LPT stage environment, the flow loss in the endwall region is also changed accordingly. The flow loss caused by the inflow vortex structures will play an important role. Also the interaction between the upstream wakes and the upstream passage vortices near the endwall region, the influence of the incoming vortex structures on endwall boundary layer, and the secondary flow structures, and other unsteady interactions will all have profound impacts on the flow loss in the LPT endwall region. Although the flow evolution and loss mechanism of the LPT endwall region under unsteady conditions have attracted more and more attention, until now, the research on this problem is not comprehensive and deep. In particular, there is a lack of targeted research that can fully consider the geometrical and aerodynamic characteristics as well as the working environment of high/ultra-high load LPT. In addition, due to the complex multi-scale vortex structures and turbulent mixing in the endwall flow, experimental methods or RANS numerical simulation are difficult to give sufficiently fine flow structures and their evolution law, which seriously restricts the understanding of turbine endwall flow. With the development of computer technology and hardware, the high-precision numerical methods such as DES, LES and even DNS have been applied in the study of three-dimensional flow in turbomachinery [193–195]. It also provides a powerful tool for further study the flow structures of the LPT endwall region in the unsteady environment [196].

4.5 Low Reynolds Number Effects in LP Turbines

Reynolds number, which represents the ratio of typical inertial forces to typical viscous forces, is the key dimensionless parameter that determines the flow condition. Researches have been shown that when the Reynolds number is lower than a certain value, the amplitude of the perturbation will gradually decrease and eventually disappear, and the flow field will return to the state before the disturbance. It means flow is stable that it will always maintain laminar flow state without transition. If the Reynolds number is high, the disturbance may gradually increase or always exist, so that the flow does not return to the state before disturbed, the flow is unstable, and will eventually induce laminar flow to transit to turbulent flow. For typical turbomachinery, since the Reynolds number is sufficiently high (mostly above the self-similarity Reynolds number), the boundary layer is considered to be turbulent, regardless laminar condition and transition processes. It brings great convenience to the design and numerical simulation. However, this may not always be the case in reality. Such as aircraft engines in the high-altitude state lower inflow density may lead LPT characteristic Reynolds number to be much lower than the self-similarity Reynolds number. This situation is more obvious in the final stage of LPT in small-scale engines that used in high-altitude unmanned aerial vehicles.

Because of low Reynolds number, the blade boundary layer will remain laminar in a large range. The transition, separation and reattachment characteristics of the laminar boundary layer are the key factors that determine the flow characteristics of the LPT. The deeply understanding of these effects is the key for LPT aerodynamic design under low Reynolds number conditions.

4.5.1 Effects of Reynolds Number on the LP Turbine Aerodynamic Performance

Ever since 1989, Hourmouziadis analyzed the flow pattern and the flow losses of the LP turbine blade suction surface boundary layer under different Reynolds numbers [197], as shown in Fig. 4.76. In the figure, red color represents the separation loss and the blue color represents the friction loss. It as can be seen that at high Reynolds number, the boundary layer is turbulent. Although the friction loss is higher than laminar flow, the resistance to separation is stronger. Only when the trailing edge adverse pressure gradient increases to a certain extent, the turbulent separation occurs and the corresponding loss increases. When the blades are operated at very low Reynolds number, the boundary layer maintains the laminar flow state. Although the friction loss is small, its anti-separation ability is weak and the large scale laminar flow separation is prone to occur under the adverse pressure gradient, leading to a sharp increase in separation loss. Researches show that the laminar boundary layer thickness increases with the decrease of Reynolds number [198, 199]. The thicker the boundary layer before separation, the larger the separation scale and the greater the separation loss is. As the boundary layer loss

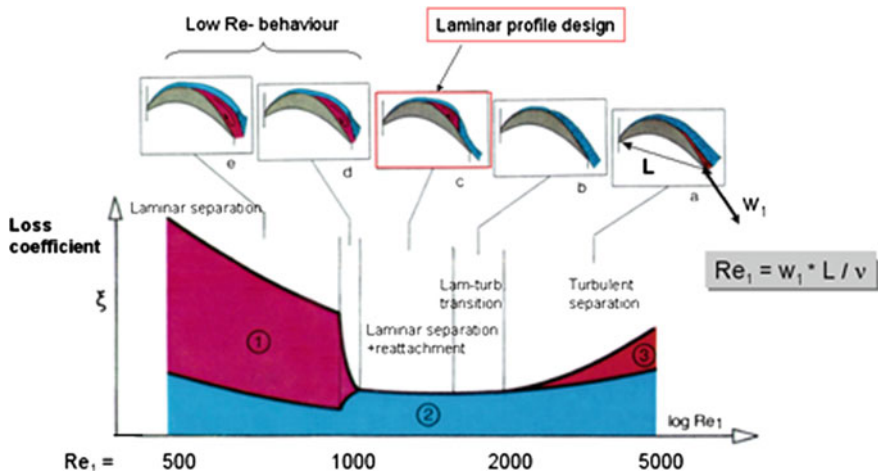


Fig. 4.76 Effects of Reynolds number on suction side boundary layer and losses in LP turbines [197]

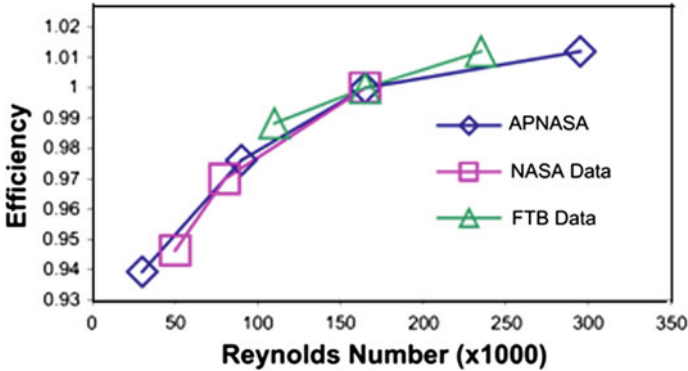


Fig. 4.77 Reynolds number effects on PW545 LP turbine efficiency [201]

dominates in the LP turbine, how to control the LP turbine blade suction surface boundary layer development in low Reynolds number conditions has become a research focus.

When the Reynolds number is lower than self-similarity range, the aerodynamic performance like the flow capacity and the aerodynamic efficiency, are affected significantly by the Reynolds number. For typical high-thrust civil large-bypass ratio turbofan engines, studies have shown that LP turbine efficiency may drop by 2% from takeoff to cruise altitude [200]. For smaller aircraft engines, the low Reynolds number effect will be more obvious. Figure 4.77 shows the plot of the LPT efficiency versus the Reynolds number in PW545 engine. Both the experimental and the numerical simulations show that when the Reynolds number is lower than the self-similarity range, the efficiency decreases with the decrease of the Reynolds number, and this trend is nonlinear, that is, in the low Reynolds number range the drop is more obvious. The lower left corner of the map corresponds to 18,288 m above sea level working Reynolds number. We can see that efficiency decreased approximately by 6% [201]. A similar situation also exists in the “Global Hawk” high altitude unmanned surveillance aircraft engine AE3007H. Data show that during high altitude 19,800 m cruise operation, the engine’s fuel consumption significant increases due to degradation of LP turbine performance [202].

MTU and the University of Stuttgart ILA laboratory investigated the low Reynolds number impact in detail on a two-stage LPT test rig and got similar impact of Reynolds number [203]. Based on this work, researchers further optimized the turbine blades and endwall of the test rig. The aerodynamic performance of the LP turbine in the design and off-design state was measured with the change of Reynolds number. In the off-design condition, the expansion ratio and rotational speed are reduced by 21% and 60%, respectively, compared with the design state, in order to realize the high attack angle in off-design case [204]. Figure 4.78 shows the mass flow rate and component isentropic efficiency changing with Reynolds number. All the data are non-dimensionalized under the corresponding conditions $Re_{v,1} = 1.8 \times 10^5$. It should be noted that, in order to compare between different

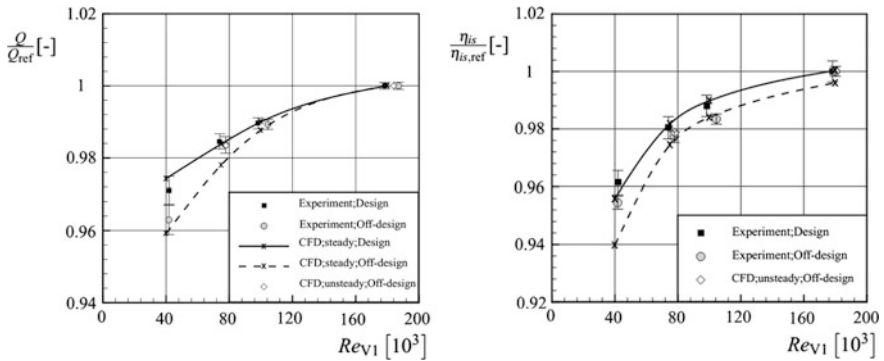


Fig. 4.78 The flow capacity and aerodynamic efficiency changing with Reynolds number in a two-stage turbine [204]

conditions, the Reynolds number is defined with the characteristic parameters of the first stage guide vane. In terms of flow capacity, test results show that the flow of turbine components operating in both the design and off-design states decreased by approximately 2.9 and 3.7%, respectively, over the tested Reynolds number range. It needs to be noted that the decline in the flow capacity shows obviously with Reynolds number lower than $Re_{v1} = 0.75 \times 10^5$. While in the range of the Reynolds number above this value, the variation of the flow capacity of turbine parts is basically the same in both design state and off-design state. The measurement results show that since the flow angle of the first stage turbine guide vanes does not change, its flow capacity varying with Reynolds number is basically consistent in different working conditions. But the second stage guide vane has a positive angle of attack of about 18° in off-design condition, which results in a greater separation at low Reynolds number conditions, and thus a greater reduction in the flow capacity of entire turbine component. In terms of aerodynamic efficiency, experimental results show that the isentropic efficiency of the turbine components drop approximately 3.9% while working in the design state at low Reynolds number. But the component efficiency has consistent trend with the changing of Reynolds number under off-design condition, though the decrease is even larger, reaching 4.6%. The authors believe that the main reason for the efficiency change is that the second-stage guide vanes are working at a large angle of attack, and the evolution of the boundary layer and the secondary flow structures in endwall region are more sensitive to the decrease of the Reynolds number.

The above research shows that it has great importance to study the internal flow structures and aerodynamic performance changing under low Reynolds number condition within LP turbine. It is the key to predict the aerodynamic performance of low-pressure turbine components under different working conditions. On the basis of this, the development of effective flow control methodologies will be an important way to improve the performance of LPT and even the whole engine under low Reynolds number condition. In order to consider low Reynolds number

impact on the performance in design phase, researchers provided aerodynamic performance correction for turbine components under low-Reynolds number conditions [205]. This correction method relies on large number of experimental data for empirical correlation, and has good applicability in a certain range. But it is worth noting that with the development of design method considering low-Reynolds number, the sensitivity of LP turbine aerodynamic performance to Reynolds number is no longer as serious as before. Thus the old correlation is not fully applicable. Thus we need to be careful [190].

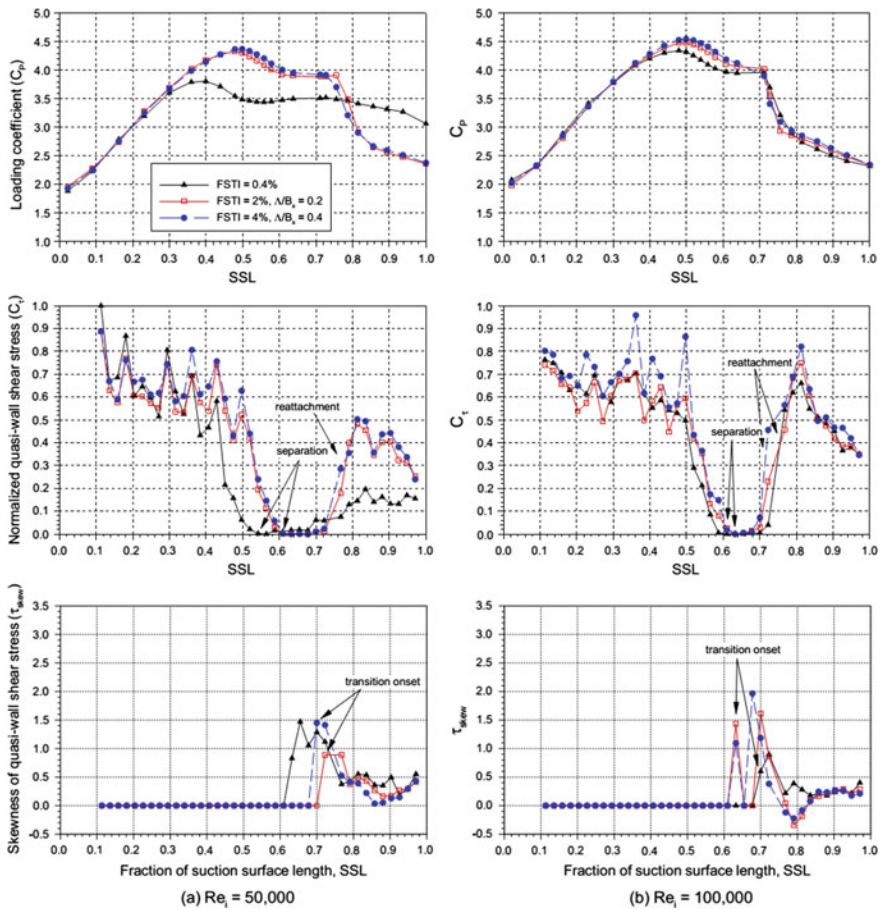


Fig. 4.79 Suction surface loading and hot-film data under different Reynolds numbers, Pack-B cascade [206]

4.5.2 LP Turbine Internal Flow Under Low Reynolds Number Conditions

Reynolds number and loading distribution, which are the key parameters to determine the state of the boundary layer, have important influence on the flow diagram in the turbine. Figure 4.79 compares the suction surface pressure distribution and the surface hot-film data of the $Z_w = 1.08$ Pack-B low-pressure turbine cascade with different background turbulence conditions in $Re = 0.5 \times 10^5$ and $Re = 1.0 \times 10^5$ operation conditions [206]. At higher Reynolds number ($Re = 1.0 \times 10^5$), the separation bubble appears near the trailing edge of the turbine blade. The influence of the turbulence on the flow structure of the suction surface is limited and the size of the separation bubble does not change. When the Reynolds number is reduced to $Re = 0.5 \times 10^5$ working condition, the size of the separation bubble near the trailing edge of the cascade increases obviously, and so do the transition position, which resulting in the re-attachment location moves downstream. In particular, when the FSTI is 0.4%, the separation of the trailing edge of the cascade will no longer re-attach but open, and the separation position moves obviously advanced. The flow loss of the Pack-B turbine cascade under different background turbulence conditions is also affected by the changes in the flow structure as shown in Fig. 4.80. In general, the effect of Reynolds number shows mainly in two aspects. On one hand, as the Reynolds number decreases, the separation bubble increases, thus the separation loss increases. On the other hand,

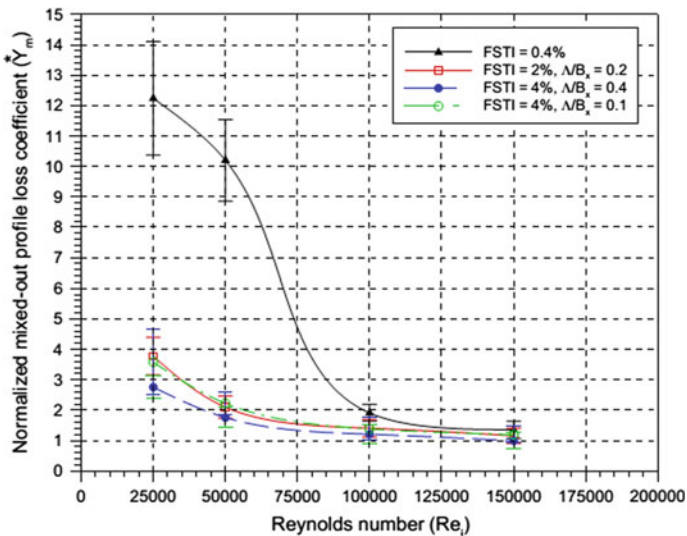


Fig. 4.80 Effects of Reynolds Number on Pack-B cascade loss [206]

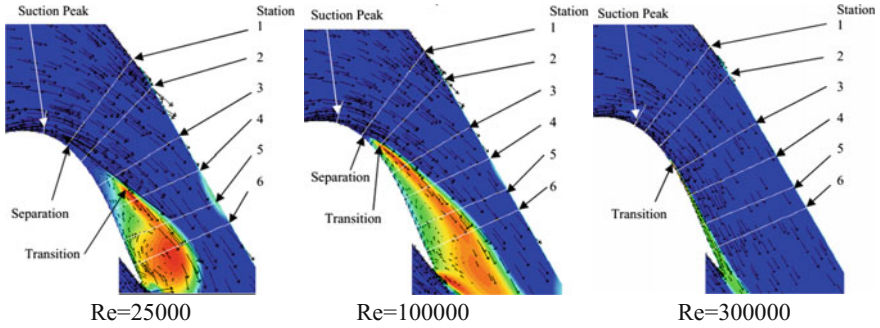


Fig. 4.81 Flow structures of high-loaded turbine cascade under different operating conditions [59, 60]

the decrease of the Reynolds number can reduce the wetting area of the turbulent boundary layer and reduce the friction loss. For the low-pressure turbine with low Reynolds number, generally the separation loss dominates, so the decrease of the Reynolds number leads to monotonous increased profile loss. As shown in Fig. 4.80, a decrease in the Reynolds number results in an open separation on the trailing edge of the Pack-B leaves under low FSTI, which results in a sharp increase in blade loss. It means that at low Reynolds number, profile loss is more sensitive to background turbulence.

As the blade loading increases, the risk of large-scale separation of the turbine cascade under low Reynolds number conditions will increase. Figure 4.81 shows a flow diagram of the turbine cascade under different Reynolds numbers [59, 60]. Experimental results and numerical simulations show that, at low turbulence (0.8%), after the Reynolds number is reduced to 1.0×10^5 , the small-size separation bubble in the boundary layer of the cascade suction surface is replaced by open separation. The profile aerodynamic loading decreased and the total pressure loss increased significantly. The boundary layer separation of the suction surface is suppressed at higher turbulence.

In the unsteady condition, the periodical sweeping wakes from upstream can effectively restrain the suction surface boundary layer separation, and the influence from wake will be affected by the Reynolds number. Figure 4.82 shows the temporal-special evolution of the boundary layer of the Pack-B cascade suction surface with $Re = 0.5 \times 10^5$ and $Re = 1.0 \times 10^5$ two Reynolds numbers [207]. The time-averaged separation and reattachment lines are shown, as well as transient separation zone, wake induced turbulence zone, and calmed region. It can be seen that the transition in wake-induced separation occurred later at the lower Reynolds number (corresponding to region C). So the separation bubble size is overall larger, which is consistent with the trend under steady-state conditions. Downstream of the separation bubble, both for the wake-affected period and the gap between wakes, the areas with high shear stress values expanded obviously as the Reynolds number increased. Correspondingly, the skewness factor values of the shear stress appear in

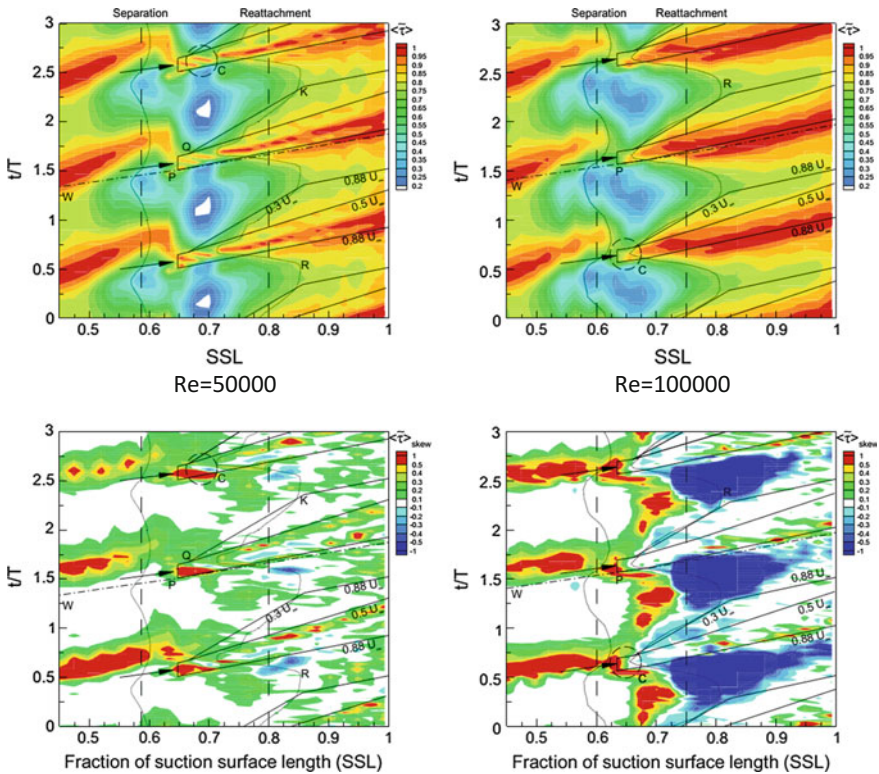


Fig. 4.82 Suction side boundary layer spatial-temporal evolution of the Pack-B cascade under different Reynolds numbers [207]

a greater range with negative and near zero values downstream of the separation bubble. This indicates that the boundary layer either in last stage of transition or in full turbulence is dominant near the cascade trailing edge under high Reynolds number condition, and the turbulent boundary layer is mainly in the wake period while the one in end phase of transition mainly exists between wakes. In contrast, at low Reynolds number, the skewness factor of the shear stress near the trailing edge of the cascade is positive in a large area, indicating that the transition process has not yet complete.

Researches show that the decrease of the Reynolds number for low pressure turbine components at high altitude not only makes the laminar flow in a larger area on the blade surface, but also increases the intensity and the area of the adverse pressure gradient in the blade loading distribution. The influence of these two factors drastically reduces the efficiency of low-pressure turbines at high altitudes [208, 209]. The effect of the low Reynolds number on turbine blade components is not only limited to profile loss, but also the development of the secondary flow in endwall region [210], which is also an important manifestation of the low Reynolds

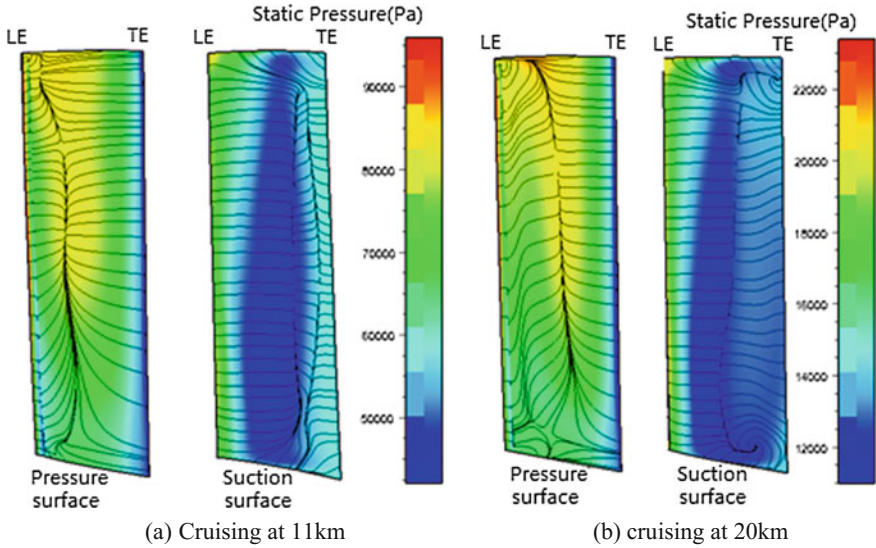


Fig. 4.83 Flow field of a LPT cruising at different altitudes [190]

number effect. Figure 4.83 shows flow field of one LPT rotor channel with corresponding working heights of 11 and 20 km [190]. It can be seen clearly from the comparison of the limited streamlines and the pressure contour on blade surface that the boundary layer of most of the blade height, changing from trailing edge separation bubble to un-reattached separation condition, when the working height of the engine from 11 to 20 km. At the same time, the small separation bubbles near the leading edge of the pressure surface are also significantly enlarged under the harsh conditions of high altitude, which has been able to affect more than half of the pressure surface at 20 km altitude. Correspondingly, the secondary flow in the endwall region of this cascade is obviously enhanced also the influence range is enlarged, which causes the related flow loss increased rapidly.

MTU and ILA laboratory in Stuttgart University measured the flow in the second stage stator passage under different Reynolds number on its two-stage low-pressure turbine test rig [203]. The distribution of the cascade efficiency is shown in Fig. 4.84 [211], with both experimental and numerical results. From the distribution of the cascade efficiency, it can be distinguish the losses induced by wake of the cascade and the endwall secondary flow. Comparing the two Reynolds number cases it shows that the wake widened obviously at low Reynolds number and the efficiency of the cascade in the wake region also decreased obviously, which is consistent with the increase of the boundary layer loss of the suction surface in low Reynolds number as mentioned before. To further quantify the width and strength of the vane wakes, which are affected by Reynolds number, Fig. 4.85, which shows the change in wake thickness (δ_1) with the Reynolds number [211]. Here, the displacement thickness is defined as:

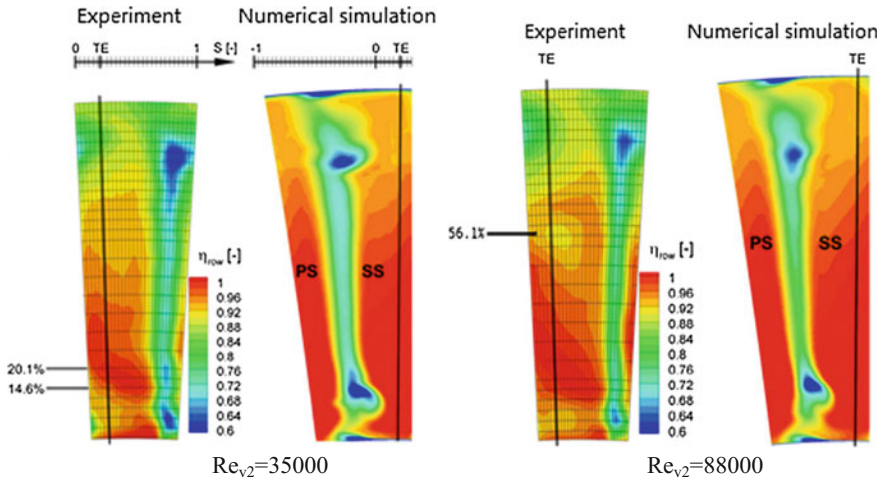
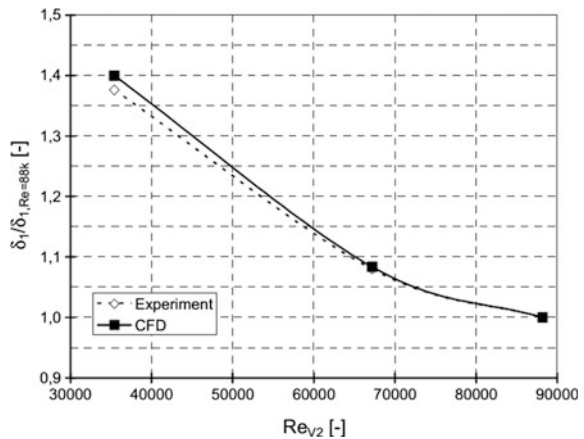


Fig. 4.84 Contour plot of blade row efficiency at exit of vane 2 under different Reynolds numbers [211]

$$\delta_{1,wake} = \int_0^t \left(1 - \frac{V_2}{V_{2,is}}\right) dt$$

where V_2 and $V_{2,is}$ represent the outlet speed and the ideal speed at cascade outlet, respectively. t is the pitch. It can be seen from the definition that the parameter represents the decrease of the flow capacity due to the loss of the wake velocity and has similar physical meaning to the velocity loss coefficient of the blade. The data given in Fig. 4.85 are data near the midspan (about 41% blade height) and are non-dimensional using the results of the Reynolds number $Re_{v2} = 0.88 \times 10^5$. The

Fig. 4.85 Relative displacement thickness of wake and loss cores at different Reynolds numbers at about 41% relative annulus height [211]



results show that when the Reynolds number decreases from $Re_{v,2} = 0.88 \times 10^5$ to $Re_{v,2} = 0.67 \times 10^5$ and $Re_{v,2} = 0.35 \times 10^5$, the flow loss near the vane increases by about 8 and 40%, respectively. The results also show that the loss of the blade loss is larger at lower Reynolds number. In terms of the secondary flow near endwall, the position of the loss core with respect to the Reynolds number change is not obvious in the experimental results and the numerical simulation results given in Fig. 4.84 (although the numerical simulation results differ slightly from the experimental results). However, those loss core regions are significantly increased, which is due to the enhanced secondary flow in endwall under low Reynolds number conditions. In addition, a high-Reynolds number of conditions at about 57% of blade height can be observed a decreased cascade efficiency region. This is mainly due to the secondary flow in the first-stage vane passage, but it vanishes due to strong mixing in the channel at lower Reynolds number condition.

References

1. Smith, S. F., & Afraes, M. A. (1965). A simple correlation of turbine efficiency. *Journal of Royal Aeronautical Society*, 69, 467–470.
2. Mayle, R. E. (1991). The role of laminar-turbulent transition in gas turbine engines. *Journal of Turbomachinery*, 113(4), 509–536.
3. Hodson, H. P., & Howell, R. J. (2005). Bladerow interactions, transition, and high-lift aerofoils in low-pressure turbines. *Annual Review of Fluid Mechanics*, 37, 71–98.
4. Zou, Z., Jian, Ye J., Huoxing, Liu H., et al. (2007). Research progress on low pressure turbine internal flows and related aerodynamic design. *Advances in mechanics*, 37(4), 551–562.
5. Howell, R. J., Ramesh, O. N., Hodson, H. P., et al. (2001). High lift and aft loaded profiles for low pressure turbines. *Journal of Turbomachinery*, 123(2), 181–188.
6. Denton, J. D. (1993). Loss mechanisms in turbomachines. *Journal of Turbomachinery*, 115(4), 621–656.
7. Curtis, E. M., Hodson, H. P., & Banieghbal, M. R., et al. (1997). Development of blade profiles for low-pressure turbine applications. *Journal of Turbomachinery*, 119(3), 531–538.
8. Rosic, B., & Denton, J. D. (2008). Control of shroud leakage loss by reducing circumferential mixing. *Journal of Turbomachinery*, 130, 021010.
9. Brear, M. J., Gonzalez, P., Harvey, N. W., et al. (2002). Pressure surface separations in low pressure turbines—Part 2: interactions with the secondary flow. *Journal of Turbomachinery*, 124(3), 402–409.
10. Wisler, D. C. (1998). *The technical and economic relevance of understanding boundary layer transition in gas turbine engines, Minnowbrook II, 1997 workshop on boundary layer transition in turbomachines*. NASA CP-206958, 1998.
11. Zou, Z., Kun, Zhou K., Peng, Wang P., et al. (2012). Research progress on flow mechanism and aerodynamic design method of high-bypass-ratio engine turbine. *Aeronautical Manufacturing Technology*, 27(13), 49–54.
12. Hodson, H. P., & Howell, R. J. (2005). The role of transition in high-lift low-pressure turbines for aeroengines. *Progress in Aerospace Sciences*, 41(6), 419–514.
13. Howell, R. J., Hodson, H. P., Schulte, V., et al. (2002). Boundary layer development in the BR710 and BR715 LP turbines—the implementation of high lift and ultra high lift concepts. *Journal of Turbomachinery*, 124(3), 385–392.

14. Weber S, & Hackenberg, H. P. (2007). *GP7000: MTU aero engines' contribution in a successful partnership*. ISABE Paper 2007-1283, 2007.
15. Praisner, T. J, Grover, E. A., & Knezevici, D. C., et al. (2008) *Toward the expansion of low-pressure-turbine airfoil design space*. ASME Paper 2008-GT-50898.
16. Goodhand, M. N., & Miller, R. J. (2010). *The impact of real geometries on three-dimensional separations in compressors*. ASME Paper GT2010-22246.
17. Garzon, V. E., & Darmofal, D. L. (2003). Impact of geometric variability on axial compressor performance. *Journal of Turbomachinery*, 125(4), 692–703.
18. Zhang, W., Zou, Z., Liu, H., et al. (2010). Effect of profile deviation on turbine performance in whole engine environment. *Journal of Engineering Thermophysics*, 31(11), 1830–1834.
19. Zhang, W., Zou, Z., Li, W., et al. (2010). Unsteady numerical simulation investigation of effect of blade profile deviation on turbine performance. *Acta aeronautica et astronautica sinica*, 31(11), 2130–2138.
20. Morkovin, M. V. (1993). *Bypass-Transition Research: Issues and Philosophy. Instabilities and Turbulence in Engineering Flows* (pp. 3–30). Netherlands: Springer.
21. Morkovin, M. V., Reshotko, E., & Herbert, T. (1994). Transition in open flow systems-a reassessment. *The Bulletin of the American Physical Society*, 39(9), 1882.
22. White, F. M. (1991). *Viscous fluid flow* (2nd ed.). New York: McGraw-Hill.
23. Goldstein, M. E., & Hultgren, L. S. (1989). Boundary-layer receptivity to long-wave free-stream disturbances. *Annual Review of Fluid Mechanics*, 21, 137–166.
24. Saric, W. S., Reed, H. L., & Kerschen, E. J. (2002). Boundary-layer receptivity to freestream disturbances. *Annual Review of Fluid Mechanics*, 34, 291–319.
25. Boiko, A. V., Grek, G. R., Dovgal, A. V., et al. (2002). *The origin of turbulence in near-wall flows*. Berlin: Springer.
26. Matsubara, M., & Alfredsson, P. H. (2001). Disturbance growth in boundary layers subjected to free-stream turbulence. *Journal of Fluid Mechanics*, 430, 149–168.
27. Jacobs, R. G., & Durbin, P. A. (2001). Simulations of bypass transition. *Journal of Fluid Mechanics*, 428, 185–212.
28. Zaki, T., & Durbin, P. A. (2005). Mode interaction and the bypass route to transition. *Journal of Fluid Mechanics*, 531, 85–111.
29. Zaki, T., & Durbin, P. A. (2006). Continuous mode transition and the effects of pressure gradient. *Journal of Fluid Mechanics*, 563, 357–388.
30. Durbin, P., & Wu, X. (2007). Transition beneath vortical disturbances. *Annual Review of Fluid Mechanics*, 39, 107–128.
31. Krishnan, L., & Sandham, N. D. (2006). Effect of Mach number on the structure of turbulent spots. *Journal of Fluid Mechanics*, 566, 225–234.
32. Wygnanski, I., Sokolov, M., & Friedmann, D. (1976). On a turbulent 'spot' in a laminar boundary layer. *Journal of Fluid Mechanics*, 78, 785–819.
33. Chen, C. P., & Blackwelder, R. (1978). Large-scale motion in a turbulent boundary layer: a study using temperature contamination. *Journal of Fluid Mechanics*, 89(2), 1–31.
34. Gad-el-Hak, M., Blackwelder, R. F., & Riley, R. J. (1981). On the growth of turbulent regions in laminar boundary layers. *Journal of Fluid Mechanics*, 110, 73–95.
35. Krishnan, L., & Sandham, N. D. (2006). On the merging of turbulent spots in a supersonic boundary-layer flow. *International Journal of Heat and Fluid Flow*, 27(4), 542–550.
36. Savas, O., & Coles, D. E. (1985). Coherence measurements in synthetic turbulent boundary layers. *Journal of Fluid Mechanics*, 160, 421–446.
37. Makita, H., & Nishizawa, A. (2001). Characteristics of internal vortical structures in a merged turbulent spot. *Journal of Turbulence*, 2(1), 1–14.
38. Horton, H. P. (1968). *Laminar separation in two and three-dimensional incompressible flow*. London: University of London.
39. Roberts, W. B. (1980). Calculation of laminar separation bubbles and their effect on airfoil performance. *AIAA Journal*, 18(1), 25–31.
40. Hatman, A., & Wang, T. (1999). A prediction model for separated-flow transition. *Journal of Turbomachinery*, 121(3), 594–602.

41. Watmuff, J. H. (1999). Evolution of a wave packet into vortex loops in a laminar separation bubble. *Journal of Fluid Mechanics*, 397, 119–169.
42. Roberts, S. K., & Yaras, M. I. (2006). Effects of surface roughness geometry on separation-bubble transition. *Journal of Turbomachinery*, 128(2), 349–356.
43. Rist, U., & Maucher, U. (2002). Investigations of time-growing instabilities in laminar separation bubbles. *European Journal of Mechanics B/Fluids*, 21(5), 495–509.
44. Alam, M., & Sandham, N. D. (2000). Direct numerical simulation of ‘short’ laminar separation bubbles with turbulent reattachment. *Journal of Fluid Mechanics*, 403, 223–250.
45. Roberts, S. K., & Yaras, M. I. (2004) *Boundary-layer transition in separation bubbles over rough surfaces*. ASME Paper GT2004– 53667.
46. McAuliffe, B. R., & Yaras, M. I. (2006). *Numerical study of instability mechanisms leading to transition in separation bubbles*. ASME Paper GT2006-91018.
47. McAuliffe B R, Yaras M I. Transition mechanisms in separation bubbles under low and elevated freestream turbulence. ASME Paper GT2007-27605, 2007.
48. Spalart, P. R., & Strelets, M. K. (2000). Mechanisms of transition and heat transfer in a separation bubble. *Journal of Fluid Mechanics*, 403, 329–349.
49. Yang, Z., & Voke, P. R. (2001). Large-eddy simulation of boundary-layer separation and transition at a change of surface curvature. *Journal of Fluid Mechanics*, 439, 305–333.
50. Ye, J. (2008). *Large-eddy simulation of blade boundary layer spatio-temporal evolution under unsteady disturbances*. Beijing: Beihang University.
51. Zhong, S., Kittichaikarn, C, Hodson, H. P., et al. (1998). *A Study of Unsteady Wake-Induced Boundary Layer Transition with Thermochromic Liquid Crystals*. International Conference on Optical Methods and Data Processing in Heat and Fluid Flow. London: IMechE Press.
52. Zou, Z., & Yun Liang, Y. (2012). *Study on flow mechanism and characteristics of boundary layer in high loading LP turbine blade*. Research Report.
53. Wu, X., Jacobs, R. G., Hunt, J. C. R., et al. (1999). Simulation of boundary layer transition induced by periodically passing wakes. *Journal of Fluid Mechanics*, 398, 109–153.
54. Ye, J., & Zou, Z. (2007). Large-eddy simulation of periodic wake/laminar separation bubble interaction under low Reynolds number conditions. *Journal of Engineering Thermophysics*, 28(2), 215–218.
55. Li, W., Zhu, J., Li, G., et al. (2011). Experimental research on boundary layer behaviors of ultra-high-lift low-pressure turbine profile based on surface-mounted hot-film. *Journal of Aerospace Power*, 26(1), 115–121.
56. Volino, R. J. (2004). *Separated flow transition mechanism and prediction with high and low freestream turbulence under low pressure turbine conditions*. ASME Paper GT2004-53360.
57. Volino, R. J. (2002). Separated flow transition under simulated low-pressure turbine airfoil conditions: Part 1-mean flow and turbulence statistics. *Journal of Turbomachinery*, 124(4), 645–655.
58. Volino, R. J. (2002). Separated flow transition under simulated low-pressure turbine airfoil conditions: Part 2-turbulence spectra. *Journal of Turbomachinery*, 124(4), 656–664.
59. Ibrahim, M., Kartuzova, O., & Volino, R. J. (2008). *Experimental and computational investigations of separation and transition on a highly loaded low pressure turbine airfoil: Part 1-low freestream turbulence intensity*. ASME Paper IMECE 2008-68879.
60. Volino, R. J., Kartuzova, O., & Ibrahim, M. (2008). *Experimental and computational investigations of separation and transition on a highly loaded low pressure turbine airfoil: Part 2-high freestream turbulence intensity*. ASME Paper IMECE 2008-68776.
61. Stadtmüller, P. (2001). *Investigation of wake-induced transition on the LP turbine cascade T106D-EIZ, test case documentation version 1.1*. München: Universität der Bundeswehr München.
62. Stadtmüller, P., & Fottner, L. (2001). *A test case for the numerical investigation of wake passing effects on a highly loaded LP turbine cascade blade*. ASME Paper 2001GT-0311.
63. Zhang, W. (2013). *Studies on flow mechanisms and aerodynamic design of low-pressure turbine*. Beijing: Beihang University.

64. Zhang, W., Zou, Z., Lei, Q., Ye, J., & Lei, W. (2015). Effects of freestream turbulence on separated boundary layer in a low-re high-lift LP turbine blade. *Computers & Fluids*, *109*, 1–12.
65. Zhang, W., Zou, Z., Zhang, H., & Ye, J. *Eddy simulations of separated shear layer behaviors in a high-lift LP turbine*. ASME paper GT2015-43054.
66. Liu, Z., Ye, J., & Zou, Z. (2013). Large-eddy simulation of separated boundary layer transition in low-pressure turbine cascade with and without wakes. *Journal of aerospace power*, *28*(12), 2803–2812.
67. Ho, C., & Huerre, P. (1984). Perturbed free shear layers. *Annual Review of Fluid Mechanics*, *16*, 365–424.
68. McAuliffe, B. R., & Yaras, M. I. (2005) *Separation-bubble transition measurements on a low-Re airfoil using particle image velocimetry*. ASME Paper GT2005-68663.
69. Mui Lin, J. C., & Pauley, L. L. (1996). Low-Reynolds-number separation on an airfoil. *AIAA Journal*, *34*(8), 1570–1577.
70. Talan, M., & Hourmouziadis, J. (2002). Characteristic regimes of transitional separation bubbles in unsteady flow. *Flow, Turbulence and Combustion*, *69*(3–4), 207–227.
71. Luo, H. (2009). *Numerical and experimental investigations on aerodynamic issues of highly-loaded blading design in low-pressure turbine*. Xi'an: Northwestern Polytechnical University.
72. Meyer, R. X. (1958). The effects of wakes on the transient pressure and velocity distributions in turbomachines. *Journal of Basic Engineering*, *80*(7), 1544–1552.
73. Smith, L. H. (1966). Wake dispersion in turbomachines. *Journal of Basic Engineering*, *88* (3), 688–690.
74. Stieger, R. D., & Hodson, H. P. (2004). *The unsteady development of a turbulent wake through a downstream low-pressure turbine blade passage*. ASME Paper GT2004-53061.
75. Howell, R. J. (1999). *Wake separation bubble interactions in low Reynolds number turbomachinery*. UK: Cambridge University.
76. Stieger, R. D. (2002). *The effects of wakes on separating boundary layers in low pressure turbines*. UK: Cambridge University.
77. Zhang, X. F. (2005). *Separation and transition control on ultra-high-lift low pressure turbine blades in unsteady flow*. UK: Cambridge University.
78. Halstead, D. E., Wisler, D. C., Okiishi, T. H., et al. (1997). Boundary layer development in axial compressors and turbines: Part 1 of 4 composite picture. *Journal of Turbomachinery*, *119*(1), 114–127.
79. Halstead, D. E., Wisler, D. C., Okiishi, T. H., et al. (1997). Boundary layer development in axial compressors and turbines: Part 2 of 4 compressors. *Journal of Turbomachinery*, *119* (3), 426–444.
80. Halstead, D. E., Wisler, D. C., Okiishi, T. H., et al. (1997). Boundary layer development in axial compressors and turbines: Part 3 of 4 LP turbines. *Journal of Turbomachinery*, *119*(2), 225–237.
81. Halstead, D. E., Wisler, D. C., Okiishi, T. H., et al. (1997). Boundary layer development in axial compressors and turbines: Part 4 of 4 computations and analyses. *Journal of Turbomachinery*, *119*(1), 128–139.
82. Schulte, V., & Hodson, H. P. (1996). *Unsteady wake-Induced boundary layer transition in high lift LP turbines*. ASME Paper 96-GT-486.
83. Dong, Y., & Cumpsty, N. A. (1990). Compressor blade boundary layers: Part 2-measurements with incident wakes. *Journal of Turbomachinery*, *112*(2), 231–240.
84. Hodson, H. P. (1985). An inviscid blade-to-blade prediction of a wake-generated unsteady flow. *Journal of Engineering for Gas Turbines and Power*, *107*(2), 337–343.
85. Stieger, R. D., & Hodson, H. P. (2003). Unsteady dissipation measurements on a flat plate subject to wake passing. *Proceedings of the Institution of Mechanical Engineers, Part A: Journal of Power and Energy*, *217*(4), 413–419.

86. Hodson, H. P., & Howell, R. J. (2000). Unsteady flow: Its role in the low pressure turbine. In: *9th International Symposium on Unsteady Aerodynamics, Aeroacoustics and Aeroelasticity of Turbomachines*, Lyon, France.
87. Stieger, R. D., & Hodson, H. P. (2003). *The transition mechanism of highly-loaded LP turbine blades*. ASME Paper GT2003-38304.
88. Stieger, R. D., Hollis, D., Hodson, H. P. (2003). *Unsteady surface pressures due to wake-induced transition in a laminar separation bubble on a LP turbine cascade*. ASME Paper GT2003-38303.
89. Vera, M., Hodson, H. P., & Vasquez, R. (2004). *The effects of roughness and unsteadiness on a high speed highly loaded low-pressure turbine blade*. ASME Paper GT2004-53822.
90. Zhang, X. F., & Hodson, H. P. (2004). *The combined effects of surface trips and unsteady wakes on the boundary layer development of an ultra-high-lift LP turbine blade*. ASME Paper GT2004-53081.
91. Chun, S., & Sung, H. J. (2003). Large-scale vortical structure of turbulent separation bubble affected by unsteady wake. *Experiments in Fluids*, 34(5), 572–584.
92. Zhang, W. H., Zou, Z. P., Ye, J., et al. (2012). *Effects of periodic wakes and freestream turbulence on coherent structures in low-pressure turbine boundary layer*. ASME Paper GT2012-69061, 2012.
93. Li, W. (2012). *Investigation on the boundary layer characteristics on ultra-high-lift low-pressure turbine airfoils under steady flow and unsteady wakes*. Beijing: Institute of Engineering Thermophysics, Chinese Academy of Sciences.
94. Liang, Y., Zou, Z., Liu, H., & Zhang, W. (2015). Experimental investigation on the effects of wake passing frequency on boundary layer transition in high-lift low-pressure turbines. *Experiments in Fluids*, 56(4), 1–13.
95. Volino, R. J. (2012). Effect of unsteady wakes on boundary layer separation on a very high lift low pressure turbine airfoil. *Journal of Turbomachinery*, 134, 011011.
96. Binder, A., Schroder, T., & Hourmouziadis, J. (1989). Turbulence measurements in a multistage low-pressure turbine. *Journal of Turbomachinery*, 111(2), 153–161.
97. Schroder, X. (1991). Investigations of blade row interaction and boundary layer transition phenomena in a multistage aeroengine low pressure turbine by measurements with hot-filmprobes and surface-mounted hot-film gauges. *Lecture Series-Von Karman Institute for Fluid Dynamics*.
98. Arndt, N. (1991). *Blade row interaction in a multistage low pressure turbine*. ASME Paper 91-GT-283.
99. Halstead D. E. (1997). Flowfield unsteadiness and turbulence in multistage low pressure turbines. In *Proceedings of the Conference on Boundary Layer Transition in Turbomachines*. Minnowbrook: Syracuse Universit.
100. Hodson, H. P., Huntsman, I., & Steele, A. B. (1994). An investigation of boundary layer development in a multistage LP turbine. *Journal of Turbomachinery*, 116(3), 375–383.
101. Huber, F. W., Sharma, O. P., Gaddis, S. W., et al. (1996). Performance improvement through indexing of turbine airfoils: Part 1-experimental investigation. *Journal of Turbomachinery*, 118(4), 630–635.
102. Griffin, L. W., Huber, F. W., & Sharma, O. P. (1996). Performance improvement through indexing of turbine airfoils: Part 2-numerical simulation. *Journal of Turbomachinery*, 118(4), 636–642.
103. Engber, M., & Fottner, L. (1996). The effect of incoming wakes on boundary layer transition of a highly loaded turbine cascade. In *AGARD Conference Proceedings*.
104. Eulitz, F., & Engel, K. (1998). *Numerical investigations of wake interactions in a low pressure turbine and its influence on loss mechanisms*. ASME Paper 98-GT-563.
105. Miller, R. J., Moss, R. W., & Ainsworth, R. W., et al. (2000). *Wake shock and potential field interactions in a 1.5 stage turbine: Part 1- vane-vane interaction and discussion of results*. ASME Paper 2000-GT-30436.
106. Li, H. D., & He, L. (2003). Blade count and clocking effects on three blade row interaction in a transonic turbine. *Journal of Turbomachinery*, 125(4), 632–640.

107. Kusterer, K., Moritz, N., Bohn, D., et al. (2010). *Transient numerical investigation of rotor clocking in 1.5 stage of an axial test turbine with a blade-to-vane ratio of 1.5*. ASME Paper GT2010-22902.
108. Arnone, A., Marconcini, M., Pacciani, R., et al. (2002). Numerical investigation of airfoiling in a three-stage low-pressure turbine. *Journal of Turbomachinery*, 124(1), 61–68.
109. Höhn, W., & Heinig, K. (2000). Numerical and experimental investigation of unsteady flow interaction in a low pressure multistage turbine. *Journal of Turbomachinery*, 122(4), 628–633.
110. Nayeri, C., & Höhn, W. (2003). *Numerical study of the unsteady blade row interaction in a three-stage low pressure turbine*. ASME Paper GT2003-38822.
111. König, S., & Stoffel, B. (2007). On the applicability of aspoked-wheel generator for clocking investigations. *Journal of Turbomachinery*, 129(11), 1468–1477.
112. König, S., Stoffel, B., & Schobeiri, M. T. (2009). Experimental investigation of the clocking effect in a 1.5-stage axial turbine—Part 1-time-averaged results. *Journal of Turbomachinery*, 131, 021003.
113. König, S., Stoffel, B., & Schobeiri, M. T. (2009). Experimental investigation of the clocking effect in a 1.5-stage axial turbine—Part 2-unsteady results and boundary layer behavior. *Journal of Turbomachinery*, 131, 021004.
114. Behr, T., Porreca, L., Mokuly, T., et al. (2005). Multistage aspects and unsteady effects of stator and rotor clocking in an axial turbine with low aspect ratio blading. *Journal of Turbomachinery*, 128(1), 11–22.
115. Schennach, O., Woisetschläger, J., Fuchs, A., et al. (2007). Experimental investigations of clocking in a one and a half stage transonic turbine using Laser-Doppler-Velocimetry and a fast response aerodynamics pressure probe. *Journal of Turbomachinery*, 129(2), 372–381.
116. Schennach, O., Pecnik, R., Paradiso, B., et al. (2008). The effect of vane clocking on the unsteady flowfield in a one-and-a-half stage transonic turbine. *Journal of Turbomachinery*, 130, 031022.
117. Dawes, W. N. (1990). *A comparison of zero and one equation turbulence models for turbomachinery calculations*. ASME Paper 90-GT-303.
118. Schlichting, H. (1966). *Boundary layer theory* (6th ed.). New York: McGraw-Hill Book Company.
119. Denton, J. D., & Cumpsty, N. A. (1987). *Loss mechanisms in turbomachines*. IMechE Paper C260/87.
120. Truckenbrodt, E. (1955). *A method of quadrature for calculation of the laminar and turbulent boundary layer in case of plane and rotationally symmetrical flow*. NASA TM 1379.
121. Dong, Y., & Cumpsty, N. A. (1989). *Compressor blade boundary layers, Part 1- test facility and measurements with no incident wakes*. ASME Paper 89-GT-50.
122. Dong, Y., & Cumpsty, N. A. (1989). *Compressor blade boundary layers, Part 2-measurements with incident wakes*. ASME Paper 89-GT-51.
123. Addison, J. S. (1990). *Wake-boundary layer interaction in axial turbomachinery*. UK: Cambridge University.
124. Addison, J. S., & Hodson, H. P. (1992). Modelling of unsteady transitional boundary layers. *Journal of Turbomachinery*, 114(3), 580–589.
125. Speidel, L. (1952). 'Beeinflussung der laminaren grenzschicht durch periodische störung der zuströmung. *Z. Flugwiss*, 5(9), 270–275.
126. Hodson, H. P. (1984). *Measurements of wake-generated unsteadiness in the rotor passages of axial flow turbines*. ASME Paper 84-GT-116.
127. Hodson, H. P., Addison, J. S., & Shepherdson, C. A. (1992). Models for unsteady wake-induced transition in axial turbomachines. *Journal Physique III*, 2(4), 545–574.
128. Vilmin, S., Hodson, H. P., Dawes, W. N., et al. (2003) *Predicting wake-passing transition in turbomachinery using an inter-mittency-conditioned modelling approach*. AIAA Paper 2003-3995.

129. Narasimha, R. (1985). The laminar-turbulent transition zone in the boundary layer. *Progress in Aerospace Sciences*, 22(1), 29–80.
130. Gostelow, J. P., & Dey, A. R. (1991). *Spot formation rates—Transitional boundary layers under zero and adverse pressure gradients*. R. Ae. Soc. Conf. Boundary Layer Transition and Control, UK: Cambridge.
131. Mayle, R. E., Dullenkopf K. A. (1989) *Theory for wake-induced transition*. ASME Paper 89-GT-57.
132. Mayle, R. E., & Dullenkopf, K. (1990). *More on the turbulent-strip theory for wake-induced transition*. ASME Paper 90-GT-137.
133. Narasimha, R. (1957). On the distribution of intermittency in the transition region of a boundary layer. *Journal of the Aeronautical Sciences*, 24(9), 711–712.
134. Denton, J. D., & Johnson, C. G. (1976). *An experimental study of the tip leakage flow around shrouded turbine blades*. CEGB Report R/M/N848.
135. Pfau, A., Treiber, M., Sell, M., et al. (2001). Flow interaction from the exit cavity of an axial turbine blade row labyrinth seal. *Journal of Turbomachinery*, 123(2), 342–352.
136. Wolter, K., Giboni, A., Peters, P., et al. (2005). *Experimental and numerical investigation of the unsteady leakage flow through the rotor tip labyrinth of a 1.5-stage axial turbine*. ASME Paper GT2005-68156.
137. Rosic, B., Denton, J. D., & Curtis, E. M. (2008). The influence of shroud and cavity geometry on turbine performance: An experimental and computational study-Part 1: Shroud geometry. *Journal of Turbomachinery*, 130, 041001.
138. Pfau, A., Schlienger, J., Rusch, D., et al. (2005). Unsteady flow interactions within the inlet cavity of a turbine rotor tip labyrinth seal. *Journal of Turbomachinery*, 127(4), 679–688.
139. Axel, P. (2003). *Loss mechanisms in labyrinth seals of shrouded axial turbines*. Zurich: Swiss Federal Institute of Technology Zurich.
140. Rosic, B., Denton, J. D., & Pullan, G. (2006). The importance of shroud leakage modeling in multistage turbine flow calculations. *Journal of Turbomachinery*, 128(4), 669–678.
141. Giboni, A., Wolter, K., Menter, J. R., et al. (2004). *Experimental and numerical investigation into the unsteady interaction of labyrinth seal leakage flow and main flow in a 1.5-stage axial turbine*. ASME Paper GT2004-53024.
142. Anker, J. E., Mayer, J. F., & Casey, M. V. (2005). The impact of rotor labyrinth seal leakage flow on the loss generation in an axial turbine. *Proceedings of the IMechE, Part A: Journal of Power and Energy*, 219(6), 481–490.
143. Porreca, L., Behr, T., Schlienger, J., et al. (2005). Fluid dynamics and performance of partially and fully shrouded axial turbines. *Journal of Turbomachinery*, 127(4), 668–678.
144. Giboni, A., Menter, J. R., Peters, P., et al. (2003). *Interaction of labyrinth seal leakage flow and main flow in an axial turbine*. ASME Paper GT2003-38722.
145. Peters, P., Menter, J. R., Pfost, H., et al. (2005). *Unsteady interaction of labyrinth seal leakage flow and downstream stator flow in a shrouded 1.5-stage axial turbine*. ASME Paper GT2005-68065.
146. Wallis, A. M., Denton, J. D., & Demargne, A. A. J. (2001). The control of shroud leakage flows to reduce aerodynamic losses in a low aspect ratio, shrouded axial flow turbine. *Journal of Turbomachinery*, 123(2), 334–341.
147. Yoon, S., Curtis, E., Denton, J., et al. (2013). The effect of clearance on shrouded and unshrouded turbines at two levels of reaction. *Journal of Turbomachinery*, 136, 021013.
148. Bohn, D. E., Balkowski, I., Ma, H., et al. (2003). *Influence of open and closed shroud cavities on the flow field in a 2-stage turbine with shrouded blades*. ASME Paper GT2003-38436.
149. Bohn, D. E., Krewinkel, R., Tummers, C., et al. (2006). *Influence of the radial and axial gap of the shroud cavities on the flow field in a 2-stage turbine*. ASME Paper GT2006-90857.
150. Peters, P., Breisig, V., Giboni, A., et al. (2000). *The Influence of the clearance of shrouded rotor blades on the development of the flow field and losses in the subsequent stator*. ASME Paper GT2000-0478.

151. Wittig, S. L. K., Dorr, L., & Kim, S. (1983). Scaling effects on leakage losses in labyrinth seals. *Journal for Engineering for Power*, 105(2), 305–309.
152. Martin, H. M. (1908). Labyrinth packing. *Engineering*, 85, 35–36.
153. Karl, T. (1986). *Non contact seal: principle and application of clearance seal and labyrinth seal* (Li J. et al., Trans.). Beijing: China Machine Press.
154. Vermes, G. A. (1961). A fluid mechanics approach to the labyrinth seal leakage problem. *Journal of Engineering Power*, 83(2), 161–169.
155. Rhode, D. L., & Allen, B. F. (2001). Measurement and visualization of leakage effects of rounded teeth tips and rub-grooves on stepped labyrinths. *Journal of Engineering for Gas Turbines and Power*, 123(3), 604–611.
156. Zhu, G. *Analysis of leakage character of a labyrinth piston compressor*. Nanjing: Nanjing University of Aeronautics and Astronautics.
157. Rosic, B., Denton, J. D., & Pullan, G. (2006). The importance of shroud leakage modeling in multistage turbine flow calculations. *Journal of Turbomachinery*, 128(4), 699–707.
158. Gier, J., Engel, K., Stubert, B., et al. (2006). *Modeling and analysis of main flow-shroud leakage flow interaction in LP turbines*. ASME Paper GT2006-90773.
159. Hunter, K. D. & Manwaringm, S. R. (2000). *Endwall cavity flow effects on gas path aerodynamics in an axial flow turbine: Part 2-source term model development*. ASME Paper GT2000-513.
160. Wang, P. (2014). *Investigations on multi-fidelity coupled method and its applications for flow simulation*. Beijing: Beihang University.
161. Zou, Z., Liu, J., Zhang, W., & Wang, P. (2016). Shroud leakage flow models and a multi-dimensional coupling CFD method for shrouded turbines. *Energy*, 103, 410–429.
162. Gier, J., Stubert, B., Brouillet, B., et al. (2003). *Interaction of shroud leakage flow and main flow in a three-stage LP turbine*. ASME Paper No. 2003-GT-38025.
163. Gao, J., Zheng, Q., Yue, G., et al. (2012). Control of shroud leakage flows to reduce mixing losses in a shrouded axial turbine. *Proc. IMechE Part C: Journal of Mechanical Engineering Science*, 226(5), 1263–1277.
164. Rosic, B., Denton, J. D., Curtis, E. M., et al. (2008). The influence of shroud and cavity geometry on turbine performance: An experimental and computational study-Part2: Exit cavity geometry. *Journal of Turbomachinery*, 130, 041002.
165. Adami, P., Milli, A., Martelli, F., et al. (2006). *Comparison of different shroud configurations in high-pressure turbines using unsteady CFD*. ASME Paper GT2006-90442.
166. Schlienger, J., Pfau, A., Kalfas, A. L., et al. (2003) *Effects of labyrinth seal variation on multistage axial turbine flow*. ASME Paper GT2003-38270.
167. Pfau, A., Kalfas, A. I., & Abhari, R. S. (2004). Making use of labyrinth interaction flow. *Journal of Turbomachinery*, 129(1), 164–174.
168. Reid, K. (2005) *Effect of leakage flows on turbine performance* (PhD thesis). Cambridge University, Cambridge.
169. Nirmalan, N. V, & Bailey, J. C. (2005). Experimental investigation of aerodynamic losses of different shapes of a shrouded blade tip section. ASME Paper GT2005-68903.
170. Auyer, E. L. (1954). *United States Patent 2685429*. USA: Assignee General Electric Company.
171. Smile, H. J., & Paulson, E. E. (1960). *United States Patent 2963268[P]*. USA: Assignee General Electric Company.
172. Turnquist, N. A., Tseng, T., Steinetz, B., et al. (1998). *Analysis and full scale testing of an aspirating face seal with improved flow isolation*. AIAA Paper 98-3285.
173. Curtis, E. M., Denton, J. D., Longley, J. P., et al. (2009). *Controlling tip leakage flow over a shrouded turbine rotor using an air-curtain*. ASME Paper GT2009-59411.
174. Hodson, H. P., & Dominy, R. G. (1987). Three-dimensional flow in a low-pressure turbine cascade at its design condition. *Journal of Turbomachinery*, 109(2), 177–185.

175. Moore, J., & Adhye, R. Y. (1985). Secondary flows and losses downstream of a turbine cascade. *Journal of Engineering for Gas Turbines and Power*, 107(4), 961–968.
176. MacIsaac, G. D., Sjolander, S. A., & Praisner, T. J. (2012). Measurements of losses and Reynolds stresses in the secondary flow downstream of a lowspeed linear turbine cascade. *Journal of Turbomachinery*, 134, 061015.
177. Gregory-Smith, D. G., Walsh, J. A., Graves, C. P., et al. (1988). Turbulence measurements and secondary flows in a turbine rotor cascade. *Journal of Turbomachinery*, 110(4), 479–485.
178. Moore, J., Shaffer, D. M., & Moore, J. G. (1987). Reynolds stresses and dissipation mechanisms downstream of a turbine cascade. *Journal of Turbomachinery*, 109(2), 258–267.
179. Lyall, M. E., King, P. I., & Sondergaard, R. (2013). Endwall loss and mixing analysis of a high lift low pressure turbine cascade. *Journal of Turbomachinery*, 135, 051006.
180. Hodson, H. P., & Dominy, R. G. (1987). The off-design performance of a low-pressure turbine cascade. *Journal of Turbomachinery*, 109(2), 201–209.
181. Hodson, H. P., & Addison, J. S. (1988). *Wake-boundary layer interactions in an axial flow turbine rotor at off-design conditions*. ASME Paper88-GT-233.
182. Yamamoto, A., & Nouse, H. (1988). Effects of incidence on three dimensional flows in a linear turbine cascade. *Journal of Turbomachinery*, 110(4), 486–496.
183. Yamamoto, A., Tominaga, J., Matsunuma, T., et al. (1994). *Detailed measurements of three-dimensional flows and losses inside an axial turbine rotor*. ASME Paper 94-GT-348.
184. Brear, M. J., Hodson, H. P., Gonzalez, P., et al. (2001). *Pressure surface separations in low pressure turbines: Part 2 of 2—Interactions with the secondary flow*. ASME Paper 2001-GT-0438.
185. Moore, H., Gregory-Smith, D. G. (1996). *Transition effects on secondary flows in a turbine cascade*. ASME Paper 96-GT-100.
186. Ingram, G. L. (2003). *Endwall profiling for the reduction of secondary flow in turbines*. Durham: University of Durham.
187. Vera, M., de la Rosa, Blanco E., Hodson, H. P., et al. (2009). Endwall boundary layer development in an engine representative four-stage low pressure turbine rig. *Journal of Turbomachinery*, 131, 011017.
188. de la Rosa, Blanco E., Hodson, H. P., & Torre, D. (2003). Influence of the state of the inlet end wall boundary layer on the interaction between pressure surface separation and end wall flows. *Proceedings of the Institution of Mechanical Engineers, Part A: Journal of Power and Energy*, 217(4), 433–442.
189. Kuerner, M., Schrack, D., Gier, J., et al. (2012). Low pressure turbine secondary vortices: Reynolds lapse. *Journal of Turbomachinery*, 134, 061022.
190. Yang, L. (2006). *Investigations of complicated flow mechanism and aerodynamic design method in low pressure turbine at low Reynolds number*. Beijing: Beihang University.
191. Schneider, C. M., Schrack, D., Kuerner, M., et al. (2013). On the unsteady formation of secondary flow inside a rotating turbine blade passage. *Journal of Turbomachinery*, 136, 061004.
192. Ciorciari, R., Kirik, I., Niehuis, R. (2013). *Effects of unsteady wakes on the secondary flows in the linear T106 turbine cascade*. ASME Paper GT2013-94768.
193. Tucker, P. G. (2011). Computation of unsteady turbomachinery flows: Part 1—progress and challenges. *Progress in Aerospace Sciences*, 47(7), 522–545.
194. Tucker, P. G. (2011). Computation of unsteady turbomachinery flows: Part 2—LES and hybrids. *Progress in Aerospace Sciences*, 47(7), 546–569.
195. Tyacke, J., Tucker, P., Jefferson-Loveday, R., et al. (2013). Large eddy simulation for turbines: Methodologies, cost and future outlooks. *Journal of Turbomachinery*, 136, 061009.
196. Ye, J. (2011). *Some improvements on the large-eddy simulation solver for complex compressible flows*. Beijing: Beihang University.

197. Hourmouziadis, J. (1989). *Aerodynamic design of low pressure turbines*. AGARD Lecture Series 167.
198. Schlichting, H., & Kestin, J. (1960). *Boundary layer theory* (4th ed.). New York: McGraw-Hill Book Company.
199. Chen, M. (2002). *Fundamentals of viscous fluid dynamics*. Beijing: Higher Education Press.
200. Volino, R. J., & Hultgren, L. S. (2001). Measurements in separated and transitional boundary layers under low-pressure turbine airfoil conditions. *Journal of Turbomachinery*, 123(2), 189–197.
201. Castner, R., Chiappetta, S., Wyzykowski, J., et al. (2002). *An engine research program focused on low pressure turbine aerodynamic performance*. ASME Paper GT2002-30004.
202. Lake, J. P., King, P. I., & Rivir, R. B. (1999). *Reduction of separation losses on a turbine blade with low Reynolds number*. AIAA Paper 99-0242.
203. Kürner, M., Reichstein, G. A., Schrack, D., et al. (2012). Low pressure turbine secondary vortices: Reynolds lapse. *Journal of Turbomachinery*, 134, 061022.
204. Lipfert, M., Marx, M., Rose, M. G., et al. (2014). A low pressure turbine at extreme off-design operation. *Journal of Turbomachinery*, 136, 031018.
205. Aero Engine Design Handbook Editorial Board. (2000). *Aero engine design handbook, volume 5, turbojet and turbofan engine performance and design*. Beijing: Aviation Industry Press.
206. Mahallati, A., McAuliffe, B. R., Sjolander, S. A., et al. (2013). Aerodynamics of a low-pressure turbine airfoil at low Reynolds numbers—Part I: steady flow measurements. *Journal of Turbomachinery*, 135, 011010.
207. Mahallati, A., & Sjolander, S. A. (2013). Aerodynamics of a low-pressure turbine airfoil at low Reynolds numbers—Part II: blade-wake interaction. *Journal of Turbomachinery*, 135, 011011.
208. Li, W., Zou, Z., & Zhao, X. (2004). The effect of Reynolds number on the characteristics of the low pressure turbine. *Journal of Aerospace Power*, 19(6), 822–827.
209. Wang, S., Liu, X., Zhou, X., et al. (2011). Aerodynamic performance analysis of low pressure turbine at low Reynolds numbers. *Turbine technology*, 53(5), 324–327.
210. Zou, Z., Ning, F., Liu, H., et al. (2004). Effect of Reynolds number on turbine cascade flow. *Engineering thermophysics*, s(2), 216–219.
211. Kürner, M., Schneider, C., Rose, M. G., et al. (2010). *LP turbine Reynolds lapse phenomena: time averaged area traverse and multistage CFD*. ASME Paper GT2010-23114.

Chapter 5

Flow Mechanism in Turbine Rear Frame Ducts

5.1 Geometrical and Aerodynamic Characteristics of Turbine Rear Frame and Their Development Trends

From the perspective of structure, turbine rear frame (TRF) is a part of the engine's load supporting system, which is designed to support the low-pressure rotor. From the perspective of aerodynamics, it is a component of the flow passage, connecting the low-pressure turbine with the exhaust nozzle, and thus it is also called exhaust casing. Figure 5.1 shows the meridian shape and geometry of TRF. In geometry, TRF is an annular pipe, and the diameters of its two ends are close; along the streamwise direction, its inlet connects to the low pressure turbine, and its outlet connects to the exhaust nozzle. Similarly, the inner casing of TRF is called hub, and there are outlet guide vanes (OGVs) between the hub and the casing. These OGVs have the functions of supporting, providing pathways for pipelines, and controlling flows. From the perspective of aerodynamics, OGVs are mainly designed to convert the outlet flow of the low-pressure turbine to axial flow at the cost of lowest total pressure loss, and meanwhile, to prevent flow separation in a wide range of working conditions. Because pipelines need to pass through the OGVs, both their minimum thickness and the 3D modeling methods are restricted. As a result, OGV design is the one of the major difficulties in TRF design. In addition, noise reduction and other factors should also be considered in TRF design.

The design objectives of modern aero-engines are to reduce weight and cost, increase turbine load, and decrease the number of stages. As a result, the inlet guide vanes of TRF always have high inlet prerotation, which makes it more difficult to carry out aerodynamic design for TRF. The structural requirements and the objective of weight reduction always result in complex 3D characteristics of TRF and engine mount recesses. For this reason, TRF designers are paying more and more attention to the influence of complex endwall geometries and engine mounting.

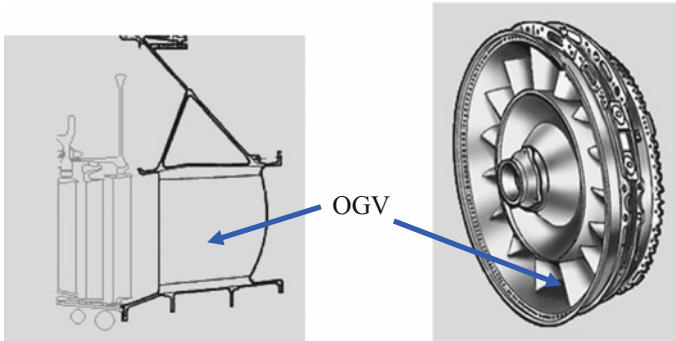


Fig. 5.1 Meridian shape (*left*) and geometry (*right*) of TRF

Table 5.1 TRF duct parameters of high-bypass-ratio turbofan engines

	CFM56-7B	GE90	E3 PW	LEAP-X	GE _{nx}
Aspect ratio	0.99	0.98	1.06	–	1.06
Number of vanes	16	14	30	19	–
Turning angle	–	About 25	43.4	–	–
Inlet reynolds number	–	–	2.88×10^5	–	–
Inlet mach number	–	–	0.503	–	–
Outlet mach number	–	–	0.372	–	–
Tangential lean or not	Yes	No	No	Yes	Yes

Geometrical and aerodynamic parameters of TRF duct of some high-bypass-ratio turbofan engines are listed in Table 5.1 [1].

As can be seen from the table, OGVs in TRF of the current high-bypass-ratio civil engines have relatively small aspect ratio, generally less than 1.2. As a result, secondary flows are strong in the flow passage. For the purpose of weight reduction, the number of OGVs in a TRF is generally less than 20, and thus the relatively low solidity brings challenges to flow control. What's more, rear engine mounts are placed on the TRF, and for the consideration of strength, the mounts are designed to be recessed into the casing to the depth as much as 30% of the inlet passage height of the TRF. However, this geometry may result in flow separation, weaken flow control effect, and seriously influence the aerodynamic performance of the TRF duct. In addition, tilted OGVs are often used in TRF. The reason for this design is that high thermal expansion of the OGVs would result in relative circumferential rotation between the hub and the casing, which can effectively reduce the thermal stress on the casing. Studies in recent years showed that tangentially-tilted OGVs, which intersect with the upstream wakes at a certain angle, can “cut” the wakes, and contribute to reducing the noise of the low-pressure turbine. Therefore, the tangentially-tilted structure has been adopted in many high-bypass-ratio civil

engines in recent years. However, this structure would result in a corner area between the OGVs and the casing or hub, where flows tend to deteriorate, and it also brings new challenges to the aerodynamic design.

From the point of aerodynamic design of turbines, improvement of low-pressure turbine efficiency would effectively increase the overall efficiency of the engine and significantly reduce specific fuel consumption. In order to improve low-pressure turbine efficiency, the outlet flow angle of the low-pressure turbine always has a great deviation from the axial direction, which reaches 30° or even higher in some cases. Undoubtedly, this would increase the difficulty in OGV design. Meanwhile, TRF duct is located downstream of the low-pressure turbine and its flow conditions are influenced by the distribution of flow at the outlet of the upstream component, so it is difficult to guarantee flow control effect and meanwhile prevent flow separation in all the working conditions.

Generally speaking, the main geometrical and aerodynamic characteristics of TRF include small aspect ratio of OGVs, few in number, hangers recessed into the casing, tangentially-tilted OGVs, large turning angle of airflow, and low Mach number at the inlet and low Reynolds number, etc.

5.2 Influence of Geometrical Parameters on Flow Structures and Performance

The number of OGVs is restricted by the requirements of structural strength and weight reduction. As the downstream unit of the low-pressure turbine, the dimensions of its inlet are known, and its outlet dimensions should be limited to a range (with the outlet area basically the same as the inlet area), so as to guarantee low Mach number and reduce leaving-velocity loss. Geometrical parameters of TRF inlet and outlet have small range of choice, and more attention should be given to meridian profile, OGV profile parameters, hanging structure in TRF, and blade surface deformations, which would influence flows in TRF ducts and its performance.

5.2.1 Influence of Meridian Profile of Duct

The meridian profile of the TRF duct has significant influence on flow field distribution, and the influence of different meridian profiles on flows is shown in Fig. 5.2. The modified casing profile moderately narrows down after the thickest point of the OGV, and the hub profile is adjusted to a form of first expanding and then narrowing down so as to match with the changes in OGV thickness. As can be seen from the figure, the modifications have some effects in improving the flow capacity of the TRF duct, reducing the total pressure loss, and changing the flow

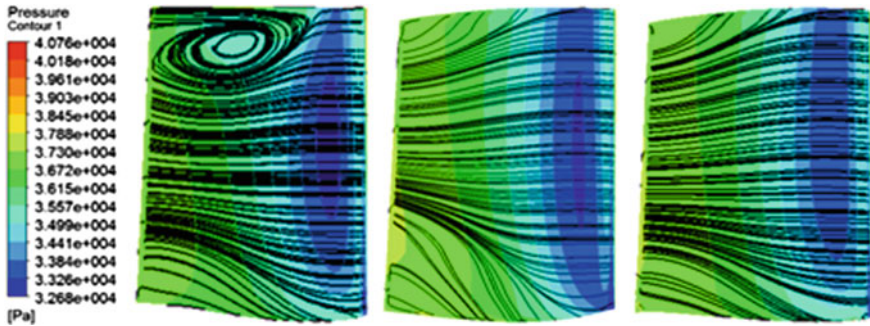


Fig. 5.2 Pressure distribution and limiting streamlines on the suction surface of the cases before and after modifications (*left* original profile; *middle* modified profile 1; *right* modified profile 2)

angle. The streamlines in the figure show the good effects of the modification of the casing profile, with flow separation disappeared completely and secondary flows only existing near the endwall regions. The hub modified profile 1 is not suitable because the range of secondary flows at the blade root shown in the figure increases obviously. From the load distribution at the blade root, it can be seen that there is a strong adverse pressure gradient after the leading-edge suction peak, but the expansion segment of the meridian hub profile in modified profile 1 is so long that it is still in the state of local deceleration after the suction peak; under the situations of deceleration and pressure gradient, the development of secondary flows accelerates obviously. In modified profile 2, the meridian hub profile is adjusted and the expansion segment is shortened. The end point is located near the leading-edge suction peak. It tries to improve the pressure gradient and slow down the development of secondary flows by the local acceleration after the suction peak. With respect to the performance parameters, the total pressure losses of the two modification modes are basically the same, but the streamlines suggest the range of secondary flows at the blade root decreases obviously in modified profile 2. In addition, the pressure distribution in modified profile 2 indicates the radial pressure gradient gets mitigated; the outlet flow angle is reasonably distributed, and the main flow is almost converted to axial flow.

5.2.2 Influence of OGVs' Profile Parameters

OGV profiling is somewhat restricted due to the influence of the oil supply pipe on the blade profile of the OGV. Thus, the influence of blade loading and thickness distribution is mainly discussed in this section.

(1) Influence of blade loading distributions

Sonoda et al. carried out a series of studies on the aerodynamic design of blade profile for TRF. They focused on studying small-scale aero-engines, which only have one low-pressure stage with low bearing requirement for the vanes, so the inlet Mach number of the TRF designed by them was much larger than that of high-bypass-ratio civil engines. In addition, the thickness of the vanes changed little. In spite of this, their design philosophy of blade profile is still useful for reference.

In 2008, Sonoda et al. designed an outlet guide vane cascade by adjusting the blade loading distribution, and concluded that, at low Reynolds number, extreme front loaded pressure distribution(ES) is more helpful to improve the vanes' aerodynamic performance than the conventional controlled diffusion airfoils (CDA) [2]. Experiments on the cascade were carried out at two working conditions respectively with high and low Reynolds numbers, and numerical simulation verification and analysis were performed as well. The experiments were carried out on the high-speed cascade testing rig of Honda Aircraft Company, and the numerical simulation was performed by using the inhouse RANS solver. The $k-\omega$ turbulence model was used at the high-Reynolds-number condition, and the SST turbulence model, supplemented by $\gamma-\theta$ transition model, was used at the low-Reynolds-number condition. The main design philosophy is about making the flow decelerate rapidly at the leading edge of the OGV by extreme front loading and thus inducing boundary layer transition earlier, so as to avoid the additional flow loss caused by laminar separation bubbles. As shown in Fig. 5.3, both the numerical simulation and experimental results suggested the loss caused by the CDA blade at low Reynolds number increased dramatically, while the loss caused by the ES blade at low Reynolds number stayed at low level; the low loss caused by the ES blade, which was significantly less than that by the CDA blade, over a wide range of attack angles.

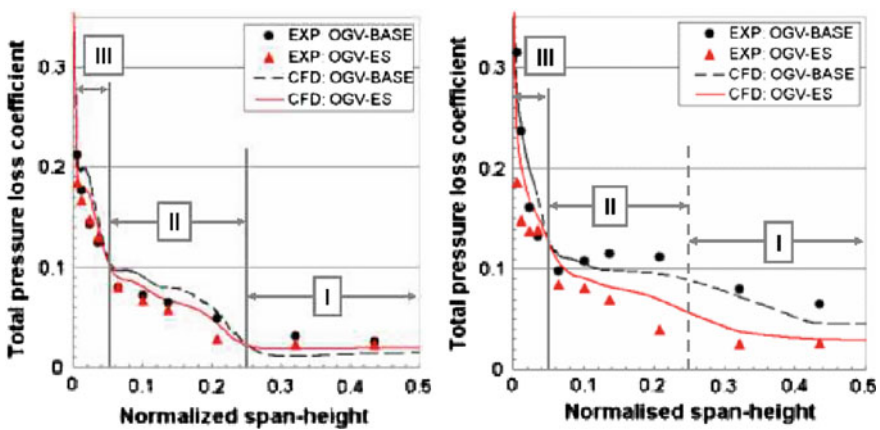
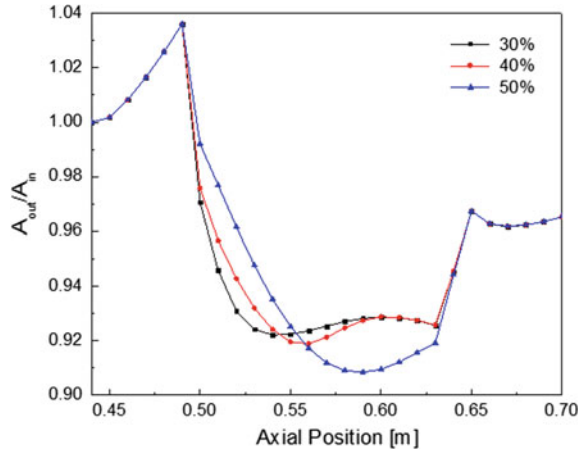


Fig. 5.3 Loss distribution at the OGV outlet in different blade loading forms [2] (left $Re = 8.6 \times 10^5$; right: $Re = 1.2 \times 10^5$)

Fig. 5.4 Flow area distributions with different OGV thickness distributions



(2) Influence of thickness distribution

The flow fields in a TRF duct with three different thickness distributions of OGV were numerically investigated. When the thickest position moved from 30% of the chord length to 40%, the overall parameters of the TRF changed very little. However, when the position further moved to 50% of the chord length, the turning ability of the flow decreased to some degree. The backward moving of the thickest position of the OGV means the contraction of the front of the flow passage becomes slow and the acceleration capability of the leading edge becomes weaker. When the position further moved to 50% of the chord length, flow separation occurred near the trailing edge, which was the main reason for the insufficient turning angle of the flow.

Figure 5.4 shows the flow area distributions in the TRF duct with different OGV thickness distributions. As can be seen from the figure, the backward moving of the thickest position resulted in longer contraction section of the flow passage and weaker acceleration capability of the leading edge, and further reduced the minimum flow area. Under the condition of constant outlet area, after the flow area reached to the minimum, the area expanding gradient would become larger, thus causing the increase of the adverse pressure gradient in the expansion section of the flow passage, which resulted in the flow separation.

5.2.3 Influence of Hanging Structure

Several rear engine mounts (3–5 in general) are installed on the outer wall of the TRF. For the consideration of structural strength, the mounts are generally designed to be recessed towards the flow passage of the TRF to the depth as much as 30% of the inlet passage height of the TRF, so as to reduce the bending moment on the

TRF. The hangers recessed towards the flow passage of the TRF may result in flow separation and the resulting great flow loss, and have negative influence on OGVs' flow control effect. These factors would all result in the decrease of TRF's aerodynamic performance.

In 2007, Hjarne et al. from Chalmers University of Technology studied the influence of hangers on flows and losses in a TRF through experimental investigations and numerical validation [3]. Figure 5.5 shows the measurements of outlet flow angle at the location 0.8 chord length from the outlet section of the OGV, and the hanging depth accounted for about 18.5% of the blade height of the TRF. Due to the influence of the hanging structure, the underturning of the flow with 1 degree deficit is formed near the casing, and the underturning angle kept increasing and reached to the maximum (about 2°) at about 75% of the blade height. Then, the influence of the hanging structure gradually reduced with the increase of the distance to the wall surface, and the underturning angle returned back to 1° at the middle blade section. The experimental results suggest that the hanging structure has significant negative influence on OGVs' flow control effect.

From the spanwise loss distribution at the outlet section, it can be seen that the flow loss at the outlet was generally decrease from the casing to the middle blade section. This is mainly because the hanging structure influenced the vortex structure close to the casing, and the thicker boundary layer caused larger flow loss. Then, the loss reached to the minimum in the area about 0.025–0.04 m from the wall surface, where the wakes were thinnest, and increased again in the area about 0.04–0.07 m from the wall surface because the rapid increase in thickness of the wakes brought about additional flow loss (see Fig. 5.6).

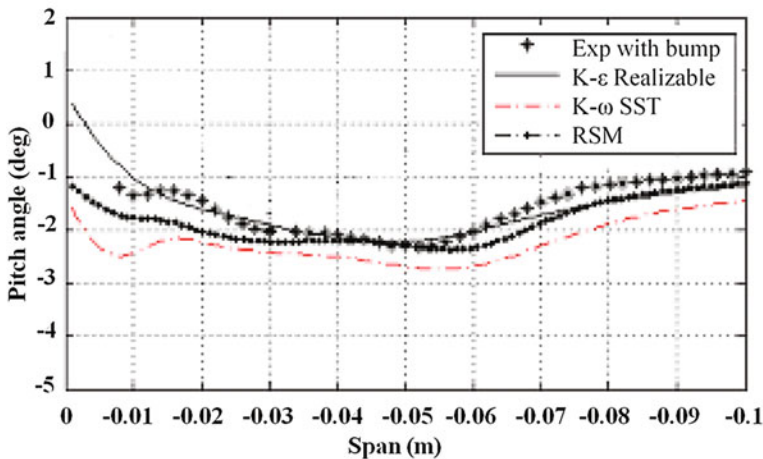
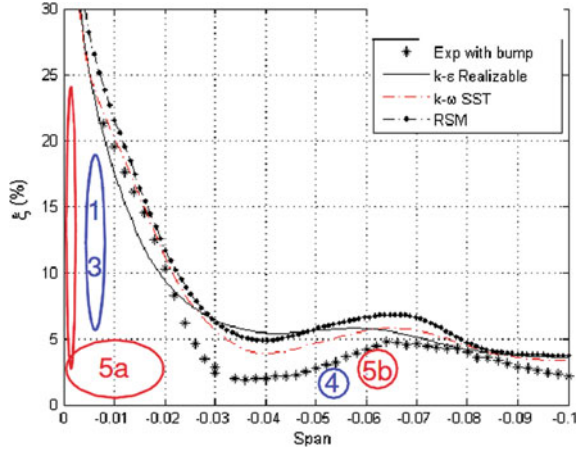


Fig. 5.5 Distribution of outflow angle [3] (from the casing to the middle blade section)

Fig. 5.6 Spanwise distribution of flow loss at the outlet section [3]



5.2.4 Influence of OGV Surface Deformations

According to the data from Volvo Aero Corporation, geometric deformations similar to welding spots would be formed on the surface of TRF of the main high-bypass-ratio turbofan engines in the process of assembly. In addition, considering the severe working conditions of the engines, high temperature erosion and other factors would also result in geometric deformations of TRF in their service period, which may make their aerodynamic performance worse. To study the potential influence of the deformations on TRF, Chernoray et al. from Chalmers University of Technology carried out an experiment study on the influence of geometric deformations in 2010 on the low-speed cascade testing rig, and performed numerical simulation for detailed analysis [4].

Figure 5.7 shows the outlet total pressure loss distributions of deformations at different positions, which can be used in quantitative analysis of deformations' influence on the flow loss in TRF. As can be seen from the figure, deformations at all the positions increased the flow loss ununiformly. However, except for the deformation near the suction peak, which caused a sharp rise in flow loss, deformations at the other positions had little influence. As can be seen from both the loss distribution and wake distribution, deformations had little influence on the near-wall boundary layer, and the additional flow loss was mainly distributed in the region from the middle of the blade to 80% of the blade height.

To find out the sensitivity of the flow in TRF to deformations, 3D numerical simulations were carried out for deformations with a diameter of 3 mm and 5 mm respectively. Both the deformations were located in the 20% axial area where their influence could reach to the highest. Figure 5.8 shows flow structure on the OGV surface with different sizes of deformations, where the red area represents the backflow area (where the axial velocity was less than 0). The comparison showed that the size of deformations had significant influence on the OGV's aerodynamic performance. When the diameter increased from 3 to 5 mm, a large range of corner

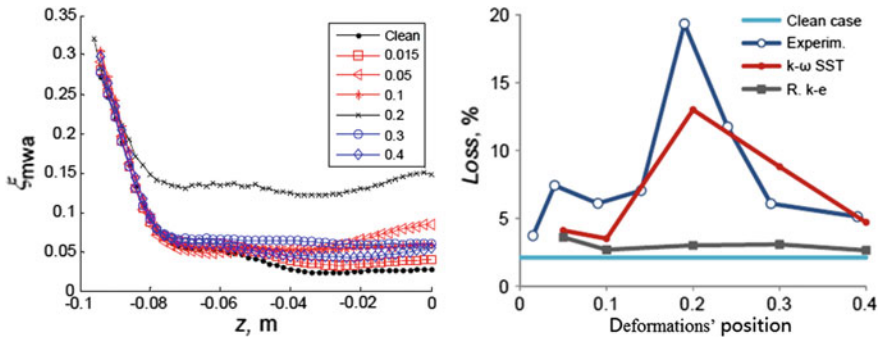
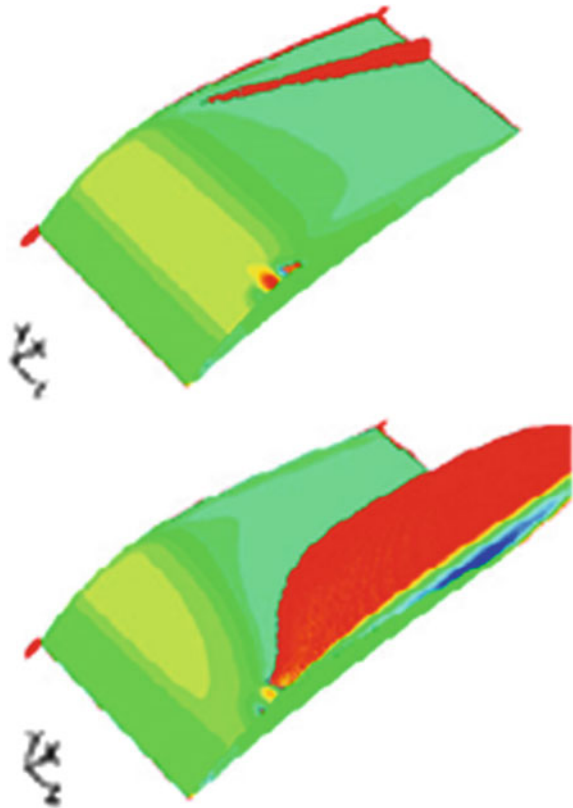


Fig. 5.7 Outlet total pressure loss distributions of deformations at different positions [4]

Fig. 5.8 Flow structures near the OGV with different sizes of deformations



separation was generated near the casing. The following conclusions can be reached: (1) the position of a deformation is the most important influencing factor, which has the largest influence on the flow, so one should try hard to prevent deformations from being generated near the suction peak at the leading edge of the

OGV suction surface; however, the influence of deformations at any position of the pressure surface is very small or even can be neglected; (2) for the deformations at the front of the suction surface of the OGV, their size has significant influence on the OGV's aerodynamic performance; however, for the part insensitive to deformations, even the relatively large deformations have very small or even negligible influence on the flow over the OGV.

5.3 Influence of Aerodynamic Parameters on Flow Structures and Performance

TRF ducts are required to be operating at a wide range of working conditions. Changes of aerodynamic parameters, which are caused by changes of working conditions of the upstream low-pressure turbine, would also influence flows in TRF ducts. The influence of inlet flow angle, turbulence intensity, and inlet Mach number is mainly discussed in this section.

5.3.1 Influence of Inlet Flow Angle

Among inlet conditions, inlet flow angle is one of the most important influencing factors. In order to increase low-pressure turbine efficiency, the outlet flow angle of the low-pressure turbine always has a great deviation from the axial direction, which reaches 30° or even higher in some engines. As a result, the turning angle of the OGVs of TRF should be large.

In 2006, Hjarne et al. carried out an experimental investigation on the low-speed cascade testing rig of Chalmers University of Technology [5], and gave a detailed analysis of the outlet flow field of the TRF ducts as well as the vortex structure. The experimental operating conditions were close to the actual OGV parameters, and parameters were measured at three working conditions, in which the inlet flow angle was respectively 30° (design condition), 20° , and 40° . The main measured parameters included streamwise vorticity and outlet loss distribution.

Figure 5.9 shows the load distribution on the OGV surface. When the inlet flow angle decreased, the load on the OGV would decrease, and so would the strength of vortex systems in the OGV passage and the strength of interaction between the vortex systems. When the inlet flow angle increased, the load on the OGV would increase, so would the strength of vortex systems in the OGV passage and the strength of interaction between the vortex systems. Meanwhile, the load increase would also result in the increase of adverse pressure gradient on the suction surface of the OGV, increase of transverse pressure gradient in the passage, and flow separation on the suction side of the OGV. Figure 5.10 shows the vorticity distribution at the outlet of the TRF passage. As can be seen from the figure, the inflow angle had influence on both the strength of secondary flows in the TRF passage and the vortex structure.

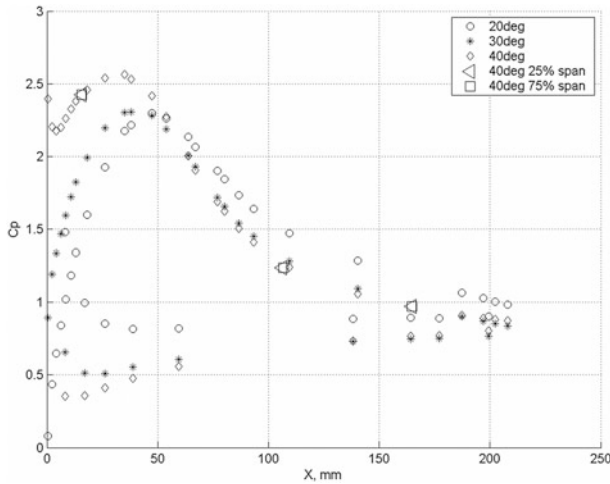


Fig. 5.9 OGV loading distribution at different inlet flow angles [5]

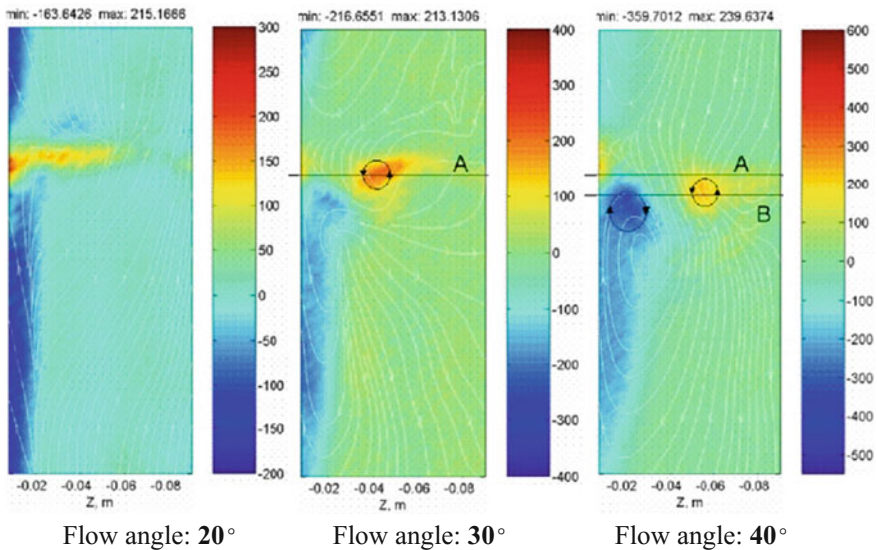


Fig. 5.10 Vorticity distribution at the outlet of the OGV passage at different inlet flow angles [5]

Researchers from Chalmers University of Technology carried out experiments on a TRF duct testing rig, compared the experimental results with numerical simulation results, and studied the influence of off-design conditions on flows and losses in TRF ducts [6]. Off-design conditions were defined as the conditions when the inlet flow angle plus or minus 10° from the design point; the inlet Reynolds number was 2.8×10^5 ; the inlet flow angles in the three conditions were

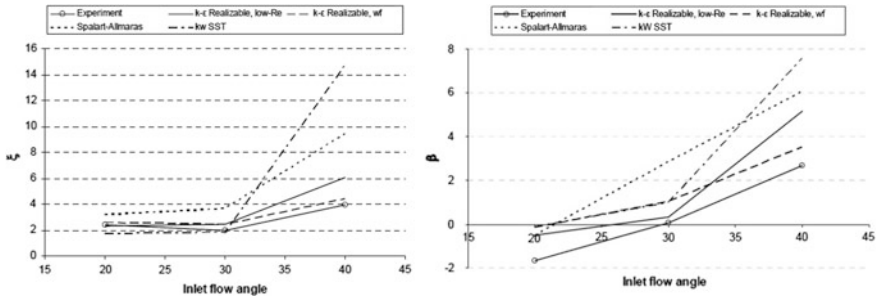


Fig. 5.11 Outlet loss distribution (*left*) and outlet flow angle distribution (*right*) at different inlet flow angles [6]

respectively 20°, 30° (design point), and 40°; the turbulence intensity was 5%. The major measured parameters included blade loading distribution, downstream wake distribution, and loss distribution.

Figure 5.11 shows the outlet loss distribution and outlet flow angle distribution at different inlet flow angle conditions. As can be seen from the figure, the flow loss at off-design points was higher than that at the design point, and the flow loss in the condition with increased deflection angle increased significantly. In the working condition with the inlet flow angle of 40°, the experimental result suggested the outlet flow was underturned by 3 degree, and nearly all the numerical simulation results of losses and flow angles in the off-design conditions were significantly higher than the experimental results.

5.3.2 Influence of Turbulence Intensity

In 2006, Hjarne et al. carried out experiments on the low-speed cascade testing rig of Chalmers University of Technology, and investigated the influence of turbulence intensity on the flow field in the TRF [6]. Changes in turbulence intensity were achieved by setting up a turbulence grid on the upstream. Flows in two turbulence intensity conditions, 5% and turbulence intensity 0.5%, were investigated.

Figure 5.12 shows the loss distribution at the outlet of the TRF duct at different turbulence intensity. With the increase of turbulence intensity, the interaction between vortex systems was enhanced. From the point of loss, in the low turbulence intensity condition, the interaction between vortex systems was relatively weak, and the non-uniformity of the loss distribution was much more obvious than that in the high turbulence intensity condition. However, with the increase of load, the influence of turbulence intensity on flow field characteristics decreased.

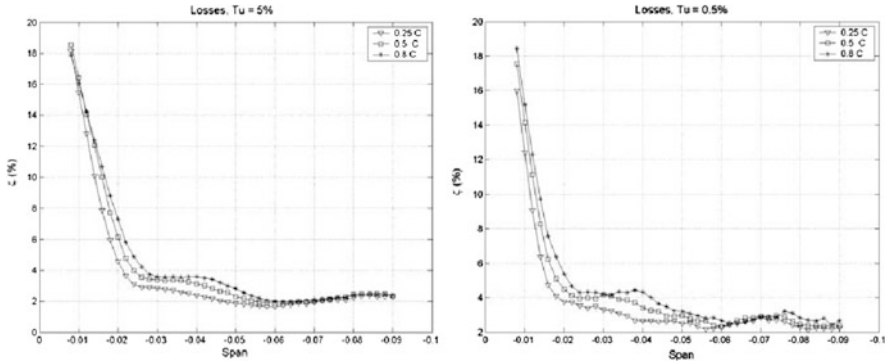


Fig. 5.12 Influence of turbulence intensity [6]

5.3.3 Influence of Inlet Mach Number

In 2006, Sonoda et al. [7] studied two different kinds of OGVs through experiments and numerical simulation. At different angles of attack, the influence of different inlet Mach numbers, especially high Mach numbers, on flows and losses in TRF ducts was studied. The range of the Mach numbers was from 0.5 to 0.87; the range of the attack angle was from -6° to 1.5° ; Re number was 1.2×10^5 . The research results are shown in Fig. 5.13. In the design condition, the loss increased with the increase of the Mach number at a slow rate; at off-design points, the loss increased rapidly with the increase of the Mach number. This trend was even more obvious when using CDA profiles.

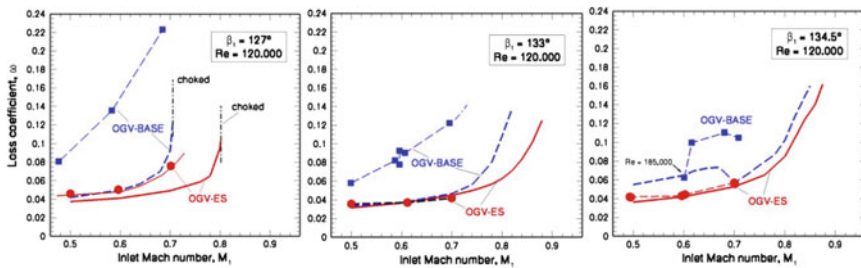


Fig. 5.13 Influence of inflow Mach number on losses at different attack angles [7]

5.4 Methods for Designing TRF Ducts with Large Turning-Angle OGVs

In terms of aerodynamic characteristics, a TRF duct with OGVs is actually similar to a row of compressor guide vanes with extremely low solidity, which operate at low Reynolds number and low Mach number, if difference in thickness and other special factors are neglected. Comparatively speaking, the degree of freedom in aerodynamic design of TRF is very low. Generally, the number of OGVs has been determined by the requirements of structural strength and weight reduction before aerodynamic design. Because the oil supply line is contained in the OGVs, the maximum thickness and stack mode have also been determined. As the downstream unit of the low-pressure turbine, the aerodynamic boundary conditions and geometrical parameters of its inlet are known, and the geometrical parameters of its outlet should be limited to a range (with the outlet area basically the same as the inlet area), so as to guarantee low Mach number and reduce leaving loss. Therefore, OGV profile and meridian passage profile are the main parameters that need to be designed. TRF ducts have two functions in aerodynamics. The first function is flow control. TRF ducts should adjust the outlet flow of the low-pressure turbine to better conditions; specifically, they should make the outlet flow direction to the axial direction, keep outlet Mach number in a reasonable range to reduce leaving loss, and provide uniform distribution of outlet flow. The second effect is noise reduction. The noise at the outlet of the low-pressure turbine could be reduced by adopting reasonable OGV layout (tangentially tilted) and using the unsteady effect of the upstream low-pressure turbine rotor and OGVs. Therefore, the following four guidelines should be followed in aerodynamic design of a TRF duct: the flow loss in the TRF duct itself should meet the qualification; the TRF duct should incur little interference to the unsteady potential of the upstream low-pressure turbine components; it should produce good flow control effects, including uniform outlet flow field, axial outlet flow, and proper outlet Mach number; it should also play a role in noise reduction.

5.4.1 Design of Duct Profile

When selecting meridian profile for a TRF duct, the following two points, which take into account the influence of different meridian profiles on flows in a TRF and its performance, should be considered:

- (1) The casing profile moderately narrows down after the thickest point of the OGV. The local acceleration caused by the meridian passage contraction is expected to reduce the separation at the expansion segment in the rear part of the passage, which results from adverse pressure gradient.

- (2) The hub profile matches with the changes in OGV thickness and the lowest point is set near the thickest point, so as to improve flow area distribution by means of area compensation.

5.4.2 Design of OGV Profile

OGV profile selection is restricted by the inner oil supply line, so the maximum thickness and stack mode have been almost determined. Thus, selection of blade loading distributions, or thickness distributions in terms of design parameters, should be mainly considered.

The flow area in the second half of the TRF passage expands rapidly due to the rapid decrease of OGV thickness after the thickest point, and thus there is relatively strong adverse pressure gradient in the flow field. Extreme front-loaded distribution is helpful to reduce the transverse pressure gradient in the expansion segment and avoid flow separation in the second half of the flow field. Meanwhile, the extreme front-loaded form can induce boundary layer transition very early, thus helping to avoid the additional flow loss caused by laminar separation bubbles. To realize the extreme front-loaded distribution, the thickest position should be placed at the front as far as possible. In this way, the axial distance to the upstream rotor will be small, so the leading-edge radius should not be too large, so as to avoid enhancing the potential interference to the upstream rotor. In addition, relatively high trailing edge thickness is helpful to improve the pressure gradient in the second half of the flow passage.

Except for the size-uniformity scheme, the non-uniformity scheme with both large and small OGVs can also be used. The basic purpose of the scheme is to separate the OGVs as supporting structures and the OGVs for guiding flows. Because supporting struts are responsible for supporting load and providing pathway for pipelines, they have higher maximum thickness and are not allowed to bear high bending. However, large thickness means greater aerodynamic loss for the guide vanes. To reduce design difficulty, increase design space, and further lower structural weight and flow loss, the supporting struts should be designed as “large struts” with large chord length and thickness, and the guide vanes should be designed as “small struts” with small chord length and thickness. In this way, the large struts can meet the structural requirements, and the small struts can meet the aerodynamic requirements for flow control as far as possible through the 3D profiling techniques, such as using skewed or swept blades.

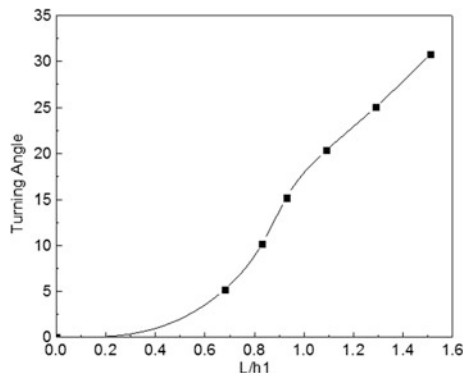
For the small struts, their trailing edge should be flush against that of the large struts in the axial direction, so as to ensure they are located in the same slot where the large struts are located. Because the small struts have shorter chord length, in the case of large deflection angle, their separation-resisting capability is lower than that of the large struts. Keeping the trailing edge flush can reduce the actual attack angle of the small struts, decrease the load, and avoid separation. In addition, this

measure can also effectively decrease the load on the rear part of the large struts, reduce the overall adverse pressure gradient on the large struts, and lower the risk of flow separation on the large struts. Their circumferential positions should be determined based on the inlet conditions. In general, the passage should be kept at basically the same degree of convergence, and the small struts could be placed uniformly in the passage of the large struts. In the case of large turning angle, the small struts could be shifted towards the suction surface of the large struts, so as to reduce the adverse pressure gradient on the suction side of the large struts and thus lower the risk of flow separation on the large struts.

5.4.3 Selection of Axial Length of the Duct

There is almost no area expansion in TRF ducts, so the most important geometrical parameter is axial length (dimensionless). Shortening the axial length is helpful to reduce engine weight. The axial length of the TRF is mainly determined by its aerodynamic load, namely the turning angle. Figure 5.14 presents the relation between load and the geometrical parameter of a TRF duct. As can be seen from the figure, with the increase of the inlet flow angle, the aerodynamic load of the TRF increases and larger relative length is required accordingly. However, the relation is not linear; the larger the inlet flow angle, the higher the required increment of relative length will be. It should be noticed that the inlet boundary conditions used here are in linear distribution. However, in actual engines, the outlet aerodynamic parameter of the low-pressure turbine is always poor in uniformity, and thus the relative length required for flow control is often larger. Therefore, by taking the curve as a boundary, the lower right area of the boundary is regarded as the “safe area”, while selecting the parameter from the upper left area may result in larger possibility of flow separation.

Fig. 5.14 Relation between turning angle and axial length of TRF ducts



References

1. Turner, M. G. (2000). *Full 3D analysis of the GE90 turbofan primary flowpath [R]*. NASACR-209951.
2. Sonoda, T., Schreiber, H. A., & Arima, T. (2008). *Endwall performance of outlet guide vane cascades with different blade loading distributions [R]*. ASME Paper GT2008-51111.
3. Hjärne, J., Chernoray, V., & Larsson, J. (2008). *Experimental investigations and numerical validation of an outlet guide vane with an engine mount recess [R]*. ASME Paper GT2008-50168.
4. Chernoray, V., Ore, S., & Larsson, J. (2010). *Effect of geometry deviations on the aerodynamic performance of an outlet guide vane cascade [R]*. ASME Paper GT2010-22923.
5. Hjärne, J., Larsson, J., & Löfdahl, L. (2006). *An experimental investigation of secondary flows and loss development downstream of a highly loaded low pressure turbine outlet guide vane cascade [R]*. ASME PaperGT2006-90561.
6. Hjärne, J., Larsson, J., & Löfdahl, L. (2006). *Performance and off-design characteristics for low pressure turbine outlet guide vanes: measurements and calculations [R]*. ASME Paper GT2006-90550.
7. Sonoda, T., & Schreiber, H. A. (2007). Aerodynamic characteristics of supercritical outlet guide vanes at low reynolds number conditions [J]. *Journal of Turbomachinery*, 129(4), 694–704.

Chapter 6

Aerodynamic Design Technologies for Turbines

6.1 Introduction to Aerodynamic Design Process for Turbines

Aerodynamic design of turbines is a process of progressive design and optimization from low dimensions to high dimensions, and the design results obtained in low-dimensional space serve as the basis of high-dimensional design. Figure 6.1 presents a typical turbine design process. In general, the first step of turbine aerodynamic design is to carry out one-dimensional aerodynamic analysis according to overall design requirements. The major work is to reasonably select dimensionless design parameters for each turbine stage to determine velocity triangles at the middle spanwise location and then work out the shape of the meridional flow passage. During this process, basic aerodynamic and geometric parameters should be reasonably selected and even fully optimized if needed after that, the design work goes to the two-dimensional space. Select a reasonable twist law for each turbine stage to obtain velocity triangles at different spanwise locations, and calculate key aerodynamic parameters of each turbine stage through S2 streamsurface inverse analysis. Then, with the inlet and outlet flow angles known, blade section profiling at different spanwise location can be carried out, with its reasonableness verified by S1 streamsurface simulation. Based on that, three-dimensional blade profiling is then carried out to organize flows in the passage by taking full advantage of stacking methods, such as skewing, sweeping and twisting. Overall performance and parameter distributions of each turbine stage are then obtained through S2 streamsurface or quasi-3D numerical simulation, and preliminary flow analysis is performed. If the design results meet relevant requirements, three-dimensional numerical simulation is then carried out to perform a more detailed diagnosis of internal flow field in the turbine and a comprehensive evaluation of the turbine's overall performance. Refined design methods are employed to organize internal flow more reasonably, furthering improving the turbine performance. Of course, aerodynamic design of turbine is an iterative process of design and optimization, in which

low-dimensional parameters can directly affect high-dimensional design results which, in turn, serve as feedback and guidance for low-dimensional optimal design. It is worth noting that accuracy of low-dimensional analysis is closely related to the prediction accuracy of the adopted aerodynamic loss models. Complete aerodynamic loss models and database, which have been established through long-term studies, are the important guarantee for a successful turbine design. Meanwhile, three-dimensional numerical simulation cannot be trusted blindly, since the accuracy is influenced by numerous factors.

This chapter mainly introduces methodologies and technologies involved in the aerodynamic design process of turbines, such as aerodynamic loss models, selection of geometric and aerodynamic parameters in low-dimensional space, blade profiling methods, three-dimensional blade stacking methods, and refined flow organizing

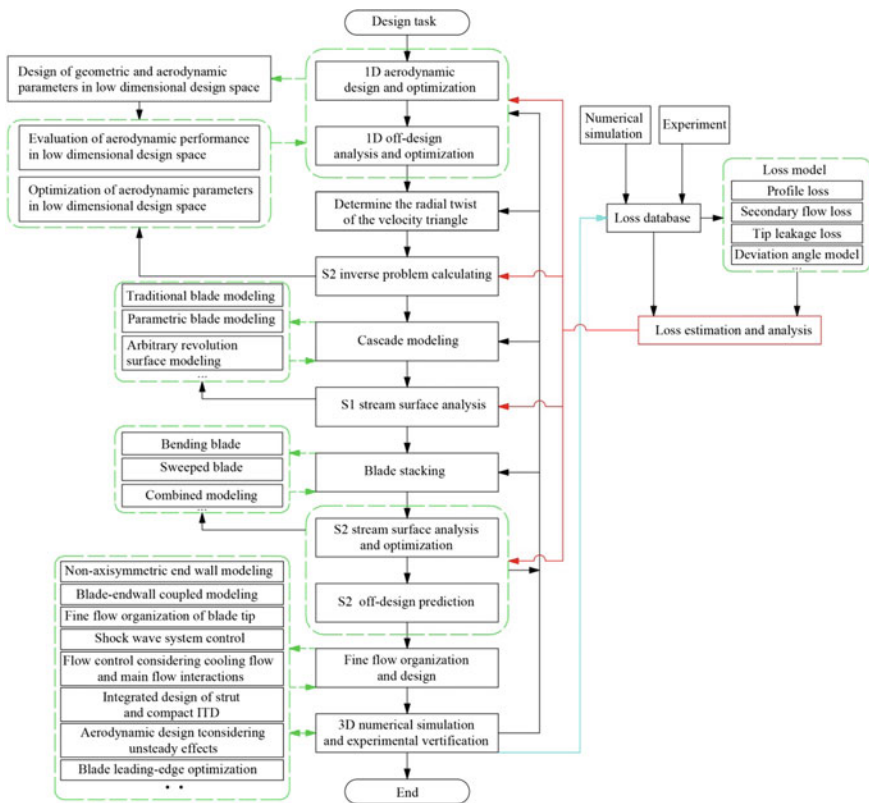


Fig. 6.1 Flowchart of aerodynamic design for turbines

and design. Due to limited space, this book does not introduce the design of turbine cooling, and more study work about this aspect can be found out from some relevant Refs [1–3].

6.2 Aerodynamic Loss Models for Turbines

Viscous flows in turbines are complicated, with strong three-dimensionality, shearing and unsteadiness. Flow features like viscous dissipation, shear mixing, and shock waves would result in various aerodynamic losses, such as profile loss, secondary loss, tip leakage loss, and cooling air mixing loss, and these losses would lead to variations of pass-flow and power capacity of the turbine. How to model and quantify these losses is of great significance in turbine design.

Profile loss refers to flow losses resulting from the boundary layer on the blade surface, wake and turbulent dissipation, and its magnitude mainly depends on blade-surface potential flow velocity, blade surface roughness, Reynolds number, blade surface area, and other factors. In addition to boundary layer loss, the vortex system caused by the separation of the boundary layer at the trailing edge and the mixing of the wake with the main flow would also result in trailing edge loss and wake mixing loss respectively. In transonic turbines, interaction between shock waves and boundary layer would also lead to loss. All the above losses can be classified as profile loss. In addition, because of the fluid viscosity and pressure gradient in flow passage, complex vortexes exist in the endwall regions, and the interaction between vortexes and the main flow would result in serious secondary loss. This phenomenon is much more obvious and complicated at the tip of the rotor blade. Leakage flows in the tip clearance would not only impair the power capacity of flows at the tip of the rotor blade, but also aggravate blockage in the tip passage. Both viscous effect of flows in the tip clearance and the mixing between the main flow and the leakage flows at the outlet of the clearance would lead to serious tip leakage loss, which is one of the main sources of turbine aerodynamic losses. Furthermore, cooling air flows in high-temperature turbines, such as air film on blades and end-wall coolant air flows, would mix with the main flow to a great extent, thus resulting in significant cooling air mixing loss. To accurately evaluate and analyze the influence of design parameters on turbine aerodynamic performance at the beginning of the turbine design process, it is of great importance and necessity to establish appropriate models to quantify these losses.

As early as the mid-twentieth century, researchers have worked out empirical correlations of loss based on analysis of aerodynamic loss mechanisms in turbines, established models for calculating aerodynamic losses in cascade passage of axial-flow turbines, and made gradual improvements to these models to quantitatively evaluate turbines' one-dimensional or mid-span section performance. For example, through a series of improvements to the Ainley and Mathieson model proposed by Ainley and Mathieson in 1957 [4], Dunham and Came established the

AMDC loss model, which has been widely applied in engineering field to predict turbine performance at both design and off-design conditions [5]. Kacker and Okapuu [6] further improved the model and established the AMDCKO model. In addition, there are many other aerodynamic loss models that can be used in aerodynamic design for turbines, such as the Soderberg model [7], Traupel model [8], Steward model [9], Balje and Binsley model [10], Craig and Cox model [11], and Denton model [12–14]. To further distinguish the sources of aerodynamic losses, researchers have also developed the Ehrich and Detra model [15], Scholz model [16], Hawthorne model [17], Boulter model [18], and Lakshminarayana model [19] to evaluate secondary loss or tip leakage loss individually, and the Ito model and Lakshminarayana model [20, 21] to evaluate cooling air mixing loss. These aerodynamic loss models have their own characteristics, and some representative models are introduced in this section. It is worth noting that different models are different in application range and precision, and thus particular attention should be paid when using them. As ranges of turbine design parameters change, loss models need to be improved continuously. Improving existing loss models or even establishing new loss models is an important research content of building the next-generation turbine design system.

6.2.1 Deviation Angle Model

The deviation between the actual flow angle and the blade metal angle, i.e. the deviation angle, shall be obtained accurately in low-dimensional design and evaluation, so as to ensure the validity of blade profiling and calculation results. For this reason, the deviation angle model needs to be established. As working condition of a turbine changes, the outlet flow angle of a blade row would change as well. According to the literature [22], the outflow angle of a blade row can be obtained by the following equation:

$$\alpha_1 = \sin^{-1}(o/s) + \Delta\alpha_1 + \delta \quad (6.1)$$

In Eq. (6.1), o is the blade throat opening; s is the blade pitch; $\Delta\alpha$ is the deviation angle; δ is the supersonic fluid deflection angle at the oblique incision of the blade cascade. It is worth noting that the outflow angle, α_1 , is defined as the included angle between the airflow direction and the tangential direction. The deviation angle and the deflection angle are mainly related to the absolute Mach number at the outlet of stator, M_{c1} :

When $M_{c1} \leq 0.5$,

$$\Delta\alpha_1 = (\Delta\alpha_1)_{M_{c1}=0.5}; \quad \delta = 0^\circ \quad (6.2)$$

When $0.5 < M_{c1} \leq 1.0$,

$$\Delta\alpha_1 = (\Delta\alpha_1)_{M_{c1}=1.0} + 2(1 - M_{c1}) \left[(\Delta\alpha_1)_{M_{c1}=0.5} - (\Delta\alpha_1)_{M_{c1}=1.0} \right]; \quad \delta = 0^\circ \quad (6.3)$$

When $M_{c1} > 1.0$,

$$\Delta\alpha_1 = (\Delta\alpha_1)_{M_{c1}=1.0}; \quad \delta = \sin^{-1} \left[\frac{\frac{\sigma}{s}}{q(\lambda_{c1})} \right] - \sin^{-1} \left(\frac{\sigma}{s} \right) \quad (6.4)$$

In Eq. (6.2), Eq. (6.3), and Eq. (6.4), deviation angles, $(\Delta\alpha_1)_{M_{c1}=0.5}$ and $(\Delta\alpha_1)_{M_{c1}=1.0}$, can be written as:

$$\begin{aligned} (\Delta\alpha_1)_{M_{c1}=0.5} &= 0.0001\alpha_{1ef}^3 - 0.00925\alpha_{1ef}^2 + 0.4135\alpha_{1ef} - 4.42875 + 4.2(s/R_c) \\ (\Delta\alpha_1)_{M_{c1}=1.0} &= C_1 + C_2\alpha_{1ef} + C_3\alpha_{1ef}^2 + C_4\alpha_{1ef}^3 \end{aligned} \quad (6.5)$$

In Eq. (6.5), α_{1ef} is the effective outflow angle; R_c is the relative radius of curvature of the suction side; coefficients, C_1, C_2, C_3, C_4 , are related to s/R_c :

When $s/R_c = 0.0 \sim 0.3$,

$$\begin{aligned} C_1 &= 7.29167(s/R_c)^3 + 3.65625(s/R_c)^2 - 4.91979(s/R_c) \\ C_2 &= 1.43056(s/R_c)^3 - 1.11875(s/R_c)^2 + 0.812153(s/R_c) \\ C_3 &= -0.125(s/R_c)^3 + 0.06375(s/R_c)^2 - 0.025875(s/R_c) \\ C_4 &= 0.002778(s/R_c)^3 - 0.00125(s/R_c)^2 + 0.0003139(s/R_c) \end{aligned}$$

When $s/R_c > 0.3 \sim 0.6$,

$$\begin{aligned} C_1 &= 1.45833(s/R_c)^3 - 10.75(s/R_c)^2 + 8.46453(s/R_c) - 2.4325 \\ C_2 &= -0.153778(s/R_c)^3 + 1.61667(s/R_c)^2 - 0.885972(s/R_c) - 4.306 \\ C_3 &= 0.025(s/R_c)^3 - 0.08(s/R_c)^2 + 0.04475(s/R_c) - 0.0123 \\ C_4 &= -0.0005533(s/R_c)^3 + 0.0011337(s/R_c)^2 - 0.0006946(s/R_c) + 0.00016 \end{aligned}$$

The deviation angle at the outlet of rotor, $\Delta\beta_2$, can be obtained by the above equations as well, in which M_{c1} should be replaced with the relative Mach number at the outlet of rotor, M_{rel2} .

6.2.2 Ainley and Mathieson Loss Model

As early as 1951, Ainley and Mathieson obtained a large number of data through a series of experiments for measuring performance parameters of conventional turbine blades, and established an aerodynamic loss model based on data analysis [4]. In this model, it is assumed that the total pressure loss coefficient of a turbine blade is unaffected by the Mach number, and that the outflow angle is unaffected by the incidence angle. The total loss is divided into three components, namely the profile loss, the secondary loss, and the tip leakage loss, and the trailing edge loss is included in the total loss by adding a correction factor. Thus, the total loss can be written as:

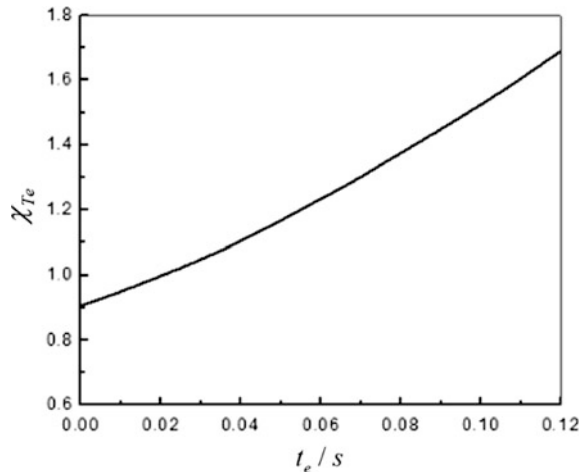
$$Y = (Y_p + Y_s + Y_{Tl}) \cdot \chi_{Te} \quad (6.6)$$

In Eq. (6.6), Y , Y_p , Y_s , and Y_{Tl} respectively represent the total loss coefficient, the profile loss coefficient, the secondary loss coefficient, and the tip leakage loss coefficient; χ_{Te} is the correction factor used to take the trailing edge loss into account, which is related to the ratio of trailing-edge thickness to blade pitch, t_{Te}/s , as shown in Fig. 6.2. The Ainley and Mathieson loss model is applicable for predicting losses of conventional turbine blades and enjoys good prediction accuracy in a wide range of working conditions: deviation of mass flow rate in turbine passage is about $\pm 2.0\%$; peak efficiency deviation is about $\pm 3.0\%$. Y_p , Y_s , and Y_{Tl} are determined as follows:

(1) Profile loss

After experimental measurements and data analysis of aerodynamic parameters of a series of turbine blades with different thickness (the relative maximum thickness $t_{\max}/c \in [0.15, 0.25]$), Ainley and Mathieson came to the conclusion that the profile loss coefficient of a blade row, Y_p , is a function of the inlet blade metal angle, β_{1k} ,

Fig. 6.2 Trailing edge correction factor in Ainley and Mathieson loss model [4]



the inflow angle, α_1 , the outflow angle, α_2 , the relative blade pitch, s/c , the relative maximum thickness, t_{\max}/c , and the relative trailing-edge thickness, t_{Te}/s , and is given by:

$$Y_{P(i=0)} = \left\{ Y_{P(\beta_{1k}=0)} + \left(\frac{\beta_{1k}}{\alpha_2} \right)^2 [Y_{P(\beta_{1k}=-\alpha_2)} - Y_{P(\beta_{1k}=0)}] \right\} \left(\frac{t_{\max}/c}{0.2} \right)^{-\frac{\beta_{1k}}{\alpha_2}} \quad (6.7)$$

where, $Y_{P(i=0)}$ is the profile loss coefficient under the design condition (zero incidence); the outflow angle, α_2 , is defined as the included angle between the airflow direction and the axial direction, and the sign convention of the angle is defined in Fig. 6.3; $Y_{P(\beta_{1k}=0)}$ is the profile loss coefficient of a cascade with $\beta_{1k} = 0$ and the same α_2 and s/c as the actual cascade; $Y_{P(\beta_{1k}=-\alpha_2)}$ is the profile loss coefficient of a cascade with $\beta_{1k} = -\alpha_2$ and the same α_2 and s/c as the actual cascade (namely, large turning angle cascade). When the relative maximum thickness of a cascade $t_{\max}/c \in [0.15, 0.25]$, the relationship between the total pressure loss coefficients, $Y_{P(\beta_{1k}=0)}$ and $Y_{P(\beta_{1k}=-\alpha_2)}$, at different outflow angles and relative blade pitches s/c is plotted in Fig. 6.4a, b.

Under off-design conditions, the profile loss coefficient can be obtained by multiplying the profile loss coefficient under the design condition by an incidence coefficient, as shown below:

$$Y_p = \chi_i Y_{P(i=0)} \quad (6.8)$$

In Eq. (6.8), χ_i is the incidence coefficient. The stall incidence angle of a blade should be first determined in order to determine χ_i , and the stall incidence angle is a function of relative blade pitch, s/c , the outflow angle, α_2 , and β_{1k}/α_2 . The procedure for determining the stall incidence angle is described as follows: (1) use Fig. 6.5b to determine the outflow angle of the “equivalent cascade”, according to the relative blade pitch of the actual blade; (2) use Fig. 6.5c to determine the stall incidence angle of the “equivalent cascade”, according to the cascade’s actual inlet blade metal angle and the outflow angle of the “equivalent cascade”; (3) use Fig. 6.5a to determine the correction of the stall incidence angle for the actual cascade relative to the “equivalent cascade”, according to the relative blade pitch of the actual cascade, and then obtain its stall incidence angle. After determining the stall incidence angle of a cascade, $i_{(stall)}$, its incidence coefficient under off-design

Fig. 6.3 Definition of angles in Ainley and Mathieson loss model



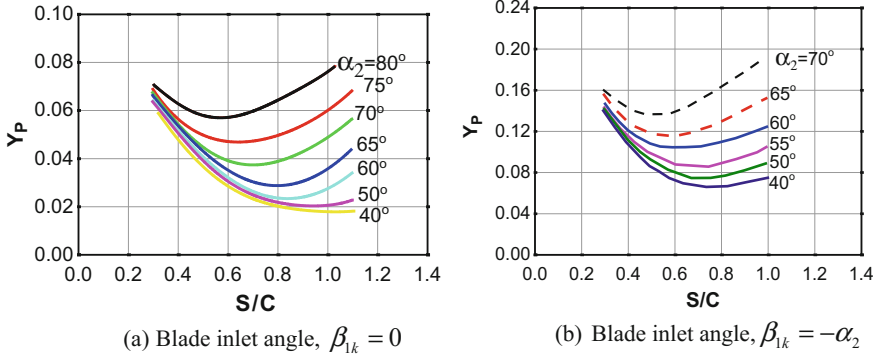


Fig. 6.4 Profile loss coefficients at zero incidence in Ainley and Mathieson loss model [4] (relative maximum thickness $t_{max}/c = 0.2$, Reynolds number $Re = 2 \times 10^5$, $M < 0.6$)

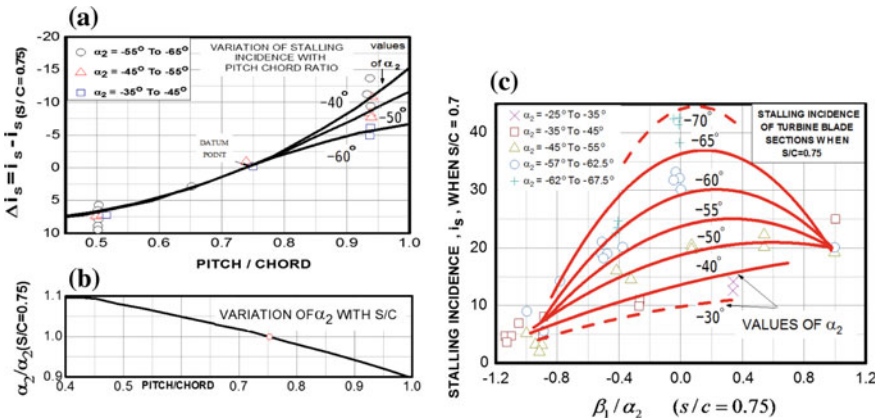


Fig. 6.5 Determination of stalling incidence for a turbine cascade in Ainley and Mathieson loss model ($Re = 2 \times 10^5$, $M < 0.6$) [4]

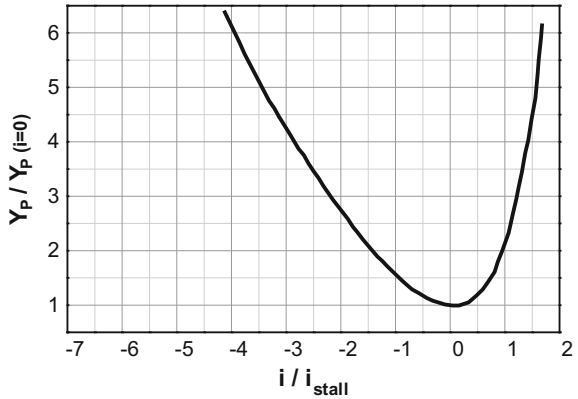
conditions, $\chi_i = Y_p/Y_{p(i=0)}$, can be then determined by using Fig. 6.6 and the ratio of incidence, i , to stall incidence angle, $i_{(stall)}$.

(2) Secondary loss

Ainley and Mathieson thought that flows in the endwall regions depend on the development of endwall boundary layer, when the tip clearance is not taken into consideration. Based on analysis of experimental data, they worked out the following equation to express the drag coefficient of secondary flows, C_{Ds} , [4]:

$$C_{Ds} = \lambda C_L^2 / (s/c) \tag{6.9}$$

Fig. 6.6 Profile loss coefficients of a turbine cascade at different incidence angles in Ainley and Mathieson loss model [4]



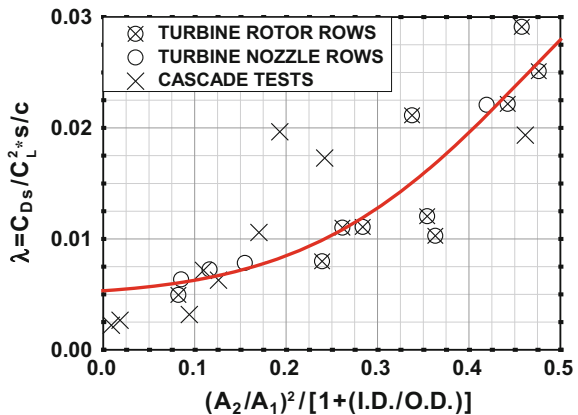
In Eq. (6.9), C_L is the lift coefficient; λ is a parameter of acceleration imparted to the gas as it flows through the blade passage, which is a function of the inlet-to-outlet area ratio of the blade row and the hub-to-shroud ratio, as shown in Fig. 6.7. In this figure, A_1 and A_2 respectively represent the inlet area and outlet area of the blade row, which are measured perpendicular to the flow direction; $I.D.$ and $O.D.$ respectively represent the hub diameter and the shroud diameter of the blade row. The lift coefficient, C_L , is a function of the relative blade pitch and the inflow and outflow angles, and is given by:

$$C_L = 2(s/c)(\tan \alpha_1 - \tan \alpha_2) \cos \alpha_m \tag{6.10}$$

where, α_1 is the inflow angle, defined as the included angle between the flow direction and the axial direction; α_m is the average flow angle of the cascade, and is given by:

$$\alpha_m = \tan^{-1}[(\tan \alpha_1 + \tan \alpha_2)/2] \tag{6.11}$$

Fig. 6.7 Secondary loss coefficient of blade row in Ainley and Mathieson loss model [4]



Having determined C_{Ds} , the secondary loss coefficient, Y_s , can be obtained by using the equation below:

$$Y_s = C_{Ds}(\cos^2 \alpha_2 / \cos^3 \alpha_m)(s/c) \quad (6.12)$$

Or,

$$Y_s = 4\lambda(\tan \alpha_1 - \tan \alpha_2)^2 \left(\frac{\cos^2 \alpha_2}{\cos \alpha_m} \right) \quad (6.13)$$

(3) Tip leakage loss

In the Ainley and Mathieson loss model, the drag coefficient, C_{Dk} , caused by the tip leakage pressure loss is written as:

$$C_{Dk} = B(k/h)C_L^2/(s/c) \quad (6.14)$$

where, k is the tip clearance height of rotor; h is the blade height; B is a constant: $B = 0.25$ for the blade row with shroud seals, $B = 0.5$ for the blade row without shroud seals.

The tip leakage loss coefficient, Y_{TI} , is given by:

$$\begin{aligned} Y_{TI} &= C_{Dk}(\cos^2 \alpha_2 / \cos^3 \alpha_m)/(s/c) \\ &= 4B(k/h)(\tan \alpha_1 - \tan \alpha_2)^2 \left(\frac{\cos^2 \alpha_2}{\cos \alpha_m} \right) \end{aligned} \quad (6.15)$$

6.2.3 AMDC Loss Model

Dunham and Came compared the results predicted by the Ainley and Mathieson loss model with the test results of 25 turbines, and found that, although this model can give accurate predictions for typical turbines in aero-engines, it is not applicable to small turbines or atypical turbines. For this reason, they took the influence of parameters like the Reynolds number, the Mach number and the aspect ratio of blades on turbines' aerodynamic losses into consideration, and made some improvements to the AMDC model. The total loss coefficient of a turbine is expressed as [5]:

$$Y = \left[(Y_p + Y_s) \left(\frac{\text{Re}}{2 \times 10^5} \right)^{-0.2} + Y_{TI} \right] \chi_{Te} \quad (6.16)$$

where, $\left(\frac{\text{Re}}{2 \times 10^5} \right)^{-0.2}$ is the multiplication factor of the Reynolds number used to correct the profile loss and secondary loss.

(1) Profile loss

Considering the influence of the Mach number, Dunham and Came made some improvements to Eq. (6.8) for calculating the profile loss coefficient. They thought the blockage effect caused by shock waves in the cascade passage, if any, would result in some supplementary loss. So, when the relative Mach number at the outlet of the blade row $M_{out} > 1$, the profile loss coefficient is given by:

$$Y_p = \left[1 + 60(M_{out} - 1)^2 \right] \chi_i Y_{p(i=0)} \quad (6.17)$$

(2) Secondary loss

Dunham and Came found that the expression of the secondary loss coefficient in the Ainley and Mathieson loss model is not applicable for blades with low aspect ratio in small turbines. For this reason, they introduced the aspect ratio, h/c , to the expression and simplified the parameter of acceleration, λ . Finally, the secondary loss coefficient is written as:

$$Y_s = 0.0334 \left(\frac{c}{h} \right) \left[4(\tan \alpha_1 - \tan \alpha_2)^2 \right] \left(\frac{\cos^2 \alpha_2}{\cos \alpha_m} \right) \left(\frac{\cos \alpha_2}{\cos \beta_{1k}} \right) \quad (6.18)$$

where definitions of the flow angles and their signs are same as those in the Ainley and Mathieson loss model.

(3) Tip leakage loss

As can be seen from Eq. (6.15), the tip leakage loss coefficient is in direct proportion to the size of the tip clearance in the Ainley and Mathieson, and the coefficient, B , is used to simply reflect the influence of shroud seals on the tip leakage flows. However, Dunham and Came pointed out that it is more reasonable to replace the linear form of the relative clearance height with its exponential form. Therefore, the following improvements were made in Eq. (6.15):

$$Y_{Tl} = 4B \frac{c}{h} \left(\frac{k}{c} \right)^{0.78} (\tan \alpha_1 - \tan \alpha_2)^2 \left(\frac{\cos^2 \alpha_2}{\cos \alpha_m} \right) \quad (6.19)$$

In Eq. (6.19), $B = 0.47$ for blades without shroud seals, $B = 0.37$ for blades with shroud seals. If there are too many labyrinths, the effective clearance value, k' , is used to replace the geometric clearance value, k :

$$k' = k \times (N)^{-0.42} \quad (6.20)$$

where, N is the number of labyrinths.

6.2.4 Kacker and Okapuu Loss Model

Kacker and Okapuu made some adjustments to the classification of losses in the AMDC loss model, and considered the influence of fluid compressibility, as well as the shock loss, in the prediction of the profile loss and the secondary loss. The improved loss model is called Kacker and Okapuu loss model or AMDCKO loss model [6]. In this model, the total loss is divided into the profile loss, the secondary loss, the tip leakage loss, and the trailing-edge loss, namely:

$$Y = \chi_{Re} Y_p + Y_s + Y_{TI} + Y_{Te} \quad (6.21)$$

In Eq. (6.21), χ_{Re} is the Reynolds number correction factor. Kacker and Okapuu thought the Reynolds number only affects the profile loss, and treated the trailing-edge loss as an independent loss component. In this model, the Reynolds number is determined by the actual chord length and flow conditions at the outlet of the cascade. χ_{Re} is obtained by the equation below:

$$\chi_{Re} = \begin{cases} \left(\frac{Re}{2 \times 10^5}\right)^{-0.4} & Re \leq 2 \times 10^5 \\ 1.0 & 2 \times 10^5 > Re > 10^6 \\ \left(\frac{Re}{10^6}\right)^{-0.2} & Re > 10^6 \end{cases} \quad (6.22)$$

(1) Profile loss

Kacker and Okapuu realized the Ainley-Mathieson model was established based on the measurements of subsonic turbine cascades and may not be well applied to high-Mach-number turbine blades. Actually, compressibility of accelerating gas in cascade passage can reduce the thickness of the boundary layer and thus inhibit flow separation. Therefore, Kacker and Okapuu brought in the Mach number correction factor, K_p , and the shock loss term, Y_{shock} , thus further turning Eq. (6.8) into:

$$Y_p = 0.914 \left(\frac{2}{3} K_p \chi_i Y_{p(i=0)} + Y_{shock} \right) \quad (6.23)$$

In Eq. (6.23), the Mach number correction factor, K_p , takes the influence of the outlet Mach number and the acceleration of gas in the cascade passage into consideration, and is a function of the mean inlet Mach number, M_{in} , and the mean outlet Mach number, M_{out} , as shown below:

$$K_p = 1 - K_2(1 - K_1) \quad (6.24)$$

where,

$$K_1 = \begin{cases} 1.0 & M_{out} \leq 0.2 \\ 1 - 1.25(M_{out} - 0.2) & M_{out} > 0.2 \end{cases}$$

$$K_2 = (M_{in}/M_{out})^2$$

Figure 6.8 shows the variations of K_1 and K_2 with the Mach number.

The shock loss coefficient is a function of the mean inlet Mach number, the mean outlet Mach number, the hub-to-shroud ratio, r_H/r_T , and the inlet-to-outlet static pressure ratio, p_{in}/p_{out} , and is given by:

$$Y_{shock} = 0.75(M_{in,H} - 0.4)^{1.75} \left(\frac{r_H}{r_T}\right) \left(\frac{p_{in}}{p_{out}}\right) \frac{1 - \left(1 + \frac{\gamma-1}{2} M_{in}^2\right)^{\frac{\gamma}{\gamma-1}}}{1 - \left(1 + \frac{\gamma-1}{2} M_{out}^2\right)^{\frac{\gamma}{\gamma-1}}} \quad (6.25)$$

where, $M_{in,H}$ is the inlet Mach number at the hub, which is a function of the mean inlet Mach number and the hub-to-shroud ratio, as shown below:

$$M_{in,H} = M_{in} \left(1 + K \left| \frac{r_H}{r_T} - 1 \right|^{2.2} \right) \quad (6.26)$$

where, K is a constant: $K = 1.8$ for the stator; $K = 5.2$ for the rotor.

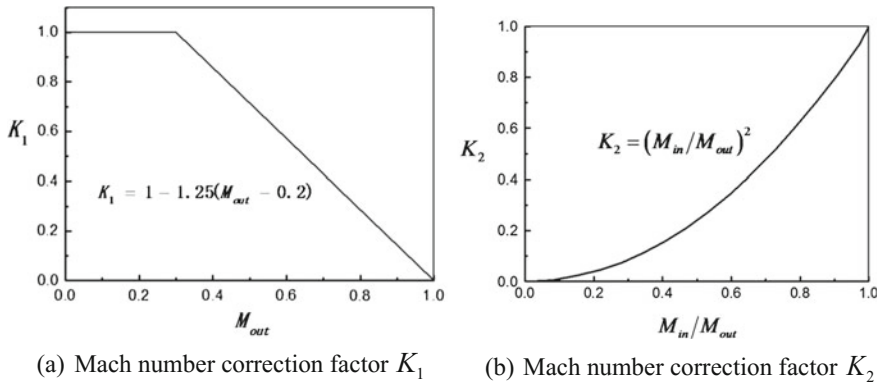


Fig. 6.8 Mach number correction factors for profile loss prediction in Kacker and Okapuu loss model [6]

In addition, for the profile with negative inlet blade metal angle, Kacker and Okapuu improved Eq. (6.7), and the profile loss coefficient at zero incidence, $Y_{P(i=0)}$, is given by:

$$Y_{P(i=0)} = \left\{ Y_{P(\beta_{1k}=0)} + \left| \frac{\beta_{1k}}{\alpha_2} \right| \left(\frac{\beta_{1k}}{\alpha_2} \right) [Y_{P(\beta_{1k}=\alpha_2)} - Y_{P(\beta_{1k}=0)}] \right\} \left(\frac{t_{\max}/c}{0.2} \right)^{\frac{\beta_{1k}}{\alpha_2}} \quad (6.27)$$

(2) Secondary loss

Kacker and Okapuu further studied the influence of the aspect ratio on the secondary loss, and made the following improvements to Eq. (6.18):

$$Y_{s,AMDC} = 0.0334 \chi_{AR} \left[4(\tan \alpha_1 + \tan \alpha_2)^2 \right] \left(\frac{\cos^2 \alpha_2}{\cos \alpha_m} \right) \left(\frac{\cos \alpha_2}{\cos \beta_{1k}} \right) \quad (6.28)$$

where, the aspect ratio factor, χ_{AR} , is:

$$\chi_{AR} = \begin{cases} \frac{1-0.25\sqrt{2-h/c}}{h/c}, & h/c \leq 2 \\ \frac{1}{h/c}, & h/c > 2 \end{cases} \quad (6.29)$$

It is worth noting that definitions of the flow angles and their signs (see Fig. 6.9) in this model are different from those in the Ainley and Mathieson loss model (see Fig. 6.3).

Considering the influence of compressibility on flows in the endwall regions, Kacker and Okapuu brought in a Mach number correction factor, K_s , for the prediction of the secondary loss, so as to correct the secondary loss in the AMDC model:

$$Y_s = 1.2 Y_{s,AMDC} K_s \quad (6.30)$$

In (6.30), K_s is a function of the aspect ratio based on the axial chord length and the Mach number correction factor, K_p , and is given by:

$$K_s = 1 - \left(\frac{1}{h/b_x} \right)^2 (1 - K_p) \quad (6.31)$$

Fig. 6.9 Definitions of angles in AMDCKO loss model



(3) Tip leakage loss

Kacker and Okapuu proposed methods of calculating the tip leakage loss coefficients for both shrouded and unshrouded blades. For shrouded rotor the tip leakage loss coefficient is given by Eq. (6.19) and Eq. (6.20) in the AMDC model; for unshrouded rotor, the tip leakage loss coefficient, as derived by Kacker and Okapuu, is given by:

$$\Delta\eta_{tt} = 0.93 \left(\frac{r_T}{r_m} \right) \left(\frac{1}{h \cos \alpha_2} \right) \eta_{tt,0} \Delta k \tag{6.32}$$

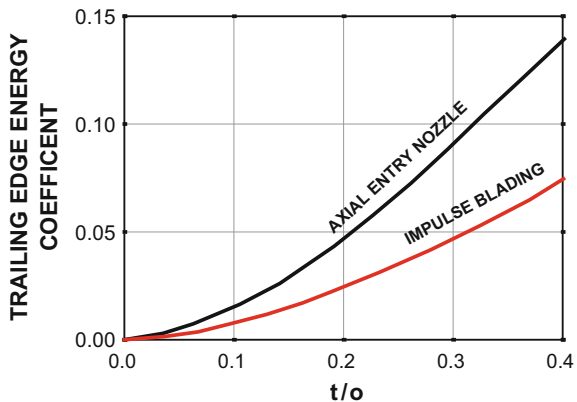
where, $\eta_{tt,0}$ is the total-to-total efficiency of the turbine stage without tip clearance; Δk is the variation of tip clearance; $\Delta\eta_{tt}$ is the variation of the total-to-total efficiency of the turbine stage, which depends on $\eta_{tt,0}$, the ratio of tip radius to mean radius, r_T/r_m , the outflow angle, α_2 , and the increment of clearance, Δk . $\Delta\eta_{tt}$ could be converted into Y_{Tl} in Eq. (6.21) through the following iteration steps: (1) determine the total-to-total efficiency of the turbine stage without tip clearance; (2) calculate the tip leakage loss and include it in the rotor loss; (3) recalculate the velocity triangle as well as other loss coefficients and obtain the new total-to-total efficiency; (4) continue the iteration until convergence is reached.

(4) Trailing-edge loss

Kacker and Okapuu considered the trailing-edge loss as an independent component, and thought that the trailing-edge loss is a function of the outlet Mach number and the trailing-edge energy loss coefficient:

$$Y_{Te} = \frac{\left[1 + \frac{\gamma-1}{2} M_{out}^2 \left(\frac{1}{1-\Delta E_{Te}} - 1 \right)^{-\frac{\gamma}{\gamma-1}} \right] - 1}{1 - \left(1 + \frac{\gamma-1}{2} M_{out}^2 \right)^{-\frac{\gamma}{\gamma-1}}} \tag{6.33}$$

Fig. 6.10 Trailing-edge energy loss coefficients of turbine cascade in Kacker and Okapuu loss model [6]



In Eq. (6.33), ΔE_{Te} is the trailing-edge energy loss coefficient, which depends on the ratio of trailing edge thickness to the throat opening, t_{Te}/o , as shown in Fig. 6.10. In this figure, the trailing-edge loss coefficients of the zero-incidence axial inflow cascade and the impulse cascade, namely $\Delta E_{Te(\beta_{1k}=0)}$ and $\Delta E_{Te(\beta_{1k}=\alpha_2)}$, are given. The trailing-edge loss coefficients of other kinds of cascades can be obtained by using the equation below:

$$\Delta E = \Delta E_{Te(\beta_{1k}=0)} + \left| \frac{\beta_{1k}}{\alpha_2} \right| \left(\frac{\beta_{1k}}{\alpha_2} \right) [\Delta E_{Te(\beta_{1k}=\alpha_2)} - \Delta E_{Te(\beta_{1k}=0)}] \quad (6.34)$$

6.2.5 Traupel Loss Model

Based on a great number of experimental results, Traupel et al. proposed a loss model in another form [8, 23]. This model not only considers the influence of geometric parameters (including the chord length, the inlet/outlet metal angles, the blade pitch, the tip clearance, etc.) and aerodynamic parameters of blades on different kinds of aerodynamic losses, but also gives a more detailed correlation for the loss caused by shroud seals, so that its predictive ability is improved. In this model, the blade row loss is divided into the profile loss, ζ_P , the secondary loss, ζ_S , the tip leakage loss, ζ_{TI} , and the fan loss, ζ_f , and is given by Eq. (6.35) and Eq. (6.36):

$$\zeta_N = \zeta_{P,N} + \zeta_{S,N} + \zeta_{TI,N} + \zeta_{f,N} \quad (6.35)$$

$$\zeta_R = \zeta_{P,R} + \zeta_{S,R} + \zeta_{TI,R} + \zeta_{f,R} \quad (6.36)$$

where, ζ is the loss coefficient; N represents the stator, and R represents the rotor.

(1) Profile loss

Traupel et al. divided the profile loss into the blade-surface boundary layer loss, the trailing-edge loss, and the shock loss, and the expression is shown as below:

$$\zeta_P = \chi_R \chi_M \zeta_{P0} + \zeta_{Te} + \zeta_C \quad (6.37)$$

where, ζ_{P0} is the basic profile loss, which is determined by the inlet/outlet flow angles; χ_R is the Reynolds number correction factor, which is used to reflect the influence of the Reynolds number and surface roughness; χ_M is the Mach number correction factor, which is used to reflect the influence of the main flow velocity; ζ_{Te} is the trailing-edge loss, reflecting the influence of wakes after the trailing edge; ζ_C is the shock loss.

The concrete value of the basic profile loss, ζ_{P0} , can be found from the empirical correlation curve in Fig. 6.11. It is worth noting that the flow angles are relative to the tangential direction. As can be seen from the figure, with the increase of the blade bending degree, boundary-layer separation may occur in part of the downstream

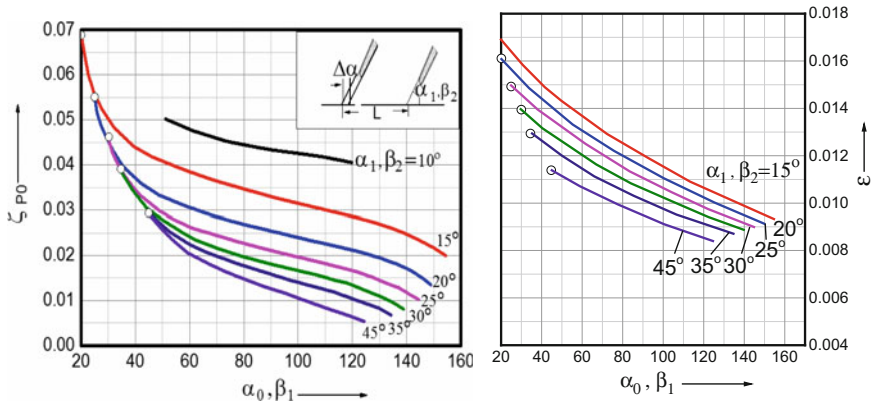


Fig. 6.11 Relation between basic profile loss and flow inlet/outlet angles in Traupel loss model [8]

deceleration area due to the thickening of the boundary layer on the suction side, thus leading to great loss. Relatively, the boundary layer on the pressure side cannot be separated easily, thus incurring little loss. It is worth noting that this method for calculating the boundary layer loss may not apply to impulse turbines.

Meanwhile, the basic profile loss related to flow conditions of blade boundary layer would also be affected by the Reynolds number and Mach number. Figure 6.12 shows the influence of the blade surface roughness and the Reynolds number on χ_R ; Curve a applies to turbines, and Curve b and Curve c apply to compressors. It can be

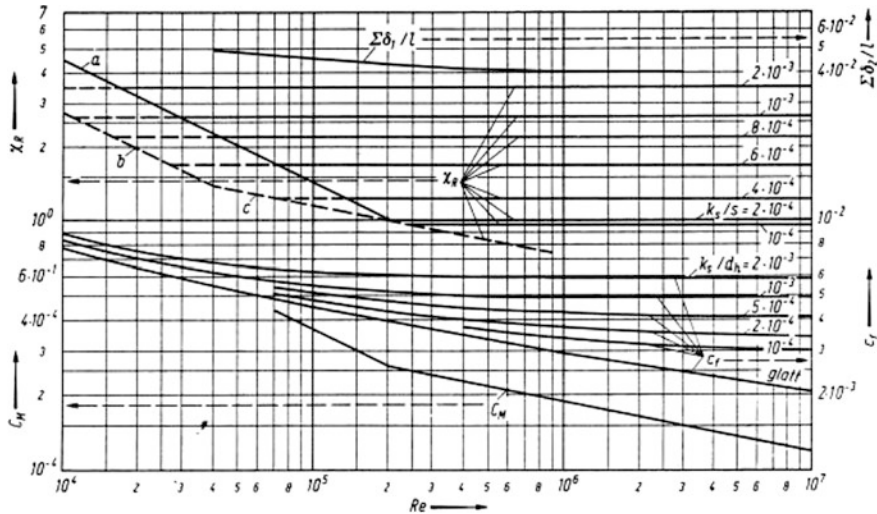


Fig. 6.12 Reynolds number correction factor for basic profile loss prediction in Traupel loss model [8]

seen that the profile loss decreases gradually with the increase of the Reynolds number because the boundary layer becomes thinner and the laminar separation bubbles decrease gradually. When the Reynolds number is greater than 2×10^5 , the profile loss will stop changing, and the state of self-modeling Reynolds number is reached. When the blade surface roughness increases, the frictional loss will become higher.

Figure 6.13 shows the influence of the outlet Mach number on the profile loss. Curve 1 and Curve 2 apply to subsonic and supersonic turbine stators respectively, and Curve 3 and Curve 4 apply to subsonic and supersonic turbine rotors respectively. Figure 6.14 shows the variation curves of the trailing-edge loss, ζ_{Te} . In nature, the trailing-edge loss results from the mixing of the low-pressure wakes and the high-pressure main flow, for the static pressure in the wake region downstream of the blade row is lower than the static pressure of the main flow. The trailing-edge loss is a function of the trailing-edge thickness, the outflow angle, ζ_{p0} , χ_R , and χ_M . As shown in the figure, the trailing-edge loss is greatly influenced by the profile and outflow angle: thicker trailing edge and smaller outflow angle would result in higher trailing-edge loss.

In the Traupel model, the shock loss is a function of the trailing-edge thickness and the outflow angle, and is given by Eq. (6.38) and Eq. (6.39).

$$\zeta_{C,N} = \left(\frac{\Delta_{\alpha,N}}{1 - \Delta_{\alpha,N}} \right)^2 \sin^2 \alpha_1 \quad (6.38)$$

$$\zeta_{C,R} = \left(\frac{\Delta_{\alpha,R}}{1 - \Delta_{\alpha,R}} \right)^2 \sin^2 \beta_2 \quad (6.39)$$

where, $\Delta_{\alpha,N} = \frac{t'_N}{t_N \sin(90^\circ - \alpha_1)}$, $\Delta_{\alpha,R} = \frac{t'_R}{t_R \sin(90^\circ - \beta_2)}$

(2) Secondary loss

Based on analysis of measured data of linear cascades, Traupel et al. established a model for calculating the secondary loss. In the model, it is assumed that there is no interaction between the secondary loss regions at both ends. Thus, the secondary loss is written as:

Fig. 6.13 Mach number correction factor for basic profile loss prediction in Traupel loss model [8]

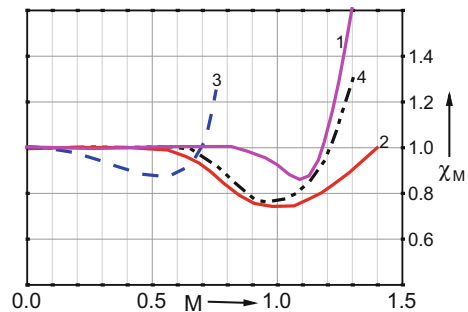
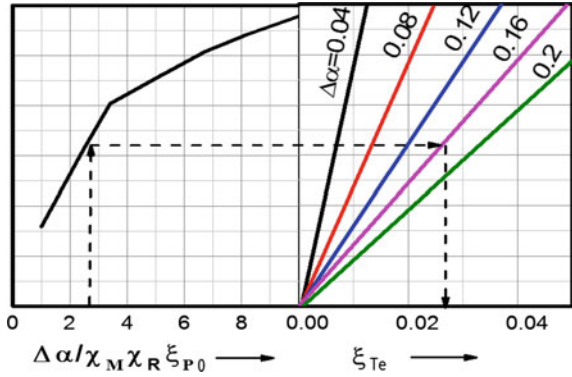


Fig. 6.14 Trailing-edge loss in Traupel loss model [8]



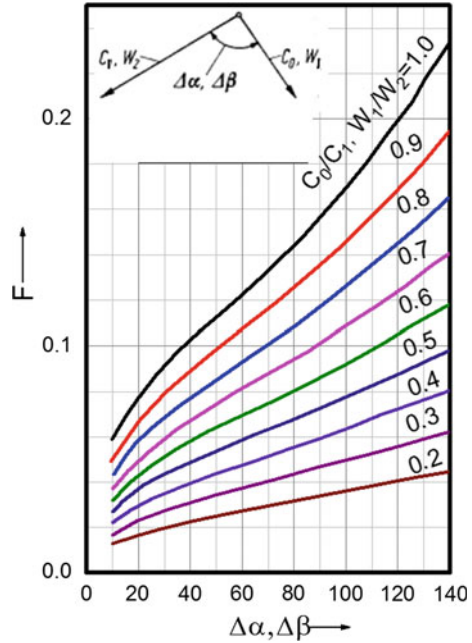
$$\zeta_s = \begin{cases} \frac{\zeta_p}{\zeta_{p0}} F\left(\frac{l}{H}\right)_k + \zeta_\alpha + A\left(\frac{l}{H} - \frac{l/t}{(H/t)_k}\right) & H/t < (H/t)_k \\ \frac{\zeta_p}{\zeta_{p0}} F\left(\frac{l}{H}\right) + \zeta_\alpha & H/t \geq (H/t)_k \end{cases} \quad (6.40)$$

where, the critical ratio of blade height to blade pitch, $(H/t)_k = B\sqrt{\zeta_p}$; $B = 7$ for stator, $B = 10$ for rotor; ζ_α is the loss caused by unsteady interaction between the stator and the rotor in the endwall region; F is a function of the flow deflection angle and the velocity ratio, which will increase with the increase of both these two parameters. The higher the value of F , the larger the secondary loss will be (see Fig. 6.15). In the model, H/t is used to represent the influence of geometric parameters on the intensity of secondary flows; namely, shorter blades or larger blade pitch would lead to stronger secondary flows and higher loss. Meanwhile, ζ_p/ζ_{p0} is used to represent the influence of relative variation of the Reynolds number, the Mach number, and the trailing-edge thickness from the reference point on the intensity of secondary flows. If H/t is smaller than the critical value, there will be interaction between secondary vortices in the endwall regions of hub and shroud, so a third term, where l is the chord length, is needed in the expression. ζ_α is the endwall loss, which is caused by boundary-layer flows of the stator and the rotor in the endwall regions and given by Eq. (6.41) and Eq. (6.42), where l_1 and l_2 are the height of the shroud; δ_{a1} and δ_{a2} are the axial length of the cascade; c_f is the friction coefficient.

$$\zeta_{a.N} = \frac{c_f \delta_{a1}}{\sin(90^\circ - a_1) l_1} \quad (6.41)$$

$$\zeta_{a.R} = \frac{c_f \delta_{a2}}{\sin(90^\circ - \beta_2) l_2} \quad (6.42)$$

Fig. 6.15 Variation of F with flow turning angle and velocity ratio in Traupel loss model [8]



(3) Tip leakage loss

Traupel treated the tip leakage loss separately for both shrouded blades and unshrouded blades. For shrouded blades, the tip leakage loss consists of two parts: the first part is the loss caused by energy dissipation of the fluid, and the other part is the loss caused by the mixing of the tip leakage flow and the main flow. Thus, the tip leakage losses of stator and rotor are written as:

$$\zeta_{TLN} = 2 \cdot (1 - R_H) \cdot \mu_N \cdot \left[1 - \left(\frac{v - v(\alpha_0^*)}{v(\alpha_0^*)} \right)^2 \right] \tag{6.43}$$

$$\zeta_{TLR} = \mu_R \cdot \left[1 - \left(\frac{v - v(\beta_1^*)}{v(\beta_1^*)} \right)^2 \right] \tag{6.44}$$

where, μ is the relative mass flow rate of the gas as it passes through the shroud seals, which depends on various factors, such as the reaction degree of the hub and the shroud, the inlet/outlet velocity, the flow area, and the number of shroud seals; $v(\alpha_0^*)$ and $v(\beta_1^*)$ are the design velocities; $1 - ((v - v(\beta_1^*)) / v(\beta_1^*))^2$ is the relative velocity ratio, which is the most important factor influencing the tip leakage loss.

For unshrouded blades, the tip leakage loss is a function of the tip clearance, the blade height, the blade chord length, the tip diameter, and the mean diameter, and is expressed as the reduction value of efficiency:

$$\Delta\eta_{tl} = K_\delta \frac{(\tau - 0.002l)D}{HD_m} \tag{6.45}$$

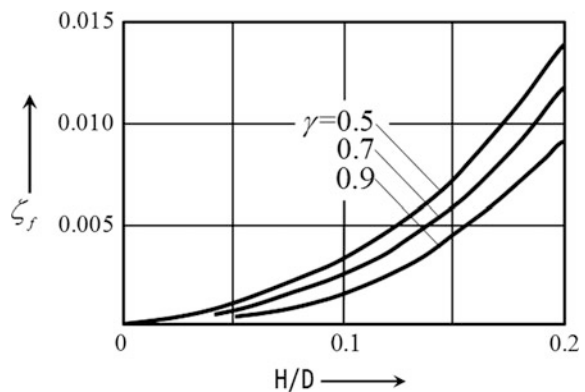
(4) Fan loss

The fan loss, ζ_f , is the comprehensive value correction term of the blade loss in the spanwise direction. For twisted blades, the value of the fan loss may be negative, and the method of integral solution is needed in some special circumstances. As for untwisted blades, the fan loss can be obtained according to Fig. 6.16, in which γ is the velocity ratio. As can be seen from the figure, ζ_f is mainly determined by the dimensionless parameter, H/D (blade height/ diameter), and increases with the increase of H/D . In addition, ζ_f is also under the influence of the velocity ratio and would decrease with the increase of the velocity ratio.

6.2.6 Craig and Cox Loss Model

Craig and Cox [11] proposed their method for estimating aerodynamic losses of axial turbines in 1970. Based on analysis of experimental data from cascade tests and turbine test rig, they divided aerodynamic losses of turbines into two major categories. The first category includes the profile loss, the secondary loss, and the annulus loss with seal structures, which are expressed as loss coefficients in the model (see Eq. (6.46)); the second category includes the rotor tip leakage loss, the stator root leakage loss, the loss caused by cooling air holes and the friction loss caused by the disc windage, which are expressed as variation of efficiency in the model. The Craig and Cox loss model allows relatively accurate prediction of aerodynamic losses of

Fig. 6.16 Variation of ζ_f in Traupel loss model [8]



turbines over a wide range of variables (including the Reynolds number, the Mach number, the aspect ratio, the aerodynamic load, etc.). Craig and Cox showed that the prediction accuracy of this model on turbine efficiency is within the range of $\pm 1.25\%$.

$$X = X_p + X_s + X_a \tag{6.46}$$

(1) Profile loss

Craig and Cox subdivided the profile loss into the basic profile loss and the additional losses caused by changes in the Reynolds number, the Mach number, the incidence, the curvature of the suction side, and the trailing-edge thickness, which can reflect the influence of aerodynamic and geometric characteristics and off-design conditions on losses. Thus, the profile loss is given by:

$$X_p = x_{pb}N_{pr}N_{pi}N_{pt} + (\Delta x_p)_t + (\Delta x_p)_{s/e} + (\Delta x_p)_m \tag{6.47}$$

where, x_{pb} is the basic profile loss coefficient, which can be determined by the lift coefficient, F_L , and the contraction ratio, CR , as shown in Fig. 6.17 (B is the outflow angle; s/b is the relative blade pitch, namely the ratio of the blade pitch to the length of the mean camber line). Figure 6.18 shows the variation curves of the lift coefficient with the inflow angle, the outflow angle, and the incidence for minimum loss, i_{min} ; the angles are defined in Fig. 6.19. Similarly, CR can be expressed by the inflow/outflow angles, A and B , and the relative blade pitch, as shown in Fig. 6.20. This model includes a trailing-edge factor, N_{pt} , and a

Fig. 6.17 Basic profile loss coefficient in Craig and Cox loss model [11]

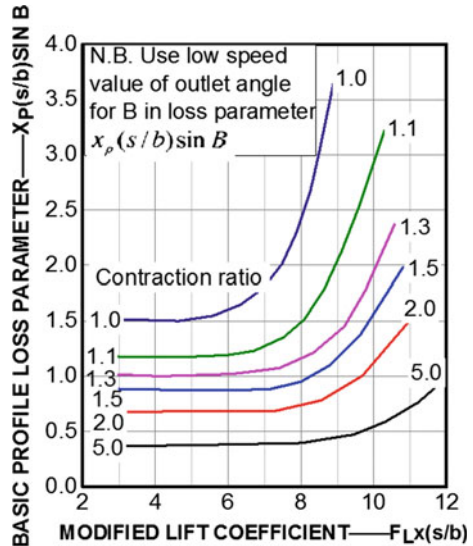


Fig. 6.18 F_L in Craig and Cox loss model [11]

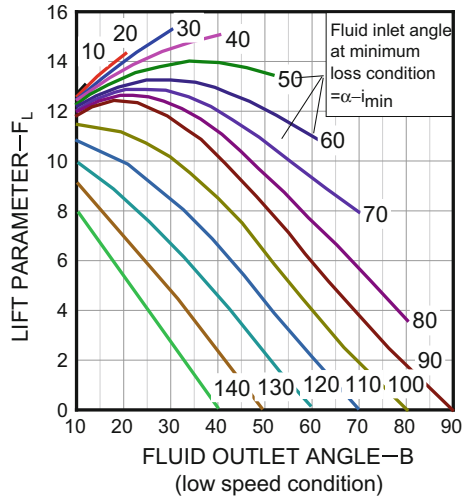


Fig. 6.19 Definitions of angles in Craig and Cox loss model



Fig. 6.20 CR with flow angles and relative blade pitch in Craig and Cox loss model [11]

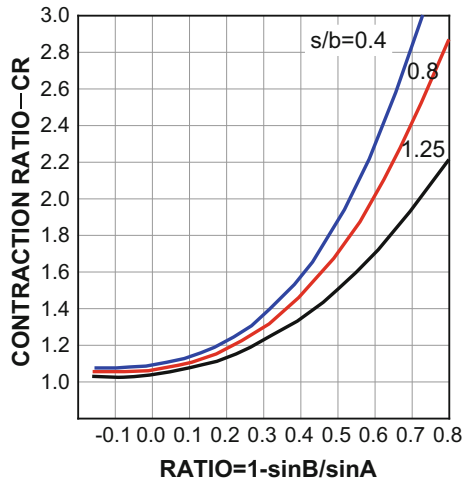
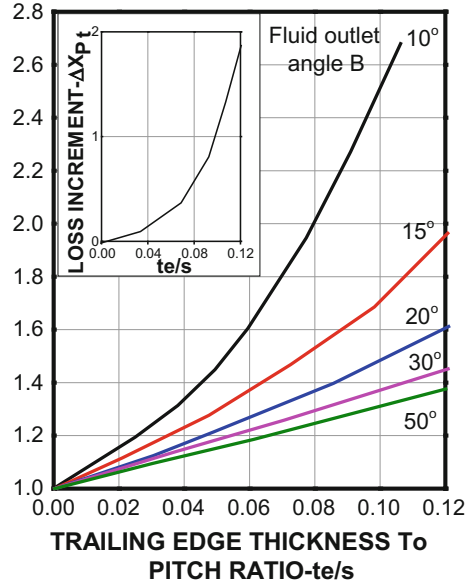


Fig. 6.21 Influence of trailing-edge thickness on profile loss in Craig and Cox loss model [11]



trailing-edge loss term, $(\Delta x_p)_t$, to reflect the influence of the trailing-edge thickness on the profile loss. Figure 6.21 shows the relation between the trailing-edge loss and the trailing-edge thickness.

Figure 6.22 presents the relation between the Reynolds number correction factor, N_{pr} , and the Reynolds number and the blade surface roughness. The influence patterns are similar to those in the Traupel loss model. The model includes a Mach number correction term, $(\Delta x_p)_m$, and a curvature correction term, $(\Delta x_p)_{s/e}$, which

Fig. 6.22 Influence of Reynolds number and surface roughness on N_{pr} in Craig and Cox loss model [11]

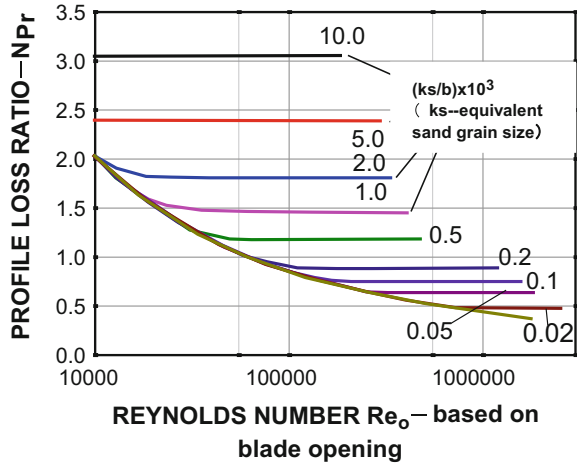


Fig. 6.23 Relation between Mach number correction term and aerodynamic and geometric parameters in Craig and Cox loss model [11]

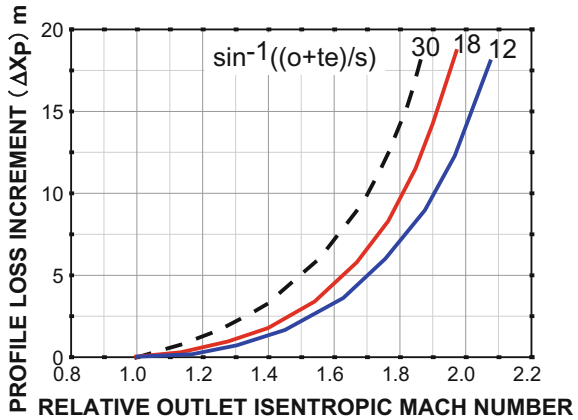
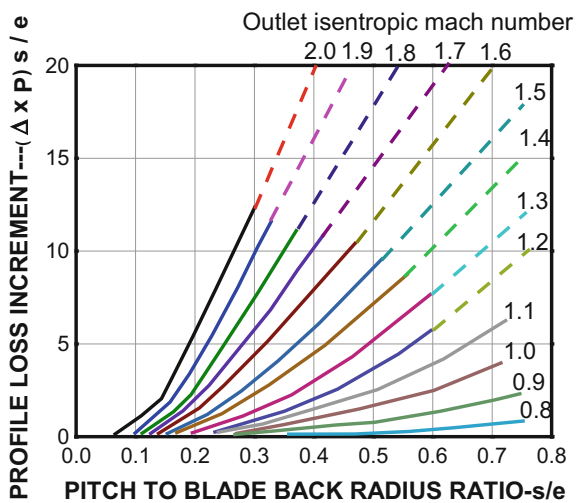


Fig. 6.24 Relation between curvature loss and aerodynamic and geometric parameters in Craig and Cox loss model [11]



are used to reflect the loss caused by transonic flows in turbines, as shown in Fig. 6.23. The Mach number loss is mainly influenced by the outlet Mach number, the blade pitch, the throat opening (o), and the trailing-edge thickness (te), while the loss caused by the curvature downstream the throat on the suction side, $(\Delta x_p)_{s/e}$, is determined by the outlet Mach number and the local curvature radius of blades, e , as shown in Fig. 6.24.

In the Craig and Cox loss model, an incidence loss coefficient, N_{pi} , is used to reflect the influence of the incidence on the profile loss (see Fig. 6.25). The incidence loss is closely related to the parameter, $(i - i_{min}) / |i_{stall} - i_{min}|$, where the stall incidence is defined in Ref. [11] as the incidence at which the profile loss is twice the minimum value. The minimum loss incidence is given by Eq. (6.48), where the parameter F is a function of the blade inlet angle and s/b , as shown in Fig. 6.26.

Fig. 6.25 Influence of incidence on profile loss in Craig and Cox loss model [11]

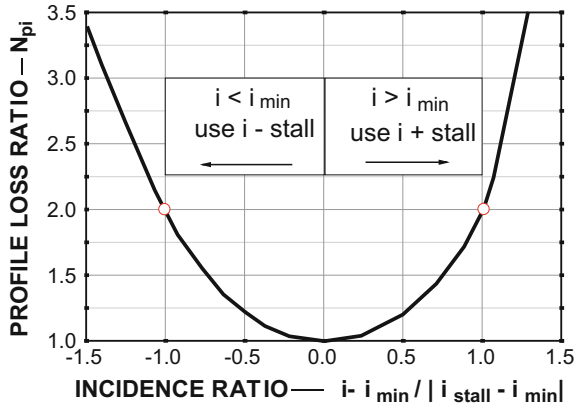
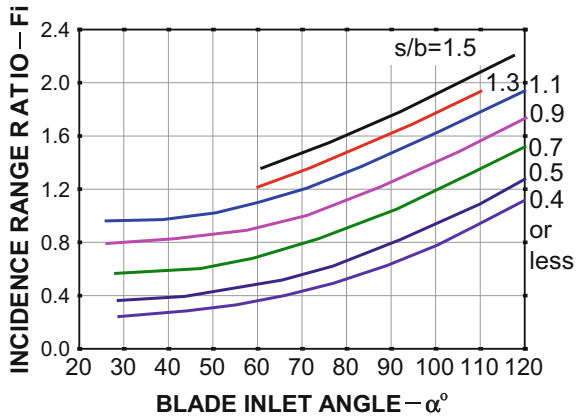


Fig. 6.26 F_i in Craig and Cox loss model [11]



$$i_{min} = \frac{(i + stall) + F_i \cdot (i - stall)}{1 + F_i} \tag{6.48}$$

where, $i + stall$ is the positive stall incidence; $i - stall$ is the negative stall incidence.

(2) Secondary loss

Craig and Cox thought that the Reynolds number and the aspect ratio have significant influence on the secondary loss. Thus, following improvements are made for the prediction of the secondary loss:

$$X_s = (N_s)_r \cdot (N_s)_{h/b} \cdot (x_s)_b \tag{6.49}$$

Fig. 6.27 Basic secondary loss in Craig and Cox loss model [11]

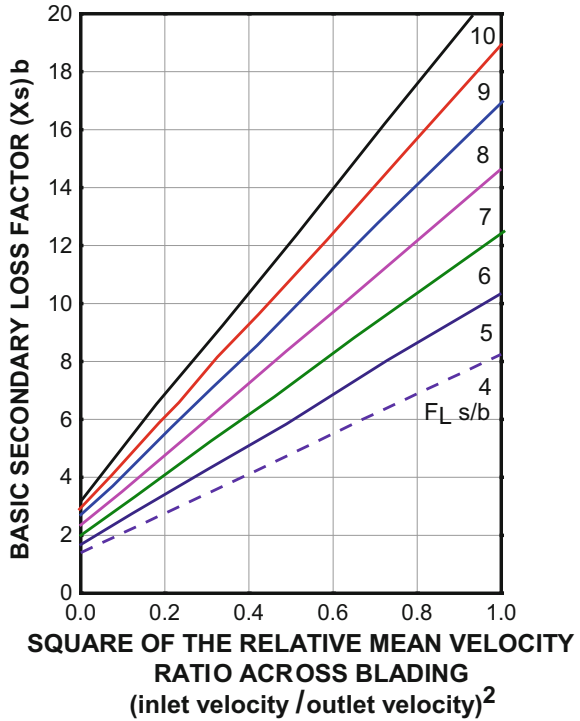
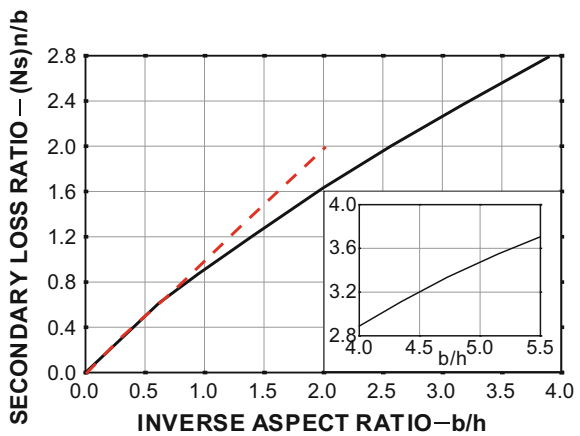


Fig. 6.28 Aspect ratio factor in Craig and Cox loss model [11]



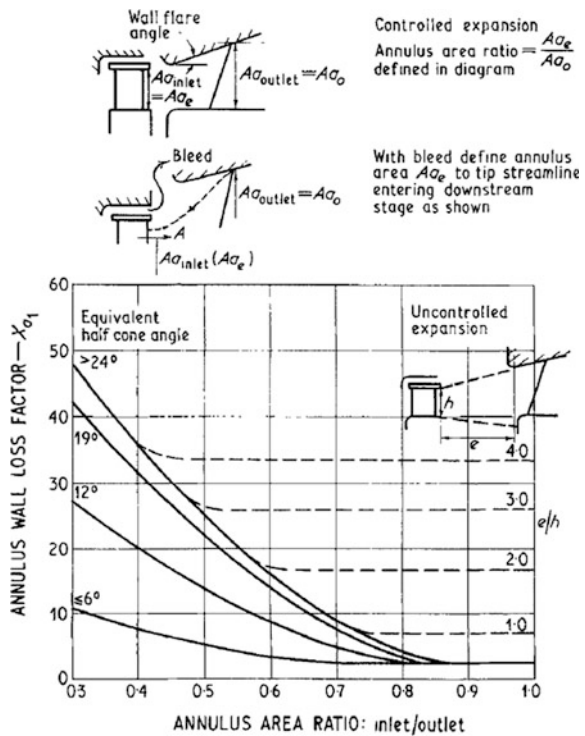
where, $(x_s)_b$ is the basic secondary loss, which is a function of the lift coefficient, F_L , the relative blade pitch, s/b , and the inlet velocity ratio, as shown in Fig. 6.27; $(N_s)_{h/b}$ is the aspect ratio correction factor and given in Fig. 6.28; $(N_s)_r$ is the Reynolds number correction factor. The influence of the Reynolds number is

similar to that in the prediction of the profile loss; when the Reynolds number increases to a certain value, its influence can be ignored.

(3) Disc cavity seal loss and other annulus wall losses

There are clearance and relevant seal structures between the rotor and the stator in actual turbines. These structures change the ideal flow passage and would result in additional losses. Craig and Cox subdivided these losses into three classes: (1) the seal loss, (2) the disc cavity loss, (3) the sudden expansion loss, which are expressed as X_{a1} , X_{a2} and X_{a3} respectively. Generally speaking, seal structures would lead to expansion of the flowpassage. When two blade rows are close in space, the expansion is considered to be controllable. The seal loss, X_{a1} , can be determined by the area ratio and the equivalent expansion angle, as shown by the solid line in Fig. 6.29. When two blade rows are far apart, the expansion is considered to be uncontrollable, and the aerodynamic loss can be determined by the area ratio and the spacing ratio, as shown by the dotted line in the figure. In this model, the disc cavity loss can be obtained by using the local flow angle, the axial clearance, the dimensions of the disc cavity, the blade height, and other key aerodynamic and geometric parameters, as shown in Fig. 6.30. The Craig and Cox model does not give a specific expression or calculation method for the third class—the sudden expansion loss.

Fig. 6.29 Seal structure loss in Craig and Cox loss model [11]



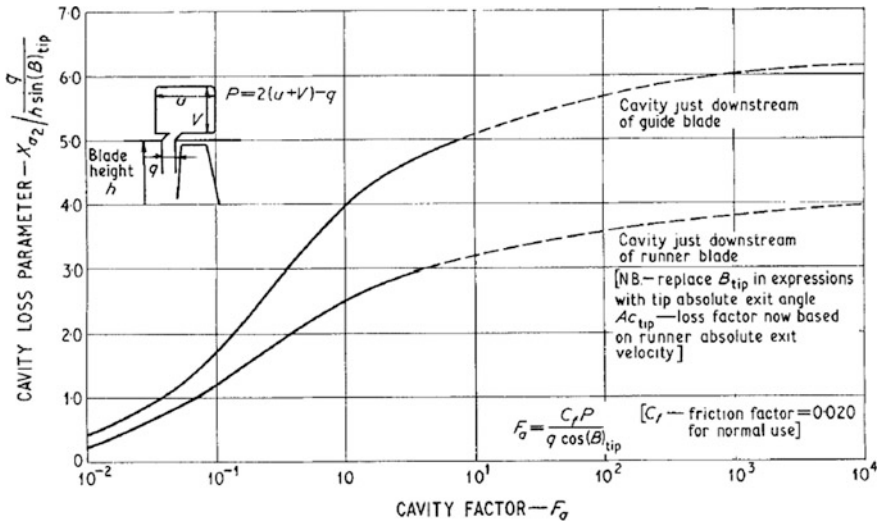


Fig. 6.30 Disc cavity loss in Craig and Cox loss model [11]

(4) Tip leakage loss

In the Craig and Cox model, the efficiency variation caused by the tip leakage loss is given by the product of the leakage coefficient, the clearance area to throat area ratio, and the efficiency at the condition of no rotor blade clearance:

$$\Delta\eta_k = F_k \frac{A_k}{A_t} \eta_{k=0} \tag{6.50}$$

where, F_k is the leakage coefficient, which is a function of the inlet-to-outlet velocity ratio at the tip clearance. Small inlet-to-outlet velocity ratio at the tip clearance means that gas is accelerated greatly in the clearance; namely, there is more gas passing through the clearance, thus leading to significant tip leakage loss. On the contrary, large inlet-to-outlet velocity ratio means small acceleration of the gas, little pressure drop, and little tip leakage loss.

(5) Other losses

Except for the above losses, the Craig and Cox model also considers the influence of the windage loss caused by the rotating disc cavity as it works on the cooling air, the partial admission loss, and the loss caused by shoulder obstruction, and even the loss caused by wet steam and condensation section in steam turbines. See Ref. [11] for more details.

6.2.7 Denton Loss Model

Denton pointed out that there are the following three sources of losses in turbomachines: (1) viscous friction in boundary layers or free shear layers (the latter also includes the loss generated in the mixing process); (2) heat transfer under finite temperature differences; (3) non-equilibrium processes, such as rapid expansion processes or shock waves [12]. He suggested defining the flow losses in turbines in terms of entropy increase so as to get rid of the dependence on selection of the reference coordinate system in the analytical process (see the equation below):

$$\zeta_s = \frac{T_2 \Delta s}{h_{02} - h_2} \quad (6.51)$$

The total cascade loss is given by the sum of the blade-surface boundary layer loss, the trailing-edge loss, the tip leakage loss, the endwall loss, the shock loss, and other losses in the cascade passage [12, 24], as shown in Eq. (6.52):

$$\zeta_N = \zeta_{Bb} + \zeta_{Te} + \zeta_{TI} + \zeta_{Eb} + \zeta_{shock} \quad (6.52)$$

(1) Blade-surface boundary layer loss

Based on analytical calculation, Denton et al. obtained the entropy increase rate in the flat-plate boundary layer, \dot{S} , as shown in Eq. (6.53), where x is the coordinate along the wall surface; ρ is the density; T_δ and V_δ are the temperature and velocity at the outer edge of the boundary layer; C_d is the dissipation factor, $C_d = 0.17\text{Re}_\theta^{-1}$ for laminar boundary layers, $C_d = 0.002$ for turbulent boundary layers. According to the definition of the loss coefficient, as shown in (6.54), the blade-surface boundary layer loss can be obtained by integrating the entropy increase rate along the pressure side and the suction side, as shown in Eq. (6.55), where p is the blade pitch; C_s is the arc length of the blade surface; α is the flow angle. It can be seen that the boundary layer loss is in direct proportion to the cube of the velocity, so the aerodynamic loss on the suction surface is greater.

$$\dot{S} = \int_0^x \frac{\rho V_\delta^3 C_d}{T_\delta} dx \quad (6.53)$$

$$\zeta_s = \frac{T \dot{S}}{m 0.5 V_{ref}^2} \quad (6.54)$$

$$\zeta_{Bb} = 2 \sum \frac{C_s}{p \cos \alpha_{ref}} \int_0^1 C_d \left(\frac{V}{V_{ref}} \right)^3 d(x/C_s) \quad (6.55)$$

(2) Trailing-edge loss

Denton employed a control volume at the blade trailing edge, and established a trailing-edge loss model through simplifying and solving the mass conservation equation, the momentum conservation equation, and the energy conservation equation, which describe the mixing process between wakes and the main flow. In this model, the trailing-edge loss is a function of the base pressure coefficient, C_{pb} , the throat opening, w , the trailing-edge thickness, t , the boundary layer displacement thickness, δ^* , and the boundary layer momentum thickness, θ , and is given by:

$$\zeta_{Te} = -\frac{C_{pb}t}{w} + \frac{2\theta}{w} + \left(\frac{\delta^* + t}{w}\right)^2 \quad (6.56)$$

where, the base pressure coefficient is given by the equation below, where P_b is the base pressure.

$$C_{pb} = (P_b - P_{ref}) / (0.5\rho V_{ref}^2) \quad (6.57)$$

In Eq. (6.56), the first term is used to describe the influence of the base pressure on the trailing edge. The reference point of the base pressure coefficient is selected based on experience, and it should be within the range of -0.1 to -0.2 as suggested by Denton. The second term is used to describe the mixing loss in the boundary layer upstream the trailing edge. The blockage effect caused by the trailing edge and the boundary layer is described by the third term.

When there is boundary layer separation at the trailing edge, a separation loss term should be added to Eq. (6.56), as shown in Eq. (6.58). It is worth noting that this additional term is generally small in value. Even when the boundary layer separation at the trailing edge contributes to 10% of the blockage, the consequential loss would be only 1%. However, the boundary layer separation would actually lead to great loss. Denton pointed out that the base pressure would decrease when there is boundary layer separation at the trailing edge; as a result, the first term of Eq. (6.56) would increase, thus reflecting the influence of the separation on aerodynamic losses.

$$\zeta_{sep} = \left(\frac{\delta^{*2} + 2t\delta^*}{w^2}\right) \quad (6.58)$$

(3) Tip leakage loss

Based on quantitative analysis of the entropy increase caused by the mixing between the tip leakage flow and the main flow, Denton established a tip leakage loss model. For shrouded turbine blades, the tip leakage and mixing can be regarded as incompressible flows, and the leakage flow rate, m_L , is a function of the main flow rate, m_m , the clearance to blade height ratio, g/h , the flow coefficient, C_c , and the inflow/outflow angles, as shown in Eq. (6.59). Further simplified analysis

suggests that the circumferential momentum difference between the leakage flow and the main flow is the main source of the leakage and mixing loss. The leakage loss is a function of the inflow angle, the outflow angle, the leakage flow rate, and the main flow rate, and is given by Eq. (6.60).

$$\frac{m_L}{m_m} = \frac{gC_c}{h} \sqrt{\sec^2 \alpha_2 - \tan^2 \alpha_1} \quad (6.59)$$

$$\zeta_{TL} = 2 \frac{m_L}{m_m} \left(1 - \frac{\tan \alpha_1}{\tan \alpha_2} \sin^2 \alpha_2 \right) \quad (6.60)$$

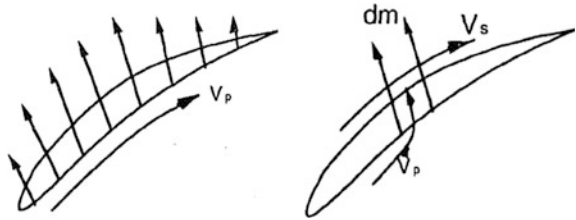
For unshrouded blades, it is considered that gas leaks from the pressure side to the suction side, driven by the pressure difference between both sides of the clearance. The velocity component along the pressure side stays unchanged in the leakage process. Once arriving at the suction side, the leakage flow would mix with local flows immediately. In the Denton model, the chordwise component of the leakage flow is divided into several independent small leakage flows with a width of dz , as shown in Fig. 6.31. The rate of each jet flow, dm , mainly depends on the local pressure difference. The velocity components at the pressure side and suction side are expressed as V_p and V_s respectively. Due to compressibility of the flows, the entropy increase, Δs_{irrev} , caused by the mixing can be obtained by Eq. (6.62). Thus, the total leakage flow loss can be obtained by integrating the entropy increase along the chord, C , and establishing simultaneous equations with Eq. (6.61), as shown in Eq. (6.63).

$$dm = C_d g \sqrt{2\Delta P} \rho dz \quad (6.61)$$

$$\Delta s_{irrev} = C_p (\gamma - 1) M^2 \left(1 - \frac{V_p}{V_s} \right) \frac{dm}{m_m} \quad (6.62)$$

$$\zeta_{TL} = \frac{2C_d g C}{h p \cos \alpha_2} \int_0^1 \left(\frac{V_s}{V_2} \right)^3 \left(1 - \frac{V_p}{V_s} \right) \sqrt{\left(1 - \left(\frac{V_p}{V_s} \right)^2 \right)} \frac{dz}{C} \quad (6.63)$$

Fig. 6.31 Denton leakage loss model for unshrouded turbines [12]



(4) Endwall loss

In the Denton model, the endwall loss includes the endwall boundary layer losses and the endwall mixing losses. The endwall boundary layer loss within a blade row can be obtained by Eq. (6.64), while the endwall boundary layer loss between blade rows can be obtained by Eq. (6.53). Thus, the total endwall boundary layer loss can be determined by establishing the simultaneous equations with Eq. (6.54) and Eq. (6.65). The endwall mixing losses include: (1) the loss caused by mixing between the upstream boundary layer and flows in the downstream blade passage; (2) the mixing loss caused by complex secondary flows in the blade passage; (3) the additional mixing loss caused by separation of endwall flows. The Denton model does not explicitly give the method for calculating endwall mixing losses, but it indicates that the upstream boundary layer mixing loss accounts for about 20% of the total endwall loss, and the secondary mixing loss accounts for about 30%. However, the proportion of the additional mixing loss caused by the separation is uncertain.

$$\dot{S}_{Ebi} = 0.25 \int_0^{c_x} \frac{C_d}{T} \frac{(V_s^4 - V_p^4)}{(V_s - V_p)} \rho w dx \quad (6.64)$$

$$\zeta_{Eb} = \zeta_{Ebi} + \zeta_{Eb,Bt} \quad (6.65)$$

(5) Shock loss

Denton pointed out that the entropy increase caused by shock waves is a function of the inlet Mach number, as shown in Eq. (6.66), where C_v is the specific heat at constant volume; γ is the specific heat ratio. The corresponding loss coefficient can be obtained by establishing simultaneous equations with Eq. (6.54).

$$\Delta s = C_v \frac{2\gamma(\gamma - 1)}{3(\gamma + 1)^2} (Ma_{in}^2 - 1)^3 \quad (6.66)$$

6.2.8 Coull and Hodson Profile Loss Model

In the process of low pressure turbine design, profile loss is one of the most critical factors influencing the turbine efficiency. In the recent 20 years, with the rapid development of technologies for high-load LP turbine design, which take the “calming” effect into account, the blade-surface boundary layer flows have become more and more complicated. Particularly, various complex flows such as laminar separation bubbles and boundary layer transition under unsteady excitation may occur simultaneously in the boundary layer at the suction side. How to deal with the influence of factors such as boundary layer transition under unsteady excitation is of

great significance to the prediction accuracy of loss models. Conventional profile loss models are powerless in this aspect. In recent years, based on studies on flow mechanisms of high-lift turbines, Coull and Hodson proposed a brand-new profile loss model and a preliminary design method for high-lift LP turbine blades [25]. The model and the design method can be used to carry out an initial assessment of the influence of key parameters, including blade loading, isentropic velocity distribution, uneven distribution of outlet velocity, and reduced frequency, on losses of high-lift blades. Considering that high-lift turbine blades are of great significance in modern aero-engine design, this subsection emphatically introduces the Coull and Hodson profile loss model, which is applicable for high-lift blades.

Since the base pressure loss in high-lift LP turbine cascades is very low, generally less than 3% [26, 27], the influence of the base pressure loss is ignored in this model. Thus, the profile loss is given by:

$$\zeta \approx \left(\frac{U_{TE}}{U_2} \right)^2 \left[\left(\frac{2 \sum \theta_{TE}}{s \cos(\alpha_2)} \right) + \left(\frac{\sum \delta_{TE}^* + t_{TE}}{s \cos(\alpha_2)} \right)^2 \right] \quad (6.67)$$

The first term within the square bracket at the right side of the above equation represents the loss in the boundary layer, where $\sum \theta_{TE}$ is the sum of the boundary layer momentum thickness at the trailing edge of the suction side and the pressure side; s is the blade pitch; α_2 is the outflow angle. The second term in the square bracket represents the loss caused by the total blockage effect of the boundary layer and blades, where t_{TE} is the trailing-edge thickness. The first term at the right side of the above equation is used to correct the difference between the trailing-edge velocity, U_{TE} , and the average outlet velocity, U_2 . Statistical results obtained by Coull and Hodson showed that the difference between the two would be more than 10% in high-lift LP turbines, and thus it cannot be ignored.

The influence of unsteady factors is considered in the modeling of the boundary layer momentum thickness at the trailing edge of the suction side, θ_{TE} , which is divided into three components representing the contributions of turbulent boundary layer, separation bubble, and unsteady wakes respectively, and is given by:

$$[\theta_{TE}] = [\theta_{TE}]_{\text{bubble}} + [\theta_{TE}]_{\text{turb}} + [\theta_{TE}]_{\text{wake}} \quad (6.68)$$

where,

$$[\theta_{TE}]_{\text{bubble}} = \theta_{\text{sep}} (6.69 \times 10^6) (\text{Re}_{\theta_{\text{sep}}})^{(-4.28 + 2.05(\Delta U^*/\Delta S^*) - 0.161f_r)} \quad (6.69)$$

$$[\theta_{TE}]_{\text{turb}} = \theta_{\text{sep}} (\text{Re}_{\theta_{\text{sep}}})^{0.322} \left(1 - \frac{S_{\text{sep}}}{S_0} \right) \left(0.166 + 3.13 \left(\frac{\Delta U^*}{\Delta S^*} \right) \right) \quad (6.70)$$

$$[\theta_{TE}]_{\text{wake}} = S_0 (7.06 \times 10^{-4}) (f_r) \quad (6.71)$$

where, θ_{sep} is the boundary layer momentum thickness at the separation point; S_{sep} and S_0 refer to the location of separation point and the arc length of the suction side respectively; $\frac{\Delta U^*}{\Delta S^*}$ is defined as $\frac{(U_{sep}-U_{TE})/U_{sep}}{(S_0-S_{sep})/S_0}$; f_r is the reduced frequency of the wake.

The boundary layer displacement thickness at the trailing edge of the suction side, δ_{TE}^* , can be obtained by using the shape factor, which is given by:

$$H_{TE} = 1.545 + (2.57 \times 10^9)(Re_{S_0})^{(-1.93DF + 0.619(\Delta U^*/\Delta S^*) - 0.085f_r - 1.77)} \quad (6.72)$$

Coull and Hodson further proposed a method for using the above model to assess the profile loss in the initial design process. With this method, the boundary layer parameters, including the blade pitch, s , θ_{sep} , and $\frac{S_{sep}}{S_0}$, are correlated to the blade loading, the trailing-edge diffusion factor on the suction side, the peak value position of isentropic velocity on the suction side, the leading-edge load on the suction side, and the outlet Reynolds number, and specific expressions are given. Figure 6.32 shows the comparison between results calculated by using this method and results of cascade experiments. It can be seen that the Coull and Hodson profile loss model has high precision (the standard deviation of data statistics is about 6.9%), and thus the model is very suitable for predicting the profile loss in the design of high-lift LP turbines.

Coull and Hodson further used this model to analyze the influence of loading distribution on the suction side on the profile loss. Figure 6.33 shows the different loading distributions of suction side with the same circulation. Table 6.1 shows the quantitative comparison between descriptive parameters of different loading

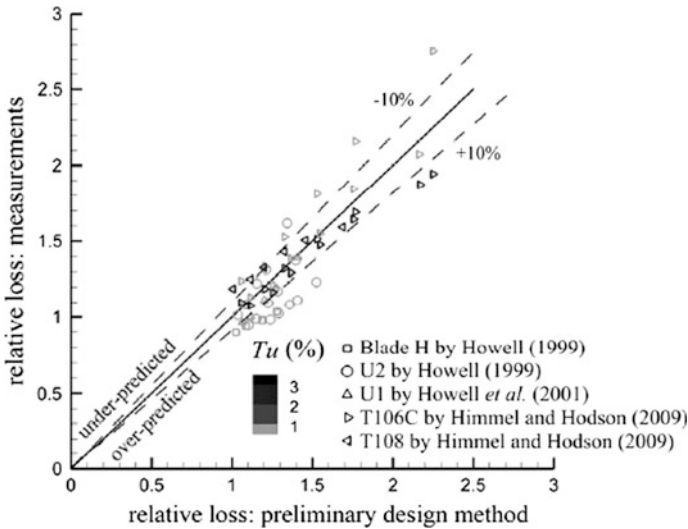


Fig. 6.32 Comparison between simulation results of Coull and Hodson profile loss model and results of cascade experiments [25]

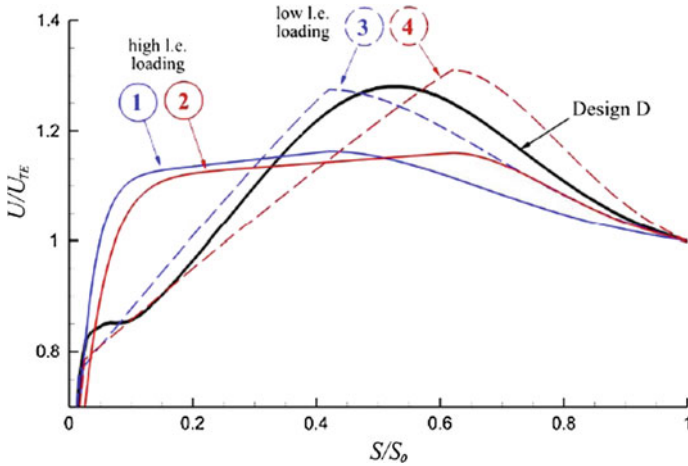


Fig. 6.33 Different suction-surface load distribution patterns [25]

Table 6.1 Quantitative comparison between descriptive parameters of different load distribution patterns [25]

Design	DF	S_{peak}/S_0	LEI	Description
D	0.28	0.52	0.47	Mid-loaded, “peaky” design
①	0.17	0.42	0.80	Front-Loaded, “flat top” design
②	0.17	0.62	0.80	Aft-loaded, “flat top” design
③	0.27	0.42	0.40	Front-Loaded, “peaky” design
④	0.31	0.62	0.40	Aft-loaded, “peaky” design

distributions. Figure 6.34 shows the assessment results about the influence of loading distributions of suction side on the profile loss at different Reynolds numbers. As can be seen from the figure, within the entire range of the Reynolds number, the aft-loaded peak-like distribution ④ has the worst performance; relatively speaking, the fore-loaded flat-top distribution ① has the best performance with low profile loss; the aft-loaded flat-top distribution ② and the fore-loaded peak-like distribution ③ give the similar performance, with the loss falling in between ① and ④; the design *D* is the mid-loaded peak-like distribution, whose performance is slightly inferior to ② and ③. These results could serve as reference for design of high-lift blades. It should be noted that, in the actual design process, attention should be paid not only to the profile loss, but also to the sensitivity of the loading distribution to the incidence, and to the influence of the load distribution on the secondary loss. The optimal loading distribution should be selected for the design through comprehensive tradeoff.

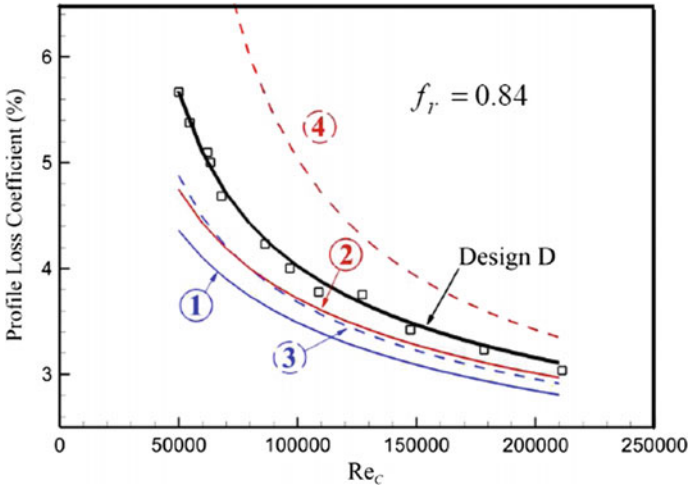


Fig. 6.34 Use Coull and Hodson profile loss model to assess the influence of load distribution on profile loss coefficient [25]

6.2.9 Cooling Flow Mixing Loss Models

As the inlet temperature of turbines increases year by year, the cooling air flow rate is becoming higher and higher, thus exerting more and more obvious influence on turbine performance. Therefore, how to establish corresponding loss models and take into full consideration of the influence of cooling flow in the design and assessment of turbines is of great significance. This subsection is devoted to introducing several cooling flow mixing loss models.

(1) Ito film cooling loss model

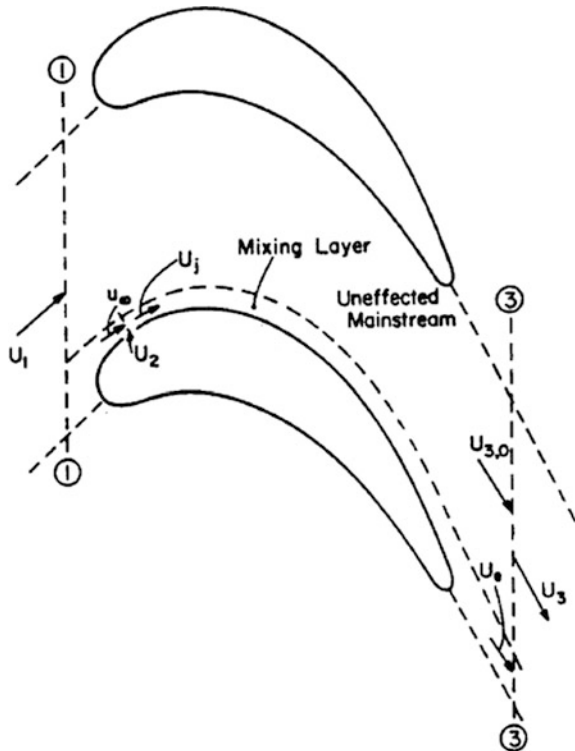
Based on the Hartsel model, Ito established a new model for predicting the film cooling loss [20]. The Hartsel model was proposed in 1972 and can be used to predict the trailing-edge flow loss of cooling air injection. According to this model, the main flow Mach number, the mass flux ratio of cooling air, the injection angle of cooling air, and the temperature ratio and velocity ratio of cooling air to main flow are the main factors influencing the cooling air mixing loss at the trailing edge slot [28].

Ito further assumed that the mixing process only occurs in a limited region on the blade surface, which is thicker than the boundary layer, as shown in Fig. 6.35. The mixing region is located within the dotted line on the suction side, similar as on the pressure side. Other regions in the main flow passage are considered to be unaffected by the cooling air injection. It is assumed that the flow in the mixing region expands isentropically, with the velocity changes from the inflow velocity, U_1 , to the velocity around the cooling air injection point, u_∞ , and after mixing with the cooling air (at the velocity of U_2) in the mixing region under the condition of constant pressure, velocity of the flow reaches to U_j . After that, velocity of the flow

in the mixing region further reaches to U_e through isentropic expansion at the outlet section (i.e. cross-section ③). As for the main flow that is unaffected by the cooling air injection, its velocity changes from the inlet velocity, U_1 , to the outlet velocity, $U_{3,0}$, through isentropic expansion. The two flows further mix together under the condition of constant pressure, and the flow velocity finally changes to U_3 . The pressure loss coefficient corresponding to the air film cooling can be obtained by using the one-dimensional method and establishing the mass conservation equation, the momentum conservation equation, and the energy conservation equation in the mixing region, and written as:

$$\begin{aligned}
 Y_{fc} &= 1 - (1 + FR) \left(1 + FR \frac{c_{p,f}}{c_{p,1}} \right) / \left(1 + FR \frac{R_f}{R_1} \right) \\
 &\quad \left(1 + \frac{(FR + \sigma) U_e}{(1 - \sigma) U_{3,0}} \right)^2 / \left(1 + \frac{FR + \sigma}{1 - \sigma} \right)^2 Y_{fc} \\
 &= 1 - (1 + FR) \left(1 + FR \frac{c_{p,f}}{c_{p,1}} \right) / \left(1 + FR \frac{R_f}{R_1} \right) \\
 &\quad \left(1 + \frac{(FR + \sigma) U_e}{(1 - \sigma) U_{3,0}} \right)^2 / \left(1 + \frac{FR + \sigma}{1 - \sigma} \right)^2
 \end{aligned} \tag{6.73}$$

Fig. 6.35 Mixing in air film cooling turbines [20]



$$\begin{aligned} \frac{U_e^2}{U_{3,0}^2} &= \frac{\left(1 + \frac{FR}{\sigma} \frac{R_f}{R_1}\right) \left(1 + \frac{FR}{\sigma} \frac{c_{p,f} T_f}{c_{p,1} T_1}\right)}{\left(1 + \frac{FR}{\sigma}\right) \left(1 + \frac{FR}{\sigma} \frac{c_{p,f}}{c_{p,1}}\right)} \left[1 - \left(\frac{u_\infty}{U_{3,0}}\right)^2\right] + \left(\frac{u_\infty}{U_{3,0}}\right)^2 \left[\frac{1 + \frac{FR}{\sigma} \frac{U_2}{U_{3,0}}}{1 + \frac{FR}{\sigma}}\right] \frac{U_e^2}{U_{3,0}^2} \\ &= \frac{\left(1 + \frac{FR}{\sigma} \frac{R_f}{R_1}\right) \left(1 + \frac{FR}{\sigma} \frac{c_{p,f} T_f}{c_{p,1} T_1}\right)}{\left(1 + \frac{FR}{\sigma}\right) \left(1 + \frac{FR}{\sigma} \frac{c_{p,f}}{c_{p,1}}\right)} \left[1 - \left(\frac{u_\infty}{U_{3,0}}\right)^2\right] + \left(\frac{u_\infty}{U_{3,0}}\right)^2 \left[\frac{1 + \frac{FR}{\sigma} \frac{U_2}{U_{3,0}}}{1 + \frac{FR}{\sigma}}\right] \end{aligned} \quad (6.74)$$

where, FR is the flow rate ratio of the cooling air to the main flow; σ is the ratio of the flow rate after mixing in the mixing region to the main flow rate before mixing; the subscript, f , indicates that the parameters are for cooling air. Other assumptions used in the model are described as follows: the pressure in the blade row is uniform, for instance, $P_1 = P_3$; the cross-sectional area of the mixing region stays the same; flows in the mixing region are incompressible. It compared the prediction results by the model with experimental results, finding that the accuracy was high. However, this method has certain limitations: (1) it would apply only to conditions with small flow rate ratio, such as $FR \leq 0.03$; (2) it is based on the assumption that there is only one cooling air hole on the blade surface.

(2) Lakshminarayana film cooling loss model

Based on the work of Kollen et al., Lakshminarayana et al. developed a new model for predicting air film cooling loss in turbines [29, 30]. The analysis object of this model is same as that in Fig. 6.35, and the difference is that flows are considered to be compressible. In this model, the enthalpy loss coefficient is given by:

$$\xi_{fc} = 1 - (1 + FR)U_3^2 / (U_{3,0}^2 + FRU_{fi}^2) \quad (6.75)$$

$$U_3 = \frac{A}{2} - \sqrt{\frac{A}{4} - \frac{2\gamma}{\gamma+1} RT_{c3}} \quad (6.76)$$

$$A = \frac{2\gamma}{\gamma+1} \left[\frac{1-\sigma}{1+\chi} U_{3,0} + \frac{\sigma+\chi}{1+\chi} U_j + \frac{p_3 A_3}{m_{in}(1+\chi)} \right] \quad (6.77)$$

$$T_{c3} = \frac{1-\sigma}{1+\chi} T_{c1} + \frac{\sigma+\chi}{1+\chi} T_{ce} \quad (6.78)$$

where, A_3 is the flow area of cross-section ③; U_{fi} is the ideal velocity of cooling air under the pressure condition in the mixing region, which can be obtained based on the assumption that the cooling air experiences isentropic expansion from the injection point to cross-section ③, and is given by:

$$U_{fi} = \sqrt{\frac{2\gamma}{\gamma-1} RT_{cf} \left[1 - \left(\frac{P_3}{P_{cf}} \right)^{(\gamma-1)/\gamma} \right]} \tag{6.79}$$

Similar to the above Ito loss model, this model is also established based on the assumption that there is only one cooling air hole on the blade surface. Both of them are established by adding cooling air to the one-dimensional flow in the blade passage. One common assumption of the models is that the pressure stays the same in the mixing process, and that the mixing between the cooling air and the main flow always takes place within a thin layer with constant cross-sectional area on the blade surface.

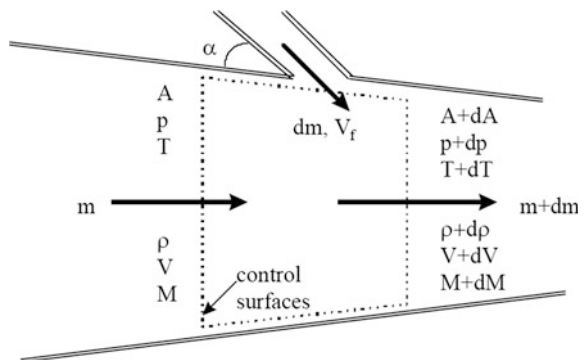
(3) Other relevant studies

Based on the Shapiro model [31], Ref. [24] proposes a film cooling mixing loss model to assess the loss of air-cooled turbines. Its analysis object is the compressible pipe flow with variable sections, which exchanges mass, momentum, and energy with the environment, as shown in Fig. 6.36. By using the mass conservation equation, the momentum conservation equation, and the energy conservation equation for the control volume, a series of equations reflecting relations between the parameters can be obtained. The relation between entropy increase and other parameters is expressed as follows:

$$ds = c_p \left[\left(1 + \frac{\gamma-1}{2} M^2 \right) \frac{dT_c}{T_c} + \frac{\gamma-1}{2} M^2 \left(4f \frac{dx}{D} + \frac{\gamma-1}{2} M^2 \left(\frac{dX}{1/2\gamma p A M^2} - 2\phi \frac{d\dot{m}}{\dot{m}} \right) + (\gamma-1) M^2 \frac{d\dot{m}}{\dot{m}} \right) \right] \tag{6.80}$$

where, f is the friction coefficient of the solid wall; A is the cross-sectional area of the flow passage; ϕ is the ratio of the cool air injection velocity to the streamwise velocity of the main flow; $d\dot{m}$ is the cooling air flow injected to the control volume; dX is the resistance caused by injection of liquid drops into the main flow, which is zero for gaseous cooling medium. The first term at the right side of the above

Fig. 6.36 One-dimensional mixing flow [24]



equation is the entropy increase caused by total temperature change, which results from heat exchange between the cooling air and the main flow. This entropy increase is not caused by the irreversible process in the cooling process, so the first term is ignored here. In addition, because the entropy increase caused by friction between the gas and blade surface is included in the profile loss, the second term at the right side can be ignored as well. Therefore, the entropy increase of the blade row is given by:

$$s_{out} - s_{in} = c_p(\gamma - 1) \sum_{i=1}^n M(x_i)^2 \left(1 - \frac{V_{fi}}{V(x_i)} \cos \alpha \right) \frac{(\Delta \dot{m}_f)_i}{\dot{m}_{in} + \sum_{k=0}^{i-1} (\Delta \dot{m}_f)_k} \quad (6.81)$$

where, $(\Delta \dot{m}_f)_i$ is the cooling air flow at the i th hole; n is the total number of cooling air holes on the blade surface. It is assumed that the cooling air is continuously and uniformly injected into the main flow passage between the inlet and outlet of the blade row. The average Mach number is written as \bar{M} , and the average velocity ratio is written as $\bar{\phi}$. Thus, the entropy increase of the blade row caused by air film cooling can be further simplified as:

$$s_{out} - s_{in} = c_p(\gamma - 1) \bar{M}^2 (1 - \bar{\phi}) \ln \left(1 + \frac{\dot{m}_f}{\dot{m}_{in}} \right) \quad (6.82)$$

where, \dot{m}_{in} is the inlet mass flow rate of the blade row; \dot{m}_f is the total mass flow rate of the cooling air injected into the blade row. To obtain the average Mach number and the average velocity ratio, the velocity distribution on the blade surface is assumed as follows: the velocity on the suction side is uniformly distributed and same as the outlet velocity of the blade row; the velocity on the pressure side is uniformly distributed and slightly lower than the inlet velocity of the blade row. This assumption is also used in the prediction of the profile loss by many researchers [14, 32–34]. According to the assumption, the average Mach number and the average velocity on the mean streamline of the S1 stream surface are given by:

$$\bar{M} = \frac{\bar{M}_{ss} + \bar{M}_{ps}}{2} = \frac{M_{out} + M_{in} - \Delta M}{2}$$

$$\bar{V} = \frac{\bar{V}_{ss} + \bar{V}_{ps}}{2} = \frac{V_{out} + V_{in} - \Delta V}{2}$$

This film cooling loss model suggests the importance of the Mach number in the prediction of loss. For the same cooling air flow rate, there is a great difference in the cooling loss between the conditions of arranging the cooling air in the leading edge area of the blade, where the Mach number is relatively low, and arranging it in the trailing edge area, where the Mach number is relatively high. It should be noted that the assumption of the model that the cooling air is continuously and uniformly injected on the blade surface may be inconsistent with engineering practice.

To give a more comprehensive consideration to the factors related to the cooling air mixing loss, Pullan et al. developed a new film cooling loss model [35] based on the work of Young et al. [36, 37]. The following assumptions were made pressure in the mixing process between the cooling air and the main flow is uniform; the mixing process takes place within a thin layer near the blade surface (as shown in Fig. 6.37); the upper boundary of the control volume is variable to ensure the mixing takes place under a constant pressure; all kinds of losses can be calculated separately and added up directly. The included angle between the cooling air and the main flow is defined as α , and the subscripts, g , c , and m , respectively represent the local main flow, the cooling air flow, and the mixed flow.

According to the assumptions, the entropy increase caused by the mixing of the cooling air and the main flow is given by:

$$\Delta \sum_{\text{mix}} = m_g \left[\int_{T_g}^{T_m} c_{pg} \left(\frac{1}{T} - \frac{1}{T_m} \right) dT - \left(\frac{V_m^2 - V_g^2}{2T_m} \right) \right] + m_c \left[\int_{T_c}^{T_m} c_{pc} \left(\frac{1}{T} - \frac{1}{T_m} \right) dT - \left(\frac{V_m^2 - V_c^2}{2T_m} \right) \right] \quad (6.83)$$

Considering the three-dimensionality of the jet flow angle (as shown in Fig. 6.38), the following equation can be obtained:

$$V_m^2 = \left(\frac{m_g V_g + m_c V_c \cos \kappa}{m_g + m_c} \right)^2 + \left(\frac{m_c V_c \sin \kappa}{m_g + m_c} \right)^2 \quad (6.84)$$

Thus, the entropy increase can be further written as:

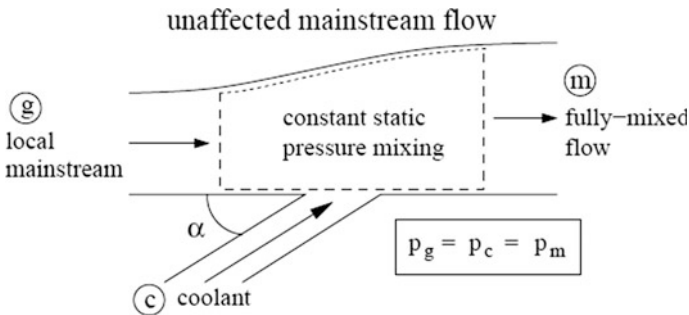


Fig. 6.37 Research object and control volume

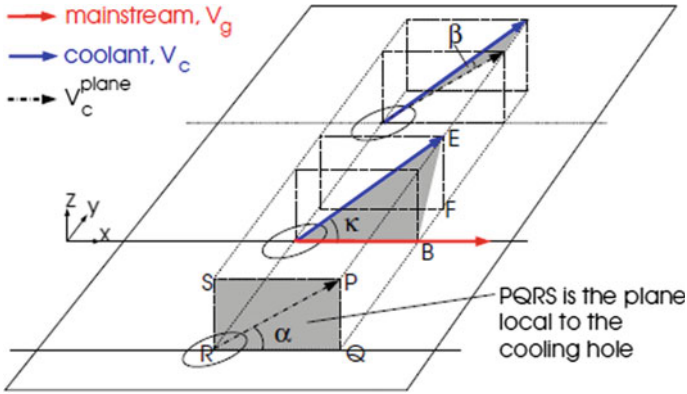


Fig. 6.38 Included angle between cooling air and main flow [35]

$$\Delta \sum_{\text{mix}} = m_g \int_{T_g}^{T_m} c_{pg} \left(\frac{1}{T} - \frac{1}{T_m} \right) dT + m_c \int_{T_c}^{T_m} c_{pc} \left(\frac{1}{T} - \frac{1}{T_m} \right) dT \quad (6.85)$$

$$+ \frac{m_g m_c}{m_g + m_c} \left(\frac{M_g^2 \gamma_g R_g T_g}{2 T_m} \right) \left[\left(1 - \frac{V_c}{V_g} \cos \kappa \right)^2 + \left(\frac{V_c}{V_g} \sin \kappa \right)^2 \right]$$

Generally, $m_g \gg m_c$, so $\frac{m_g}{m_g + m_c} \approx 1$, $T_m \rightarrow T_g$; thus, the entropy increase can be further written as:

$$\Delta \sum_{\text{mix}} = m_c \int_{T_c}^{T_g} c_{pc} \left(\frac{1}{T} - \frac{1}{T_g} \right) dT + \frac{m_c \gamma_g R_g M_g^2}{2} \left[\left(1 - \frac{V_c}{V_g} \cos \kappa \right)^2 + \left(\frac{V_c}{V_g} \sin \kappa \right)^2 \right]$$

$$= m_c c_{pc} \left(\ln \frac{T_g}{T_c} + \frac{T_c}{T_g} - 1 \right) + \frac{m_c \gamma_g R_g M_g^2}{2} \left[\left(1 - \frac{V_c}{V_g} \cos \kappa \right)^2 + \left(\frac{V_c}{V_g} \sin \kappa \right)^2 \right]$$

$$= m_c \frac{\gamma_c}{\gamma_c - 1} R_c \left(\ln \frac{T_g}{T_c} + \frac{T_c}{T_g} - 1 \right) + \frac{m_c \gamma_g R_g M_g^2}{2} \left[\left(1 - \frac{V_c}{V_g} \cos \kappa \right)^2 + \left(\frac{V_c}{V_g} \sin \kappa \right)^2 \right] \quad (6.86)$$

Finally, the efficiency of air-cooled turbines is given by:

$$\eta_c = \frac{P_{\text{gross}}}{P_{\text{gross}} + \bar{T} \Delta S_{CR}} = \frac{P_{\text{gross}}}{P_{\text{gross}} + \bar{T} (\Delta \sum_{\text{basic}} + \Delta \sum_{\text{mix}})} \quad (6.87)$$

where, $\Delta \sum_{basic}$ is the entropy production without cooling, including the profile loss, the endwall loss, and so on; P_{gross} is the actual output work; \bar{T} is $\frac{h_{03} - h_{03e}}{s_3 - s_{3e}}$ (see Ref. [35] for details).

6.3 Selection of Geometrical and Aerodynamic Parameters in Low-Dimensional Design Space

Aerodynamic design of turbines is a process of design and optimization from low dimensions (one dimension and two dimensions) to high dimensions (three dimensions, four dimensions of time and space considering unsteady effect, etc.), and the design results obtained in low-dimensional space serve as the basis of high-dimensional design. Although design and optimization in high-dimensional space can effectively improve the aerodynamic performance of turbines, but they are heavy work-loaded and long time-consuming. In addition, accuracy and precision of the current three-dimensional numerical simulation methods still mainly rely upon experience. Regardless of how advanced the employed three-dimensional design and optimization method is, any overlook of physical nature in the design process may lead to failure of turbomachinery design. The failure of the design of the PW6000 turbofan engine is a typical example. Relatively, although low-dimensional aerodynamic design method relies more on experience and requires deeper understanding of physical nature, it is helpful to grasp the most essential physical essence of a turbine and determine the performance level of the designed turbine to a great extent, if properly used. Thus, the method plays a decisive role and serves as a key link in the design process, which is also one of the core technologies of aero-engine companies. In the importance of low-dimensional aerodynamic design method, this section is devoted to introducing the methods for assessing aerodynamic performance of turbines in low-dimensional design space, and investigating the methods and criteria for selecting low-dimensional design parameters for various kinds of turbines, such as multi-stage LP turbines, variable-speed power turbines, versatile core-engine turbines, and counter-rotating turbines, so as to provide some reference for low-dimensional aerodynamic design of turbines.

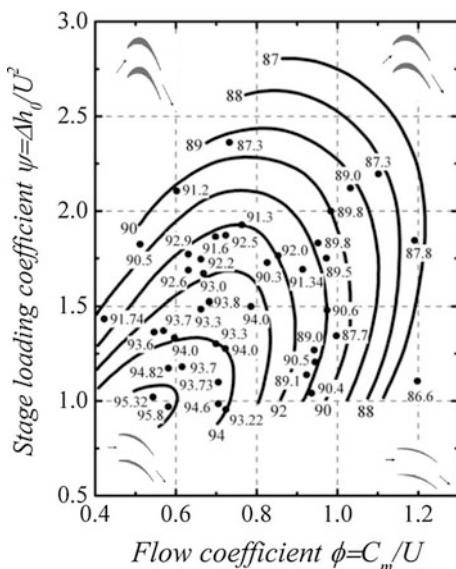
6.3.1 *Methods for Assessing Aerodynamic Performance of Turbines in Low-Dimensional Design Space*

One-dimensional aerodynamic design is the first step of aerodynamic design of turbines. The primary mission in this step is to obtain the meridional flow passage, number of turbine stages, velocity triangle of each stage, and other key parameters according to the performance requirements, boundary conditions and various constraints at the design point. The performance requirements include a series of parameters such as design-point flow rate, expansion ratio, and efficiency (or

power). The boundary conditions include parameters like the revolution speed of rotor, total temperature, pressure and flow angles at the turbine inlet, and cooling air parameters, and the constraint conditions include parameters of axial and radial dimensions, aerodynamic parameters at the outlet (outflow angle, outlet Mach number, etc.), structural strength, weight, and so on. Under the premise that the distribution of the work for each of the turbine stages is determined, the velocity triangle of each turbine stage is determined by five dimensionless parameters: the loading coefficient, H_T , the flow coefficient, ϕ , the reaction degree, Ω , the axial velocity ratio, K , and the inlet to outlet mean diameter ratio, D .

Among the parameters above, the value of the axial velocity ratio, K , and the inlet to outlet mean diameter ratio, D , change little in conventional turbines, thus they have little influence on aerodynamic performance of turbines, while the other three parameters: the loading coefficient, H_T , the flow coefficient, ϕ , and the reaction degree, Ω , play a vital role in determining aerodynamic performance of turbine stages. The classical Smith chart is used to describe the empirical correlations between the efficiency of a turbine stage and the loading coefficient, H_T , and the flow coefficient, ϕ , at $\Omega = 0.5$ [38], which has become an important reference for selecting low-dimensional design parameters of a turbine stage. For a certain design, there is an optimal combination of parameters that can obtain the best aerodynamic performance of a turbine stage. Actually, the three dimensionless parameters influence the performance of a turbine stage versatily. They would not only have influence on the aerodynamic performance, but also the dimensions, structure per-

Fig. 6.39 Classical Smith chart—variation of turbine efficiency with loading coefficient and flow coefficient [38]



formance, and strength performance. Figure 6.39 also shows the typical blade profiles corresponding to different parameter ranges, and it is clear that the blade profile is related to the value of the flow coefficient and loading coefficient.

It is worth noting that the empirical correlations in the Smith chart are based on turbines designed in the 1960s. However, with the development of turbine design techniques and the changes of design requirements, influence of some new parameters such as the lift coefficient and Reynolds number of high-lift blades, which are not taken consideration into in the Smith chart, is gradually increasing, while the classical Smith chart cannot indicate the influence of these parameters on turbine performance. In order to resolve these deficiencies, some researchers analyzed the influence of low-dimensional design parameters by using the one-dimensional meanline assessing method with modifying the empirical models in recent years. For instance, Coull and Hodson analyzed the influence of the flow coefficient, the lift coefficient, and the Reynolds number on the performance of LP turbines by using this method [39, 40].

6.3.1.1 Meanline Methods for Assessing Turbine Performance by Using Loss Models

Regarding a concrete specific problem or a certain kind of design problems, the following question should be answered first: how to select a velocity triangle for each turbine stage or is it possible to give an optimal range for the selection. Generally, solution of this question mainly depends on designers' experience or the low-dimensional model based on the experience. In other words, if these one-dimensional parameters are correlated with the aerodynamic performance of a turbine stage, it is possible to realize reasonable selection and optimization of design parameters in the low-dimensional space with the meanline method. Although the models are semi-theoretical and semi-experimental correlation equations or even totally depend on experience, they can reflect the relation between the crucial flow mechanisms in turbines and the aerodynamic performance in the most concise way and serve as the important tool for assessing turbines' aerodynamic performance in low-dimensional space. What follows is a brief introduction to the model in Ref. [22].

The model is built to correlate turbine efficiency with the dimensionless parameters (namely the five variables: the loading coefficient, H_T , the flow coefficient, φ , the reaction degree, Ω , the axial velocity ratio, K , and the inlet to outlet mean diameter ratio, D). For single turbine stage, the aerodynamic efficiency can be expressed as [22]:

$$\eta = \frac{2H_T\eta_\delta}{\left\{ \begin{aligned} &\varphi^2 \left[\left(\frac{1}{\zeta_r^2} - 1 \right) + K^2 \left(\frac{1}{\zeta_s^2} - 1 \right) \right] + \frac{H_T^2}{4} \left(\frac{1}{\zeta_s^2} + \frac{1}{\zeta_r^2} - 2 \right) \\ &+ H_T \left\{ (1 - \Omega) \left(\frac{1}{\zeta_s^2} - 1 \right) + [D - (1 - \Omega)] \left(\frac{1}{\zeta_r^2} - 1 \right) + 2 \right\} \\ &+ [D - (1 - \Omega)]^2 \left(\frac{1}{\zeta_r^2} - 1 \right) + (1 - \Omega)^2 \left(\frac{1}{\zeta_s^2} - 1 \right) \end{aligned} \right\}} \tag{6.88}$$

where, η_δ represents the tip leakage loss efficiency; ζ_r and ζ_s represent the velocity loss coefficients of the rotor and stator respectively. The velocity loss coefficients of the blade row can be calculated by the following equation:

$$\zeta_r, \zeta_s = \sqrt{1 - (\xi_p + \xi_s)} \tag{6.89}$$

where, ξ_p and ξ_s represent the profile loss coefficient and the secondary loss coefficient respectively. The profile loss coefficient of the stator is calculated by:

$$\xi_p = \frac{0.003}{\left(0.09 \frac{K_{p1}}{\sin \alpha_1} + 0.46 \right) (K_{p2} - \sin \alpha_1) + 0.085} + 0.017 \tag{6.90}$$

where, α_1 represents the outflow angle of the stator; K_{p1} and K_{p2} represent the coefficients determined by specific profile parameters, and are calculated by:

$$\left\{ \begin{aligned} &\text{when } \alpha_0 + \alpha_1 < 90^\circ, K_{p1,a} = \sin \alpha_0 \sin(\alpha_0 + \alpha_1), K_{p2,a} = \sin \alpha_0 \\ &\text{when } \alpha_0 + \alpha_1 \geq 90^\circ \text{ and } \alpha_0 \leq 90^\circ, K_{p1,a} = \frac{\sin \alpha_0}{\sin(\alpha_0 + \alpha_1)}, K_{p2,a} = \sin \alpha_0 \\ &\text{when } \alpha_0 > 90^\circ, K_{p1,a} = \frac{1}{\sin \alpha_0 \sin(\alpha_0 + \alpha_1)}, K_{p2,a} = \frac{1}{\sin \alpha_0} \end{aligned} \right. \tag{6.91}$$

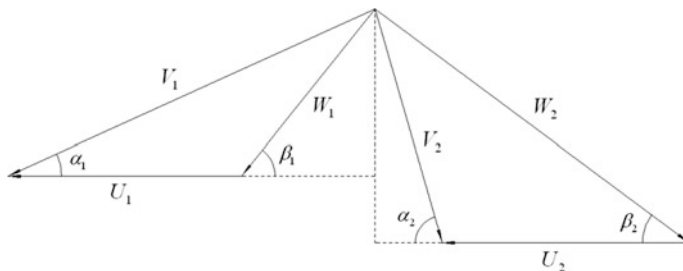


Fig. 6.40 Typical velocity triangle of a turbine stage

where, α_0 represents the inflow angle of the stator. The secondary loss coefficient is calculated by:

$$\zeta_s = 0.0474 \frac{\sin \alpha_1}{\sin \alpha_0} \left[\frac{\cot \alpha_0 + \cot \alpha_1}{\left(\frac{h}{b}\right)} \right] K_s + 0.0118 \quad (6.92)$$

where, $\frac{h}{b}$ represents the aspect ratio; K_s represents the coefficient related to the aspect ratio, and is calculated by:

$$\begin{cases} \text{when } \left(\frac{h}{b}\right)_{sa} \geq 2, & K_{s,a} = 1 \\ \text{when } \left(\frac{h}{b}\right)_{sa} < 2, & K_{s,a} = 1 - 0.25\sqrt{2 - \left(\frac{h}{b}\right)_{sa}} \end{cases} \quad (6.93)$$

Similar calculations could be performed for the rotor of a turbine stage to obtain the velocity loss coefficient of the rotor blade, ζ_r (see Ref. [22] for details).

The quantitative relations of the five dimensionless parameters used to define the velocity triangle (as shown in Fig. 6.40) and flow angles are given in Eq. (6.94):

$$\begin{cases} \alpha_1 = \arctan \frac{\varphi K}{\frac{H_T}{2} + (1-\Omega)} \\ \alpha_2 = \arctan \frac{\varphi}{\frac{H_T}{2} - (1-\Omega)} \\ \beta_1 = \arctan \frac{\varphi K}{\frac{H_T}{2} - \Omega} \\ \beta_2 = \arctan \frac{\varphi}{\frac{H_T}{2} - (1-\Omega) + D} \end{cases} \quad (6.94)$$

So far, the aerodynamic efficient of a turbine stage can be calculated by using the five dimensionless parameters of the velocity triangle and the aspect ratio of blades.

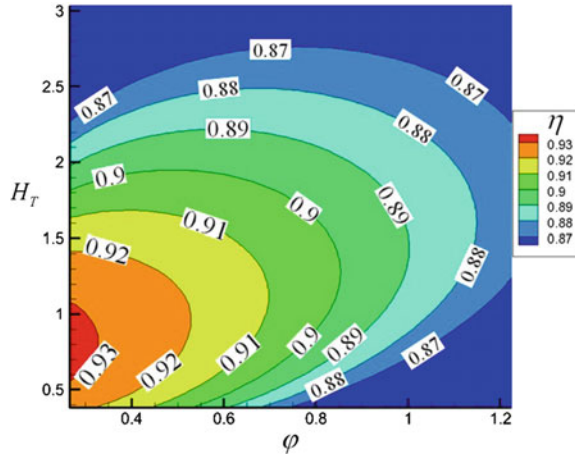
In multi-stage turbines, except for the above-mentioned five parameters of each turbine stage, the work distribution coefficient, λ_n , is added to the model; the subscript, n , means the n th turbine stage. In other words, the relation between the total power of turbine, P_T , and the power of each turbine stage, P_n , is written as:

$$P_n = \lambda_n P_T \quad (6.95)$$

In addition, the work distribution coefficient, λ_n , is subject to the following constraint:

$$\sum_1^N \lambda_n = 1 \quad (6.96)$$

Fig. 6.41 Influence of flow coefficient and loading coefficient on efficiency of turbine stage [41]



Then, for the design of a N -stage turbine, the total efficiency of turbine, η_T , is calculated by:

$$\eta_T = \frac{\sum_1^N P_n}{\sum_1^N \frac{P_n}{\eta_n}} = \frac{\sum_1^N P_T \lambda_n}{\sum_1^N \frac{P_T \lambda_n}{\eta_n}} = \frac{1}{\sum_1^N \frac{\lambda_n}{\eta_n}} \tag{6.97}$$

The aerodynamic efficiency of a single-stage turbine is calculated with the correlation equations above. Figure 6.41 shows the correlation between the flow coefficient, the loading coefficient, and the efficiency of the turbine. In the calculation, the reaction is set as 0.5; both the axial velocity ratio and the inlet-to-outlet mean diameter ratio are set as 1; the aspect ratio of blades is set as 1.7; the tip leakage loss efficiency is set as 0.99. It can be seen that the variation trend of turbine efficiency given in Fig. 6.41 is same as that shown in the classical Smith chart [38, 41].

Obviously the ability and accuracy of this method in the prediction of turbine performance depend on the accuracy and application range of the employed loss model. When using the method users can select a loss model based on their experience and even modify relevant empirical coefficients to obtain the best results.

For supersonic turbines, the kinetic energy of the gas exhausted from the outlet of rotor cannot be recovered, which is called the exhausted velocity loss. Therefore, the impact of the exhausted velocity loss on turbine performance has to be considered when selecting velocity triangles for supersonic turbines. In addition, the flow direction at the outlet of the rotor always deviates from the axial direction according to the characteristics of supersonic turbines. When the flow enters the exhaust nozzle with a high tangential velocity, significant friction occurs between the flow and the wall of the exhaust nozzle, so that the tangential velocity of the flow would suffer a great loss. Meanwhile, the total pressure recovery coefficient of the exhaust nozzle would decline sharply, thus causing an adverse influence on turbine performance. Therefore, when designing the velocity triangle for a

supersonic turbine, the impact of both the flow losses in the turbine and the exhaust loss on its performance have to be considered.

When calculating the influence of the exhausted velocity loss on turbine efficiency, the exhausted flow loss coefficient, Z_E , is defined. The coefficient represents the ratio of kinetic energy of exhausted flow to the rim work [42], and is written as:

$$Z_E = \frac{V_2^2}{2Lu} \quad (6.98)$$

Finding the relations between the physical quantities in the above equation and the basic parameters of the velocity triangle and replacing them with the basic parameters, we can obtain:

$$Z_E = \frac{\bar{C}_{2a}^2 + (1 - \frac{\mu}{2} - \Omega)^2}{2\mu} \quad (6.99)$$

With the loss coefficient in Ref. [42], the turbine efficiency can be written as:

$$\eta = 1 - Z_s = 1 - \frac{Z}{Z+1} = \frac{1}{Z+1} \quad (6.100)$$

For the total-to-total efficiency given in the above equation, the corresponding loss coefficient is calculated by:

$$Z_{internal} = \frac{1}{\eta_{tt}} - 1 \quad (6.101)$$

Thus, the total efficiency is expressed by:

$$Z_{all} = Z_{internal} + Z_E \quad (6.102)$$

$$\eta = \frac{1}{Z_{all} + 1} \quad (6.103)$$

Now, the total-to-total efficiency and total turbine efficiency (with exhaust loss being taken into consideration) can be calculated with every group of the selected basic parameters of the velocity triangle. For a single-stage supersonic turbine, the problem of matching the annulus area at the outlet of the rotor should be considered as well. For example, the annulus area of the outlet can't be taken consideration into when designing the velocity triangle, for the influence that the flow loss would increase caused by the large divergence angle of the flow passage. The inlet-to-outlet annulus area ratio of the rotor can be estimated by using the following method. According to the mass conservation of the rotor, the mass can be calculated:

$$\dot{m} = K \frac{P_1^*}{\sqrt{T_1^*}} A_1 q(\lambda_1) \sin \alpha_1 = K \frac{P_2^*}{\sqrt{T_2^*}} A_2 q(\lambda_2) \sin \alpha_2 \quad (6.104)$$

where, $q(\lambda_1)$ and $q(\lambda_2)$ represent the density flow functions of the inlet section and outlet section of the rotor, which can be calculated according to the velocity triangle; P_1^* is the total pressure at the inlet of the rotor, which can be obtained when calculating the internal flow loss; T_1^* is determined by design requirements; the corresponding T_2^* can be determined by the specified average radius, revolution speed, and selected loading coefficient; P_2^* can be derived from the total-to-total efficiency. Thus, the inlet-to-outlet area ration of the rotor can be estimated with Eq. (6.104), providing some reference for selection of the design parameters. Based on the assessment method above, the efficiency of supersonic turbines can be further expressed as a function of the dimensionless parameters of the velocity triangle. Supersonic turbines are always designed as impulse turbines; namely, the reaction degree is zero, so as to improve the power output of a single stage as possible. However, the flow in the impulse turbine only changes direction in the rotor passage but does not expand at all. Thus, it needs to overcome a strong adverse pressure gradient at the trailing edge of the suction side, which would cause the separation easily so as to lower down turbine efficiency. In addition, negative reaction degree would occur easily at the blade root. Both the separation and the negative reaction degree should be avoided as possible. Therefore, the reaction degree is set as 0.1 for the velocity triangle analysis in this section. Figure 6.42 shows the contours of the variation of supersonic turbine efficiency with the loading coefficient and the flow coefficient respectively at $\kappa = 1.0, 1.2$ and 1.5 . The axial velocity ratio, $\kappa = \frac{C_{2a}}{C_{1a}}$, is defined as the inlet-to-outlet axial velocity ratio of rotor. The contours on the left show the variation of the total-to-total turbine efficiency obtained by the conventional assessment method with the design parameters, while the contours on the right show the variation of the total turbine efficiency (with exhaust loss being taken into consideration) with the design parameters. Obviously, there are difference between the contours above in both quantitative distribution and qualitative distribution, which highlighting the necessity of the exhausted velocity considered at the initial design process.

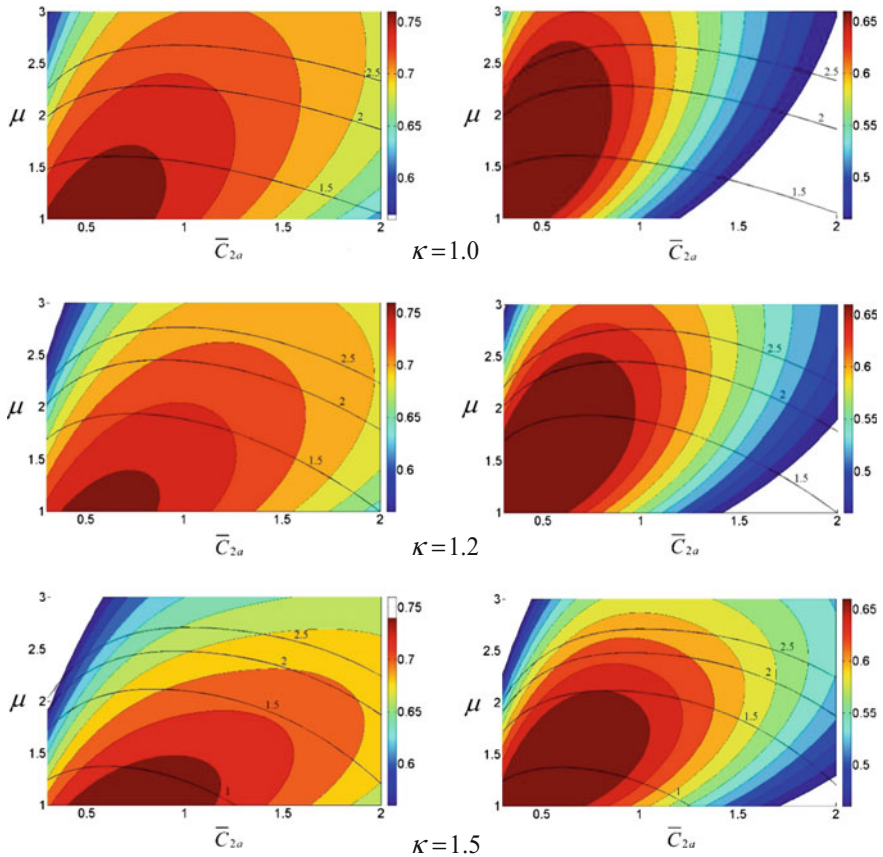


Fig. 6.42 Variation of supersonic turbine efficiency with design parameters

6.3.1.2 Assessing Turbine Performance by Using the Combination of One-Dimensional Euler Equations and Body Force Method

Except the meanline method, the method of assessing turbine performance with the combination of Euler equation and body force has also received much attention in recent years. This method can be used in one-dimensional, two-dimensional, and three-dimensional assessment of turbine performance, even under unsteady condition. What follows takes one-dimensional performance assessment as example. Adam and Léonard developed a method for rapid assessment of turbine performance by introducing the body force source term to the one-dimensional Euler equation. Aerodynamic parameters at the mean diameter of the runner can be obtained by using the finite volume method to solve the equations, and aerodynamic performance of multi-stage turbines under different conditions can be then found [43, 44]. Relevant research has also been carried out and codes have been

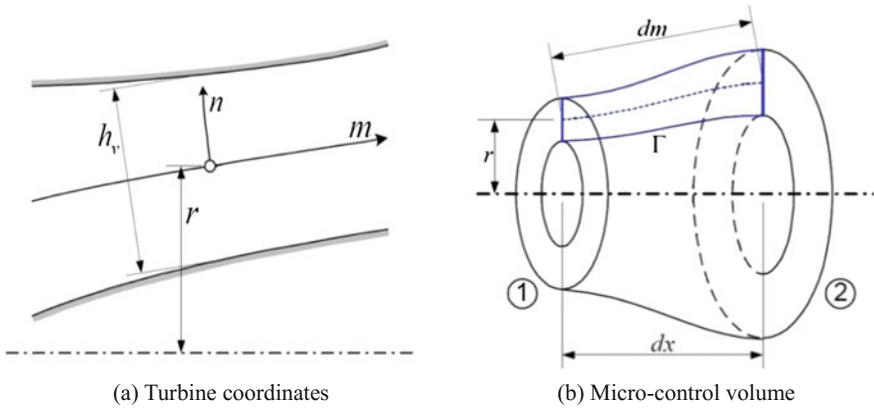


Fig. 6.43 Coordinates and control volume [43]

developed for calculating aerodynamic performance of multi-stage axial-flow turbines [41, 45]. There is a brief introduction to the method in this subsection.

The meridional flowpassage of the turbine under study is shown in Fig. 6.43a. Only variations of aerodynamic parameters along the flow direction are considered in one-dimensional assessment, while variations along the direction normal to the flowpassage are ignored. Based on that, the curvilinear coordinate system (m, n, θ) is established, where m is the coordinate along the flow direction; n is the normal coordinate; θ is the circumferential coordinate. The control volume is shown in Fig. 6.43b, with its upper boundary defined as the shroud and lower boundary defined as the hub. Section ① is assumed as the inlet section, and Section ② is assumed as the outlet section. Then, the Euler differential equation is established as follows:

$$\frac{\partial U}{\partial t} + \frac{\partial F}{\partial m} = Q \tag{6.105}$$

where,

$$U = \begin{bmatrix} \rho S \\ \rho V_m S \\ \rho V_\theta S \\ \rho e^\circ S \end{bmatrix} \quad F = \begin{bmatrix} \rho V_m S \\ (p + \rho V_m^2 S) \\ \rho V_m V_\theta S \\ \rho \left(e^\circ + \frac{p}{\rho} \right) V_m S \end{bmatrix}$$

$$Q = Q_b + Q_f + Q_g + Q_c$$

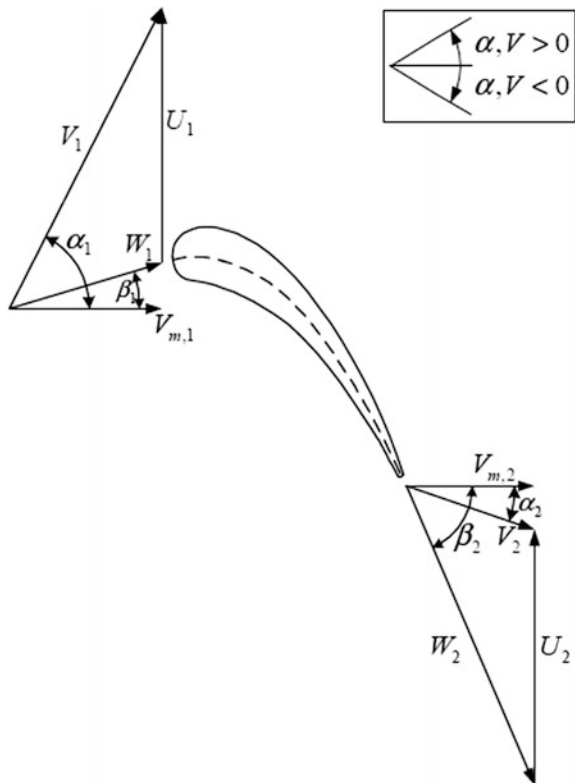
where, ρ represents the density of the fluid; S represents the cross-sectional area of the meridional flowpassage; t represents time; V_m represents the component of the absolute fluid velocity along the meridional direction; V_θ represents the component

of the absolute fluid velocity along the circumferential direction; r represents the radius to the central axis of the turbine; p represents the static pressure of the fluid; e° represents the total internal energy of the fluid. The body force source term, Q , includes four components: Q_b represents the non-viscous blade force source term; Q_f represents the viscous force source term; Q_g represents the geometric force source term; Q_c represents the cooling air source term. Of them, Q_b and Q_f are mainly related to the velocity triangles of the blade rows; Q_g is mainly related to the geometry of the meridional flowpassage; Q_c is mainly related to cooling flow.

Determination of the source terms is of vital importance to the prediction accuracy and ability of the method. To analyze the source terms, the velocity triangle at the mid-span section of the blade is shown in Fig. 6.44, where r_1 represents the mean diameter of the blade inlet and $V_{\theta,1}$ represents the corresponding circumferential velocity; r_2 represents the mean diameter of the blade outlet and $V_{\theta,2}$ represents the corresponding circumferential velocity; q_m represents the flow rate in the passage; Vol represents the gas volume in the blade row.

The circumferential component of the non-viscous blade force, $F_{b,\theta}$, can be calculated by using the angular momentum conservation equation; namely, the sum of the moments on the gas within the blade row is equal to the momentum increment between the inlet and outlet of the blade row. Thus, the circumferential

Fig. 6.44 Velocity triangle [43]



component, $F_{b,\theta}$, and the streamwise component, $F_{b,m}$, of the non-viscous blade force on the gas in unit volume can be written as:

$$rF_{b,\theta} = \frac{q_m}{Vol} (r_2 V_{\theta,2} - r_1 V_{\theta,1}), F_{b,m} = -F_{b,\theta} \frac{W_\theta}{V_m} \quad (6.106)$$

The increasing of the entropy of the flow along the streamline would be caused by the viscous force (the entropy increase can be obtained by using the Kacker and Okapuu model or other loss models). Thus, the viscous force vector, \vec{F}_f , and its streamwise component, $\vec{F}_{f,m}$, and circumferential component, $\vec{F}_{f,\theta}$, are calculated by:

$$|F_f| = \rho T \frac{W_m}{W} \frac{\partial S}{\partial m}, \vec{F}_{f,m} = -|\vec{F}_f| \frac{\vec{W}_m}{|\vec{W}|}, \vec{F}_{f,\theta} = -|\vec{F}_f| \frac{\vec{W}_\theta}{|\vec{W}|} \quad (6.107)$$

The geometric force source term mainly reflects the influence of the shape of the meridional flowpassage, specifically the influence of variations of the mean diameter and the area of the section perpendicular to the average meridional streamline. The streamwise component, $F_{g,m}$, and circumferential component, $F_{g,\theta}$, are given by:

$$F_{g,m} = \frac{\rho V_\theta^2}{r} \frac{\partial r}{\partial m}, F_{g,\theta} = -\frac{\rho V_m V_\theta}{r} \frac{\partial r}{\partial m} \quad (6.108)$$

The cooling air source term is mainly related to the cooling air. It is convenient to idealize that the cooling air only has impact on the mass conservation equation and the energy conservation equation (namely, the cooling air could change gas flow as well as enthalpy in the passage), and does not influence the momentum conservation equation and the angular momentum conservation equation along the flow direction. This assumption is reasonable when the proportion of the cooling air is small.

To sum up, the body force source terms are expressed as:

$$\begin{aligned} \mathbf{Q}_b &= \begin{bmatrix} 0 \\ F_{b,m}S \\ F_{b,\theta}S \\ F_{b,\theta}\Omega rS \end{bmatrix} & \mathbf{Q}_f &= \begin{bmatrix} 0 \\ F_{f,m}S \\ F_{f,\theta}S \\ F_{f,\theta}\Omega rS \end{bmatrix} & \mathbf{Q}_g &= \begin{bmatrix} 0 \\ F_{g,m}S + p \frac{\partial S}{\partial m} \\ F_{g,\theta}S \\ F_{g,\theta}\Omega rS \end{bmatrix} \\ \mathbf{Q}_c &= \begin{bmatrix} q_{cool} \\ 0 \\ 0 \\ q_{cool} \cdot h_{cool}^\circ \end{bmatrix} \end{aligned}$$

The turbine performance can be obtained by solving the one-dimensional Euler equation that contains the source term. Figure 6.45 presents the simulation results of the one-dimensional body force model on the performance of a two-stage LP

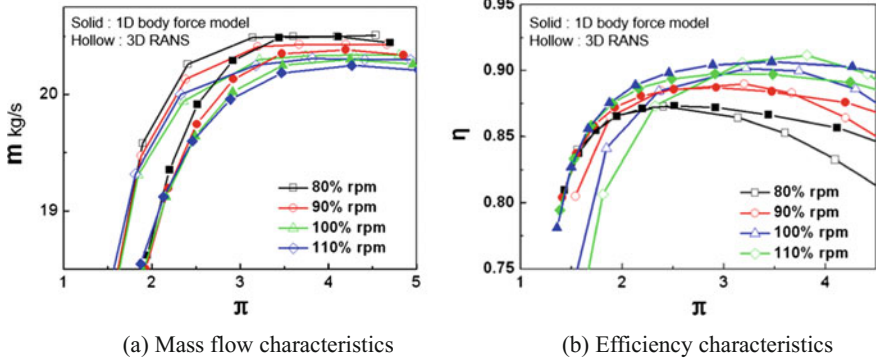


Fig. 6.45 Comparison between results obtained by 1D body force model and 3D RANS [46]

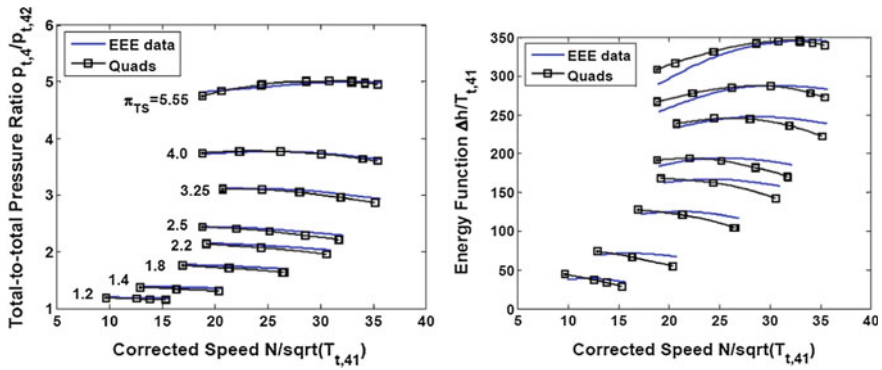


Fig. 6.46 Comparison between results obtained by one-dimensional body force model and experimental results [43]

turbine and compares them with the three-dimensional RANS calculation results [46]. Figure 6.46 presents the comparison between the results obtained by the one-dimensional body force model and the experimental results of the cooled HP turbine of the E³ engine [43]. These results suggest that the one-dimensional body force model has good accuracy in the prediction of turbine performance and can serve as an effective method for analyzing low-dimensional design parameters of turbines.

6.3.2 Selection and Optimization of Aerodynamic Parameters for Multi-stage LP Turbine in Low-Dimensional Design Space

6.3.2.1 Influence of Design Parameters on LP Turbine Performance

The influence of one-dimensional parameters on aerodynamic performance of turbines can be analyzed by one-dimensional performance assessing methods and mathematical statistics and analysis tools. Analysis of the influence of the dimensionless parameters of velocity triangle of a single stage turbine with the meanline method and the range analysis method in the reference [47]. In the study, the inflow/outflow angles of the turbine are all relative to the axial direction, and the ranges of all the dimensionless parameters cover the typical value ranges of conventional LP turbine components; the sample number is 13, and the samples are at the same interval. The concrete data is shown in Table 6.2. The experiment was carried out based on the data above, and 371,293 (13^5) samples were obtained. Range analysis of these samples was carried out, and the results are shown in Table 6.3. The data in the table shows that the levels of the influence of the 5 parameters in typical ranges on efficiency can be divided into three. The loading coefficient has the highest influence level, for its efficiency range value is significantly higher than that of other parameters. The flow coefficient and the reaction degree have the intermediate influence level. The axial velocity ratio and the inlet-to-outlet mean diameter ratio have the lowest influence level, for their efficiency range values are smaller than that of the loading coefficient by an order of magnitude. These data suggests that the loading coefficient, the flow coefficient, and the reaction degree should be considered primarily in aerodynamic design and optimized reasonably, moreover that the first priority should be given to the loading coefficient. Based on that, the influence of the axial velocity ratio and inlet-to-outlet mean diameter ratio was not taken into consideration in the following analysis of a two-stage turbine, and only the influences of 7 parameters were studied, including the work distribution coefficient, W_D , and the loading coefficient, the flow coefficient, and the reaction degree of each stage. In this way, the total sample number was largely reduced. The sample number is 13 for each parameter, and the samples are at the same interval. As shown in Table 6.4, the loading coefficient of each stage has the most significant influence, while the flow coefficient, the reaction degree,

Table 6.2 Samples of one-dimensional parameters of single-stage turbine

	Minimum value	Maximum value	Levels
Loading coefficient H_T	0.7	3.1	13
Flow coefficient φ	0.42	1.28	13
Reaction degree Ω	0.17	0.53	13
Axial velocity ratio K	0.7	1.3	13
Inlet-to-outlet mean diameter ratio D	0.82	1.18	13

Table 6.3 Range analysis results of single-stage turbine, η_{EDA} (%)

	Loading coefficient H_T	Flow coefficient φ	Reaction degree Ω	Axial velocity ratio K	Inlet-to-outlet mean diameter ratio D
Efficiency range η_{EDA} (%)	5.42	1.84	1.42	0.50	0.43

and the work distribution coefficient have similar influence level. The inflow/outflow angles of the turbine are all relative to the axial direction, so that the velocity triangles of the two turbine stages are under different restrictions, such as the first stage is set in axial admission while the second stage is set in axial discharge. As a result, influence levels of the parameters of the two stages are slightly different. Zhdanov et al. optimized more parameters by using the meanline method and the Soderberg loss model, and analyzed their influence levels. The results are shown in Table 6.5 [48]. Influence levels of the parameters are somewhat different from those in Ref. [47] due to different loss models and value ranges of the parameters, but the results also indicate that the loading coefficient, the flow coefficient, and the reaction degree have the greatest influence on turbine efficiency.

With the development of high-loaded design technologies for modern LP turbines and the widening of the turbine working range, influence characteristics of the design parameters on LP turbine performance are changing constantly. Except for the loading coefficient, the flow coefficient, and the reaction degree, which have

Table 6.4 Range analysis results of two-stage turbine, η_{EDA} (%)

	First stage			Second stage			W_D
	H_T	φ	Ω	H_T	φ	Ω	
Efficiency range η_{EDA} (%)	2.27	0.35	0.27	1.22	0.58	0.51	0.31

Table 6.5 Influence of design parameters on turbine efficiency [48]

Design parameter name	Design parameter range	Average gain in percentage points of TTE (%)
H_T	0.5–3.0	3.65
φ	0.2–1.0	12.13
Ω	0–1.0	7.26
c_1	100–300 m/s	0.31
c_{x2}/c_{x3}	0.8–1.2	0.94
U_2/U_3	0.8–1.2	1.68
$(H/b)_N$	0.5–3.0	0.38
$(H/b)_R$	0.5–3.0	1.82
Z_N	0.6–1.4	1.25
Z_R	0.6–1.4	0.62

significant influence on turbine performance, the blade lift coefficient, the Reynolds number, and other parameters have also become important performance-influencing factors. For this reason, Coull and Hodson analyzed the influence of the flow coefficient, the lift coefficient, and the Reynolds number of high-loaded blades on LP turbine performance by using the one-dimensional meanline method [39], and this work is beyond the capability of the classical Smith chart. Considering the importance of the loss model to the accuracy of calculation results, they first analyzed and compared the prediction ability and accuracy of a series of loss models including the Denton model, the Coull and Hodson model, the Ainley and Mathieson model, the Dunham and Came model, the Kacker and Okapuu model, the Craig and Cox model, the Traupel model, and the Benner model to guarantee reliable results. The results suggest that the Coull and Hodson loss model shows good ability and accuracy in prediction of the profile loss, while the Craig and Cox loss model and the Traupel loss model perform better in prediction of the secondary loss. Based on that, they analyzed the influence of the lift coefficient on turbine efficiency by using different combinations of the Coull and Hodson profile loss model and the Traupel/Craig and Cox secondary loss model. Figure 6.47 shows the superposition of the efficiency—loading coefficient—flow coefficient relation graphs which were obtained under different circulation coefficients (C_o , as previously defined in Sect. 1.12). As can be seen from the figure, increase of the lift coefficient would result in efficiency drop. Because different areas in the Smith chart correspond to different blade profiles (see Fig. 6.39), the efficiency drop is different in different areas. For example, Point A and Point B are located in different areas of the Smith chart. When C_o increases from 0.7 to 0.8, the efficiency at Point A ($\varphi = 0.8$, $H_T = 2.2$) drops by 0.56%. However, when C_o increases from 0.7 to 0.8, the efficiency at Point B ($\varphi = 1.0$, $H_T = 1.8$) drops by 0.86%. This means the design scheme B with large flow coefficient is more sensitive to the increase of the lift coefficient. Figure 6.48 shows the influence of the Reynolds number on the efficiency of LP turbines with different lift coefficients. It can be seen that, when the Reynolds number is less than a critical value, the efficiency drop with the Reynolds

Fig. 6.47 Influence of lift coefficient on LP turbine efficiency [39]

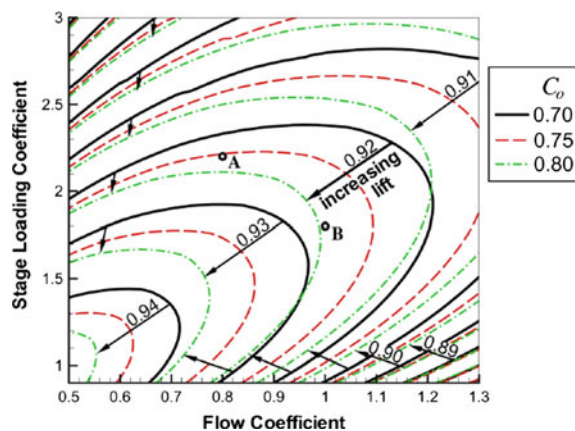
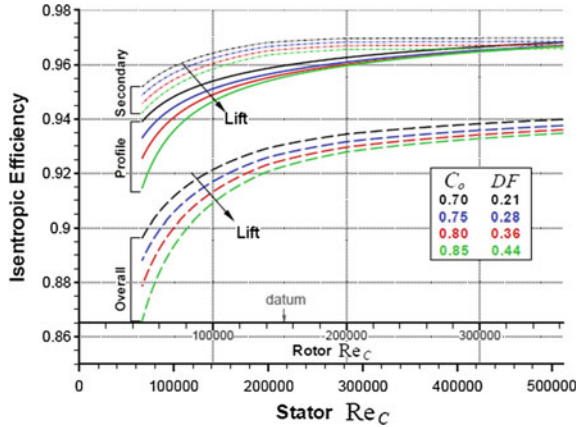


Fig. 6.48 Influence of Reynolds number on LP turbine efficiency [39]



number accelerates; namely, the lower the Reynolds number, the more significant its negative influence on performance will be. By comparing the influence of the Reynolds number on the profile loss and the secondary loss, it can be seen that the Reynolds number has very significant influence on the profile loss, which is the main cause of changes in efficiency, and that the profile loss of the blades with high lift coefficient is most sensitive to the Reynolds number. Relatively, the secondary loss also increases with the decrease of the Reynolds number, but its amplitude of variation is lower and there is little difference in sensitivity of blades with different lift coefficients to the Reynolds number.

6.3.2.2 Optimization of Multi-stage LPT Design Parameters in 1D Design Space

Based on the one-dimensional model above for multi-stage turbines, conjugate optimization methods can be used to optimize one-dimensional aerodynamic parameters of multi-stage LP turbines. Generally speaking, optimal design of one-dimensional parameters of multi-stage LP turbines is a constraint optimization problem, which is mainly about restricting the form of the meridional flowpassage. If the optimization algorithm takes only turbine efficiency as the objective without considering any restrictions on the form of the meridional flowpassage, the optimization results of design parameters of turbine stages will inevitably lie in the high efficiency area of the Smith chart; however, the meridional flowpassage determined by this group of design parameters is unacceptable in most cases. Based on the considerations above, a method for optimizing one-dimensional parameters of multi-stage LP turbines by combining the particle swarm optimization (PSO) with the one-dimensional model is proposed, and the feasibility of this method through an improvement scheme for a 6-stage LP turbine is verified in Ref. [41]. The results of S2 direct calculation suggest that the aerodynamic efficiency of the LP turbine

Table 6.6 Some 1D parameters before and after optimization [41]

		Stage 1	Stage 2	Stage 3	Stage 4	Stage 5	Stage 6
W_D	Original	0.136	0.157	0.173	0.182	0.182	0.170
	Optimized	0.136	0.164	0.177	0.180	0.187	0.156
μ	Original	1.540	1.555	1.575	1.615	1.645	1.585
	Optimized	1.507	1.613	1.620	1.618	1.691	1.442
\bar{C}_{2a}	Original	0.610	0.490	0.460	0.510	0.640	0.800
	Optimized	0.591	0.467	0.452	0.512	0.655	0.820
Ω	Original	0.400	0.400	0.400	0.400	0.400	0.425
	Optimized	0.600	0.539	0.540	0.536	0.540	0.514

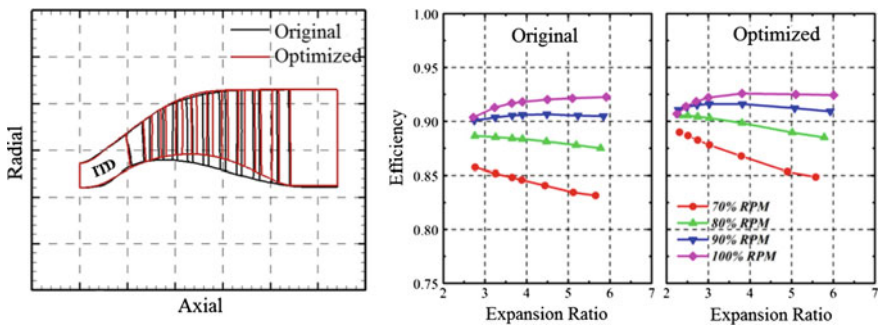


Fig. 6.49 Flow passage and efficiency characteristics of LP turbine before and after optimization [49]

increased by 0.8% after applying the above optimization method. The values of turbine parameters before and after the optimization are compared in Table 6.6, including the work distribution coefficient, the loading coefficient, the flow coefficient, and the reaction degree. After the optimization, the work of the first stage and the fourth stage of the turbine was basically the same as that before the optimization; the work of the last stage decreased greatly, while work of the other three stages increased to different degrees; the loading coefficient of the first stage and the last stage decreased, while the loading coefficient increased to different degrees in the other four stages; the flow coefficient of the first three stages of the optimized turbine decreased, while the flow coefficient of the last three stages increased somewhat; the reaction degree became larger in all the stages after the optimization, and this helps to improve the turbine efficiency. This method was also used for improving a 5-stage LP turbine. Figure 6.49 compares the three-dimensional numerical simulation results of flow passage and efficiency characteristics before and after the optimization. The results suggest that not only did the performance of the turbine increases at the design revolution speed, but also the performance improvement at off-design revolution speeds was even greater [49].

6.3.3 Design of Low-Dimensional Design Parameters for Variable-Speed Power Turbines

6.3.3.1 Aerodynamic Characteristics of Variable-Speed Power Turbines

In recent years, NASA proposed the VSPT (Variable-Speed Power-Turbine) research program in the aerodynamic research project of LCTR (Large Civil Tilt-Rotor) [50–52]. The program is mainly intended to enable LP turbines to operate with high efficiency at two or more revolution speeds. Taking VSPT for example, there are great differences between the revolution speeds at the taking off and cruise conditions, so are the speed in different cruise tasks. If the speed changes only by a speed reducer, it would be difficult to design the structure of the reducer, and the gearbox would be much more complicated, heavier and less reliable. These problems can be avoided by abandoning the speed reducer, but a new problem would then arise that the design requirements for power turbines are significantly different from those for conventional turbines because the power turbine needs to perform efficiently in a wide range of speed. The VSPT program follows the latter idea to study the design methods for variable-speed power turbines.

Table 6.7 shows the design requirements for VSPT in the LCTR project [53]. As can be seen, the power turbine needs to cruise respectively at 54%, 61.5%, 75%, and 100% of its physical speed and take off at 100% of the speed, and the corresponding reduced speeds are respectively 60.8%, 69.7%, 85.1%, 112.7%, and 102.3%. The range of working speed of the power turbine is much wider than that of conventional turbines. Because the power turbine needs to operate at these speeds for long hours, its performances under different conditions have significant

Table 6.7 Design requirements for VSPT in LCTR project [53]

Flight point	Take-off	Cruise	Cruise	Cruise	Cruise
Altitude (kft)	2	28	28	28	28
VSPT speed ($N/N_{100\%}$) (%)	100	54	61.5	75	100
Main-rotor tip-speed (ft/s)	650	350	400	500	650
Power, SHP	4593	2328	2330	2329	2330
VSPT mass flow rate, lb_m/s	22.03	12.22	11.71	11.63	11.55
Specific power (SHP/ lb_m/s)	208.5	190.5	200.2	200.2	201.8
PT inlet temp ($T_{4.5}$), R	2204	1812	1798	1795	1818
PT inlet pres. ($P_{0.4.5}$), psia	58.0	26.76	26.3	26.1	26.6
PR_{TT}	4.04	5.34	5.25	5.21	5.30
Corrected flow, lb_m/s	11.51	12.54	12.41	12.18	11.95
Corrected speed ($N_c/N_{c100\%}$), %	102.3	60.8	69.7	85.1	112.7

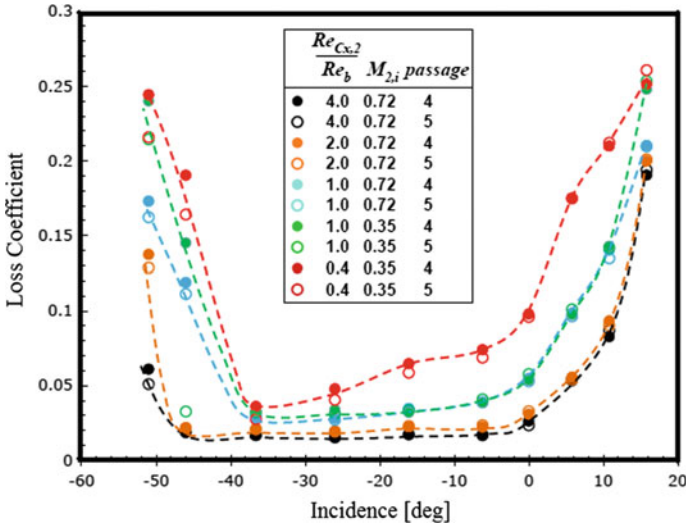


Fig. 6.50 Influence of Reynolds number on range of high-efficiency incidence [246]

influence on the economy of the engines. How to guarantee good performance of the power turbine at different operating conditions with significant difference in speed is of great importance to the dynamic design of tilt rotors.

One of the core problems of the LCTR program is the design of variable-speed power turbines. This challenge also goes for the design of power turbines for the turboprop engines. From the perspective of aerodynamic design, this problem differs from the design technologies for conventional power turbines in the following aspects: due to the great difference in operating speeds, the low-dimensional design parameters should be selected and optimized reasonably to give consideration to the performance at different operating conditions; blade profiling should guarantee a good adaptability to variations of inflow incidence in an ultra-wide range (in VSPT, variation range of inflow angle is as much as 50° – 57° under different conditions); performance of the turbine at low Reynolds number should be guaranteed (the low Reynolds number effect can not only reduce the efficiency of the power turbine at the design point, but also diminish the insensitive range of changes of incidence; see Fig. 6.50). The influence of low-dimensional VSPT design parameters on performance and the parameter optimization by taking the VSPT-relevant research progresses of NASA and Williams International as example are mainly discussed in this subsection.

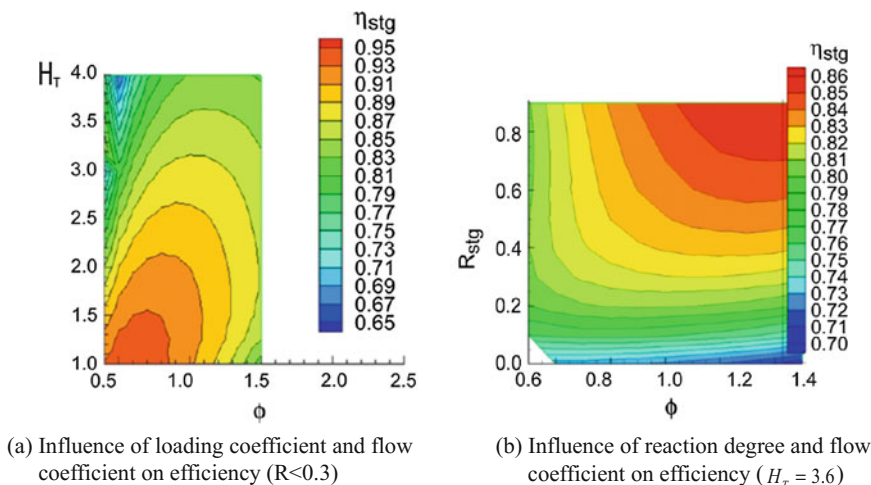


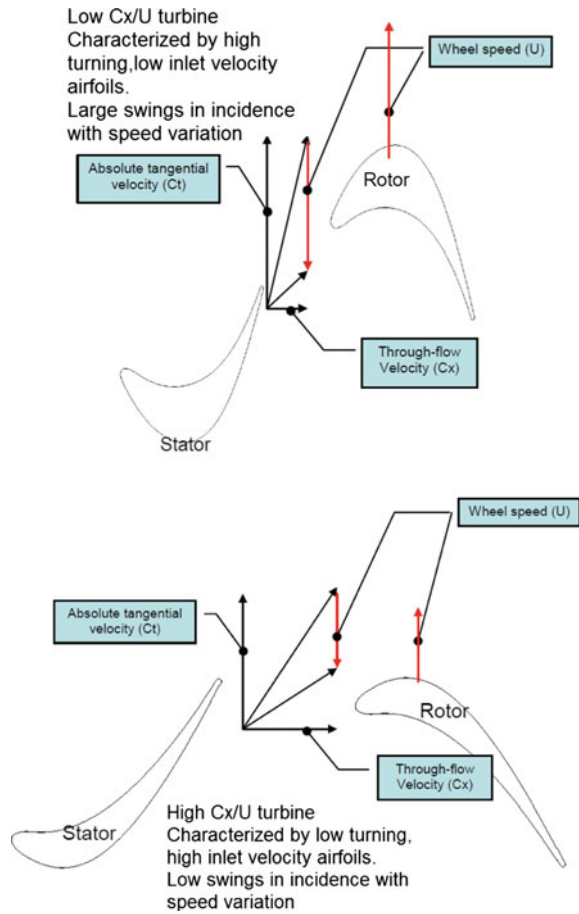
Fig. 6.51 Influence of loading coefficient, flow coefficient, and reaction degree on turbine efficiency [53]

6.3.3.2 Influence of Design Parameters on VSPT Performance

Among the VSPT design parameters, the revolution speed, the number of stages, the flow coefficient, the reaction degree, the loading coefficient, and the Reynolds number have significant impact on turbine performance. Their result would be analyzed one by one in the following.

The first to be analyzed is the influence of the flow coefficient, the reaction degree, and the loading coefficient. Variation in the flow rate of the power turbine with a specific geometry is less than 5% when the physical speed changes from 54% to 100%. It is thus clear that the flow coefficient is approximately in inverse proportion to speed, which would lead to significant difference in the flow coefficient at different operating conditions. Generally speaking, turbines operating at different flow coefficients have different geometrical characteristics (see Fig. 6.52). Turbine blades with small flow coefficient generally have large deflection angle and low inlet velocity, and changes in revolution speed would lead to significant changes in incidence. The situation is just the opposite for turbine blades with large flow coefficient. Therefore, studies on the influence of the flow coefficient and the revolution speed are essential for design of this kind of turbines. Welch et al. analyzed the influence of the flow coefficient, the loading coefficient, and the reaction degree by using the one-dimensional meanline method and the AMDCKO loss model [53]. The results obtained at zero clearance, the hub-to-shroud ratio of 0.7, the aspect ratio of 5.0, the Reynolds number of 5×10^5 , the outlet Mach number of 0.7, and the Zweifel coefficient of 0.8 are represented in Fig. 6.51. These results also confirm that the optimal aerodynamic efficiency can be obtained

Fig. 6.52 Blade characteristics corresponding to different flow coefficients [50]



through reasonable selection of the loading coefficient, the flow coefficient, and the reaction degree. The study also shows that efficiency drop caused by increase of the loading coefficient is more evident in the high loading coefficient area. However, the loading coefficient of the VSPT at the cruising speed of 54% is about 3.5 times higher than that at the taking-off speed of 100%, and the flow coefficient changes for about 1.85 times accordingly. So, how to give consideration to both the two extreme conditions is particularly important in design.

Suchezky et al. studied the influence of different design speeds and the number of stages by using the one-dimensional meanline method [50], and found that both 54% and 100% are not the optimal design speed. If the cruising condition at the speed of 54% is selected as the design point, the turbine will have ideal design performance with its aerodynamic efficiency being about 91%, but it will perform poorly at the cruising speed of 100% with its aerodynamic efficiency dropping to 70%. If the cruising condition at the speed of 100% is selected as the design point,

Table 6.8 Oil consumption rate and efficiency when setting design point at different speeds [50]

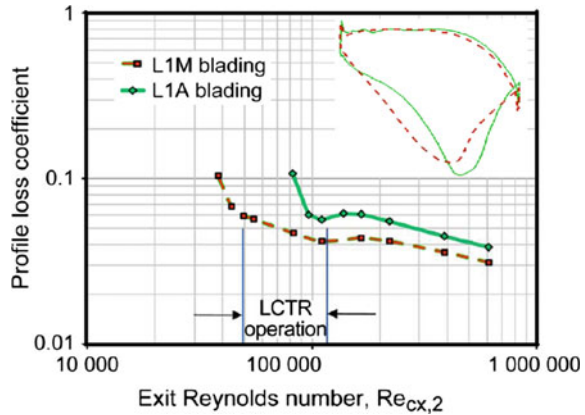
% Speed	Design RPM	Fuel burn%	ETA 1	ETA 2	ETA 3	ETA 4
<i>High CX/U</i>						
53.8	8045	-3.29	73.34	68.62	69.34	91.39
69.2	10,343	-7.88	88.33	84.71	84.12	88.62
84.6	12,642	1.41	92.95	90.84	90.63	74.87
100.0	14,941	23.20	91.25	91.58	92.80	57.42
<i>Low CX/U</i>						
53.8	8045	-2.22	69.98	66.62	69.30	90.20
69.2	10,343	-7.80	87.58	83.60	82.85	89.14
84.6	12,642	-1.84	92.00	89.60	89.44	78.15
100.0	14,941	24.30	89.29	89.78	91.43	57.00

Table 6.9 Comparison between 3-stage and 4-stage schemes [50]

% speed	Design RPM	Fuel burn%	ETA 1	ETA 2	ETA 3	ETA 4
<i>3 stage</i>						
53.8	8045	-1.11	70.57	66.14	67.52	89.72
69.2	10,343	-4.51	78.24	74.89	74.04	89.63
84.6	12,642	-7.19	93.53	91.76	91.60	84.44
100.0	14,941	-6.36	92.35	92.49	93.53	66.26
<i>4 Stg Hi loading (1)</i>						
53.8	8045	-0.84	78.77	71.42	69.10	87.45
69.2	10,343	-7.98	90.15	87.28	87.13	87.37
84.6	12,642	-8.31	93.67	92.32	92.37	85.64
100.0	14,941	-3.68	93.96	93.59	94.26	79.31

the design performance of the turbine will be kept around 92%, but the off-design performance will also deteriorate seriously, with the aerodynamic efficiency at the speed of 54% being less than 58%. Table 6.8 shows the oil consumption rate of the engine and the turbine efficiency when selecting the condition at the speed of 54%, 69%, 85%, and 100% as the design point. ETA1, ETA2, ETA3, and ETA4 represent the four condition points respectively. The results suggest that, when the design speed is selected at 69%, not only could high turbine efficiency and low oil consumption rate at the design point be guaranteed, but also the off-design performance would be desirable; namely, this is an ideal selection that can bring good performance under both design conditions and off-design conditions; relatively, the flow coefficient has little influence on turbine performance. The main reason for this finding is described as follows. Performance of turbine blades at negative inflow incidence is generally much better than that at positive inflow incidence, while blades are in the positive incidence state and negative incidence state when the turbine is operating at low speed and high speed respectively. So, most of off-design operating conditions of the turbine can be made in the negative incidence state by

Fig. 6.53 Influence of blade load distribution on low Reynolds number effect [53]



selecting the condition at relatively low speed as the design point, so as to ensure a good performance under off-design conditions. Afterwards, Suchezky et al. analyzed the influence of the number of stages through comparison between different schemes. Table 6.9 shows the comparison between a 3-stage turbine and a 4-stage high-loaded turbine. It can be seen that the 4-stage scheme with high loading coefficient, in which the design point is set at the speed of 69%, has obvious advantage in both design performance and off-design performance.

As for the influence of the Reynolds number, high-lift blades are more sensitive to the decrease of the Reynolds number, as previously discussed in Sect. 6.3.2. For the reason, it is suggested the blades with moderate lift coefficient are suitable for the program, such as the blades with a Zweifel coefficient between 0.8 and 1.0, instead of the high lift blades or ultra high lift blades. Another benefit of choosing blades with moderate lift coefficient is that the blades support a greater range of incidence, which apparently is very important to VSPT. In addition, the influence of blade loading distribution on the Reynolds number effect is also very critical and should be carefully considered in the actual design process (see Fig. 6.53) [42, 53].

6.3.3.3 Optimization of Low-Dimensional Design Parameters of VSPT Turbines

To make the VSPT schemes reach the best performance in the initial concept design step, Hendricks et al. optimized the low-dimensional design parameters for the 4-stage VSPT scheme [54]. The optimization code for parameters at the mid-span section OTAC, developed by NASA Glenn Research Center, coupling Kacker and Okapuu loss model and the SNOPT optimization algorithm were used in this study. The cruising condition at the speed of 54% was selected as the initial design point. The taking-off condition and the cruising condition at 54% were mainly considered in the optimization process. Therefore, the optimization objective was to reach the maximum weighted efficiency of the two conditions. The results suggest that the

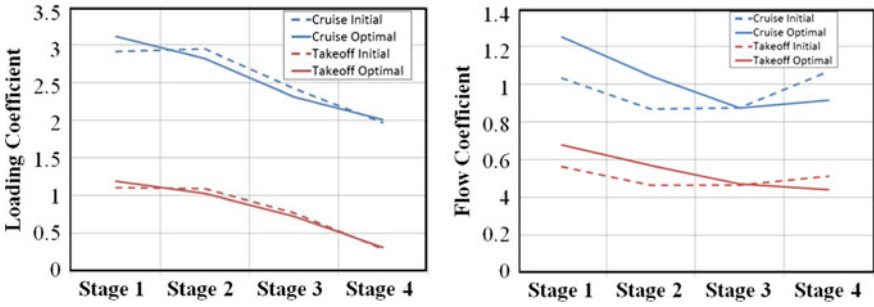


Fig. 6.54 Comparison of loading coefficient and flow coefficient before and after optimization [54]

low-dimensional optimization resulted in significant changes in the velocity triangle and the geometric flow passage, and increased the turbine performance at both the taking-off condition and the cruising condition by more than 1%, indicating that selection of low-dimensional design parameters is of great significance in turbine design. The comparison of the loading coefficients and flow coefficients of each stage before and after the optimization is shown in Fig. 6.54. It should be noted that all the above studies are based on the meanline method, and the predication ability and accuracy of loss models at off-design points have great influence on calculation results.

Zou and Zhang [55] from Beihang University proposed a new index for evaluating comprehensive turbine performance with the consideration of the factors such as contribution of the engine mission envelope and turbine to engine fuel consumption:

$$\eta_M = \sum_{seg=1}^{nseg} \eta_{iseg} \frac{Time_{iseg}}{\sum_{seg=1}^{nseg} Time_{iseg}} \frac{W_{fuel_iseg}}{W_{fuel_design}} \quad (6.109)$$

where, $Time_{iseg}$ represents the flight time under a certain flight condition; W_{fuel_iseg} represents the fuel consumption under a certain flight condition; W_{fuel_design} represents the fuel consumption at the selected design point. This defining equation can reasonably reflect the comprehensive turbine performance for the full mission envelope with the consideration of time-weighted turbine operating conditions and engine fuel consumption under different conditions. They also proposed a one-dimensional method for solving the congestion problem in turbines, and established and verified a model for calculating the one-dimensional characteristics, which can provide accurate predictions on turbine performance. Based on that, Zou and Zhang [55] developed a method for optimizing one-dimensional turbine design, which considers comprehensive turbine performance at multiple operating points, and discussed the criteria for choosing design parameters, loss models, and optimization algorithms. This method can fully balance turbine performance at various

operating points in the one-dimensional design process. A variable-speed power turbine, which was designed by using this method, can keep at a basically invariable efficiency level under different conditions including cruise at high altitude, maximum continuous operation, and take-off, and achieve optimal turbine performance in the entire flight process.

6.3.4 Selection of Low-Dimensional Design Parameters for Versatile Core-Engine Turbines

The core engine is the key component of the gas turbine engine that consists of a high-pressure compressor, a combustor, and a high-pressure turbine. The core engine technology is the core technology of gas turbines. The core engine is mainly characterized by short blades, high ambient temperature, high pressure, high revolution speed, and high stress, which is the reason for the high failure rate. The core engine is made of expensive materials through complicated processes, and the proportion of both the money and the time cost of the development of the core engine is large. This makes the core engine the most key-technology-intensive component, and the main embodiment of advancement and complexity of gas turbines [56]. A series of gas turbines that are used in different fields can be derived by adding various low-pressure components (low-pressure compressors/fans, low-pressure turbines/power turbines) to the core engine, such as F110-series low-bypass ratio turbofan engines and CFM56-series high-bypass ratio turbofan engines, which were developed based on the F101 core engine [57]. On the other hand, development cost and lead time of gas turbines keep increasing with the improvement of their performance. The cost is so high that even the United States cannot afford. Therefore, the United States announced in the VAATE program that they will lower down the life cycle cost by 50% while improving engine performance [58]. One of the key technologies to realize this objective is the versatile core engine technology. As stated in the VAATE program, the versatile core engine research is intended to guarantee the necessary versatility by means of high surplus power, high combustion efficiency, durable design, high efficiency, and wide range of flow rate, which eventually lower down the life cycle cost [59].

Centering on the characteristics of the versatile core-engine turbine components, a parameter is proposed to describe the versatility of aerodynamic performance of turbines, and the influence of the velocity triangle and other turbine parameters on the versatility of aerodynamic performance as well as the criteria for selecting low-dimensional design parameters of the versatile core-engine turbine components is discussed in this subsection [60].

6.3.4.1 Discussion on Parameters Used to Describe Versatility of Turbine Components

From the perspective of aerodynamic performance, the following parameters used to describe the versatility of turbine components would be taken into consideration: efficiency value, scope of high efficiency area, and revolution speed. The efficiency value is the efficiency at the design point—the higher, the better, in theory. The scope of high efficiency area refers to the region, in which the efficiency is above the specified benchmark value (namely, higher than the benchmark coefficient, η_{Tcir}), which represents the gentleness degree of the efficiency curve variation from the design point to the off-design point at the same revolution speed, to some degree. The gentler the efficiency curve, the better the versatility of the turbine will be. When a turbine is operating at off-design revolution speed, the high efficiency area at the off-design speed and range of flow rate variation should be considered as well. With these factors taken into consideration, the parameter used to describe the versatility of aerodynamic performance of turbines is defined as follows:

$$T = g(T_1, T_2, \dots, T_n) = \sum_{m=1}^n N_m T_m \quad (6.110)$$

where, N_1, N_2, \dots, N_n are the weighting coefficients at different speeds, representing the degree of influence of the efficiency curve at different speeds on the versatility; $\sum_{m=1}^n N_m = 1$; T_n represent the parametric component used to describe the versatility at different speeds, and is given by:

$$T_n = a_1 E_n^{k_1} + a_2 D_n^{k_2} + a_3 M_n^{k_3} + a_4 R_n^{k_4} \quad (6.111)$$

where, k_1, k_2, \dots, k_n are the weighting coefficients for the influence of different parameters on the versatility and can be determined by experience; E_n is the efficiency factor at the corresponding speed, which represents the maximum turbine efficiency and is expressed by dimensionless parameters; D_n and M_n are the derivative factor of the efficiency curve at different speeds and the flow factor at the corresponding speed (from the view of design, they can be expressed as below: the derivative factor $D_n = aD_L + bF + cD_R$, where $F = \pi_{\max} - \pi_{\min}$, π_{\max} and π_{\min} are the two expansion ratios corresponding to the benchmark efficiency η_{Tcir} , used to reflect the scope of the high efficiency area in which the turbine efficiency is above the benchmark efficiency; D_L and D_R are used to reflect the gradient of the left branch and the right branch of the turbine efficiency curve, namely the derivative of the efficiency with respect to the expansion ratio π ; $M_n = \left| \frac{\phi_{\max} - \phi_{\min}}{\phi_{\max}} \right|$; is used to reflect the range of flow corresponding to the high efficiency area); R_n is the speed factor at the corresponding speed, $R_n = - \left| \frac{\eta_{T\max}|_{n=100\%} - \eta_{T\max}|_{n=ville}}{\eta_{T\max}|_{n=100\%}} \right|$, namely the relative difference between the maximum value of the efficiency curve at off-design speeds

and the maximum efficiency value at the design speed; a, b, c , and a_1, a_2, a_3, a_4 are the weighting coefficients and can be determined by experience. It should be highlighted that the expansion ratio of the turbine is used in the definition of the versatility. For the convenience of analysis in the design process, the relation between the expansion ratio and the parameters of the velocity triangle is given below. According to the relation between the critical sound speed and the outlet speeds of the stator and the rotor, the energy equation in the form of mechanical energy in relative coordinates, total pressure at the inlet and outlet of the rotor blade, and the relation between the relative total pressure and the static pressure, the expansion ratio can be expressed as:
$$\pi = \left[\left(1 - \frac{C_2^2}{2CpT_1 - 2H_T U^2} \right) \cdot \left(\frac{2CpT_1^*}{w_2^2 - w_1^2} \right) \right]^{\frac{k}{k-1}}$$

According to the relations with the parameters of the velocity triangle, C_2, w_1 , and w_2 in the equation can be expressed by ϕ, Ω, H_T and K . So, the expansion ratio of the turbine can be fully correlated with the parameters of the velocity triangle. Analysis of the performance of several turbine components proves that this definition can well describe the versatility of turbine performance [61].

Influence of E_n, D_n, M_n , and R_n on the versatility parameter is described as follows. (1) The efficiency factor— E_n . The efficiency curve of the versatile core-engine turbine components is required to be gentle; namely, the efficiency should change little across a wide range of the expansion ratio. Meanwhile, the efficiency curve is expected to have ideal absolute value. In other words, for the same changing pattern of the efficiency curve, the larger the mean efficiency value the better the versatility. (2) The derivative factor— D_n . As required by the versatile core engine, the turbine components should possess a large high efficiency area; namely, under the premise of a high mean efficiency value, the efficiency curve is expected to be gentle across a wide range. The derivative of the efficiency with respect to the expansion ratio can be used to describe the changing trend. (3) The flow factor— M_n . Higher value of the flow factor means larger flow range corresponding to the high efficiency area and better versatility. (4) The speed factor— R_n . This factor is used to describe the variation of efficiency with the speed. Little variation of efficiency value with the speed means good versatility of the turbine.

With the increase of the loading on turbine stages, design points of the turbine are generally after the blocking point. Therefore, it is very difficult to get a relatively wide flow range within a wide range of the expansion ratio without any regulating measures. However, it is possible to get a gently changing high efficiency area within a wide range of the expansion ratio by means of aerodynamic design. Therefore, for versatile core-engine turbine components, more attention should be paid to the way to make the turbine having larger high efficiency area without any regulating measures.

6.3.4.2 Influence of Turbine Aerodynamic Parameters on Versatility

With the loss model, turbine performance can be correlated with the parameters of the velocity triangle namely $\eta_T = f(\phi, \Omega, H_T, K, D, N)$. Thus, the efficiency factor, E_n , the derivative factor, D_n , the flow factor, M_n , and the speed factor, M_n , can be

determined, and the relation between the versatility parameter, T , and the parameters of the velocity triangle can be finally obtained. The specific process is described in Ref. [60]. It is worth noting that the prediction ability and accuracy of the loss model for off-design points are very important to versatility-related studies, and the loss model should be selected or the empirical coefficient should be corrected according to users' experience in actual use to obtain more ideal results.

The influence of the reaction degree, Ω , the loading coefficient, H_T , and the axial velocity ratio, K on the versatility parameter, T (see Fig. 6.55) are described in Ref. [60]. As the figure shown: (1) within the scope of the study, increase of the reaction degree would lead to increase of the versatility parameter of turbine performance, and the efficiency factor, E_n , is the most important parameter; namely, increase in

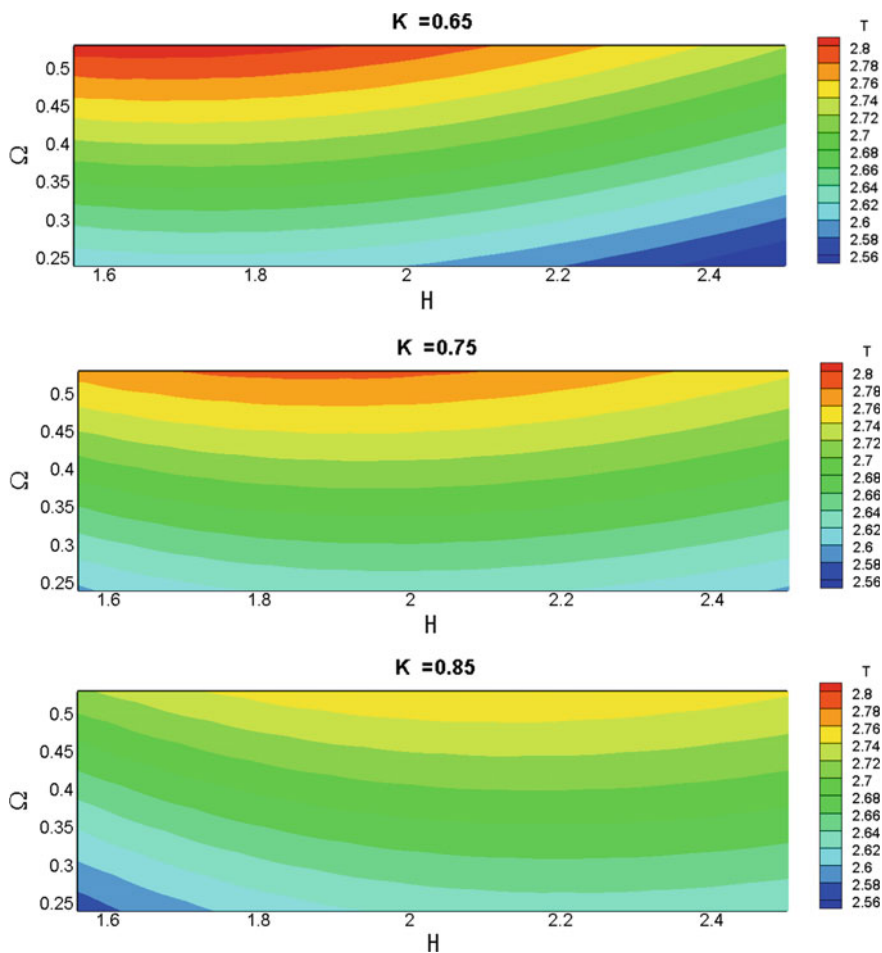
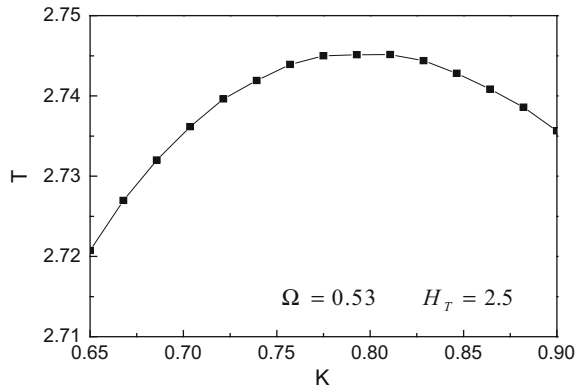


Fig. 6.55 Influence of reaction degree, loading coefficient, and axial velocity ratio on versatility [60]

Fig. 6.56 Influence of axial velocity ratio on turbine efficiency and versatility [60]



the reaction degree would make the mean efficiency value in the high efficiency area increase significantly; (2) when the loading coefficient changes, there is an optimal loading coefficient that makes the versatility parameter reaching to the maximum due to the joint influence of the efficiency factor, E_n , and the derivative factor, D_n , and the optimal value is related to the axial velocity ratio and the flow coefficient; when $K = 0.75$, $\Omega = 0.45$ (as shown in the figure), the optimal loading coefficient H_T is about 2.0; (3) within the scope of the study, increase in the axial velocity ratio would result in a generally decreasing trend of the versatility parameter, but there is also an optimal axial velocity ratio in a certain range; when $\Omega = 0.53$, $H_T = 2.5$, (as shown in Fig. 6.56), the optimal axial velocity ratio is about 0.8.

6.3.5 Selection of Low-Dimensional Design Parameters for Counter-Rotating Turbines

A counter-rotating turbine is a type of turbine that the rotors of the two adjacent turbine stages in a dual-rotor or multi-rotor gas turbine are arranged with opposite rotation direction. Due to the opposite rotation direction, the downstream stage can make full use of the prewhirl generated by the outlet flow of the upstream rotor. As for the aerodynamic performance, since the downstream turbine stage can make full use of the prewhirl generated by the upstream rotor, the deflection angle of the guide vane can be reduced, so that it is possible to reduce the number of guide vane in the downstream stage, even disuse the downstream guide vane. As for the cooling design, decrease in the number of the guide vane or disuse of the guide vane can reduce the cooling air demand of the guide vane, while the cooling air demand of the rotor is increased due to increase in the reaction degree and weakening of the expansion and acceleration in the guide vane. As for the structure and weight, decrease in the number or even disuse of the guide vane helps to reduce the

weight and decrease the axial length, resulting in much more compact layout of structure. As for the rotor dynamics, counter-rotating rotors can decrease or neutralize the gyroscopic moment applied by single-direction rotors on the airplane, and thus improve the motility and maneuverability of the plane.

Researchers have made a large number of studies on design techniques for counter-rotating turbines, for the importance of counter-rotating turbines to the development of aero-engines [62]. As early as 1957, Wintucky et al. analyzed the variation patterns of parameters of a 1+1/2 counter-rotating turbine, such as the efficiency, the output power ratio, and the weight, with the outflow prewhirl of the high-pressure turbine guide vane, velocity and work ratios of high/low pressure turbines, outflow prewhirl of the low-pressure turbine, and rotating speed of high/low pressure turbines [63]. Louis et al. discussed the variation patterns of efficiency of a 1+1/2 and 1/2+1/2 counter-rotating turbine with the loading coefficient under both design and off-design conditions [64]. In addition, Huberr, Yamamoto, et al. carried design and experiments of counter-rotating turbines, according to different application background and requirements [65, 66]. A great amount of fruitful work in the field were carried out in the Institute of Engineering Thermophysics, Chinese Academy of Sciences, Beihang University, and Northwestern Polytechnical University. The influence of the relative flow angle at the outlet of high pressure rotor, the relative Mach number, the loading coefficient, and the axial velocity ratio on turbine efficiency and the output power ratio [67, 68] were studied systematically. The criteria for selecting relevant design parameters of counter-rotating turbines were studied systematically [60, 69], as well as blade profiling and design methods for counter-rotating turbines [70, 71], and aerodynamic and thermal characteristics and design methods of counter-rotating turbines in variable cycle engines [72].

These studies suggest that counter-rotating turbines not only present superior aerodynamic performance than conventional turbines, but also have different flow characteristics. So, the criteria for selecting low-dimensional design parameters are quite different from those for conventional turbines. The criteria for selecting low-dimensional design parameters of different types of counter-rotating turbines is discussed in the subsection.

6.3.5.1 Description of Velocity Triangle of Typical Counter-Rotating Turbines and Fundamental Formulae

There are many types of counter-rotating turbines. As for a counter-rotating turbine with one high pressure turbine stage and one low pressure turbine stage, the conventional type (1+1 counter-rotating turbine) and the low pressure vaneless type (1+1/2 counter-rotating turbine and 1+N/2 counter-rotating turbine) are the most common ones. Compared to conventional turbines, LP counter-rotating turbines have their own characteristics in velocity triangle design (see Fig. 6.57). For

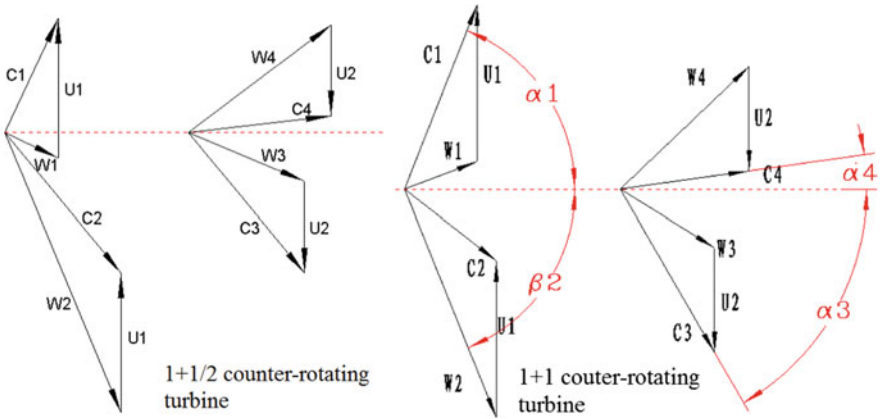


Fig. 6.57 Velocity triangle of counter-rotating turbine

conventional turbines, a group of five independent parameters can determine the velocity triangle of a single-stage turbine, and ten independent parameters are needed to determine the velocity triangles of a two-stage turbine. However, because the LP turbine of a LP vaneless counter-rotating turbine is not equipped with guide vanes and the rotor inlet velocity of the LP turbine is totally determined by the flow conditions at the outlet of the HP rotor (ignore velocity changes in the axial gap between the LP turbine and HP turbine), only eight independent parameters are needed to determine the velocity triangles of the LP vaneless counter-rotating turbine. Design of velocity triangles for the 1 + 1 counter-rotating turbine is not completely the same as that for two independent single-stage LP&HP turbine combination. The main difference is that the LP-to-HP output power ratio of the counter-rotating turbine is related to the outflow angle of the HP turbine, and the LP turbine should be designed to make full use of the prewhirl generated by the outflow of the upstream HP turbine. However, axial admission at the LP turbine inlet is assumed in design of conventional turbines.

There are many ways to select the independent parameters of the velocity triangle for a counter-rotating turbine, which may be related to the designer's practice and experience. The following parameters could be selected based on the characteristics of the counter-rotating turbine. Select U_1 as the reference parameter, the absolute flow angle at the outlet of the guide vane, α_1 , the flow coefficient, ϕ , the relative flow angle at the outlet of the rotor, β_2 , and the inlet-to-outlet axial velocity ratio of the rotor, K_{21} as the independent parameters of the HP turbine, and the HP-to-LP turbine revolution speed ratio, U_{r12} , the inlet-to-outlet axial velocity ratio of LP rotor, K_{43} , and the absolute outflow angle, α_4 as the independent parameters of the LP turbine. As for conventional counter-rotating turbines, the absolute flow angle at the outlet of LP guide vane, α_3 , and the inlet-to-outlet axial velocity ratio of

LP guide vane, K_{32} are the two additional parameters for the LP turbine. Some of these parameters are defined as follows:

$$\phi = C_{1x}/U_1 \quad (6.112)$$

$$K_{21} = C_{2x}/C_{1x} \quad (6.113)$$

$$U_{r12} = U_1/U_2 \quad (6.114)$$

$$K_{43} = C_{4x}/C_{3x} \quad (6.115)$$

$$K_{32} = C_{3x}/C_{2x} \quad (6.116)$$

For a single stage turbine, the efficiency is given by:

$$\eta = \frac{L_u}{L_u + L_r} = \frac{U \cdot \Delta C_u}{U \cdot \Delta C_u + (1/\varphi_s^2 - 1)C_1^2/2 + (1/\varphi_r^2 - 1)W_2^2/2} \quad (6.117)$$

The equation above only considers the kinetic energy loss within the blade row, and regards the kinetic energy loss as the difference between the kinetic energy of gas obtained through actual expansion in the blade row and that obtained through isentropic expansion. For a blade row, the velocity loss coefficient and kinetic energy loss coefficient are given by:

$$\varphi_s = C_1/C_{1ad} \quad (6.118)$$

$$\xi_s = \frac{L_r}{E_a} = \frac{(C_{1ad}^2 - C_1^2)/2}{C_{1ad}^2/2} \quad (6.119)$$

According to the basic relations with the parameters of the velocity triangle, the rim work of the turbine, as well as the loading coefficient, can be obtained by the independent parameters. Then, the efficiency of the turbine stage can be written as:

$$\eta = \frac{H_t}{H_T + \frac{\xi_s}{2} \left(\frac{\phi}{\sin \alpha_1}\right)^2 + \frac{\xi_r}{2} \left(\frac{K_{21}\phi}{\sin \beta_2}\right)^2} \quad (6.120)$$

The equation above shows the relation between the efficiency of the turbine stage and selected basic parameters of the velocity triangle. Under certain assumptions, the efficiency of the single turbine stage is a function of four independent parameters of the velocity triangle:

$$\eta = f(\phi, \alpha_1, \beta_2, K_{21}) \quad (6.121)$$

6.3.5.2 Velocity Triangle Analysis of 1 + 1 Counter-Rotating Turbines

The efficiency of a single-stage HP turbine and LP turbine is given in Eq. (6.117). According to the relation between the HP-to-LP axial velocity ratio and revolution speed, the aerodynamic efficiency of the LP turbine can be also written as:

$$\eta_2 = \frac{H_{t2}}{H_{t2} + \frac{\xi_{s2}}{2} \left(\frac{K_{21} K_{32} \phi U_{r12}}{\sin \alpha_3} \right)^2 + \frac{\xi_{r2}}{2} \left[\left(\frac{K_{43} K_{21} K_{32} \phi U_{r12}}{\sin \alpha_4} \right)^2 + 2K_{43} K_{32} K_{21} \phi U_{r12} \cot \alpha_4 + 1 \right]} \quad (6.122)$$

Without considering reheat, the total efficiency of both the HP and LP turbine can be expressed as:

$$\eta = \frac{\Delta h_1^* + \Delta h_2^*}{\Delta h_1^*/\eta_1 + \Delta h_2^*/\eta_2} = \frac{\eta_1 \eta_2 (H_{t1} U_{r12}^2 + H_{t2})}{\eta_2 H_{t1} U_{r12}^2 + \eta_1 H_{t2}} \quad (6.123)$$

The output power ratio of the HP and LP turbine is calculated by:

$$SWR = \frac{L_{u1}}{L_{u2}} = \frac{H_{t1}}{H_{t2}} U_{r12}^2 \quad (6.124)$$

Generally speaking, the turbine revolution speed ratio is mainly determined by the compressor. In the overall thermodynamic design process of the cycle, the range of revolution speed ratio suitable for the turbine component can be preliminarily obtained through analyzing the influence on turbine performance, which can provide guidance for determining the revolution speed ratio of the gas turbine.

Figure 6.58a shows the variation curves of the output power ratio with the flow coefficient at different β_2 and α_3 under the revolution speed ratio of 1.2. Based on the approximate ranges of parameters for the conventional turbines and the restriction that the outflow of the low pressure turbine is axial, some of the parameters are given as below: $\alpha_4 = 90^\circ$, $K_{32} = 1.2$, $K_{43} = 1.2$, $K_{21} = 1.2$, $U_{r21} = 1.2$, $\alpha_1 = 20^\circ$. It can be seen that both β_2 and α_3 have great impact on the output power ratio of the turbine. For a specific α_3 , the output power ratio would decrease with the decrease of β_2 . For a specific β_2 , the output power ratio would decrease with the increase of α_3 . When α_3 is relatively small, the output power ratio is at high levels on the whole. As indicated by the black line in the figure, regardless of β_2 , the minimum output power ratio is above 1.5. For a specific β_2 , the output power ratio drops dramatically with the increase of α_3 . Therefore, the output power ratio can be reduced effectively by either increasing α_3 or decreasing β_2 [73].

Figure 6.58b, c show the variation curves of the output power ratio with the flow coefficient under the revolution speed ratio of 1.0 and 1.5 respectively. By comparing Fig. 6.60b, c with Fig. 6.58a, it can be seen that the variation trends of the output power ratio with the flow angles are similar under different revolution speed ratios, but lower revolution speed ratio would result in lower output power ratio

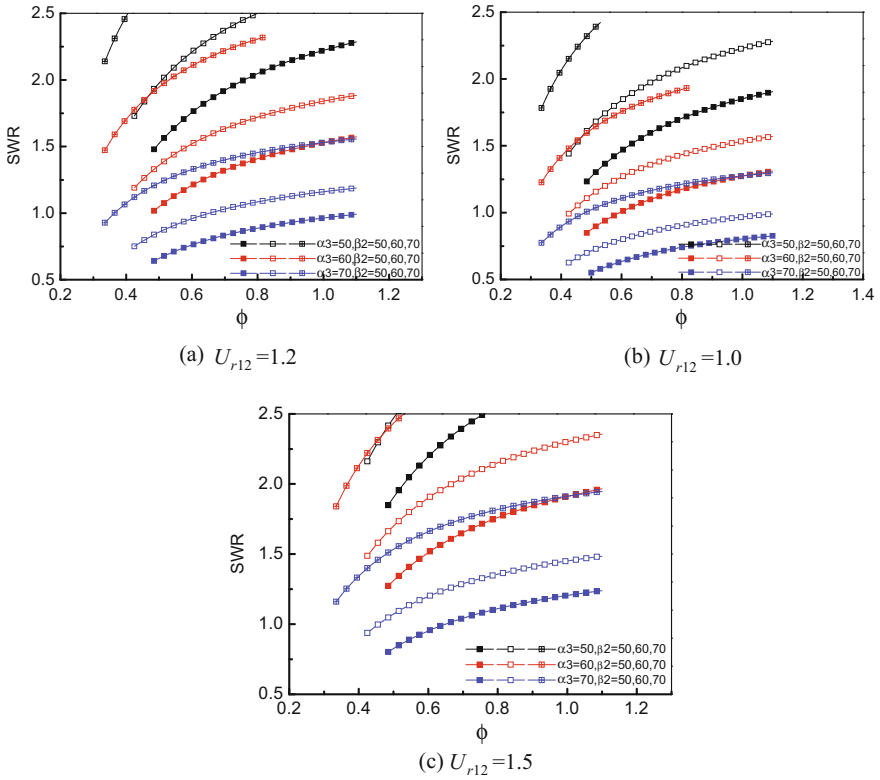
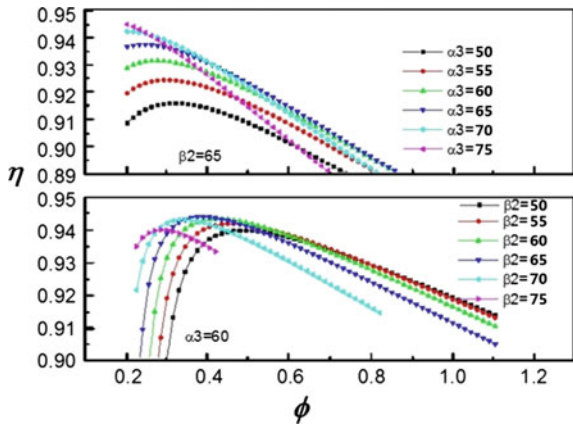


Fig. 6.58 Variation of output power ratio with flow angles at different rotating speed ratios [69]

Fig. 6.59 Variation of HP/LP turbine efficiency with flow angles



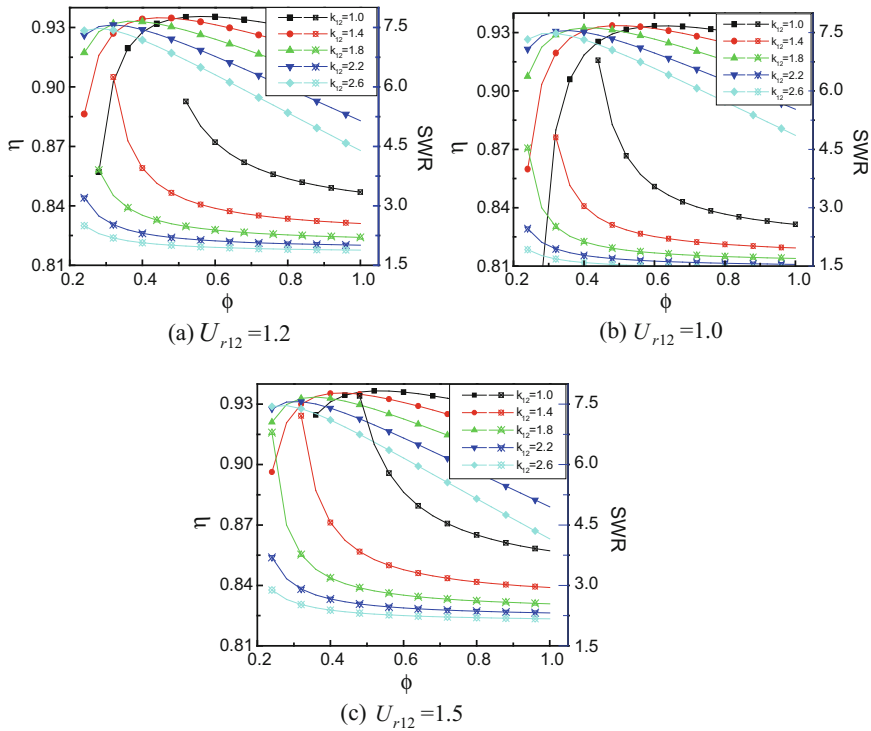


Fig. 6.60 Variation of total efficiency and output power ratio with basic parameters [69]

when all the other conditions are the same. If the revolution speed ratio is 1.5 and α_3 is 40° , the minimum output power ratio is above 1.8, even when β_2 is as low as 40° . When α_3 is 20° , the output power ratio can be selected appropriately across a wide range of β_2 . Through the comparison above, it can be found that the variation trends of the output power ratio with the flow angles and flow coefficient are basically the same at different revolution speed ratios, except that the overall level of the output power ratio is different among the conditions. To further analyze the influence of the flow angles, the efficiency curves of the HP turbine and LP turbine at the output power ratio of 1.2 are given in Fig. 6.59. Efficiency of the HP turbine only depends on the flow angle at the rotor outlet and the flow coefficient. With the increase of β_2 , the maximum efficiency first increases and then decreases, but the flow coefficient corresponding to the maximum efficiency decreases gradually. Seeing that the absolute flow angle at the outlet of the HP turbine rotor shall not be greater than that at the outlet of the LP turbine guide vane, the larger the value of β_2 , the narrower the range of the flow coefficient of the HP turbine that meets the condition will be. For example, when $\beta_2 = 15^\circ$ and $\alpha_3 = 30^\circ$, the flow coefficient of the HP turbine shall not exceed 0.4. If α_3 continues declining, the range of flow coefficient of the HP turbine would further decrease. The LP turbine efficiency is unaffected by β_2 .

The larger the value of α_3 , the higher the maximum efficiency and the smaller the corresponding flow coefficient will be.

It is thus clear that the HP-to-LP revolution speed ratio has great influence on the output power ratio of the 1 + 1 counter-rotating turbine. In addition, the output power ratio can be adjusted by changing the two independent parameters: the flow angle at the outlet of the HP turbine rotor and the flow angle at the outlet of the LP turbine guide vane. So, special considerations are in need when selecting these two parameters.

Characteristics of the velocity triangle of the 1 + 1 counter-rotating turbine are described as follows. The loading coefficient, the flow coefficient, the reaction degree, and the axial velocity ratio of the HP and LP turbines are at the same level as conventional turbines. The difference between the counter-rotating turbine and conventional turbines lies in the LP guide vane. Specifically, the flow deflection angle of the LP guide vane decreases significantly (by about 2/3) from 100° to 30°–40°. This would bring the following two benefits. (1) The weight of the engine could be reduced. Research has shown that the number of the LP guide vane can be reduced by 1/3 nearly. (2) The LP loading will increase if the efficiency remains unchanged, or the efficiency of the LP turbine will increase if the loading keeps constant. Therefore, the efficiency of the 1+1 counter-rotating turbine is higher than that of the conventional turbines, if the basic parameters and the dimensions of the flow passage are the same.

6.3.5.3 Velocity Triangle of Analysis of 1 + 1/2 Counter-Rotating Turbines

The efficiency of the HP stage in a LP vaneless count-rotating turbine can be expressed in the similar form as the 1 + 1 counter-rotating turbine. Because the LP turbine is equipped without guide vanes, the kinetic energy loss caused by guide vanes is zero. Thus, the LP turbine efficiency can be simplified as:

$$\eta_2 = \frac{L_{u2}}{L_{u2} + L_{r2}} = \frac{U_2 \cdot \Delta C_{u2}}{U_2 \cdot \Delta C_{u2} + (1/\varphi_{r2}^2 - 1)W_4^2/2} \quad (6.125)$$

Considering the relations the parameters of the velocity triangle, the loading coefficient and efficiency of the LP turbine can be written respectively as:

$$H_{t2} = L_{u2}/U_2^2 = (K_{21} \cdot \phi \cdot \cot \beta_2 - 1 + K_{21}K_{43}\phi \cdot \cot \alpha_4)U_{r12} \quad (6.126)$$

$$\eta_2 = \frac{H_{t2}}{H_{t2} + \frac{\xi_{r2}}{2} \left[\left(\frac{K_{21}K_{43}\phi U_{r12}}{\sin \alpha_4} \right)^2 + 2K_{21}K_{43}\phi U_{r12} \cot \alpha_4 + 1 \right]} \quad (6.127)$$

Expressions of the total efficiency and the output power ratio are the same as those of conventional turbines. As for LP vaneless counter-rotating turbines, the number of independent parameters of the velocity triangle of the HP and LP turbine is reduced to seven. To compare with conventional counter-rotating turbines, the

convected velocity of the HP turbine, U_1 , is taken as the reference parameter, and the seven independent parameters are ϕ , α_1 , β_2 , K_{21} , U_{r12} , K_{43} , and α_4 . Similarly with the above method, three different revolution speed ratios were first chosen for the discussion, and the parameters were preliminarily determined as below: $\alpha_1 = 20^\circ$, $\beta_2 = 20^\circ$, $K_{43} = 1$, $\alpha_4 = 0$. Figure 6.60a shows the variation curves of the total efficiency and the output power ratio with the flow coefficient and the inlet-to-outlet axial velocity ratio of the HP turbine, at the HP-to-LP turbine revolution speed ratio $U_{r12} = 1.2$. As is shown in the figure, the inlet-to-outlet axial velocity ratio of the HP turbine has great influence on both the efficiency of the LP vaneless counter-rotating turbine and the output power ratio. The flow coefficient corresponding to the extreme point of the counter-rotating turbine efficiency changes greatly with different axial velocity ratio. For a given axial velocity ratio, the efficiency firstly increases and then decreases with the increase of the flow coefficient. The higher the axial velocity ratio, the smaller the flow coefficient corresponding to the maximum efficiency will be and the larger the efficiency decreasing amplitude after the extreme point will be. The axial velocity ratio has significant influence on the output power ratio of the vaneless counter-rotating turbine. For a given flow coefficient, the higher the axial velocity ratio, the more contributions it will make to reducing the output power ratio of the counter-rotating turbine. In addition, when the axial velocity ratio is at high level (such as $K_{21} = 2.6$ in Fig. 6.60a), the output power ratio of the LP vaneless counter-rotating turbine first declines to a low level rapidly and then decreases gradually with the increase of the flow coefficient. Although the increase in the axial velocity ratio would significantly reduce the output power ratio of the vaneless counter-rotating turbine, the output power ratio does not decrease much after the axial velocity ratio increases to a certain level. For a given flow coefficient, if the flow coefficient is 0.6, the output power ratio will decrease from 2.95 to about 2.4 as the axial velocity ratio increases from 1.4 to 1.8, and the output power ratio will decrease gently from 2.15 to about 2.0 as the axial velocity ratio increases from 2.2 to 2.6. The figure also indicates that, at a specific axial velocity ratio, the output power ratio changes evidently around the flow coefficient corresponding to the extreme value of the total efficiency, and then changes gently as the flow coefficient further increases. Therefore, the influence of the efficiency and the output power ratio should be fully considered when selecting flow coefficient, and the appropriate flow coefficient should be slightly higher than the value corresponding to the maximum efficiency.

Figure 6.60c, d present the variation curves of the efficiency and output power ratio under the revolution speed ratios of 1.0 and 1.5, which can be used to further discuss the influence of the HP-to-LP turbine revolution speed ratio on the total efficiency and the output power ratio of the LP vaneless counter-rotating turbine. As revealed by the comparison, the variation trends of the turbine efficiency and output power ratio with the flow coefficient are basically the same at different revolution speed ratios. For a given K_{21} , the maximum efficiency is slightly different at different speed ratios, and the higher the revolution speed ratio, the larger the maximum efficiency will be. Variations of the revolution speed ratio would lead to a

significant change of the output power ratio. The higher the revolution speed ratio, the larger the HP-to-LP turbine output power ratio will be. At the revolution speed ratio of 1.5, the minimum output power ratio is greater than 2 over the ranges of the parameters under study. Therefore, the influence of the total efficiency and the output power ratio should be considered when selecting the revolution speed ratio.

Through the above analysis, it can be concluded that the HP-to-LP turbine revolution speed ratio has little impact on the total efficiency of the LP vaneless counter-rotating turbine. The extreme value of the total turbine efficiency increases slightly with the increase of the revolution speed ratio, but the increment is insignificant. The HP-to-LP turbine revolution speed ratio has great influence on the output power ratio, and decrease in the revolution speed ratio can significantly reduce the output power ratio. The higher the inlet-to-outlet axial velocity ratio of the HP turbine, the more contributions it will make to reducing the output power ratio, but the decline of the HP-to-LP turbine output power ratio slows down with the increase of K_{21} .

Figure 6.61 presents the variation curves of the total efficiency and the inlet-to-outlet axial velocity ratios of the HP/LP turbine with the flow coefficient at different α_1 (when $\beta_2 = 20^\circ$, $\alpha_4 = 80^\circ$, and the HP-to-LP turbine output power ratio = 2.0), which can be used to discuss the criteria of selecting of the flow angles. The maximum efficiency value almost keeps unchanged as α_1 changes. The flow coefficient corresponding to the maximum efficiency value would decrease as α_1 increases. For a given α_1 , the total efficiency would first increase and then decrease with the increase of the flow coefficient, and this variation trend can be explained qualitatively by the change of the velocity triangle. As shown in Fig. 6.62, the velocity triangle changes from black to blue as ϕ increases, which is manifested as the decrease of W_2 and the increase of C_1 and W_4 . Decrease in velocity helps to

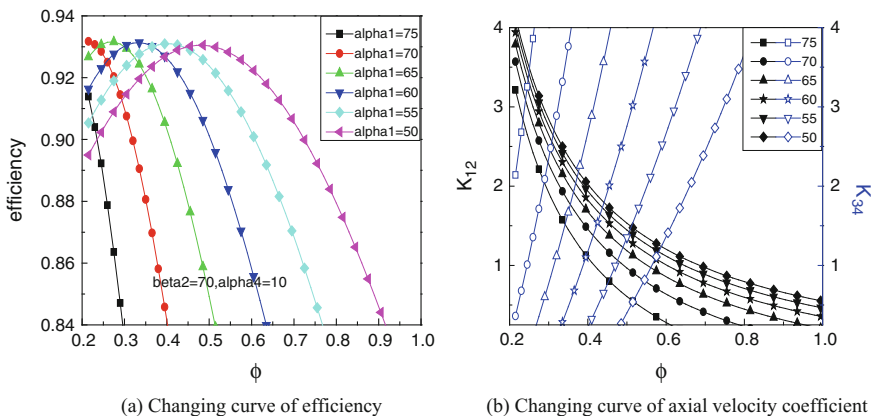
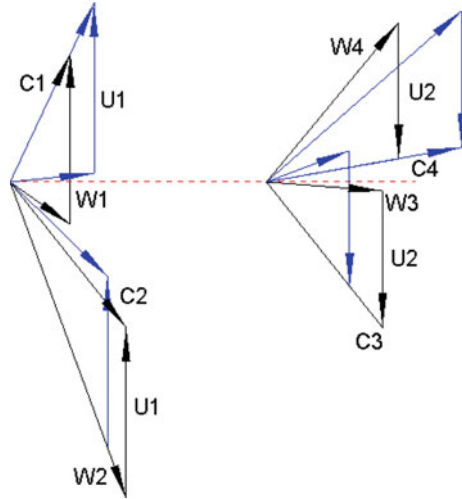


Fig. 6.61 Relations between turbine performance parameters and flow coefficient at different α_1 (Output power ratio = 2.0) [69]

Fig. 6.62 Changes of velocity triangle as flow coefficient changes



reduce the loss. Therefore, if the decrease of W_2 is greater than the increase of C_1 and W_4 , the total efficiency will increase; otherwise, the total efficiency will decrease. By comparing (a) and (b) in Fig. 6.61, it can be drawn that the corresponding inlet-to-outlet axial velocity ratio of the HP rotor should be high to guarantee a high efficiency of the counter-rotating turbine. For example, when $\alpha_1 = 25^\circ$ and the flow coefficient is about 0.28, the efficiency reaches to the extreme value and the corresponding K_{21} and K_{43} are 2.5 and 0.9 respectively.

Figure 6.63 presents the variation curves of the efficiency, K_{21} , and K_{43} with the flow coefficient at different α_1 (output power ratio = 2.2), which can be used to further analyze the criteria of selecting of the flow angles at different output power ratios. At the higher output power ratio, the maximum efficiency is slightly higher at each α_1 , and the range of the flow coefficient corresponding to the high efficiency area is wider. For a given α_1 , the flow coefficient corresponding to the maximum efficiency value becomes higher. In terms of changes in axial velocity ratios, the axial velocity ratios of both the HP and LP turbines decrease at the maximum efficiency point, and the ratio of the LP turbine changes more significantly. For example, when $\alpha_1 = 25^\circ$ and the flow coefficient corresponding to the maximum efficiency point is about 0.35, the corresponding K_{21} and K_{43} are 2.1 and 0.25 respectively. Increasing the flow angle at the guide vane outlet is one of the effective approaches to solve the problem of excessively low axial velocity ratio of the LP stage; when $\alpha_1 = 20^\circ$ and the flow coefficient corresponding to the maximum efficiency point is about 0.29, the corresponding K_{21} and K_{43} are about 2.4 and 0.8 respectively.

In a word, there is great difference in the selection of the velocity triangle between LP vaneless counter-rotating turbines and conventional counter-rotating turbines at the same general parameters. To meet the requirement on the unit power

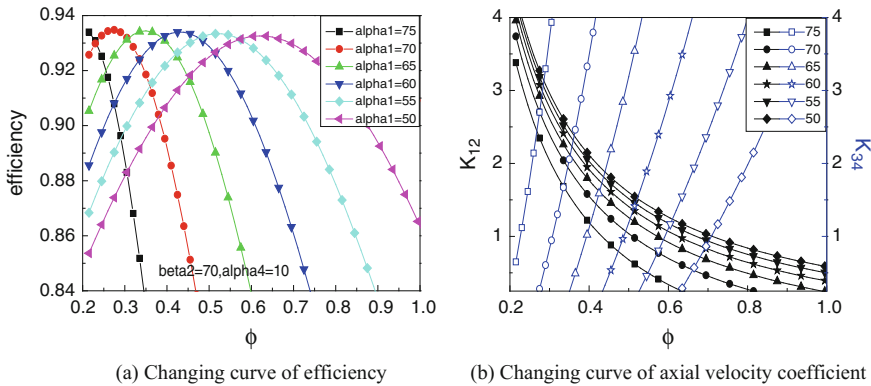


Fig. 6.63 Relations between turbine performance parameters and flow coefficient at different α_1 (Output power ratio = 2.2) [69]

of the HP/LP turbines and achieve high efficiency, the flow coefficient should be much lower than that of conventional counter-rotating turbines, while the inlet-to-outlet axial velocity ratio of the HP turbine should be much higher, which would lead to the higher Mach number at the HP turbine rotor outlet. All of these bring challenges to the design of LP vaneless counter-rotating turbines. LP vaneless counter-rotating turbines have the advantage of low weight due to the reducing or even disusing of the guide vane. However, due to the lower flow coefficient at the operating point, the mean radius of LP vaneless counter-rotating turbines should be larger than that of the conventional turbines to achieve the same flow rate. This would result in the increase of the weight of turbine disk. So, concrete analysis is needed to determine whether LP vaneless counter-rotating turbines are lighter than conventional counter-rotating turbines.

6.3.5.4 Velocity Triangle Analysis of 1 + 3/2 Counter-Rotating Turbines

If the first stage of the LP turbine of a 1+3/2 counter-rotating turbine is close to or greater than the conventional one-stage LP turbine in power capability, then the matching characteristics between the HP turbine and LP turbine of the 1+3/2 counter-rotating turbine are similar to those of the 1+1/2 counter-rotating turbine, and their design parameters can be selected by using those of the 1+1/2 counter-rotating turbine as reference. However, 1 + 3/2 counter-rotating turbines are also facing an unique problem, namely the work distribution for the two LP turbine stages. The influence of the work distribution coefficient of the LP turbine on the total efficiency of the LP turbine at different HP turbine loading coefficients is analyzed in this subsection.

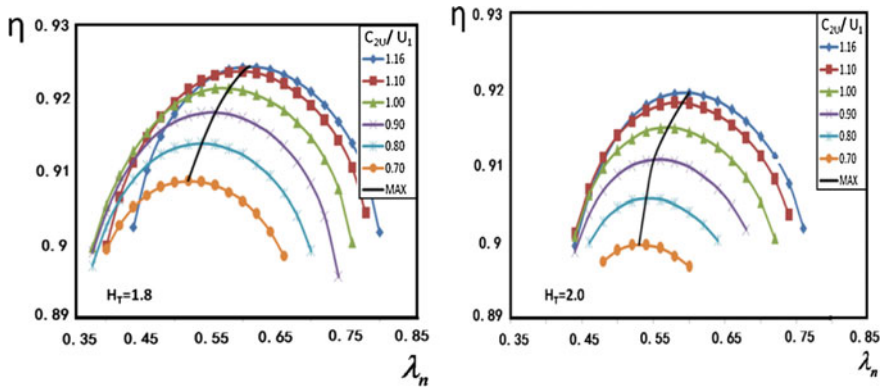


Fig. 6.64 Relation between LP turbine efficiency and work distribution coefficient (HP turbine loading coefficient = 1.8)

Figure 6.64 shows the variation curves of the total efficiency of the LP turbine with the LP turbine work distribution coefficient at different HP turbine outlet prewhirl, C_{2U}/U_1 (HP turbine loading coefficient = 1.8, 2.0). The vertical coordinate represents the total efficiency of the LP turbine, and the horizontal coordinate represents the LP turbine work distribution coefficient, λ_n . The parameter at the right side is the HP turbine outlet prewhirl, C_{2U}/U_1 , and the maximum AN^2 is obtained at 1.16. As can be seen from the figure, when the HP turbine outlet prewhirl is given, there exists an optimal LP turbine work distribution coefficient corresponding to the maximum total efficiency of the LP turbine. The optimal LP turbine work distribution coefficient would change with the prewhirl value. As the HP turbine outlet prewhirl decreases, the optimal LP turbine work distribution coefficient would decrease accordingly, so would the maximum total efficiency of the LP turbine. At the higher turbine loading coefficient, influence of the HP turbine outlet prewhirl on the optimal work distribution coefficient becomes weaker. Within the allowable range of AN^2 , the maximum total efficiency of the LP turbine can be increased with the increasing of the HP turbine outlet prewhirl.

6.3.5.5 Discussion on Reaction Degree of Counter-Rotating Turbines

Generally speaking, the reaction degree of a turbine is defined as “the ratio of the expansion and acceleration of gas in the rotor cascade to that in the stator cascade”. A low reaction degree indicates that the degree of acceleration from expansion is high in the stator while low in the rotor; otherwise, the degree of acceleration from expansion is low in the stator while high in the rotor. Zero reaction degree means all the acceleration from expansion occurs in the stator and the turbine is an impulse

turbine. If following with this definition, there will be two unexplainable questions in velocity triangle analysis of 1 + 1/2 counter-rotating turbines. The first one is that why could the reaction degree of the HP turbine of 1 + 1/2 counter-rotating turbines be greater than 1.0, and the second one is that how to define the reaction degree of the LP turbine without any stators.

Actually, the reaction degree is originally defined as “the ratio of the static enthalpy drop in the rotor to the total enthalpy drop” or “the ratio of the increment in relative kinetic energy in the rotor to the rim work” [74], and given by:

$$\Omega = \frac{h_1 - h_2}{h_1^* - h_2^*} \quad \text{or} \quad \Omega = \frac{\frac{1}{2}(W_2^2 - W_1^2)}{L_u} \quad (6.128)$$

Since no rim work is produced in the stator, the reaction degree is not directly related to the stator, but only to the rotor. Therefore, the second question is answered quite naturally. The following analysis is presented to answer the first question. First, the reaction degree is redefined as:

$$\Omega = \frac{h_1 - h_2}{L_u} = \frac{h_1 - h_2}{(h_1 - h_2) + \frac{1}{2}(C_1^2 - C_2^2)} \quad (6.129)$$

The total enthalpy of the working medium would decrease in the rotor and the rim work (or output shaft power) is generated. There are two sources of the turbine shaft power. The first one is the static enthalpy or micro energy of the working medium (including internal energy and pressure potential energy), and the second is the kinetic energy or macro energy of the working medium. Physically, the definition of the reaction degree represents the ratio of the two sources of the shaft power. Thus, zero reaction degree means static enthalpy of the working medium keeps constant and the shaft power all results from changes in kinetic energy, which is the work principle of impulse turbines. If the reaction degree is between 0 and 1, both the two sources contribute to the shaft power. If the reaction degree is 1, kinetic energy of the working medium keeps constant and the shaft power all results from static enthalpy. If the reaction degree is greater than 1, static enthalpy of the working medium converts not only to the shaft power, but also to kinetic energy. Turbines with the reaction degree greater than 1 are widely used in production practice, such as the turbines used in tidal power generation and wind power generation. For low-speed incompressible gas, the outlet flow direction will inevitably deviate from the axial direction to produce a torque according to velocity triangle analysis, and the axial velocity at the inlet is equal to that at the outlet under the incompressible condition. Therefore, the absolute velocity at the outlet of the wind turbine blade is higher than that at the inlet. In other words, the static enthalpy of air is converted into the shaft power and kinetic energy. In this condition, the reaction degree of the turbine is greater than 1.

Then, how do the “misunderstandings” above about the turbine reaction degree come into being. The reason is described as follows. Because the outlet velocity of conventional gas turbines (such as turbines with low aerodynamic loading, used in third-generation or earlier-generation aero-engines) is generally in axial direction and the expansion ratio of a single-stage turbine is limited, the inlet velocity and outlet velocity of the turbine stage are basically the same, namely $C_0 \approx C_2$. Thus, $\frac{1}{2}(c_1^2 - c_2^2) \approx \frac{1}{2}(c_1^2 - c_0^2)$. After substituting it into the reaction degree expression, the following equation can be obtained:

$$\Omega = \frac{h_1 - h_2}{L_u} = \frac{h_1 - h_2}{(h_1 - h_2) + \frac{1}{2}(C_1^2 - C_2^2)} = \frac{\frac{1}{2}(W_2^2 - W_1^2)}{\frac{1}{2}(W_2^2 - W_1^2) + \frac{1}{2}(C_1^2 - C_0^2)} \quad (6.130)$$

where, the numerator represents the increment in kinetic energy of the gas in the rotor cascade, namely the degree of acceleration from expansion, and the denominator represents the sum of the degree of acceleration from gas expansion in both the rotor cascade and stator cascade. Therefore, the reaction degree is given the “physical significance” of “the ratio of degree of acceleration from gas expansion in the rotor cascade to that in the stator cascade”. It is thus clear that this definition of the reaction degree is established on the assumptions that “the turbine has guide vanes” and “ $C_0 \approx C_2$ ”, so it is applicable to conventional turbines. However, the assumptions that “the turbine has guide vanes” and “ $C_0 \approx C_2$ ” may not be appropriate to counter-rotating turbines. For example, $C_0 < C_2$ in the HP turbine of 1 + 1 counter-rotating turbines, and $C_0 < C_2$ in the HP turbine of 1 + 1/2 counter-rotating turbines, which are not equipped with guide vanes. Therefore, the two questions above arise with respect to the conventional understanding of the turbine reaction degree.

Hence, the two misunderstandings on the turbine reaction degree in 1 + 1 and 1 + 1/2 counter-rotating turbines result from the assumptions on “conventional turbines”, while they are not in conflict with the original definition and physical significance of the turbine reaction degree. Therefore, the definition and physical significance of the turbine reaction degree are totally applicable in velocity triangle analysis of counter-rotating turbines.

The motion reaction degree, Ω' , is also a commonly used parameter in design of conventional turbines, and is defined as:

$$\Omega' = \frac{W_{2u} - W_{1u}}{2U} = 1 - \frac{C_{1u} - C_{2u}}{2U} \quad (6.131)$$

This parameter is directly related to the tangential components of the velocity triangle, and is usually used in the velocity triangle analysis. Under incompressible conditions, the motion reaction degree can be used as the substitution of the original definition, while it could only reflect the actual reaction degree partially under compressible conditions. Through simple derivation of the parameters of the

velocity triangle, the relation between the reaction degree and the motion reaction degree can be written as:

$$\Omega = \Omega' + \frac{\psi(1 - K_{12}^2)}{2 \cot^2 \beta_2} \left(\frac{1}{2} + \frac{\Omega'}{\psi} \right)^2 \quad (6.132)$$

In general, the axial velocity ratio, K_{12} , is less than 1.0, so $\Omega' < \Omega$. However, with the increase of the reaction degree, the difference between the two will become larger. Therefore, when analyzing the physical significance of the reaction degree, the motion reaction degree cannot be used as the substitution of the original reaction degree particularly in counter-rotating turbines [72].

6.4 Multi-dimensional Numerical Evaluation System of Turbine Aerodynamic Performance

In the aerodynamic design process of turbines, numerical evaluation systems in different dimensions can make the design process concise and efficient, reduce design cost and shorten design cycle. For this reason, companies and institutes have developed various kinds of distinctive and practicable numerical evaluation systems based on their usual design practice and requirements. Each of the numerical evaluation methods of different dimensions has both merits and demerits. For example, S2 calculation has the advantage of high calculation speed, but the accuracy of the results relies heavily on the experience or losses models employed by the user. 3-D CFD methods have high accuracy (depends mainly on the universality of the turbulence model) and are less dependent on experience than S2 calculation, but large amounts of computation are required. Thus, numerical evaluation methods of different dimensions are important in the design process, and can meet different levels of demands in the design system by completing each other and giving full play to their features [75–77].

6.4.1 S2 Calculation for Air-Cooled Turbines

Figure 6.65 shows the flow chart of the multi-stage S2 streamsurface calculation procedure. This procedure is mainly designed to calculate the S2 streamsurface parameters of multi-stage gas turbines, analyze the reasonability of the spanwise distribution of S2 streamsurface parameters, and determine the flow rate, power,

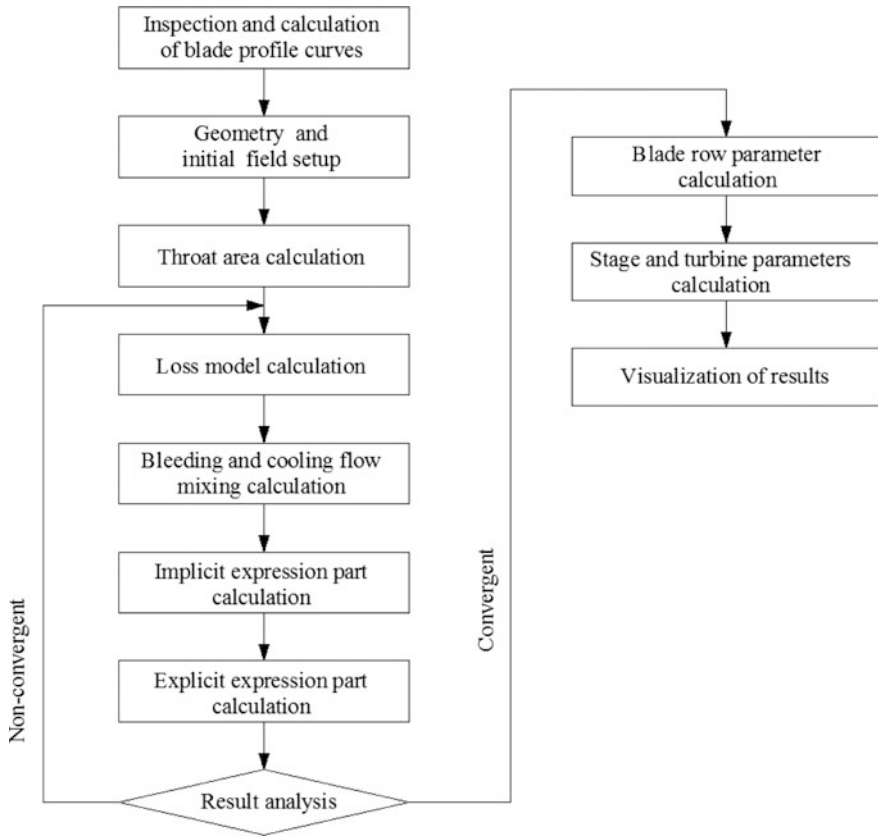


Fig. 6.65 Direct problem calculation procedure

efficiency, and other overall parameters. Thus, it plays a very important role in aerodynamic design process of turbines. This subsection mainly introduces the fundamental principles of S2 direct problem calculation.

6.4.1.1 Fundamental Equations for S2 Direct Problem Calculation

I. Three-dimensional viscous flow equations in cylindrical coordinate system

For turbomachineries, the equations for unsteady 3-D viscous flow with mass source are as follows:

$$\begin{aligned} \frac{\partial \rho}{\partial t} + \nabla \cdot (\rho \vec{w}) &= \dot{m} \\ \frac{\partial(\rho \vec{w})}{\partial t} + \nabla \cdot (\rho \vec{w} \vec{w} + Ip - \Pi') &= \dot{m} \vec{V}_c - \rho \frac{d\omega}{dt} \\ \frac{\partial(\rho e)}{\partial t} + \nabla \cdot [(\rho e + p) \vec{w} - \Pi' \cdot \vec{w} - \lambda \nabla T] &= \dot{m} H_C + r \rho \omega^2 w - r \rho w \frac{d\omega}{dt} \\ e &= \int C_v dT + \frac{W^2}{2} \end{aligned}$$

ω is the angular velocity of the rotor, and Π' is the stress tensor. In the cylindrical coordinate system, the 3-D viscous flow equations can be expanded as:

$$\frac{\partial}{\partial t}(rU) + \frac{\partial}{\partial z}(rF) + \frac{\partial}{\partial r}(rG) + \frac{1}{r} \frac{\partial}{\partial \varphi}(rH) = Q \quad (6.133)$$

where,

$$U = \begin{bmatrix} \rho \\ \rho u \\ \rho v \\ \rho w \\ \rho e \end{bmatrix} \quad (6.134)$$

$$F = \begin{bmatrix} \rho u \\ \rho u^2 + P \\ \rho uv \\ \rho uw \\ \rho(e + \frac{p}{\rho})u \end{bmatrix} \quad (6.135)$$

$$G = \begin{bmatrix} \rho v \\ \rho uv \\ \rho v^2 + p \\ \rho vw \\ \rho(e + \frac{p}{\rho})v \end{bmatrix} \quad (6.136)$$

$$H = \begin{bmatrix} \rho w \\ \rho uw \\ \rho vw \\ \rho w^2 + p \\ \rho(e + \frac{p}{\rho})w \end{bmatrix} \quad (6.137)$$

$$Q = \begin{bmatrix} r\dot{m} \\ r\dot{m}V_{cz} + f_z \\ r\dot{m}V_{cr} + f_\varphi + p + \rho(w + \omega r)^2 \\ r\dot{m}V_{c\varphi} + f_\varphi - \rho v(w + 2\omega r) - r^2\rho \frac{d\omega}{dt} \\ r\dot{m}H_C + \omega^2 r^2 \rho v - r^2 \rho w \frac{d\omega}{dt} + \phi + N_f \end{bmatrix} \quad (6.138)$$

where

$$\begin{aligned} f_z &= \vec{i}_z \cdot (\nabla \cdot \Pi') \\ f_r &= \vec{i}_r \cdot (\nabla \cdot \Pi') \\ f_\varphi &= \vec{i}_\varphi \cdot (\nabla \cdot \Pi') \\ \vec{f} &= \nabla \cdot \Pi' \\ \phi &= \Pi' : \nabla \vec{W} \\ N_f &= \vec{f} \cdot \vec{W} \end{aligned}$$

\dot{m} is the mass of the cooling medium, exhaust gas, or condensed gas in unit time and unit volume. For convenience, the mass is expressed as the mass unit, \dot{m} , which is equal to the mass of gas flowing into or out of a unit volume in unit time, and it is specific to the source term of continuity equations with sources.

If a mass unit is composed by n components, the ratio of each component to the original mass is written as: $\alpha_i = \delta m_i / \delta m_o$, where α_i is the mass distribution function or the mass ratio of each component in a mass unit. Then, the mass density of each component is given by:

$$C_i = \frac{\delta m_i}{\delta m_o + \delta m_1 + \delta m_2 + \cdots + \delta m_n} = \frac{\alpha_i}{1 + \alpha_1 + \cdots + \alpha_n} \quad i = 1, \dots, n$$

Sum it up: $C_0 + C_1 + \cdots + C_n = 1$

The original mass must follow the following continuity equation:

$$\frac{\partial}{\partial t}(r\rho C_0) + \frac{\partial}{\partial Z}(r\rho u C_0) + \frac{\partial}{\partial r}(r\rho v C_0) + \frac{\partial}{r\partial\varphi}(r\rho w C_0) = 0$$

Replace C_0 with the above equation:

$$\begin{aligned} \frac{\partial}{\partial t}(r\rho) + \frac{\partial}{\partial z}(r\rho u) + \frac{\partial}{\partial r}(r\rho v) + \frac{\partial}{r\partial\varphi}(r\rho w) &= \frac{\partial}{\partial t}[r\rho(C_1 + \cdots + C_n)] \\ + \frac{\partial}{\partial z}[r\rho u(C_1 + \cdots + C_n)] + \frac{\partial}{\partial r}[r\rho v(C_1 + \cdots + C_n)] &+ \frac{\partial}{r\partial\varphi}[r\rho w(C_1 + \cdots + C_n)] \end{aligned}$$

and,

$$C_0 = \frac{\alpha_0}{1 + \alpha_1 + \cdots + \alpha_n} \alpha_0 = \frac{\delta m_0}{\delta m_0} = 1$$

So,

$$C_i = \frac{\alpha_i}{1 + \alpha_1 + \cdots + \alpha_n} = \alpha_i C_0$$

Then, the continuity equation can be rewritten as:

$$\frac{\partial}{\partial r}(r\rho) + \frac{\partial}{\partial z}(r\rho u) + \frac{\partial}{\partial r}(r\rho v) + \frac{\partial}{r\partial\phi}(r\rho w) = r\rho C_0 \left[\frac{d\alpha_1}{dt} + \frac{d\alpha_2}{dt} + \cdots + \frac{d\alpha_n}{dt} \right]$$

We can obtain:

$$r\dot{m} = r\rho C_0 \left[\frac{d\alpha_1}{dt} + \cdots + \frac{d\alpha_n}{dt} \right]$$

When $n = 1$, the value is δm_0 at the moment t_0 , and after a time interval dt , the value is $\delta m_0 + \delta m_1$. Then,

$$\begin{aligned} r\dot{m} &= r\rho \frac{d(\alpha_1 C_0)}{dt} = r\rho \frac{1}{\delta t} \left(\frac{\delta m_1}{\delta m_0} \frac{\delta m_0}{\delta m_0 + \delta m_1} \right) \\ &= r \frac{\delta m_0 + \delta m_1}{\partial V} \frac{\delta m_1}{\delta t} \frac{1}{(\delta m_0 + \delta m_1)} \\ &= r \frac{1}{\delta V} \frac{\delta m_1}{\delta t} \end{aligned}$$

Then, we can obtain:

$$\dot{m} = \frac{1}{\delta v} \frac{\delta m_1}{dt}$$

In addition, the following supplementary equations are needed:

$$J \frac{d\omega}{dt} = \sum M \quad (6.139)$$

$$p = f(\rho, T) \quad (6.140)$$

$$i = u + \frac{p}{\rho} \quad (6.141)$$

For the steady problem, $\frac{d\omega}{dt} = 0$, Eq. (6.139) and corresponding terms in the equations can be removed.

II. Simplification of viscous flow equations

The viscous force in the momentum equations, $\vec{f} = \nabla \cdot \Pi'$, can be simplified and solved approximately by using the equation below:

$$\vec{f} = \frac{-\rho \bar{w} \bar{w}}{w^2} \cdot T \nabla S = -\frac{\bar{w} \phi}{w^2}$$

In the cylindrical coordinate system, it can be expanded as:

$$(f_z, f_r, f_\phi) = -\frac{r\phi}{u^2 + v^2 + w^2} (u, v, w) \quad (6.142)$$

The following equations can be derived:

$$\begin{aligned} r\rho T \frac{DS}{dt} = r\dot{m} \{ H_c - i - \frac{1}{2} (V_{cz}^2 + V_{cr}^2 + V_{c\phi}^2) \\ + \frac{1}{2} [(V_{cz} - u)^2 + (V_{cr} - v)^2 + (V_{c\phi} - w)^2] \} + r\phi \end{aligned} \quad (6.143)$$

Or written as:

$$\begin{aligned} r\rho T \frac{Ds}{dt} = r\rho C_0 \sum_{j=1}^n \{ H_{cj} - i_j - \frac{1}{2} (V_{czj}^2 + V_{crj}^2 + V_{c\phi j}^2) \\ + \frac{1}{2} [(V_{czj} - u)^2 + (V_{crj} - v)^2 + (V_{c\phi j} - w)^2] \} \frac{Dx_j}{dt} + r\phi \end{aligned} \quad (6.144)$$

σ is defined as the entropy increase resulting from viscosity, and then we can obtain:

$$\Phi = \rho T \frac{D\sigma}{dt} \quad (6.145)$$

σ can be calculated by using the loss value. For flows without mass sources, σ only depends on Φ . Then Eq. (6.143) and Eq. (6.144) can be simplified.

For the energy equation, $\phi \approx -\vec{f} \cdot \vec{w}$. The viscous force term can be removed in the energy equation. Thus, $\phi + N_f = 0$ in Eq. (6.138). In addition, boundary conditions of the simplified equations are greatly different from those of the actual viscous flow equations. The main difference is that the simplified equations adopt the wall boundary conditions of inviscid equations.

III. S2 stream surface equations

By using the circumferentially-averaged equations,

$$\begin{aligned}\frac{\partial \bar{q}}{\partial z} &= \frac{1}{\tau} \frac{\partial(\tau \bar{q})}{\partial z} - \frac{\Delta q}{\Delta \varphi} \frac{\partial \varphi_m}{\partial z} - \frac{1}{\tau} \frac{\partial \tau}{\partial z} \bar{q} \\ \frac{\partial \bar{q}}{\partial r} &= \frac{1}{\tau} \frac{\partial(\tau \bar{q})}{\partial r} - \frac{\Delta q}{\Delta \varphi} \frac{\partial \varphi_m}{\partial r} - \frac{1}{\tau} \frac{\partial \tau}{\partial r} \bar{q}\end{aligned}$$

Equation (6.133) can be written as:

$$\frac{\partial}{\partial t}(r\tau\bar{U}) + \frac{\partial}{\partial z}(r\tau\bar{F}) + \frac{\partial}{\partial r}(r\tau\bar{G}) = \bar{Q} \quad (6.146)$$

where, $\bar{U}, \bar{F}, \bar{G}$ are the average quantities, and the terms contained in them are the same as those in U, F, G (as shown in Eq. (6.133)), but:

$$\bar{Q} = \begin{bmatrix} \tau r \dot{m} \\ \tau r \dot{m} V_{cz} + \tau f_z + r p \frac{\partial \tau}{\partial z} \\ \tau r \dot{m} V_{cr} + \tau f_r + \tau p + r p \frac{\partial \tau}{\partial r} + \tau p (w + \omega r)^2 + r \tau \frac{\Delta p}{\Delta \varphi} \frac{\partial \varphi}{\partial r} \\ \tau r \dot{m} V_{\varphi} + \tau f_{\varphi} - \rho \tau v (w + \omega r) - \tau r^2 \rho \frac{dw}{dt} \\ \tau r \dot{m} H_c + \tau \omega^2 r^2 \rho v - \tau r^2 \rho w \frac{dw}{dt} \end{bmatrix} \quad (6.147)$$

The stream surface equation is given by:

$$u \frac{r \partial \varphi}{\partial z} + v \frac{r \partial \varphi}{\partial r} - w = 0 \quad (6.148)$$

IV. Equations in curvilinear coordinate system

In the curvilinear coordinate system (or body-fitted coordinate system),

$$\begin{aligned}\xi &= \xi(z, r, \varphi) \\ \eta &= \eta(z, r, \varphi) \\ \zeta &= \zeta(z, r, \varphi)\end{aligned} \quad (6.149)$$

Equation (6.133) can be written as:

$$\frac{\partial \tilde{U}}{\partial t} + \frac{\partial \tilde{F}}{\partial \xi} + \frac{\partial \tilde{G}}{\partial \eta} = \tilde{Q} \quad (6.150)$$

where,

$$\begin{aligned}\tilde{U} &= \frac{\tau r \bar{U}}{J} \\ \tilde{F} &= \frac{\tau r}{J} (\bar{F}_{\xi_z} + \bar{G}_{\xi_r}) \\ \tilde{G} &= \frac{\tau r}{J} (\bar{F}_{\eta_z} + \bar{G}_{\eta_r}) \\ \tilde{Q} &= \frac{\bar{Q}}{J} \\ J &= \frac{\partial(\xi, \eta, \zeta)}{\partial(z, r, \varphi)}\end{aligned}$$

6.4.1.2 Loss Model for S2 Direct Problem Calculation

The S2 direct problem calculation procedure has a wide application range, and employs many loss models. In practice use, users can choose appropriate loss models as required. This subsection gives a brief introduction to a commonly used loss model for air-cooled turbines in aero-engines, namely the BТИ loss model.

The BТИ loss model is a method of predicting the turbine loss, which is proposed based on comprehensive analysis of large amounts of experimental data. The model not only considers the profile loss, the trailing-edge loss, the shock loss, the leakage loss, and the incidence loss, but also corrects the loss of conventional straight cascades under the fan-shaped conditions (namely, the 3D loss) based on ЦКТИ's experimental data and МЗИ's empirical data. In addition, it further corrects the loss coefficients by introducing the relative blade pitch and the outlet velocity coefficient, λ_{2T} .

This model gives a detailed subdivision of losses in the cascade passage and establishes empirical equations for all of them. The data used in this model is the experimental data of complete turbines or turbine stages designed in modern times, so it can reflect the actual level of modern turbine design and produce highly reliable results.

The methods for calculating the losses in the BТИ loss model are described as follows:

When calculating the loss in the cascade, the model adopts the parameter, K , which is defined as:

$$K = \frac{r_1 \Delta r \cos \bar{\tau}_1 \sin \beta_1}{r_2 \Delta r \cos \bar{\tau}_2 \sin \beta_2} \quad (6.151)$$

where, r_1 is the inlet radius of the cascade; r_2 is the outlet radius of the cascade; Δr is the thickness of the stream sheet; r is the meridian angle of the passage.

The profile friction loss, ζ_{TP} , is given by:

$$\zeta_{TP} = 0.00874C_1 \left\{ \frac{\theta}{C_3 57.3} \left[C_2 \left(\phi + \frac{C_1}{C_2 \sqrt{K}} \right) \right]^2 \right\}^{\frac{1}{3}} \quad (6.152)$$

where, $C_1 = \frac{0.01380}{\sin^2 \frac{\theta}{2}} - 0.634$, $C_2 = 1.22 \text{tg} \frac{\theta}{4} + 0.323$, $C_3 = 1.92 - \frac{0.00850}{\sin^2 \frac{\theta}{2}}$, θ is the deflection angle of the fluid, and

$$\phi = \begin{cases} 0.23K^2 - 1.545K + 2.75, & K < 2 \\ [\sqrt{K}(1.1K - 1)]^{-1}, & K \geq 2 \end{cases}$$

The trailing edge loss, ζ_{KP} , is given by:

$$\zeta_{KP} = 0.33 \frac{d_2}{t_2 \sin^2 \beta_2}, \quad (6.153)$$

d_2 : trailing edge radius

When $\lambda_{2T} > 1$, $\sin \beta_2$ in the equation above is given by:

$$\sin \beta_2 = \sin \beta_{2P} \left(\frac{R+1}{\theta} \right)^{-\frac{1}{k-1}} \left(1 - \frac{k-1}{k+1} \lambda_{2T}^2 \right)^{-\frac{1}{k-1}} \lambda_{2T}^{-1}$$

β_2 : outflow angle

β_{2P} : effective metal angle at the outlet

λ_2 : dimensionless velocity at the outlet

The shock loss, ζ_{sh} , is given by:

$$\zeta_{sh} = (0.0144 - 0.00268\beta_{2P})(M_{2T}^3 - 1) \quad (6.154)$$

where, M_{2T} is the Mach number corresponding to λ_{2T} .

The incidence loss, ζ_{AT} , is written as:

$$\zeta_{AT} = 0.028 \left(\frac{d_1}{t_1 \sin \beta_1} \right)^{-\frac{2}{3}} \sigma_1 + \sigma_2 \quad (6.155)$$

where, d_1 is the minor diameter of the leading edge; t_1 is the blade pitch at the cascade inlet;

$$\sigma_1 = \left(\frac{\lambda_1 \cos \bar{r}_1}{\lambda_{2T}} \right)^2 - \left(\frac{\lambda_{\delta 1}}{\lambda_{2T}} \right)$$

$\sigma_2 = \left(\frac{\lambda_{\delta 1}}{\lambda_{2T}}\right)^2 \sin^2 \Delta\beta_1 \cos^3 \beta_2$; $\Delta\beta_1$ is the incidence;

$\lambda_{\delta 1}$ is determined by the q-relation aerodynamic function:

$$q(\lambda_{\delta 1}) = \frac{q(\lambda_1 \cos \bar{\tau}_1) \sin \beta_1}{\sin \beta_{\delta 1}}$$

$\beta_{\delta 1}$ is the inflow angle corresponding to the inlet metal angle; $\lambda_{\delta 1}$ is the dimensionless velocity of the inflow angle corresponding to the inlet metal angle.

The endwall loss, ζ_{EW} , is given by:

At the root of the fan-shaped cascade, the endwall loss is given by:

$$\zeta_{EW} = \left[\frac{F_n (1 + \lambda_{2T}^2 \operatorname{tg} \tau_1) (1 + \theta_B \operatorname{tg} \tau_2)}{(D/l)^{1.15}} + 1 \right] \zeta_{TP} \quad (6.156)$$

where,

τ_1 and τ_2 are the inclinations (relative to the meridian) of the inlet and outlet endwalls of the cascade;

θ_B : fluid deflection;

$$F_n = \begin{cases} 8, & X_n < 0.25 \\ \frac{0.0895}{X_n^2} + \frac{5.228}{X_n} - 11.027 + 7.06X_n, & 0.25 < X_n < 0.7 \\ 0.9 - 0.5(X_n - 0.7), & X_n > 0.7 \end{cases}$$

$$X_n \approx \frac{(\lambda_1 \cos \beta_1 + \lambda_2 \cos \beta_2)^2 (\theta_B)^{0.25}}{1 + \operatorname{tg} \tau_2}$$

When λ_{2T} deviates from the optimal value, $\lambda_{2T_{opt}}$, the loss correction, $\Delta\zeta_\lambda$, is given by:

$$\Delta\zeta_\lambda = \left(6.05 \left(\frac{\lambda_{2T}}{\lambda_{2T_{opt}}} \right)^3 - 11.8 \left(\frac{\lambda_{2T}}{\lambda_{2T_{opt}}} \right)^2 + 6 \frac{\lambda_{2T}}{\lambda_{2T_{opt}}} - 0.25 \right) (\zeta_{TP} + \zeta_{KP}) \quad (6.157)$$

If $\lambda_{2T} > 1$, take $\lambda_{2T} = 1$ into the Eq. (6.157);

$\lambda_{2T_{opt}}$: optimal outlet angular velocity;

When the relative blade pitch, t , deviates from the optimal blade pitch, t_{opt} , the loss correction, $\Delta\zeta_t$, is given by:

$$\Delta\zeta_t = \left[\frac{\Delta\bar{t}_{\text{opt}}}{0.38\bar{t}_{\text{opt}} + 0.058} \right]^2 \zeta_{\text{TP}} \quad (6.158)$$

where, $\Delta\bar{t}_{\text{opt}} = \frac{\bar{t} - \bar{t}_{\text{opt}}}{\bar{t}_{\text{opt}}}$, \bar{t}_{opt} is determined after obtaining \bar{t}'_{opt} according to K and θ at $\lambda_{2T} = 0.8$

$$\bar{t}_{\text{onT}} = \begin{cases} 0.815(1 + \delta) \left(1 - 0.1 \sqrt{\frac{2.7}{K+0.7}} \ln \frac{\theta}{27} \right), & K > 1.5 \\ 0.815(1 + \delta) \left(1 - 0.1 \sqrt{\frac{2.7}{K+0.7}} \ln \frac{\theta}{27} \right) \left(\frac{54.5}{\theta} \right)^{\frac{0.175}{K} - 0.25}, & 1 \leq K \leq 1.5 \end{cases}$$

$$\delta = \begin{cases} 0.1, & \lambda_{2T} < 0.56 \\ 0.575 - 0.707\lambda_{2T} + \frac{0.574(\lambda_{2T} - 0.955)}{0.045 + \lambda_{2T}}, & 0.56 < \lambda_{2T} < 1.25 \\ -0.3b, & \lambda_{2T} > 1.25 \end{cases}$$

6.4.2 Error Analysis of Various Factors in CFD-Based Air-Cooled Turbine Calculation

As aerodynamic design is carried out in higher and higher dimensions, the design methods can solve more problems, and meanwhile, need to take more factors into consideration. Therefore, the key point that a designer should pay attention to in 3-D numerical calculation is how to improve the reliability of the numerical simulation. This subsection mainly describes the problems that need to be paid attention to in the current 3-D numerical calculation for air-cooled turbines. Conventional problems of numerical accuracy are not discussed here which can be found in relevant literature.

6.4.2.1 Turbulence Model and Calculation Accuracy

Calculation software should be verified in the calculation for air-cooled turbines. The calculation accuracy should be assessed in the following two aspects: (1) Assess the prediction ability of the 3-D calculation on the turbines' aerodynamic parameters and overall aerodynamic performance under the condition of air film cooling; (2) Simulate air-cooled turbines with film cooling holes and assess the prediction ability of the 3-D calculation on temperature field on the blades. What follows gives a brief review on content in this field.

Fully 3-D calculation for GE's E³ turbine (two-stage HP turbine and five-stage LP turbine, 14 blade rows in all) was carried out by the 3-D calculation software

Fig. 6.66 Comparison of total pressure

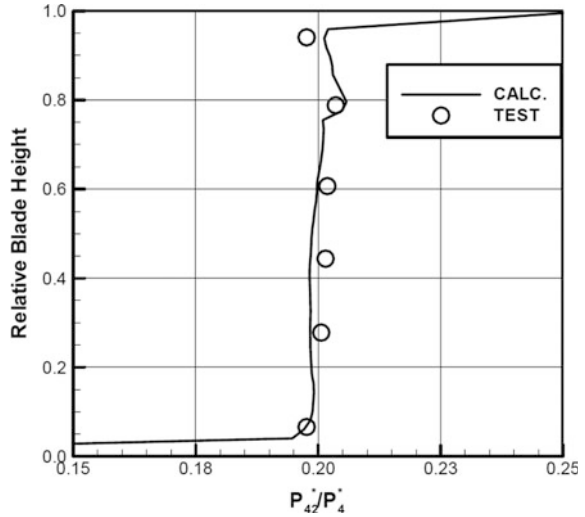
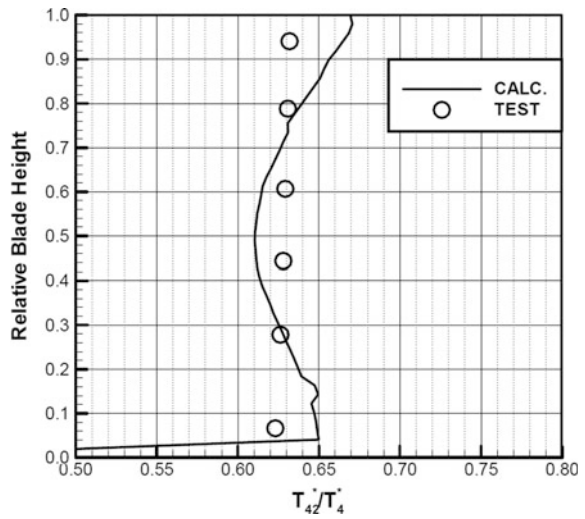


Fig. 6.67 Comparison of total temperature



(CFX) and a comparison between the simulation results and experimental results was performed [78]. The transition SST turbulence model was employed, which can produce more accurate results than the models only with the ϵ equation, under the flow condition with adverse pressure gradient. Figure 6.66, Figure 6.67, and Figure 6.68 respectively show the comparison of the absolute total pressure at the turbine stage outlet, the absolute total temperature at the turbine stage outlet, and the blade outflow angle, between calculated results and design values. The subscript “4” in the figures represents the inlet section of the HP turbine, and the subscript “42” represents the outlet section of the HP turbine. It can be seen that the

Fig. 6.68 Comparison of outflow angle

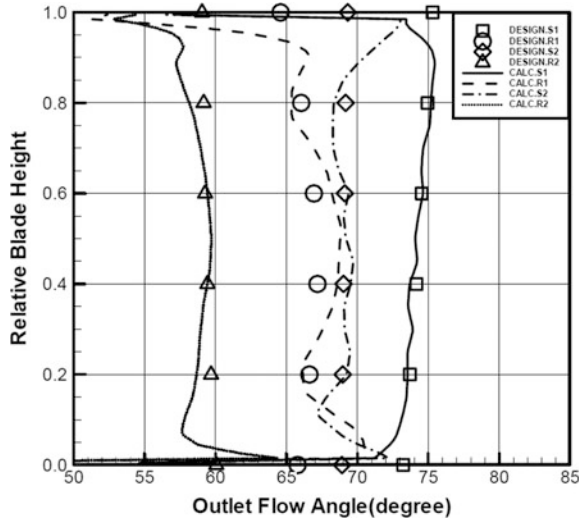


Table 6.10 Comparison of overall performance

	Experimental results	Numerical results
Inlet flow rate kg/s	10.9	11.0
Total expansion ratio π^*	5.01	5.00
Efficiency η_t	0.925	0.927

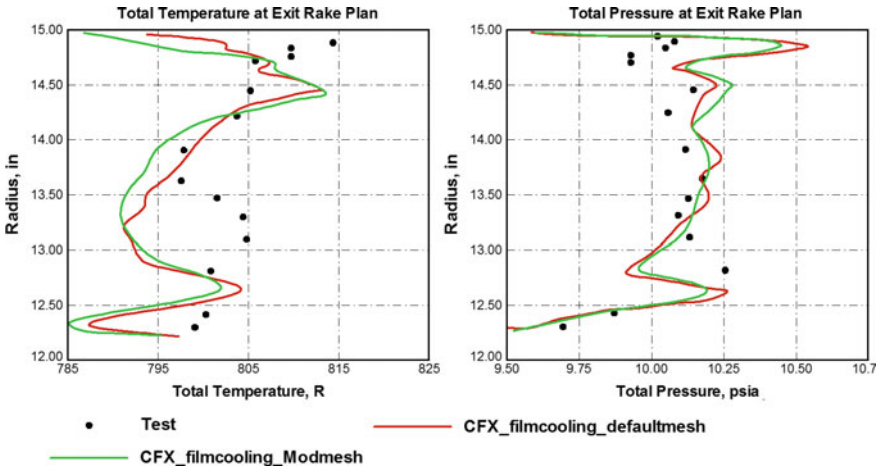


Fig. 6.69 Comparison of outlet total temperature and total pressure

Fig. 6.70 Comparison of flow characteristic between experimental results and calculated results

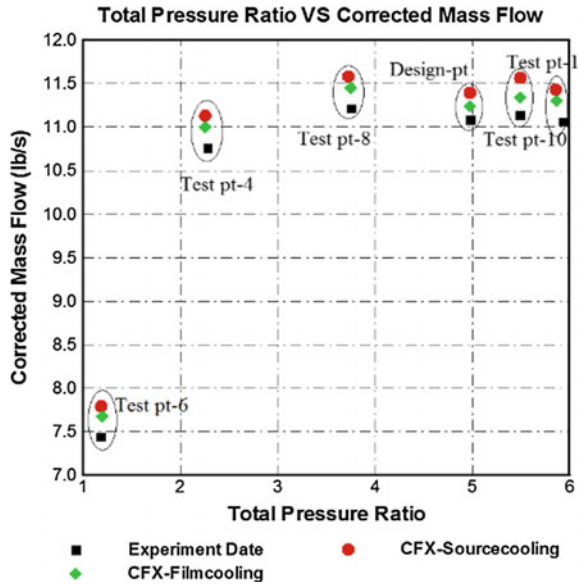
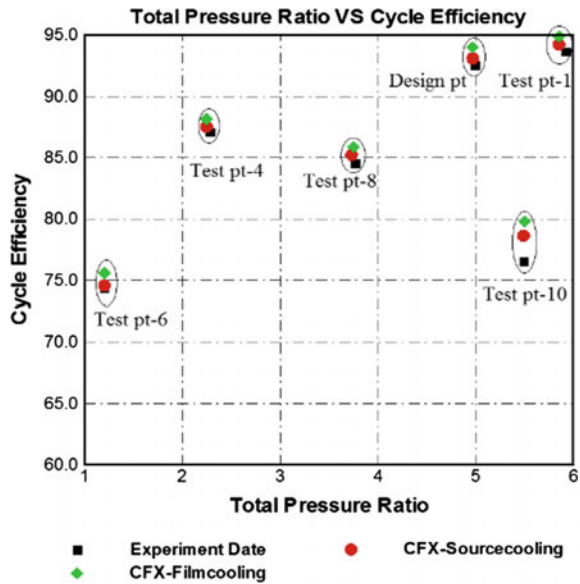


Fig. 6.71 Comparison of efficiency characteristic between experimental results and calculated results



simulation results of the parameters agree well with the experimental results in all areas except the endwalls.

Table 6.10 shows the comparison between the performance and experimental results of the HP turbine. The total parameters and the spanwise distribution suggest good agreement between the simulation results and experimental results, thus

Fig. 6.72 Comparison of mid-span section wall temperature distribution on blade

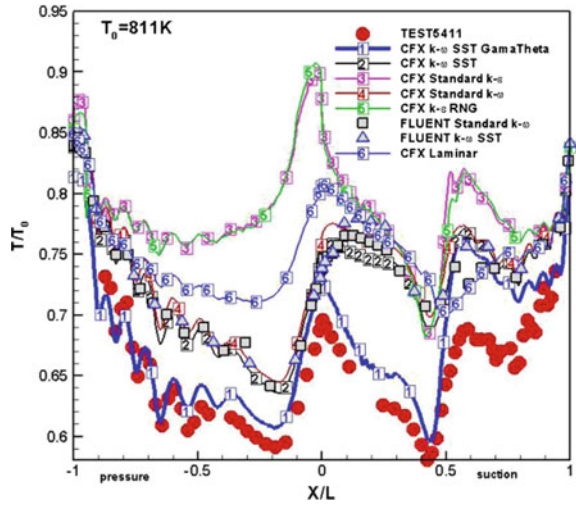
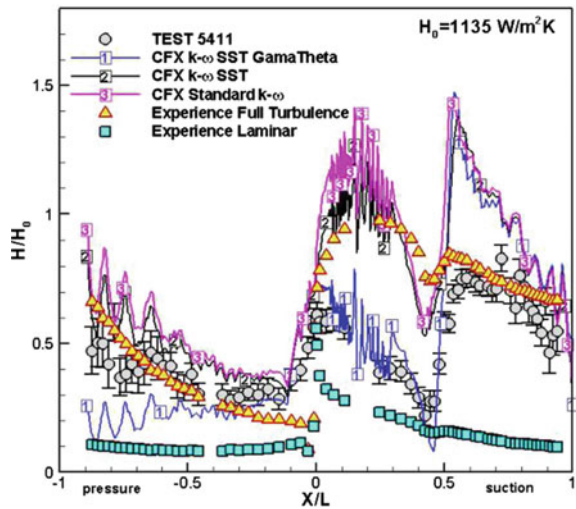


Fig. 6.73 Comparison of mid-span section wall heat transfer coefficient distribution on blade



proving that the simulation results obtained by the above turbulence model and cooling air processing mode are reliable.

3-D viscous numerical simulation of GE's E³ two-stage HP turbine was also carried out under multiple operating conditions by CFX, with the transition SST turbulence model employed [79]. Figure 6.69 shows the comparison of the outlet total temperature and total pressure between simulation results and experimental results under a specific operating condition. Figure 6.70 and Figure 6.71 present the comparison of the flow characteristic and efficiency characteristic with expansion ratio at different points between simulation results and experimental results. In

Fig. 6.74 Comparison of mid-span section wall temperature distribution on blade

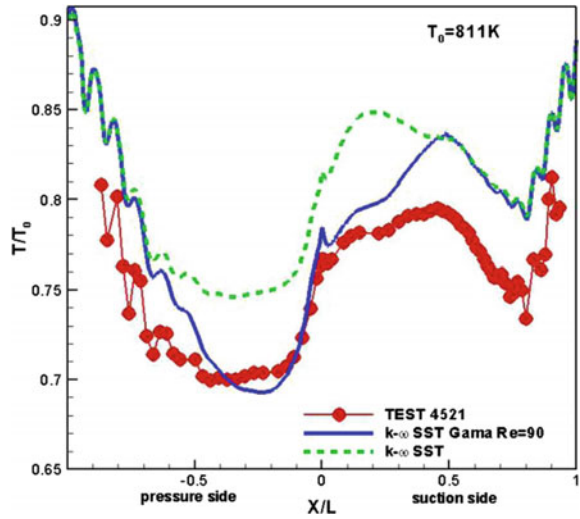
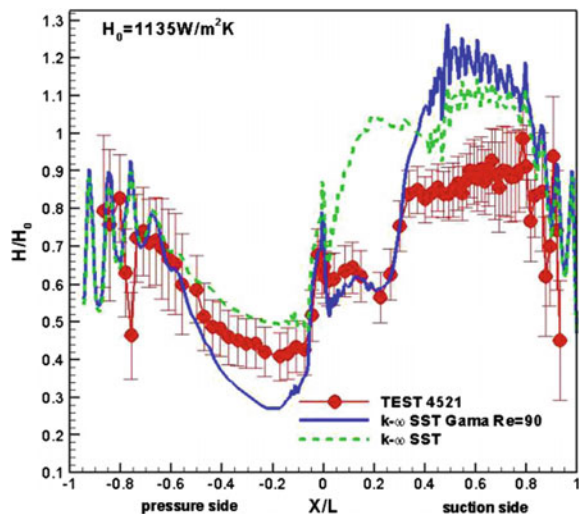


Fig. 6.75 Comparison of mid-span section wall heat transfer coefficient distribution on blade



addition, the simulation results obtained by CFX and Fine-Turbo respectively were compared as well.

There is some difference in the spanwise distribution of the total temperature between simulation results and experimental results, while good agreement can be seen in the total pressure distribution. The simulation results under different operating conditions, which were obtained by different softwares, agree well with the experimental results.

To find out the influence of turbulence models in 3-D numerical calculation for HP turbines, researchers carried out conjugate heat transfer numerical simulations

Fig. 6.76 Mid-span section static pressure distribution on outside surface of blades

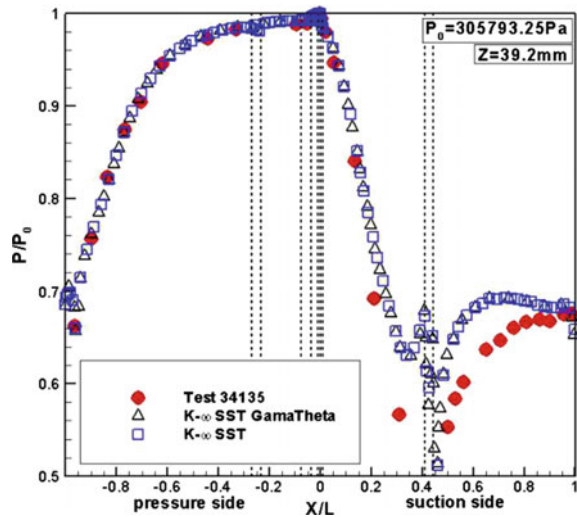
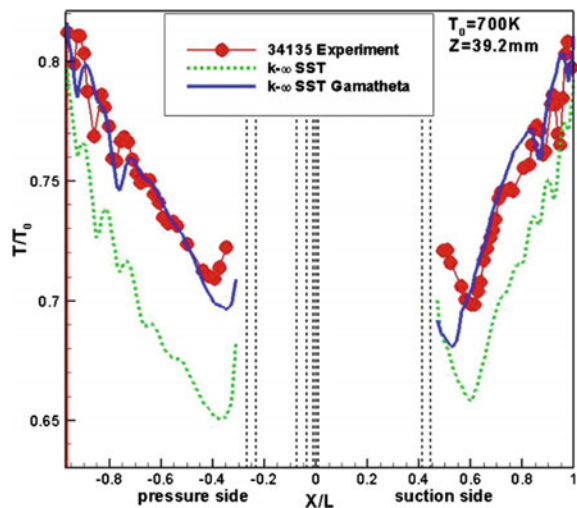


Fig. 6.77 Mid-span section static pressure + temperature distribution on outside surface of blades



for the turbine blades without film cooling—MarkII and C3X under the 5411 condition and 4521 condition respectively by using different turbulence models [80]. With respect to the numerical simulation for MarkII, simulation results of the wall temperature distribution and wall heat transfer coefficient, which were obtained by different turbulence models, and experimental results are compared in Fig. 6.72 and Fig. 6.73 respectively. With respect to the numerical simulation for C3X, the simulation results obtained by different models and experimental results are compared in Fig. 6.74 and Fig. 6.75.

Conjugate heat transfer numerical simulation was carried out for the modified C3X profile under the 4313 condition, with the presence of film cooling. Simulation and experimental results are compared in Fig. 6.76 and Fig. 6.77.

Among the turbulence models employed in CFX, the results of the above conjugate heat transfer numerical simulation obtained by using the SST turbulence model with $\gamma - Re_\theta$ transition model agree well with the experimental results. This turbulence model can reflect the flow and heat transfer in the HP turbine truthfully, while great difference can be found in the description of the suction side. For this reason, the strategy of secondary development based on commercial softwares (such as Fluent, CFX, etc.) has been gradually accepted. With this strategy, the defects of the employed models could be corrected, and the advantages of the commercial softwares could be made full use of in the meantime, thus lowering the difficulties of self-programming for high-performance CFD codes, and improving working efficiency.

There are many ways to improve the accuracy of CFD calculation. One of the relatively efficient and practical methods is to solve some specific problems in CFD softwares by means of secondary development. For example, it is very necessary to accurately predict the eddy-viscosity coefficient and the scalar diffusion coefficient of the turbulence models when using the RANS method to solve heat transfer problems of air-cooled turbines. That's because conventional turbulence models assume that the eddy-viscosity coefficient and scalar diffusion coefficient are isotropous, which is inconsistent with both theoretical and experimental results. To solve these problems, researchers have proposed relevant solutions, such as the AAEV-AASF (anisotropic algebraic eddy viscosity—anisotropic algebraic scalar flux) correction method, which can improve the prediction accuracy of the Reynolds stress as well as the accuracy of film cooling flow field in air-cooled turbines.

6.4.2.2 Influence of Multiple Components

In the actual operating process of air-cooled turbines, the cooling medium is air, while the working medium in the mainstream area is gas. The two have great difference in thermophysical properties. When the flux of the cooling air is low, the calculation of turbine performance without considering cool air component diffusion is acceptable. With the development of engines, the ratio of the mass flow rate of the cooling air to the inflow of air-cooled turbines has been as high as 20% or even 30%. There is significant diffusion between different components, and its influence on flows and heat transfer cannot be neglected. Comparative study on the influence of multicomponent diffusion on aerodynamic and heat transfer performance of a two-stage HP turbine was carried out, where two numerical simulation cases under different conditions were set up [81]. The first one, which was called

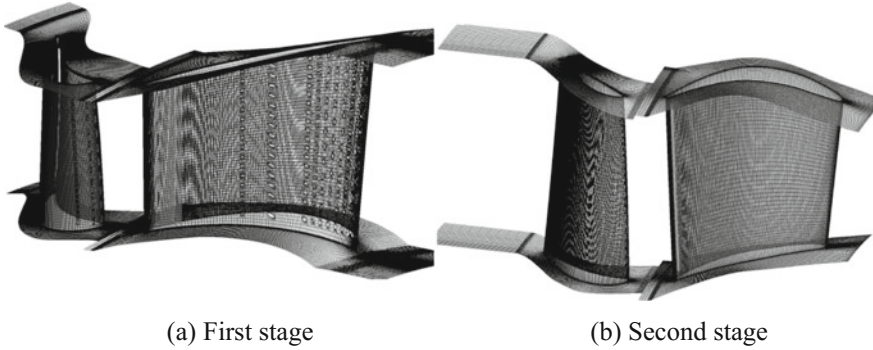


Fig. 6.78 Blade surface grid distribution in computing domain

Table 6.11 Comparison of overall parameters between Scheme c1 and Scheme c2

	Unit	Scheme c1		Scheme c2	
		First stage	Second stage	First stage	Second stage
$W\sqrt{T_0^*/P_0^*}$	$\text{g}\sqrt{\text{K}}/\text{s Pa}$	0.866		0.866	
FC		1.033	0.967	1.032	0.968
Ω		0.360	0.445	0.360	0.446
$\Delta h/U^2$		1.347	1.137	1.344	1.135
$U/C1$		1.308	1.182	1.307	1.180
π^*		2.159	2.258	2.159	2.258
α_2		85.867		85.816	
ηt (%)		90.68		90.50	

Scheme c_1 , was under the condition of multicomponent diffusion, where gas was chosen as the working medium and air as the cooling medium. The other one, which was called Scheme c_2 , was under the condition of single working medium, where gas was chosen.

In the calculation, the specific heat at constant pressure of the gas, $C_p(T)$, was expressed as a function of temperature through polynomial fitting,

$$C_p(T) = a^*T^2 + b^*T + c \quad (6.159)$$

where, $a = -5.1489 \times 10^{-5} \text{ J}/(\text{kg}\cdot\text{K}^3)$, $b = 0.2991 \text{ J}/(\text{kg}\cdot\text{K}^2)$, $c = 942.7613 \text{ J}/(\text{kg}\cdot\text{K})$, $120 \text{ K} \leq T \leq 3000 \text{ K}$.

Both the heat transfer coefficient, $\lambda(T)$, and the dynamic viscosity, $\mu(T)$, of the gas were expressed as functions of temperature by using Sutherland's formula,

$$\frac{\lambda(T)}{\lambda_{ref}} = \frac{T_{ref} + T_{\lambda suth}}{T + T_{\lambda suth}} \left(\frac{T}{T_{ref}} \right)^n \quad (6.160)$$

$$\frac{\mu(T)}{\mu_{ref}} = \frac{T_{ref} + T_{\mu th}}{T + T_{\mu th}} \left(\frac{T}{T_{ref}}\right)^n \tag{6.161}$$

where $n = 1.5$, $T_{ref} = 300.00$ K, $\lambda_{ref} = 1.9830 \times 10^{-5}$ W/(m*K), $T_{\lambda_{suth}} = 78.06$ K, $\mu_{ref} = 0.02624$ Pa*S, $T_{\mu th} = 246.50$ K. The thermophysical properties of the air were set as constant values. The molar mass of the air was 28.96 kg/kmol, while the molar mass of the gas is 28.93 kg/kmol.

Experimental operating conditions of the two-stage HP turbine were chosen as the boundary conditions, where the total cooling air flow for the two stages accounts for about 26% of the inlet air flow. Numerical simulations was carried out under the adiabatic condition. The Shear-Stress Transport turbulence model and the $\gamma - Re\theta$ transition model were adopted. 6.5 million grids were applied, as shown in Fig. 6.78.

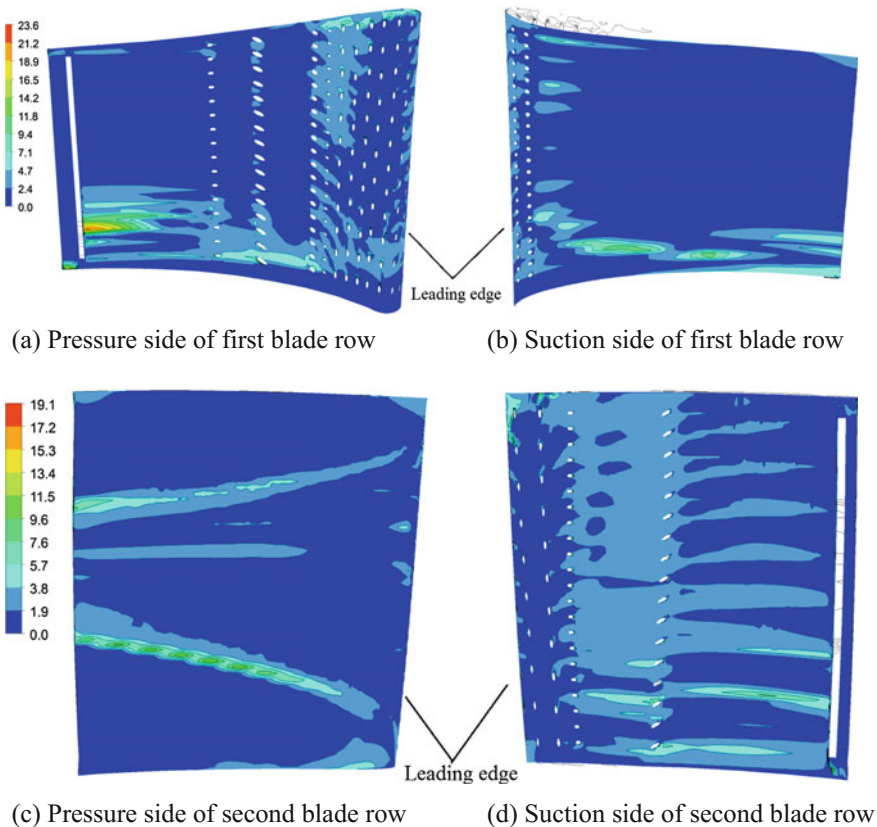


Fig. 6.79 Difference in adiabatic wall temperature between Scheme c1 and Scheme c2

Table 6.11 presents the comparison of the overall performance parameters obtained for the two schemes. As can be seen, the difference in the overall performance parameters between the schemes is small. As for the turbine efficiency, η_t , the difference is 0.18%. The main reason for the difference is that different cooling mediums with different power abilities are used for the two schemes.

Figure 6.79 shows the difference in adiabatic wall temperature. Although the wall temperatures cannot reflect the real blade temperature field due to the adiabatic wall assumed, the influence of different cooling mediums on film cooling efficiency can be seen to some extent. The average adiabatic temperatures of each blade row in Scheme c1 and Scheme c2 are respectively 497.9 K(496.8 K), 501.1 K(499.5 K), 506.2 K(505.4 K), and 451.9 K(451.8 K). As can be seen from Fig. 6.79 a), the maximum local temperature difference of the first blade row is 23.6 K, which is about 5% of the average adiabatic temperature on the blade surface. The maximum temperature difference values of the other blade rows drop dramatically. Except for the first row, areas with maximum blade-surface temperature difference are all located in the margin around the passage vortexes on the suction side. The entrainment effect of passage vortexes makes cooling air in the region more concentrated. Specific heat of air is smaller than that of gas, so using air as the cooling medium would result in obvious rise of cool air temperature as well as adiabatic wall temperature. This is more obvious in areas where cool air is more concentrated.

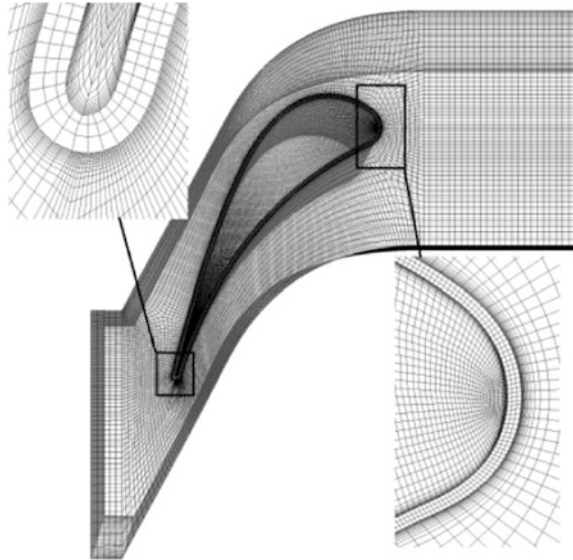
The two numerical examples above suggest that different cooling mediums at the cool air ratio of 26% would result in insignificant difference in the flow rate and other overall performance parameters, but a difference of 0.18% in aerodynamic efficiency. Influence of different cooling mediums on aerodynamic efficiency cannot be neglected. Difference in cooling mediums has some influence on local temperature field on the blade surface. The average temperatures in different schemes are close, but the maximum adiabatic temperature difference of the first blade row is near 5%. Areas with maximum temperature difference on the other blade rows are all located in the margin around the passage vortexes. Influence of different cooling mediums on cooling effect cannot be neglected.

6.4.2.3 Influence of Thermal Radiation

To achieve higher thrust-weight ratio and efficiency, the inlet gas temperature of turbines has been increasing constantly and has reached to 2000 K or even higher. As the temperature increases, the influence of thermal radiation on temperature of turbine blades can no longer be ignored. This subsection presents researches on the influence of thermal radiation on blade temperature field through numerical simulation under the condition of conjugate heat transfer [8].

A turbine stator blade with an inner cavity is taken as an example. The cooling air comes from the last stage of the compressor and is guided from the blade tip to the blade root through the inner cavity. To simplify the model, the end walls are assumed to be adiabatic. The temperature field and flow field in the fluid domain

Fig. 6.80 Calculation model and grids in computing domain



and solid domain inside and outside of the blade are calculated by using the conjugate heat transfer method. The grids in the computing domain are all hexahedral unstructured grids. There are 2.49 million grids in the outer fluid domain, 1.39 million in the inner fluid domain, and 0.27 million in the solid domain. The calculation model and grids are shown in Fig. 6.80.

The components of the working medium have great influence on radiation calculation. When considering thermal radiation, diatomic molecules (such as O_2 and N_2) have little influence on the results, while the influence of triatomic molecules is great. Therefore, the influence of diatomic molecules on thermal radiation is ignored in the calculation, while the influence of CO_2 and H_2O on the radiation is considered. The gas-oil ratio is 0.022. The gas obtained at complete combustion of the fuel is regarded as the working medium, and numerical simulation of thermal radiation is carried out. Mole fractions of CO_2 and H_2O are close and both set as 6%. The spectrum is divided into 4 bands, and the absorption coefficients of the working medium are specified. The absorption ability and release ability of the working medium in different bands are compensated by adding

Table 6.12 h_i, B_i, c_i values

	$i = 1$	$i = 2$	$i = 3$	$i = 4$
$h_i [m^{-1} * atm^{-1}]$	0	0.94	9.4	130
B_i	0.4092	0.284	0.211	0.0958
$C_i [K^{-1}]$	7.53×10^{-5}	2.58×10^{-5}	-6.54×10^{-5}	-3.57×10^{-5}

Table 6.13 Blade temperature in different schemes

	1a	1b	2a	2b
T_{av} [K]	947.41	964.07	1425.41	1517.49
T_{max} [K]	1094.93	1105.15	1730.93	1769.10
T_{min} [K]	812.56	836.37	1111.12	1245.32
$max(\Delta T)$ [K]	0	28.10	0	154.1

weights. The band absorption coefficient of the working medium, Ab_i , is defined by Eq. (2.30), and the weight, Wg_i , is defined by Eq. (2.31).

$$Ab_i = [h_i * (F_{CO_2} + F_{H_2O})] * P (i \leq 4) \tag{6.162}$$

$$Wg_i = B_i + C_i * T \quad (i \leq 4, T \leq 2400) \tag{6.163}$$

where, values of $h_i (i \leq 4)$, $B_i (i \leq 4)$, and $C_i (i \leq 4)$ are shown in Table 6.12; P is the pressure of the working medium (unit: atm).

The Shear-Stress Transport turbulence model and the $\gamma - Re\theta$ transition model are adopted. The Discrete Transfer Model is used as the radiation model. This model uses a single radiation ray to replace all the radiation effect from the radiation surface at a solid angle, and its accuracy is mainly affected by the number of rays and grid density. Under the two conditions where the inlet total temperature is set at 1260 and 2000 K respectively, the flow conditions and temperature field of the blade are investigated, and the flow rate and inlet total temperature of the cooling air are set constant. Under the condition of conjugate heat transfer, changes of blade temperature field caused by radiation after a great increase of the inlet temperature are mainly investigated, and the influence of changes in the gas viscosity, resulting from changes in the boundary layer temperature, on the aerodynamic efficiency is ignored. For comparison, two groups of numerical simulation cases with different boundary conditions are set up. The first group includes Scheme 1a with no radiation considered and Scheme 1b with radiation considered, where both the inlet total temperature is set to be 1206 K. The other group includes Scheme 2a with no

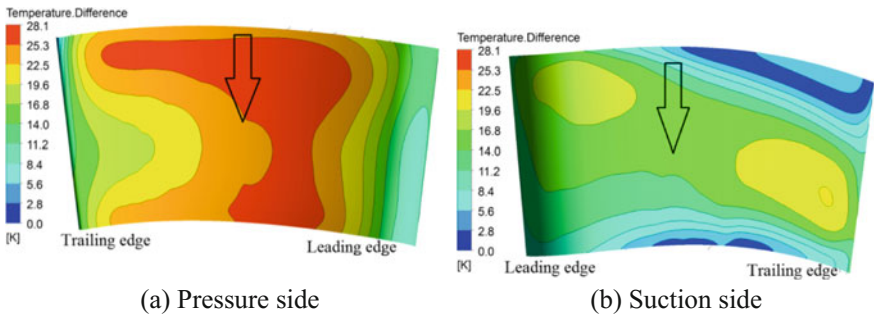


Fig. 6.81 Blade temperature difference between Scheme 1a and Scheme 1b

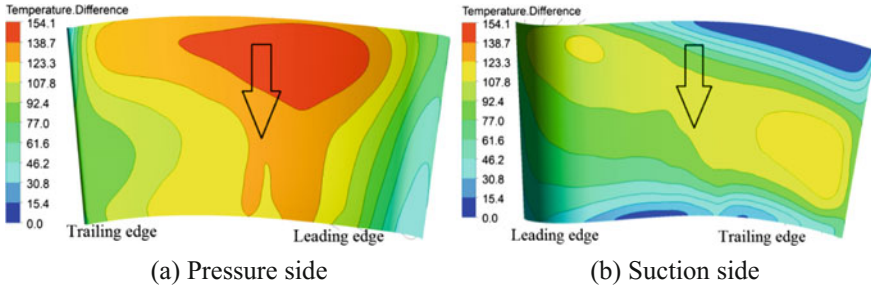


Fig. 6.82 Blade temperature difference between Scheme 2a and Scheme 2b

radiation considered and Scheme 2b with radiation considered, while the inlet total temperature is set to be 2000 K. The average temperature T_{av} and the maximum temperature T_{max} on the blade surface in different schemes are shown in Table 6.13. In the table, $\max(\Delta T)$ represents the maximum temperature rise on the blade surface caused by radiation.

As shown in Table 6.13, when the inlet total temperature is 1206 K with radiation considered, the average temperature on the blade surface rises by 16.66 K, the maximum temperature rises by 10.22 K, and the minimum temperature rises by 23.81 K. While when the inlet total temperature increases to 2000 K with radiation considered the average temperature on the blade surface rises by 92.08 K, the maximum temperature rises by 38.17 K, and the minimum temperature rises by 134.20 K. As the inlet total temperature increases, influence of radiation on the blade temperature field would become stronger, and influence of the temperature rise in such a magnitude on blade life is non-negligible.

Figure 6.81 shows the temperature difference on the blade surface caused by radiation at the inlet total temperature of 1260 K, where the direction of the cooling air flow in the inner cavity is indicated by the arrow. The maximum temperature difference is 28.1 K which is located at the pressure side of the blade. The temperature rise caused by radiation in the high-temperature areas of the blade, which are around the leading edge near the hub and the trailing edge on the suction side near the shroud, is relatively small.

Figure 6.82 shows the temperature difference on the blade surface caused by radiation at the inlet total temperature of 2000 K, where the direction of the cooling air flow in the inner cavity is indicated by the arrow. The maximum temperature difference is 154.1 K, which is located at the pressure side of the blade. Similarly, the temperature rise caused by radiation in the high-temperature areas of the blade, which are around the leading edge near the hub and the trailing edge on the suction side near the shroud, is relatively small.

Through the calculation above, it can be seen that influence of thermal radiation would increase sharply with the increase of the inlet temperature. In addition, radiation has great influence on the blade temperature field in the areas with relatively low blade temperature, while little influence in high temperature areas. As the

inlet temperature keeps increasing, influence of radiation on blade temperature field would be non-negligible. Therefore, influence of radiation should be considered in the current heat transfer design.

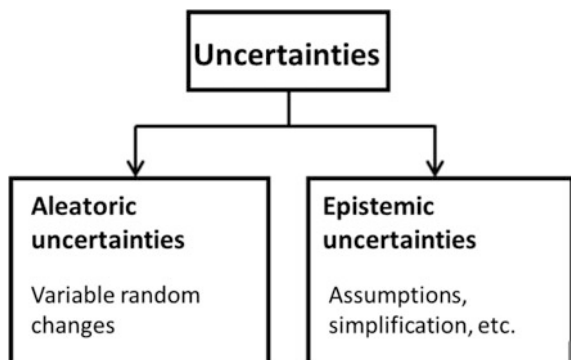
6.4.3 Numerical Simulation Methods with Geometric/ Aerodynamic Uncertainty Being Considered

6.4.3.1 Introduction to Probabilistic Numerical Simulation Methods

In actual engineering applications, performance of turbomachinery may be inconsistent with expected results due to machining errors, installation errors, geometrical errors caused by encrustment and abrasion, and uncertainty of operating conditions. In other words, uncertainties of geometry and operating conditions may invalidate the fine design efforts made to improve aerodynamic performance, or even result in disqualification of design schemes. One of the reasons is that the current aerodynamic design systems are all established based on certainty. With the current aerodynamic design systems, it is possible to work out optimal schemes for given input conditions, while impossible to consider the influence of uncertainties of machining and operating conditions. As a result, dramatic decrease of aerodynamic performance may occur when there are deviations in geometric and aerodynamic conditions. To solve the problems, a large number of studies on the influence of geometric deviations of airfoils, uncertain incoming flow conditions, and other uncertainties on aerodynamic performance of turbomachinery have been carried out in recent years, with the hope of developing new aerodynamic design technologies for turbomachinery that take various uncertainties into consideration.

Uncertainty and error are not clearly distinguished in most engineering practice. For this reason, Oberkampf et al. gave unambiguous definitions of them in the AIAA Guide (see Ref. [82]), and indicated their differences. Errors refer to recognizable deficiencies in the process of modeling and simulations, which are not

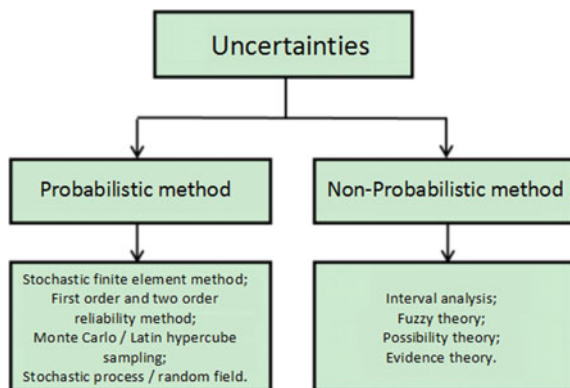
Fig. 6.83 Classification of uncertainties



due to lack of knowledge. That is, the deficiency caused by an error is knowable in advance, or unknowable in advance but can be detected through debugging and other methods. Therefore, errors can be divided into acknowledged errors and unacknowledged errors. Uncertainties refer to potential deficiencies in the process of modeling and simulations, which are due to lack of knowledge. Uncertainties can be also divided into accidental uncertainties and cognitive uncertainties. Cognitive uncertainties, also known as reducible uncertainties, are related to assumptions and simplifications in physical models such as turbulence model and periodic simplification, which can be reduced by improving the physical models through multiple tests. Accidental uncertainties, also known as unreducible uncertainties, are related to physical variables describing the object of study or the environment, such as material properties, boundary conditions, and machining deviations. Due to some objective conditions, accidental uncertainties cannot be reduced. So, the general approach to deal with these uncertainties is to carry out additional experimental design through probabilistic simulation based on values of model variables. Figure 6.83 shows the comparison of uncertainties.

This subsection mainly presents the methods for studying accidental uncertainties. What follows takes machining deviations of blades for example. In analysis of the accidental uncertainty, an uncertainty model is needed to describe deviations of airfoils in high fidelity, which can be established according to the data of blade samples. According to practical experience, the machining deviations in actual blade machining process can be divided into systematic deviations and random deviations, and the latter are mainly discussed here. Random machining deviations of blades refer to machining errors, position errors, clamp errors, and deformations caused by residual stress, which result from the random variation of the cutting force during the sequential processing of a batch of work pieces. Usually, the variation of the cutting force is related to a lot of random factors in the process system, such as grinding, foreign objects damage, and uneven blank allowance or hardness. The magnitude and direction of the machining deviations vary randomly. Generally speaking, these random deviations are subject to statistical rules, so principles and methods of mathematical statistics can be adopted. The analysis

Fig. 6.84 Classification of uncertainty analysis methods



methods which are commonly used can be divided into two major categories, which are the probabilistic methods and the non-probabilistic methods [83–85], as shown in Fig. 6.84. The theoretical basis of the probabilistic methods is the probability density function, which describes system uncertainties using random variables, random processes, and random fields. The probabilistic methods are mainly used to deal with inexact problems related to true values of parameters.

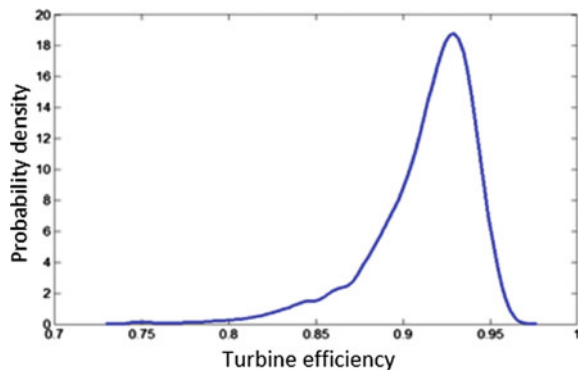
6.4.3.2 Applications of Probabilistic Methods in Turbine Performance Analysis

Random machining deviations of turbine blades are one of the main sources of performance uncertainty. Acknowledgment and reasonable description of uncertain parameters are the premise of studies on the influence of geometrical uncertainties. There are two methods for modeling geometrical uncertainties of blades, which are the parametric method and the coordinate method. The parametric method describes the geometrical deviations of blades by establishing probability distribution functions, with characteristic parameters such as the incidence angle, the chord length, the leading edge thickness, etc. [86]. While the coordinate method extract the geometrical deviations of blades from measured coordinate data of samples by methods like PCA (principal component analysis), and then establish the coordinate-based high-precision model [87]. There are advantages and disadvantages to both of the methods. The geometrical deviations of blades are directly described by design parameters in the parametric method, making it easy to couple the modeling with the design process. However, it cannot be guaranteed that the selected parameters are enough to describe all the geometrical deviations, so geometrical parameters that have significant influence on performance may be ignored. The coordinate method requires to measure and process large amounts of data, but it can cover the entire blade geometry and avoid the limitations of the parametric method.

As MIT and other institutes apply probabilistic methods in design of compressors and other turbomachines, applications of the methods in design and analysis of aircraft gas turbines have been getting more attention. Taking air-cooled turbines as objects, Bunker [88] from GE Company systematically studied changes of the temperature on metal surface caused by machining deviations of various cooling structures, with the Monte Carlo Method. This study clearly demonstrates the great advantages of probabilistic methods in analysis and evaluation of gas turbine performance, pointing the direction of future applications of probabilistic methods. With the probabilistic analysis methods like Monte Carlo Method and the Probabilistic Collocation Method, Montomoli et al. [89–92] studied the influence of geometrical uncertainties caused by blade coating and other factors, and discussed the influence of the distribution of random parameters on the predicted results, as

well as the relation between acknowledgement and accidental uncertainties. This study greatly pushed forward the application of probabilistic methods in the analysis of turbine performance. Based on the pilot study on influence of turbine clamp deviations, Guo and Zou [93] from Beijing University of Aeronautics and Astronautics gradually explored applications of probabilistic methods in predication and diagnosis of gas turbine performance, and developed a systematical numerical analysis method. To analyze the influence of geometrical random deviations of turbine blades, they developed a method for describing geometrical deviations of blades based on the coordinate method, and proposed a dimension reduction method for the geometrical deviation model based on principal component analysis, thus achieving modeling of geometrical deviations of turbine blades with high restoration degree. Based on that, they studied the influence of geometrical deviations, as well as the magnitude, at different areas of turbine cascades on the aerodynamic performance of cascades, and discussed the sensitivity of turbine cascade uncertainty to operating conditions and design parameters of blades. The results show that geometrical deviations of the leading edge and suction surface of turbine blades contribute most to the uncertainty of performance, and that there is certain interaction in the significance of the influence of geometric system deviations of blades on random deviations, which should be considered conjugately. In addition, Guo and Zou developed a method for describing the geometrical deviations based on the parametric method, which keeps the most crucial geometrical characteristics while lowering down the dimensionality of the model, and developed a joint probability distribution model with good universality for multiple geometrical deviations based on Gaussian kernel density estimation. To evaluate the performance uncertainty for a single turbine stage, Guo and Zou [93] carried out test point design by the Latin hypercube sampling method to reduce the required sample size and accelerate CFD simulation, and developed a response surface modeling and simplification method based on significance analysis. Based on high-precision restoration of sample distribution characteristics, they considered the interaction, simplified the response surface model, and extracted key influencing factors. Analysis of typical random deviations of the incidence angles of guide

Fig. 6.85 Probability density distribution of single-stage turbine efficiency under the influence of typical random geometrical deviations [93]



vanes and rotor blades, as well as those of the tip clearance, of a single-stage HP turbine indicates that the turbine performance showed strong discreteness (i.e. uncertainty) and great negative bias (i.e. performance is generally lower than that in design conditions) under the influence of the above geometrical deviations, as shown in Fig. 6.85. In addition, the random variation of the aerodynamic conditions is an important factor, which induces the uncertainty of turbine performance. Guo and Zou took the MARK-II air-cooled turbine blade as object, and analyzed the influence of random variations in the mainstream turbulence, the total temperature, the outlet Mach number, and the outlet Reynolds number on the aerodynamic and heat transfer performance of the blade by numerical simulation. The results are consistent with those obtained by Hylton experimentally [94]. Analysis results by the probabilistic method indicate that the mainstream turbulence contributes most to the uncertainty of the heat transfer performance.

6.4.4 Numerical Simulation Methods with Multi-dimensional Coupling

6.4.4.1 Introduction to Numerical Simulation Methods with Multi-dimensional Coupling

In calculation of complex fluid systems, dimensionality reduction is a method commonly used in engineering practice to meet the comprehensive requirements of simulation accuracy, calculation speed, and computing resources. For example, the traditional calculation method for aero-engine air systems is to first abstract flow structures into a series of one-dimensional models and then determine the flow rate, pressure, and other parameters by solving non-linear simultaneous equations. This method was widely used in various engineering fields and well developed [95–99]. However, with the development of modern engineering technologies, fluid system design has become more and more complicated and subtle, and the accuracy requirement has accordingly become higher and higher. However, the one-dimensional network method, which depends too much on empirical criteria and fails to capture the complexity and diversity of flows, cannot meet this requirement in many cases. Actually, two-dimensional and three-dimensional CFD technologies have been widely used in engineering design, which are capable to capture complex flows and obtain detailed flow structures. In recent years, many researchers have shifted their attention from CFD simulation of traditional components to flow structures that were analyzed through one-dimensional calculation or even neglected before, such as air systems with complex geometry, cool air mixing, shroud leakage flows, other flows outside of the main flow passage, and their interactions with the main flow, which are difficult to consider effectively in the simulation of the main flow passage [100–104]. However, in most cases, three-dimensional or even two-dimensional CFD calculation can be performed only to some components or local flows in the system due to the limitations of

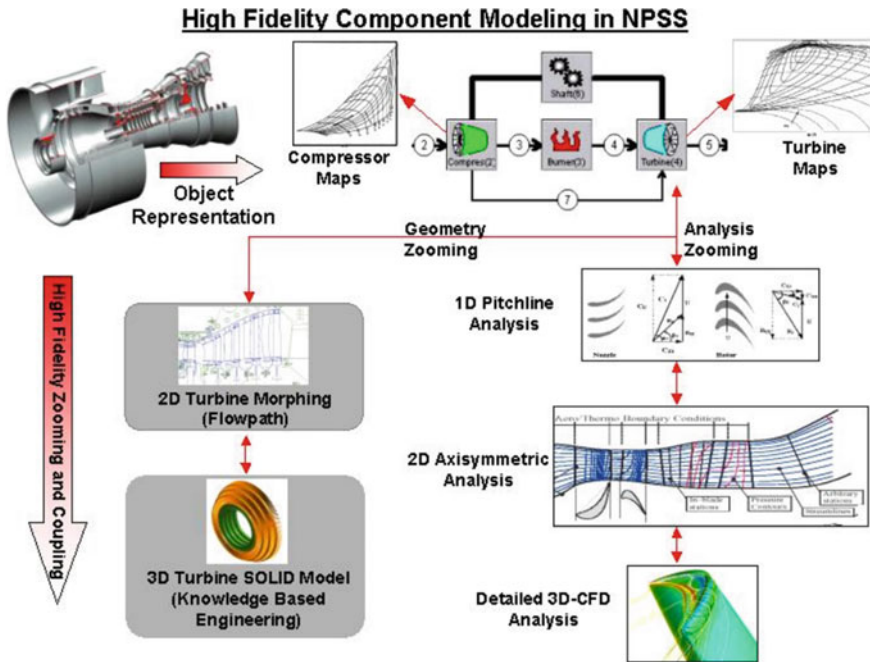


Fig. 6.86 Variable complexity analysis of NPSS [247]

computing resources, engineering design cycle, CFD development level, and other factors, and it is very difficult to perform complete CFD calculation for the entire system in engineering evaluation. It is clear that it is very difficult to carry out reasonable simulation of complex fluid systems by using single-dimensional calculation. Thus, it is necessary to employ multiple complementary calculation methods in different dimensions (i.e. multi-dimensional coupling calculation) to deal with complex simulation tasks. Currently, systematic studies and engineering applications in this field have been carried out. The variable complexity analysis (i.e. seamless automatic integration of high-fidelity component analysis modules and the whole simulation system) is a typical example, which is a research focus in the NPSS (Numerical Propulsion System Simulation) program organized and implemented by NASA Glenn Research Center [105] (see Fig. 6.86). This program provides an important support for the advantages of the United States in the field of aviation and aerospace technologies. Presumably, the coupling calculation can play a very positive role in engineering design in relevant areas, making it is very necessary to thoroughly study the coupling calculation methods and their applications. Meanwhile, it would be very cumbersome to manually do the relevant work such as solver controlling and coupling data transferring, and human-caused errors would easily occur in this process. Particularly for complex systems, the work cannot be carried out at all, so it is hardly acceptable in engineering practice. For this reason, a high-performance automatic coupling calculation platform is needed to assist the research and realization of the coupling methods.

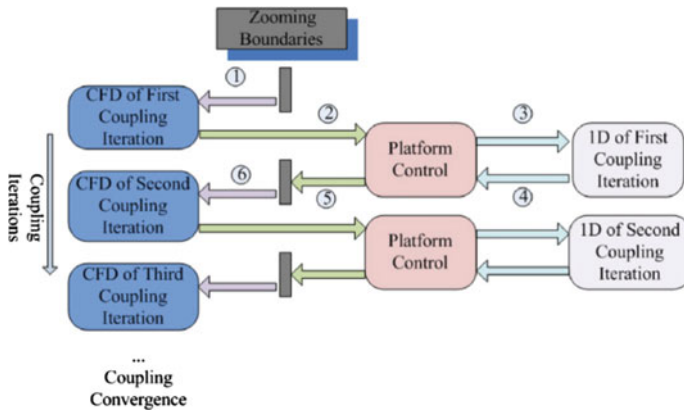


Fig. 6.87 Iterative process of coupling between one-dimensional CFD and certain-dimensional CFD

Just as the name of coupling calculation implies, the relation between subsystems of different dimensions is not independent calculation or one-way data transmission, but two-way data transmission with appropriate frequencies at corresponding interfaces. That’s to say, the coupling data transmission at the interfaces does not start until the simulations of the subsystems of the same dimension reach specific iteration steps or converge, and then the subsystems restart their respective simulations and exchange data bilaterally after convergence. This inter-iteration process continues until the relevant parameters at the boundaries between different dimensionalities become stable. Figure 6.87 shows the iteration process by taking the coupling between one-dimensional CFD and a certain dimensional CFD as an example. Flow rate and pressure are the two important parameters to be calculated in the prediction of flows in complex systems. In the coupling method to be presented, flow-based parameters are passed along the design flow direction at the scaled boundaries between different dimensionalities, and pressure-based parameters are passed along the opposite direction. In the traditional one-dimensional network method, inner cavities and other structures in the fluid system are often regarded as nodes, and corresponding non-linear simultaneous equations are then established for these nodes by residual modification. With respect to the coupling calculation in Fig. 6.87, the CFD calculation can be regarded as the internal node of the system, but this node is no longer a simple zero-dimensional calculation point and is provided with some flowing characteristics. P , T , and L represent the pressure, temperature, and geometric size respectively, and then the mass flow rate of the j th one-dimensional unit, which connects with the i th CFD unit in the system, is given by:

$$\dot{m}_{ij} = f_{ij}(P_{ij1}, P_{ij2}, \dots, T_{ij1}, \dots, L_{ij2}, \dots)$$

According to the principle of mass conservation, the algebraic sum of the mass flow rate of the fluid flowing into and out of each internal CFD unit in a steady-state

system is zero. Assume there are m one-dimensional units that connect with the i th CFD unit and n internal CFD units within the system, then we can obtain:

$$\sum_{j=1}^m \dot{m}_{Lj} = \sum_{j=1}^m f_{ij}(P_{ij1}, P_{ij2}, \dots, T_{ij1}, \dots, L_{ij2}, \dots) = 0; \quad i = 1, 2, \dots, n$$

At the beginning of the coupling calculation, flow parameters at the inlet and outlet of each CFD unit are unknown, and the inlet flow rate and outlet pressure can be assumed according to the boundary conditions of the system. Then, flow residual would be generated at the inlet and outlet, and is given by:

$$\sum_{j=1}^m \dot{m}_{ij} = \Delta \dot{m}_i \neq 0; \quad i = 1, 2, \dots, n$$

According to the relations above and flow characteristics of the CFD unit, we can get:

$$\begin{aligned} \dot{m}_{CFD,i} &= f_{CFD,i}(P_{CFD,i,1}, P_{CFD,i,2}, \dots, T_{CFD,i,1}, \dots, L_{CFD,i,2}, \dots) \dot{m}_{CFD,i} \\ &= f_{CFD,i}(P_{CFD,i,1}, P_{CFD,i,2}, \dots, T_{CFD,i,1}, \dots, L_{CFD,i,2}, \dots) \end{aligned}$$

Then, the inlet and outlet parameters of the CFD unit can be corrected gradually through coupling iteration as follows:

$$\dot{m}_{ik}' = \dot{m}_{ik} + \Delta \dot{m}_{ik}; \quad P_{il}' = P_{il} + \Delta P_{il}; \quad i = 1, 2, \dots, n; \quad k = 1, \dots; \quad l = 1, \dots$$

Where, k and l are the number of inlets and outlets of the CFD unit respectively. The coupling iteration continues with the newly obtained parameter values until all the residuals of the CFD unit meet the convergence criteria. Similarly, according to the principle of energy conservation, temperature equilibrium at the scaled boundaries between different dimensionalities can be realized by continuous corrections in the coupling iteration.

Reasonable dimensionality scaling is of great importance during boundary data transmission between different dimensionalities, which is equivalent to the process of determining the boundary conditions of each flow unit in a more reasonable way. Reasonableness of the boundary conditions directly determines the reliability of calculated results. The major criterion for judging the scaling method is whether it can well reflect the actual physical nature. The method is aimed at passing the key flow parameters to the upstream or downstream as accurate as possible in the process of scaling and avoiding distortions in the calculation to meet the accuracy requirement. A reasonable averaging method is needed to ensure conservation in the “scaling-down” process from high dimensions to low dimensions, which can be easily achieved generally. In the “scaling-up” process from low dimensions to high dimensions, reasonable distribution for the high-dimensional boundaries should be determined by using average values obtained in low dimensions, and in-depth

studies are needed in this respect. For example, with respect to the data transmission from a one-dimensional model to a two-dimensional model, \bar{F} is a boundary parameter obtained through one-dimensional calculation; $F(x)$ is the distribution function of actual flow at the boundary of the two-dimensional model; $F'(x)$ is the given distribution function in the coupling calculation. Then, the following equation can be obtained:

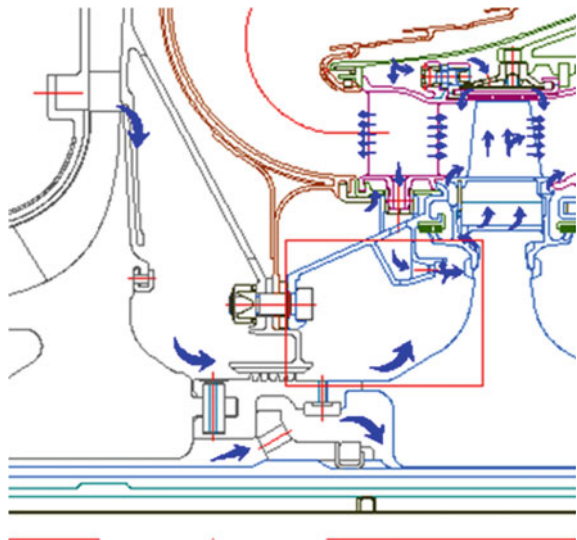
$$\bar{F} \Rightarrow F'(x, Re, Ma, L \dots) \approx F(x)$$

Namely, reasonable distribution function can be obtained based on one-dimensional calculation results and local flow parameters and geometric parameters, by the methods of theoretical analysis and experimental studies or numerical calculation. In addition, the characteristics of the function shall ensure that results, which are obtained in the entire coupling iteration process, can agree well with the actual distribution function. If uniform distribution is assumed and no consideration is given to actual flows, the characteristics of the two-dimensional flow will probably be distorted, thus reducing the accuracy of the coupling calculation greatly. In this case, the coupling will be meaningless.

6.4.4.2 Application of Numerical Simulation Methods with Multi-dimensional Coupling in Complex System Flows

Application of numerical simulation methods with multi-dimensional coupling in shroud leakage flows and their advantages have been described above. Actually, advantages of numerical simulation methods with multi-dimensional coupling are

Fig. 6.88 Flow passage of actual air system in an aero-engine



even more evident in studies on complex system flows, which have more obvious multi-scale characteristics. Multi-scale complex system flows exist extensively in various engineering fields, such as automotive engines, etc. BMW [106], Mitsubishi [107], and other companies have developed mature multi-dimensional coupling numerical simulation platforms based on dimensionality scaling technologies, which play an important role in their research and development of automotive engines. Beihang University and other organizations have also carried out systematical research in recent years and achieved good results [108–110].

Wang [108] developed a multi-dimensional coupling numerical simulation platform with friendly interactive interfaces based on Tkinter—the default graphic user interface in Python. In the rapid modeling platform WYSIWYG (What You See Is What You Get), different icons were employed to represent the calculation units of different types, which are allowed to be dragged from the cell library to the modeling area. Various kinds of software including the one-dimensional flow passage system solvers like Flowmaster and Flownet, and CFD softwares like Fluent and CFX, are integrated in the platform, making the platform capable to meet most of the demands of multi-dimensional coupling numerical simulation in the field of aero-engines. With this platform, multi-dimensional coupling numerical simulation of the actual air system in an aero-engine (see Fig. 6.88) were carried out, and the influence of the dimensions of the CFD calculation on the coupling numerical simulation results was analyzed.

Figure 6.89 shows the one-dimensional model of the air system in Flowmaster. The disc cavity component in the red box corresponds to the front cavity of the HP turbine, which is the flow region for the CFD simulation during the coupling calculation. As can be seen from Fig. 6.88 and Fig. 6.89, the front cavity of the HP

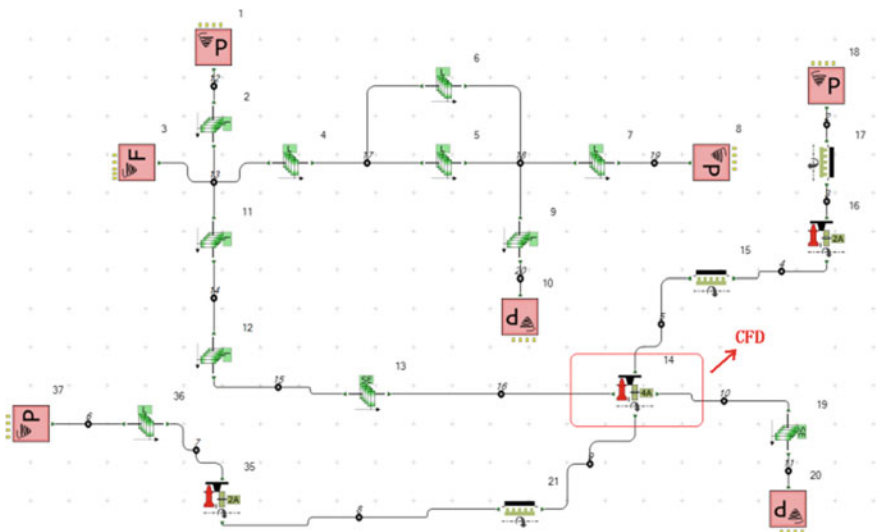


Fig. 6.89 One-dimensional model of air system

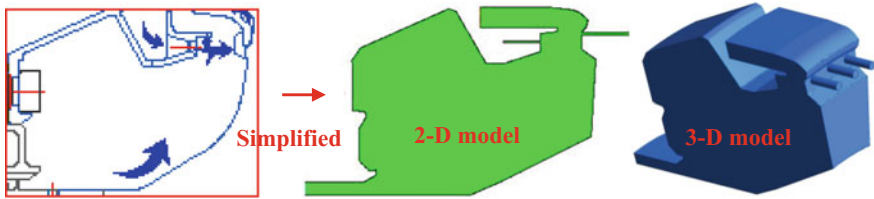


Fig. 6.90 Simplified disc cavity models

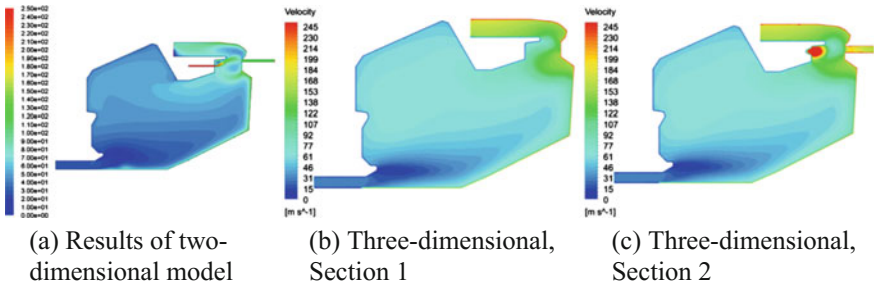


Fig. 6.91 Comparison of velocity distribution in disc cavity (m/s)

turbine with two inlets and outlets is chosen as the CFD simulation object, and all the inlets and outlets are connected to a one-dimensional network unit. The one-dimensional networks in each one-dimensional unit differ from each other in complexity, and are connected only by the CFD units. The disc cavity is simplified as the two-dimensional model and three-dimensional model during the CFD simulation, as shown in Fig. 6.90. Figure 6.91 shows the comparison of velocity distribution of disc cavity under different dimensionalities in the coupling simulation. The velocity distribution of two different sections of the three-dimensional model are given. It can be seen that the two-dimensional model and the three-dimensional model present similar overall distribution of the velocity. The three-dimensional CFD results show that the flows in the disc cavity are of strong three-dimensionality due to the three-dimensionality of the geometry and inlet and outlet conditions, which is even more obvious around the inlets and outlets. However, the above phenomenon cannot be observed in the two-dimensional CFD calculation model. Thus, for this coupling model, the coupling calculation by the three-dimensional model is more reliable than that by the two-dimensional model, while the three-dimensional model would lead to a great increase in calculation amount. Comparison of the boundary conditions at the inlet and outlet of the disc cavity shows that prediction error of the two-dimensional and three-dimensional coupling calculation can reach up to 20%. In addition, Wang also proposed a method of interface dimensionality scaling, which is similar to that used in shroud multi-dimensional coupling numerical simulation. Comparison analysis lead to the conclusion that the importance of reasonable dimensionality scaling varies in

different flow systems, while reasonable dimensionality scaling is indispensable to achieve more accurate coupling simulation.

6.5 Blade Profiling Methods

Turbine blades are the carriers of energy conversion (from the internal energy of gas to mechanical energy), and the blade profile is the main factor determining turbine performance. Since the blades are operating under conditions of high pressure, high temperature and high revolution speed, the blade profiling process shall not only meet the aerodynamic performance requirements, but also give comprehensive considerations to strength, lifetime, cooling, material, manufacture, and other aspects. As for the blade profiling, the three-dimensional blade is obtained by stacking profiles of a number of sections along the blade span according to certain rules, so two-dimensional profiles are the bridge connecting low-dimensional design parameters with three-dimensional blades. The blade profiling level determines the aerodynamic performance of turbines to a great extent.

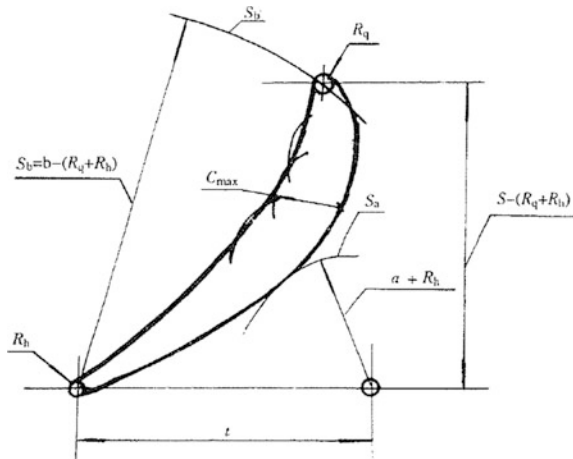
In general, blade profiling methods can be divided into two categories, namely the inverse method and the direct method. The inverse method aims to inversely work out the profile that meets the given velocity or pressure distribution on blade surface. In the early stage, inverse problem design mainly adopted the S1 stream surface design method based on the potential flow theory. For example, Garabedian et al. [111] carried out blade profile design by conformal transformation. Schmidt et al. [112] developed the inverse method for S1 stream surface design of cascades, based on the potential-stream function. In addition, fully three-dimensional inverse methods were also developed, which can be used to inversely derive the blade profile with the specific circumferential averaged circulation [113, 114]. These inverse methods are characterized by rigorous derivation and small calculation amount. However, due to the assumptions of non-viscosity, incompressibility, and irrotationality, these inverse methods are not applicable for conditions with shock waves and strong vortex flows. Massachusetts Institute of Technology developed the famous S1 direct and inverse calculation program—MISES [115]. In the program, computational grids are generated along streamlines, and simultaneous solution is performed in the calculation process by dividing the entire flow field into an inviscid region outside of the boundary layer where the Euler equations are solved, and a viscous region inside the boundary layer where the von Karman integral momentum equation and energy integral equation are solved. In the iteration process of the inverse problem, changes in streamlines and boundary layer displacement thickness are made to correct the blade profile according to the given aerodynamic loading, until convergence is reached. As for the inverse problem design of subsonic turbine blades, the program can work out the target profile rapidly. However, convergence problems may occur in the program when there are transonic flows. Chen et al. carried out systematic studies in this field and successfully developed two-dimensional and three-dimensional inverse problem

calculation and design procedures, and applied them in the aerodynamic design of compressors and turbines (see Ref. [116] for details). The key to the inverse problem design is to give the optimal blade loading distribution at the beginning of the design. On the contrary, the direct method first constructs curves directly and obtains geometric coordinates of the profile with the selected profile profiling parameters, and then checks whether the profile can generate a reasonable flow field and aerodynamic performance through numerical calculation. If the profile does not meet the design requirements, adjust the profiling parameters and curve parameters until the desirable profile is obtained. The direct profiling method can make full use of the data and empirical formulae obtained previously through large amounts of experimental studies on cascade performance, making it widely used in engineering design. Direct problem profiling methods include the traditional blade profiling method represented by the graphical method and the parametric profiling method that can make full use of computer-aided technologies to conduct direct control of curves. Both of them are described in the following.

6.5.1 Traditional Blade Profiling Methods

As for the traditional design method of turbines, such key geometric parameters like the number of blades, the blade solidity, the axial chord length, the metal angles, the stagger angle, the throat width of the blade channel, the leading edge radius, the trailing edge radius, the wedge angles, the trailing edge bending angle, and the maximum blade thickness are first selected according to the inflow and outflow angles and velocity, with the help of the database and empirical formulae, and then

Fig. 6.92 Graphical blade modeling method [22]



blade profiling is directly carried out by giving the mean camber line and thickness distribution or using the graphical method [117, 118].

What follows gives a brief introduction to the graphical blade profiling method described in Ref. [22], as shown in Fig. 6.92:

- (1) Use the tangential direction as reference, take two points at a distance of the cascade pitch, t , and draw two circles by taking the two points as the centers and trailing-edge radius, R_h , as the radius; these are the trailing-edge circles.
- (2) Determine the trailing edges of the main profile and the adjacent profile according to the deflection of inflow/outflow angles of the blade row; draw an arc, S_a , by taking the center of the trailing edge circle of the adjacent trailing edge as the center and the sum $(a + R_h)$ of throat width, a , and trailing edge radius, R_h , as the radius; the arc is the control line of the throat width.
- (3) Draw a line along the tangential direction, which is located at the distance of $S - (R_q + R_h)$, upstream the point-to-point line of the two centers of the trailing edge circles (S is the axial chord length of the blade profile); draw an arc, S_b , by taking $b - (R_q + R_h)$ as the radius (b is the chord length of the blade profile), and the center of the trailing edge circle of the main profile as the center; the intersection point of the line and the arc is the initial center of the leading edge circle.
- (4) Select a suitable curve (arc, parabola, hyperbola, lemniscate, or combination of these types of curves) and make it tangential to the leading-edge and trailing-edge circles and the arc, S_a ; the curve is the initial curve of the suction side. It is worth noting that curvature of the curve should decrease gradually from the leading edge to the trailing edge within the subsonic scope.
- (5) Draw arcs by taking several points on the curve of the suction side as circle centers and the maximum thickness, C_{\max} , as the radius to guarantee the maximum thickness of the profile.
- (6) Select a suitable curve or combination of different curves and make it tangential to the leading-edge and trailing-edge circles and an arc with a radius of C_{\max} ; the curve is the initial curve of the pressure side.

Once the initial profile is established, it is necessary to examine of the profile, such as the metal angles, the wedge angle, and the trailing edge bending angle. If the parameters do not meet the requirements, adjustments needs to be carried out accordingly. As shown in Fig. 6.93, if the leading-edge metal angle is not within the preset range, the profile curves should be exchanged or the center and radius of the leading-edge circle should be adjusted. Similarly, if the trailing-edge metal angle is not within the preset range, the profile curves should be exchanged or the trailing edge radius should be adjusted. The trailing-edge bending angle reflects the curvature variations at the oblique incision of the curve of the suction side, which should be determined according to the outlet Mach number. In addition, to avoid local pressure expansion around the throat, the trailing-edge bending angle should be greater than the trailing-edge wedge angle. The trailing-edge bending angle can be controlled by adjusting the profile curves or the location of the center of the

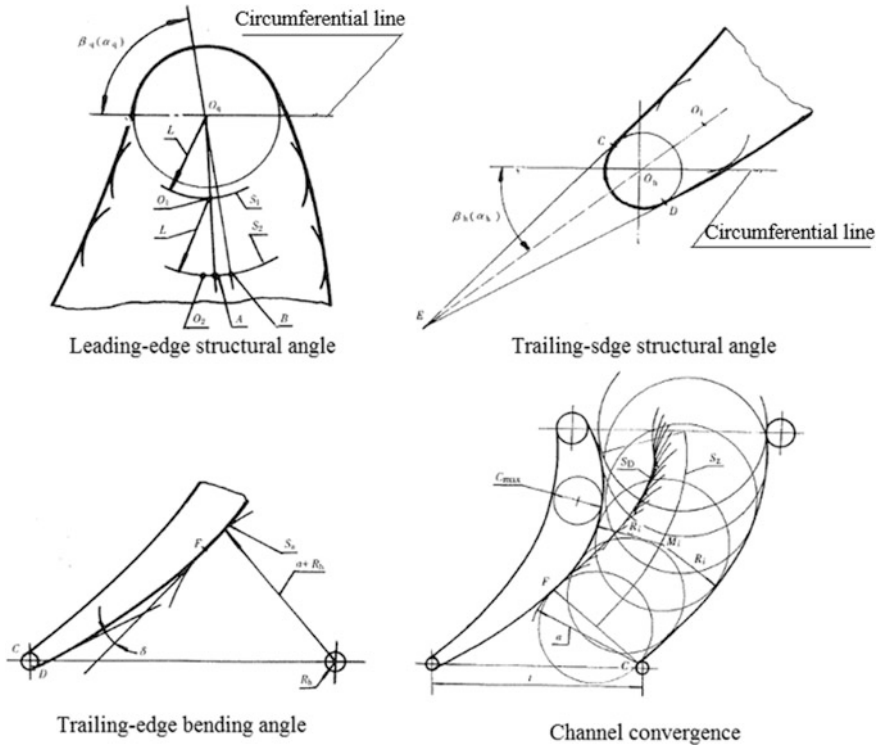


Fig. 6.93 Examination and adjustment of key profile parameters [22]

leading-edge circle. As for the turbine cascade, the channel should be kept in gradual convergence from the inlet to the outlet. If there is local expansion, it should be eliminated by adjusting the profile curves or the leading edge location, the maximum thickness, and other parameters. If necessary, the throat width can be modified for re-profiling. After all of the examinations, S1 stream surface calculation should be carried out to confirm whether the profile is desirable. If not, the parameters should be adjusted, and the iteration should be continued until design requirements are met.

6.5.2 Parametric Blade Profiling Methods and Procedures

As for traditional blade profiling methods, selection of profile parameters depends much on experimental database, and the profiling process would be affected by designers' experience. To solve these problems, researchers further developed parametric blade profiling methods, which regard the profile as analytic curves

controlled by several characteristic geometric parameters and realize optimization of the profile by adjusting the parameters.

6.5.2.1 Parametric Blade Profiling Methods

To reduce flow losses, profile curves should be smooth without inflection points. In other words, it is necessary to guarantee the continuity of the first-order and second-order derivatives of the profile curves. Therefore, in the early phase, combination of relatively simple curves including hyperbolic spirals, secondary arc curves, and high-order polynomial curves are used for parametric blade profiling [118]. This profiling method can guarantee the continuity of curvature in each curve section. However, only continuity of one-order derivative can be guaranteed at the joints of curve sections, while smooth transition of the curves cannot be realized. If the point of curvature discontinuity happens to be located around the leading edge or the throat on the suction side, there would be local jumps of flow velocity [119]. Korakianitis et al. carried out systematic studies on parametric blade profiling methods and the influence of curve types on curvature continuity [120–122]. To avoid excessive expansion of the fluid around the leading edge, the structural curves of the pressure side and suction side as well as thickness distribution were applied to describe the shape of the leading edge, as shown in Fig. 6.94a. The structural curves are polynomial curves that pass the leading-edge stagnation point, and can be expressed by Eq. (6.164), where e is the correlation coefficient used to describe

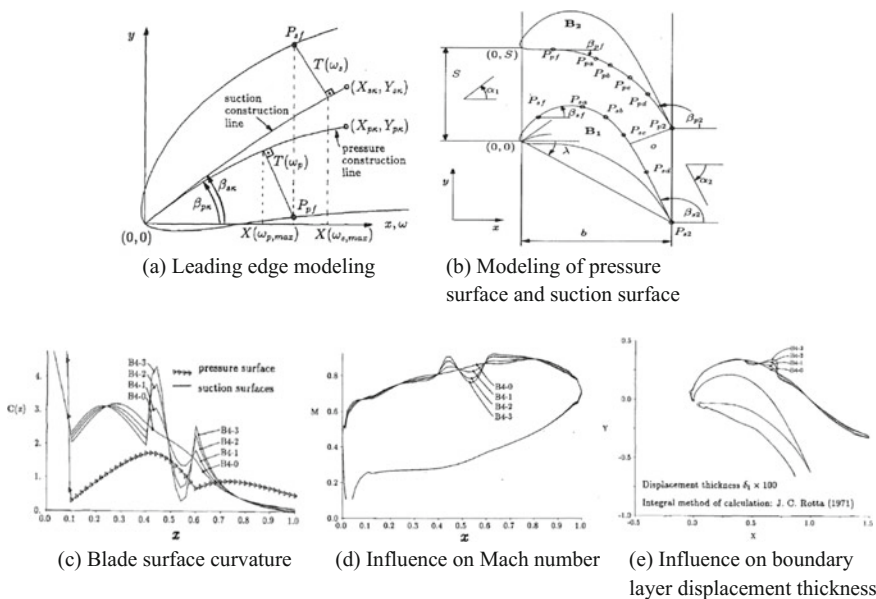


Fig. 6.94 Influence of curvature continuity on flows in parametric modeling [120]

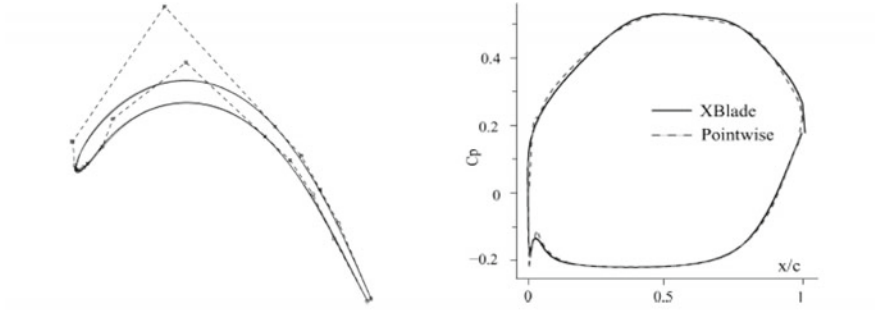
the curves. Thickness distributions on the suction side and the pressure side is given by Eq. (6.165) and Eq. (6.166) respectively (see Fig. 6.94b), where δ and c are the control parameters. Three different profiling methods were used for the profile after the leading edge. The combination of cubic polynomial, quintic polynomial, and septic polynomial was used in the first profiling method to describe the profile, as shown in Fig. 6.94c–e. From the profile curve B4-0 to the profile curve B4-3, the influence of the discontinuity on Mach number distribution and boundary layer displacement thickness becomes greater with the increase in the degree of curvature discontinuity at joints of the curves on the suction side, thus deteriorating the flow. Therefore, the quartic spline was used in the second method to guarantee continuity of the third-order derivative at the joints and the flow was improved effectively. However, the calculation amount is high for this method. The combination of polynomials and Bezier curves was adopted in the third method, and the smoothness of Mach number distribution was guaranteed.

$$L(\omega) = e_0 + e_1\omega + e_2\omega^2 \quad (6.164)$$

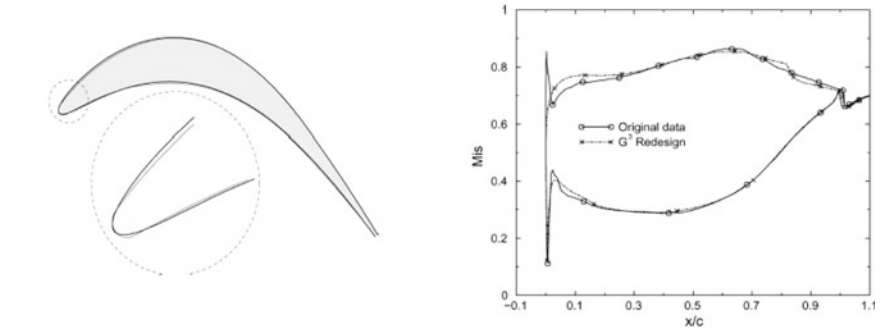
$$T_s(\omega) = \delta_s\sqrt{\omega} + c_{s1}\omega + c_{s2}\omega^2 + c_{s3}\omega^3 + c_{s4}\omega^4 \quad (6.165)$$

$$T_p(\omega) = \delta_p\sqrt{\omega} + c_{p1}\omega + c_{p2}\omega^2 + c_{p3}\omega^3 + c_{p4}\omega^4 \quad (6.166)$$

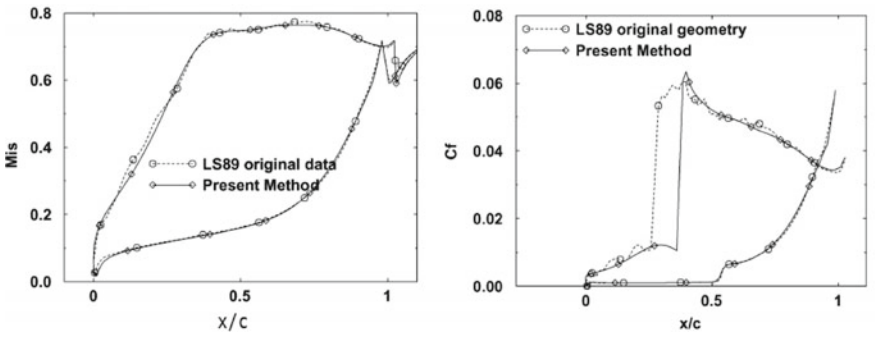
With the development of mathematics and computer technology, Bezier curves have been widely used in the field of parametric profiling thanks to their advantages of good curvature continuity, simple calculation, and mature theories and algorithms. For example, to guarantee curvature continuity, Corral et al. used two groups of fourth-order Bezier curves to carry out profiling of the pressure side and suction side, with the leading edge point included [123]. The used Bezier curves are given by Eq. (6.167), where P_i is the control point, $B_{i,n}(u)$ is the Bernstein primary function, given by Eq. (6.168), and u is the curve parameter. As shown in Eq. (6.169) and Eq. (6.170), the curvature K and its derivative along the profile curve are guaranteed to be continuous when constructing the Bezier curves. In Fig. 6.95a, it can be seen that this profiling method requires very few control points to describe the thin blade profile of a LP turbine and obtains the pressure distribution that is almost exactly the same as that of the original profile. In the subsequent studies, they made the best of the curvature continuity of the fourth-order Bezier curves and modified the leading edge of the turbine blade where suction peaks were observed, as shown in Fig. 6.95b. The results suggest that the modified profile was free from suction peaks without affecting both key aerodynamic parameters and aerodynamic loading. The fourth-order Bezier curves was also adopted to improve the performance of the LS89 turbine cascade. The calculated isentropic Mach number and friction coefficient are shown in Fig. 6.95c. It can be seen that, although the aerodynamic loading of the new profile was almost exactly the same as that of the original profile, the transition point was moved backward for about 10% of the axial chord length due to the fact that the Bezier curve is smoother, and the flow loss was reduced by 12% compared with the original value.



(a) LP turbine blade modeling



(b) Modification to leading edge



(c) Influence of modeling methods on transition

Fig. 6.95 Blade modeling with fourth-order Bezier curves [123]

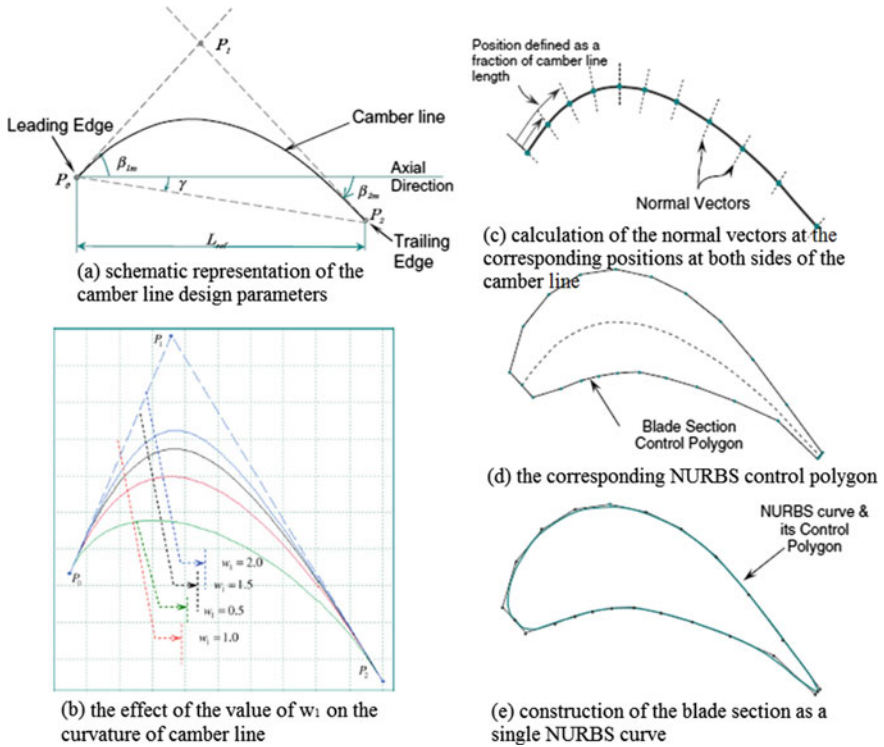


Fig. 6.96 NURBS modeling method [126]

Similarly, Anders et al. developed the parametric profiling method of using quintic Bezier curves and leading edge circle to describe the blade profile, which was integrated into the blade design system [124]. Trigg et al. optimized turbine blades by combining the Bezier curve parametric profiling with genetic algorithm and expressing blade profile as design parameters and aerodynamic loss as the objective function [125].

$$C(u) = \sum_{i=0}^n B_{i,n}(u)P_i \tag{6.167}$$

$$B_{i,n}(u) = \frac{n!}{i!(n-i)!} u^i(1-u)^{n-i} \tag{6.168}$$

$$K^- = K^+ \tag{6.169}$$

$$\left. \frac{dK}{ds} \right|^- = \left. \frac{dK}{ds} \right|^+ \tag{6.170}$$

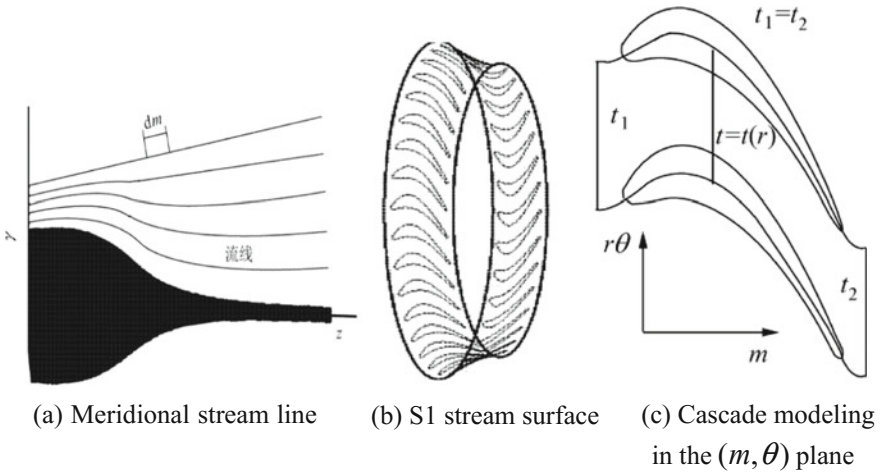


Fig. 6.97 Arbitrary revolution surface modeling procedures [127]

For parametric profiling methods, curvature continuity at the joints of curve sections can be guaranteed not only by increasing the order, but also by new topologies of profiling curves. For example, Koini et al. proposed a blade profiling method of using a non-uniform rational B-spline (NURBS) to construct the mean camber line and the thickness distribution [126]. This method uses one curve to describe the entire profile, avoiding the problem of curvature discontinuity directly. Figure 6.96 shows the procedures of blade profiling by using the NURBS. First, define the mean camber line by using the axial chord length, the stagger angle, and the inlet and outlet metal angles. The mean camber line is determined by three control points p_0 , p_1 , and p_3 , as shown in the figure. As can be seen, the shape of the mean camber line can be controlled by adjusting the weight of p_1 , with the parameters of the line stay unchanged. Second, the distance between each point on the profile in the curvilinear coordinate system and the mean camber line (namely, the blade thickness) is expressed as a function of its projective position on the mean camber line. The NURBS is then used to describe the function. After determining the control points, the profile can be then formed. Because the NURBS curve is a closed curve from the trailing edge and back to the trailing edge, the problem of curvature discontinuity at joints of curves is avoided.

It is worth noting that the profiling method described above can be used directly to design the two-dimensional profile on the cylindrical revolution surface for conventional turbines. However, for the turbines with flowpassage of large expansion ratio where the slope of the meridional streamline of the S2 stream surface is high, as well as intermediate turbine duct with large climb angle, the blade profiling on the cylindrical revolution surface will not only result in geometric deviations, but also lead to aerodynamic errors due to the failure to consider the

normal components of aerodynamic parameters on the revolution surface. The arbitrary revolution surface profiling method is an ideal choice to solve this problem [127]. This method follows the following procedures. First, select the meridional stream line, generate S1 stream surface by rotation, and obtain aerodynamic parameters along the stream surface. Then, develop the revolution surface into a two-dimensional dimensionless plane (m, θ) , carry out 2-D cascade modeling in the plane. Finally, convert the profile into three-dimensional coordinate system, as shown in Fig. 6.97. This modeling method can fully inherit the current 2-D cascade profiling methods, and variation characteristics of the meridional stream line can be obtained by surface transformation.

6.5.2.2 Parametric Blade Profiling Procedures

What follows takes the Pritchard 11-parameter method as an example to describe the specific parametric blade profiling procedures. This method divides the profile into three curves representing the leading edge, the pressure surface, and the suction surface respectively. 11 parameters including the number of blades, the radius of blade section, the diameter of leading-edge circle, the diameter of trailing-edge circle, the chord length, the stagger angle, the leading edge wedge angle, the trailing edge wedge angle, the trailing edge bending angle, the inlet metal angle, and the outlet metal angle are used as the basic profile parameters with the aim of controlling the important physical quantities in the aerodynamic design process conveniently (see Fig. 6.98) [128]. The blade profile is divided into the leading-edge circle, the trailing-edge circle, the profile curve of the pressure side, the profile curve of the anterior part of the suction side, and the profile curve of the posterior

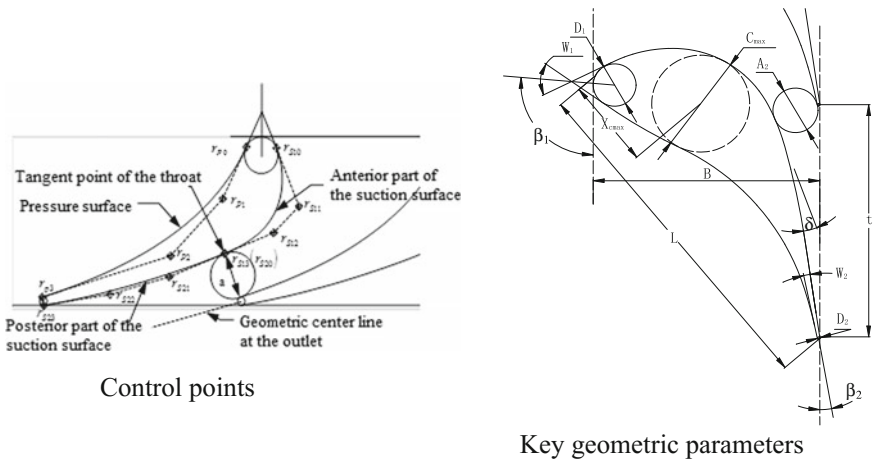


Fig. 6.98 Geometric parameters and control points in Pritchard 11-parameter parametric blade profiling

part of the suction side. The pressure side and suction side of the profile are formed by third-order polynomial curves, and the anterior part of the trailing edge is formed by arcs. The five profile points include two endpoints on the pressure side, two endpoints on the suction side, and an interior point. The multi-point Bezier curve is used to replace the rational Bezier curve. The advantage of this profiling method is that the meaning of the parameters is definite. On the other hand, there are two disadvantages. One is that except the 11 basic parameters, there are no other degree of freedom to modify the curves, and the other is that inflection points are inevitable in polynomial curves. The specific design procedures are described as follows:

- (1) Input geometric parameters: including inlet (outlet) metal angle, leading (trailing) edge wedge angle, leading (trailing) edge circle, trailing edge bending angle, pitch (or section radius and number of blades), axial (chordwise) chord length.
- (2) Fix the leading-edge circle and make it as the reference point; determine the location of the trailing-edge circle according to the chord length and stagger angle; with the diameters of both the leading and trailing edge circle known, the leading and trailing edge circles can be determined.
- (3) Around the leading edge, determine the two tangent points, r_{P0} and r_{S10} , between the leading-edge circle and the profile curve of the pressure side and the profile curve of the anterior part of the suction side according to the inlet metal angle and leading edge wedge angle; around the trailing edge, determine the two tangent points, r_{P3} and r_{S23} , between the trailing-edge circle and the profile curve of the pressure side and the profile curve of the posterior part of the suction side in a similar way.
- (4) The trailing-edge circle of the adjacent blade can be obtained according to the cascade pitch; diameter of the incircle representing the throat can be obtained according to the outlet metal angle; the tangent point $r_{S13}(r_{S20})$ of the incircle and the profile curve of the suction side, which is determined along the direction perpendicular to the geometric center curve at the trailing by taking the center of the trailing-edge circle of the adjacent blade as the center and the radius of the throat incircle as the radius, can be obtained, and this point divides the profile curve of the suction side into two segments: the anterior part and the posterior part.
- (5) As for the profile curve of the pressure side, profile curves of the anterior part and the posterior part of the suction side, two end control points and tangential directions of the profile curve at the points can be obtained; take two appropriate middle control points in along the tangential directions of each segment, and then there are four control points in each section; put the coordinates of the four control points into the profile curve generating function, carry out curve construction for each segment, and then all the profile curves of the profile can be obtained; perform S1 calculation to examine whether the profile meets the requirements; if not, adjust the parameters and re-profile the blade.

- (6) Repeat step 1 to step 6 for each reference blade section along the blade height (root, middle and tip for example), and generate the profile for each reference section.
- (7) According to the profile of the reference section, many other sections at different radius, which are used for calculation and machining, can be obtained through spanwise interpolation.
- (8) Carry out 3-D blade stacking, and check the design result by numerical methods so as to determine whether it meets the design requirements.

6.5.3 Blade Leading Edge Profiling/Modifying Methods and Applications

If smooth transition between the leading edge curve and the blade curves cannot be guaranteed at the leading edge of the blade, the inflow may experience overexpansion around the circular leading edge and a suction peak may occur as a result. Especially when the turbulence and Reynolds number of the inflow are low, there would be a separation bubble behind the suction peak, thus causing losses. Therefore, it is possible to weaken the suction peak and separation bubble by controlling the curvature of the profile curves and organizing the flow around the leading edge to prevent overexpansion, and thus improving the turbine performance. For example, an elliptic leading edge could guarantee the radius of curvature increase gradually from the leading-edge stagnation point to the tangent point on the blade curves, thus reducing the adverse pressure gradient of the flow around the leading edge and inhibiting overexpansion and weakening the suction peak. In addition, it can also largely increase the range of incidence, at which the turbine operates efficiently [129, 130].

6.5.3.1 Introduction to Blade Leading Edge Profiling Methods

Leading edge profiling can be realized by different types of curves, such as the cubic-spline-based leading-edge curve and the elliptic-curve-based leading-edge curve. The cubic-spline-based leading-edge profiling method uses the leading edge point and control points on the suction and pressure side to conduct cubic spline interpolation and obtain the leading edge curve when the profile curves are given. This method is very simple and practicable, and can guarantee smooth transition between the leading edge curve and the blade curves. However, there is obvious limitation of this method. Namely, when the blade curves are determined, the leading edge curve will be determined only by the location of the leading edge point. In other words, this profiling method only has one degree of freedom, which can not meet the requirements of aerodynamic performance and structural strength on the leading edge curve simultaneously, in some cases. The elliptic-curve-based

leading-edge profiling method has much more degrees of freedom. When the direction of the symmetry axis is given, an elliptic curve can be determined by three parameters, which are the coordinates of the center point, the long axis length, and the short axis length, or the coordinates of an end, the length of an axis, and the ellipticity. If the short axis length of the elliptic curve is determined by the distance between the endpoints of the suction side curve and the pressure side curve, then the coordinates of the leading edge point of the ellipse and the ellipticity can be given according to the requirements of aerodynamic performance and structural strength. For example, the leading edge profiling program developed in Ref. [131] adopts this method. However, this method has the deficiency that it needs the support of other methods to realize smooth transition between the leading edge curve and the blade curves, which will increase the workload of profiling.

To give consideration to the requirements of aerodynamic performance and structural strength on the leading edge shape, and realize smooth transition between the leading edge curve and the blade curves, Zhang, Zou, et al. developed a polynomial-based leading edge profiling method [132]. The curve used in this profiling method can be written as:

$$\frac{y}{c} = \sqrt{\frac{x}{c}} \cdot S\left(\frac{x}{c}\right) \quad (6.171)$$

where, the origin of the coordinates is set at the leading edge point, x is the length along the mean camber line of the profile, y is the half thickness of the profile, c is the reference dimension, and S represents the polynomial. The first term of the expression, $\sqrt{\frac{x}{c}}$, determines that the curve passes the leading edge point of the mean camber line ($y_{x=0} = 0$, i.e. leading edge point of the profile) and is perpendicular to the mean camber line ($y'_{x=0} \rightarrow \infty$) at the leading edge point ($x = 0$), which guarantees that the curve meets the requirements on the shape of the leading edge. The second term, $S(\frac{x}{c})$, determines the specific shape of the curve, namely the thickness distribution and curvature distribution of the leading edge. The leading edge curve is required to meet the requirements of four physical quantities, which are the curvature radius of the leading edge point, the coordinates of joint points between the leading edge curve and the blade curves, the slope, and the curvature. To meet these four quantities, $S(\frac{x}{c})$ shall be at least a cubic polynomial. If more terms are added in $S(\frac{x}{c})$, the degree of freedom of the leading edge curve will be higher, while the workload and complexity would also be higher. When $S(\frac{x}{c})$ is assumed as a cubic polynomial, it can be written as:

$$S\left(\frac{x}{c}\right) = A_0 + A_1\left(\frac{x}{c}\right) + A_2\left(\frac{x}{c}\right)^2 + A_3\left(\frac{x}{c}\right)^3 \quad (6.172)$$

Setting the reference dimension, c , as the length of the mean camber line at the leading edge, the independent variable of the polynomial is non-dimensionalized between 0 and 1, and the solution is simplified. Substituting the above equation in Eq. (6.171), we can obtain:

$$\tilde{y} = \sqrt{\tilde{x}} \cdot (A_0 + A_1\tilde{x} + A_2\tilde{x}^2 + A_3\tilde{x}^3) \left(\tilde{y} = \frac{y}{c}, \tilde{x} = \frac{x}{c}, \tilde{x} \in [0, 1] \right) \quad (6.173)$$

Thus, the design of the leading edge curve is changed to the problem of determining the coefficients in the equation above according to the requirements on the leading edge curve. Taking the derivative of the terms, we can obtain the slope distribution of the leading edge curve:

$$\tilde{y}' = \sqrt{\tilde{x}}(A_1 + A_2\tilde{x} + A_3\tilde{x}^2) + \frac{A_0 + A_1\tilde{x} + A_2\tilde{x}^2 + A_3\tilde{x}^3}{2\sqrt{\tilde{x}}} \quad (6.174)$$

The second-order derivative distribution can be obtained by taking the derivative of the terms again. Thus, the curvature distribution of the leading edge curve can be expressed as:

$$\begin{aligned} \tilde{k} = Abs & \left(\sqrt{\tilde{x}}(2A_2 + 6A_3\tilde{x}) + \frac{A_1 + 2A_2\tilde{x} + 3A_3\tilde{x}^2}{\sqrt{\tilde{x}}} \right. \\ & \left. - \frac{A_0 + A_1\tilde{x} + A_2\tilde{x}^2 + A_3\tilde{x}^3}{4\tilde{x}^{3/2}} \right) \\ & / \left(1 + \left(\sqrt{\tilde{x}}(A_1 + 2A_2\tilde{x} + 3A_3\tilde{x}^2) + \frac{A_0 + A_1\tilde{x} + A_2\tilde{x}^2 + A_3\tilde{x}^3}{2\sqrt{\tilde{x}}} \right)^2 \right)^{3/2} \end{aligned} \quad (6.175)$$

When $\tilde{x} \rightarrow 0$, the curvature radius of the leading edge point described above only depends on A_0 :

$$\tilde{R}_L = \frac{A_0^2}{2} \quad (6.176)$$

It is observed that Eq. (6.171), which describes the leading edge curve, provides a simple and direct approach to the control of curvature radius of the leading edge point, and meanwhile, guarantees the coefficients can be easily calculated.

6.5.3.2 Influence of Modifications to Blade Leading Edge on Performance

The polynomial-based leading edge profiling method described above was adopted to modify the leading edge of the HD turbine blade. The effectiveness was verified by RANS and LES. The results are shown in Fig. 6.99, in which HD represents the original turbine blade profile, and C1 represents the profile after the modification. It

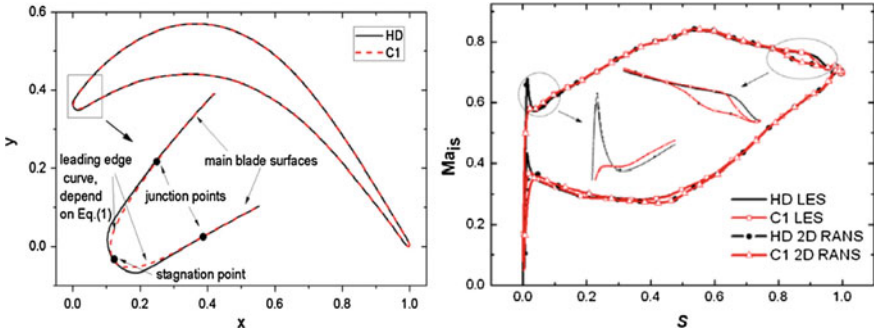


Fig. 6.99 Comparison before and after modification to leading edge of HD blade [132]

can be seen from the isentropic Mach number distribution that LES and RANS results are very close on the whole, though there is some difference between the two in the description of the separation bubble around the trailing edge. The calculated results suggest that there was an obvious suction peak around the leading edge of the HD profile and strong adverse pressure gradient after the peak, which was clear on both the suction side and pressure side. After the modification to the leading

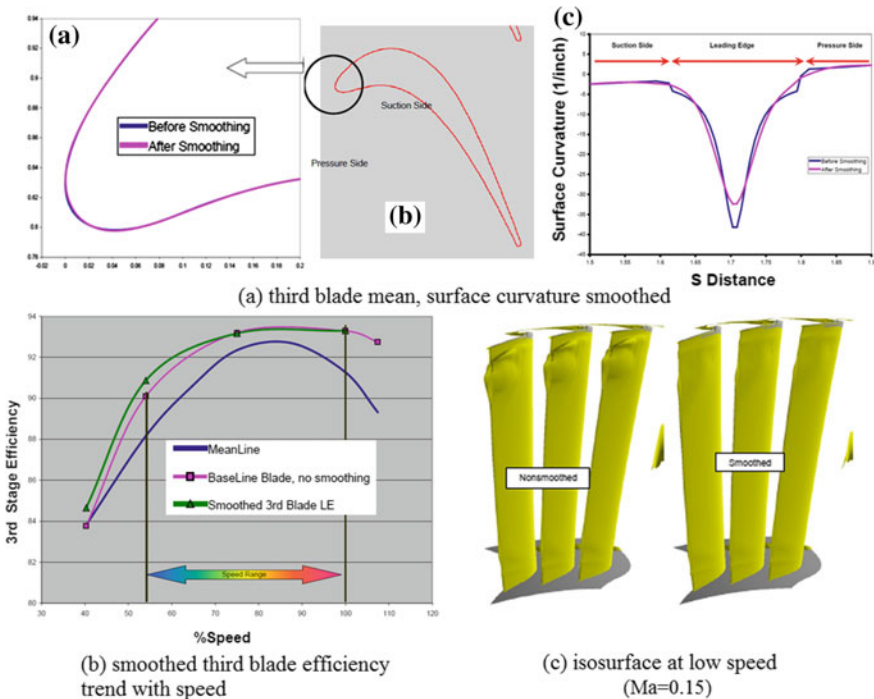


Fig. 6.100 Influence of leading edge curvature on off-design conditions [50]

edge, the C1 profile was free from the suction peak on both the suction side and pressure side around the leading edge while keeping pressure distribution at other locations basically unchanged. In addition, flow loss in the boundary layer of the suction side was reduced by 10% compared with the original profile, and off-design performance was improved significantly as well.

Reasonable leading edge profiling/modifying helps widening the high-efficient operating range of turbine blades. Suchezky et al. carried out smoothing modifications to the leading edge curvature of turbine blades, and analyzed the influence of the leading edge modifications on the high-efficient range of incidence [50]. The corresponding relations between curvature and coordinates of the profile curves were worked out, as well as the curvature gradient of the points on the profile curves, and then fine adjustments were made to the normal positions of the coordinate points through iteration until smooth transition of curvature distribution was reached. It can be seen from Fig. 6.100a that the curvature peak at the leading edge became gentle after the smoothing modification, while changes to the leading edge shape were quite little. The calculated results also suggest that the curvature smoothing barely has any influence on the performance at the design point. In addition, the speed-efficiency curve in Fig. 6.100b indicates that the curvature smoothing could improve the turbine stage efficiency in a large range of the low speed area. Figure 6.100c presents the isosurface at low speed, while the Mach number is 0.15. Since the Mach number of the main flow is far above 0.15, the isosurface in the figure represents the boundary layer and separation bubble area. It can be seen that the separation bubbles on the suction surface under off-design conditions were eliminated after the curvature smoothing. Reference [130] also suggests that reasonable selection of leading edge shapes can greatly improve off-design performance. Benner et al. conducted a similar study, and pointed out that the leading edge wedge angle is closely related to the continuity of leading-edge curvature and has influence on leading edge loss under off-design conditions. So, the wedge angle should be as large as possible to avoid the influence of discontinuous curvature [133].

6.6 Influence of 3D Blade Stacking on Turbine Flows and Performance

6.6.1 Basic Concept of 3D Profiling

In the turbine design process, 3-D blade profiling generally refers to the process of assembling 2-D profiles at different blade height together along the spanwise direction according to the stacking line and thus forming the geometry of the entire blade. At the beginning, a straight line was used as the stacking line, while in order to realize the control of secondary flows and shock waves, different types of stacking lines have been developed, such as curved lines, leaned lines, and compound lines. Accordingly, turbine blades have developed from the original straight

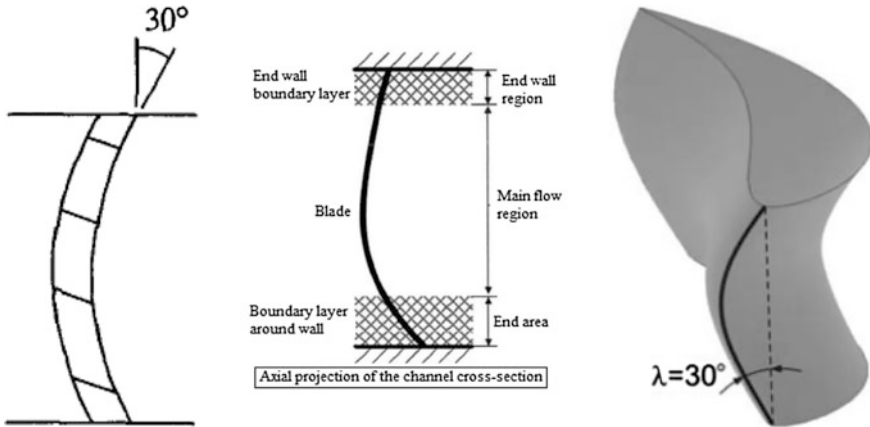


Fig. 6.101 Curved blade and its stacking line [135–137]

blades to twisted blades and even curved-twisted-swept blades. This subsection mainly presents an description of the applications of blade curving, blade sweeping, and combination of the two in turbine design.

The basic concept of blade curving was proposed jointly by Filippov from the former Soviet Union and Wang Zhongqi from Harbin Institute of Technology in 1960s, which was then referred to as composite aerodynamic profiling of curved-twisted blades [134]. Different from traditional blade stacking methods, “curving” refers to the geometric degree of freedom of staggered stacking of spanwise profiles along the direction perpendicular to the flow direction, as shown in Fig. 6.101 [135–137]. The key parameter to describe the degree of curving is the curving angle, which was defined as the included angle between the tangential direction at the end of the stacking line and the radial direction and generally accepted [138]. If the included angle between the pressure side and the endwall is an acute angle, then it is called positive curving, otherwise, it is called negative curving. The fundamental objective of using blade curving is to make the radial component of the force between the flow and blade nonzero by curving or leaning the blade in the circumferential direction, thus controlling the spanwise distribution of pressure, and reducing the radial secondary loss and the tip leakage loss.

Blade sweeping is originated from high-speed airfoils. Seeing the successful application of blade sweeping in external flows, designers have employed this method in blade profiling for turbomachineries, such as compressors and turbines. The key parameter to describe the degree of sweeping is the sweeping angle. In external flows, it is defined as the included angle between the normal direction (pointing to the wing tip) of the longitudinal symmetry plane of an aircraft and the characteristic line of the wing [139]. While in internal flows, it is redefined as the complementary angle of the included angle between the vector of the local relative inflow velocity and the tangential direction at the leading edge. Actually, “sweeping” is the degree of freedom of staggered stacking of spanwise profiles along/against the flow direction.

With the continuous development of turbine blade design technologies, 3-D profiling technologies such as compound leaning, blade tip curving, and forward/backward sweeping have been widely used to reduce flow losses and expand stable operating range, providing more degrees of freedom for 3-D design and optimization of turbine blades. The former can improve the flow in the endwall regions, and the latter can reduce the normal Mach number of the inflow. With respect to geometric design of endwalls, curvature control, in addition to convergent-divergent control, can be also carried out to realize the optimal control of radial distribution of axial Mach number and reduce the loading in the endwall regions.

6.6.2 Influence of Blade Curving on Turbine Flows and Performance

Since 1970s, curved blades have been successfully used in compressors, gas turbines, and aero-engines. Essentially, circumferential blade curving provides a new degree of freedom to the aerodynamic design of turbines. By reasonably matching blade curving with the original degrees of freedom (i.e. spanwise twist), it is possible to further optimize the flow field. The basic principle of blade curving is firstly described.

As for the traditional straight blades or conventional twisted blades, the radial component of the blade's acting force on the flow is very small [F_r in Eq. (6.177)], which can be ignored in general cases due to the fact that it barely has any influence on the distribution of flow parameters. Curved blades are mainly designed to make advantage of the radial component force to control the static pressure distribution in the flow passage. Effective adjustment and control of this radial force is helpful not only to improve the flow in the root region of the rotor blade, but also to weaken the radial flows in the blade surface boundary layer as well as the accumulation of low energy fluid in the root region of the stator blade, thus reducing energy loss. The radial force should be in the same order of magnitude as the inertial centrifugal force of the fluid element.

The radial equilibrium equation is given in as:

$$\frac{1}{Q} \frac{\partial p}{\partial r} = \frac{V_u^2}{r} + \frac{w_m^2}{r_m} \cos \sigma - \frac{dw_m^2}{dm} \frac{\sin \sigma}{2} + F_r \quad (6.177)$$

where, $F_r = -\frac{n_r}{n_u r} \frac{\partial p}{\partial \theta}$.

It can be seen that variation of the radial pressure in the cascade passage is determined by the four terms at the right side of the equation above. The first term is the inertial centrifugal force due to the rotation of the fluid element in the revolution surface, which always makes positive contribution to the radial pressure gradient. The second term is the radial component of the inertial centrifugal force due to the curvilinear motion of the fluid element in the meridian plane. When the stream line

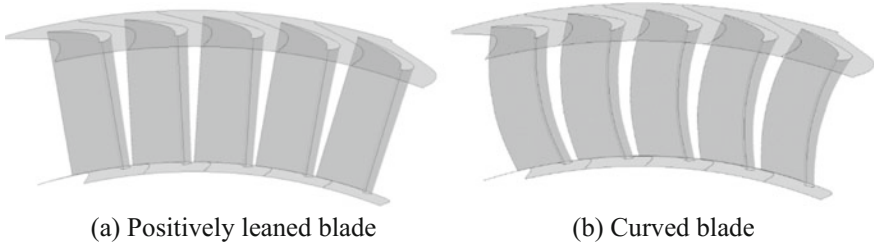


Fig. 6.102 Positively leaned blade and curved blade

is concave, this term is at a negative value, thus reducing the radial component of the static pressure. In the controlled vortex design, this term can be used to control the spanwise pressure distribution. In the axial clearance between the stator and the rotor, concave curvature can correct the distribution of the reaction degree and make it tend to be uniform along the spanwise direction. For this reason, controlled vortex methods are also called controlled reaction degree methods. The third term is the radial component of the meridional acceleration inertia force due to the motion of the fluid element on the stream surface, which is opposite to the direction of the acceleration. In symmetric flows,

$$\frac{1}{2} \frac{dW_m^2}{dm} \sin \sigma = \frac{1}{2} \frac{\partial W_m^2}{\partial m} \sin \sigma \quad (6.178)$$

The expression above defines the radial component of the acceleration inertia force of the fluid element in the meridian plane. Since $\sigma = 0$ in the meridian plane between the stator and the rotor, this term is close to zero.

The fourth term is the radial component of the blade's acting force on the flow, whose influence on the radial pressure gradient may be positive or negative. When blades are positively curved (see Fig. 6.102), the circumferential partial derivative of pressure is negative, so as the radial component of the unit normal vector of the stream surface. Thus, for positively leaned blades, the fourth term at the right side would reduce the pressure gradient along the spanwise direction, which is opposite to that of the first term at the right of the equation. If the influence of the fourth term on the radial pressure gradient is greater than the total influence of the other three terms, the radial pressure gradient may be negative.

Figure 6.103 shows the spanwise distribution of the static pressure for three kinds of blades. For the traditional radial blade, the radial component of the blade's acting force on the flow, namely the fourth term at the right side of Eq. (6.177), is so small that it can be ignored. Then, the radial pressure gradient is mainly influenced by the inertial centrifugal force due to the tangential velocity component in the revolution surface, so positive pressure gradient along the spanwise direction is obtained (see Fig. 6.103). For the positively leaned blade, as stated above, if the influence of the fourth term is greater than the total influence of the other three terms, the radial pressure gradient may be negative. For the curved blade, its lower

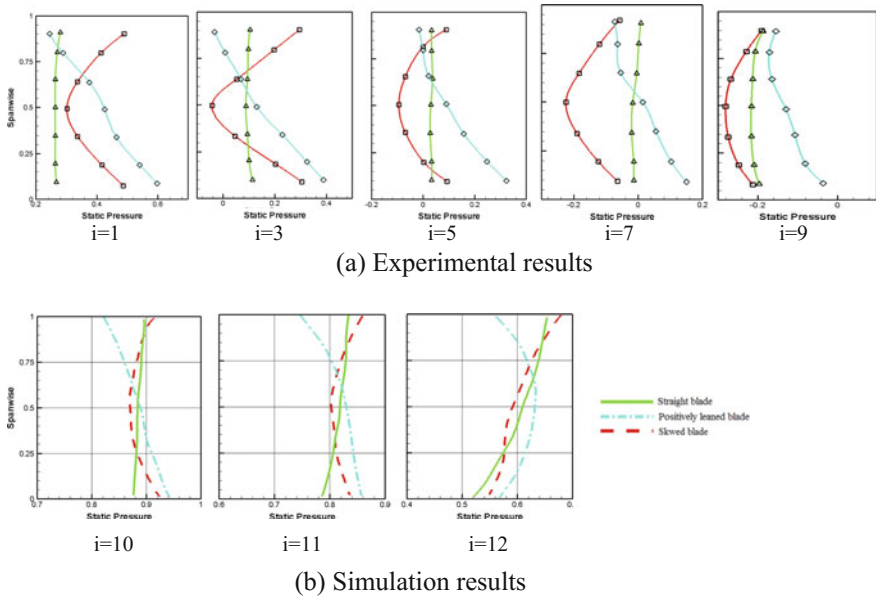
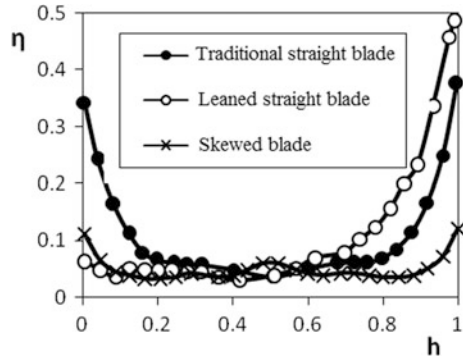


Fig. 6.103 Spanwise distribution of the static pressure

half is equivalent to a positively leaned blade, which would reduce the radial pressure gradient. If the inclination angle at the root is large enough, negative radial pressure gradient along the spanwise direction can be obtained. The upper half of the curved blade is equivalent to a negatively leaned blade, which would increase the radial pressure gradient. Thus, the C-shaped pressure distribution, as shown in Fig. 6.103, is obtained. Part (a) and Part (b) show the experimental and calculated results of the static pressure distribution respectively.

Studies have shown that the intensity of the radial secondary flows is mainly determined by the viscous effect of the wall and the wall pressure gradient [138]. Due to the great positive pressure gradient along the spanwise direction, the boundary layer, which moves radially along the suction surface from the tip to the root, would join with the boundary layer, which moves transversely on the lower wall, in the corner zone formed by the suction side and the lower wall, thus resulting in thickening and accumulation of the boundary layer in the corner zone. These low-energy flows move along the suction side near the root and are possible to separate when passing through a diffusion section from the throat to the outlet edge, thus resulting in rapid increase of energy loss in the root near the suction side. The boundary layer, which moves radially along the pressure side from the top down, would not accumulate in the corner zone formed by the pressure side and the lower wall. Under the action of transverse pressure gradient, it would continue moving from the pressure side to the suction side along the lower wall, thickening the boundary layer in the corner zone formed by the suction side and the lower end wall [140].

Fig. 6.104 Spanwise distribution of energy loss in stator blade



To eliminate the radial motion of the boundary layer, which moves radially along the suction side and pressure side, the positive pressure gradient on the suction side and pressure side of conventional blades should be changed. Negative radial pressure gradient can be obtained by using positively leaned blades (as shown in Fig. 6.102). This kind of blades can prevent radial drift of the boundary layer along the suction side and pressure side from the top down, thus reducing the energy loss in the root of the blade. However, there may be boundary layer movement from the bottom up, which would lead to increase in the energy loss at the top of the blade. Thus, the total energy loss of the blade may not be decreased. Sometimes, energy loss in positively leaned blades may be greater than that in traditional blades (see Fig. 6.104).

When curved blades are adopted (namely, the included angles between the suction side and the shroud and hub are all acute angles), the spanwise C-shaped distribution of the static pressure on the suction side and pressure side can be obtained. Under the effect of this C-shaped pressure distribution, the boundary layers at both ends would be driven to the middle and then taken away by the main flow, so the energy loss in the two endwall regions would be decreased (see Fig. 6.104). As low-energy flows in both the endwall regions are driven to the middle and taken away by the main flow, some energy of the main flow would be consumed. As a result, energy loss in a range of the middle region would increase. However, the increment of the energy loss in the middle region is generally insignificant, so the total energy loss of the blade would be reduced in this case.

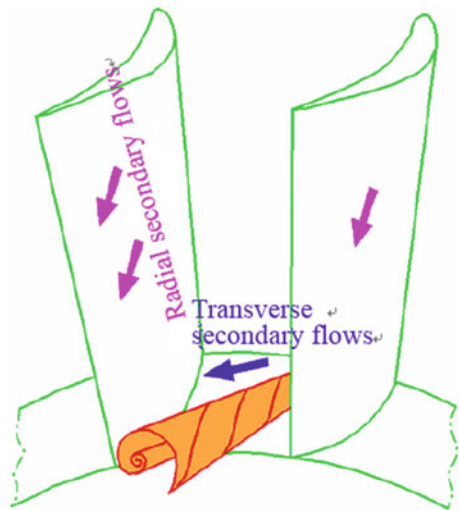
Based on studies on curved blades, Wang Zhongqi proposed the boundary layer migration theory, trying to explain the mechanism of composite aerodynamic profiling of curved-twisted blades. According to the theory, the boundary layer on the suction side moves radially from the blade tip to the root due to the large positive pressure gradient along the spanwise direction, and meets with the boundary layer, which moves transversely along the hub, in the corner zone on the suction side, thus resulting in accumulation of boundary layer in the corner zone. According to the boundary layer migration principle, the only way to eliminate this radial movement of boundary layer along the suction side is to change the pressure gradient in the blade passage. By leaning or curving the blades, a radial force can be

generated, which can serve as a new control factor in the radial equilibrium equation, namely the radial component of the blade force— F_r . By adjusting the magnitude and direction of the blade force, it is possible to control the magnitude and direction of the radial pressure gradient as well as the development of boundary layers. In this way, the radial secondary flows that are bad for aerodynamic performance can be weakened or even eliminated.

The curved blades are firstly used in turbines. The flows in turbines are generally accelerated and the boundary layers on the blade surface do not separate easily. If positively curved blades are used, the static pressure distribution with negative pressure gradient in the root region and positive pressure gradient in the tip region, i.e. the C-shaped static pressure distribution with high values at the ends and low values in the middle, can be obtained, as shown in Fig. 6.106. The lower half of the curved blade is positively leaned, so it would result in negative pressure gradient pointing from the blade root to the middle. On the contrary, the upper half is negatively leaned, which would result in positive pressure gradient pointing from the blade tip to the middle. In this case, low-energy flows near the two endwalls would be driven into the main flow, thus eliminating the boundary layer accumulation in the corner zone on the suction side, reducing endwall loss, and increasing the aerodynamic performance of the blade. This C-shaped static pressure distribution has been proved by many studies. For example, Hourmouziadis et al. [141] came to the conclusion that positively curved blades can not only reduce the blade loading near the endwall, but also reduce the static pressure in the middle of the blades. As a result, the low-energy flows are effectively prevent from moving to the corner zone on the suction side.

Curved blades have significant influence on the blade loading distribution. Harrison studied three kinds of high-loaded low-aspect-ratio cascades, which are straight blades, leaned blades, and curved blades [135]. The results show that blade

Fig. 6.105 Radial and transverse secondary flows [248]



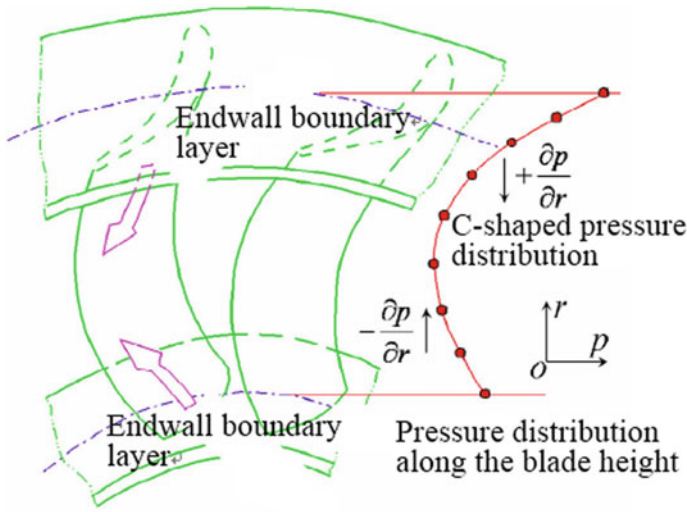


Fig. 6.106 C-shaped pressure distribution in curved blades [248]

leaning has significant influence on the blade loading distribution (especially near the middle of the chord), the loss distribution, the suction side flow conditions, and the endwall boundary layer flow conditions. It would result in acceleration and thinning of the boundary layer on one endwall, while deceleration and thickening of the boundary layer on the other endwall. On the high-pressure endwall, most fluids in the incoming boundary layer leave the blade surface along the separation line, and the boundary layer downstream of the separation line is relatively thin. However, the boundary layer on the other endwall is relatively thick. Loss in straight blades is concentrated in blade endwall regions. Blade curving makes the flow deflecting excessively in the middle of the blade while insufficiently at endwalls, making the spanwise variations of the average outflow angle decrease

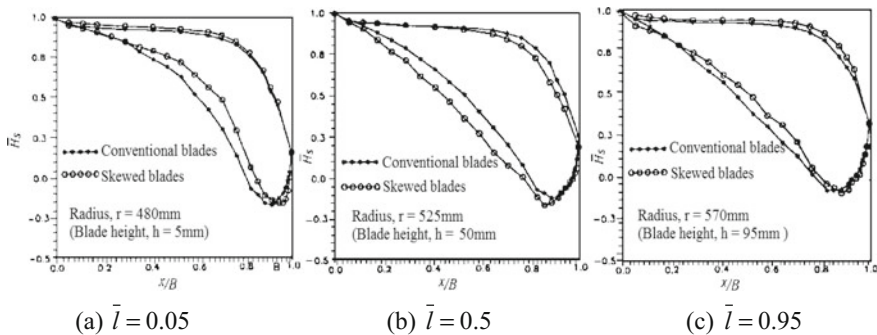


Fig. 6.107 Blade surface pressure distribution at different blade height

significantly. In addition, curved blade would lead to higher loading in the middle of the blade, thicker wakes downstream of the middle of the blade, and higher ratio of mixing loss. Therefore, curved blades can increase the flow turning angle and decrease mixing loss at the downstream and spanwise variations of the average outflow angle, so they can increase the turbine efficiency greatly, particularly in the cases with changes in blade loading being considered.

Figure 6.107 shows the influence of curved blades on the pressure difference between the pressure side and suction side, where (a), (b) and (c) show the measured results at the blade root, middle, and tip respectively. The pressure difference between the pressure side and suction side of curved blades in endwall regions is significantly lower than that in conventional blades, which suggests that the transverse secondary flows on the two endwalls become weaker, and that the corresponding secondary loss decreases. In the middle of the blade, the pressure difference in curved blades is higher than that in conventional blades, indicating that the work in the middle of the curved blades increases, and that the loading of the turbine stage increases. Therefore, variations of the pressure difference at the tip and middle of the curved blades are all beneficial. So, curved bladed can not only reduce the total loss by inhibiting radial secondary flows and reducing transverse secondary flows, but also increase the power capability in the middle of the blade.

Experimental measurements of the turbine stage performance are very necessary to verify the effectiveness and reliability of curved blades. Schobeiri et al. studied the influence of 3-D curved blades on turbine performance with a three-stage HP turbine test rig [142]. The results show that curved blades can effectively reduce the range of the secondary flows in the endwall regions, reduce the secondary loss, and increase the efficiency of the turbine stage. Bohn et al. carried out an in-depth analysis of 3-D complex unsteady flows in both straight blades and curved blades based on experiments [143]. The results show that curved blades can not only reduce the secondary flows in endwall regions of all the blade rows, but also weaken the non-uniformity of the flow field at the outlet of the upstream blade row, thus increasing the turbine stage efficiency.

Fully 3-D viscous simulation suggests that J-shaped curved stator blades are beneficial to reducing the loss [144]. In actual blade rows, radial equilibrium would result in spanwise pressure gradient. However, positive curving at the root can just prevent accumulation of low-energy fluid at the root, which is just the advantage of J-shaped blades. Studies on highly-curved turbine cascade show that the forward sweeping at the end, resulting from circumferential curving, has the effect of weakening the passage vortices and horseshoe vortices [145].

Impulse turbines have the characteristics of small difference between inlet and outlet velocity, low pressure drop, large flow turning angle, and great energy loss in the middle of blades [146]. For this type of blade, it should be according to actual the situation to determine which kind of blade curving needs to be adopted [147]. Negative curving may be suitable for cases with serious separation in the middle of the blade, while positive curving may be appropriate for cases, in which endwall loss accounts for the major proportion and no separation occurs in the middle of the blade. Lindner described the secondary vortex characteristics, the total pressure

loss, and the development of streamwise vortexes in both leaned blade passage and curved blade passage [148].

Due to the significant effectiveness of flow controlling, the method of blade curving has been applied in more and more turbine design cases. Based on systematic studies on the influence of curved blades on turbine flows and performance, researchers from Harbin Institute of Technology carried out modification design for a small-scaled turbojet engine. Speaking of the turbine efficiency, the original turbine scheme, which was designed by the free vortex method, performed poorly. The modification was carried out to the guide vane by using the two degrees of freedom of curving and twisting. The modified turbine guide vane is shown in Fig. 6.108. Experimental results show that the stage efficiency of the modified turbine with curved blades was higher than that of the original turbine at all the revolution speeds, as shown in Fig. 6.109. Within the range of the tested speeds, the turbine stage efficiency was increased by 3–4%, with the engine thrust increased by about 3.5%. Similar experimental results obtained by Kawagishi et al. indicates that, although straightly leaned blades cannot reduce energy loss of the blades, they

Fig. 6.108 Turbine IGV before (*right*) and after (*left*) modification [149]

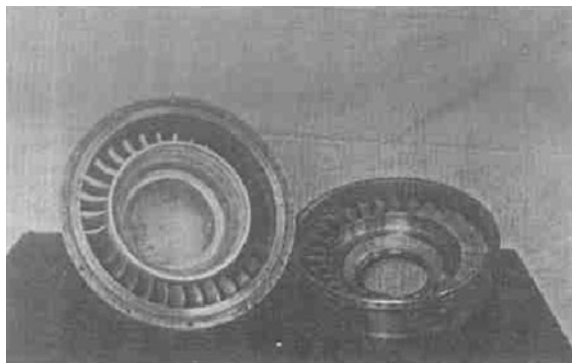
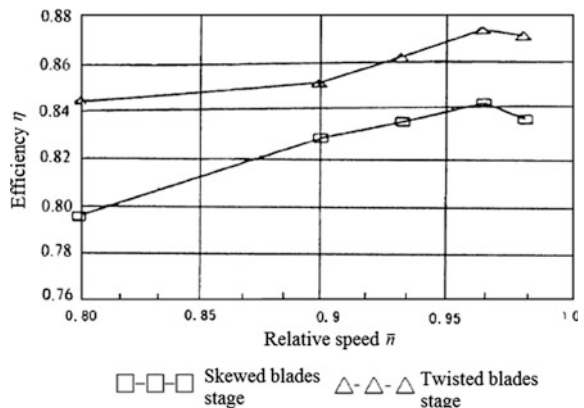


Fig. 6.109 Relation between curved blades and efficiency [149]



can increase the reaction degree at the root of the turbine stage, which helps to increase the efficiency of the turbine stage.

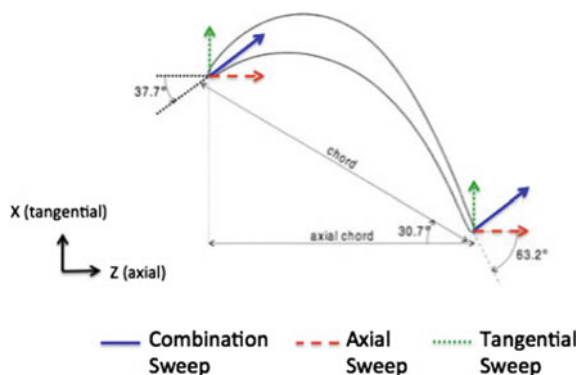
GEC Company modified the blades of the last stage in a steam turbine [150]. The last stage are operating in harsh conditions of large volume flow rate, high loading, and drastic radial changes of static pressure, and there are separation and blockage of flows in the root region of the blades. To increase the reaction degree at the blade root, the guide vane was redesigned by using composite aerodynamic profiling methods of axial positive curving and radial twisting. The experimental results show that the reaction degree at the root was increased by 30%, and the flow conditions in the root region of the rotor blade passage were improved significantly. Meanwhile, the reaction degree in the blade tip region was decreased by more than 15%, and the tip leakage loss was reduced.

A large number of experimental studies have shown that blade curving can not only control the magnitude and variation rules of the radial pressure gradient, but also change the spanwise distribution of the reaction degree of turbine stages (increasing the reaction degree at the root and decreasing the reaction degree at the tip). Thus, it can effectively control flow separation in the root region and enhance the flow capacity of the turbine stage. Therefore, curved blade profiling can improve 3-D flows of blade rows and largely decrease energy loss in the blade passage, thus improving the overall performance of the turbine stage.

6.6.3 Influence of Blade Sweeping on Turbine Flows and Performance

Swept blades are widely used in compressors. Blade sweeping design can be used to improve the secondary flow distribution in the endwall regions and control the strength of shock wave system, thus improving the efficiency and stall margin of compressors. Over the years, aerodynamic studies on swept blades of compressors have been extensively carried out, while there are still few analyses and discussions

Fig. 6.110 Relation between axial sweeping, tangential sweeping, and combination sweeping [151]



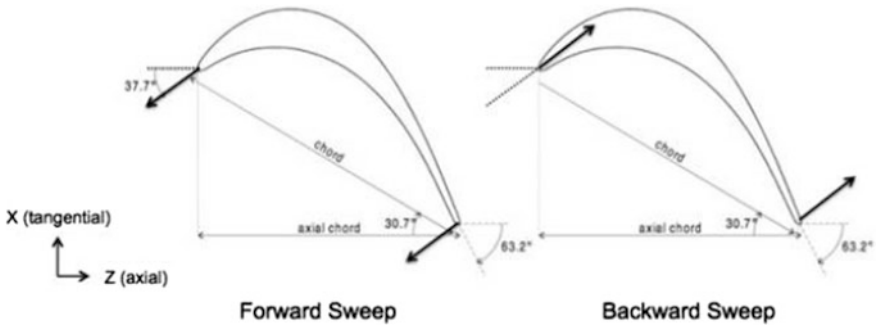


Fig. 6.111 Forward sweeping and backward sweeping [152]

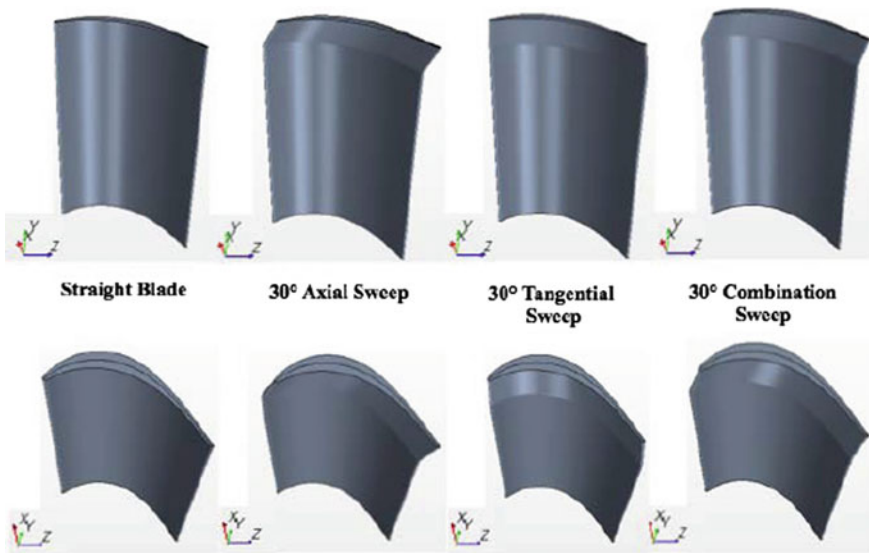


Fig. 6.112 Blade profiling by using axial sweeping, tangential sweeping, and combination sweeping [151]

on swept blades in turbines. Actually, orthogonal design in turbine blade design is a sort of blade sweeping design. According to the existing calculated and experimental results, swept blades of turbines and swept blades of compressors are similar in principle. However, there is a great difference in the radial pressure gradient between compressors and turbines because that compressors and turbines have different pressure distribution patterns along the flow direction. In addition, influence of swept blades on the shape of shock surface varies greatly between turbines and compressors.

In some respects, blade sweeping is similar to blade curving. Both blade sweeping and curving can change the radial pressure gradient, which would result

in radial movement of boundary layers and influence the original distribution of the secondary flows and the vortex systems. However, blade sweeping and curving are different in the mechanism of changing the radial pressure gradient. So, the ability of controlling and changing the flow structure is also different.

Currently, studies on the influence of blade sweeping on flows in LP turbines are more common. As shown in Fig. 6.110, blade sweeping can be subdivided into axial sweeping, tangential sweeping, and combination sweeping [151]. It is anticipated that chordwise sweeping may be developed following the combination of axial sweeping and tangential sweeping. In LP turbines, blade sweeping is generally used at 10% blade height from the tip to reduce leakage flow and leakage loss. Generally, the forward sweeping would make blades more sensitive to the incoming flow and result in easy separation at the blade tip on the pressure side, enhancing the leakage vortices in both size and strength. On the contrary, the backward sweeping would reduce the sensitivity of the blade to the incoming flow, and in this case, flows do not separate easily at the blade tip on the pressure side, weakening the leakage vortices in both size and strength. With the increase in the sweeping angle, these variation trends are more obvious [152]. It should be noted that the abovementioned forward sweeping and backward sweeping are not axial sweeping but the sweeping along the direction of the incoming flow, as shown in Fig. 6.111. The forward sweeping refers to the inclination of the leading edge curve of the blade against the direction of the incoming flow, and the backward sweeping is just the opposite.

Figure 6.112 shows the 3-D blade models generated by using axial sweeping, tangential sweeping, and combination sweeping at different sweeping angles. Studies on the influence of blade sweeping on flows in LP turbine cascades have shown that although the backward sweeping would increase the tip leakage flow, it would result in the reduction of the turbulent kinetic energy. Decrease in the turbulent kinetic energy would weaken the size and strength of the leakage vortices, thus contributing to the reduction of energy loss. It should be noted that variation of the leakage flow and turbulent kinetic energy is related to the form of sweeping.

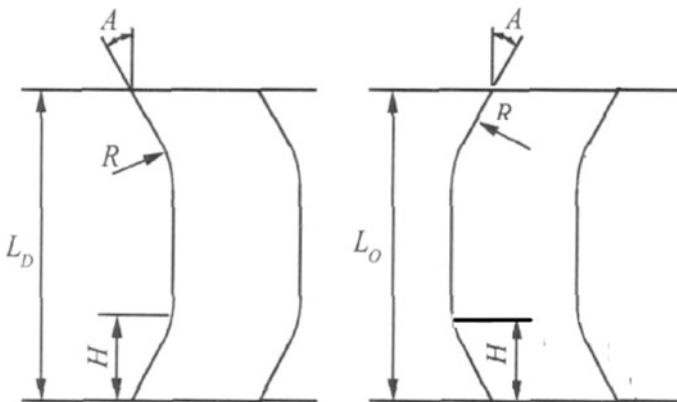


Fig. 6.113 Forward sweeping and backward sweeping of inlet vanes in a turbine

Actually, this sweeping design for rotor blade tips belongs to the category of spanwise part-span sweeping.

Blade sweeping is also widely used in the design of turbine guide vanes. Figure 6.113 shows the axial forward sweeping and the backward sweeping of the guide vane in a turbine. When the forward sweeping is adopted, the average static pressure coefficient of flows in the meridional stream surface presents an inverse-C-shaped distribution. With the increase in the sweeping height, H , the inverse-C-shaped pressure distribution is enhanced. Under the effect of the inverse-C-shaped pressure distribution, the boundary layers in the endwall regions are driven to the two endwall regions and are hard to be taken away by the main flow. As a result, low-energy flows would accumulate in the two endwall regions and the total loss in the endwall regions would be increased.

The backward sweeping works just in the opposite way. With the backward sweeping adopted, the average static pressure coefficient of flows in the meridional stream surface presents a C-shaped distribution. With the increase in the sweeping height, H , the C-shaped pressure distribution is enhanced. Under the effect of the C-shaped pressure gradient distribution, the boundary layers in the endwall regions are taken away by the main flow. As a result, accumulation of low-energy flows in the two endwall regions would be reduced and the total pressure loss in the endwall regions would be decreased. In summary, The forward sweeping would reduce the loss in the middle of the blades, enhance the transverse secondary flows in the endwall regions, and worsen the flow conditions in the endwall regions. As a result, the loss in the endwall regions would be increased. The backward sweeping would increase the loss in the middle of the blades and weaken the transverse secondary flows around the endwalls, thus decreasing the loss in the endwall regions. Variations in the strength of the secondary flows and the total pressure loss are in direct proportion to both the sweeping angle and sweeping height, which is to say, with the increase in the forward/backward sweeping angle and the sweeping height, the total loss would increase accordingly. In addition, blade sweeping can not only improve the aerodynamic performance, but also influence the acoustic characteristics to a certain extent.

In turbofan engines, the intermediate turbine duct is designed with meridional flowpassage of large expansion angle, which brings great difficulties to the aerodynamic design, including severe flow conditions at the outlet of the HP turbine,



Fig. 6.114 Swept strut in a intermediate turbine duct

large radial deflection of the flow passage, and short axial distance. In this case, the swept struts can be used to keep flows unseparated as possible, as shown in Fig. 6.114. The swept struts can not only improve the aerodynamic performance under design conditions, but also keep flows unseparated in the duct in a wide range of off-design conditions.

In addition to the influence of blade sweeping on mechanisms of turbine flows, attention has also been paid to the ways of considering the influence of blade sweeping in preliminary design. Pullan from University of Cambridge have made some contributions in this area. The blade loading coefficient, Z_w , was corrected, and the influence of blade sweeping on the flows in the middle and root of the blade passage was taken into consideration. Results indicates that blade sweeping design can reduce the secondary loss in the endwall regions, while increase the profile loss in the middle of the blade in the mean time. Therefore, tradeoff should be made in the design.

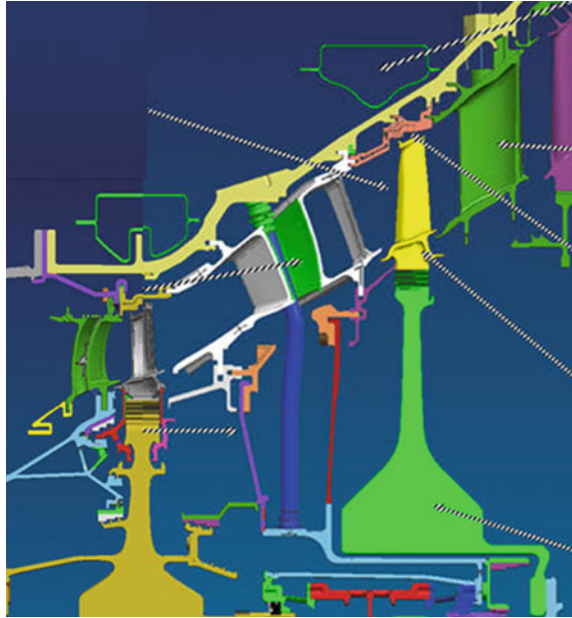
6.6.4 Influence of Combination Blade Profiling on Turbine Flows and Performance

With the requirements of turbine performance increasing rapidly, it is insufficient to meet the requirements of flow control only by blade curving or sweeping. Due to the gradually in-depth comprehension of regularities of 3-D complex flows in turbines, blade curving and sweeping have always been used simultaneously. The composite method of blade profiling, which is formed through optimization and combination of blade sweeping and sweeping, could bring much more benefits. In fact, the 3-D design of the flow passage is also included in the fully 3-D profiling methods of the existing design system of turbines.

Mechanisms of how blade curving and sweeping influence the flows and turbine performance, which has been obtained by studies on blade curving and sweeping, can serve as the reference and basis for 3-D profiling of turbine blades. In fact, blade curving, blade sweeping, and other 3-D profiling methods are similar in the basic principle of flow controlling. Comparison of the analytic results and 3-D numerical simulation results indicates that the pressure distribution plays a fundamental role in flow controlling. Mechanisms of all the 3-D blade profiling methods lie in the changing of the chordwise or the radial pressure distribution through geometric adjustments to realize flow controlling [139].

Therefore, 3-D curved or swept blades are designed to control flows by changing the 3-D pressure field in the blade passage, thus reducing the energy loss and improving the turbine efficiency. Extensive experimental studies show that the secondary flows are inhibited and the turbine aerodynamic performance is improved effectively, with the adoption of blade curving or sweeping. From the perspective of design, blade curving, twisting and sweeping are all degrees of freedom, and every newly added degree of freedom indicates larger space and new possibilities in the design.

Fig. 6.115 Application of curving-sweeping profiling in HP turbine of Trent 1000 engine [153]



Composite blade profiling technologies, which are based on the idea of making comprehensive use of various 3-D profiling methods to realize better control of flows in turbines, have been used in the design of advanced engines or included in 3-D aerodynamic design technologies of the new generation. In recent years, 3-D blade profiling technologies have been implemented in the design of turbines in high-performance large-bypass-ratio turbofan engines to improve turbine performance, such as Trent1000, LEAP-X, etc. Figure 6.115 shows the turbines in Trent 1000 engine, in which curving-twisting profiling was used in the design of guide vanes in the HP turbine, and blade sweeping with a large sweeping angle was used in the design of rotor blades in the intermediate pressure turbines [153]. The composite blade profiling method of large-angle sweeping and curving was used for designing guide vanes in the LP turbine, which plays an important role in turbine performance improvement. A 3-D aerodynamic design technology of the new generation was used for designing the LP turbine in LEAP-X engine as well [154].

It should be noted that applications of blade curving, blade sweeping and other profiling methods are under certain restrictions. For example, the composite curving-twisting profiling is suitable for designing guide vanes of large-aspect-ratio LP turbines. However, effectiveness of curving and twisting on guide vanes of small-aspect-ratio HP turbines is unobvious due to the short blade. In this case, better results can be obtained for the turbines by combining small-angle sweeping with other 3-D profiling methods such as nonaxisymmetric endwall. In addition, structural strength and machining processes should also be considered when using the composite blade profiling methods.

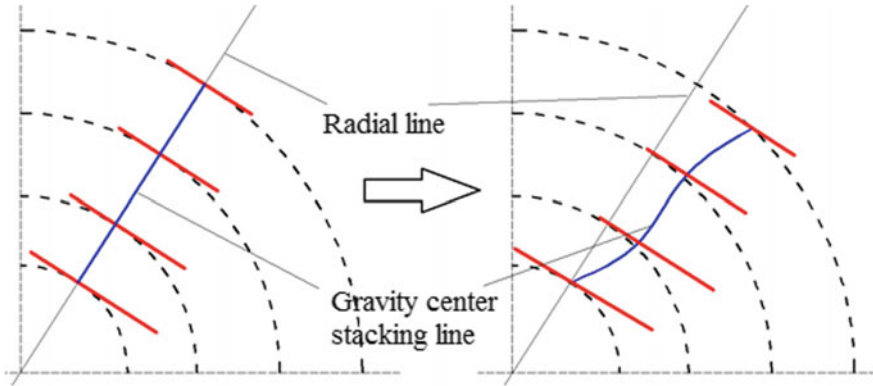


Fig. 6.116 Stacking lines before and after adjustment to the center of gravity

6.6.5 Influence of Blade Stacking Errors

During turbine design, it is necessary to put all the profiles at special positions of the stacking line, so as to form a complete blade. In the stacking process, influence of aerodynamic force, axial force, centrifugal force, and surface stress in practice on blade deformation is always neglected due to the limited knowledge. For example, for rotor blades where the center of gravity is adopted as the stacking position, the stacking line is strictly a radial line on the meridional plane. Due to the factors mentioned above, deformation and twist of the profiles may emerge, which would result in a certain deviation of the center of gravity. To counterweigh the centrifugal force moment and circumferential aerodynamic force moment, manual adjustments to the position of the center of gravity should be made, which are also necessary to reduce blade surface stress and adjust the inherent frequencies at the first few orders. This problem is even more prominent in design of air-cooled turbines. The cooling structure may cause bigger deviation to the position of the center of gravity. However, there is no specific design of the cooling structure in the process of aerodynamic design and profiling, so deviation of the center of gravity is unknown. Figure 6.116 shows the details about this problem.

During the design process of turbines, strength verification of the blade is necessary, right after the aerodynamic design and cooling design. An important task is to adjust the stacking positions and the amount of twist of the blade. These adjustments will be bound to exert some influence on the aerodynamic performance of the blade, particularly on the distribution of cooling air injected from film cooling holes.

Table 6.14 Reduced rotating speed and flow rate of a turbine

	Unit	Stage 1	Stage 2
$N/\sqrt{T_0^*}$	rad/(s \sqrt{K})	23.22	20.09
$W\sqrt{T_c^*}/P_0^*$	g \sqrt{K} /S Pa	1.437	

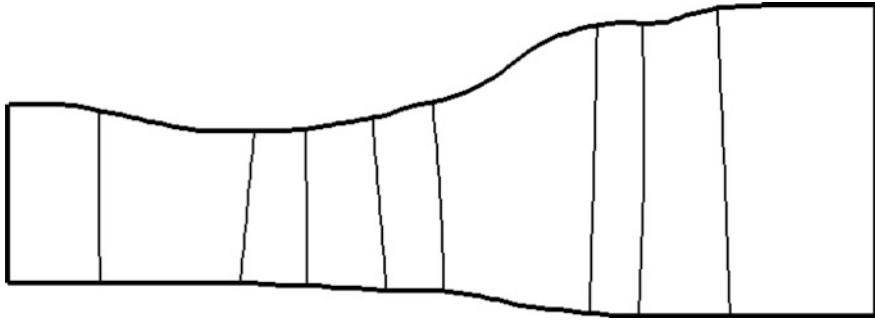


Fig. 6.117 Flow passage of a HP-LP turbine

Table 6.15 Deviations of stacking positions after adjustments to the center of gravity

Blade number	$\overline{\Delta l}$			$\overline{\Delta t}$		
	Root section	Middle section	Tip section	Root section	Middle section	Tip section
1S	0	/	0	0	/	0
1R	0.0139	/	-0.0357	0.0036	/	0.0046
2S	0.0359	0.0077	-0.0030	-0.0015	0.0022	0.0027
2R	-0.0107	-0.0411	-0.0518	0.0026	0.0026	0.0034

To solve the above problems, this subsection is devoted to determining the influence of adjustments to the center of gravity on the aerodynamic and heat transfer performance through numerical simulation of a two-stage air-cooled turbine. 6.6 million grids are adopted to this two-stage HP and LP air-cooled turbine, in which the total cooling air flow accounts for 20.08% of the turbine inflow. Table 6.14 shows the overall parameters of the turbine, with the meridional flow-passage shown in Fig. 6.117.

Table 6.15 shows the relative values of the axial and circumferential profile deviations of the blades after adjustments to the center of gravity. Stator blades of the first stage were not adjusted. $\overline{\Delta l}$ and $\overline{\Delta t}$ are defined in Eq. (6.179) and Eq. (6.180), in which Δl is the absolute axial offset of the profile, B is the axial chord length of the profile, Δt is the circumferential offset of the profile, R is the radius of the profile. Only the influence of deviations in axial position and circumferential position on the aerodynamic and heat transfer performance is considered in this subsection, while that of deviations in the amount of blade twist caused by the adjustments during the strength verification is not taken into consideration.

$$\overline{\Delta l} = \Delta l / B \tag{6.179}$$

$$\overline{\Delta t} = \Delta t / R \tag{6.180}$$

Table 6.16 Comparison of aerodynamic performance before and after adjustments of blade parameters

	Stage1	Stage2
FC	1.191/1.195	0.809/0.805
Ω	0.332/0.319	0.326/0.325
$\Delta h/U^2$	1.380/1.383	0.864/0.859
α_2	86.72/86.08	
η_t	88.64%/88.53%	

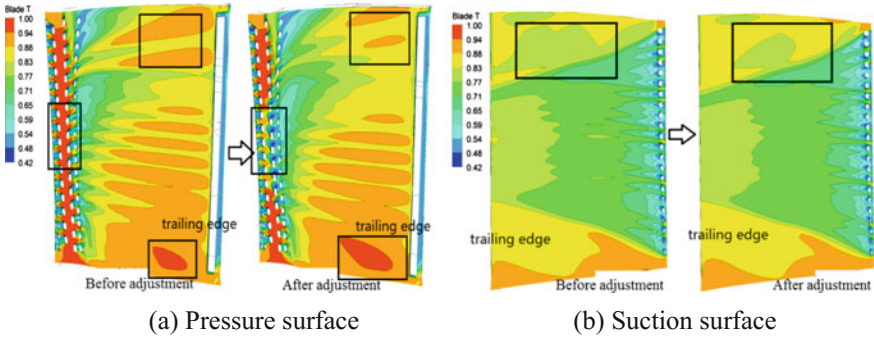


Fig. 6.118 Rotor blade surface temperature distribution before and after adjustments

Table 6.15 shows the comparison of the calculated results. As can be seen, the adjustment range for the turbine is very small, and the influence of blade twist is ignored. Table 6.16 shows the comparison of some key aerodynamic parameters, indicating that the adjustments to the blade lead to the increment of 0.11% in the aerodynamic efficiency and the increment of 0.20% in the turbine inflow angle. Therefore, the influence of adjustments to blade position in the later strength check process on aerodynamic performance is non-negligible.

There are no film cooling holes on the stator blade of the first turbine stage, which were not adjusted. To analyze the heat transfer performance, the rotor blades with six film cooling holes of the first stage, which have been adjusted, were selected as the object. Figure 6.118 shows the influence of the deviation of the blade position on film cooling. Figure 6.118a shows the temperature distribution on the pressure side of the rotor blades. It can be seen that, after the adjustments, cooling conditions in the tip region and leading edge region of the blades on the pressure side became better, while the conditions in the root region became worse slightly. Figure 6.118b shows the temperature distribution on the suction side. It can be seen that, after the adjustments, heat transfer conditions in the tip region of the blades on the suction side became worse slightly, while the other regions were unaffected basically. The averaged temperature of the blade decreased by 10 K, and thus the adjustments to the blade positions had favorable influence on film cooling.

Results of heat transfer analysis of the rotor blades show that, the adjustments to blade positions were beneficial for the cooling in the tip region on the pressure side, while detrimental to the cooling in the root region on the pressure side and the tip region on the suction side. The averaged temperature of the entire blade dropped by about 10 K, and the overall cooling effect was slightly enhanced. However, it should be noted that due to the highest temperature in the root region on the pressure side, the temperature rise in this region was to the disadvantage of life span of the blade.

It is thus clear that aerodynamic design and heat transfer design should be combined with structural strength analysis so as to shorten the entire turbine design cycle and improve reliability of aerodynamic design and heat transfer design. This, from another perspective, reflects the importance and necessity of multidisciplinary concurrent design.

6.7 Fine Flow Organizing and Design Technologies

6.7.1 Basic Concept of Fine Flow Organizing and Design

The traditional turbine design technologies, which are based on conventional cascade profiling and 3D stacking, have been much more mature through decades of development, and the design capability and design level of turbine have been improved greatly. However, as the power of aircraft is getting more and more demanding, traditional turbine design technologies have been unable to meet the demand of further improvement of turbine performance for the future aero-engines. Therefore, it is necessary to carry out in-depth and systematic studies on details and characteristics of flows, which are ignored in traditional design system. It is also necessary to explore specific fine flow organizing methods for turbines, add new degrees of freedom to the aerodynamic design, and further improve turbine design methods and tools. Only through these efforts, turbine design capabilities can be further improved. This is also a hot topic in the field of turbine aerodynamics.

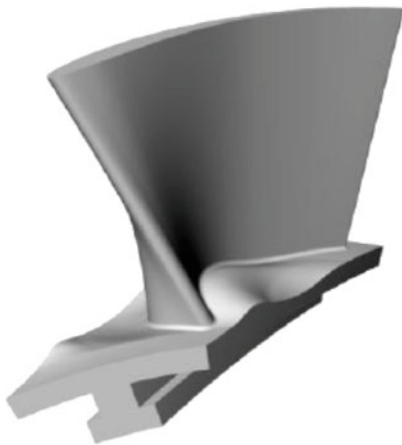
Focusing on fine flow organizing and design, this section gives a brief introduction to the current applications of a series of typical technologies in turbine design, including nonaxisymmetric endwall modeling technologies, blade-endwall integration design technologies, fine organizing technologies for rotor blade tip leakage flows, fine organizing technologies for shock wave systems in supersonic blades, flow organizing technologies considering the interference effect of cooling air to the main flow, integration design technologies for struts and intermediate turbine duct, and aerodynamic design technologies considering unsteady effects.

6.7.2 Applications of Fine Flow Organizing and Design

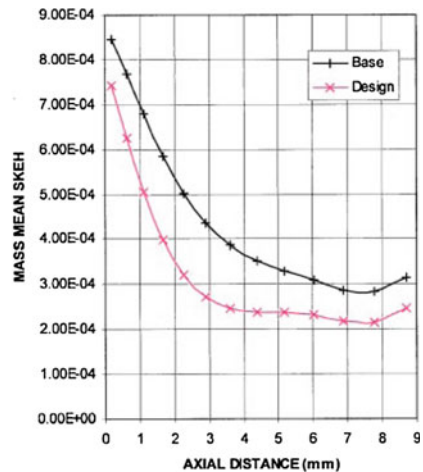
6.7.2.1 Nonaxisymmetric Endwall Modeling Technology

The secondary loss in endwall regions of a turbine is one of the main sources of turbine flow losses, which is also a key factor influencing the matching of the small-aspect-ratio blade rows. How to control secondary loss is critical to aerodynamic design of high-performance turbines. Blade curving and sweeping are good for controlling the secondary loss, which have been used extensively. However, it is difficult to adopt blade curving and sweeping directly to air-cooled turbines, due to the additional difficulties that they would bring to the structural strength and machining of air-cooled blades. Thus, it is imperative to develop new technologies to control the secondary flows in the endwall regions, among which the nonaxisymmetric endwall modeling technology has gained great attention and has been successfully used in turbine design [155, 156].

The nonaxisymmetric endwall modeling technology is compared with traditional turbine design technologies which adopt the design of axisymmetric endwalls. The original intention of this technology is to change the pressure distribution in the endwall regions of the flow passage by building the surface of the hub and then reduce the secondary flow intensity and control the secondary loss, as shown in Fig. 6.119a. Based on this idea, Kopper et al. used nonaxisymmetric geometries to regulate and control local flow structures as early as 1981, and reduced the flow loss by 17%, as the experimental results indicated [157]. However, due to the limitation



(a) Nonaxisymmetric endwall structure



(b) Intensity of secondary vortices [160]

Fig. 6.119 Application of nonaxisymmetric endwall modeling in HP turbine of TRENT engine

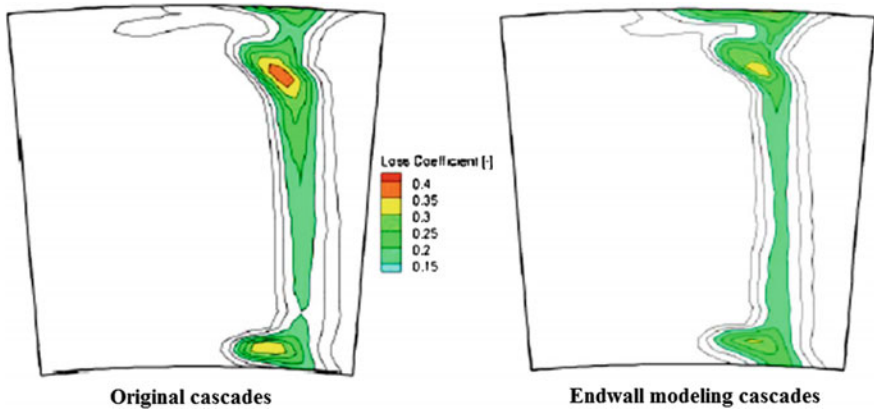


Fig. 6.120 Loss distribution on outlet section of first-stage guide vanes [162]

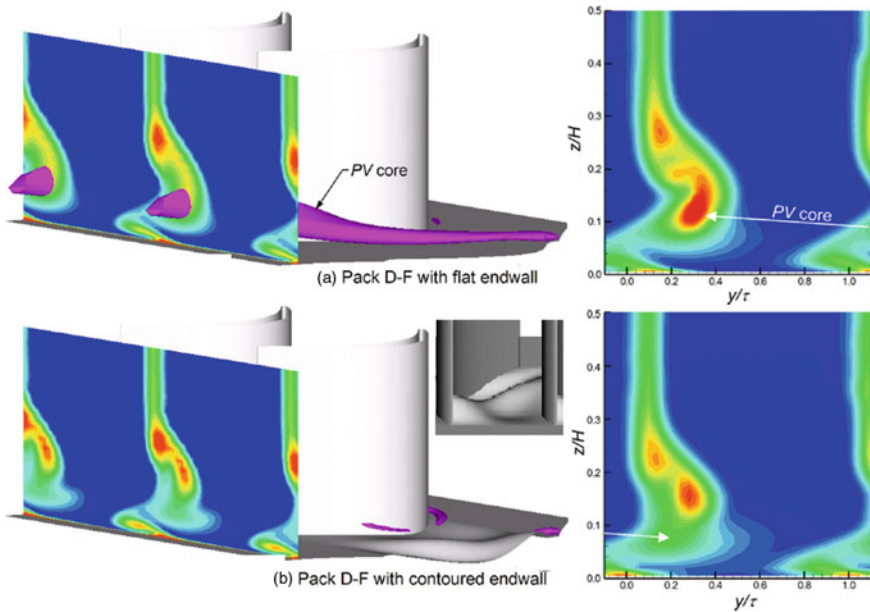


Fig. 6.121 Passage vortices and outlet TKE in high-loaded LP turbine cascades with nonaxisymmetric endwall [164]

of the research level and technical conditions of the time, the study did not fully consider the influence of endwall design on downstream flows. With the development of technologies, researchers have begun to use fully 3-D viscous numerical calculation and other methods to carry out studies on the nonaxisymmetric endwall modeling technology, and developed relevant design methods. The most

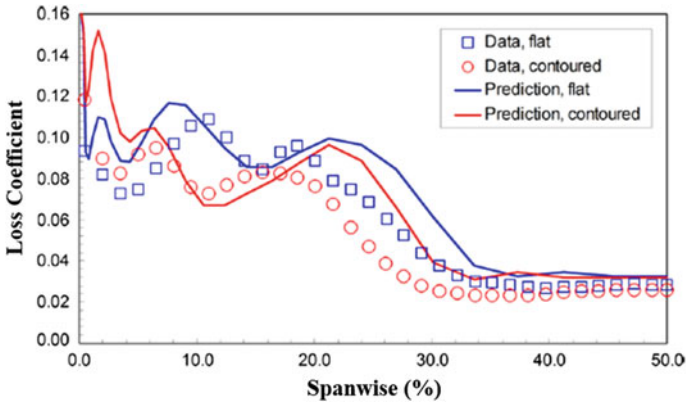


Fig. 6.122 Radial distribution of loss with nonaxisymmetric endwall [164]

representative example of these methods is the continuous cooperation research carried out by Durham University (England) and Rolls-Royce Company. Rose et al. first used the sinusoidal endwall modeling method to weaken the pressure peak in the endwall region between the guide vane and the rotor in a HP turbine and succeeded in reducing the coolant air flow [156]. After that, Hartland et al. from Durham University further developed a nonaxisymmetric endwall design method, which was verified by low-speed cascade tests. The results suggested that the transverse pressure gradient was weakened and the secondary loss was reduced by 34%. Meanwhile, the excessive deflection of the flow angle in the endwall region at the outlet, which is due to the influence of the small vortexes induced by the endwall surface, was weakened [158, 159]. Based on these studies, they applied this nonaxisymmetric endwall modeling technology to the design of the HP turbine of TREN500 engine. Figure 6.119b presents the comparison of the calculated results of the axial distribution of SKEH at the outlet of guide vanes with axisymmetric endwall design and nonaxisymmetric endwall design. The results showed that nonaxisymmetric endwall design could significantly reduce the intensity of the secondary flows at the hub. Experimental results also suggest that nonaxisymmetric endwall design could increase the efficiency by $0.59\% \pm 0.25\%$ [160, 161]. Germian et al. from MTU successfully improved the efficiency of a 1.5-stage high-power turbine by the nonaxisymmetric endwall modeling technology [162, 163], and the experimental results showed that not only the turbine efficiency was increased by $1.0\% \pm 0.4\%$ but also the flow conditions at the mid-span section were improved to some extent. Reduction in the loss of the upstream blade rows helps to improve the inlet conditions of the downstream blade rows, as shown in Fig. 6.120. These comprehensive factors contribute to the great improvement of the turbine performance.

The nonaxisymmetric endwall modeling technology is also effective in controlling the increase of the secondary loss in the endwall regions in high-loaded LP turbines. Praisner et al. from Pratt & Whitney Company made a useful attempt in

this area, and succeeded in applying the nonaxisymmetric endwall modeling technology in the ultra-high-loaded LP turbine cascade with a Zweifel coefficient as high as 1.4 [164, 165]. Figure 6.121 shows the development of passage vortices in the cascades and the corresponding TKE at the outlet, where PV represents the passage vortices. It can be seen that the development of the passage vortices was inhibited effectively by the nonaxisymmetric endwall design, and the secondary loss was decreased significantly. Figure 6.122 gives the radial distribution of the loss, from which it can be seen that the loss in the regions that covers a wide range of blade height was decreased significantly by as much as 13.3%. This technology has also been successfully used in the design of the high-loaded LP turbine in Rolls-Royce TRENT900 engine [166].

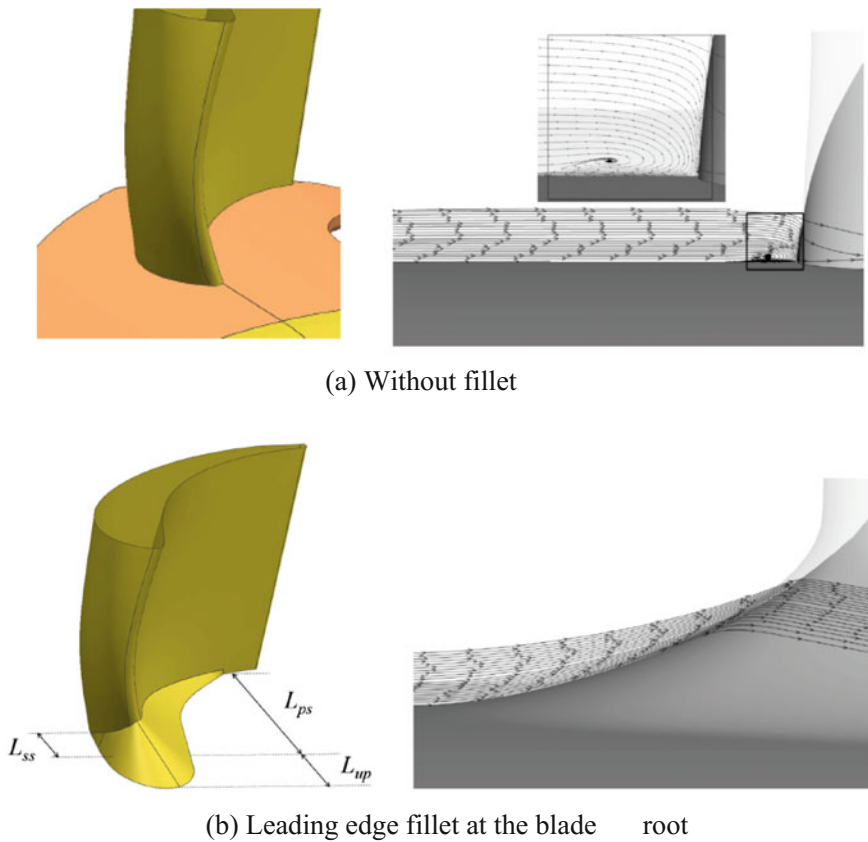


Fig. 6.123 Influence of leading edge fillet at the blade root on development of horseshoe vortex [169]

6.7.2.2 Blade-Endwall Integration Design Technology

Besides the nonaxisymmetric endwall modeling technology, the blade-endwall integration design technology is also helpful to reduce the secondary loss in endwall regions [167, 168]. The geometry at the junction between the blade and the endwalls has influence on local pressure field and flows. Particularly, the shape of the leading edge at the root has an important influence on the development of horseshoe vortices. With the blade-wall integration design technology, fine adjustments are made to the geometry, thus the flows can be organized effectively so that the secondary flow would be weakened.

The modification method of creating a leading edge fillet at the blade root can accelerate the incoming boundary layer and reduce the radial pressure gradient at the leading edge of the blade in the endwall region, thus inhibiting the development of the horseshoe vortices. As shown in Fig. 6.123, when there was no fillet at the blade root, the flow would stagnate at the leading edge, move towards the endwalls driven by the radial pressure gradient, and then roll up, thus forming a horseshoe vortex. While, when a leading edge fillet is created, the flow would accelerate bypass the leading edge and thus the horseshoe vortex could be eliminated [169]. The numerical simulation and experimental studies by Zess and Thole suggest that, when the fillet is as much as the thickness of the inflow boundary layer in height and twice as much as the thickness in length, the secondary flows would be controlled to the full extent [170]. Turgut et al. from Pennsylvania University combined this technology with the nonaxisymmetric endwall modeling technology, and lowered the flow losses in the endwall regions significantly, with the loss at the guide vane outlet reduced. Flow losses in the endwall regions were significantly decreased, and the loss at the guide vane outlet was reduced by 1.84% [169] as shown in Fig. 6.124. Then, they further studied the interaction between the main gas flow and the coolant air from the hub, and pointed out that, because that the transverse flows at the hub are weakened by the leading edge fillet, the momentum

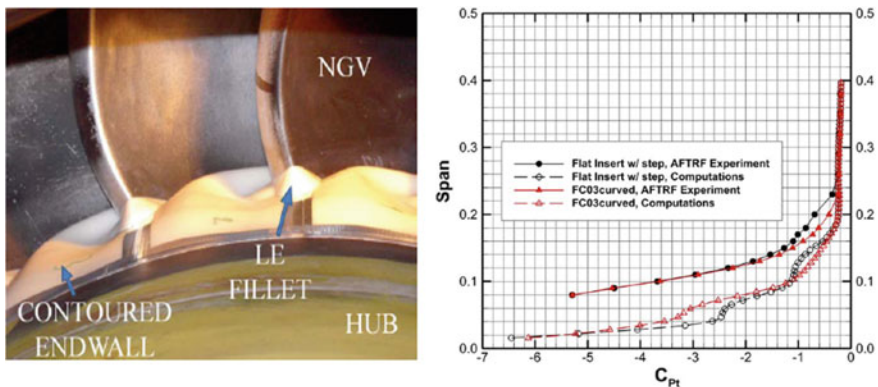
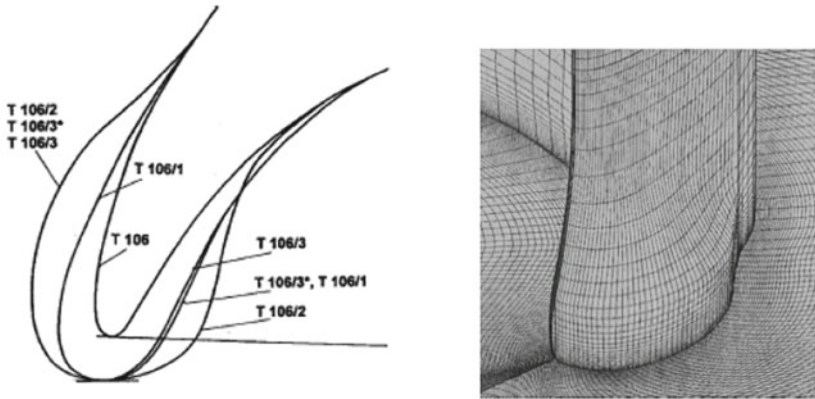
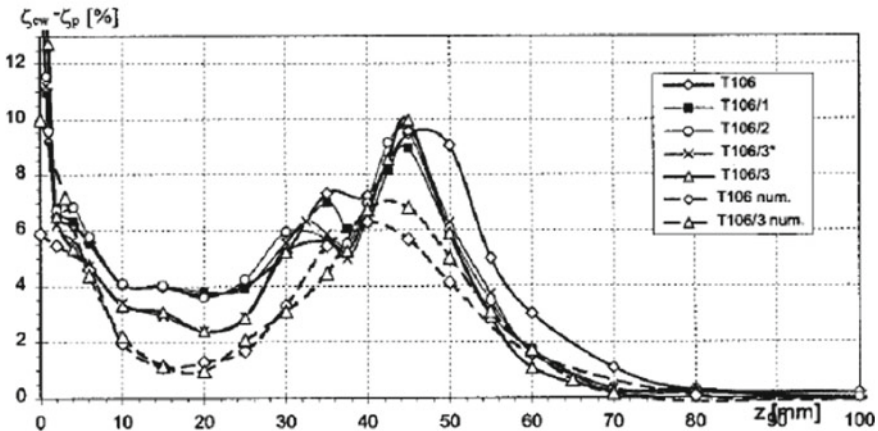


Fig. 6.124 Combination of leading edge fillet and nonaxisymmetric endwall [169]



(a) Leading-edge small bulb



(b) Spanwise distribution of loss coefficient

Fig. 6.125 Secondary loss control by using leading-edge small bulb [172]

loss of the boundary layer can be reduced and the loss due to the mixing of the main flow and the downstream coolant air can be then lowered [171].

Sauer et al. were the first to use the small bulb at the leading edge of the blade root to weaken the outlet passage vortex by enhancing the branch of the horseshoe vortex on the suction side, which rotates in the opposite direction to the passage vortex. As shown in Fig. 6.125, when the volume of the small bulb on the suction side is larger than that on the pressure side, the secondary loss in the endwall regions was greatly reduced by as much as 50% [172]. Whereafter, Becz and Majewski studied the integration of root fillet and two spherical structures (both small and large) with experiments [173]. The results showed that the leading edge with the fillet and the small spherical structure can reduce the secondary loss

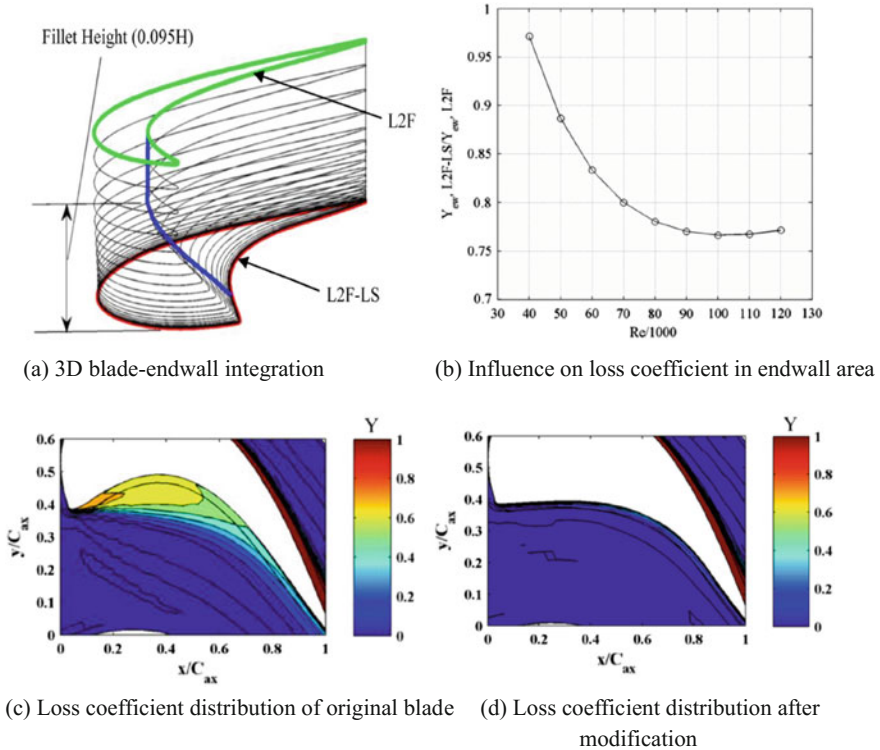


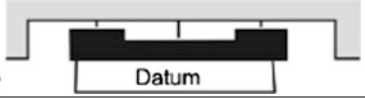



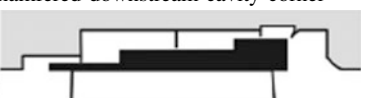
Fig. 6.126 Blade root and endwall integration in a high-loaded turbine [174]

effectively, while the leading edge with the large fillet and the small spherical structure would increase the secondary loss on the contrary. They also pointed out that the leading edge fillet and the small spherical structure can be integrated in optimization design since they are different in the mechanism of reducing the aerodynamic loss. Lyall et al. applied the blade-endwall integration design technology to the high-loaded turbine cascade with a Zweifel coefficient as high as 1.57 to reduce the losses in endwall regions. Figure 6.126 shows the model at the blade root and the distribution of the loss coefficient. It can be seen that the separation flow on the pressure side was eliminated, and the secondary loss in the endwall regions was reduced. Experimental measurements suggested that the flow losses in the endwall regions were reduced by about 23% [174, 175].

6.7.2.3 Fine Organizing Technology for Rotor Blade Tip Leakage Flows

There is a clearance between the rotating blade and the fixed casing in a turbine, and the main gas flow would produce leakage flow at the blade tip driven by the

Table 6.17 Influence of changes in shroud geometric parameters on turbine performance [177]

Geometry	$\eta/(\Delta\eta)$ [%]	
	Leakage 1.48%	Leakage 1.78%
 <p>A Datum</p>	89.84	89.42
<p>Minimised inlet cavity</p>  <p>B</p> <ul style="list-style-type: none"> - Reduced mixing losses in the cavity, - Improved flow field in the rotor, - Reduced leakage fraction 	90.12 (+0.28)	89.77 (+0.35)
<p>5 mm extended shroud overhang</p>  <p>C</p> <ul style="list-style-type: none"> - Reduced main passage fluid ingress - Reduced circumferential pressure non-uniformity in the inlet cavity 	90.20 (+0.36)	89.86 (+0.44)
<p>Radial deflector in the exit cavity</p>  <p>D</p> <ul style="list-style-type: none"> - Redirected leakage jet: reduced jet radial velocity component - Reduced separation at the cavity downstream edge - Improved downstream stator secondary flows - Reduced leakage fraction 	90.38 (+0.54)	90.09 (+0.67)
<p>Chamfered downstream cavity corner</p>  <p>E</p> <ul style="list-style-type: none"> - Further reduction in corner separator - Improved downstream stator secondary flows 	90.44 (+0.60)	90.17 (+0.75)

pressure difference between both sides of the gap. As a result, the power capacity of the flow would decrease, and the mixing loss would increase. In addition, the turbine performance would deteriorate further with significant changes in the inlet conditions of the downstream blade row. Therefore, it is very important to reduce the tip loss. Besides the conventional methods such as adjusting the loading distribution of the blade tip, active control of the tip clearance, etc., optimization design of the tip geometry and fine organizing of the flows can be also used to reduce the leakage flow and additional aerodynamic losses. What follows are the

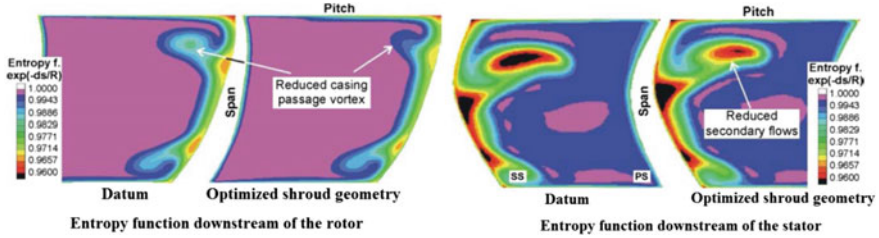


Fig. 6.127 Entropy function contours before and after shroud optimization [177]

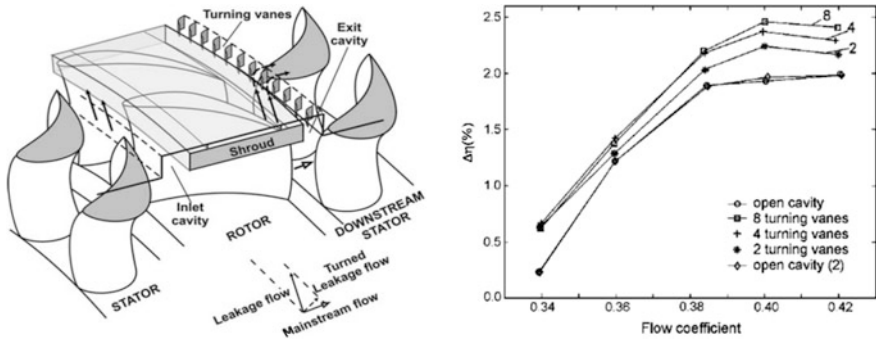


Fig. 6.128 Shroud leakage flow control by outlet turning vanes [179]

introduction of the fine organizing methods for tip flows, which are suitable for shrouded turbines and unshrouded turbines respectively.

(1) Tip flow organizing for shrouded turbines

In shrouded turbines, there is significant momentum difference between the leakage jets and the main flow, causing great mixing losses. In addition, the downstream blade row would be in the negative-incidence state, thus causing more loss. Therefore, to reduce aerodynamic losses, it is necessary to organize the leakage jets, such as the jet angle of the leakage flow in the meridional plane and along the tangential direction. Schlienger et al. were the first to use the method of modifying the endwall to organize the leakage flow in the meridional plane, realizing the control of the the pressure distribution on the endwall of the downstream blade effectively, as well as the secondary loss [176]. Whereafter, Rosic systematically studied and compared the influence of different shroud geometries and meridional jet patterns at the outlet on the aerodynamic losses [177]. They used baffles, the axial and radial guide plates to control the outflow of the shroud, and pointed that reducing radial velocity of the jet flow is one of the effective methods of reducing the mixing loss and avoiding negative influence on the downstream blade rows.

Based on that, they studied the influence of the shroud parameters by numerical simulation. Table 6.17 shows the influence of changes in shroud geometric parameters on the performance of two turbines with different tip clearances. The 0.75 mm clearance is the corresponding clearance of the tip leakage flow 1.48%, while the 1.00 mm clearance corresponds to the tip leakage flow 1.78%. It can be seen that the turbine efficiency could be increased by 0.6%–0.75%, with the shroud geometric parameters optimized. Figure 6.127 shows the entropy function contours at the outlet sections of the rotor and the downstream stator, before and after the optimization of the 1.00 mm clearance (corresponding to A and E in Table 6.17 respectively). Obviously, with the clearance optimized, the loss near the rotor casing was decreased and the flow field at the outlet of the rotor was improved. As a result, the secondary flows in endwall regions of the downstream stator casing was weakened, with the secondary loss reduced. In addition, because that the shroud leakage flow is not deflected through blade rows and is affected by the friction with the casing, there would be an obvious circumferential momentum difference between the leakage flow and the main flow, which is one of the main sources of the blade tip loss in shrouded turbines [178]. For this reason, Rosic and Denton used the method of arranging small turning vanes in the cavity at the shroud outlet to control the tangential velocity of the leakage jet flow and reduce mixing loss and additional secondary loss, as shown in Fig. 6.128. Experimental verification was carried out on the turbine test rig of University of Cambridge, and results suggested that the efficiency under the design condition (flow coefficient = 0.384) was increased by 0.4%, and that the efficiency could improved in a wide operating range by reasonable flow organizing. The study also indicated that control effect of the turning vanes in the cavity at the shroud outlet is closely related to the geometry and the pitch of the blade [179].

(2) Tip flow organizing for unshrouded turbines

The tip leakage flow in unshrouded turbines will not only reduce the power capability and cause mixing loss, but also increase local thermal load at the blade tip. Therefore, fine organizing of flow structures at the blade tip, as well as the local

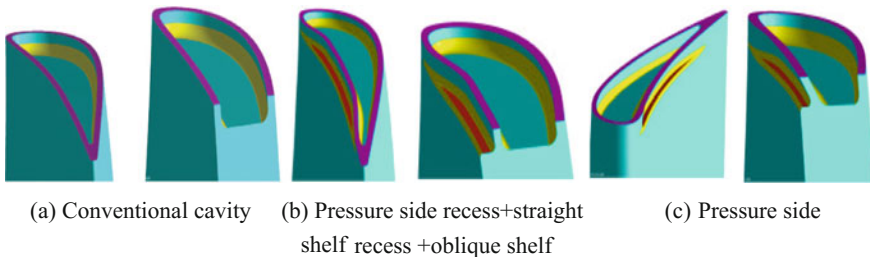


Fig. 6.129 Schematic of different tip geometries [185]

aerodynamic load, should be carried out to reduce the flow losses and thermal load. Currently, fine modifications of the blade tip geometry are the most commonly studied method for the tip flow organizing, such as tip cavity, combination of cavity and ribs, tip winglet, and chordwise variable tip clearance. Tip cavities can reduce the tip leakage flow by increasing the kinetic energy loss in the clearance and thus reduce the mixing loss of the leakage flow. Tip winglets can control the leakage flow by changing the velocity distribution on both sides of the blade tip to reduce the pressure difference between the two sides, especially by increasing the velocity on the pressure side. Compared with flat tips, tips with cavity have huge superiority in aerodynamic performance, which can reduce the leakage flow significantly [180, 181]. Among different tips with cavity, semi-tips with rib on the suction side are the best to control the jet coefficient and flow losses [182]. Geometry and parameters of tip cavities have significant influence on the tip heat transfer [183, 184]. GE Company carried out a comparative study on its patented product, namely composite structure of tip cavity and pressure side concave, with the conventional cavity structures, as shown in Fig. 6.129. The results suggested that the composite structure of pressure side concave and oblique rib is helpful to reduce the tip leakage flow and to reach the ideal efficiency [185]. Currently, GE Company has successfully applied the tip cavity technology in the design of the HP turbine for LEAP-X and other large-bypass-ratio turbofan engines. Besides the tip cavity technology, the tip winglet technology has also become one of the important methods for controlling the leakage flows. For example, Booth et al. discussed the application of tip winglets in low-aspect-ratio transonic turbines of engines, and increased the efficiency of the rotor by 0.6% at the design point and by 1.05% at the highest speed allowed in the experiment [181]. Pate increased the efficiency of a

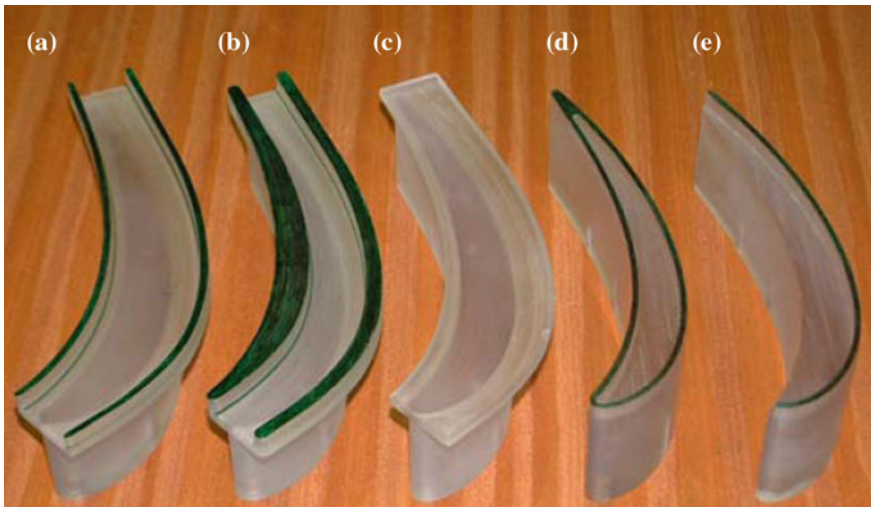
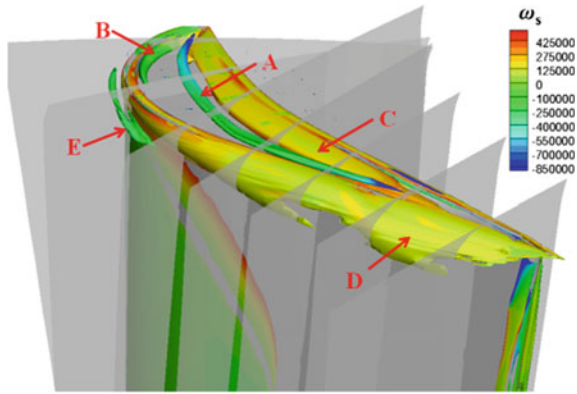


Fig. 6.130 Different combinations of tip cavity and winglet [187]

Fig. 6.131 Typical vortex structures around blade tip with cavity [188]



turbine stage by 1.2% by the similar method [186]. In addition, the combination of rib and winglet has gained more attention in recent years. For example, Schabowski and Hodson from University of Cambridge carried out a comparative study on different combinations of tip rib and winglet, including rib with winglet, only winglet, tip with cavity, and rib on the suction side, by detailed experiments and numerical simulations. Experimental results show that the combination of rib with winglet is the optimal, which can reduce the loss by 22% compared with the original flat tip [187]. Zou et al. [188] from Beihang University analyzed the development and evolvement of the vortex structures in the squealer tip, and came to the conclusion that the vortex structures lingering in the rotor tip cavity may cause blocking effect on the leakage flow, thus inhibiting the leakage flow and changing key parameters of the leakage flow including the momentum and flow angle, as shown in Fig. 6.131. They also found and preliminarily confirmed the existence of the dominating vortex in the cavity, as well as the basic characteristics

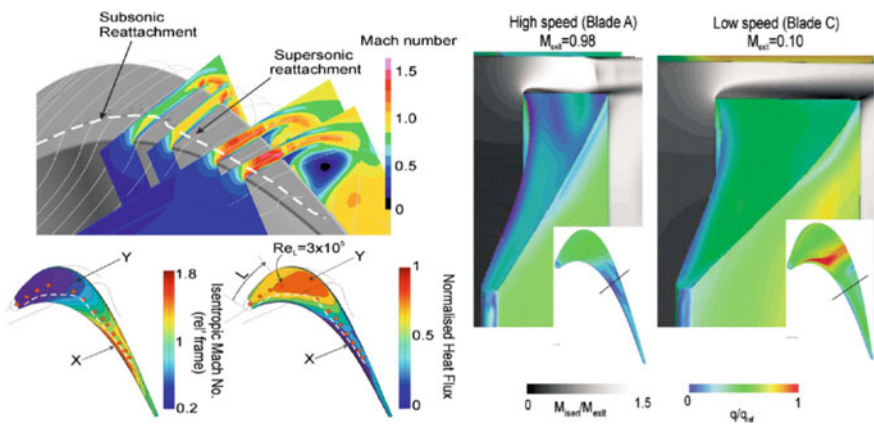


Fig. 6.132 High-speed tip flow and comparison of heat transfer between high-speed and low-speed tip flows [189]

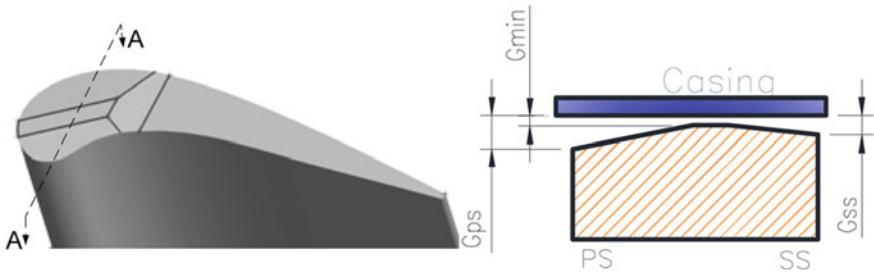


Fig. 6.133 Flow organizing method of convergent-divergent tip design [190]

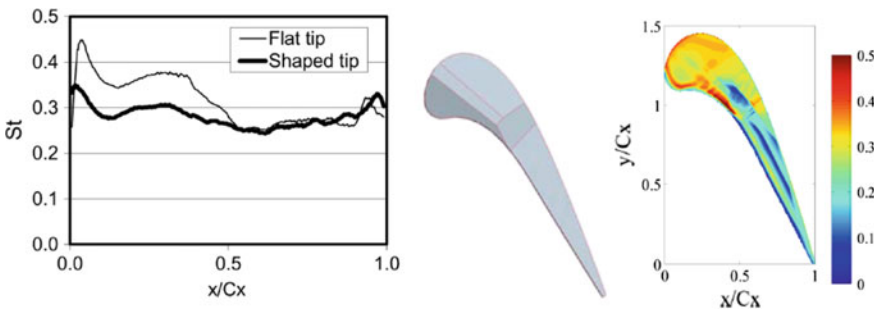


Fig. 6.134 Influence of tip shape on heat transfer [190]

of this dominating vortex, by studying the variation in the distribution of key parameters (including leakage flow rate and momentum) under different cavity geometries, and proposed thoughts of controlling the leakage flow, which are based on reasonably organizing of the vortex systems in the tip region, providing a new and potential method of controlling the tip leakage flow and its influence effectively. In addition, they have preliminarily realized effective control on the tip leakage flow through optimization design of the tip shape and reasonable use of vortex structures, and increased the aerodynamic efficiency of a turbine rotor by more than 0.5%. This achievement proves the huge potential and value of reasonable organizing of the the tip vortex system for controlling the tip leakage flow.

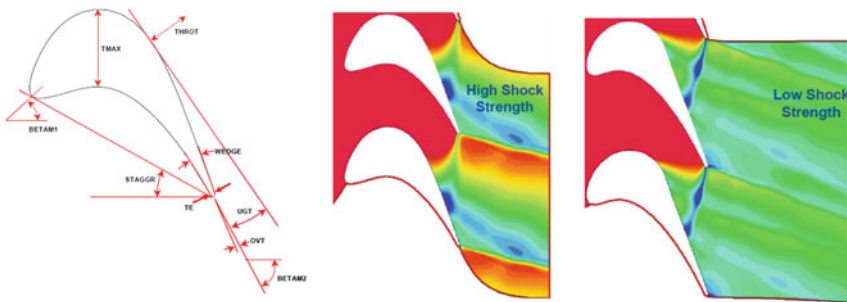
(3) Difference in tip flow heat transfer between high-speed and low-speed inflow conditions and its influence on design

It is worth noting that there is obvious difference in the tip flow between high-speed inflow condition and low-speed inflow condition, which may even lead to opposite heat transfer characteristics of the tip flow. Since the inlet Mach number at the blade tip of HP turbines is relatively high, the tip flows are generally transonic. For this reason, the research results on the heat transfer performance of the tip flow, obtained in low-speed incompressible cascade experiments, should be interpreted

carefully before used in design. He et al. from University of Oxford found that, compared with low-speed tip flows, the heat transfer performance of transonic tip flows would be influenced by both the heat transfer coefficient and the recovery temperature drop [189]. In high-speed tip flows, the separation bubble on the pressure side would re-attach rapidly in the accelerating process of the tip flow. If the outlet Mach number at the blade tip increases from 0.1 to 1.0, the length of the separation bubble would be halved. In addition, the interaction between the tip shock waves and the boundary layer would change the boundary layer at the tip. All these changes of the flow structures would finally cause significant changes of heat transfer coefficient of the tip. In addition, the high Mach number ($M > 1.5$) in the tip region would lead to obvious local changes of the recovery temperature, as shown in Fig. 6.132. Compared with low-speed tip flows, high-speed transonic tip flows are lower in turbulent dissipation and less sensitive to the turbulence models in numerical simulation. Based on these studies, they proposed a flow organizing method to control the heat transfer performance of the tip by designing of the tip shape. As shown in Fig. 6.133, the convergent-divergent design was adopted at the blade tip to accelerate the leakage flow to supersonic speed, thus reducing the thermal load at the tip. Meanwhile, the aerodynamic throat would also lead to the decrease of the leakage flow [190]. Figure 6.134 presents the comparison of the experimental results of the averaged circumferential St number before and after blade modeling, as well as the distribution contour of St number after the improvement to the tip shape. The results prove the effectiveness of this method.

6.7.2.4 Fine Organizing for Shock Wave Systems in Supersonic Blades

As the expansion ratio of a turbine stage and the outlet Mach number increase constantly, the shock loss has become an important component of the flow losses in



(a) Profile parameter optimization (b) Static pressure distribution in original turbine
 (c) Static pressure distribution in optimized turbine

Fig. 6.135 Comparison of flow field between original and modified turbine [195]

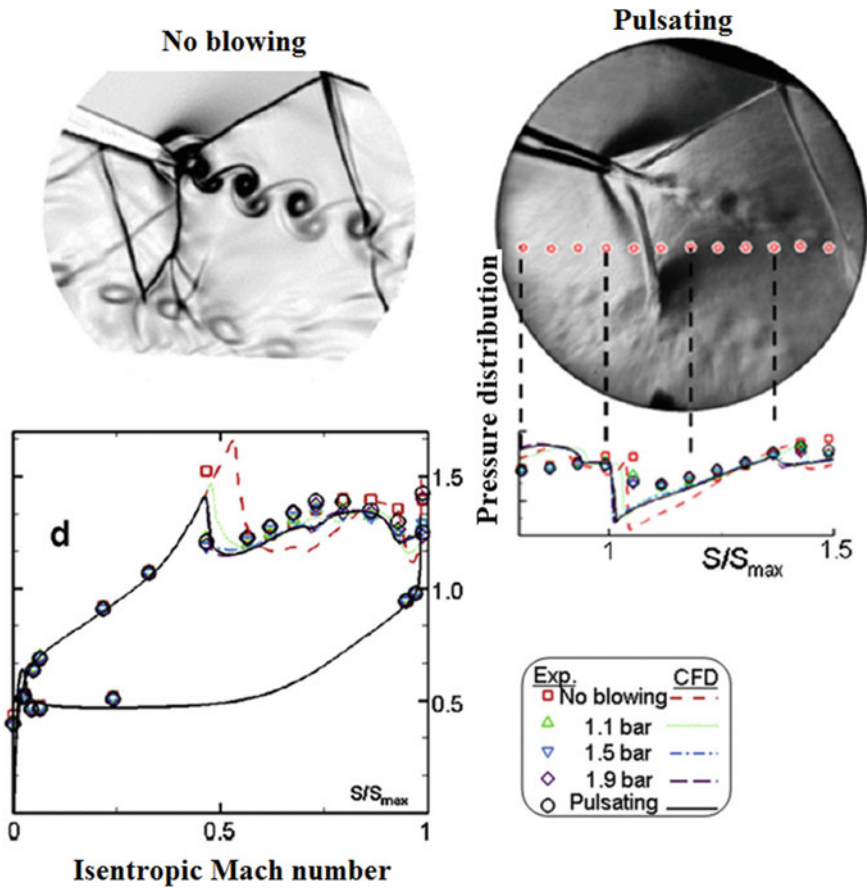


Fig. 6.136 Reducing shock loss by pulse coolant jet at the trailing edge [196]

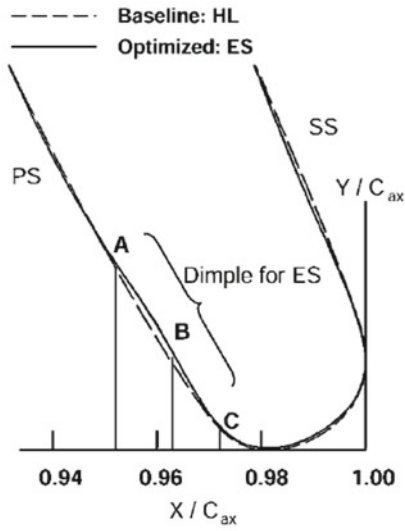
transonic turbines. Particularly, the shock loss at the trailing edge of the blade may account for up to 1/3 of the entire aerodynamic losses in transonic turbines. Factors including the outlet pressure, the boundary layer thickness, the profile characteristics, and the trailing-edge coolant jet would influence the strength of the shock wave, as well as the aerodynamic loss [191]. In addition, the unsteady force caused by the shock wave in the upstream row sweeping and going into the blade passage in the downstream row would also bring problems such as high-cycle fatigue of the turbine blade [62, 192]. Therefore, it is an important way to organize the wave systems reasonably to reduce the aerodynamic loss and the unsteady force, thus improving the performance and reliability of transonic turbines.

(1) Organizing of complex shock wave systems in high-loaded transonic turbine blades

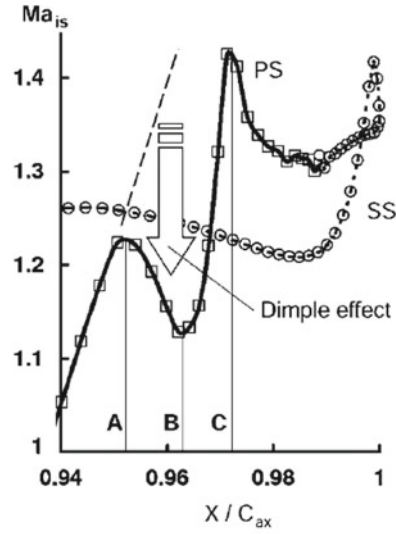
The shock loss in the blade passage is closely related to the profile characteristics. For example, the shock loss can be reduced by adjusting the curvature of the blade after the throat [193]. The trailing edge thickness would also directly influence the strength of the trailing-edge shock waves and even the shock wave interaction between the blade rows. Studies have shown that increment of the trailing edge thickness would lead to increase of the shock loss in the present blade row, while decrease of the shock reflection loss in the downstream row, thus reducing the total loss [191, 194]. A series of practical measures for reducing the shock loss in supersonic turbines have been proposed in the Highly-Loaded Turbine Research Program (HLTRP) which was jointly implemented by NASA and GE, including adopting the convergent-divergent profile, reducing the trailing-edge bending angle, optimizing the stagger angle and the deviation angle, adopting the straight suction side with the trailing-edge thickness reduced, optimizing the trailing-edge wedge angle, etc. [195], as shown in Fig. 6.135. The wave systems in the supersonic blade of a single-stage HP turbine, whose expansion ratio is 5.5, was organized and the strength of the shock wave was significantly weakened. Experimental results suggested that the efficiency of the HP turbine can be increased by 2%, with the loading coefficient increased by 33%. In addition, the slot cooling is frequently adopted in HP turbines. Research shows that reasonable control of the coolant jets from the trailing-edge slots can also reduce the shock loss. Saracoglu et al. studied the method of adopting the pulse coolant jet at the trailing edge to control the shock loss [196]. Figure 6.136 shows the isentropic Mach number distribution of the blade with and without the pulse coolant jet and the comparison of the results obtained by schlieren visualization. It can be seen that, with the pulse coolant jet at the trailing edge employed, the shock wave was weakened obviously, and the inclination angle of inner tail waves was also changed significantly.

(2) Profile optimizing technology for high-loaded transonic turbine

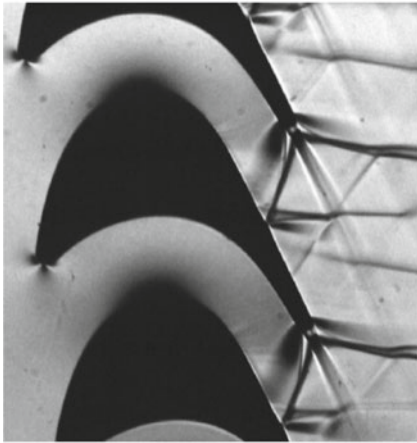
With the deep-going studies on aerodynamic design technologies for turbines and the enhancement of computing power, optimization methods have been gradually applied in the field of fine organizing of the wave systems in supersonic blades in recent years. Sonoda et al. from Honda Company optimized the profile of a highly-loaded transonic turbine by genetic algorithm [197]. After the optimization, changes were observed in the position of maximum thickness, as well as the profile curves near the trailing edge on both the pressure side and the suction side, such as the negative curvature of the pressure side near the trailing edge. Due to these changes of the blade profile, the strong inner tail waves of the original blades were substituted by the double shock waves which are weaker in strength, as shown in Fig. 6.137. Finally, the aerodynamic loss was reduced by 12%, and the deviation angle was decreased in the meantime. Figure 6.138 shows the local schlieren diagram of the separation bubble of the original blade. As can be seen, the incoming laminar boundary layer separated under the effect of the strong shock waves, and the separation bubble brought two reflected shock waves. In the optimized blades, a



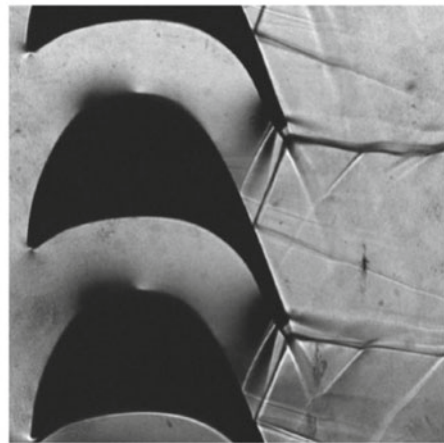
(a) Trailing edge profile



(b) Distribution of isentropic Mach number near the trailing edge



(c) Wave system of the original blade



(d) Wave system of the optimized blade

Fig. 6.137 Optimizing wave system by genetic algorithm in supersonic turbine blades [197]

deceleration region was formed on the suction side, which bring forward the flow transition and development into full turbulence in the boundary layer, thus improving the anti-separation ability of the boundary layer. Hence, not a single separation bubble was observed.

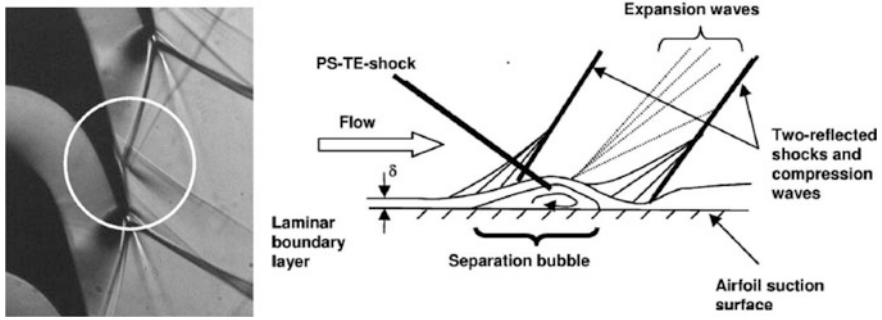


Fig. 6.138 Separation bubble generated by interaction of shock waves and boundary layer [197]

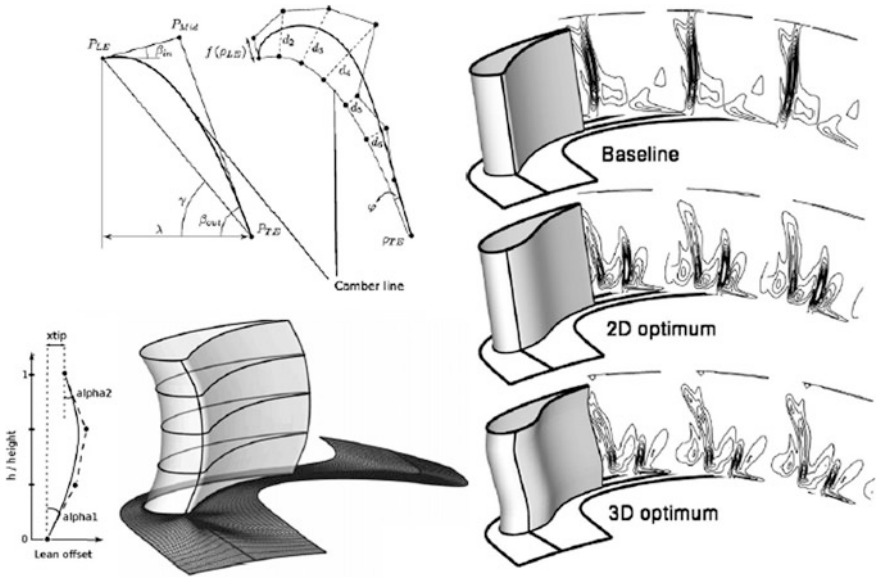


Fig. 6.139 Optimization results of supersonic turbine blades [192]

(3) Influence of shock wave in highly-loaded transonic turbines on unsteady force in downstream blade rows

It should be noted that two aspects of negative influence would be brought in by the shock waves, which are the aerodynamic loss and the unsteady aerodynamic force. With the increase of the expansion ratio of HP turbines, this phenomenon will be more prominent. Therefore, the influence of both the aerodynamic performance and the unsteady aerodynamic force should be considered in blade optimization design for advanced transonic turbines. Joly et al. from Von Karman Hydrodynamics Institute (Belgium) carried out a series of studies in this area [198, 199]. They

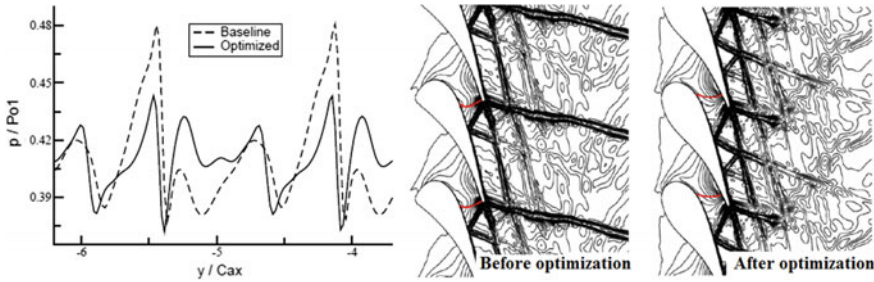
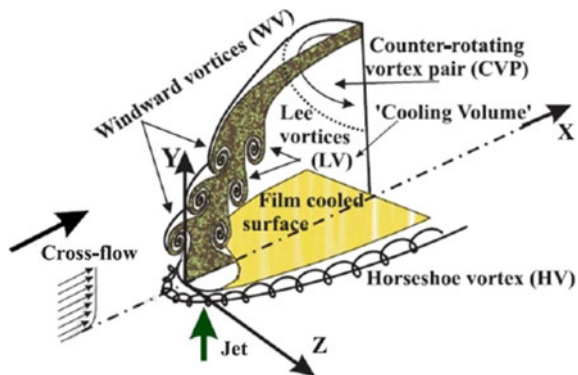


Fig. 6.140 Static pressure and density gradient at the outlet of guide vanes before and after optimization [192]

Fig. 6.141 Vortex systems induced by film cooling jet flows



developed a multi-objective optimization algorithm, which was based on parametric 2-D blade modeling and 3-D stacking, and made 3-D optimization and modifications to the transonic turbine to reduce the unsteady force caused by the shock waves in the downstream blade row (namely, to reduce the circumferential non-uniform degree of the static pressure at the outlet of the guide vane and the aerodynamic loss), as shown in Fig. 6.139. Figure 6.140 presents the comparison of the results before and after the optimization. It can be seen that the circumferential fluctuating amplitude of the pressure at the outlet of the guide vane was decreased, the cascade passage was changed from the convergent passage to the convergent-divergent passage, and the outer tail waves were weakened [192]. Similar research were carried out in NASA Ames Research Center. The shock wave systems were optimized to reduce the unsteady force caused by shock waves in the downstream blade row, by the combination of the response surface method and the neural network method. The results suggested that the fluctuating amplitude of the unsteady aerodynamic force was reduced, on the premise that the tangential force on the rotor, the output power, and the efficiency were all kept unchanged [200, 201].

Table 6.18 Summary of manufacturing factors and their effect levels on cooling [203]

Code	Factor	Tolerance	Effect of factors on cooling design parameter							
			Discharge coefficient	Internal HTC	Friction factor	External HTC	Film effectiveness	Aero load or loss	External heat flux	
A1	Aerodynamic profile/shape	± 0.05 mm	L	L	L	M	M	M	M	
A2	Airfoil incidence angle	$\pm 2^\circ$	L	L	L	M	M	M	M	
A3	Surface roughness (initial)	$+1 \mu$	L	L	L	H	M	M	H	
B1	Bondcoat thickness	± 0.025 mm	L	L	L	L	L	L	L	
B2	TBC thickness	± 0.05 mm	L	L	L	L	L	M	H	
B3	Local wall thickness	± 0.125 mm	L	L	L	L	L	L	L	
C1	Film hole diameter (effective)	$\pm 10\%$	M	L	L	M	M	H	M	
C2	Film hole L/D	$\pm 6\%$	M	L	L	L	L	M	M	
C3	Film hole angle to surface tangent	$\pm 5^\circ$	M	L	L	M	M	H	M	
C4	Film hole orientation to external flow	$\pm 5^\circ$	M	L	L	M	M	H	M	
C5	Film hole orientation to internal flow	$\pm 5^\circ$	H	L	L	L	L	M	M	
C6	Film hole P/D	$\pm 10\%$	L	M	L	M	M	H	H	
C7	Film hole shaped exit spec	$\pm 30\%$	H	L	L	H	H	H	H	
D1	Impingement hole diameter	$\pm 10\%$	L	L	L	L	L	L	L	
D2	Impingement array X/D or Y/D	$\pm 10\%$	L	H	M	L	L	L	L	

(continued)

Table 6.18 (continued)

		Effect of factors on cooling design parameter									
		±20%	±10%	±10%	±10%	±10%	±10%	±10%	±10%	±10%	±10%
D3	Impingement Z/D	L	H	L	L	L	L	L	L	L	L
D4	Crossover hole diameter	H	H	L	L	L	L	L	L	L	L
E1	Cool. no passage turn aspect ratios	L	H	H	L	L	L	L	L	L	L
E2	Passage H/W (or aspect ratio)	L	M	M	H	H	L	L	L	L	L
F1	Turbulator e/D (blockage)	M	H	H	L	L	L	L	L	L	L
F2	Turbulator radius r/e	L	M	M	H	H	L	L	L	L	L
F3	Turbulator P/e	L	M	M	H	H	L	L	L	L	L
F4	Turbulator angle	M	H	H	L	L	L	L	L	L	L
F5	Turbulator end wrap-around	L	M	M	M	M	L	L	L	L	L
F6	Turbulator lean	L	M	M	M	M	L	L	L	L	L
G1	Pin diameter	L	L	L	M	M	L	L	L	L	L
G2	Pin fillet r/H	L	M	M	H	H	L	L	L	L	L
G3	Pin array S/D	L	H	H	L	L	L	L	L	L	L
G4	Pin H/D	L	M	M	H	H	L	L	L	L	L
H1	TE channel blockage e/H	L	M	M	M	M	L	L	H	M	M
H2	TE exit slot or hole H/W (aspect ratio)	M	M	M	H	H	M	M	M	M	M
H3	TE lip thickness to slot height ratio t/H	H	L	L	L	L	H	H	H	M	H

6.7.2.5 Flow Organizing Considering the Interaction Between Cooling Flow and the Main Flow

The inlet temperature of the turbine in modern aero-engines has been far higher than the temperature tolerance of materials. Therefore, various cooling methods such as convection, impingement, and air film are extensively used to cool down the turbine, and coolant air is used in the disc cavity between the rotor and stator to prevent gas invasion. Most coolant air finally joins into the main flow, so it would influence the flow structures and the turbine performance [202].

(1) Flow organizing considering the interaction of the cooling air and the main flow

There are dramatic momentum transport and temperature transport between the cooling air and the gas in air-cooled turbines. As shown in Fig. 6.141, entrainment and mixing between the cooling jet flows and the main flow would induce the kidney-shaped vortex pairs, the horseshoe vortices, the leading-edge vortices, and the trailing-edge vortices. These complex flow structures would not only result in the mixing loss and the performance drop, but also influence the heat transfer characteristics and the cooling effect. This process is under the influence of both aerodynamic parameters (including the air blowing ratio, the momentum rate, the density ratio, the turbulence intensity of the inflow, the Reynolds number, etc.) and geometric parameters (including the blade shape, the cool air injection angle, the shape and position of the cooling air holes, the pitch of holes, the arrangement of the holes, the wall curvature, the wall roughness, etc.). Table 6.18 systematically shows the influence of the shape and machining error of the film cooling holes on the cooling effectiveness and the aerodynamic loss [203]. It can be seen that optimization of the cooling jet flows can improve the cooling effect and reduce the additional aerodynamic loss. However, it should be noted that both the processing cost and the aerodynamic proceeds should be taken into consideration in the design process.

(2) Flow organizing considering the interaction of coolant air with the main flow

The sealing structures are generally used in the position between the rotating components and stationary components of the actual turbines, to prevent gas with high temperature from flowing into the disc cavity. However, these complex geometric structures would induce additional flows, and even if the coolant air flow is zero, the sealing structures would still change the local flow structures and cause the aerodynamic loss [204]. Meanwhile, the coolant air jets would also influence the flow structures in the endwall regions and cause the mixing loss. The practice of ignoring the sealing structures and their influence on the flow structures in design and calculation would result in great deviation of the calculated results from experimental measurements [205]. Fine organizing of the coolant air flow is necessary for further improving the turbine performance. Studies have shown that it is possible to weaken the viscous shear layer near the hub, as well as the enhancement of the secondary vortices in the endwall regions by the coolant air, by reducing the

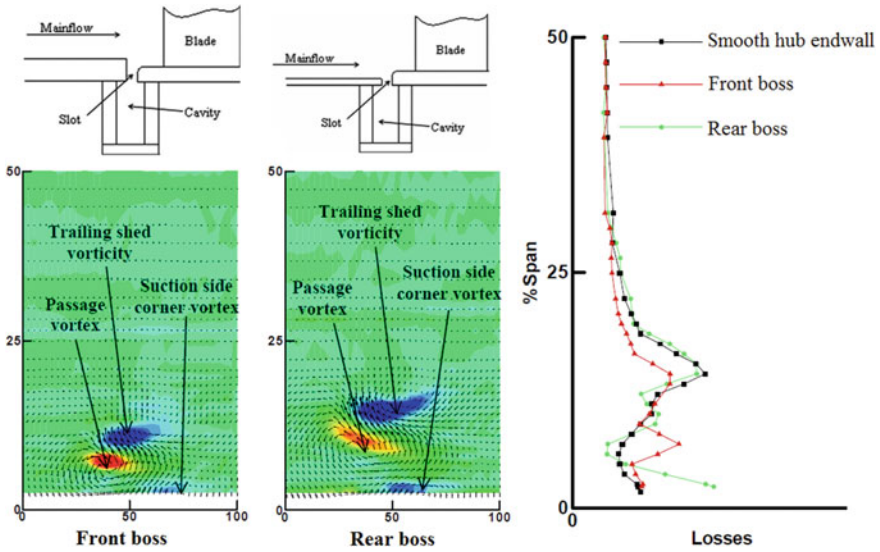


Fig. 6.142 Influence of boss structures on downstream secondary flows, vorticity, and loss coefficient distribution [209]

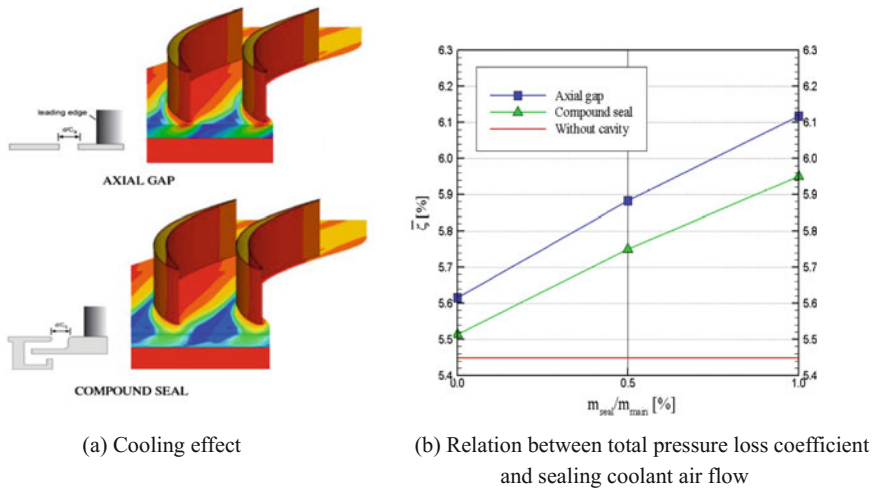


Fig. 6.143 Cooling effect of different sealing structures and aerodynamic loss [211]

radial momentum of the coolant air and the circumferential momentum difference between the coolant air and the main flow [206, 207]. Flows in the endwall regions of turbines can be improved by applying pre-whirl to the coolant air and optimizing geometry of the sealing endwall. The method of applying pre-whirl to the coolant air can diminish or even eliminate the velocity difference between the cooling air

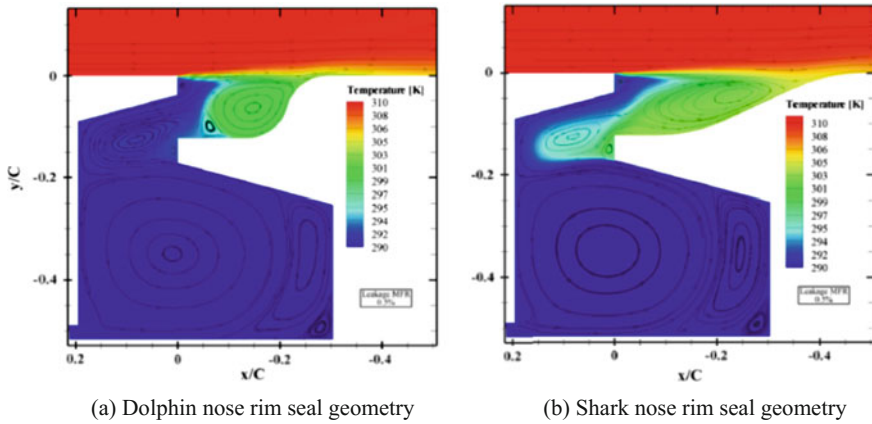


Fig. 6.144 New-type shark nose and dolphin nose rim seal geometries [213]

and the gas, thus reducing the mixing loss. Meanwhile, as the negative-incidence status at the blade root caused by the coolant air is improved, the enhancement of the secondary flows in the endwall regions can be reduced [208]. As for the geometry of the endwall, Blanco et al. from University of Cambridge systematically studied the influence of the front boss and rear boss at the rotor-stator junction on the secondary flows in the endwall regions of a LP turbine [209]. The study shows that the boss can significantly change the structure and strength of the secondary flows in the endwall regions. The front boss can inhibit the interaction between the branch of the horseshoe vortices and the separation bubble on the pressure side, as shown in Fig. 6.142. Compared with the smooth hub endwall and the rear boss, the front boss can reduce the strength of the secondary vortex and the aerodynamic loss in the endwall regions. In the subsequent studies, it is pointed out that, for different coolant air flow and different tangential velocity of the coolant air, the front boss can avoid interaction between the secondary flows and the separation bubble on the pressure side, thus resulting in low aerodynamic loss [210]. As for the optimization of sealing structures at the hub, it is beneficial to replace the simple axial sealing structure with the composite sealing structures and circular fillets, which can increase the sealing effectiveness and improve the temperature distribution at the blade root. Meanwhile, the composite sealing structure can weaken the radial migration of the low-energy leakage flow and the enhancement of the passage vortices, thus reducing the additional aerodynamic loss [211, 212].

In recent years, with the development of aerodynamic design technologies, researchers have started to optimize the rim seal geometries and take into comprehensive consideration of the influence of the rim seal geometries on the aerodynamic performance and the thermal load. For example, Erickson et al. proposed the “shark nose” and “dolphin nose” rim seal geometries, and compared their influence on the aerodynamic and cooling efficiency, as shown in Fig. 6.144. The results showed that the “dolphin nose” could produce higher cooling efficiency than the “shark nose” at

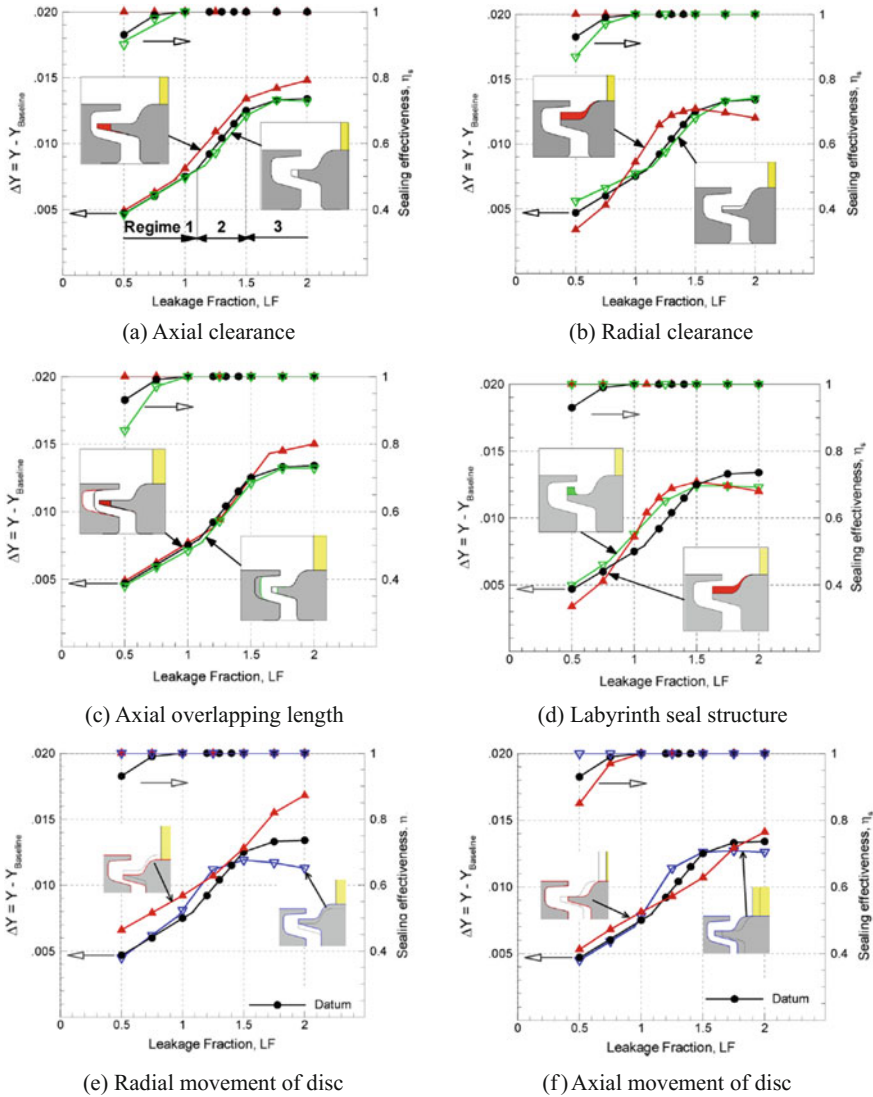


Fig. 6.145 Influence of seal structures parameters of on sealing effectiveness and aerodynamic loss [218]

different air blowing ratios, while would result in relatively large secondary loss due to the rapid lift of cooling air [213]. Similar conclusions were obtained in the researches by Zhang et al. , where pressure-sensitive paint and liquid crystal thermography were used to study the cooling efficiency and the thermal load in the endwall regions [214, 215]. Popovic et al. from University of Cambridge carried out systematical studies on the influence of the sealing outflow on flows and heat transfer

of a highly-loaded cascade [216–219]. The results showed that the loss would increase with the increase of the coolant air flow, and that the influence of the coolant air flow on the loss and the sealing effectiveness, which tends to be nonlinear, can be divided into three obvious regimes, as shown in Fig. 6.145a. In addition, because most of the coolant air is entrained to the passage vortexes, the cooling effect for the hub is limited [216, 217]. Based on that, they further studied the influence of the sealing structures and the geometric parameters on the sealing effectiveness and the aerodynamic loss, and pointed that the backflow vortexes at the outlet of the sealing structures very important the sealing effectiveness and the aerodynamic loss [218, 219]. Figure 6.145 shows the influence of various geometric parameters (including the axial clearance, the radial clearance, the axial contact ratio, the labyrinth sealing structure, the radial deformation of rotor disc, the axial float of rotor disc, etc.) on the loss coefficient and sealing effectiveness at different leakage flow rates. It can be seen that the optimal geometry and size of the sealing cavity, which can produce best sealing effectiveness and aerodynamic performance in the entire flow range, do not exist. Therefore, optimization should be carried out in combination with specific aerodynamic parameters in the engineering design process.

6.7.2.6 Integrated Design of Strut and Aggressive Intermediate turbine Duct with Large Climbing Angle

Due to the economical requirement, the bypass ratio of modern aero-engines is being increased continually, which will inevitably lead to larger radius difference between the HP turbine and LP turbine of the conventional turbofan engines. In order to lighten the intermediate turbine duct (ITD) and alleviate the problems of support and axis rigidity resulting from longer intermediate turbine duct, the aggressive intermediate turbine duct with large climbing angle has attracted more attention. Compared with the turbine, the intermediate turbine duct is simpler in structure, while flows in the duct are equally complex. For example, the intermediate turbine duct operates under highly 3-D unsteady conditions, and great pressure gradient in the passage may result in separations of the endwall boundary layer and the strut boundary layer. In addition, great changes in curvature may lead to strong secondary flows, and thick struts may cause potential effect. Therefore, it is very necessary to develop effective design methods to guarantee good inflow adaptability, low flow loss, and uniform outlet flow field (to provide good inlet conditions for the downstream LP turbine) of the aggressive intermediate turbine duct with large climbing angle has become one of the current research focuses. Chalmers University of Technology (Sweden), Graz University (Austria), and Von Karman Hydrodynamics Institute (Belgium) have carried out systematic studies in this research field [220, 221].

(1) Fine design and optimization technologies for intermediate turbine duct

In the design of intermediate turbine ducts with struts, the area distribution and the climbing angle are the key parameters which have a great impact on performance.

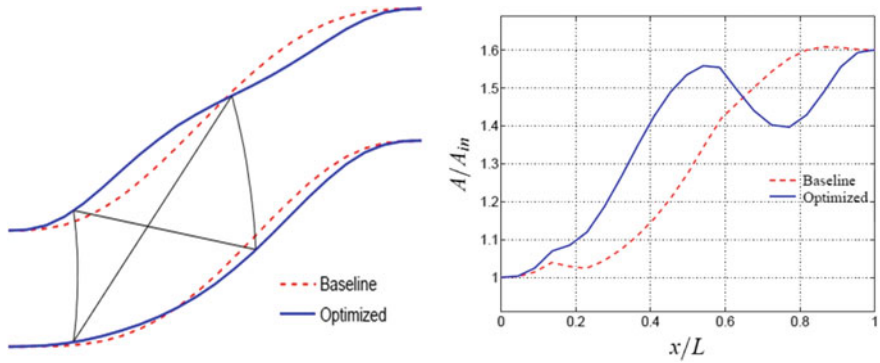


Fig. 6.146 Optimization of duct geometry and area distribution [222]

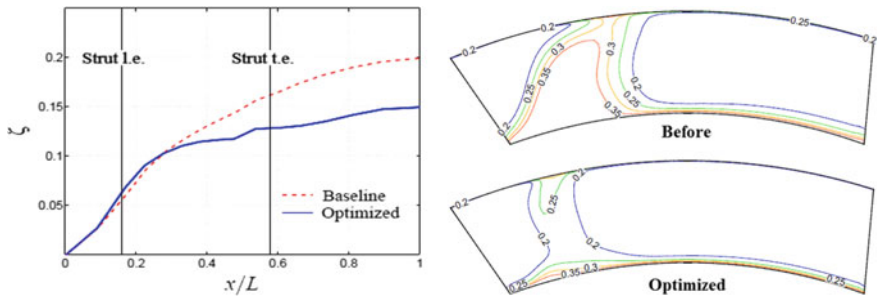


Fig. 6.147 Axial loss distribution and outlet loss distribution before and after optimization [222]

Wallin et al. from Chalmers University of Technology (Sweden) optimized an aggressive intermediate turbine duct by the response surface method [222]. Figure 6.146 shows comparison of the duct and area distribution between the optimized and the baseline. It can be seen that, after the optimization, the expansion of the ITD in the first bend is more aggressive and the flow area is increasing rapidly, while there is an obvious area decrease around the strut, which is conducive to control the separation of boundary layers in the outlet of the strut. The axial loss distribution and the outlet loss distribution shows that the flow loss was reduced by about 25% compared with the original duct, proving the effectiveness of optimization, as shown in Fig. 6.147. The application of nonaxisymmetric endwall modeling technology in intermediate turbine duct design was successful, which reduced the loss coefficient by 10% [223]. In addition, Wallin et al. proposed the method of using vortex generators to control separation of the boundary layer in aggressive intermediate turbine ducts [224]. Figure 6.148 shows the loss coefficient distribution contours of the intermediate turbine duct with and without vortex generators. It can be seen that there was separation around the casing in the original intermediate turbine duct, while the separation was completely eliminated by the use of vortex generators, reducing the loss of the intermediate turbine duct by 15%.

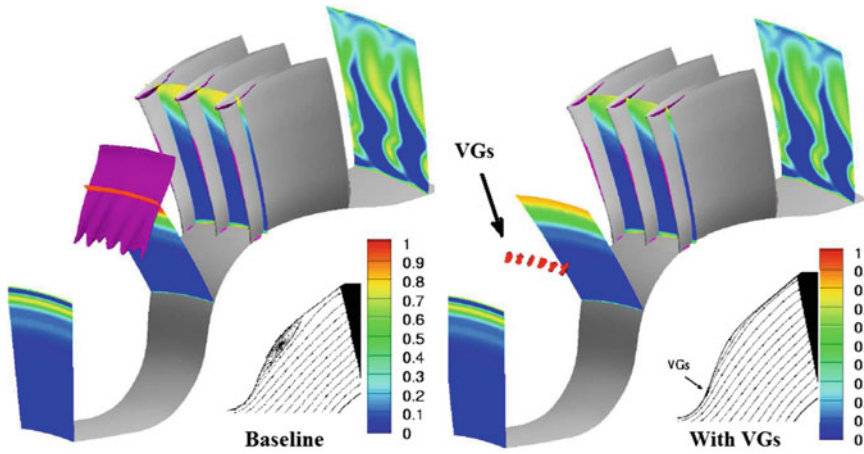


Fig. 6.148 Loss coefficient distribution in intermediate turbine duct with and without vortex generator [224]

(2) Integration of intermediate turbine duct struts and LP turbine guide vane

To further reduce the axial length of intermediate turbine ducts with large climbing angle and engine weight, Marn and Göttlich et al. from Graz University (Austria) proposed a design concept of integrating the intermediate turbine duct struts with the first-stage guide vane of the LP turbine [225] which is to substitute the first-stage guide vane of the LP turbine with the intermediate turbine strut that has been carefully profiled. Based on this concept, the integrated design of an intermediate turbine duct was accomplished, as shown in Fig. 6.149. The shorter axial length and fewer blades result from the integrated design contributed to a decrease

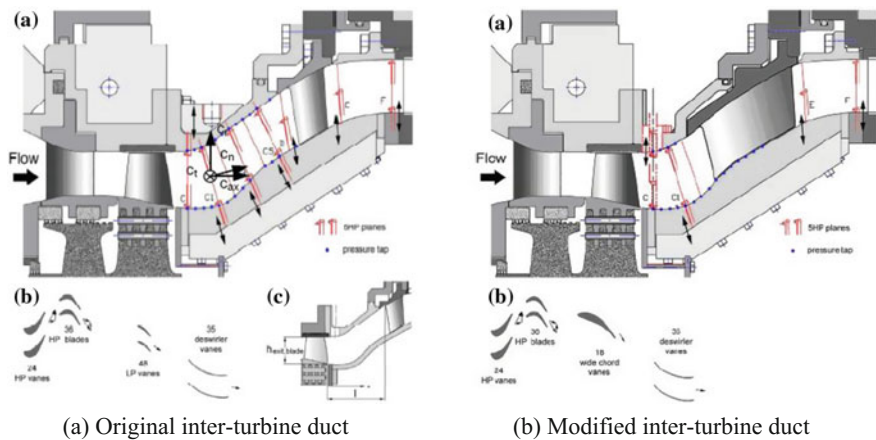


Fig. 6.149 Integrated design of intermediate turbine struts and LPT IGV [225]

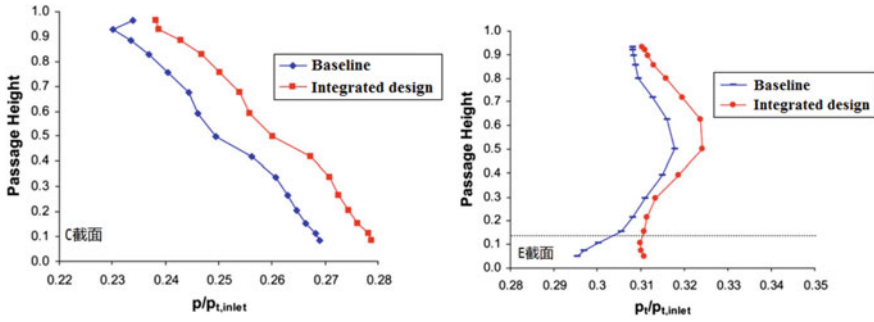


Fig. 6.150 Radial distribution of circumferential averaged total pressure before and after integrated design [225]

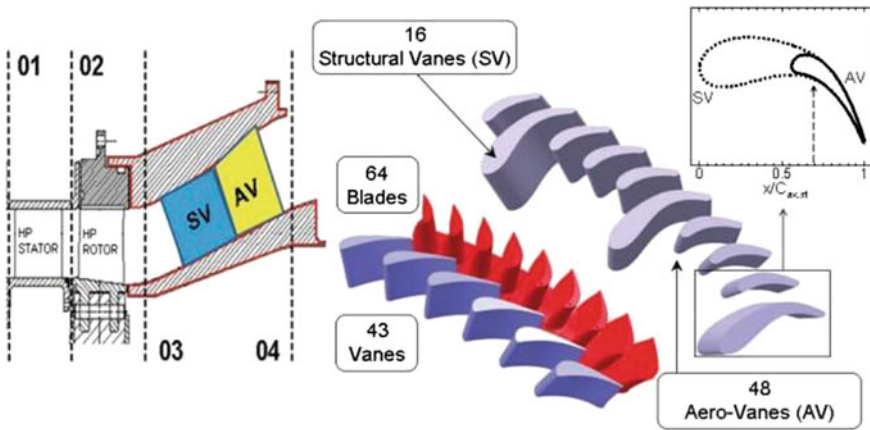


Fig. 6.151 Transition duct with splitter vanes [226]

of 20–39% in the weight of the intermediate turbine duct. Figure 6.150 shows the comparison of the results between the integrated design and the baseline. The results show that the modified struts could hardly influence the flow field at the outlet of the HP turbine (cross-section C), and that the aerodynamic parameters at the outlet of the intermediate turbine duct (cross-section E) were close to those of the original duct. Meanwhile, the total pressure loss coefficient in the intermediate turbine duct dropped from 4.4% to 4.3%. Undoubtedly, this technology can greatly improve the engine performance.

(3) Integrated design of structural vanes and splitter vanes in ITDs

Actually, the intermediate turbine strut is always used as supporting structure, with various kinds of pipelines arranged inside, such as oil pipes. Therefore, the strut is

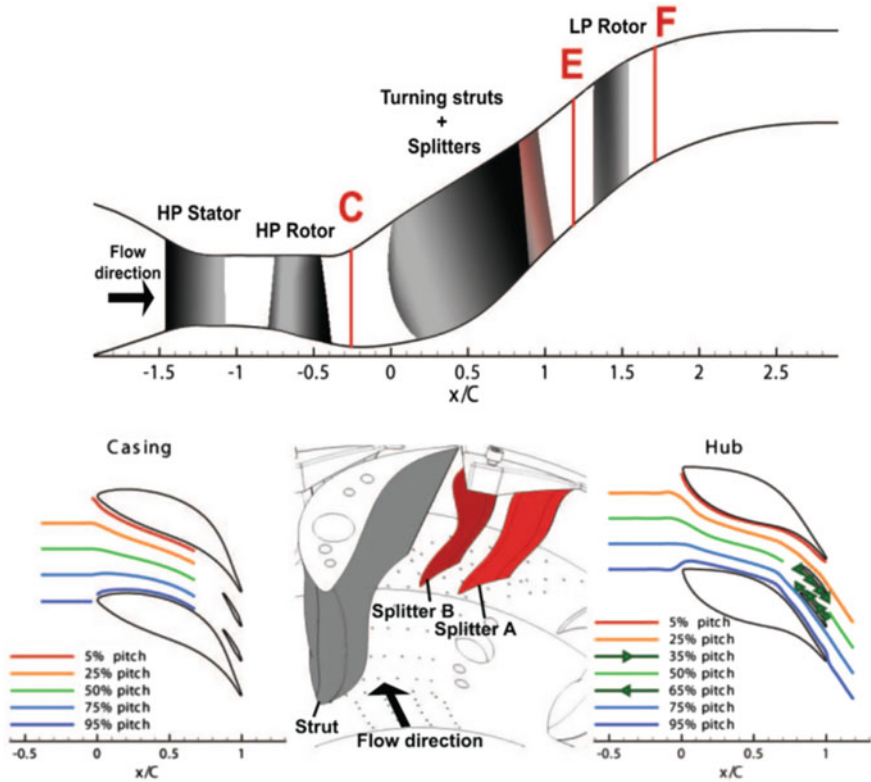


Fig. 6.152 Alternatively placed structural vanes and LP turbine guide vanes [228]

generally thick, which brings some difficulties to design. Especially when the inflow angle changes greatly, the flow may easily get worse rapidly. To solve this problem, Lavagnoli et al. from Von Karman Hydrodynamics Institute (Belgium) proposed a strut structure with splitter vanes, aiming at further reduction of the axial length and the weight of the engine. As shown in Fig. 6.151, the large strut, also called structural vane, is used for supporting, and the splitter vane, also called aero-vane, is used for guiding flows [226, 227]. The study shows that the structural vane has significant influence on the splitter vane, which should be noted in design. Spataro, Göttlich, et al. from Graz University further discussed this design, in which the structural vane and the splitter vane are placed alternately in the intermediate turbine duct, with the purpose of weakening the wakes of the structural vane and the secondary flows at the rotor inlet of the downstream LP turbine [228]. As shown in Fig. 6.152, two LP turbine guide vane are placed between the structural vanes. The experimental results showed that this combination design method can effectively inhibit the corner separation at the trailing edge of the structural vane in the hub region, weaken the secondary vortexes, and finally achieve more reasonable flows downstream of the structural vane. Meanwhile, the performance of the LP turbine

Fig. 6.153 Comparison of oil flow visualizations on the strut suction side for baseline and multisplitter setups (view from downstream) [228]

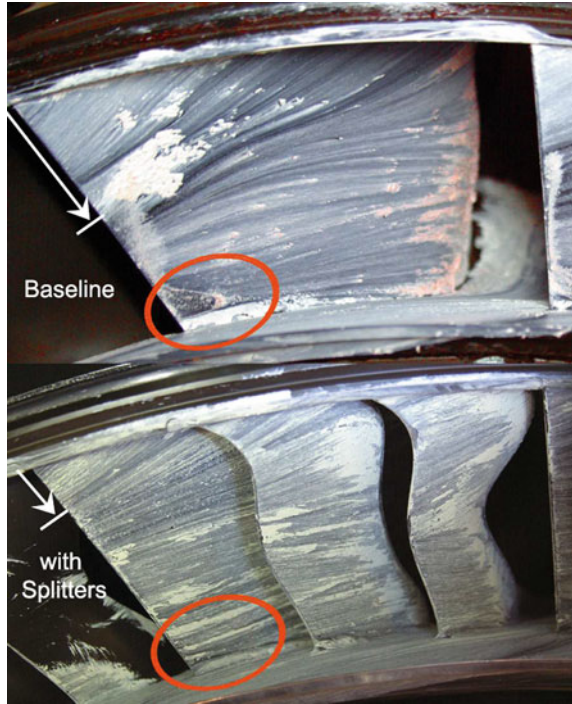
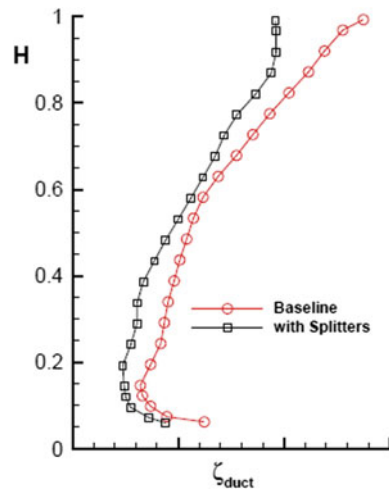


Fig. 6.154 Losses through the duct for baseline and embedded design setups [228]



was increased significantly due to the better flow conditions at the rotor inlet, as shown in Fig. 6.153 and Fig. 6.154. The total pressure recovery coefficient of the intermediate turbine duct was increased by 3.71%, and the relative value of the LP turbine efficiency was increased by 6.08%.

6.7.2.7 Aerodynamic Design with Unsteady Effect Being Considered

Unsteadiness is the essential feature of flows in turbine. Most of the traditional turbine design systems are established based on the steady assumption, in which high-performance turbomachineries can be designed by grasping the main characteristics of flows. However, with the continuous increase of the aerodynamic loading of turbine in advanced aero-engines, turbines become more compact, and thus the unsteady interaction between blade rows becomes more prominent. The inherent unsteadiness of flows in turbines cannot be ignored any longer. To further improve the aerodynamic performance of turbines, it is necessary to consider the influence of the unsteady flows in turbine design. This subsection gives a brief introduction to the applications of unsteady effects in turbine design by taking the clocking effect, the hot streak, and the calming effect for instance.

(1) Clocking effect and its application

Clocking effect refers to the performance variation resulting from the relative position of the upstream and downstream rotors or the relative position of the upstream and downstream stators. When wakes of the upstream stator (or rotor) strike on the leading edge of the downstream stator (or rotor), the aerodynamic efficiency of the turbine would increase. While when wakes of the upstream stator (or rotor) strike on the middle region of the downstream stator (or rotor) passage, the aerodynamic efficiency of the turbine would decrease [229]. The main reason for this phenomenon is that, when wakes of the upstream stator (or rotor) fixedly act on different circumferential positions of the downstream stator (or rotor), they would change the status of the boundary layer of the downstream stator (or rotor) or the mixing between the wakes and the main flow, thus changing the aerodynamic performance of the turbine, the aerodynamic actuation on the downstream blade, and the heat transfer on the blade surface [230]. Clocking effect has great influence on the performance of multi-stage turbines. Research results have shown that variations of the circumferential relative position of the stator of multi-stage LP turbines can result in an efficiency variation of 0.5%. The obtained efficiency gain

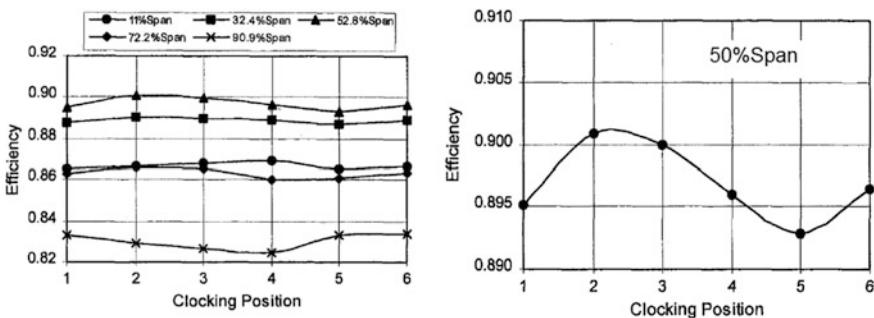


Fig. 6.155 Spanwise efficiency versus clocking position [231]

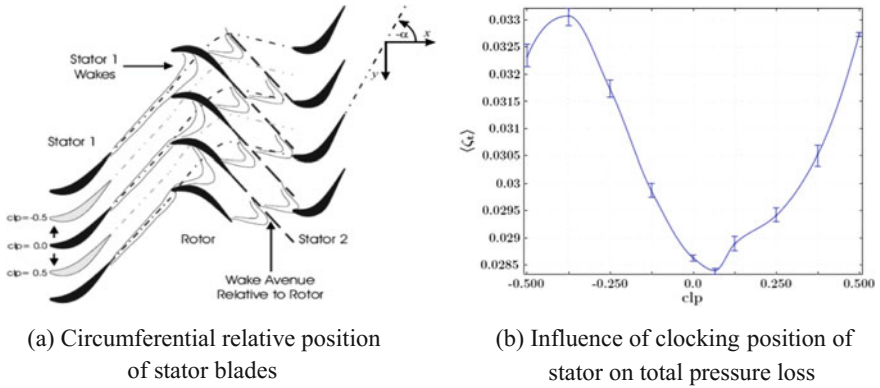


Fig. 6.156 Clocking effect in multi-stage turbine [232]

would change with the radial position, and reach to the maximum of 0.8% at the midspan as shown in Fig. 6.155 [231]. Figure 6.156 shows the results of the study carried out by König et al. of the impact of the variations in the circumferential relative position of the stator blades in a 1.5-stage turbine. As can be seen, variation of the circumferential relative position of the stator would influence the outflow angles of both the rotor and the second stator, as well as the total pressure loss of the second stator. There is a separation bubble on the suction side of the second stator, where the high-lift blade is adopted. When the wakes of the first stator strike on the leading edge of the second stator, they would change the length of the separation bubble as well as the development of the boundary layer, and the total pressure loss would also be changed, as shown in Fig. 6.156 [232]. From the perspective of unsteady aerodynamic force, He et al. pointed out that the number of blades and the circumferential relative position should be regarded as design parameters and optimized, and that the unsteady aerodynamic force can be reduced by making the wakes of the upstream guide vane sweeping over the suction side of the downstream stator [233].

Since the number of the upstream rotor (or stator) does not always equal to that of the downstream rotor (or stator), it is very difficult to make all the wakes of the upstream stator (or rotor) strike on the leading edge of the downstream stator (or rotor) along the whole blade height, with the 3-D blade profiling and other factors taken into consideration. Therefore, benefits of the clocking effect in actual application will be less ideal than those obtained in test rigs.

(2) Hot streaks and corresponding control measures

Hot streaks refer to the local high-temperature regions at the outlet of the combustor. This highly-uneven distribution of the inlet temperature would directly influence the thermo-aerodynamic performance, the blade heat transfer, and the mechanical properties of the turbine. Therefore, it is important to control the migration of the hot streaks and eliminate their adverse effects. In general, wakes

can be regarded as “inverse jet flows”, which tend to accumulate towards the suction side in the downstream blade passage, while hot streaks are just the opposite. Because that heating would result in velocity increase, hot streaks can be regarded as “direct jet flows”, which tend to accumulate towards the pressure side in the downstream blade passage. When wakes meet with the hot streaks in the passage, the two would inhibit each other. As a result, both the accumulation of wakes around the suction side of the downstream blades and the accumulation of hot streaks (i.e. high-temperature fluid) around the pressure side can be relieved as shown in Fig. 6.157b [234]. In 3-D environment, migration of the hot streaks would be influenced by the interaction between the secondary vortexes in the blade row and the secondary flows induced by temperature, then the situation would be more complex, as shown in Fig. 6.158 [235]. Firstly, the streamwise shed vortexes of the upstream blades would have impact on the radial migration of the hot streaks, for example, the shedding vortexes of the guide vane would drive the hot streaks (high-temperature fluid) towards the hub. Meanwhile, the density gradient caused by the hot streaks would create normal vortexes at the inlet. Being stretched deflected, the normal vortexes would induce spanwise vortexes as they spread in the blade passage, thus enhancing the radial movement in the passage [236]. Under the influence of the tip leakage flow, the radial movement of high-temperature fluid on blade surface would be further enhanced, thus increasing the influence range of the hot streaks and the thermal load on the rotor blade [237]. In addition, cold and hot fluid would flow in different directions in the S1 stream surface. The high-temperature fluid would migrate to the pressure side, while the low-temperature fluid would migrate to the suction side, which would further increase the temperature on the pressure side [238]. The direction of the swirling flow at the inlet also has significant impact on the migration of the hot streaks [239]. When the hot streaks strike on the leading edge of the guide vane, the backward

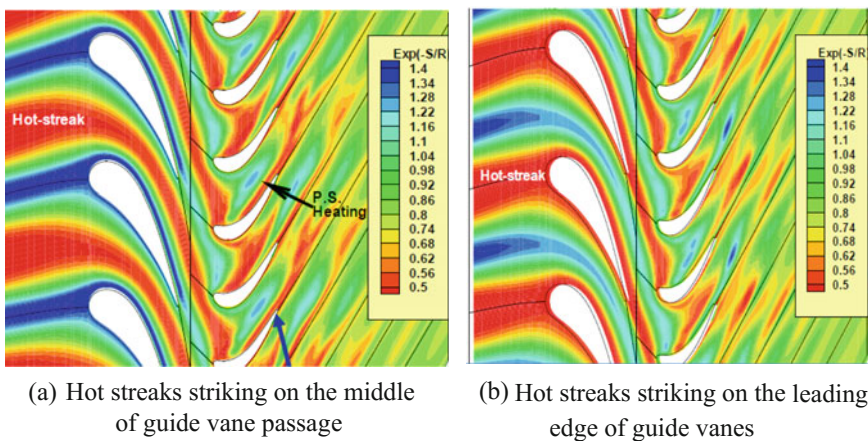


Fig. 6.157 Transient entropy distribution at midspan section [234]

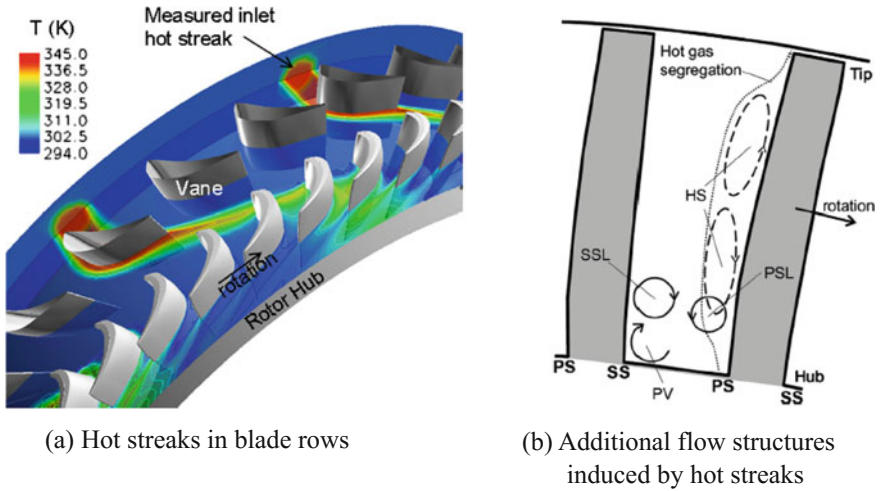


Fig. 6.158 Hot streak migration in turbine [235]

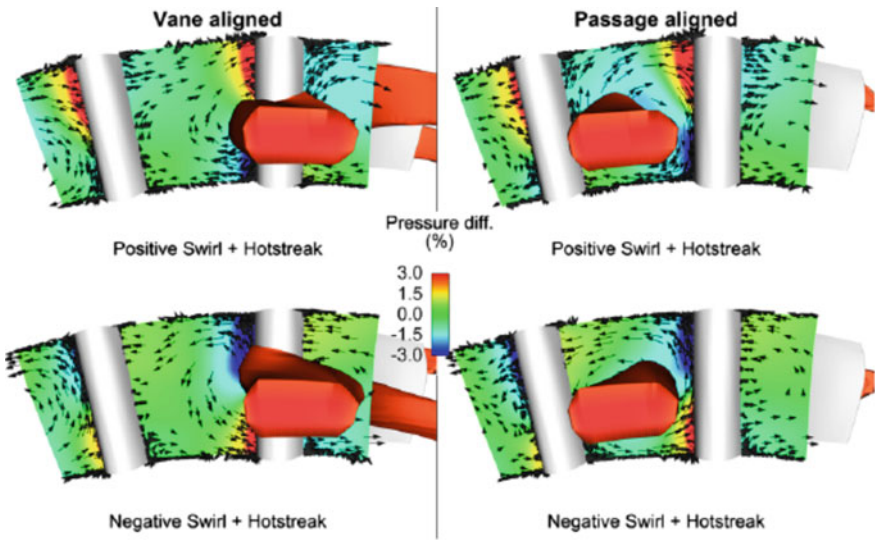


Fig. 6.159 Hot streak migration in guide vane passage under conditions with different swirling inflows [239]

swirling flow would increase the pressure loss around the tip, while the forward swirling flow would increase the pressure loss around the hub. When the hot streaks strike on the middle region of the guide vane passage, the forward swirling flow would increase the loss in the corner zone on the suction side of the tip while the backward swirling flow would decrease the tip loss. In the rotor passage where there is strong radial migration on the pressure side, the direction of the swirling

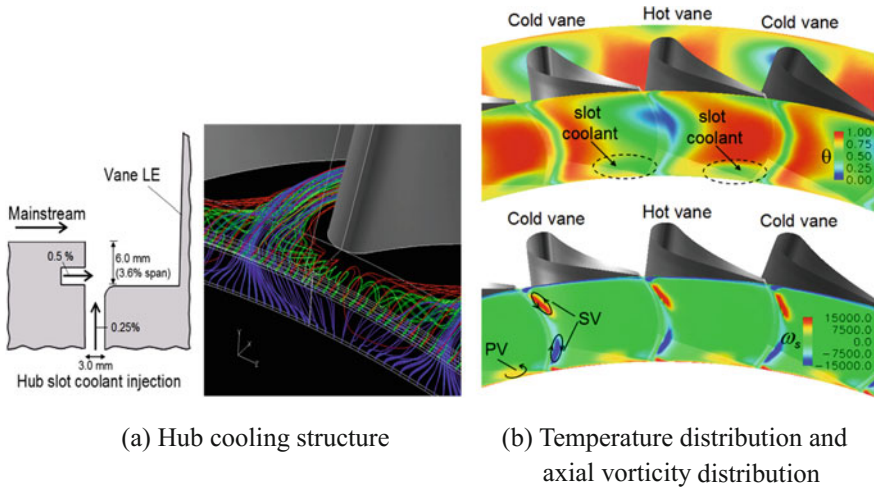


Fig. 6.160 Use cooling air to relieve hot-streak high temperature gas accumulation [235]

flow and the position of the hot streaks have significant impact on the heat transfer performance on the blade surface of the rotor, as shown in Fig. 6.159.

During highly 3-D migration of the hot streak, the high-temperature fluid migrates from the middle region of the blade, where the blade is fully cooled, to the endwall regions, thus influencing both the reliability and the life span of the blade. Therefore, it is necessary to organize the hot streak to reduce the thermal load on the blade. Dorney, Gundy-Burlet et al. reduced the influence of the radial migration of the hot streak by adjusting the circumferential position of the stator [240]. Ong et al. carried out fine organizing of the cooling air, making it being entrained by the suction-side branch of the shedding vortices at the trailing edge of the upstream guide vane and transferred to the blade root on the pressure side where the high-temperature fluid in the hot streak accumulates and obtained good cooling effectiveness, as shown in Fig. 6.160 [235].

(3) Calming effect and its application

In recent years, the calming effect has become one of the focuses in the field of aerodynamic research on highly-loaded LP turbines. In nature, it is the interaction between the upstream wakes and the suction-side boundary layer of the downstream blade row, which would cause great changes in the profile loss. Reasonable utilization of the calming effect in turbine design can improve the anti-separation capability of the suction surface of the blade and reduce the friction loss, thus improving the blade load and the turbine performance [241]. Hodson et al. from Cambridge university have been studying for more than two decades and have made outstanding contributions in the field. Studies on the influence of the loading distribution on the suction side, the Reynolds number, and the reduced frequency

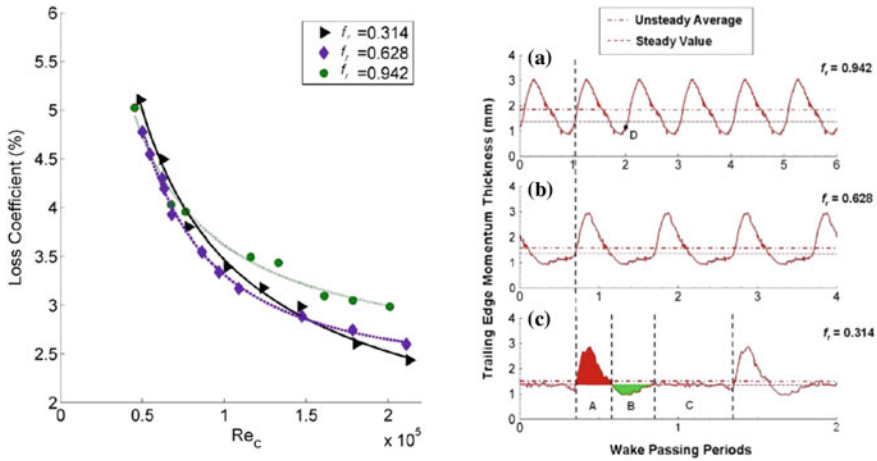


Fig. 6.161 Influence of wake passing frequency on loss coefficient and trailing edge momentum thickness [242]

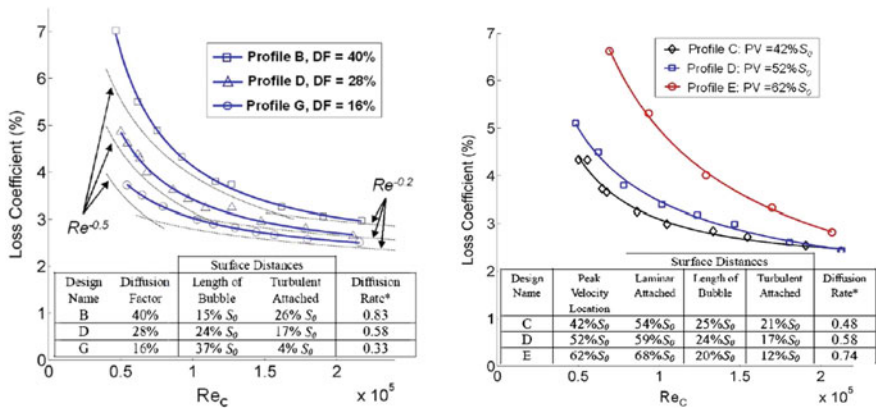


Fig. 6.162 Influence of suction-side diffusion factor and suction peak position on loss coefficient [242]

on the losses in highly-loaded LP turbines, were carried out by plate experiments. Figure 6.161 shows the influence of the passing frequency of the wakes on the loss and the trailing-edge momentum thickness. The results suggest that, at high Reynolds number conditions, the separation bubble is small and the loss is mainly caused by the turbulent boundary layer, so increasing wake passing frequency would increase the loss. While at low Reynolds number conditions, the separation bubble is larger and is the main source of the loss, so higher wake passing frequency would suppress the separation bubble, thus reducing the loss. Therefore, selection of the wake passing frequency in turbine design depends on the status of

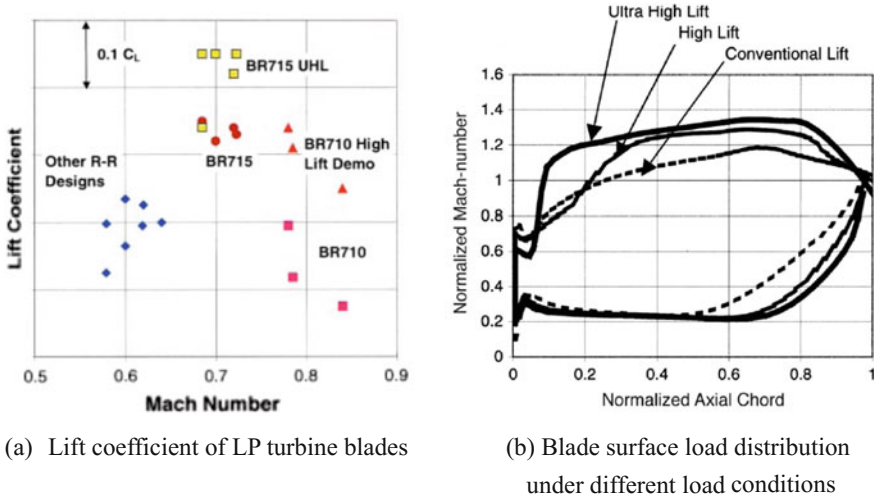


Fig. 6.163 Lift coefficient of turbine blades and surface load distribution [244]

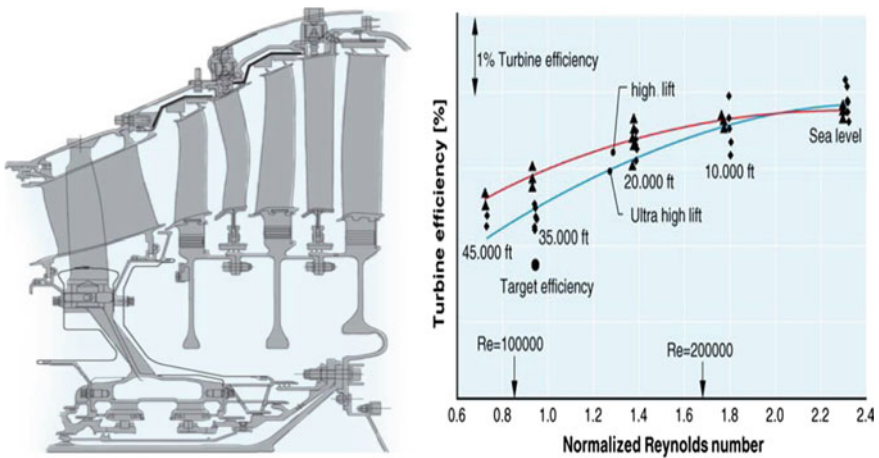


Fig. 6.164 BR715 LP turbine efficiency [245]

the boundary layer. Parameters of the loading distribution on the suction side such as the trailing edge diffusion factor, the position of the suction peak, etc. have significant impact on the loss, as shown in Fig. 6.162. For example, increment of the trailing edge diffusion factor would results in higher loss caused by the separation bubble and larger wetted area of turbulence flows. Based on that, three parameters were optimized, including the wake passing frequency, the Reynolds number and the trailing edge diffusion factor. The results showed that, when the

wake passing frequency and the Reynolds number under the design condition are given, there would be an optimal position of the suction peak, which corresponds to a specific trailing edge diffusion factor. In turn, when the trailing edge diffusion factor and the Reynolds number are given, there would be an optimal wake passing frequency, which corresponds to a specific position of the suction peak. These results can serve as good reference for the design of blades in high-lift LP turbines. Figure 6.163 shows the evolution of the lift coefficients of several Rolls-Royce LP turbine blades, together with the comparison of blade loading distribution between different loading conditions, where UHL represents the ultra-high-lift blade and HL represents the high-lift blade. Both of these two blades are the application examples of the calming effect. It can be seen that the calming effect can be used to greatly increase the aerodynamic load of the blades.

Nowadays, the design method with the calming effect being considered has been used extensively in the design of LP turbines for advanced aero-engines, such as, Rolls-Royce BR710, BR715, TRENT500, and TRENT900 aero-engines [166, 243, 244]. Figure 6.164 presents the comparison of the experimental results between the UHL blade and the HL blade, which are used in the LP turbine of the BR715 engine [245]. The number of the UHL blade is 11% less than that of the HL blades. The results show that the aerodynamic efficiency of the LP turbine equipped with the UHL blade is 0.5% higher than the target value. The LP turbine equipped with the UHL blade is more sensitive to the decrement of the Reynolds number than that equipped with the HL blade, and efficiency difference between the two at the design point (cruising at the height of 35,000 ft) is about 0.5%. However, the aerodynamic efficiency of the LP turbine equipped with the UHL blade drops by 1.5% from takeoff to cruise, which is still lower than that (2%) in conventional LP turbines.

References

1. Han, J. C., Duffa, S., & Ekkad, S. V. (2000). *Gas turbine heat transfer and cooling technology*. New York: Taylor & Francis.
2. U.S. Department of Energy, et al. (2006). *The gas turbine handbook*. <http://www.netl.doe.gov/research/coal/energy-systems/turbines/publications/handbook>.
3. Aero Engine Design Handbook Editorial Board, Wang, H., et al. (2001). *Aero engine design handbook, volume 16, air system and heat transfer analysis*. Beijing: Aviation Industry Press.
4. Ainley, D. G., & Mathieson, G. C. R. (1951). *A method of performance estimation for axial-flow turbines* (pp. 2974–2974). USA: Defense Technical Information Center.
5. Dunham, J., & Came, P. M. (1970). Improvements to the Ainley-Mathieson method of turbine performance prediction. *Journal for Engineering for Power*, 92(3), 252–256.
6. Kacker, S. C., & Okapuu, U. (1982). A mean line prediction method for axial flow turbine efficiency. *Journal for Engineering for Power*, 104(1), 111–119.
7. Soderberg, C. R. (1949). *Gas turbine laboratory*. Massachusetts Institute of Technology (Unpublished Notes).
8. Traupel, W. (1977). *Thermische Turbomaschinen Zweiter Band Geländerte Betriebsbedingungen, Regelung, Mechanische Problem, Temperature problem*. Berlin, Heidelberg, New York: Springer.

9. Stewart, W. L., Whitney, W. J., & Wong, R. Y. (1960). A study of boundary-layer characteristics of turbomachine blade rows and their relation to over-all blade loss. *Journal of Basic Engineering*, 82(3), 588–592.
10. Balje, O. E., & Binsley, R. L. (1968). Axial turbine performance evaluation. Part A—Loss-geometry relationships. *Journal for Engineering for Power*, 90(4), 341–348.
11. Craig, H. R. M., & Cox, H. J. A. (1970). Performance estimation of axial flow turbines. *Proceedings of the Institution of Mechanical Engineers*, 185(1), 407–424.
12. Denton, J. D. (1993). *Loss mechanisms in turbomachinery*. ASME Paper 93-GT-435.
13. Denton, J. D. (1993). Loss mechanisms in turbomachines. *Journal of Turbomachinery*, 115(4), 621–656.
14. Denton, J. D. (1990). *Entropy generation in turbomachinery flows*. SAE Technical Paper.
15. Ehrich, F., & Detra, R. (1954). Transport of the boundary layer in secondary flow. *Journal of Aeronautical Sciences*, 21(2), 136–138.
16. Scholz, N. (1954). Secondary flow loss in turbine cascades. *Journal of Aeronautical Sciences*, 21(10), 707–708.
17. Hawthorne, W. R. (1955). *Some formula for the calculation of secondary flow in cascades*. A R. C. Report.
18. Boulter, R. A. (1962). *The effect of aspect ratio on the secondary losses in a cascade of impulse turbine blade* (Unpublished Pamertrada Report).
19. Lakshminarayana, B. (1970). Methods of predicting the tip clearance effects in axial flow turbomachinery. *Journal of Basic Engineering*, 92(3), 467–480.
20. Ito, S., Eckert, E. R. G., & Goldstein, R. J. (1980). Aerodynamic loss in a gas turbine stage with film cooling. *Journal for Engineering for Power*, 102(4), 964–970.
21. Lakshminarayana, B. (1996). *Fluid dynamics and heat transfer of turbomachinery*. USA: Wiley-Inter Science.
22. Aero Engine Design Handbook Editorial Board, Huang, Q., et al. (2001). *Aero engine design handbook, volume 10, turbine*. Beijing: Aviation Industry Press.
23. Traupel, W. (1985). *Thermische Turbomaschinen*. Beijing: China Water & Power Press.
24. Ning, W. (2000). *Significance of loss models in aerothermodynamic simulation for axial turbines*. Royal Institute of Technology.
25. Coull, J. D., & Hodson, H. P. (2012). Predicting the profile loss of high-lift low pressure turbines. *Journal of Turbomachinery*, 134, 021002.
26. Curtis, E. M., Hodson, H. P., Banieghbal, M. R., Howell, R. J., & Harvey, N. W. (1997). Development of blade profiles for low-pressure turbine applications. *ASME Journal of Turbomachinery*, 119(3), 531–538.
27. Roberts, Q. D. H. (1998). *The trailing edge loss of subsonic turbine blades*. Ph.D. thesis, Cambridge University.
28. Hartsel, J. E. (1972). *Prediction of effects of mass-transfer cooling on the blade-row efficiency of turbine airfoils*. AIAA Paper 1972-11.
29. Lakshminarayana, B. (1996). Crossflow in a turbine cascade passage. *Journal of Engineering for Power*, 102(4), 886–892.
30. Kollen, O., & Koschel, W. (1985). *Effect of film cooling on the aerodynamic performance of a turbine cascade*. AGARD CP 227.
31. Shapiro, A. H. (1953). *The dynamics and thermodynamics of compressible fluid flow*. New York: The Ronald Press.
32. Zweifel, O. (1946). Optimum blade pitch for turbomachines with special reference to blades of great curvature. *The Engineers' Digest*, 7(11), 358–360.
33. Stewart, W. L., Whitney, W. J., & Wong, R. Y. (1960). A study of boundary-layer characteristics of turbomachine blade rows and their relation to over-all blade loss. *Journal of Fluids Engineering*, 82(3), 588–592.
34. Baljé, O. E., & Binsley, R. L. (1968). Axial turbine performance evaluation, Part A—Loss-geometry relationship. *Journal of Engineering for Power*, 90(4), 341–348.
35. Lim, C. H., Pullan, G., & Northall, J. (2010). *Estimating the loss associated with film cooling for a turbine stage*. ASME GT2010-22327.

36. Young, J. B., & Wilcock, R. C. (2002). Modeling the air-cooled gas turbine: Part 1—General thermodynamics. *Journal of Turbomachinery*, 124(2), 207–213.
37. Young, J. B., & Wilcock, R. C. (2002). Modeling the air-cooled gas turbine: Part 2—Coolant flows and losses. *Journal of Turbomachinery*, 124(2), 214–222.
38. Smith, S. F. (1965). A simple correlation of turbine efficiency. In *Proceedings of the Seminar on Advanced Problems in Turbomachinery*. Von Karman Institute for Fluid Dynamics.
39. Coull, J. D., & Hodson, H. P. (2011). *Blade loading and its application in the mean-line design of low pressure turbines*. ASME Paper GT2011–45238.
40. Murthy, S. V. R., & Kumar, S. K. (2012). *Parametric study of axial flow turbine for mean-line design and blade element*. GTINDIA 2012-9589.
41. Yao, L. (2013). *Studies on an optimal method of low dimensional aerodynamic design for multistage low pressure turbine*. Beijing: Beihang University.
42. Yang, L. (2006). *Investigations of complicated flow mechanism and aerodynamic design method in low pressure turbine at low reynolds number*. Beijing: Beihang University.
43. Adam, O., & Léonard, O. (2007). *A quasi-one dimensional model for axial turbines*. ISABE 2007-1215.
44. Adam, O., & Léonard, O. (2008). A quasi-one dimensional model for multistage turbomachines. *Journal of Thermal Science*, 17(1), 7–20.
45. Zhang, X., Liu, J., & An, B. (2011). Investigation on the computational method of axial turbine aerodynamic characteristics based on 1.5 dimensional Euler equations. *Journal of Engineering Thermophysics*, 32(4), 569–572.
46. He, J., Zou, Z., & Yao, L. (2014). *A one-dimensional simulation method to calculate turbine performance based on body forced model*. Research Report, Beihang University.
47. Zhang, W. (2013). *Studies on flow mechanisms and aerodynamic design of low-pressure turbine*. Beijing: Beihang University.
48. Zhdanov, I., Staudacher, S., & Falaleev, S. (2013). *An advanced usage of meanline loss systems for axial turbine design optimisation*. ASME Paper GT2013-94323.
49. Yao, L., Zou, Z., Zhang, W., et al. (2013). An optimal method of one-dimensional design for multistage low pressure turbine based on particle swarm optimization. *Journal of Propulsion Technology*, 34(8), 1042–1043.
50. Suchezky, M., & Cruzen, G. S. (2012). *Variable-speed power-turbine for the large civil tilt rotor*. NASA CR-217424.
51. D'Angelo, M. (1995). *Wide speed range turboshaft study*. NASA CR-198380.
52. Clark, J. P., Koch, P. J., & Ooten, M. K. (2009). *Design of turbine components to answer research questions in unsteady aerodynamics and heat transfer*. AFRL-RZ-WP-TR-2009-2180.
53. Welch, G. E. (2010). *Assessment of aerodynamic challenges of a variable-speed power turbine for large civil tilt-rotor application*. NASA TM-216758.
54. Hendricks, E. S., Jones, S. M., & Gray, J. S. (2014). *Design optimization of a variable-speed power-turbine*. AIAA Paper 2014-3445.
55. Zhang, S. (2015). *Study on aerodynamic design method of variable-speed turbine*. Beijing: Beihang University.
56. Jiang, H., Huang, S., & Zhou, R. (2004). Idea of aero-engine development by “core-engine” in series and derivation. *Gas Turbine Experiment and Research*, 17(1), 1–5.
57. Bolin, G. W., Field, J., Kevin, J. B., et al. (1999). *F414 engine today and growth potential for 21st century fighter mission challenges*. ISABE Paper 99-7113.
58. Zane, D., & Gastineau, Ph. D. (2002). *Propulsion technology planning for engine health management*. Air Force Research Laboratory.
59. Squadron, L. R. (2001). *Turbine engine research in the United States air force*. IEEE AERO 2001-931393.
60. Fu, C. (2010). *Study on some key technologies related to high performance turbine aerodynamics design*. Beijing: Beihang University.

61. Fu, C., Zou, Z., Liu, H., et al. (2011). Turbine aerodynamic design criteria of versatile core. *Journal of Propulsion Technology*, 32(2), 165–174.
62. Zhou, K., Zou, Z., Liu, H., et al. (2012). Aerodynamic design of counter-rotating turbine for aero-engine. *Science & Technology Review*, 30(15), 61–74.
63. Wintucky, W. T., & Stewart, W. L. (1957). *Analysis of two-stage counter-rotating turbine efficiencies in terms of work and speed requirements*. NACA, RM E57 L05.
64. Louis, J. F. (1985). *Axial flow counter-rotating turbines*. ASME Paper 85-GT218.
65. Huber, F. W., Branstrom, B. R., Finke, A. K., et al. (1993). *Design and test of a small two stage counter-rotating turbine for rocket engine application*. AIAA Paper 93-2136.
66. Yamamoto, A., Matsunuma, T., Ikeuchi, K., et al. (1994). *Unsteady tip-clearance flows and losses due to turbine rotor-stator interaction*. ASME Paper 94-GT-461.
67. Ji, L., Quan, X., & Xu, J. (2001). A primary design of one counter-rotating turbine. *Journal of Engineering Thermophysics*, 22(4), 438–440.
68. Ji, L. (2000). *A preliminary study on complex flow field simulation and design and experiment of counter rotating turbines*. Beijing: Institute of Engineering Thermophysics, Chinese Academy of Sciences.
69. Ya, Zhou. (2014). *Investigations of aerodynamic design techniques for advanced counter-rotating turbine*. Beijing: Beihang University.
70. Fang, X. (2003). *Aerodynamic analysis of supersonic and transonic highly loaded vaneless contra-rotating axial new concept turbines*. Beijing: Beihang University.
71. Yan, X. (2003). *Research on pneumatic design method of rotating turbine*. Xi'an: Northwestern Polytechnical University.
72. Zhou, K. (2014). *Investigations of aerodynamic design techniques for counter-rotating turbine in adaptive cycle engine*. Beijing: Beihang University.
73. Zhou, Y., Liu, H., & Zou, Z. (2010). Aerodynamics design of two-stage vaneless counter-rotating turbine. *Journal of Propulsion Technology*, 31(6), 689–695.
74. Aungier, R. H. (2005). *Turbine aerodynamics: Axial-flow and radial-inflow turbine design and analysis*. ASME Press.
75. Jiang, H. (2001). Some experiences and enlightenment of developing fan/compressor design system abroad. *Aeroengine*, 2, 31–45.
76. Yuan, N., Zhang, Z., Wang, S., et al. (2000). Aerodynamic design system adapting to three dimensional turbine. *Journal of Propulsion Technology*, 21(2), 1–4.
77. Huang, H., Feng, G., Wang, Z., et al. (1999). A three -dimensional design system applicable to naval steam turbines. *Journal of Engineering for Thermal Energy and Power*, 14(80), 119–121.
78. Zeng, J., Wang, L., & Wang, B. (2011). Full-3D simulation and analysis of flow in GE energy efficient engine turbine component. In *ANSYS 2011 China User Conference*, Sanya, China.
79. Sridhar, M., Sunnam, S., Goswami, S., et al. (2011). *CFD aerodynamic performance validation of a two-stage high pressure turbine*. ASME Paper, GT2011-45569.
80. Dong, P. (2009). *Research on conjugate heat transfer simulation of aero turbine engine air-cooled vane*. Harbin Institute of Technology.
81. Lu, S. (2014). *Research on turbine aerodynamic design system with optimization of film cooling and conjugate heat transfer*. Harbin: Harbin Institute of Technology.
82. Oberkampf, W. L., Sindir, M. N., & Conlisk, A. T. (1998). *AIAA guide for the verification and validation of computational fluid dynamics simulations*. American Institute of Aeronautics & Astronautics.
83. Ghanem, R. G., Spanos, P. D., & Spanos, P. (2003). *Stochastic finite element: A spectral approach* (p. 224). New York, Berlin: Springer.
84. Schuëller, G. I. (1997). A state-of-the-art report on computational stochastic mechanics. *Probabilistic Engineering Mechanics*, 12(4), 197–321.
85. Tatang, M. A. (2010). *Direct incorporation of uncertainty in chemical and environmental engineering systems*. Massachusetts Institute of Technology.

86. Dow, E. A. (2014). *Robust design and tolerancing of compressor blades*. Massachusetts Institute of Technology.
87. Garzón, V. E. (2003). *Probabilistic aerothermal design of compressor airfoils*. Massachusetts Institute of Technology.
88. Bunker, R. S. (2009). The effects of manufacturing tolerances on gas turbine cooling. *Journal of Turbomachinery*, 131(4), 1–11.
89. D’Ammaro, A., & Montomoli, F. (2013). Uncertainty quantification and film cooling. *Computer & Fluids*, 71, 320–326.
90. Montomoli, F., Hodson, H., & Haselbach, F. (2010). Effect of roughness and unsteadiness on the performance of a new low pressure turbine blade at low Reynolds numbers. *Journal of Turbomachinery*, 132, 031018.
91. Montomoli, F., Carnevale, M., D’Ammaro, A., et al. (2015). *Uncertainty quantification in computational fluid dynamics and aircraft engines*. Berlin: Springer.
92. Montomoli, F., Massini, M., & Salvadori, S. (2011). Geometrical uncertainty in turbomachinery: Tip gap and fillet radius. *Computer & Fluids*, 46, 362–368.
93. Guo, Xiangkun. (2016). *Uncertainty analysis of the geometric deviations on turbine performance*. Beijing: Beihang University.
94. Hylton, L. D., Mihelc, M. S., Turner, E. R., et al. (1983). *Analytical and experiment evaluation of the heat transfer distribution over the surface of turbine vane*. NASA Technical Report CR168015.
95. Schallhorn, P., Palmiter, C., Farmer, J., et al. (2000). Interfacing the generalized fluid system simulation program with the SINDA/G thermal program. In *AIAA-2000-2504, 36th AIAA/ASME/SAE/ASEE Joint Propulsion Conference and Exhibit*, Alabama, USA.
96. Holt, K., Majumdar, A., Steadman, T., & Hedayat, A. (2000). Numerical modeling and test data comparison of propulsion test article helium pressurization system. In *AIAA-2000-3719, 36th AIAA/ASME/SAE/ASEE Joint Propulsion Conference and Exhibit*, Alabama, USA.
97. Sözen, M. (2002). *A computational method for determining the equilibrium composition and product temperature in a LH2/LOX combustor*. NASA/CR-2003-212397. The NASA Faculty Fellowship Program Research Reports, Marshall Space Flight Center.
98. Schallhorn, A., & Hass, E. (2004). Forward looking pressure regulator algorithm for improved modeling performance within the generalized fluid system simulation program. In *AIAA-2004-3667, 40th AIAA/ASME/SAE/ASEE Joint Propulsion Conference and Exhibit*, Florida, USA.
99. Meitner, L. (2003). Procedure for determining 1-D flow distributions in arbitrarily connected passages without the influence of pumping, GT2003-38061. In *Proceeding of the ASME Turbo Expo*, Barcelona, Spain, Atlanta, Georgia, USA.
100. Okita, Y. (2006). Transient thermal and flow field in a turbine disk rotor-stator system, GT2006-90033. In *Proceeding of the ASME Turbo Expo*, Barcelona, Spain.
101. Bianchini, C., Da Soghe, R., Facchini, B., et al. (2008). Development of numerical tools for stator-rotor cavities calculation in heavy-duty gas turbines, GT2008-51268. In *Proceeding of the ASME Turbo Expo*, Berlin, Germany.
102. Young, C., & Snowsill Guy, D. (2002). CFD optimization of cooling air offtake passages within rotor cavities, GT2002-30480. In *Proceeding of the ASME Turbo Expo*, Amsterdam, The Netherlands.
103. Andreini, A., Da Soghe, R., Facchini, B., et al. (2008). Turbine stator well CFD studies: Effects of cavity cooling air flow, GT2008-51067. In *Proceeding of the ASME Turbo Expo*, Berlin, Germany.
104. Dixon, J. A., Brunton, I. L., & Scanlon, T. J. (2006). Turbine stator well heat transfer and cooling flow optimization, GT2006-90306. In *Proceeding of the ASME Turbo Expo*, Barcelona, Spain.
105. Jin, J. (2003). A summary of numerical propulsion simulation system(NPSS) by NASA. *Gas Turbine Experiment and Research*, 16, 57–62.
106. Flowmaster Automotive Case Study. (2007). BMW Motoren.

107. Masahik, Kubo. (2005). *Introduction of coupling simulation of automatic vehicle cooling system*. Minato: Mitsubishi Auto Co., Ltd.
108. Wang, P. (2014). *Investigations on multi-fidelity coupled method and its applications for flow simulation*. Beijing: Beihang University.
109. Zhou, Z., & Sun, R. (2006). *Study on one-dimensional model and CFD coupled air system analysis method*. Zhuzhou: China Aviation Power Machinery Research Institute.
110. Wang, P., Zheng, Y., Zou, Z .P., et al. (2013). A novel multi-fidelity coupled simulation method for flow systems. *Chinese Journal of Aeronautics*, 26(4), 868–875.
111. Garabedian, P., & Korn, D. (1976). A systematic method for computer design of supercritical airfoils in cascade. *Communications on Pure and Applied Mathematics*, 29(4), 369–382.
112. Schmidt, E. (1980). Computation of supercritical compressor and turbine cascades with a design method for transonic flows. *Journal of Engineering for Gas Turbines and Power*, 102 (1), 68–74.
113. Borges, J. E. (1990). A three-dimensional inverse method for turbomachinery: Part I—Theory. *Journal of Turbomachinery*, 112(3), 346–354.
114. Dang, T. Q. (1993). A fully three-dimensional inverse method for turbomachinery blading in transonic flows. *Journal of Turbomachinery*, 115(2), 354–361.
115. Mark, D., & Harold, Y. (1998). *A user's guide to MISES 2.53*. MIT Computational Aerospace Sciences Laboratory.
116. Chen, N. X. (2010). *Aerothermodynamics of Turbomachinery: Analysis and design*. John Wiley & Sons(Asia) Pte Ltd.
117. Zhu, F. *Aerodynamic design of axial-flow aero-turbomachine*. Xi'an: Northwestern Polytechnical University Aviation Major Teaching Materials Editing Room.
118. Alonov, B. M. (1980). *Modeling of aviation gas turbine blades*. Beijing: National Defence Industry Press.
119. Pritchard, L. J. (1985). *An eleven parameter axial turbine airfoil geometry model*. ASME Paper 85-GT-219.
120. Korakianitis, T. (1993). Hierarchical development of three direct-design methods for two-dimensional axial-turbomachinery cascades. *Journal of Turbomachinery*, 115(2), 314–324.
121. Korakianitis, T. (1993). Prescribed-curvature-distribution airfoils for the preliminary geometric design of axial-turbomachinery cascades. *Journal of Turbomachinery*, 115(2), 325–333.
122. Korakianitis, T., & Papagiannidis, P. (1993). Surface-curvature-distribution effects on turbine-cascade performance. *Journal of Turbomachinery*, 115(2), 334–341.
123. Corral, R., & Pastor, G. (2004). Parametric design of turbomachinery airfoils using highly differentiable splines. *Journal of Propulsion and Power*, 20(2), 335–343.
124. Anders, J. M., & Haarmeyer, J. (1999). A parametric blade design system. In *Von Karman Institute for Fluid Dynamics: Lecture Series 1999–2002 Turbomachinery Blade Design Systems*.
125. Trigg, M. A., Tubby, G. R., & Sheard, A. G. (1999). Automatic genetic optimization approach to two-dimensional blade profile design for steam turbines. *Journal of Turbomachinery*, 121(1), 11–17.
126. Koini, G. N., Sarakinos, S. S., & Nikolos, I. K. (2009). A software tool for parametric design of turbomachinery blades. *Advances in Engineering Software*, 40(1), 41–51.
127. Fang, X., Liu, S., & Wang, P. (2007). Research of 3d design method for rotor of supersonic high loaded contra turbine with large expansile meridional channel. *Acta Aeronautica et Astronautica Sinica*, 28(01), 25–31.
128. Pritchard, L. J. (1985). *An eleven parameter axial turbine aerofoil geometry model*. ASME Paper 85-GT-219.
129. Walraevens, R. E., & Cumpsty, N. A. (1995). Leading edge separation bubbles on turbomachine blades. *Journal of Turbomachinery*, 117(1), 115–125.

130. Bai, T., Zou, Z., Zhang, W., et al. (2014). Mechanism of effect of leading-edge geometry on the turbine blade cascade loss. *Journal of Aerospace Power*, 06, 1482–1489.
131. Feng, T. (2006). *Some problems of flow analysis and design in turbomachinery*. Beijing: Beihang University.
132. Zhang, W. H., Zou, Z. P., & Ye, J. (2012). Leading-edge redesign of a turbomachinery blade and its effect on aerodynamic performance. *Applied Energy*, 93, 655–667.
133. Benner, M. W., Sjolander, S. A., & Moustapha, S. H. (1997). Influence of leading-edge geometry on profile losses in turbines at off-design incidence: Experimental results and an improved correlation. *Journal of Turbomachinery*, 119(2), 193–200.
134. Filippov, G. A., & Wang, Z. (1963). The calculation of axial symmetric flow in a turbine stage with small ratio of diameter to blade length. *Journal of Moscow Power Institute*, 47, 63–78.
135. Harrison, S. (1992). The influence of blade lean on turbine losses. *Journal of Turbomachinery*, 114(1), 184–190.
136. Fischer, A., Reiss, W., & Seume, J. R. (2004). Performance of strongly bowed stators in a four-stage high-speed compressor. *Journal of Turbomachinery*, 126(3), 333–338.
137. Rosic, B., & Xu, L. (2011). Blade lean and shroud leakage flows in low aspect ratio turbines. *Journal of Turbomachinery*, 134, 031003.
138. Zhong, J. (1995). *An experimental investigation by using curved blade to control secondary flow in compressor cascade*. Harbin: Harbin Institute of Technology.
139. Zou, Z., Zhao, L., Chen, M., et al. (1998). Three-dimensional blading and its influence on blade aerodynamic loading. *Journal of Aerospace Power*, 13(3), 235–240.
140. Wang, Z., & Zheng, Y. (2000). Research status and development of the bowed-twisted blade for turbomachines. *Engineering Science*, 2(6), 40–48.
141. Hourmouziadis, J., & Hubner, N. (1985). *3D design of turbine airfoils*. ASME Paper 85-GT-188.
142. Schobeiri, M. T., Suryanarayanan, A., Jermann, C., et al. (2004). *A comparative aerodynamic and performance study of a three-stage high pressure turbine with 3-D bowed blades and cylindrical blades*. ASME Paper GT2004-53650.
143. Bohn, D. E., Ren, J., & Tummars, C. (2005). *Unsteady 3D numerical of the influence of the blading design on the stator-rotor interaction in a 2-stage turbine*. ASME Paper GT2005-68115.
144. Chen, N. (1995). *A comparative study on different leaned and skewed bladings in a turbine stator by 3-D Navier-stokes analysis*. AIAA Paper 95-2189.
145. Ye, X. (1995). *Research on three-dimensional flows in bending blade and unstructured mesh methods*. Beijing: Beihang University.
146. Han, W., Han, C., et al. (1991). Effect of blade leaning on the development of passage vortices and losses in the passage of turbine cascade with a great turning angle. In *Proceedings of the Chinese society of Engineering Thermophysics*, 912034.
147. Wang, Z., Su, J., & Zhong, J. (1994). New progress of investigation into mechanism of reducing energy loss in cascades with curved and twisted blades. *Journal of Engineering Thermophysics*, 15(2), 147–152.
148. Lindner, E. (1995). *Numerical and experimental analysis of secondary flow in modern state-of-the-art low pressure guide vane rows*. ASME Paper 95-GT-189.
149. Kawagishi, H., & Kawasaki, S. (1991). *The effect of nozzle lean on turbine efficiency*. PWR-Vol. 13, Design, Repair, and Refurbishment of Steam Turbines. ASME Paper.
150. Hesketh, J. A., Tritthart, H., & Aubry, P. (1994). *Modernization of steam turbines for improved performance*. Symposium on Steam Turbine and Generators.
151. Trehan, R., & Roy, B. (2013). *Investigation of turbine cascade blades with part-span sweep with an open end*. ASME Paper GT2013-95314.
152. Trehan, R., & Roy, B. (2012). *Application of sweep to low pressure turbine cascade blade for tip flow containment*. AIAA Paper GT2012-3878.
153. Chen, G. (2009). Design characteristics of Trent 1000. *Aero Engine*, 35(4), 1–6.
154. Julian, F. (2008). First steps for CFMI leap-X. *Interavia Business and Technology*, 700, 4–6.

155. Bagshaw, D. A., Ingram, G. L., Gregory-Smith, D. G., et al. (2008). An experimental study of three-dimensional turbine blades combined with profiled endwalls. *Proceedings of the Institution of Mechanical Engineers, Part A: Journal of Power and Energy*, 222(1), 103–110.
156. Rose, M. G. (1994). *Non-axisymmetric endwall profiling in the HP NGV's of an axial flow gas turbine*. ASME Paper 94-GT-249.
157. Kopper, F. C., Milanot, R., & Vancot, M. (1981). Experimental investigation of endwall profiling in a turbine vane cascade. *AIAA Journal*, 19(8), 1033–1040.
158. Harvey, N. W., Rose, M. G., Taylor, M. D., et al. (2000). Nonaxisymmetric turbine end wall design: Part 1 three-dimensional linear design system. *Journal of Turbomachinery*, 122(2), 278–285.
159. Hartland, J. C., Gregory-Smith, D. G., Harvey, N. W., et al. (2000). Nonaxisymmetric turbine end wall design: Part 2 experimental validation. *Journal of Turbomachinery*, 122(2), 286–293.
160. Brennan, G., Harvey, N. W., Rose, M. G., et al. (2003). Improving the efficiency of the Trent 500-HP turbine using nonaxisymmetric end walls: Part 1 turbine design. *Journal of Turbomachinery*, 125(3), 497–504.
161. Rose, M. G., Harvey, N. W., Seaman, P., et al. (2001). *Improving the efficiency of the Trent 500-HP turbine using nonaxisymmetric end walls: Part 2 experimental validation*. ASME Paper 2001-GT-0505.
162. Germain, T., Nagel, M., & Raab, I. (2010). Improving efficiency of a high work turbine using nonaxisymmetric endwalls—Part I: Endwall design and performance. *Journal of Turbomachinery*, 132, 021007.
163. Schüpbach, P., Abhari, R. S., & Rose, M. G. (2010). Improving efficiency of a high work turbine using nonaxisymmetric endwalls—Part II: Time-resolved flow physics. *Journal of Turbomachinery*, 132, 021008.
164. Praisner, T. J., Allen-Bradley, E., Grover, E. A., et al. (2013). Application of nonaxisymmetric endwall contouring to conventional and high-lift turbine airfoils. *Journal of Turbomachinery*, 135, 061006.
165. Knezevici, D. C., Sjolander, S. A., & Praisner, T. J. (2010). Measurements of secondary losses in a turbine cascade with the implementation of nonaxisymmetric endwall contouring. *Journal of Turbomachinery*, 132, 011013.
166. González, P., & Lantero, M. (2006). *Low pressure turbine design for Rolls-Royce Trent 900 Turbofan*. ASME paper GT2006-90997.
167. Sun, H., Song, L., & Li, J. (2013). Optimization design of nonaxisymmetric end wall profiling for turbine cascade. *Journal of Xi'an Jiaotong University*, 47(9), 35–40.
168. Tian, Y., Ji, L., Li, W., et al. (2013). Applicability of blended blade and endwall under different operating conditions. *Journal of Aerospace Power*, 28(8), 1905–1913.
169. Turgut, Ö. H., & Camcı, C. (2012). *Experimental investigation and computational evaluation of contoured endwall and leading edge fillet configurations in a turbine NGV*. ASME Paper GT2012-69304.
170. Zess, G. A., & Thole, K. A. (2002). Computational design and experimental evaluation of using a leading edge fillet on a gas turbine vane. *Journal of Turbomachinery*, 124(2), 167–175.
171. Turgut, Ö. H., & Camcı, C. (2013). *Influence of leading edge fillet and nonaxisymmetric contoured endwall on turbine NGV exit flow structure and interactions with the rim seal flow*. ASME Paper GT2013-95843.
172. Sauer, H., Muller, R., & Vogeler, K. (2001). Reduction of Secondary flow losses in turbine cascades by leading edge modifications at the endwall. *Journal of Turbomachinery*, 123(2), 207–213.
173. Becz, S., & Majewski, M. S. (2003). *Leading edge modification effects on turbine cascade endwall loss*. ASME Paper GT2003-38898.

174. Lyall, M. E., King, P. I., Clark, J. P., et al. (2014). Endwall loss reduction of high lift low pressure turbine airfoils using profile contouring—Part I: Airfoil design. *Journal of Turbomachinery*, 136, 81005.
175. Sangston, K., Little, J., Lyall, M. E., et al. (2014). End wall loss reduction of high lift low pressure turbine airfoils using profile contouring—Part II: Validation. *Journal of Turbomachinery*, 136, 81006.
176. Schlienger, J., Pfau, A., Kalfas, A. I., et al. (2003). *Effects of labyrinth seal variation on multistage axial turbine flow*. ASME Paper GT2003-38270.
177. Rosic, B., Denton, J. D., Curtis, E. M., et al. (2008). The influence of shroud and cavity geometry on turbine performance: An experimental and computational study-part ii: exit cavity geometry. *Journal of Turbomachinery*, 130, 41002.
178. Wallis, A. M., Denton, J. D., & Demargne, A. A. J. (2001). The control of shroud leakage flows to reduce aerodynamic losses in a low aspect ratio, shrouded axial flow turbine. *Journal of Turbomachinery*, 123(2), 334–341.
179. Rosic, B., & Denton, J. D. (2008). Control of shroud leakage loss by reducing circumferential mixing. *Journal of Turbomachinery*, 130, 21010.
180. Yang, D., & Feng, Z. (2007). Study on tip leakage flow and heat transfer for a squealer tip blade. *Journal of Engineering Thermophysics*, 28(6), 936–938.
181. Booth, T. C., Dodge, P. R., & Hepworth, H. K. (1981). *Rotor-tip leakage, Part I—Basic methodology*. ASME Paper 81-GT-71.
182. Camci, C., Dey, D., & Kavurmacioglu, L. (2005). Aerodynamics of tip leakage flows near partial squealer rims in an axial flow turbine stage. *Journal of Turbomachinery*, 127(1), 14–24.
183. Kwak, J. S., & Han, J. (2003). Heat transfer coefficients on the squealer tip and near squealer tip regions of a gas turbine blade. *Journal of Heat Transfer*, 125(4), 669–677.
184. Nasir, H., Ekkad, S. V., Kontrovitz, D. M., et al. (2004). Effect of tip gap and squealer geometry on detailed heat transfer measurements over a high pressure turbine rotor blade tip. *Journal of Turbomachinery*, 126(2), 221–228.
185. Prakash, C., Lee, C. P., Cherry, D., et al. (2005). *Analysis of some improve blade tip concepts*. ASME Paper GT2005-68333.
186. Patel, K. V. (1980). *Research on a high work axial gas generator turbine*. SAE Technical Paper.
187. Schabowski, Z., & Hodson, H. P. (2007). *The reduction of over tip leakage loss in unshrouded axial turbines using winglets and squealers*. ASME Paper GT2007-27623.
188. Zou, ZP., Shao, F., Li, YR., et al. (2017). Dominant flow structure in the squealer tip gap and its impact on turbine aerodynamic performance. *Energy*, 138, 167–184.
189. Wheeler, A. P. S., Atkins, N. R., & He, L. (2011). Turbine blade tip heat transfer in low speed and high speed flows. *Journal of Turbomachinery*, 133, 41025.
190. Zhang, Q., & He, L. (2013). Tip-shaping for HP turbine blade aerothermal performance management. *Journal of Turbomachinery*, 135, 51025.
191. Denton, J. D., & Xu, L. (1990). The trailing edge loss of transonic turbine blades. *Journal of Turbomachinery*, 112(2), 277–285.
192. Joly, M. M., Verstraete, T., & Paniagua, G. (2013). Differential evolution based soft optimization to attenuate vane–rotor shock interaction in high-pressure turbines. *Applied Soft Computing*, 13(4), 1882–1891.
193. Shi, W. (2011). *Numerical and experimental study of cascade flow in turbo-machinery*. Beijing: Beihang University.
194. Jennions, I. K., & Adamczyk, J. J. (1997). Evaluation of the interaction losses in a transonic turbine HP rotor/LP vane configuration. *Journal of Turbomachinery*, 119(1), 68–76.
195. Giel, P. W. (2007). *NASA/GE highly-loaded turbine research program*. NASA Fundamental Aeronautics 2007 Annual Meeting.
196. Saracoglu, B. H., Paniagua, G., Salvadori, S., et al. (2012). Trailing edge shock modulation by pulsating coolant ejection. *Applied Thermal Engineering*, 48, 1–10.

197. Sonoda, T., Arima, T., Olhofer, M., et al. (2004). A study of advanced high-loaded transonic turbine airfoils. *Journal of Turbomachinery*, 128(4), 650–657.
198. Joly, M. M., Verstraete, T., & Paniagua, G. (2010). *Attenuation of vane distortion in a transonic turbine using optimization strategies: Part I—Methodology*. ASME Paper GT2010-22370.
199. Joly, M. M., Paniagua, G., & Verstraete, T. (2010). *Attenuation of vane distortion in a transonic turbine using optimization strategies: Part II—Optimization*. ASME Paper GT2010-22371.
200. Palm, B., & Gardens, F. L. (1999). *Neural net-based redesign of a gas generator turbine for improved unsteady aerodynamic performance*. AIAA Paper 99-2522.
201. Rai, M. M., Madavan, N. K., & Huber, F. W. (2000). *Improving the unsteady aerodynamic performance of transonic turbines using neural networks*. AIAA Paper 2000-0169.
202. Liu, H. X., An, Y. G., & Zou, Z. P. (2014). *Aerothermal analysis of a turbine with rim seal cavity*. ASME Paper GT2014-25276.
203. Bunker, R. S. (2008). *The effects of manufacturing tolerances on gas turbine cooling*. ASME Paper GT2008-50124.
204. De la Rosa Blanco, E., & Hodson, H. P. (2006). *Effect of the leakage flows and the upstream platform geometry on the endwall flows of a turbine cascade*. ASME Paper GT2006-90767.
205. Turner, M. (1995). *Multistage turbine simulation with blade-vortex interaction*. ASME Paper 95-GT-288.
206. McLean, C., Camci, C., & Glezer, B. (2001). Mainstream aerodynamic effects due to wheel-space coolant injection in a high-pressure turbine stage: Part I—Aerodynamic measurements in the stationary frame. *Journal of Turbomachinery*, 123(4), 687–696.
207. McLean, C., Camci, C., & Glezer, B. (2001). Mainstream aerodynamic effects due to wheel-space coolant injection in a high-pressure turbine stage: Part II—Aerodynamic measurements in the rotational frame. *Journal of Turbomachinery*, 123(4), 697–703.
208. Ong, J., Miller, R. J., & Uchida, S. (2012). The effect of coolant injection on the endwall flow of a high pressure turbine. *Journal of Turbomachinery*, 134, 51003–51008.
209. de la Rosa Blanco, E., & Hodson, H. P. (2005). *Effect of upstream platform geometry on the endwall flows of a turbine cascade*. ASME Paper GT2005-68938.
210. Blanco, E., La Rosa, De, Hodson, H. P., et al. (2009). Effect of the leakage flows and the upstream platform geometry on the endwall flows of a turbine cascade. *Journal of Turbomachinery*, 131, 11004–11009.
211. Schuler, P., Kurz, W., Dullenkopf, K., & Bauer, H. J. (2010). *The influence of different rim seal geometries on hot-gas ingestion and total pressure loss in a low-pressure turbine*. ASME Paper GT2010-22205.
212. Schuler, P., Dullenkopf, K., & Bauer, H. J. (2011). *Investigation of the influence of different rim seal geometries in a low-pressure turbine*. ASME Paper GT2011-45682.
213. Erickson, R., & Simon, T. W. (2009). Effects of stator/rotor leakage flow and axisymmetric contouring on endwall adiabatic effectiveness and aerodynamic loss. In *International Symposium on Heat Transfer in Gas Turbine Systems*, August 9–14, Antalya, Turkey.
214. Zhang, L., & Moon, H. K. (2011). *Comparison of two axisymmetric profiles on blade platform film cooling*. ASME Paper GT2011-45102.
215. Zhang, L., Lee, D. H., Yin, J., et al. (2013). *The effect of axisymmetric profile on turbine blade platform heat transfer distribution*. ASME Paper GT2013-94335.
216. Popovic, I., & Hodson, H. P. (2010). *Aerothermal impact of the interaction between hub leakage and mainstream flows in highly-loaded HP turbine blades*. ASME Paper GT2010-22311.
217. Popović, I., Hodson, H. P., Janke, E., et al. (2013). The effects of unsteadiness and compressibility on the interaction between hub leakage and mainstream flows in high-pressure turbines. *Journal of Turbomachinery*, 135, 61015.
218. Popović, I., & Hodson, H. P. (2013). The effects of a parametric variation of the rim seal geometry on the interaction between hub leakage and mainstream flows in high pressure turbines. *Journal of Engineering for Gas Turbines and Power*, 135, 112501.

219. Popović, I., & Hodson, H. P. (2013). Improving turbine stage efficiency and sealing effectiveness through modifications of the rim seal geometry. *Journal of Turbomachinery*, 135, 61016.
220. Göttlich, E. (2011). Research on the aerodynamics of intermediate turbine diffusers. *Progress in Aerospace Sciences*, 47(4), 249–279.
221. Axelsson, L., Osso, C. A., Cadrecha, D., et al. (2007). *Design performance evaluation and endwall flow structure investigation of an S-shaped intermediate turbine duct*. ASME paper GT2007-27650.
222. Wallin, F., Eriksson, L., & Nilsson, M. (2006). *Intermediate turbine duct design and optimization*. 25th International Congress of the Aeronautical Sciences.
223. Wallin, F., & Eriksson, L. (2007). *Non-axisymmetric endwall shape optimization of an intermediate turbine duct*. ISABE 2007-1300.
224. Wallin, F., & Eriksson, L. (2008). *Design of an aggressive flow-controlled turbine duct*. ASME Paper GT2008-51202.
225. Marn, A., Göttlich, E., Cadrecha, D., et al. (2009). Shorten the intermediate turbine duct length by applying an integrated concept. *Journal of Turbomachinery*, 131, 041014.
226. Lavagnoli, S., Yasa, T., Paniagua, G., et al. (2010). *Aerodynamic analysis of an innovative low pressure vane placed in a S-shaped duct*. ASME Paper GT2010-22546.
227. Solano, J. P., Pinilla, V., Paniagua, G., et al. (2011). Aero-thermal investigation of a multi-splitter axial turbine. *International Journal of Heat and Fluid Flow*, 32(5), 1036–1046.
228. Spataro, R., Göttlich, E., & Lengani, D. (2013). *Development of a turning mid turbine frame with embedded design—Part I: Design and steady measurements*. ASME paper GT2013-95279.
229. Griffin, L. W., Huber, F. W., & Sharma, O. P. (1996). Performance improvement through indexing of turbine airfoils: Part 2—Numerical simulation. *Journal of Turbomachinery*, 118(4), 636–642.
230. Billiard, N., Paniagua, G., & Dénos, R. (2005). *Effect of clocking on the heat transfer distribution of a second stator tested in a one and a half stage HP turbine*. ASME Paper GT2005-68462.
231. Huber, F. W., Johnson, P. D., Sharma, O. P., et al. (1996). Performance improvement through indexing of turbine airfoils: Part 1—Experimental investigation. *Journal of Turbomachinery*, 118(4), 630–635.
232. König, S., Stoffel, B., & Taher Schobeiri, M. (2009). Experimental investigation of the clocking effect in a 1.5-stage axial turbine—Part I: Time-averaged results. *Journal of Turbomachinery*, 131, 021003–021003.
233. Li, H. D., & He, L. (2003). Blade count and clocking effects on three-bladerow interaction in a transonic turbine. *Journal of Turbomachinery*, 125(4), 632–640.
234. He, L., Menshikova, V., & Haller, B. R. (2004). *Influence of hot streak circumferential length-scale in transonic turbine stage*. ASME Paper GT2004-53370.
235. Ong, J., & Miller, R. J. (2012). Hot streak and vane coolant migration in a downstream rotor. *Journal of Turbomachinery*, 134, 51002–51010.
236. Hawthorne, W. R. (1986). Secondary circulation in fluid flow. *Proceedings of the Royal Society of London, Series A: Mathematical and Physical Sciences*, 1951(206), 374–387.
237. Dorney, D. J., & Sondak, D. L. (2000). Effects of tip clearance on hot streak migration in a high-subsonic single-stage turbine. *Journal of Turbomachinery*, 122(4), 613–620.
238. Dorney, D. J., Davis, R. L., Edwards, D. E., et al. (1992). Unsteady analysis of hot streak migration in a turbine stage. *Journal of Propulsion and Power*, 8(2), 520–529.
239. Khanal, B., He, L., Northall, J., et al. (2013). Analysis of radial migration of hot-streak in swirling flow through high-pressure turbine stage. *Journal of Turbomachinery*, 135, 041005.
240. Dorney, D. J., & Gundy-Burlet, K. (1996). Hot-streak clocking effects in a 1-1/2 stage turbine. *Journal of Propulsion and Power*, 12(3), 619–620.
241. Howell, R. J., Hodson, H. P., Schulte, V., et al. (2002). Boundary layer development in the BR710 and BR715 LP turbines—The implementation of high-lift and ultra-high-lift concepts. *Journal of Turbomachinery*, 124(3), 385–392.

242. Coull, J. D., Thomas, R. L., & Hodson, H. P. (2008). *Velocity distributions for low pressure turbines*. ASME Paper GT2008-50589.
243. Ulizar, I., & González, P. (2001). *Aerodynamic design for a new five stage low pressure turbine for the Rolls-Royce Trent 500 Turbofan*. ASME Paper 2001-GT-440.
244. Haselbach, F., Schiffer, H., & Horsman, M. (2002). The application of ultra high lift blading in the BR715 LP turbine. *Journal of Turbomachinery*, 124(3), 45–51.
245. Hodson, H. P., & Howell, R. J. (2005). Bladerow interactions, transition, and high-lift aerofoils in low-pressure turbines. *Annual Review of Fluid Mechanics*, 37, 71–98.
246. Flegel-McVetta, A. B., Giel, P. W., & Welch, G. E. (2013). *Aerodynamic measurements of a variable-speed power-turbine blade section in a transonic turbine cascade at low inlet turbulence*. NASA TM-218069.
247. Rajiv, S., Rohinton, I., Mahadevan, B., et al. (2004). *High fidelity system simulation of aerospace vehicles using NPSS*. AIAA-2004-371.
248. Deng, Q. (2013). *Investigation of turbine pressure controlled vertex design technology*. Harbin: Harbin Engineering University.

Chapter 7

Flow Control Technologies

In gas turbines, relatively few stages of turbine cause high pressure and temperature gradient and high blade loading the cooling system including metal material cooling, hub and shroud sealing, etc. also further increases the complexity of such a flow field. Design of high-performance turbine has presented new requirements for flow organizing, such as the control over the separation of low pressure turbines with a low Reynolds number and a high load, the control over secondary flow and tip leakage flow, and turbine working condition variation through minor local changes, etc. The conventional turbine design methods usually fail to satisfy requirements above within an application range extensive enough; or, a great cost may be required to meet such requirements. Relatively speaking, if minor control actions over critical areas are taken, such as boundary layer, end walls, tip clearance and throat, etc., the flow state of main flow can be changed to a large extent so as to further achieve the purpose of organizing flow field and improving turbine performance. The approach of obtaining large flow gains of main flow based on minor flow corrections is referred to as flow control.

7.1 Introduction to Flow Control Technology

The idea of flow control begins to develop together with modern fluid mechanics. In 1904, Prandtl not only illustrated the boundary layer theory, but also introduced several methods for boundary layer control, in “On the motion of a fluid with very small viscosity” [1]. The flow control technology can be roughly classified into passive control and active control. As to the former, it refers to the control measures that have been determined during design. Generally, it depends on mechanical structures or wall shapes, such as a vortex generator in a mechanical form. With regard to the latter, it is exerted in the process of working and usually requires consuming energies, such as the blowing/suction boundary layer. In addition, such

two categories of flow control methods have their own advantages and disadvantages. To be specific, the passive control is provided with a simple structure. However, as the control mechanism always exists in the flow channel, it can disturb the flow and further give rise to losses instead of gains in conditions that no controls should be exerted. Although the active control is able to exert controls of different levels on the actual condition of flow and generate preferable control effects, the corresponding active control mechanism is rather complex in most cases. Consequently, not only the reliability of it is much lower than the passive control, but extra energies are needed in the process of control implementation to drive the control device. Furthermore, the active flow control can be subdivided into preset control and interaction control (see Fig. 7.1). In detail, the former does not change with variations in flow conditions (although such an approach itself is non-steady and time-varying) while the latter continuously monitors flow state variations by virtue of a sensor and makes an adjustment for its control mode correspondingly.

At present, the developing flow control technologies that have been applied into turbines mainly consist of those as follows.

- (1) Vortex Generators (VGs) Technology. The basic VGs technology adopts a mechanical spoiler, pore or slot structure. By shearing with main flow, a specific vortex structure is formed. Typical geometric construction of a VG is given in Fig. 7.2. Figure 7.2a, b respectively show a VG in a shape of two-dimensional rectangular or triangular spoiler and a VG with a more complex three-dimensional structure. The major shape and location parameters of the VG include a dimensionless height of spoiler h/δ , a dimensionless length of spoiler e/h , a dimensionless spoiler spacing $\Delta z/h$ and a declination angle β . Mechanical VGs technology commonly falls into a category of passive flow control, while blowing and suction are also able to induce local jet. Combined actions of shearing and choking controllable jet on main flow finally generate the required vortex structure, as shown in Fig. 7.3. All these means are the jets vortex generator technology that belongs to the active flow control.
- (2) Surface Treatment Technology. That trip wires are mounted on the surface of blade (see Fig. 7.4) can advance the transition of flow field so as to acquire a

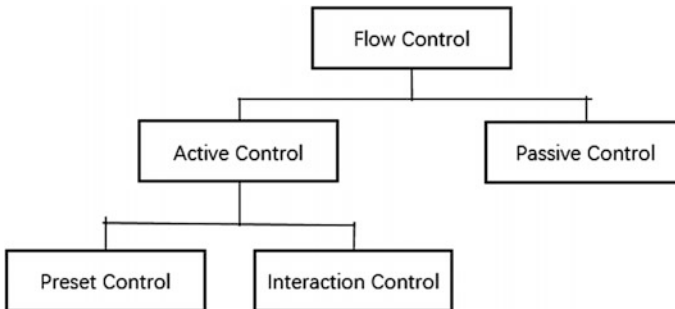


Fig. 7.1 Classification of flow control technology

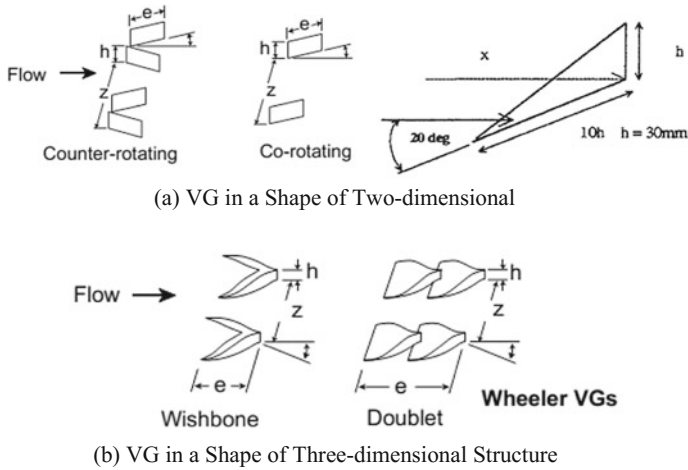


Fig. 7.2 Geometric structure of mechanical VGs [2]

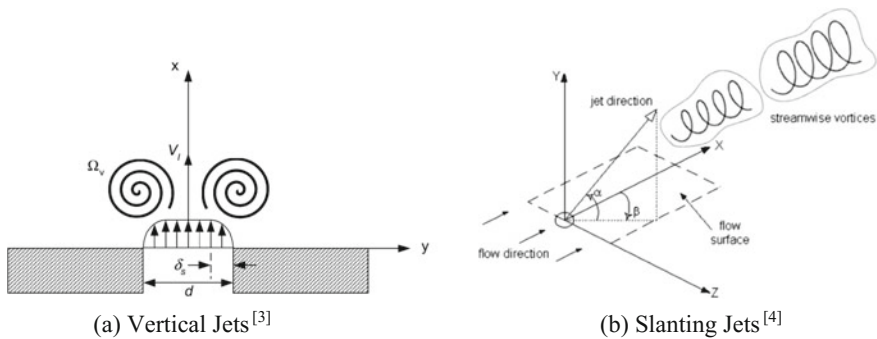


Fig. 7.3 Schematic of a jet vortex generator

turbulent boundary flow field with a stronger separation-resistant ability. Similarly, setting of the appropriate blade surface roughness can effectively control flow separation in the blade passage of turbine.

- (3) Variable Blade Technology. Metal angle of the turbine blade is one of the key factors that determine working conditions of turbine. By adjusting setting angle of the turbine blade or metal angle for part of its chord lengths, critical parameters of the turbine, such as flow rate, reaction degree and expansion ratio, etc., can be changed based on variable blade (see Fig. 7.5) technology. In the end, working condition adjustment is realized for the turbine. Such a technology falls into the category of active control.
- (4) Aerodynamic Jet Technology. Airstreams are injected onto the turbine blade surface and its tip, etc. at a certain flow rate and angle. In this way, key flow

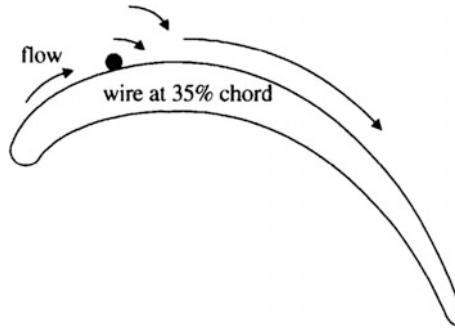


Fig. 7.4 Schematic of trip wires on the suction surface of a turbine blade [5]

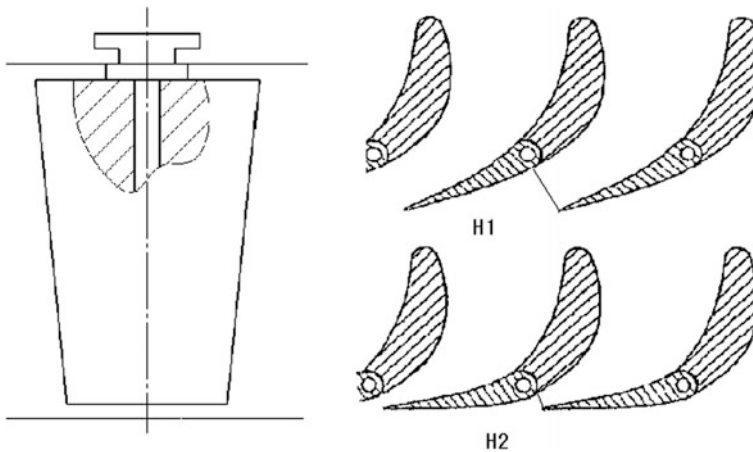


Fig. 7.5 Schematic diagram of variable blade

structures are changed, including boundary layer and vortex system, etc. This technology falls into the category of active control. Aerodynamic jet is able to not only directly exert momentum on local flow field to set up the flow field structure required, but form vortices shearing with the main flow so as to affect the relevant flow field based on such vortices (that is, vortex generator jets technology mentioned above). Figure 7.6 shows a jet VG for low-pressure turbine blade. In line with the sequential control law of jets, the aerodynamic jets technology can be further divided into steady jet and pulsed jet. As for jets in turbine parts, they erupt in pinhole arrays usually or from grooves which is known as the Air Curtain Technology. The jet required by flow control in turbine is commonly derived from compressor. Due to a small flow rate, no significant influences can be generated on thermodynamic cycle of its engine.

- (5) Plasma Technology. Plasma is a nearly electroneutral aggregation constituted by positive and negative charged particles. As well, it intensively interacts with

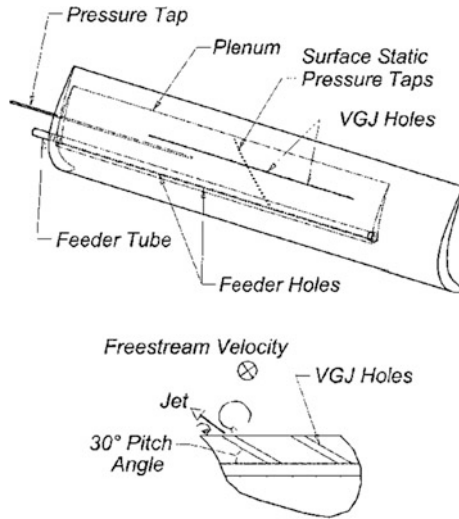


Fig. 7.6 Jet VG for low-pressure turbine blade [6]

neutral gas background. In a flow field that needs to be controlled, controllable electric field is exerted by a plasma actuator (shown in Fig. 7.7) to form plasma, induce local flow field movement and ultimately affect the flow field structure of main flow. Hence, the goal of flow control is achieved [7]. This is the plasma flow control technology falling into the category of active control.

The flow control technology is a cutting-edge technique in aerospace, which has giant application potentials in the drag reduction, lift enhancement and operation of aircraft, the internal flow control of engine and the flow control around rotor wing, etc. In comparison with external flow issues related to aircraft, extremely complex working conditions of the internal flows in a gas turbine have presented challenges

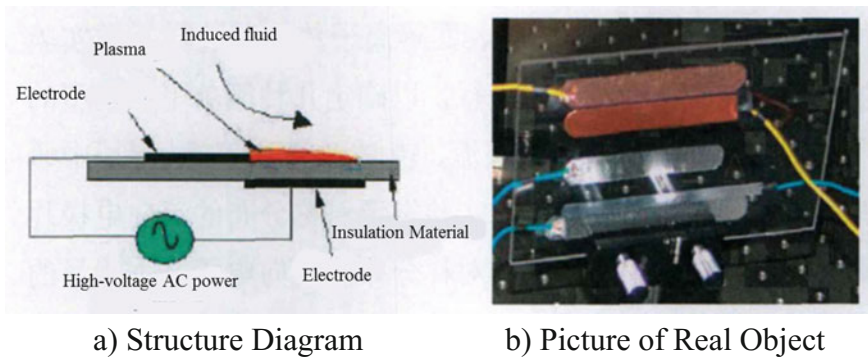


Fig. 7.7 Plasma actuator

to the application of the corresponding flow control technology. Due to high speed revolution of engine rotor, strict restrictions on its structural strength, complex geometrical shape of its flow channel, excessively high gas temperature and a wide working parameter variation range of it, etc., many effective methods that are applicable to external flow control over aircraft cannot be utilized in the flow control of gas turbine. In this chapter, several typical flow control technologies and their applications in gas turbines are introduced according to the flow characteristic of turbine components.

7.2 Flow Control Technology for Boundary Layer

As described in Chap. 4, due to a small Reynolds number in blade passage of large bypass ratio low pressure turbine, the flow field is in a laminar condition. Relatively, it is much likely for separation of boundary layer to take place and its flow field parameters (blade loading distribution, Reynolds number, incoming flow turbulence, etc.) determine the generation of separation/reattachment and the position of separation/reattachment point, etc. Moreover, the low pressure turbine blade of a high bypass ratio turbofan engine has a rather great aspect ratio between 3:1 and 7:1 in general cases. Considering this, the areas under influences of secondary flows, including horseshoe vortex, corner vortex and leakage vortex, etc., in end walls or tip region are very limited. Therefore, the secondary flow loss only occupies a very small proportion. Under such circumstances, losses caused by the separation of boundary layer turns into the most important flow losses inside a low-pressure turbine and a major influencing factor on its aerodynamic efficiency. During unsteady design for the low pressure turbine, high turbulence and upstream wake can be both adopted to induce bypass transition of the boundary layer and control boundary layer separation. However, the corresponding control effects are subjected to impacts of load, Reynolds number and wake frequency, etc. As a consequence, the relevant issues cannot be solved completely dependent on this approach [8]. As another effective means to restrict flow separation of boundary layer, the flow control technology either independently acts on the suction surface boundary layer of a low Reynolds number high load low pressure turbine, or exerts combined actions together with the wake to reduce separation losses and implement high load turbine design for turbine parts.

7.2.1 *Transition Inducing Technology Based on Surface Trip Wires*

As for the suction surface flow field of a low Reynolds number high load turbine blade with an excessively large adverse pressure gradient, unsteady wakes cannot be relied on to sufficiently control the separation of boundary layer in an effective manner.

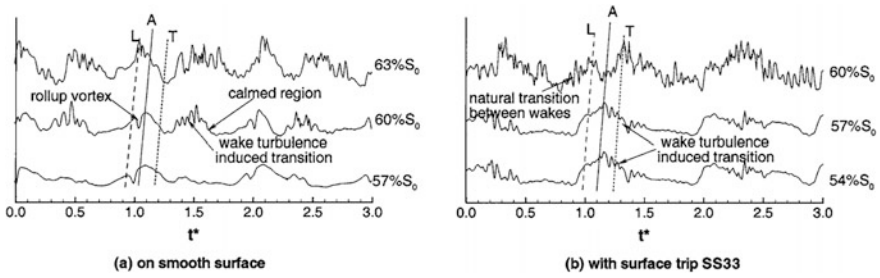


Fig. 7.8 Advanced transition under trip wires and wakes [9]

Taking T106C Blade Profile Turbine Cascade as the example, when the Reynolds number is as low as 174,000, transition induced by wake jet is significantly delayed and the calmed region formed by it also lasts for a short time as shown in Fig. 7.8a. Thus, the length reduction of separation bubble is insignificant and decreases in boundary layer losses are also under substantial restrictions (see Fig. 7.9). On this basis, trip wires are set up to apply disturbances so as to evidently shorten the delay between transition and wake, as given in Fig. 7.8b. Under such circumstances, the length of separation bubbles can be shortened evidently and the loss of boundary layer can be significantly brought down correspondingly (see Fig. 7.9). In addition, Figure 7.9b also indicates that the technique of advancing transition with trip wires and reducing boundary layer loss is effective within a considerably extensive scope of Reynolds number.

The effect of trip wire controlling transition in advance is closely related to both height and shapes of the trip wires. The optimal trip wire height should be about 60% of the local boundary layer displacement thickness. Compared with round trip

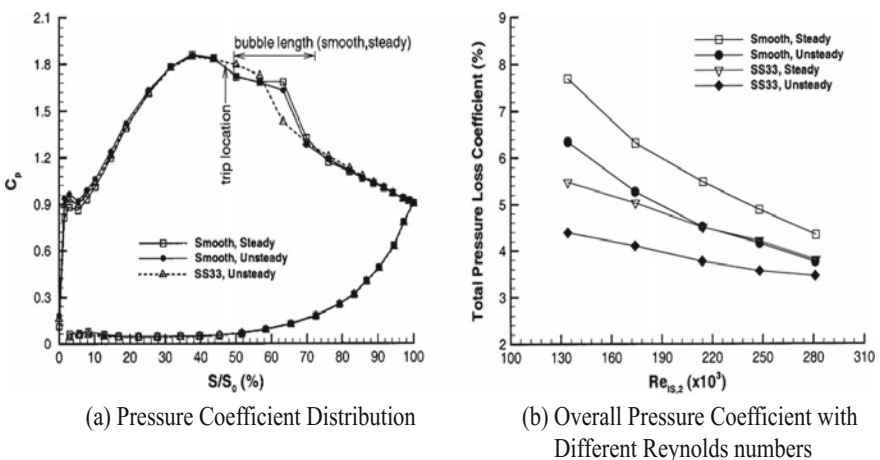


Fig. 7.9 Combined effects of trip wires and wakes on separation and boundary loss [9]

wires, those in stepped profiles can give rise to better control effects, while wave-shaped trip wires have the capability to cause effect of advancing transition in circumstances independent of wakes [9, 10]. However, a trip wire control mode for the purpose of advancing transition increases wetted area of the turbulent flow. Therefore, in order to reduce frictional loss of turbulent boundary layer, aft-loaded profile is appropriate [11].

7.2.2 Transition Controlling Technology Based on Rough Surface

Similar to trip wires, rough blade surface can cause disturbance to boundary layer. On the suction surface of a low Reynolds number high load turbine, flow separation, transition and the corresponding flow losses incurred by local adverse pressure gradient are all under influences of surface roughness. J. P. Bons [12] draws conclusions about studies on the surface roughness controlling over boundary layer flow separation. In his opinion, boundary layer flow separation can be controlled by appropriately increasing local surface roughness. Such control is implemented by virtue of advancing transition [13], or plays a role in laminar boundary layer only. In other words, reattachment of separated flow fields is facilitated by enhancing momentum exchange instead of transition [14].

During experimental studies, blade surface roughness is usually quantitatively simulated by randomly distributed roughness elements. Targeted at aft-loaded ultra-high load turbines, Maria Vera et al. [8] carried out cascade tests that incorporate unsteady effects of wakes. As a result, rough surface controlling blade suction surface separation is proved to play a role in boundary layer loss reduction. Stephen K. Roberts et al. [13] taked advantage of flexible walls to simulate load distributions of turbine and study control actions of roughness element arrays on boundary layer transition inception and separation bubble sizes on a flat plate. Relevant researches demonstrate that although the roughness element array is unable to obviously change the frequency of transition inceptions, the initial disturbance amplitude of these inceptions evidently increases (as shown in Fig. 7.10 in which PSD refers to Power Spectral Density). This is the key to advancing the transition on the rough wall surface. Moreover, further studies also show that the height of a roughness element array plays a dominant role, which is followed by effects of spacing and arraying directions.

There are also many studies in this field in China. In Institute of Engineering Thermophysics, Chinese Academy of Sciences, numerical simulations are employed to study impacts of surface roughness in high load low pressure turbine [15]. The study results show that, based on rough bands, not only can transition be advanced for the boundary layer on high load low pressure turbine blade surface, but length of the separation bubble on suction surface can be controlled. In this way, blade profile losses decrease. By contrast, the rough band based on variable

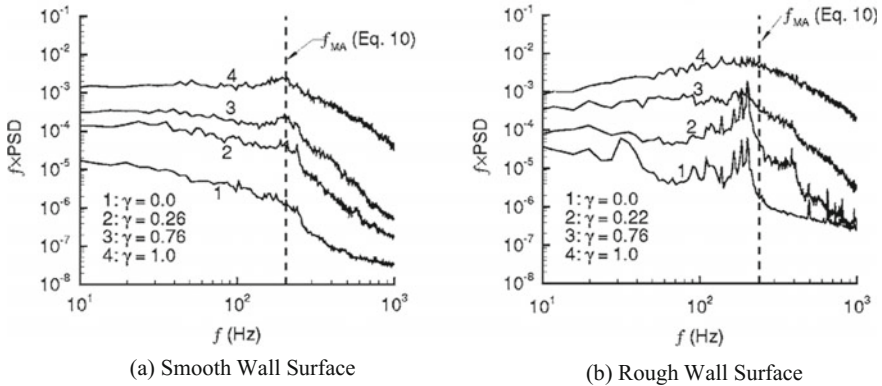


Fig. 7.10 Boundary layer power spectrum with different Roughness

roughness height generates better effects. In Beihang University (BUAA), influences of the roughness are studied under circumstances of different Reynolds numbers [16]. Corresponding results indicate that increase in blade surface roughness intensifies transport and mixing inside the boundary layer and plumps the velocity profile of boundary layer. The roughness has different influencing laws on turbine cascade in a condition of different Reynolds numbers. When the Reynolds number is rather small and that separation bubbles exist on the suction surface, blade surface roughness weakens the separation of boundary layer or avoids the generation of boundary layer separation bubbles. Hence, boundary layer losses can be reduced. However, in the case that the Reynolds number is rather high and that boundary layers are not separated, increase in roughness may accelerate boundary layer transition, which that can give rise to a rise of boundary layer friction losses.

7.2.3 Vortex Generator Technology

After the shear between a mechanical vortex generator and the incoming flow, vortices are generated inside rear space of an obstacle so that a series of ordered longitudinal vortices take form. The strong movement of these longitudinal vortices facilitates momentum and energy exchanges between fluids near wall surfaces and those in main flow area. Besides, strong flow disturbances play a role in weakening or destroying the boundary layers. In other words, with a series of vortices generated, intense mass, momentum and energy exchanges take place between low velocity fluid at the bottom of boundary layer and high velocity fluid at the top of vortex generator. On this basis, changes occur to velocity field, temperature field and pressure field of near-wall fluids. In the case that a vortex generator is mounted on the suction surface of a high load low Reynolds number

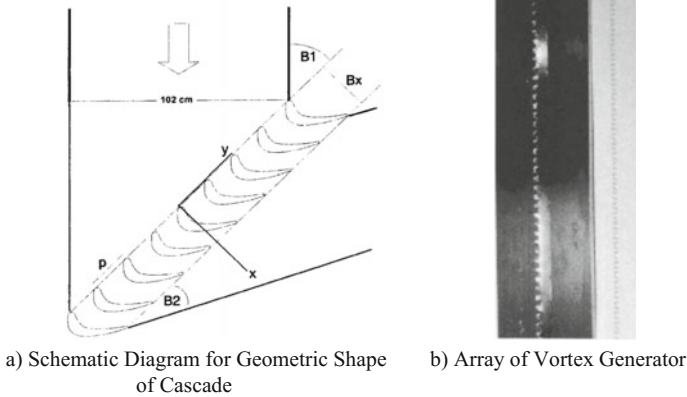


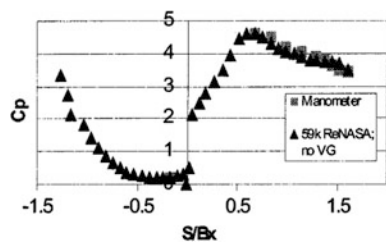
Fig. 7.11 Experimental studies on vortex generator application in a LPT flow separation control [17]

low pressure turbine blades, flow separation can be also controlled, as shown in Fig. 7.11 [17].

The vortex generator used for the experiment has a height of about 1 mm ($h \approx 1$ mm) (determined by materials and processing technique), which is equivalent to the boundary layer thickness. Experimental results are given in Fig. 7.12, a diagram of blade loading distributions. In this figure, pressure surface parameters are on the left of the vertical axis, while suction surface parameters are on its right. Suction load distribution curve (in triangular data points) for a turbine without vortex generator is presented as a platform near the position of $S/B_x = 1$. This phenomenon signifies that boundary layer separation takes place at this position. However, that curve exhibits a tendency of smooth decline at this position (in rectangular data points) after the mounting of a vortex generator, which indicates that boundary layer separation is removed by such a vortex generator.

Mechanical vortex generator control depends on a spoiler that is fastened onto the blade surface during turbine design and manufacturing. In general cases, its geometric structure cannot be changed according to flow control requirements. Therefore, it falls into the category of passive flow control technology. In recent years, development of the shape memory alloy technology forces the implementation of a vortex generator spoiler whose folding or unfolding is controllable [18],

Fig. 7.12 Separation removing by vortex generator on suction surface of high Re low turbulence LPT [17]



with which certain experimental accomplishments have been achieved in airfoil flow control studies. Nevertheless, this technology cannot be used for the control over high temperature flow field inside the turbine. The vortex generator flow control technology of flow in turbine puts more emphases on aerodynamic jet, as shown in Fig. 7.6. Figure 7.3a shows that the jet injected into the main flow vertically can give rise to symmetrical vortex pairs in reverse directions on both sides of jet holes. If these jet holes are provided with a certain slant angle α and an offset angle β , as given in Fig. 7.3b, the vortex pairs become no longer symmetrical and the vortex that forms a small included angle with flow direction is more intense. Under actions of main flow, such a strong vortex deflects towards the flow direction to be close to wall surface and is further intensified, and thus, individual streamwise vortices are formed.

Vortex generator jets (VGJs) control boundary layers are based on two mechanisms. First, during movement and development of streamwise vortex along with the main flow, high-energy fluids outside the boundary layer can be constantly pumped into its interior to facilitate momentum and energy exchanges. As a result, it has a stronger ability to resist separation. Secondly, based on unsteady effects of vortex, periodic shedding of streamwise vortices provides unstable disturbances for laminar boundary layers on turbine blade surface with a low Reynolds number, which facilitates its transition into turbulent boundary layer, and plays a role in resisting separation.

Blowing ratio B of aerodynamic jet is defined as the ratio of flux density of jet to the local mainstream's, that is, $B = (\rho u)_{jet} / (\rho u)_{local}$. If densities of jet and main flow are approximately equal to each other, the corresponding blowing ratio is just the specific value between flow velocities of jet and main flow. The jet controlling a turbine flow field is generally derived from compressor. Consequently, performances of gas turbine engine are affected inevitably. On the premise of guaranteeing flow control effects, a lower blowing ratio is better. Experimental studies indicate that, although increase in blowing ratio of steady jet is beneficial to enhancing flow control effect and reducing boundary layer separation losses, a trend of saturation is exhibited after it reaches a certain value, as shown in Fig. 7.13. As for a particular turbine blade boundary layer, there exists a minimum blowing ratio B_{min} to make the boundary layer separation effectively restricted. Furthermore, B_{min} is also one of the objectives during design of VGJs.

Replacement of steady jet with pulsed vortex generator jets (PVGJs) can bring the blowing ratio one and even more magnitude down provided that flow control effects remain unchanged, which is demonstrated in Fig. 7.13. Pulsed jet is only jetted in part of each jet period. Start and termination of pulsed jet in each period cause disturbances to the controlled turbine flow field. Similar to the vortex shedding disturbance of steady vortex generator, such disturbances give rise to earlier transition for laminar boundary layers. This is the principal principle for boundary layer flow control based on the PVGJs technology. Above arguments have been verified by boundary layer energy spectrum under the control of jet (see Fig. 7.14). In this figure, the energy spectrum peak of steady jet corresponds to the shedding frequency of vortex (500 Hz), while that of pulsed jet corresponds to both pulse frequency (10 Hz) and its frequency multiplication.

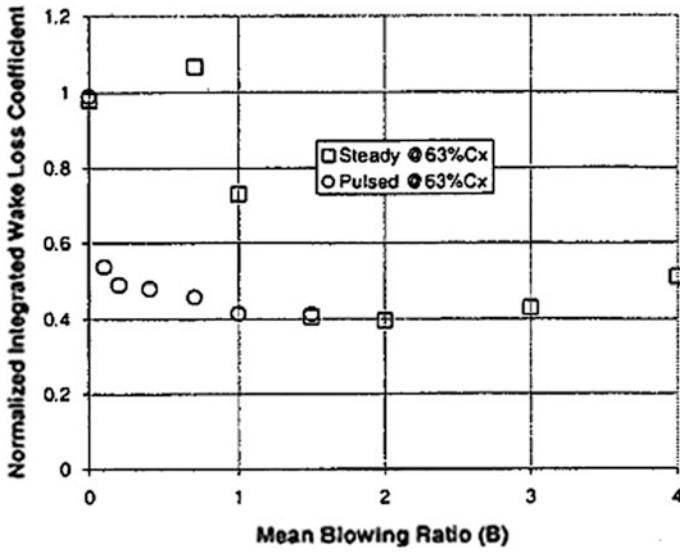


Fig. 7.13 Influence of blowing ratio on boundary layer separation [19]

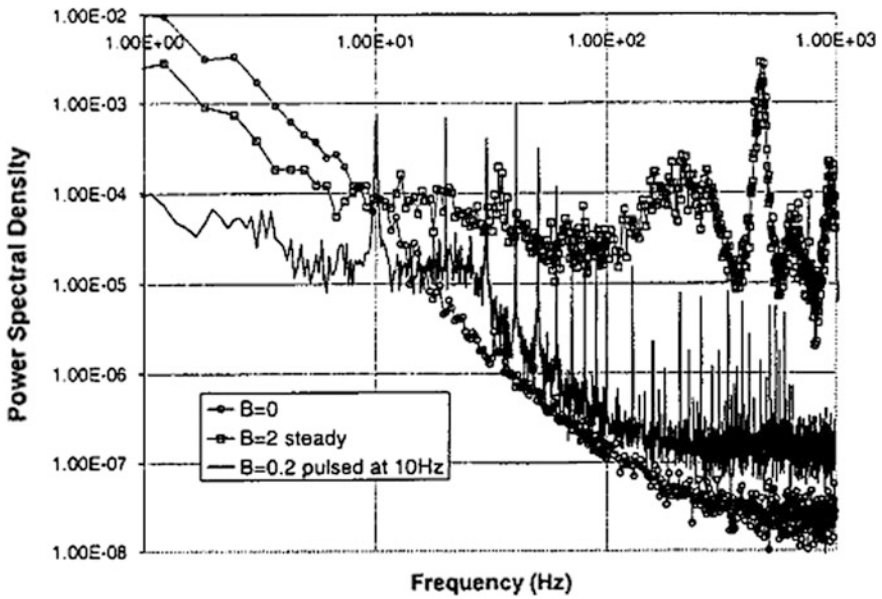


Fig. 7.14 Boundary layer energy spectrum with different jets [19]

On the basis of this principle, main functions of PVGJs depend on abrupt start and termination of jet, not the shedding of jet vortex. Therefore, duty ratio can be enormously reduced as long as pulse waveforms are guaranteed to be steep by the PVGJs. Hence, time average blowing ratio is brought down, and thus jetting air demands of the flow control technology is reduced so as to diminish its influences on gas turbine performance. Besides, higher pulse frequency not necessarily gives rise to better cases. The reason is that if the frequency is over high, cavity effect of jet air sources leads to a phenomenon that the pulse waveform is approximate to the sinusoidal wave [19]. As a consequence, effectiveness of abrupt jet start and termination cannot be exerted.

The VGJs flow control technology sufficiently uses technological accumulations in turbine gas film cooling field for references, except its merits as an active control method. Air film cooling is a rather mature technology related to high pressure turbine and it has been abundantly accumulated in terms of blade machining and cool air jetting, etc. Generally speaking, PVGJs have an equivalent flow control effect with steady jet. Considering that air entraining content of jet can be reduced from a perspective of order of magnitude, this technology has more application potentials.

7.2.4 Plasma Boundary Layer Exciting Technology

Aerodynamic jet technology controls over movement of fluid by directly exerting mass and momentum towards it in essence. However, in order to realize such a goal, air injection from wall surface to flow field is not the only method. A plasma actuator is mounted on the suction surface of a low pressure turbine blade to exert momentum on fluid directly by means of body force, similar to the aerodynamic jet, as shown in Fig. 7.15.

Figure 7.15 shows that two electrodes of the plasma actuator do not overlay with each other, but are slightly staggered. While the upper bias electrode is placed at the upstream of cascade flow field, the lower bias electrode is located at its downstream. After the application of alternating voltage, a strong electric field is formed between such two electrodes. Furthermore, their superposition part is just the position with the strongest electric field where the plasma takes form. Under actions of electric body force, the plasma moves towards the lower electrode and ultimately induces the local fluid to move towards wall surface and the downstream. Such an inducing effect is expanded to the downstream flow field. Experimental studies of Junhui Huang et al. are targeted at control actions of plasma actuator on low pressure turbine cascade flow field [20]. In the case that the plasma actuator is located at 40% of chord, pressure coefficients of blade surface under circumstances of different plasma excitation voltages are distributed as those curves shown in Fig. 7.16. When no plasma excitation is exerted, suction surface boundary layers separates at a position equivalent to about 70% of chord and the reattachment takes place at 95% of chord approximately. After excitation voltage loading, the

flow separation control effects of plasma, the reattachment position no longer moves forward after it is up to a certain value under circumstances of a certain flow field condition and a definite exciting position. In other words, there exists certain saturation excitation voltage. Researches above indicate that the plasma flow control technology can effectively control flow separation on suction surface of low Reynolds number low pressure turbine blade.

It is important to note that technologies, such as trip wire, surface roughness and PVGJs, etc. that control suction surface boundary layer flow separation of low Reynolds number low pressure turbine by virtue of advancing transition may not come into play when turbulence of the incoming flow is high enough. Separation transition may occur to turbine suction surface boundary layer with a high turbulence at this circumstance and reattachment then takes place even free of any flow control. The unsteady effect of wake has the capability to further bring down boundary layer separation losses to an acceptable level so that no flow control is required. For active control technologies including PVGJs, jet can be closed in circumstances that the turbine requires no flow control. Hence, extra flow losses are avoided. However, with regard to passive control technologies such as trip wires and surface roughness, flow losses of the flow field are inevitable. Therefore, the relative size between gains obtained when they play a role in flow control and losses in the case that they fail to come into play should be estimated at the stage of turbine design, so as to make a tradeoff.

7.3 Flow Control Technology for Secondary Flow

In turbine blade passages, the main flow deflects along the blade and those transverse motions in inconsistency with main flow direction are popularly referred to as the secondary flow. In end wall of turbine, the secondary flow is primarily constituted by passage vortex, horseshoe vortex, leakage vortex and corner vortex, etc. Reasons for their formation cover the circumferential pressure gradient between suction surface and pressure surface of blade, the flow around leading edge of blade, end-wall boundary layer, rotating and clearance leakage, etc., as given in Fig. 7.17. Due to these secondary flows, the flow at the end walls of turbine channel exhibits strong three-dimensionality and consumes the turbine shaft power that should be output originally. In addition, flow losses incurred take a percent of 30% in the total loss of turbine stage [21]. A suitable flow control technology can be adopted to control the development of secondary flows at a small cost on the premise of no substantial modifications to turbine design. Hence, the corresponding flow loss is effectively reduced. The development of horseshoe vortex pressure surface branches is a decisive factor of secondary flow. Considering this, many flow control technologies specific to the secondary flow in end walls are aimed at these branches.

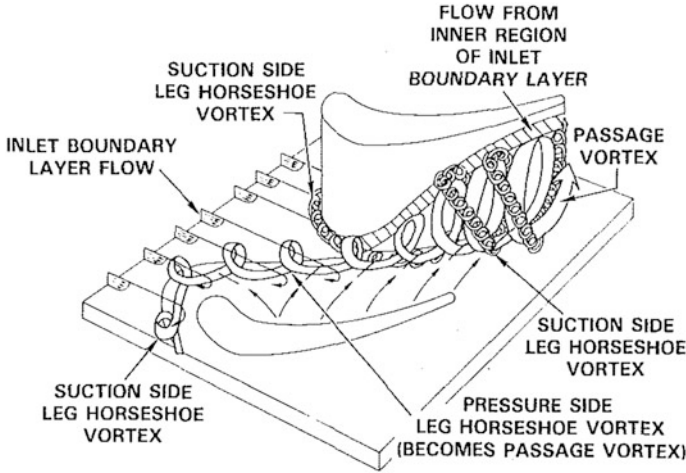
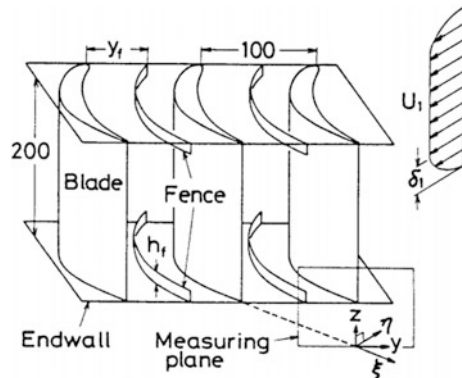


Fig. 7.17 Secondary flow model of Sharma and Butler [22]

7.3.1 Control Technology Based on End-Wall Fence

As a typical feature of the secondary flow in end walls is the transverse flow, installation of a fence onto the end-wall to obstruct transverse flows in a near-wall region is a simple and effective control approach. Figure 7.18 is a schematic diagram of mounting the fence on end-wall of turbine cascade. The crooked fence keeps consistent with the direction of turbine blade and thus plays a role in cutting off transverse flows in the near-wall region, obstructing vortices and carding the relevant flow field. Essential geometric parameters of the fence mainly consist of the height h_f and the installation site along cascade pitch y_f . Non-dimension processing for h_f and y_f is carried out by boundary layer thickness of cascade inlet and pitch respectively.

Fig. 7.18 Schematic of fence on a turbine cascade endwall [23]



As for the flow of turbine cascade outlet without flow control, rather strong passage vortex P, corner vortex C and blade wake vortex T measured are presented in Fig. 7.19a. If the fence is mounted with $y_f = 0.5t$ and $h_f = 0.3\delta_1$, non-dimensionalized vorticity for the cross section of cascade outlet is shown in Fig. 7.19b. A very weak passage vortex P_{II} is measured on the left of fence (the side near blade pressure surface). In addition, the other weak passage vortex P_I is also detected on a point next to the passage vortex P presented in Fig. 7.19a. It indicates that the fence not only obstructs the pressure surface branches of horseshoe vortex, but cuts off and weakens blade passage vortices. Besides, another weak corner vortex C_f is formed between the fence and the blade suction surface, despite that the fence evidently brings down the intensity of corner vortex C. As for the blade wake vortex T, it is also weakened. Such a fence gives rise to the formation of a new streamwise vortex F in direction opposite to the passage vortex. Although flow losses increase locally, excessive transition of flows in the end walls can be restricted.

Height and position of the fence have a decisive influence on its flow control effect. The related study indicates that $h_f = 0.3\delta_1$ is the optimal fence height. It is the minimum height where the fence is just able to obstruct the pressure surface branches of horseshoe vortex. The best fence installation position is $y_f = 0.5t$.

The above fence with a uniform height mounted on the end-wall is the most fundamental form. Except this, Kawai et al. [24] mounted fences on the blade suction surface to exert a combined action with the end-wall fence. The combined fences are able to cut off three-dimensional secondary flow vortex structures on the end-wall or in the near-wall region of blade suction surface. If compared with independent use of end-wall fence or blade suction surface fence, better flow

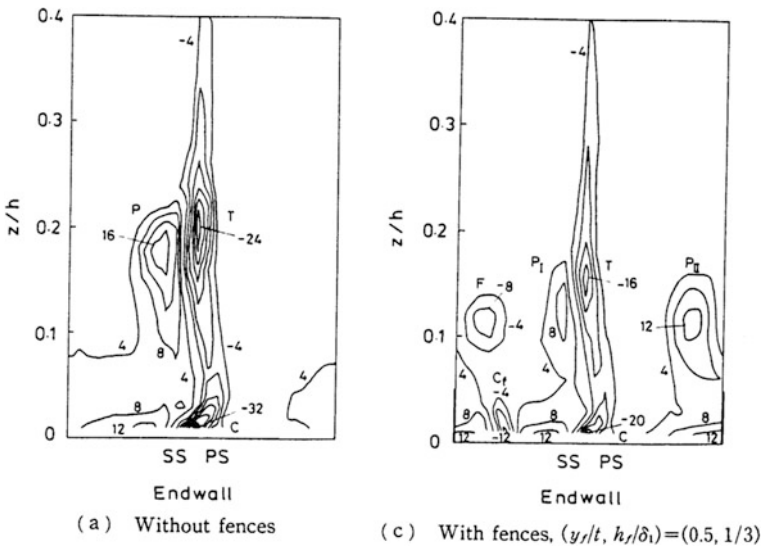


Fig. 7.19 Secondary vorticity on a turbine cascade outlet [23]

control effects can be achieved with combined fences. Kumar et al. [25] develop a fence whose height linearly changes from the leading edge to the trailing edge so as to control passage vortices with constant increase in heights. Optimal leading edge and trailing edge heights (h_f) of such fences are $\delta_1/6$ and $\delta_1/3$ respectively; and, its optimal position stays the same at $y_f = 0.5t$ (see Fig. 7.20 and Fig. 7.21).

7.3.2 Control Technology Based on Vortex Generator

The function of a fence is to prevent secondary flows from performing transverse motions in a near-wall region so as to control passage vortices. Considering that these passage vortices have a three-dimensional streamwise structure in the entire channel, designer can make use of the streamwise vortex in revolve direction opposite to the passage vortices to suppress passage vortex development [26]. This is also the application of vortex generator technology in flow control of secondary flows in end walls. Figure 7.22 displays a semi-delta wing vortex generator on the

Fig. 7.20 Schematic of combined fence [24]

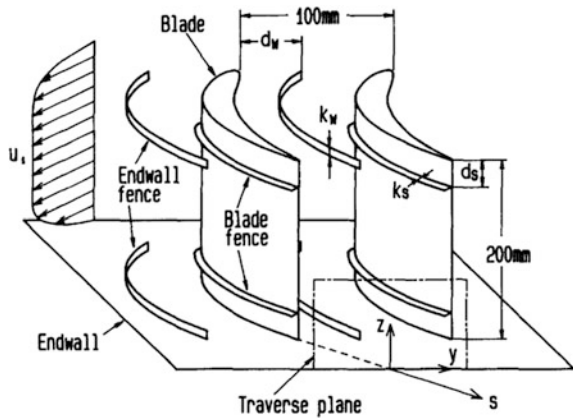


Fig. 7.21 Fence with linear changes in height [25]

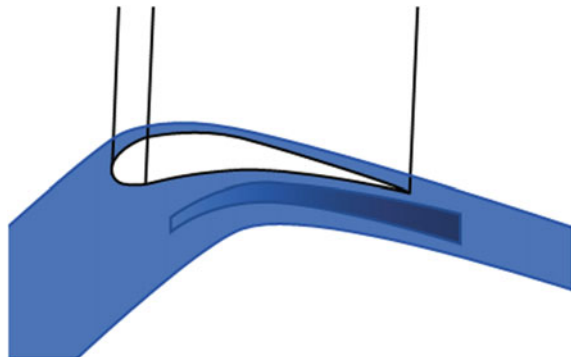
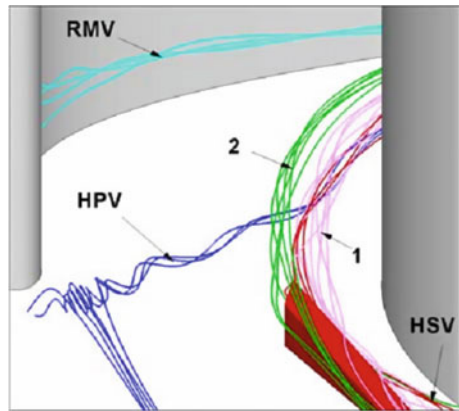


Fig. 7.22 Streamwise vortex generator mounted on the end wall [27]



Fig. 7.23 Turbine end wall vortex structures under the control of vortex generator [27]



leading edge end-wall of a plane cascade. When the incoming flow passes this semi-delta wing at a certain incidence angle, it rapidly separates and immediately rolls up after bypassing backward-swept wing surface edge. In this way, not only is steady shed vortex generated, but lateral motions are incurred during its development towards the downstream. Then, streamwise vortices take the form near the trailing edge of such a semi-delta wing, as Vortex 1 shown in Fig. 7.23. In the end walls flow field of a turbine blade, pressure surface branches (HPV) of horseshoe vortex cause insufficient transition to flow fields inside cascade channel while excessive transition in the middle of this channel. It is just the other way around in terms of Vortex 1 generated by a vortex generator. Under actions of transverse pressure gradient, HPV moves towards the Vortex 1 near suction surface. As a result, Vortex 1 interacts with HPV in the cascade channel, which ultimately restrains HPV development.

Positive effects of that semi-delta wing vortex generator controls over secondary flows in the end walls are described above. In fact, in addition to streamwise vortex 1 generation, the semi-delta wing also leads to streamwise vortex 2 in a direction opposite to it. Vortex 2 is generated due to the inducement of Vortex 1 and its revolve direction is identical to that of HPV. Therefore, it is able to combine Vortex 1 with HPV in certain conditions to increase secondary flow loss. Additionally, if the transverse position of a semi-delta wing is excessively close to blade pressure

surface, local load reduction takes place at blade root of the pressure surface. Consequently, a radial pressure gradient from blade center to its root is formed. As separation bubbles may occur to blade pressure surface of a high load low pressure turbine, their low energy fluids under effects of radial pressure gradient migrates to blade root to form associated secondary vortex RMV correspondingly.

The end walls secondary flow control effects of semi-delta wing are expressed in a total pressure loss coefficient of cascade, as shown in Fig. 7.24. The turbine cascade outlet without flow control has two obvious core zones of total pressure loss. They are generated by passage vortex and end-wall vortex induced by them respectively. The core of a passage vortex is located at 20% span approximately. In the case that a semi-delta wing vortex generator is mounted in a position next to the suction surface, the core zone position of passage vortex basically remains unchanged, and the range of such a vortex and the total pressure loss significantly go down. In addition, an associated total pressure loss area is formed at 10% span under the passage vortex which is caused by mixing between vortex 2 mentioned above and the main flow. However, the intensity of Vortex 2 is significantly less than that of the passage vortex. As a whole, semi-delta wing vortex generator flow control is still able to effectively decrease secondary flow losses in end walls.

Flow control effects of a semi-delta wing vortex generator are closely related to its transverse position. This generator needs to stay close to the suction surface (SS-V). In this way, it can make use of the acceleration of suction surface flow field to make Vortex 1 strong enough to validly generate HPV. If the vortex generator is located in the middle of the cascade pitch (MID-V), Vortex 1 turns out to be not strong enough to weaken HPV that is intensified by Vortex 2 otherwise. Consequently, its control effect is lowered (which is still valid in general). Furthermore, if the generator is situated at the middle of the cascade pitch (MID-V),

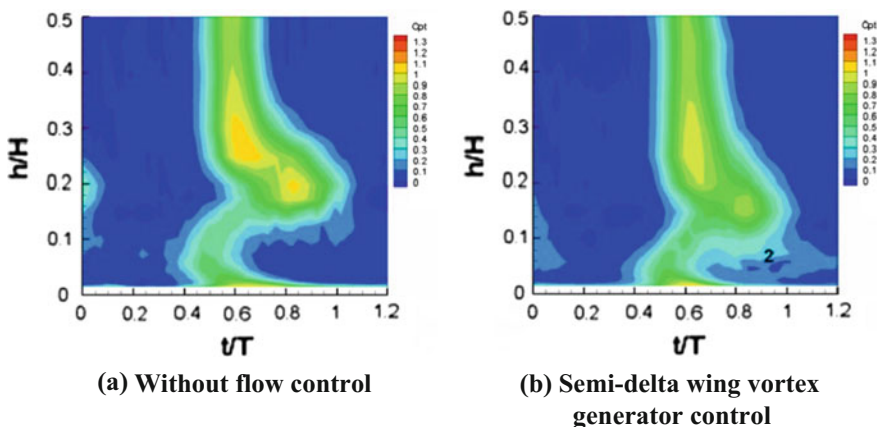


Fig. 7.24 Total pressure loss coefficient distribution on cascade outlet [27]

Vortex 1 is strongly compressed, the corresponding vorticity drops, and very strong associated secondary vortex RMV takes form near the suction surface. In the end, the intensity of passage vortex is enhanced, which leads to increase in secondary flow losses.

7.4 Tip Leakage Flow Control Technology

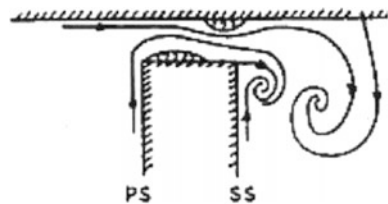
Under actions of static pressure differentials between pressure edge and suction edge in the tip, gas within the clearance between rotor blade and stationary casing in shroudless turbine enters the tip clearance from a pressure edge at a high speed. After these fluids flow out of the suction edge, they roll up due to joint actions of transverse pressure gradient and radial underflow inside the corresponding passage. As a result, leakage vortex takes form (see Fig. 7.25). Tip clearance leakage flow is one of the major sources for flow losses in shroudless turbine. Flow control over such a problem is of great significance in flow loss reduction and performance improvement of turbine. The basic concept of control is to obstruct leakage flow channel. Without doubt, it is impossible for physical blocking to be implemented because of high-speed revolve. Therefore, the blocking based on air injection becomes its solution logically.

7.4.1 Blade Tip Jet Technology

In tip aerodynamic jet technology, jet holes are designed at the tip of turbine rotor blade (see Fig. 7.26). Thus, aerodynamic jet can be utilized to reduce tip leakage flow and the corresponding flow loss. It is an effective active control technology for tip leakage flow.

The effect of tip jet on turbine tip leakage flow is presented in Fig. 7.27 where TV refers to tip leakage vortex. After the gas flow is injected into tip clearance, jets act like circular cylinders to block the leakage flow. It leads to generation of pressure gradient on the upper stream of jet holes. Due to effects of the pressure gradient, Vortex V_2 takes form on the upstream of jet holes and it induces velocity in the direction of the jet velocity but reversed with tip leakage flow. The stream line of leakage flow deflects towards casing under the act of V_2 , which has the same

Fig. 7.25 Schematic of tip leakage vortex [27]



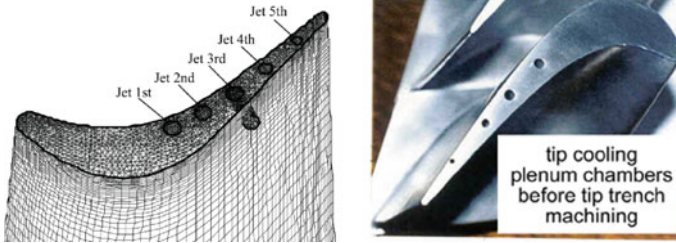


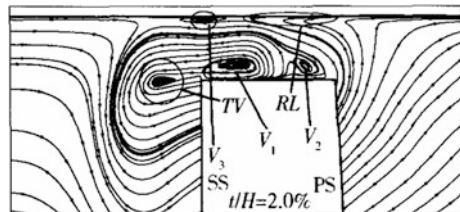
Fig. 7.26 Rotor blade tip jet holes [28, 30]

effect as a shortened tip clearance. By summarizing the above actions, jet columns ejected from tip holes and the Vortex V_2 obstruct the tip leakage flow together. In fact, Vortex V_1 symmetrical to V_2 has the same blockage function. Besides, relative motion between casing and rotor blade gives rise to the generation of a scraping vortex V_3 next to casing wall and its revolve direction goes against that of the leakage vortex. Furthermore, under actions of viscosity, the casing drives fluids in the near-wall region to flow from suction side to pressure side (RL given in the figure) in a direction opposite to that of leakage flow. These are the active role played by casing on leakage flow control.

On one hand, aerodynamic tip jet can reduce leakage flow and loss corresponding. On the other hand, it mixes with the main flow and increase the loss. The acquisition of positive flow control effects depends on measurement of such two opposite actions. The effect of jet on leakage flow reduction is closely related to jet hole positions and jet flow rate. Therefore, the successful application of tip aerodynamic jet technology into the turbine tip leakage flow control is largely depends on the selection of suitable jet hole positions and jet flow rate. Numerical simulation performed by Li Wei [29] et al. indicates that in the case that clearance height is equal to 2% blade height, the optimal jet hole position should be approximately at a point of 70% axial chord length and the optimal injection flow is about 0.2% of the flow rate of main flow. Tip aerodynamic jet flow control is able to make turbine efficiency 0.35% higher roughly.

Rao et al studied how the injection holes which are directed towards the pressure side control the leakage flow with the tip gap heights of 1.40% and 0.72% of the blade height. The cases presented included results for different injection holes location and different coolant injection rates [30, 31]. They find that the leakage

Fig. 7.27 Stream lines on cross section in tip clearance region [29]



flow greatly obstructs the main flow and clearance reduction will weaken this blockage. To be specific, when $\tau/h = 0.72\%$ rises up to $\tau/h = 1.40\%$, it is clear that the leakage vortex size decreases by 50%. The coolant injection rate should be 0.41% of the main flow for the purpose of the best leakage vortex control effects. By contrast, to obtain an optimal control effect over the whole situation, the amount of cooling air should be 0.63% of the main flow. The coolant injection makes leakage vortex much closer to the upper end-wall as well as reducing the transverse size and pressure loss of the vortex. The position of the leakage vortex with a coolant injection of 0.63% or 0.72% is much higher in radial direction, which weakens its interaction with the passage vortex so that air injection is able to reduce mutual effects of leakage vortex, upper passage vortex and wakes. If the coolant injection rate takes a percent larger than 0.63%, air injection will influence the leakage flows of the adjacent passages, because tip air injection faces the pressure surface and the cooling air with high momentum changes static pressure distributions of both casing and pressure surface.

In the experiment of influence of air injection holes location on tip clearance leakage flow, four axes positions as well as their combinations are studied by analyzing the total pressure coefficient of outlet channel and total pressure coefficient distributions along the blade height of rotor blade (shown in Fig. 7.28). Air injection from 61, 71 or 81% axis position can bring down shed vortex and turn the leakage flow to the trailing edge. In this manner, the size of leakage vortex drops. In detail, air injection at 81% axis position is able to reduce the total pressure loss of vortex core to the greatest extent, which shows that the total pressure loss primarily takes place at the 80% axis position. While air injection at 91% axis position close to the trailing edge has insignificant control effects over leakage flow and a lower total pressure coefficient for channel flows at the clearance position. The combined injection is successful in moving the tip leakage vortex closer to the blade suction-side and its control effect is preferable.

7.4.2 Casing Air Injection Control Technology

Casing air injection is another air injection control technique. By arranging small holes leaning to the blade pressure surface on diverse axes positions on the casing, high pressure cooling air is injected into the rotor passage to control clearance flow, as shown in Fig. 7.29. Thus, air injection is able to block clearance leakage flows, bring down leakage flow, push the leakage vortex move backward and reduce leakage losses consequently.

Behr et al. [32] carried out experimental studies about the casing air injection's effect on rotor blade clearance leakage flow and secondary flow in high load turbine. The research covers unsteady interactions among air injection, tip leakage flow and secondary flow. According to studies on cooling air holes of diverse sizes, cooling air flow rates and axial positions, both intensity and size of upper passage and leakage vortexes would be reduced on the rotor blade with cooling air injected.

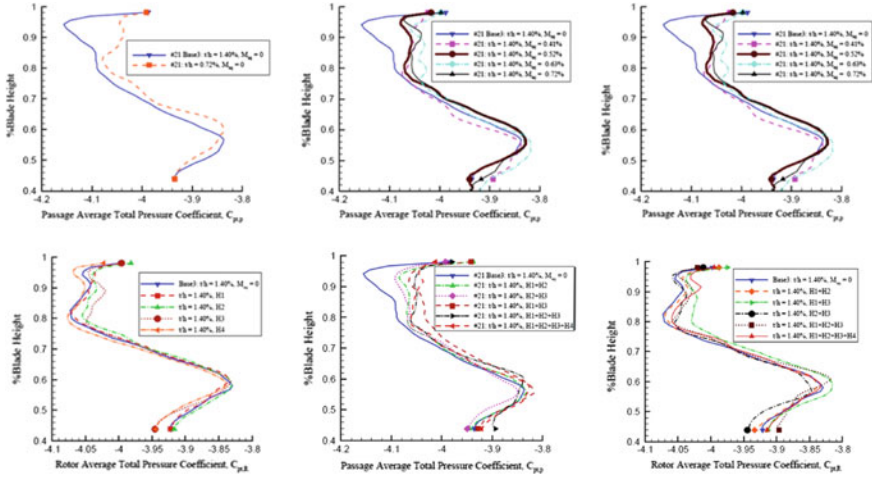


Fig. 7.28 Total pressure coefficient distribution on outlet along blade height [31] (H1, H2, H3 and H4 refer to axes positions at 61, 71, 81 and 91%)

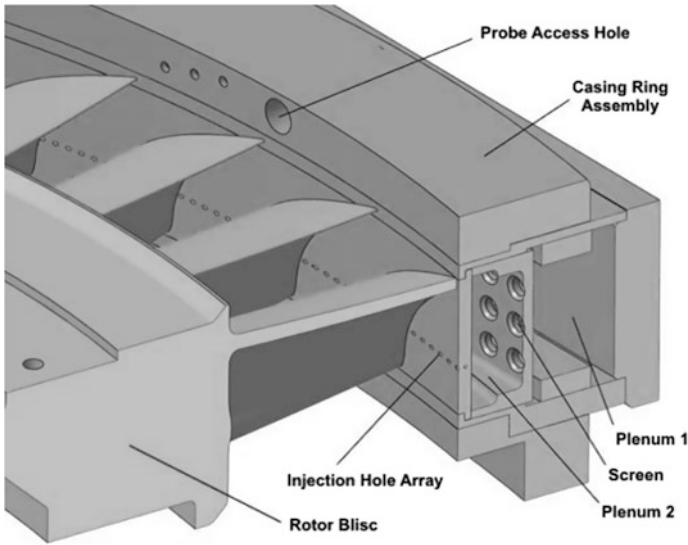


Fig. 7.29 Schematic of casing air injection [32]

The tip casing region can be divided into two areas by measuring the average static pressure of rotor blade tip, as shown in Fig. 7.30. The grey area stands for a transverse flow area from the pressure side to the suction side and a scraping vortex

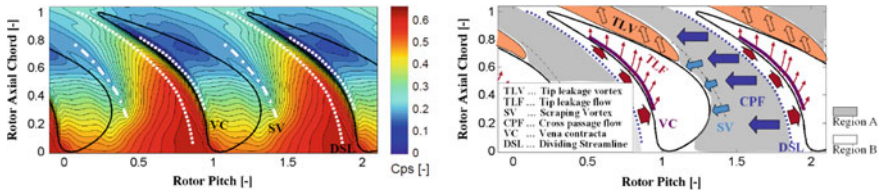


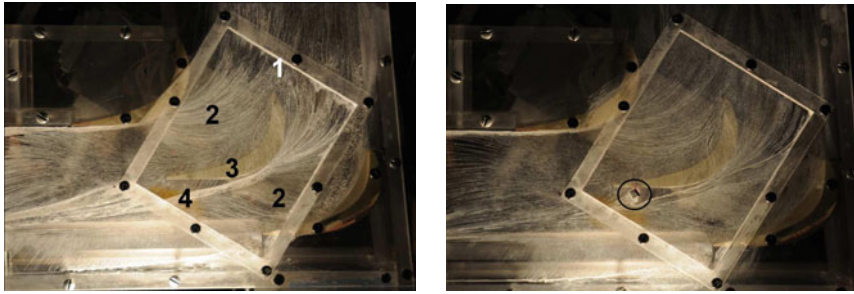
Fig. 7.30 Casing static pressure distribution and flow model [32]

on the suction side; while, the tip area stands for the transverse flow from pressure side to suction side, which is able to form a leakage vortex. As for air injected at 30% axial chord length, the velocity of the injection is opposite to that of the leakage flow, which makes the pressure near the upstream of leakage flow holes increases and the momentum between gas jet and leakage flow gas exchanges. Considering this, the leakage flow discharges at the place near the downstream of suction side. In addition, leakage vortex intensity at outlet would be weakened and become much closer to the suction surface.

7.4.3 Vortex Generator and Plasma Exciting Control Technology

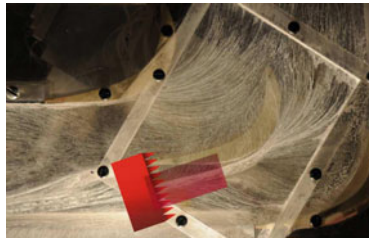
Except for coolant injection control technology, both the vortex generator technology and the plasma control technology have the same capabilities to effectively control turbine tip leakage flows. Stephens et al. [33] adopt oil flow tests to exhibit effects of tip leakage flow control implemented on plane cascade, as shown in Fig. 7.31. By comparing Fig. 7.31a with b, we find that a vorticity of opposite sign is introduced to dissipate the tip-clearance vortex. This was done by placing vortex generators on the casing wall, on the suction side of the center blade. The surface visualization also suggests that the tip-leakage vortex is quite dissipated by one chord length downstream of the blade. The plasma actuator on casing wall surface given in Fig. 7.31c exerts a similar control effect.

Douville et al. [34] studied the plasma actuator fixed on the blade tip, as shown in Fig. 7.32. This actuator generates body forces that fluctuate in a high frequency and act on unsteady tip leakage flow to control flow losses. Under a specific excitation frequency, such technology can effectively reduce flow losses incurred by tip leakage flow. Daniel et al. [35] employ plasma actuator and squealer on suction side to study controls over tip clearance leakage flow of plane cascade under different Reynolds number conditions. They find that the plasma actuator is inversely proportional to the Reynolds number and able to enhance static pressure on the end wall. In addition, its increment is associated with excitation frequency. In



(a) Cascade without Flow Control

(b) Vortex Generator Mounted on Casing



(c) Plasma actuator Mounted on Casing

Fig. 7.31 Oil flow visualization on turbine cascade casing with tip clearance [33]

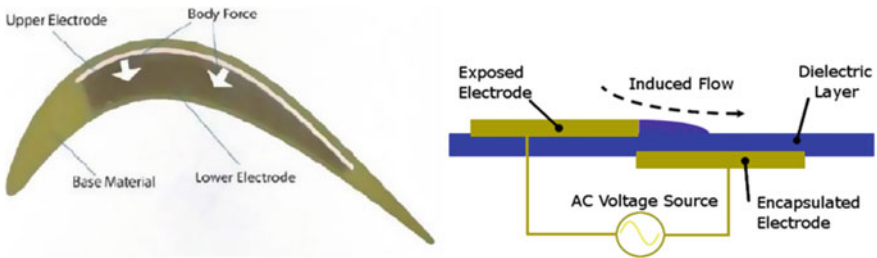


Fig. 7.32 Plasma actuator on blade tip [34, 35]

a condition of low Reynolds number, plasma actuator gives rise to an effect similar to that of squealer. They carry out relevant experiments in a low speed condition, because it is technologically difficult for them to arrange plasma actuator on a narrow tip with high temperature and pressure in actual conditions.

7.4.4 Shroud Air Curtain Jet Technology

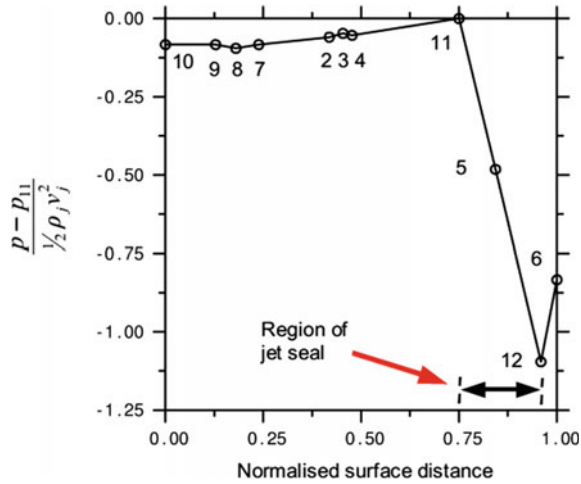
As for shrouded turbine rotor, giant differences lie in velocities and directions of shroud leakage flow and main flow, bringing substantial flow losses. Moreover, interactions between shroud leakage flow and main flow can also intensify unsteadiness of main flow. Circumferentially continuous and uniform air curtain injected from casing to shroud is an active control technology targeted at the shroud leakage flow, as shown in Fig. 4.62 of Chap. 4. The principle of air curtain jet control technology can be illustrated by the simplified model given in Fig. 4.62a [36] where \dot{m}_1 is the flow rate of leakage flow required to be controlled while \dot{m}_j is the flow rate of air curtain jet. The essence of air curtain jet control technology is to offset pressure differential $p_1 - p_2$ between inlet and outlet of shroud cavity by consuming the momentum of slanting jet. The ultimate objective of this technology is to maintain the mass and momentum conservations of cavity when the inlet flow rate of shroud cavity is zero. This technology consists of two mechanisms. First, the curvature of the air-curtain jet flow requires a transverse (axial) pressure gradient which generates the sealing pressure drop. Second, downstream of First, the curvature of the air-curtain jet flow requires a transverse (axial) pressure gradient which generates the sealing pressure drop. Second, downstream of its impact point the seal jet will mix out and it is assumed that this leads to a uniform flow with velocity $2v$ leaving the shroud cavity. There will be a static pressure rise in this mixing process so that the pressure acting on the downstream face of the jet is lower than the blade exit pressure p_2 . Thus, the shroud leakage flow is further restrained. When the inlet flow rate of shroud cavity is zero ($\dot{m}_1 = 0$), that is, the shroud leakage flow is just under control, the pressure differential between turbine rotor blade inlet and outlet (nondimensionalized by dynamic pressure of the jet) which can be resisted but the air curtain at a given velocity v_j and along a given inclination α is derived out based on mass and momentum conservations. It is written into the following equation.

$$\frac{p_1 - p_2}{1/2\rho_j v_j^2} = 2 \frac{A_j}{A_c} \left(\frac{\rho_j A_j}{\rho_2 A_c} + \cos \alpha \right) \quad (7.1)$$

The above equation shows that if inclination α decreases or A_j/A_c increases, that is, geometric structure of air curtain becomes much closer to axial injection, the shroud leakage flow control effect of air curtain jet can be improved. In a situation that its geometric structure has been established, increase in jet flow velocity (flow rate) has the same effects. In the case that $\alpha = 45^\circ$ and $A_j/A_c = 0.26$, and supposing that the density of injected air is equal to the shroud cavity outflow, the right side of the equation above approaches to 0.5. At this time, air curtain jet control is able to resist a pressure differential roughly equivalent to the half of dynamic pressure of the jet.

Mechanism of the air curtain jet control can be further illustrated by the pressure distributions inside shroud cavity, as shown in Fig. 7.33. It displays the case that the shroud leakage flow is just under the control of air curtain jet. In addition, vertical coordinates are the differences between the non-dimensionalized pressures

Fig. 7.33 Pressure distribution inside shroud cavity with air curtain jet [36]



at diverse measuring positions and the non-dimensionalized peak pressure. The curves in this figure indicate that a very large pressure drop exists in the zone of action of air there is a large pressure drop between upstream (location 11) and downstream of the jet nozzle (location 12). There is also evidence that there is some pressure recovery downstream of the jet nozzle before the flow leaves the shroud cavity and enters the mainstream. Such phenomena coincide with the above discussions about air curtain jet mechanism.

Despite that the increase in flow rate of air curtain flow can bring down the flow rate of shroud leakage flow, it is also able to result in losses due to interactions between the jet and main flow. Therefore, except reductions in the flow rate of leakage flow, the quantitative study on effects of air curtain jet control technology should also take variations in turbine efficiency into account, as shown in Fig. 7.34.

Figure 7.34a shows that increasing the jet mass flow rate decreased the leakage flow leaving the mainstream and passing into the shroud cavity. Perfect sealing was achieved for approximately 3.5% air curtain seal flow where $m_1 = 0$. In this case, the air curtain jet is just able to control shroud leakage flow. The flow rate of such air curtain jet is roughly equal to 70% of that of the shroud leakage flow independent of flow control. However, Figure 7.34b signifies that the air curtain jet flow rate that results in the maximum increase in turbine efficiency is lower than the above value and it is about 1.2% of the main flow rate, that is approximately 1/3 of the flow rate of shroud leakage flow without flow control. The reason is that the air curtain jet used for flow control also needs to consume energies. Curves presented in Fig. 7.34b correspond to the air curtain jet derived from independent air bleed channels. Therefore, ideal work of turbine should contain corresponding terms of the air curtain jet. In general cases, air curtain jet is considered being incompressible. Then, its ideal work is cubic proportional to jet flow rate. When the flow rate of air curtain jet is low, the increment of jet ideal work is also small and the turbine efficiency linearly rises along with the jet flow rate approximately. By

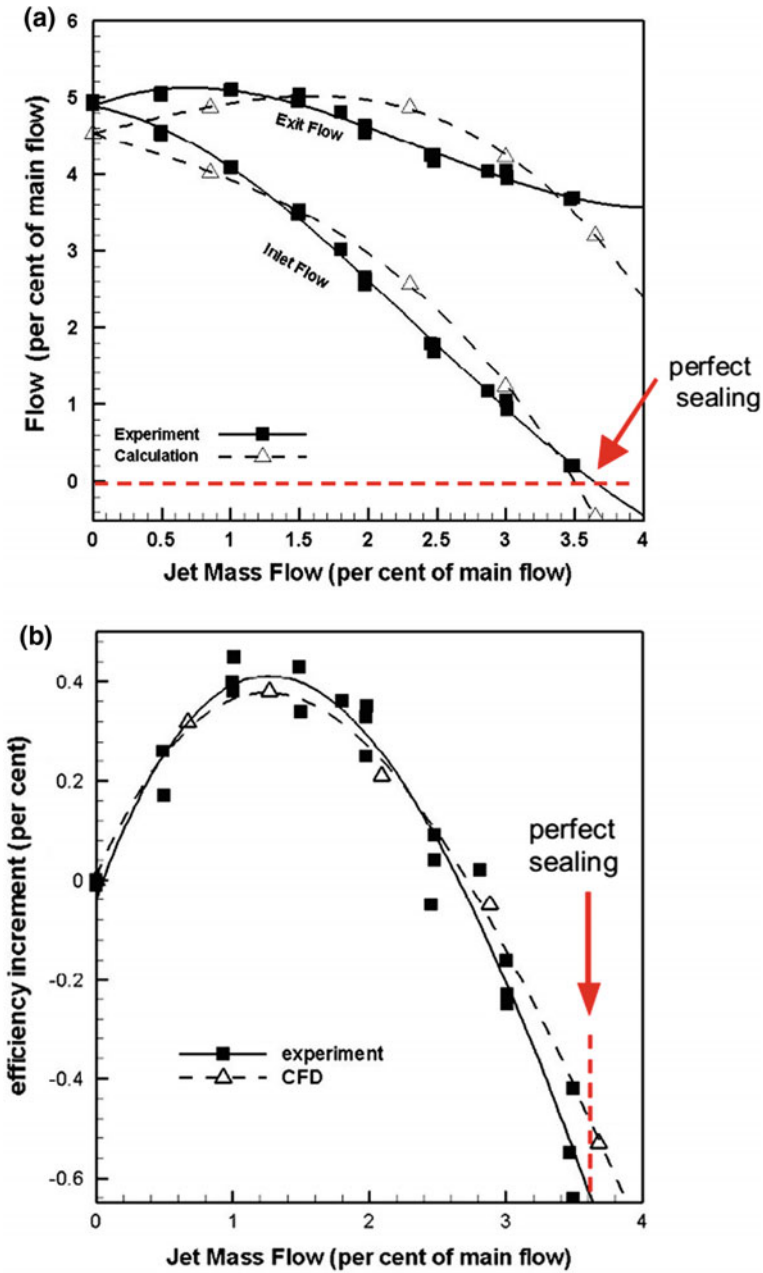


Fig. 7.34 Air curtain jet control effects [36]

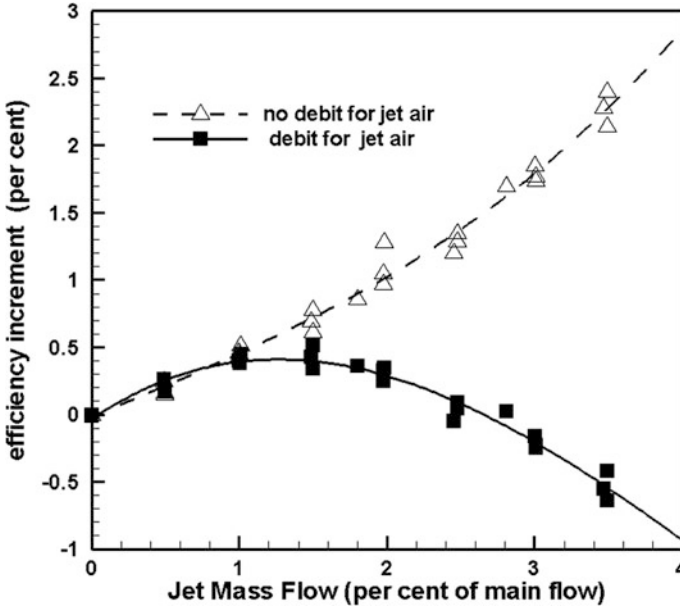


Fig. 7.35 Turbine efficiency with different air curtain jets [36]

contrast, if the air curtain jet flow rate is large, the ideal work of jet increases as a cubic function. As a consequence, denominator of the turbine efficiency sharply goes up and the corresponding efficiency value abruptly declines. Such a tendency is displayed in Fig. 7.34b. At that time, dependent on air curtain jet control, the peak value of turbine efficiency can increase by 0.4%.

However, there are also exceptions. In the case that the air curtain jet is derived from cooling air in turbine, ideal work of turbine should not include the corresponding terms of air curtain jet. In this way, the turbine efficiency increment obtained is greater than curves given in Fig. 7.34b (see Fig. 7.35).

Further researches show that [37], the narrower the air curtain jet channel is designed, the more likely for air curtain jet with a rather small inclination to exert its ability of turbine efficiency improvement it will be. In addition, the jet position should be appropriately close to the shroud cavity outlet (not too close as the air curtain should be guaranteed to be effectively injected onto the shroud surface). High temperature in the combustor of an aero-engine fades effects of air curtain jet control over shroud leakage flow of high pressure turbine, while rising reaction degree is beneficial to increase the suitable jet injection velocity, and improve turbine performance.

7.5 Turbine Working State Adjustment Technology

Versatile core engine technology that brings down costs by realizing high intercommunity and the variable cycle engine (VCE) that is applicable to broaden working ranges by changing geometry are both important technical means

upgrading performances levels of existing the turbojet and turbofan engines. Moreover, they are also cutting-edge technologies in the field of aero gas turbine at present. In terms of the versatile core engine technology, Yin Zeyong et al. from the China Aviation Powerplant Research Institute point out that its turbine should be equipped with a wide high efficiency zone and flow adaption range so as to adapt to the changes in inlet flow rates, corrected rotational speed and expansion ratio of various engines. Such a wide flow rate adaption range can be achieved according to specific requirements by a few local adjustments in engines of different types [38]. As for the variable cycle engine based on a core driven fan stage (CDFS), its turbine parts are required to adjust and control flow rate during working of the engine with an aim to change turbine power and further modify rotational speed differences between high and low pressure turbines. In this way, they are able to match with the working conditions of both fans and compressors. Such two technologies have presented different requirements for turbine working state regulation. In detail, during the working of a versatile core engine, there is no need to adjust flow rate. However, turbine flow rate should be variable in the process of its operating as far as the VCE is concerned. The turbine working state regulation technology is developed based on the two technologies above. The technique means consist of geometric adjustment and aerodynamic adjustment.

The geometric adjustment technique of turbine state is essentially based on two typical stream surfaces S1 and S2 of the turbine channel. In other words, the adjustment method based on S1 stream surface is utilized to implement flow rate regulation by changing the angle of turbine nozzle blade. It is specifically achieved by changing the blade angle or the latter part of nozzle blade, as shown in Fig. 7.36, a schematic diagram of adjustable guide vane. These two geometric adjustment methods are first put forward by company R-R. In 1971, R-R reported [39] that these approaches would result in flow rate change of 17.5% in experiment. Although the relevant experimental conditions are not clear, it has proven that such variable-geometry methods can give rise to substantial changes in turbine flow rate. Therefore, they are still in use. With regard to the other adjustment method based on a S2 stream surface, wedges (BLOCK) are brought into turbine channel in a mechanical manner to block the turbine channel area of S2 stream surface and hence change the flow rate of turbine, as given in Fig. 7.37. Nevertheless, mechanical introduction of blocks in the wedge fails to increase turbine flow rate. Considering that the actual internal temperature of turbine is very high, wedge block stuffing has many problems in terms of the structure and cooling. Therefore, this method has a poor feasibility.

7.5.1 Geometric Adjustment Technology for Turbines

According to the geometric adjustment technology for turbine state, working state of the turbine is usually controlled by changing throat area. As shown in Fig. 7.36a, when the blade angle goes up or down (in this Chapter, increase in blade angle

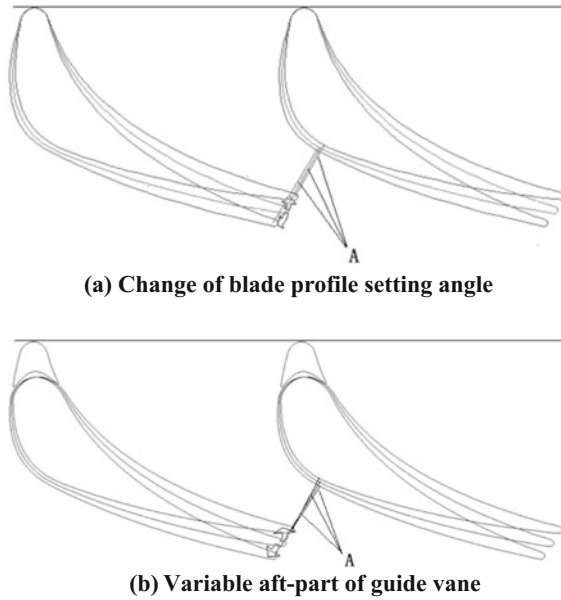


Fig. 7.36 Schematic of variable guide vanes [40]

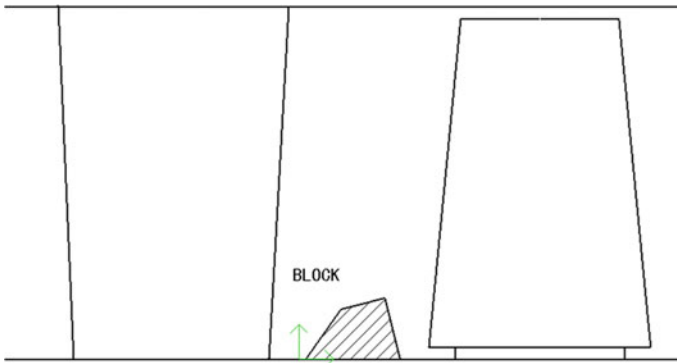


Fig. 7.37 Passage area change for regulating flow rate [40]

means that the guide vane revolves to increase the throat area; the case is just the other way around if the blade angle decreases), the throat area of guide vane also changes correspondingly and the turbine flow rate rises or drops approximately linearly with the rotating angle. A numerical simulation study on an aft-loaded high pressure turbine shows that [40] blade angle variation of $\pm 3^\circ$ can lead to a turbine flow rate change of $\pm 20\%$. Simultaneously, turbine efficiency also varies. In the

case that blade angle becomes smaller, Ma at guide vane throat enlarges, shock waves turn to be stronger and interactions between them and the boundary layer are intensified. As a result, the separation area after shock waves near the trailing edge of guide vane suction surface is expanded, which increases the guide vane loss and decreases turbine efficiency. In comparison, after the guide vane blade angle increases by 3° , Ma at guide vane throat significantly drops and the separation area almost completely disappears. However, the negative incidence will give rise to separation at pressure side of rotor blades, as shown in Fig. 7.38 and Fig. 7.39. This study signifies that in the case of guide vane blade angle reduction, the maximum turbine efficiency value becomes lower while the turbine efficiency curves become smoother; by contrast, if the guide vane blade angle increases, such a maximum values goes up and the efficiency value sharply declines along with the relevant turbine expansion ratio when this ratio is rather high. While adjusting the maximum flow rate by changing the guide vane blade angle, flow rate variation tendencies (increase or decrease) should be taken into account at the very beginning of turbine design. Accordingly, reasonable distributions of guide vane surface loading can be selected during design to preferably control shock strength at the throat and adverse pressure gradient at the trailing edge of suction surface. In this way, it is guaranteed that changes in maximum flow rate of turbine cannot give rise to substantial reduction of turbine efficiency; or, its efficiency can even be improved with a certain range of expansion ratio.

The other geometric adjustment method is shown in Fig. 7.36b. The guide vane profile is divided into two segments. While the former segment is ensured to be

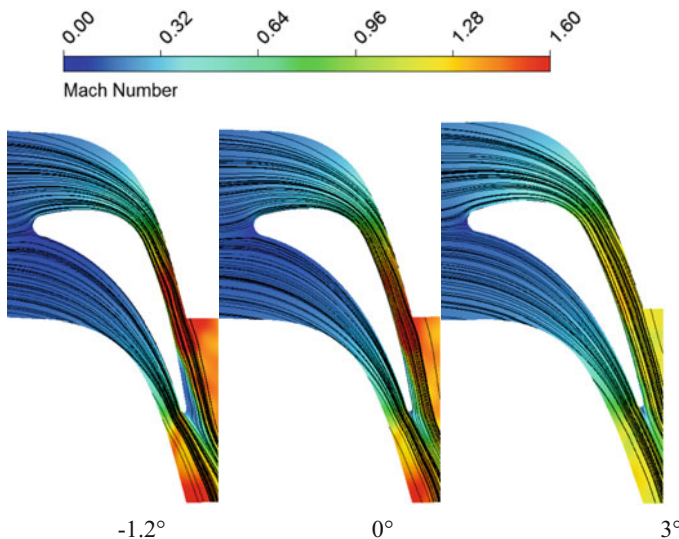


Fig. 7.38 Streamlines and relative Ma in guide vane root section with diverse setting angles [40]

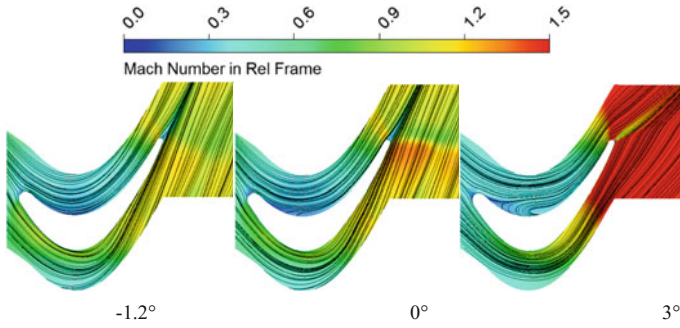


Fig. 7.39 Streamlines and relative Ma in rotor root section with diverse setting angles [40]

immovable, the latter revolves at a certain angle by using its leading edge point as the center of circle. In this way, throat area is changed and the purpose of regulating turbine state is achieved. CFD approach is adopted to study influences of changing guide vane blade angle and regulating its latter segment on turbine flow rate and efficiency. The corresponding results are given in Fig. 7.40. It shows that when the blade angle of the guide vane or the latter segment becomes smaller, effects of such two regulation methods on flow rate adjustment are basically the same. However, there is almost no impact on turbine efficiency if the latter segment of guide vane is adjustable. Under the circumstance of an identical turning angle, guide vane blade angle changes can lead to substantial reduction in turbine efficiency. In the case that the blade angle of guide vane or the turning angle of latter segment goes up, adjustable latter segment of the guide vane gives rise to a less obvious flow rate regulation effect than that of the guide vane blade angle variation. When the turning angle rises to 1.8° , flow rates regulated by them have a difference of 3% roughly. At the same time, changes in guide vane blade angle result in 0.5% increase of turbine efficiency when the turning angle goes up to 1.5° . By contrast, turbine efficiency obtained based on the adjustable latter segment of guide vane remains the same basically.

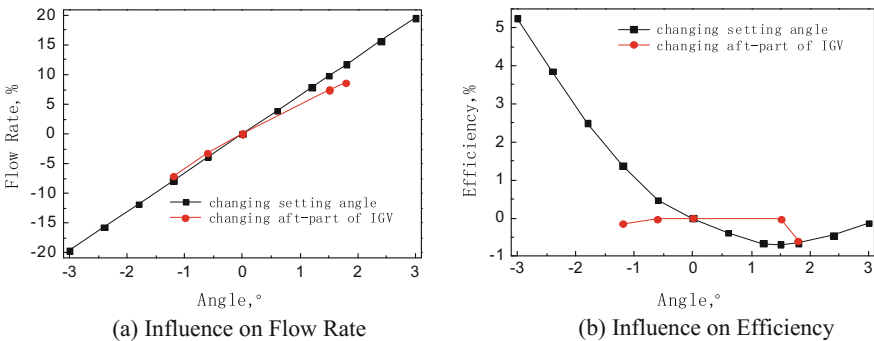


Fig. 7.40 Geometric regulation on flow rate and efficiency [40]

Same with the method of changing blade angle, geometric adjustment of changing the latter segment turning angle of a guide vane also faces some problems, such as losses generated when the Ma at pressure side of rotors and the separation losses created when turning angle increases. Besides, the latter is confronted with a peculiar issue—the leakage flow in guide vane gaps, as shown in Fig. 7.41. It can be clearly seen from the figure that in all three states the flow at the seam is driven by the pressure difference from the pressure side to the suction side. But, the flow at the seam is not strong enough to have a giant influence on the flow inside guide vane channel. Therefore, when applying the method of adjustable latter segment of guide vane is applied into engines, influences of circumferential pressure gradients at the leading edge of guide vane on the flow at seams should be taken into consideration at the very beginning of its design. Designing the leading edge of this guide vane to be symmetrical or independently designing a symmetrical straightening head to add in front of the original blade profile will eliminate the flow from pressure side to suction side at the seams. Meanwhile, in terms of actual engines, cooling air needs to be ejected at seams between the former and latter segments of the guide vane considering cooling of turbine blade, which also obstructs the flow from pressure surface to suction surface.

7.5.2 Aerodynamic Adjustment Technology for Turbines

According to the aerodynamic adjustment technology for turbine states, controllable gases injected near the trailing edge of blade pressure surface will make the main flow deflect, change turning angle and flow rate in the blade passage, and finally change the working state of the turbine, as shown in Fig. 7.42.

The R-R Company attempted to adopt the aerodynamic adjustment method to change turbine flow rate at the earliest [39]. They introduced secondary jets into the turbine endwall and change the injection positions (upper/lower parts of end-wall; front/back/throat of guide vanes) as well. Their experimental results indicate that

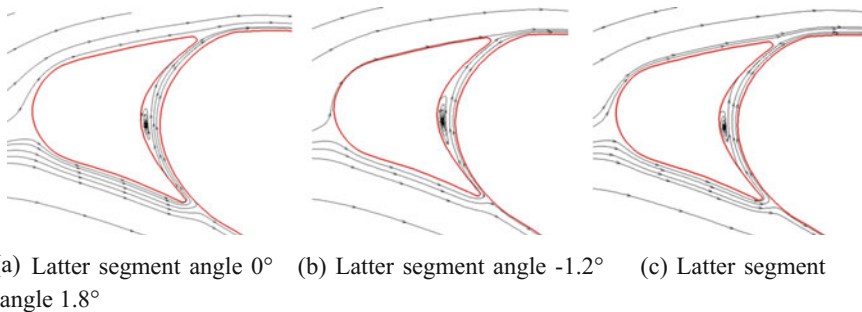


Fig. 7.41 flow in seams of guide vane [40]

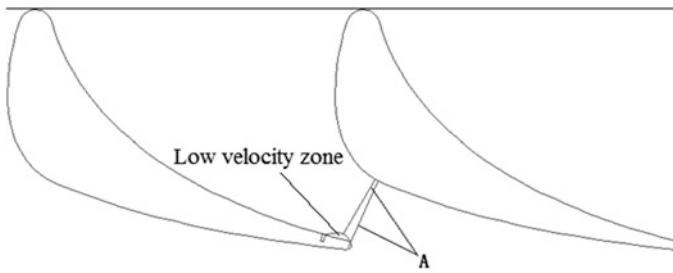


Fig. 7.42 A schematic of pneumatic regulation [40]

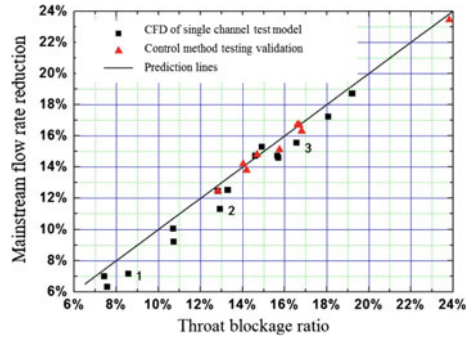
such a method is able to realize effective regulation flow rate. However, due to limitations of research techniques at the time, aerodynamic adjustment may result in dramatic efficiency drop.

Due to improvement of three-dimensional numerical simulation techniques and experimental measurement technologies, the aerodynamic adjustment technology attracts attentions of researchers once again. For example, corresponding studies in this field have been performed in the BUAA and Northwestern Polytechnical University (NWPU), etc. [40–42]. Numerical simulation researches indicate that [43] the flow rate reduction of main flow realized by aerodynamic adjustment is approximately in direct proportion to throat blockage ratio (the specific value between blockage width and the geometric throat width), as shown in Fig. 7.43. It signifies that the basic principle of aerodynamic adjustment is to form a low velocity zone by air injection near the geometric throat so as to block the throat, and thus bring down the related flow rate by flow area reduction.

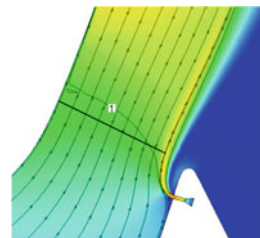
Some parameters, such as air injection flow rate, air injection angle, air injection velocity and air injection position are critical to the aerodynamic adjustment technology. Researches have been made to understand the effect of those parameters. In those researches, periodic turbine cascades are replaced by single passage test model and numerical simulation methods are combined. The result indicates that the main flow mass flow rate of turbine decreases with the increase of air injection flow rate; and, the increase in air injection angle magnifies the effect of the air injection flow. The closer the air injection position is to the geometric throat, the stronger the ability of aerodynamic adjustment to reduce main flow mass flow rate will be, but the smaller the gains are brought. Besides, the selection of air injection positions is limited by the geometric dimension of air injection holes, the blade thickness and the cooling configuration. Therefore, all these factors are required to be taken into account during air injection position design.

In a specific cascade working state (confirmed isentropic Mach number at outlet) and a certain air injection angle, the flow rate control effect is governed by the actual flow status of air injection holes: overexpansion, optimum expansion or underexpansion. At the state of overexpansion, air injection velocity and flow rate affect aerodynamic adjustment simultaneously. Flow rate reduction caused by unit variation is relatively large. At the state of underexpansion, the air injection velocity

Fig. 7.43 Throat blockage ratio on flow rate [43]



(a) Throat blockage on flow rate variation



(b) schematic of aerodynamic throat width

keeps invariant, and its flow rate (or, total pressure of air injection hole inlet) determines the corresponding control effect. In addition, the flow rate reduction caused by flow rate variation is rather small and the relevant control effect exhibits a tendency of linear variation basically. The complete expansion state serves as demarcation point on aerodynamic adjustment curves and it is used to distinguish the above two states.

Both geometric adjustment methods and aerodynamic adjustment methods have their own advantages and disadvantages. Hence, different flow rate adjustment approaches should be selected according to diverse purposes of them. Aerodynamically, the principle of geometric adjustment method is rather visual and the flow rate range regulated by it can be also very broad. After flow rate changes, changes in absolute flow angle at outlet can be compensated to a certain degree due to guide vane blade angle variations. Hence, the incidence angle of rotor inlet and loss slightly change. However, geometric adjustment will also result in multiple problems related to structure and cooling, etc. In terms of the structure, turbine as a high temperature subsystem has prominent cooling and sealing issues. Therefore, flow rate adjustment based on the geometric adjustment method requires an additional set of complicated mechanism, which is a giant challenge for structure design. As far as the relevant reliability is concerned, complex structure and the increase of turbine parts, incurred by revolve of the latter segment of turbine guide vane will seriously influence the reliability and service life of the engine.

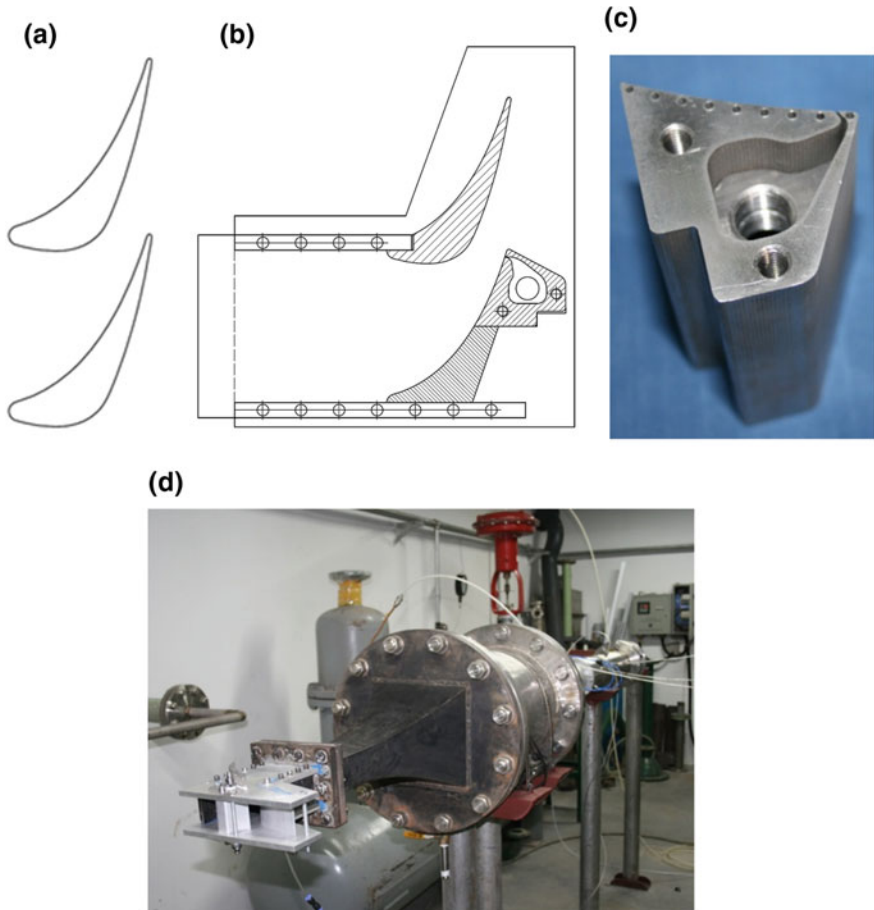


Fig. 7.44 Single channel test of convergent turbine cascade [43]

Aerodynamically, as the latter segment of guide vane is movable, additional sealing and cooling must be carried out to prevent the flow from going through the seams instead of expanding in the blade passage. This will inevitably create much more low energy gases which lead to turbine efficiency reduction. Regarding the engine, increase in turbine cooling and sealing gases may make more gases extracted from the compressor. As a consequence, gases that work in the turbine reduce, which affect thrust/power of the engine. Meanwhile, considering that a set of complex regulating mechanism is mounted additionally, weight of the engines increases so that its thrust-weight ratio drops otherwise.

Comparing with geometric adjustment, aerodynamic adjustment has some obvious superiorities in spite of some defects. With a simple structure, air injection

used for aerodynamic adjustment is able to adopt the existing secondary flow system without dramatically modifying the existing structure of this turbine. Therefore, it has little impacts on thrust-weight ratio and service life of the engine. However, the aerodynamic adjustment is restricted to factors including the ratio of total pressures between air injection hole inlet and blade row inlet, relative flow rate of air injection, and turbine efficiency, etc. Considering this, it is still very difficult to apply the aerodynamic adjustment method into high pressure turbine due to limitations of the existing technology. Nevertheless, it can be used in low pressure turbine guide vane.

References

1. Prandtl, L. (1904). Über Flüssigkeitsbewegung bei sehr kleiner Reibung. In *Proceedings, 3rd International Mathematics Congress*, Heidelberg, Germany.
2. Lin, J. C. (1999). *Control of turbulent boundary-layer separation using micro-vortex generators*. AIAA Paper 99-3404.
3. Utturkar, Y., Holman, R., Mittal, R., et al. (2003). *A jet formation criterion for synthetic jet actuators*. AIAA Paper 03-636.
4. Postl, D. (2005). *Numerical Investigation of Laminar Separation Control using Vortex Generator Jets*. Arizona : The University of Arizona.
5. James, L., Paul, K., Richard, R. (2000). *Low Reynolds number loss reduction on turbine blades with dimples and V-Grooves*. AIAA Paper 00-0738.
6. Sondergaard, R., Rivir, R. B., & Bons, J. P. (2002). Control of low-pressure turbine separation using vortex-generator jets. *Journal of Propulsion and Power*, 18(4), 889–895.
7. Li, Y., & Wu, Y. (2012). Progress of research on plasma flow control technology. *Journal of air force engineering university (natural science edition)* 13(3):1–5.
8. Howell, R. J., Ramesh, O. N., Hodson, H. P., et al. (2001). High lift and aft-loaded profiles for low-pressure turbines. *Journal of Turbomachinery*, 123(2), 181–188.
9. Zhang, X. F., & Hodson, H. (2004). Combined effects of surface trips and unsteady wakes on the boundary layer development of an ultra-high-lift LP turbine blade. *Journal of Turbomachinery*, 127(3), 479–488.
10. Vera, M., Hodson, H. P., & Vazquez, R. (2004). The effects of a trip wire and unsteadiness on a high-speed highly loaded low-pressure turbine blade. *Journal of Turbomachinery*, 127(4), 747–754.
11. Zhang, B., Li, W., Lu, X. (2012). Ultra-high-lift low-pressure turbine blade boundary layer passive control in different flow conditions. *Journal of Aerospace Power*, 127(4):747.
12. Bons, J. P. (2010). A review of surface roughness effects in gas turbines. *Journal of Turbomachinery*, 132, 21004.
13. Roberts, S. K., & Yaras, M. I. (2006). Effects of surface-roughness geometry on separation-bubble transition. *Journal of Turbomachinery*, 128(2), 349–356.
14. Simens, M. P., & Gungor, A. G. (2013). The effect of surface roughness on laminar separated boundary layers. *Journal of Turbomachinery*, 136, 31014.
15. Sun, Sh, Lei, Z., & Zhu, J. (2014). Effects of roughness on boundary layer of ultra-high-lift low-pressure turbine. *Journal of Propulsion Technology*, 35(3), 347–355.
16. Bai, T., Liu, J. Y., Zhang, W. H., & Zou, Z. P. (2014). Effect of surface roughness on the aerodynamic performance of turbine blade cascade. *Propulsion and Power Research*, 32(3), 82–89.

17. Van, T. K. W., Simon, T., Von, K. M., et al. (2001). Measurements in a turbine cascade flow under ultra low Reynolds number conditions. *Journal of Turbomachinery*, 124(1), 100–106.
18. Todd, Q., Robert, M., Glen, W. (2010). *Development and testing of deployable vortex generators using SMA actuation*. AIAA Paper 2010-4686.
19. Bons, J. P., Sondergaard, R., & Rivir, R. B. (2001). Turbine separation control using pulsed vortex generator jets. *Journal of Turbomachinery*, 123(2), 198–206.
20. Huang, J., Corke, T. C., & Thomas, F. O. (2006). Plasma actuators for separation control of low-pressure turbine blades. *AIAA Journal*, 44(1), 51–57.
21. Denton, J. D. (1993). Loss mechanisms in turbomachines. *Journal of Turbomachinery*, 115(4), 621–656.
22. Sharma, O. P., Butler, T. L. (1987). *Predictions of endwall losses and secondary flows in axial flow turbine cascades*. *Journal of Turbomachinery*, 109(2), 229–236.
23. Kawai, T., Shinoki, S., & Adachi, T. (1989). Secondary flow control and loss reduction in a turbine cascade using endwall fences. *JSME International Journal. Ser. 2, Fluids Engineering, Heat Transfer, Power, Combustion, Thermophysical Properties*. 32(3): 375–387.
24. Kawai, T. (1994). Effect of combined boundary layer fences on turbine secondary flow and losses. *JSME International Journal. Series B, Fluids and Thermal Engineering* 37(2):377–384.
25. Kumar, K. N., & Govardhan, M. (2011). Secondary flow loss reduction in a turbine cascade with a linearly varied height streamwise endwall fence. *International Journal of Rotating Machinery* 2011.
26. Qi, L. (2010). *Investigations of unsteady interaction mechanism and flow control in the turbine endwall regions*. Beijing: Beihang University.
27. Sjolander, S. A., & Amrud, K. K. (1987). Effects of tip clearance on blade loading in a planar cascade of turbine blades. *Journal of Turbomachinery*, 109(2), 237–244.
28. Li, W., Qiao, W., Xu, K., et al. (2009). Numerical simulation of active control on tip leakage flow in axial turbine. *Chinese Journal of Aeronautics*, 22(2), 129–137.
29. Li, W., Qiao, W., & Xu, K. (2008). Numerical simulation of active control on tip leakage flow in axial turbine. *Journal of Aerospace Power*, 23(7), 1260–1265.
30. Rao, N. M., Camci, C. (2004). *Axial turbine tip desensitization by injection from a tip trench: Part 1—effect of injection mass flow rate*. ASME Paper GT2004-53256.
31. Rao, N. M., Camci, C. (2004). *Axial turbine tip desensitization by injection from a tip trench: Part 2 leakage flow sensitivity to injection location*. ASME Paper GT2004-53258.
32. Behr, T. (2007). *Control of rotor tip leakage and secondary flow by casing air injection in unshrouded axial turbines*. Germany: Dresden University of Technology.
33. Stephens, J., Corke, T., Morris, S. (2009). *Control of a turbine tip leakage vortex using casing vortex generators*. AIAA Paper 2009-299.
34. Douville, T., Stephens, J., Corke, T., et al. (2006). *Turbine blade tip leakage flow control by partial squealer tip and plasma actuators*. AIAA Paper 2006-20.
35. Van Ness, D. K. II, et al. (2008). *Tip clearance flow visualization of a turbine blade cascade with active and passive flow control*. ASME Paper GT2008-50703.
36. Curtis, E. M., Denton, J. D., Longley J P, et al. (2009). *Controlling tip leakage flow over a shrouded turbine rotor using an air-curtain*. ASME Paper GT2009-59411.
37. Auld, A., Hilfer, M., Hogg, S., et al. (2013). *Application of an air-curtain fluidic jet type seal to reduce turbine shroud leakage*. ASME Paper GT2013-94198.
38. Zhou, K. (2014). *Investigations of aerodynamic design techniques for counter-rotating turbine in adaptive cycle engine*. Beijing: Beihang University.
39. Rolls-Royce, L. T. D. (1971). *Variable flow turbines*. British.
40. Fu, C. (2010). *Study on some key technologies related to high performance turbine aerodynamics design*. Beijing: Beihang University.
41. Yang, Y. (2009). *An Aerodynamic method to control the flux in turbine nozzle blade*. Beijing: Beihang University.

42. Luo, H., Qiao, W., & Xu, K. (2008). Numerical study of active flow control using jet-flap for a low-pressure turbine cascade. *Journal of Aerospace Power*, 23(2), 347–354.
43. Shi, W. (2012). *Numerical and experimental study of cascade flow in turbo-machinery*. Beijing: Beihang University.

Chapter 8

Multidisciplinary Coupling Analysis and Design

8.1 Conjugate Heat Transfer Problems

8.1.1 Conjugate Heat Transfer in Turbines

Increasing turbine inlet temperature is an important method to improve cycle efficiency of gas turbines. A previous study has shown that a 40K increasing of turbine inlet temperature would result in a 10% increase in output power of gas turbines and a 1.5% increase in cycle efficiency [1]. The study [1] summarizes the changing trend of turbine inlet temperature of aircraft engines (see Fig. 8.1) that the turbine inlet temperature of engines in 3rd generation fighter is about 1600-1700K, as well as that of engines with weight ratio of 10 in 4nd generation fighter is about 1900-2000K. Future fighters require further advanced aircraft engines, with the turbine inlet temperature of the next-generation aircraft engine more than 2200 K [2]. Due to the strict requirements of lifetime and reliability, although turbine inlet temperature of civil aircraft engines is under restrictions, it is still over 1600 K. Such high temperature exceeds beyond the toleration normal materials, thus advanced heat-resistant materials and manufacturing processes as well as advanced cooling technology have been widely used in modern gas turbines to ensure turbine safe working state. According to the related statistics, turbine inlet temperature increases by about 22 K each year, in which only 8 K is contributed by improvement of heat resistance capability, yet the remaining 14 K is achieved by cooling technology [3]. Therefore, high-efficiency cooling system plays a very important role in the reliability of gas turbines and their components.

With the continuous increase of turbine inlet temperature, more cooling flow is needed to cool down turbine components. Currently, cooling flow in high-pressure turbines of aircraft engines is even more than 20% of turbine inlet flow, leading to intenser interaction between cooling flow and main gas flow [4]. Therefore, it is of great significance for turbine design that carrying out further studies on the mechanism of conjugate convective heat transfer in turbines, cooling system

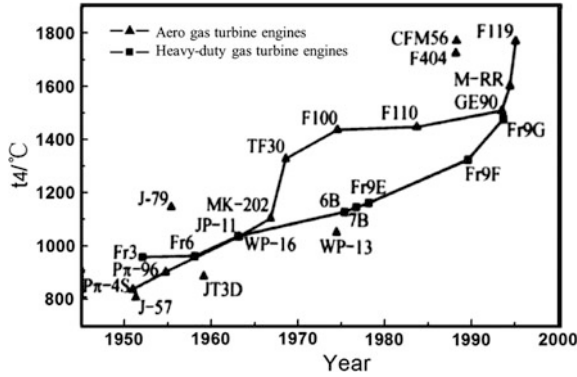


Fig. 8.1 Trend of turbine inlet temperature [1]

optimization, and cooling flow reduction AITEB (Aero-thermal Investigations of Turbine Endwalls and Blades) program was carried out in the Sixth Framework Programme (2003) of the EU with the aim of researching on the aero-thermal characteristics of turbine endwalls and blades with high lift and high exit Mach number, as well as developing advanced cooling technology, etc. [5]. Figure 8.2 shows the typical turbine blade cooling system [6]. In this system, the temperature distribution and thermal stress in blades are determined by both flow condition and interaction of cooling flow and external gas flow. Heat conduction at the solid-wall boundary layer has influence on local heat transfer parameters and flow characteristics as well as the interaction between the cooling flow and the main flow may change the aerodynamic mixing loss in turbines. This interaction between the fluid

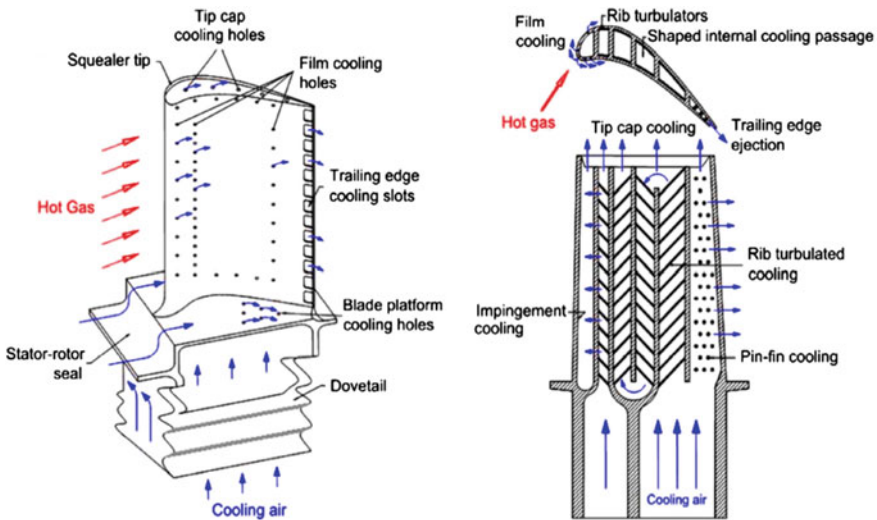


Fig. 8.2 Diagram of a typical turbine blade cooling system [6]

and the solid domain lead to the conjugate heat transfer problem. Only with fully considering and characterizing the interaction between the temperature field and the flow field can we obtain the correct thermal loads of turbine components and the flow structure which is more consistent with the reality.

8.1.2 Research Methods for Aerodynamic-Heat Transfer Coupling in Turbines

8.1.2.1 Traditional Non-conjugate Numerical Research Methods for Aerodynamic-Heat Transfer Coupling

In early stage, fluid network and boundary layer calculation programs were generally used in engineering design to evaluate a convective heat transfer evaluation of turbines and cooling system [7, 8]. Based on the fluid network method, the complex flow passage of flow system is simplified into a network system composed by nodes and components, then the pressure, temperature, flow rate and other parameters could be calculated by solving the non-linear equations which are established by topology of the network. Boundary layer calculation programs could obtain external heat transfer coefficient of turbine blades by solving two-dimensional boundary layer equations, for instance, the famous STAN5 program is widely used in engineering design, which solves the parabolized turbulent boundary layer equations by Patankar-Spalding finite difference scheme to acquire flow and heat transfer parameters. This boundary layer calculation method is suitable for evaluating the thermal loads on the middle of blades and other components where the flow has obvious two-dimensional characteristics and small pressure gradient, However, error would increase significantly if shock waves and complex endwall flows exist.

With the development of computing method and capacity, CFD method has also been used in thermal analysis of turbines. CFD model can simulate and describe the three-dimensional flow field structure in detail, thus the CFD method can be used to obtain the heat transfer parameters closely related to flow conditions. These cases are called non-conjugate computing method, in which first boundary conditions are generally used to define wall temperature distribution then to obtain local heat flux density. For example, Ameri, Bunker, Saha, etc. worked out the convective heat transfer coefficient distribution at the blade tip through CFD with the boundary condition of adiabatic wall and isothermal wall. Roy obtained the convective heat transfer coefficient distribution on the surface of a rotor disk using this method, indicating that flow structure in the disk cavity has significant effect on the thermal load of rotor disk [9–11]. Similarly, this method has also been widely used in researching the influence of the hub-endwall thermal load and inlet hot spots on heat transfer [12, 13]. If more accurate temperature distribution is needed, the

equations could be further solved by adding the convective heat transfer information on the surface to a solid heat transfer solver, as well as forming an external iteration combining CFD and heat conduction calculations to consider the conjugate heat transfer problems, so as to improve the prediction accuracy of temperature distribution.

Especially, the selection of reference temperature, which is generally based on experience, would make a difference to the results in non-conjugate calculation. Furthermore, the boundary parameters selection are generally based on the data accumulated through long-term studies. Particularly when the flow structure is complex or heat conduction itself would influence heat transfer parameters, it would be hard to give appropriate and accurate boundary conditions thus the accuracy would be degraded greatly. In these cases, the results may misguide designers, so it is necessary to analyze them carefully [14].

8.1.2.2 Conjugate Heat Transfer Numerical Methods

Conjugate Heat transfer (CHT) method, which is used to calculate the heat transfer and solid heat conduction simultaneously, could make the thermal analysis be independent of the selection of reference temperature, thus to achieve a more accurate thermal load distribution. Generally, there are two methods to solve the conjugate heat transfer problem. One is global discretization and solution and another is local solution and boundary coupling. With respect to the first method, heat transfer processes in different areas are combined into a unified heat transfer process and the general governing equations are used for both the fluid and the solid domains, in which the only difference occurs in terms of generalized diffusion coefficients (viscosity coefficient and coefficient of heat conduction) and generalized source terms, moreover, the interface between the fluid and the solid would be included in the inner part of the computational domain. When solving discrete equations by the finite volume methods, the continuity condition on the interface could be satisfied generally. NASA's Glenn-HT (CHT) solver, using this computational method which sets solid density as a constant solves as well as simplifies energy equation with the solid velocity of 0, while the discretization method and numerical method are consistent for both the fluid domain and the solid domain [15]. However, the computing stability would be influenced by this method because that the flux and gradient on the interface is so hard to calculate accurately, which could be different with thousands of times at the two sides of the flow structure interface [16]. For another method, the solution is carried out respectively in both the fluid domain and the solid domain. The N-S equations are solved in the fluid domain while temperature field is determined by solving heat conduction equations in the solid domain. Temperature, heat flux, and other information are then transmitted through the interface between the fluid domain and the solid domain to link the fluid them together. This method can make full use of the existing high-precision CFD solvers with good stability, so it is widely used in turbomachinery conjugate heat transfer studies (such as the famous CHT-Flow solver) [17].

Conjugate heat transfer calculations, involving flow field and temperature field, have strict demands on the accuracy of flow simulation, conjugation methods, as well as computational models, thus it is necessary to carefully analyze factors which influences the accuracy of the calculations. The relevant studies in China, Li, Zou, et al. (Beihang University) studied on the influence of different turbulence model parameters and transition models on numerical results of conjugate heat transfer simulation using the experimental database of the MarkII inner-cooling turbine cascade, and obtained the limiter which is suitable for *Chien k- ϵ* model by analysis and derivation, then developed a three dimensional conjugate heat transfer solver based on preprocessing methods, which has satisfactory accuracy [18, 19]. Li et al. [20] (Harbin Institute of Technology) did a series of meaningful work on conjugate thermal-flow-elastic multi-field numerical simulation and then developed a platform based on finite difference method for conjugate thermal-flow-elastic multi-field numerical simulation. Aiming at porous medium-based transpiration cooling structure analysis, Zhang, Zou, et al. established a 3D numerical simulation method for conjugate porous/fluid/solid domains, which could serve as a simulation tool for studies on advanced transpiration cooling technology and porous cooling technology for high-speed aircrafts [21, 22].

However, the current 3D conjugate heat transfer computational methods cannot be directly used in engineering design due to their insufficient predictive ability and limited precision, in which the influence factors on simulation accuracy is various. Firstly, it is difficult for the turbulence model to accurately simulate the influence of flow phenomena (transition, separation, etc.) and roughness of solid wall surface, which have significant influence on heat transfer. Secondly it is difficult to obtain accurate and detailed aero-thermodynamic and geometric boundary conditions. In addition, other factors, such as numerical simulation methods, grid, etc., could also lead to uncertainty of the results [23, 24]. Because of the above reasons, results of the current 3-D conjugate heat transfer calculations have to be only a reference basis for analysis, as well as be interpreted carefully and cannot be trusted blindly.

8.1.2.3 Experimental Methods for Aerodynamic-Heat Transfer Coupling in Turbines

Because of the limitations of turbines thermal analysis methods in terms of precision and convergence. The experiment is still an important method for studying aerodynamic heat transfer, so as to check the numerical simulation methods, as well as to study the mechanism of conjugate heat transfer, to establish physical models, and to assess design schemes. The measurement of temperature field is very important for turbine CHT experiments, in which the commonly used methods includes contact measurement techniques (using thermocouples, etc.) and

non-contact measurement techniques (such as, liquid crystal thermography, infrared thermometry, etc.) [4, 25–27]. Figure 8.3 shows the typical techniques used in turbine aerodynamic heat transfer experiments.

It is worth noting that, it is generally difficult for gas turbines to carry out the results under real working conditions due to the limitations of experiment conditions and test equipments. Thus, similar flow conditions are used in most of the experiments to simulate real flows in turbines with the condition of normal or medium temperature. Under this condition, the similarity criteria used in the experiments are of great significance to the experimental results, and it is a key point that using the similarity criteria to model the boundary conditions. In addition, it is of great importance for further understanding of the mechanism of conjugate heat transfer and diagnosis design by developing the advanced test methods and technologies under the condition of little disturbance to test flow field.

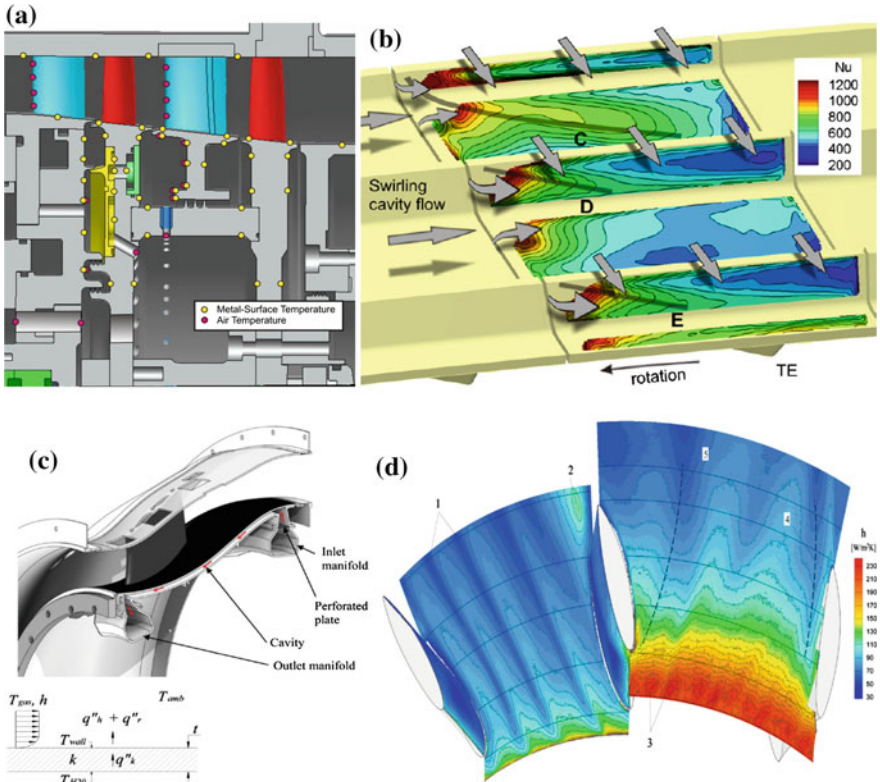


Fig. 8.3 Techniques used in turbine aerodynamic-heat transfer measurements [25, 27].
a Thermocouple techniques, **b** Liquid crystal thermography, **c** Infrared thermometry, **d** Heat transfer coefficient distribution in a ITD

8.1.3 Mechanism of Interaction Between Flow Field and Temperature Field in Turbines

Flow field and temperature field in turbines are highly conjugate and closely interacted. On the one hand, complex flow structures in turbines such as shock waves, secondary vortices, leakage flows, and sealing/cooling jet flows have significant influence on heat transfer characteristic and thermal load of these components. On the other hand, flow structures and turbine performance are influenced by boundary heat transfer in the fluid domain, as well as interaction between cooling outflow and the main flow, etc. Therefore, it is very important to analyze the mechanism of interaction between flow field and temperature field from these two aspects. The interaction between cooling flow and the main flow has been presented in Chap. 2, and the repetition is saved here.

Adiabatic wall assumption, which is considered that heat transfer has no influence on turbines' aerodynamic performance, is usually used in traditional turbomachinery design and flow mechanism study. Generally, this assumption is coincident for most of turbomachineries. However, the assumption not always appropriate in some gas turbines, such as micro-turbines, high cooling flow turbines, etc., in which influence of heat transfer at solid wall boundary on flows and performance is non-negligible. For example, as for boundary layer flows, a previous study has shown that thermal environment has very significant influence on space-time evolution characteristics of boundary layers that wall heating or cooling would directly make a influence on the transition process of boundary layers, advancing or delaying the transition and further influencing turbine flows and performance. On the other hand, flow structures would also effect the heat transfer on the wall surface, and thus the interaction between flow and wall surface lead to the highly conjugate problem [28]. Using the DNS method, Wu et al. studied the small-scale vortex structures in the flat plate transitional boundary layer and turbulent boundary layer with heat transfer and obtained coherent structures in the heating boundary layer (as shown in Fig. 8.4). As the results, turbulent spots in the transition zone are fully filled with closely distributed and relatively isolated hairpin vortices, which would move downstream with the turbulent spots and enter the downstream turbulent boundary layer, changing with heating condition, then it would change these coherent structures [29]. Shafi et al. and Krogstad et al. [30, 31] gained the similar conclusions. In addition, in low-velocity gas flows, the buoyancy lift caused by temperature gradient is also an important driving force, thus the influence of boundary temperature on flows must be considered particularly in studies of internal flows in cooled turbine blades [32].

There are several flow phenomena (transition, separation, etc.) and some complex flow structures (shock waves, secondary vortices, etc.) in turbines, which have significant influence on heat transfer characteristics and temperature field. Giel et al. [33] from NASA analyzed the influence of flows in blade passage on surface heat transfer of turbine blades by liquid crystal thermography and other techniques. Figure 8.5 shows the Stanton Number distribution on blade surface. On the suction surface, the Stanton

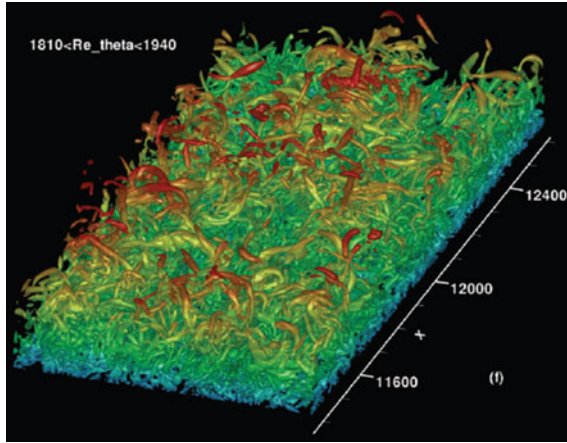


Fig. 8.4 Coherent structures in heating flat-plate boundary layer [29]

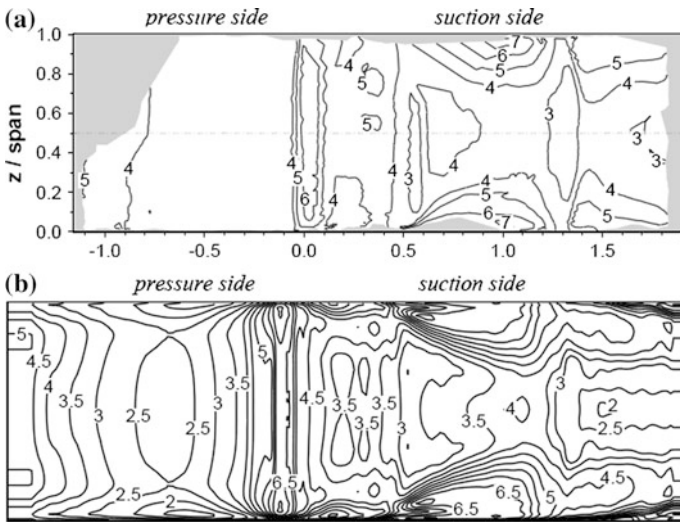


Fig. 8.5 Stanton number distribution on turbine blade surface ($\times 1000$). **a** Experimental results (gray means no-data points) [33], **b** Computational results [34]

Number at the middle blade gradually decreases from the maximum value at the leading-edge stagnation point, and then increases rapidly due to the transition. Because the velocity reduces and heat transfer intensity decreases with the effect of adverse pressure gradient, the Stanton Number decreases again after reaching the maximum point and reaches to the minimum value at the position where the chord length is about 50% of the blade height. Then the effect of secondary vortices begins to emerge, and then as increases the Stanton Number around the upper and lower endwalls significantly. This

region expands gradually to the middle of the blade with the migration of passage vortexes. At the position where the chord length is 130% of the blade height, the oblique shock wave formed at the outlet of adjacent blades results in the interaction between shock wave and boundary layer on the suction surface, which increases the thickness of the boundary layer gradually, and as a result, the Stanton Number decreases again. As the influence of shock waves weakens at the downstream endwall region, the effect of secondary flows increases rapidly, and regions with intensive heat transfer appear again around the upper and lower endwalls.

In turbines, thermal loads of components would also be influenced by tip leakage flows, sealing cooling flows, and other flows in the endwall region. As for unshrouded turbine rotor blades, tip clearance leakage flows would lead to high local thermal loads, which may result in oxidation and ablation of the blades, which is closely related to flow structures. Figure 8.6 shows the Nusselt Number distribution of several typical blade tip structures. Corresponding typical flow structures are marked in the figure, in which black solid circles and hollow circles show the points with the maximum and minimum thermal load respectively. It is shown that high local leakage flow mass and backflow vortexes would increase the thermal loads, hence the influence of blade tip structure on thermal loads must be considered when optimizing the structure [35]. At the hub, thermal loads of the turbine disk and blade roots are closely related to sealing cool flow in obturation. Particularly when local gas influx, the heat transfer would turn more complex (as shown in Fig. 8.7a). Obtaining correct thermal loads of components is based on accurate description of flow structure and the mechanism of energy transport. Figure 8.7b shows the temperature distribution of the sealed cavity and turbine components, which is obtained by the CHT method [4]. The figure show that there is a obvious temperature difference between the sealing flow and the main flow, thus temperature gradient in the solid components is high. In this case, local temperature is determined by heat transfer coefficient, and conversely, wall temperature variation would influence local convective heat transfer coefficient. Meanwhile, heat transfer characteristics that are consistent with physical reality could be only obtained by the CHT method [36].

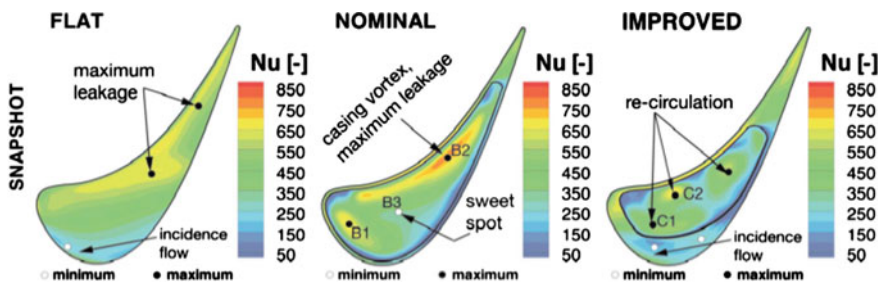


Fig. 8.6 Nusselt number distribution of typical blade tip structures [35]

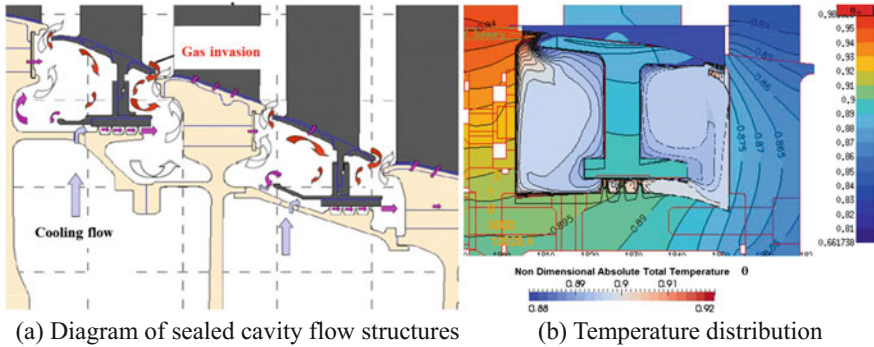


Fig. 8.7 Typical sealed cavity flow structures and temperature distribution [4]

8.2 Flow-Structure Interaction Problems

8.2.1 Flow-Structure Interaction Problem in Turbines

The working principle of a turbine results in the intense interaction between the solid in a turbine and the fluid in it. Because the internal flow field is unsteady essentially, hence the force applied on the surface of blades and other solid components is also unsteady, which may result in blade vibration. Conversely, blade deformation or vibration may lead to unsteady changes of boundary conditions of the flow field which may affect the flow graphs and the interaction between the fluid and the solid. Thus it can be seen that the conjugate problem between the flow and structure is inevitable.

The interactive relations between various forces in the generalized conjugate process between the fluid and the solid are described in Fig. 8.8 [37]. The process has the basic characteristic that both the interaction between the flow aerodynamic and solid movement are realized through the conjugate interfaces. In addition, both aerodynamic forces and solid movements at the interfaces are determined specifically by solving the entire conjugate system systematically, which could be unknown presciently.

According to the discipline classification, the sub-discipline dealing with the fluid-structure interaction problem in turbomachinery is generally called turbomachinery aeroelasticity. According to the response patterns of blade, turbomachinery aeroelasticity problems can be generally divided into static aeroelasticity problems, forced response, and flutter [38]. Generally, the static aeroelasticity discuss the elastic deformation of structures. for example the deformation, which is different from original cold-state shapes, of blade with the centrifugal force and aerodynamic force. The deformation is static and generally independent from vibration, and the effect of static aeroelasticity on performance of turbine components can be inhibited by back-stepping the geometrical machining parameters as well as by machining

and assembly. For example, pre-twisting and other methods are often used in installation of typical low-pressure turbine blades with high aspect ratio so as to eliminate this effect. Because the deformation changes linearly with different rotate speed the effect of blade deformation should be considered in evaluating the performance at off-design rotate speed. For example, Wilson et al. [39] studied the effect of the large fan blade elastic deformation at different speeds on performance by using a non-linear model. Forced response generally refers to the structural vibration of blades, which is caused by periodic unsteady aerodynamic force when the blades pass through the upstream blade row wake region or the blade row potential region between the upstream and downstream. If the frequency of the periodic force is equal to the inherent frequency of the elastic structure, resonance would occur with sharply increased vibration amplitude. Regarding to the forced response problem, the external force that results in vibration of the elastic structure is independent on its own vibration. Changes of the external force with time may be simple-harmonic, stepped, or stochastic. This kind of aeroelasticity problems is also called aeroelastic dynamic response problems. Flutter is generally defined as unsteady self-excited vibration of a structure for its interaction with gas flows. When flutter occurs, unsteady aerodynamic force, inertia and damping of the structure, as well as elastic force on the structure are in an unbalanced state. The aerodynamic force, working on the structure, results in the increase of vibration amplitude which in return leads to larger unsteady aerodynamic force. The essential difference between flutter and forced response is that the force in this problem, which has alternative aero-elastic effects in vibration, is only related to the elastic vibration system itself. The core of the flutter problem is whether flutter occurs or not, which is also called aeroelastic stability problem. Sometimes, narrowly-defined aeroelasticity problems refer solely to the flutter problem.

8.2.2 Forced Response of Turbine Blades

In a turbine, rotor blade rows the relative motion as well as position of rotor blade row and stator blade row result in that the non-uniform distribution of pressure around the circumferential direction and the vortex in flow field would make an influence on the blade in upstream and downstream, making the blade disturbed by unsteady aerodynamic forces. These acting forces is led by unsteady disturbances including incoming flow distortions (including pressure, temperature, velocity, and density distortions), adjacent blade row potential field (including shock waves), wake of the upstream blade row and secondary flows, unsteady flows in the blade row passage, and so on. These unsteady disturbances are collectively called forcing effects. Based on the stress on blades, these forcing effects would eventually apply periodic disturbing lift and resistance on blades, thus force them to vibrate through influencing velocity distribution or pressure distribution. When the frequency of an aerodynamic actuation is equal to the inherent frequency of blades, resonance would occur with the sharp increase of vibration amplitude. Blades may be

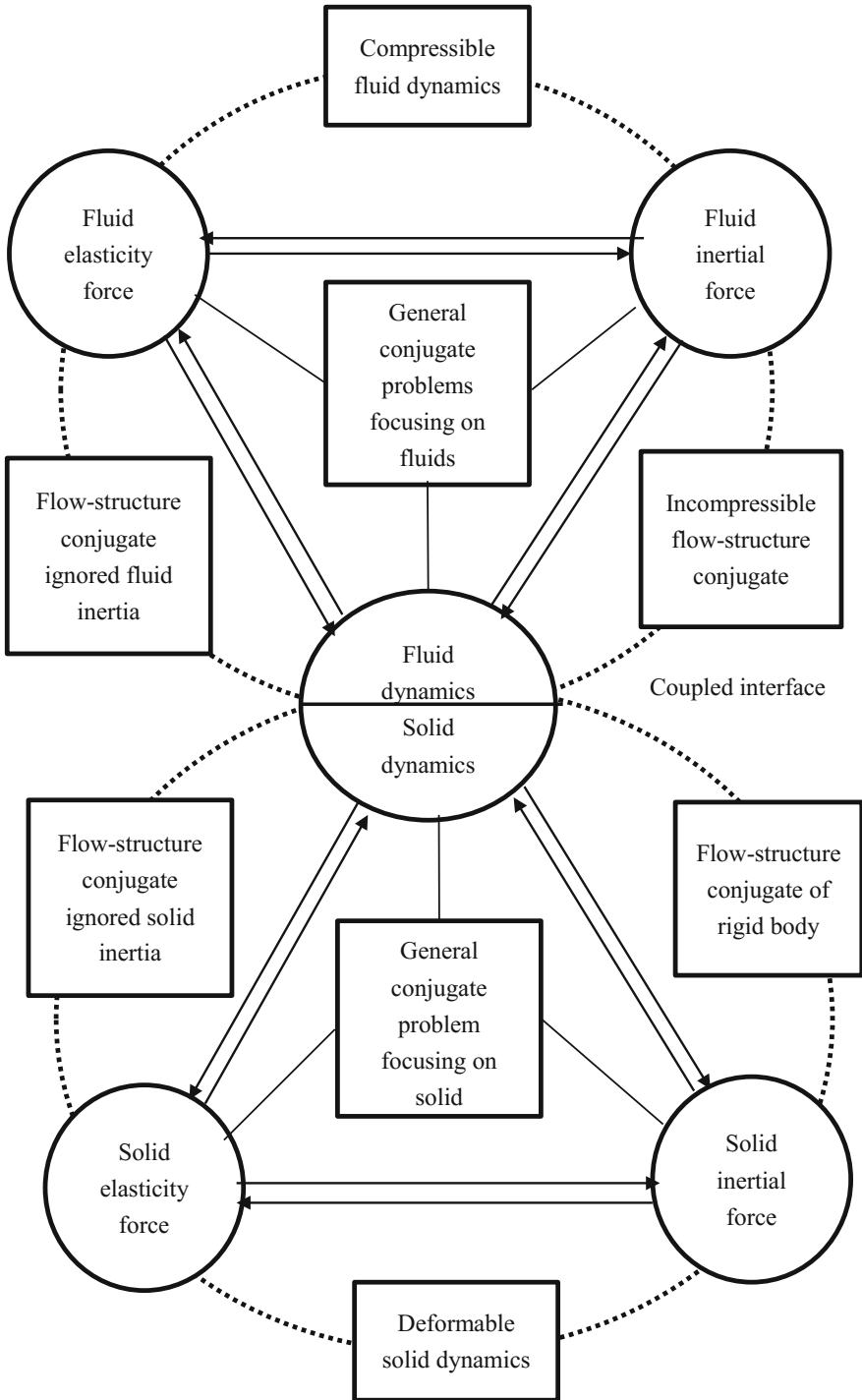
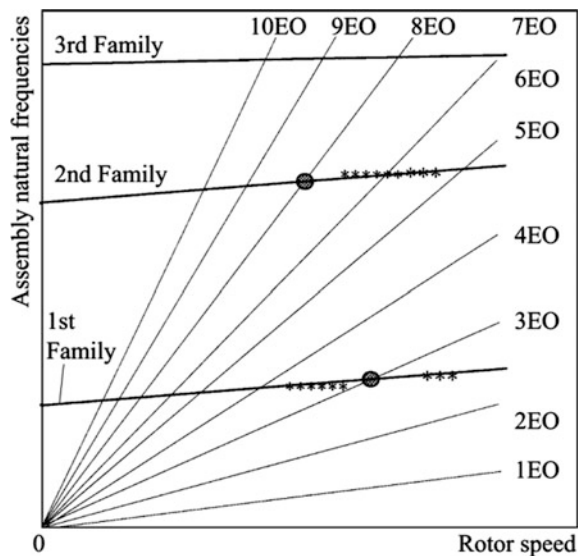


Fig. 8.8 Interactive relations between forces in flow-structure interaction problem [37]

damaged by excessively large vibration stress. Blade resonance would always lead to a serious HCF (High-Cycle Fatigue) problem, which is a key factor of destroy structural integrity and reliability of turbine components. In order to solve this problem, American and British aviation industries carried out a special research program and regarded engine HCF-related maintenance cost reduction as an important index in their IHPTET (Integrated High Performance Turbine Engine Technology) programs [40]. Because of the significance of forced vibration, it has been universally accepted that forced response analysis of turbine components must be included in the design of not only aircraft engines but also gas turbines. When force response of blade occurs, blade movement is a function of the unsteady aerodynamic force. The key unsteady flows in turbine components are essentially related to the rotate speed, so the blades forced response caused by the unsteady aerodynamic force could be analyzed by a Campbell diagram plot [41] (see Fig. 8.9), in which the dot represents the forced resonance point and the asterisk represents the flutter point.

Li, Li, et al. (from Beihang University) have done a large number of systematic works in the field about the forced response problem of blades under the actuation of unsteady flows. In the paper [42], they used the transient analysis method to estimate displacements and stresses of rotor blades with wake excitation of upstream stator blades. 3D unsteady simulations were carried out for the flow field, and the obtained 3D unsteady aerodynamic force was then introduced to finite element calculations for rotor blades, so as to do a transient analysis of the forced response problem of blades with wake excitation. They also analyzed the influence

Fig. 8.9 Typical Campbell diagram [41]



of the anharmonic design of asymmetric stator blade distribution, and the results showed that the excitation force on the rotor changed from single-frequency high-amplitude excitation force in the case of uniform stator blade distribution to multi-frequency-component low-amplitude excitation force, indicating that the anharmonic design of asymmetric stator blade distribution could effectively decrease the wake excitation force on rotor blades thus increase fatigue life [43]. Gong et al. analyzed the changes of flow graphs before and after conjugation by the flow-structure interaction numerical simulation method [44, 45], and the results show that, as for high-aspect-ratio blade passage flows, there were great differences in overall flow field parameters with the conjugation taken into account or not. Meanwhile, flow in the passage would also be significantly influenced by blade deformations, and that the flow field was more sensitive to structural deformations in off-design conditions. Figure 8.10 compares the standard deviations of blade-surface static pressure coefficients in a low-pressure turbine with design conditions between the two simulation models: flow-structure interaction model and non-conjugate model. Although the difference of time averaged load and the load distribution on blades between the two simulation models was not large, the unsteady characteristic of the flow field in blade passage was quite different, in which the flow field unsteadiness obtained in the flow-structure interaction simulation is weakened significantly [44]. Thus it can be seen that the flow-structure interaction analysis method not only has great importance on the studies of blade

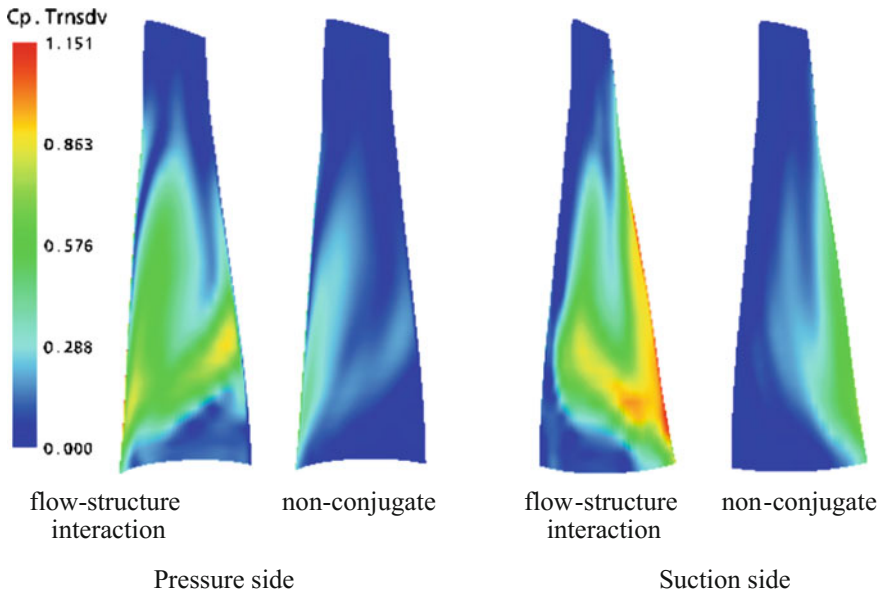


Fig. 8.10 Standard deviations of static pressure coefficients of turbine rotor blades [44]

vibration problem, but also can effectively improve the capability of capturing the real unsteady flow field in turbines.

8.2.3 *Blade Flutter*

Another important problem of aerodynamic conjugation is the aeroelastic stability problem, which is named the flutter problem. Although turbomachinery aeroelasticity problems have been studied for more than half a century, there are still no completely reliable methods that can accurately predict the flutter stability of blades and other typical structures.

Experimental research is an important approach to solve the flutter problem and also a necessary step of verifying numerical simulation results. Flutter experiments can be carried out for both individual components and the whole machine. However, the whole machine experiment is more complex and difficult than component experiment. Therefore, detailed, specific, and parameterized analysis of flutter phenomena have to be carried out on the basis of component experiments. However, because component experiments are performed in relatively ideal environments, in which not all flutter influencing factors can be considerable. For example, the influence of adjacent blade rows cannot be modeled in cascade flutter experiments. Thus, compared to experimental research, numerical simulation can obtain more flow field data as well as blade stress and vibration data. With the development of numerical simulation methods, numerical simulation has become more and more important in blade flutter studies. Generally methods of numerical investigations on the flutter problem can be divided into classical and conjugate methods. Classical methods ignore the conjugate relation between the fluid and the structure and solve problems in the two domains separately, while conjugate methods solve them with conjugation taken into account. Classical methods mainly include actuator disk method, eigenvalue method, energy method, etc. Because these methods do not consider problems that need to be solved in a conjugate manner, their requirement for computing capability is low. So, they were widely applied in the early stage of research. However, the accuracy of these methods in predicting the flutter problem is relatively lacking, and thus their applicability is limited to a certain problem [46, 47]. Conjugate methods acknowledge interaction between the fluid and the structure, which is just the essential difference between conjugate methods and classical methods. Conjugate methods are consistent with the fact, and require more non-linear factors to be considered in the analysis of the fluid and the structure. Thus, the researcher could not only predict the moment when the flow turn unstable and flutter occur, but also predict the limit cycle characteristics of the instability. A large number of experimental results suggest that turbine blade flutter usually occurs in the form of limit cycle vibration with different amplitudes, so predicting the size of the amplitude is more important than predicting the occurrence of flutter. It is because that limit cycle movement with a small amplitude may not seriously impact the operation of turbomachinery. It is

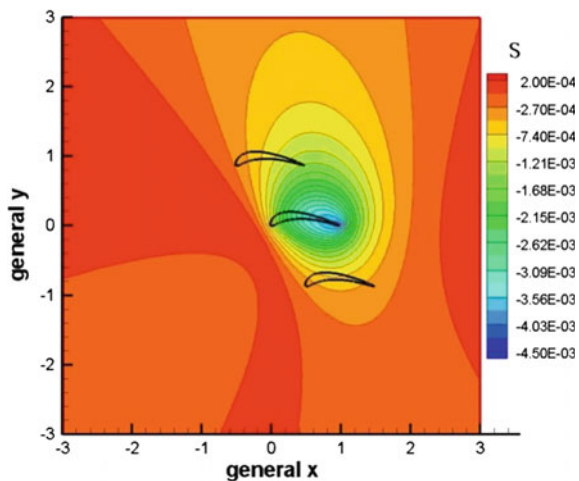
more important for designers to predict and avoid high-amplitude vibration. Therefore, prediction results obtained by conjugate methods are always more meaningful for engineering applications. However, the current conjugate methods require high computing capability, and their accuracy still needs to be further enhanced.

Because of the importance of the flutter problem, researchers have studied the mechanism of turbomachinery blade flutter stability, parametric flutter prediction, and flutter parameterization measures for a long time with great achievements. There are many factors influencing flutter stability in turbomachinery environment, so that studies on the flutter problem are generally carried out by taking a certain design parameter as the judgment criterion. Thus, rules of flutter stability with this parameter can be obtained through a systematic study on the parameter. In the design of primary stage of gas turbine, parameters such as reduced frequency, vibration mode, inflow incidence, and Mach Number are commonly used to evaluate stability of the blade flutter. For example, inflow incidence angle have influence on the load on blades and flow within blade rows by directly effecting the triangle of velocities, hence finally affect flutter stability. Carta et al. studied cascade flutter stability of a linear compressor and present an idea that the reduced frequency, at which flutter occurs, decreases with the increase of the incidence angle and is unrelated to rotating stall [48]. Increasing the incidence angle would result in the decrease of flutter stability, in which flow separation at the leading edge of blades will be the main factor influencing flutter stability when the incidence angle exceeds a critical value. Ellenberger et al. indicated that things will be different when there are shock waves in flows. They studied torsional flutter in a compressor cascade and found that shock waves have a great influence on flutter stability than separation bubbles [49], which is not exactly the same in turbines. He et al. carried out experimental investigations on unsteady flows with different incidence angles in a torsional vibration cascade of a low-pressure turbine of which the results show that separation bubbles on the pressure surface would reduce flutter stability, while flows after the reattachment point would increase flutter stability. On the whole, the incidence angle has little influence on flutter stability [50]. With the deepening study of turbomachinery flutter problems, the important influence of vibration mode on flutter stability has been paid more attention. Bendiksen et al. studied oscillating cascade flows at bending and torsional vibration in a series of flow conditions by the analytic method, of which the results show that there is a big difference in flutter stability between bending vibration and torsional vibration [51]. Using the stability parameter diagram method, Panovsky et al. systematically studied the influence of vibration modes in a 2D cascade on flutter stability [52, 53]. In this method, rigid motion assumption is used and all the possible vibration modes are transformed into torsional motions. The stability parameter diagram relating to torsional center and stability parameters of torsional motions could be obtained, which clearly indicates the flutter stability of all possible rigid motions. The results show that vibration modes have significant influence on flutter stability as well as the influence of geometrical parameters is also non-negligible. Yang, He, et al. studied the influence of blade tip clearance in a compressor cascade on flutter stability, and the results

show that tip leakage flows can reduce flutter stability compared to the case with sealed tips [54].

As for numerical prediction of flutter stability, Wang (from Beihang University) has made a large number of fruitful studies [55–58] that a 3D turbomachinery aeroelasticity computing software based on the time-domain method has been developed, which can be used to make forced response and flutter analysis. Wang also systematically made analysis of several factors influencing aeroelastic stability of turbomachinery blades, in which a study on blades of a compressor reveals that blade modal and inter blade phase angle have crucial influence on flutter of turbomachinery blades, and that shock waves on the suction surface and post-wave separation zone are the important factors inducing blade flutter. With respect to determination of flutter stability, Zhang et al. carried out flow-structure interaction numerical simulation investigations on the flutter problem of fan and turbine blades by taking the influence coefficient method into 3D unsteady numerical simulation. Based on the rigid motion assumption, modal superposition principle and the idea of all rigid motions can be expressed as torsional rigid motions, then they established the stability parameter contour map that can describe all the possible rigid motions and stability parameter relations as well as discussed the influence of the key parameters on flutter stability [59–61]. Figure 8.11 shows the diagram of relations between the stability parameters of a turbine blade profile and the position of rotation axis, in which the region with the stability parameter $S < 0$ covers the torsional center positions of all the unstable rotational modes of the turbine blade profile under the research conditions. It is shown that the most unstable region is located in an oval area with the trailing edge of the reference blade as its center, and a “reverse-C” region at the leading edge vertex of the reference blade has the highest stability parameter. In addition, the stability parameter is relatively large along the extension direction of the trailing edge. As for low-pressure turbines, a stability parameter contour map suggests that vibration mode has the greatest

Fig. 8.11 Relations between typical turbine stability parameters and position of torsion shaft [59]



influence on flutter stability. A tiny change of vibration mode would make a great difference on flutter stability. Reduced frequency, inlet flow angle, and Mach Number have relatively small influence on flutter stability, meanwhile, influence of tip clearance is the weakest among the discussed parameters. Stability parameter distribution of the subsonic low-pressure turbine and the transonic fan rotor discussed in the study show the same distribution trends, indicating that there is certain similarity in flutter stability between turbine blades and fan blades.

8.3 Aero-acoustic Conjugate Problems

8.3.1 *Noise and Aero-acoustic Conjugate Problems in Turbine*

As great progress has been made in terms of aerodynamic characteristics, reliability, and maintainability of turbines, noise problem is getting more and more attention. In aviation, for example, aircraft noise may seriously influence residents near airports. With the development of the air transport industry, the aircraft noise pollution problem is further exacerbated across the world. Aero-engines are the main source of aircraft noise, hence all the western aviation powers have implemented specific research programs, aiming at the noise problem, such as AST of NASA and QAT in America. These programs are mainly intended to significantly reduce aero-engine noise and other pollutions so as to meet demand for intensive air transport [62]. Jet noise is the main constituents of noises generated by aero-engines that were used previously. However, with the bypass ratio of modern civil aero-engines increasing, jet noise was reduced greatly and large-size fans became another main source of engine noises [63]. Therefore, a large number of studies on fan noise reduction have been carried out in aviation field since 1970s consequently fan noise was greatly reduced as well. Thus, the turbine noise problem, which was “neglected” in previous, became more and more obvious. For example, in the approaching and landing process of aircrafts with their engines set at idling rating, the interaction between rotor and stator noise of low-pressure turbines has become one of the main noise sources of aero-engines. Therefore, more and more institutes and researchers have paid great attention to tahte how to reduce low-pressure turbine noise in design. For example, the Sixth Framework Programme of the EU regards noise reduction technologies for low pressure turbines as an important research subject [64]. Figure 8.12 shows the sources of noises generated by a typical civil airplane during take-off and landing. It be seen that noise level of turbine exceeds jet noise even approaches fan noise level, becoming the second largest source of engine noise [65]. Figure 8.13 shows the influence of noises generated by components on overall noise of a typical modern aero-engine with a bypass ratio of 8 in the process

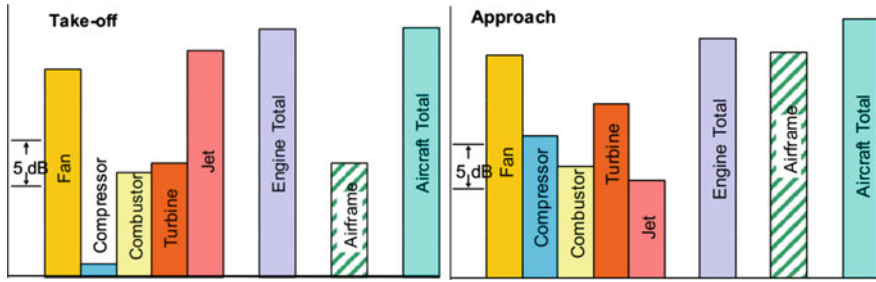
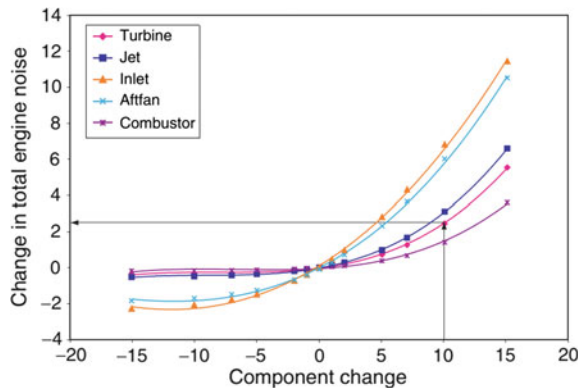


Fig. 8.12 Sources of aircraft noises during take-off and landing [65]

Fig. 8.13 Influence of noises generated by components on overall noise of a typical bypass ratio 8 aero-engine in landing [64]



of landing. The results show that an increase of 10 dB in turbine component noise would lead to an increase of about 2.5EPNdB (even up to 4EPNdB in some cases) in overall equivalent perceived noise of the engine [64].

Turbomachinery noise reduction methods can be generally divided into two kinds: (1) sound source control method which reduce noise generation from the source by optimization design of turbomachinery. (2) propagation path control methods which reduce noise by installing devices (i.e. acoustic liners), which have sound absorption function or effect the propagation paths of noise. Both of the above two kinds of methods have been explored effectively and have been successfully applied in the field of reduction of aero-engine fan noise. However, because working temperature of turbine components is very high and may beyond the temperature limit of acoustic treatment materials, application of acoustic liners in turbines is limited in particular. In this case, aerodynamic optimization design for turbines, which aimed at sound sources and acoustic problems, becomes one of the key point reducing turbine noise. Currently, research institutes have carried out a large number of studies on low-pressure turbine noise reduction based on a large quantity of experimental data. Meanwhile, the empirical models for predicting turbine noise based on

aeroacoustics theories and a large quantity of experimental data for engine noise have been developed. Also, correlations among noise have been established with turbine dimensions, rotation speed, flow rate, output work, temperature, and other parameters so as to evaluate the noise generated by turbine, which make it possible to consider turbine noise reduction at the initial stage of aerodynamic and structural design for low-pressure turbines [66, 67]. Sun (from Beihang University) has done a lot of basic research of aeroacoustics and has made fruitful achievements as well [68, 69] (see Fig. 8.14).

It's worth noting that aerodynamic performance of low-pressure turbine is crucial to the economic efficiency of the engine. Therefore, noise reduction and aerodynamic performance of low-pressure turbines should be considered together. In other words, influence of all the noise reduction measures on low pressure turbine aerodynamic performance must be taken into account, which needs to be considered in the process of aerodynamic design. Effective aero-acoustic conjugate design refers to the design method, in which the influence of turbine parameters on both aerodynamic and acoustic performance is considered during the entire process

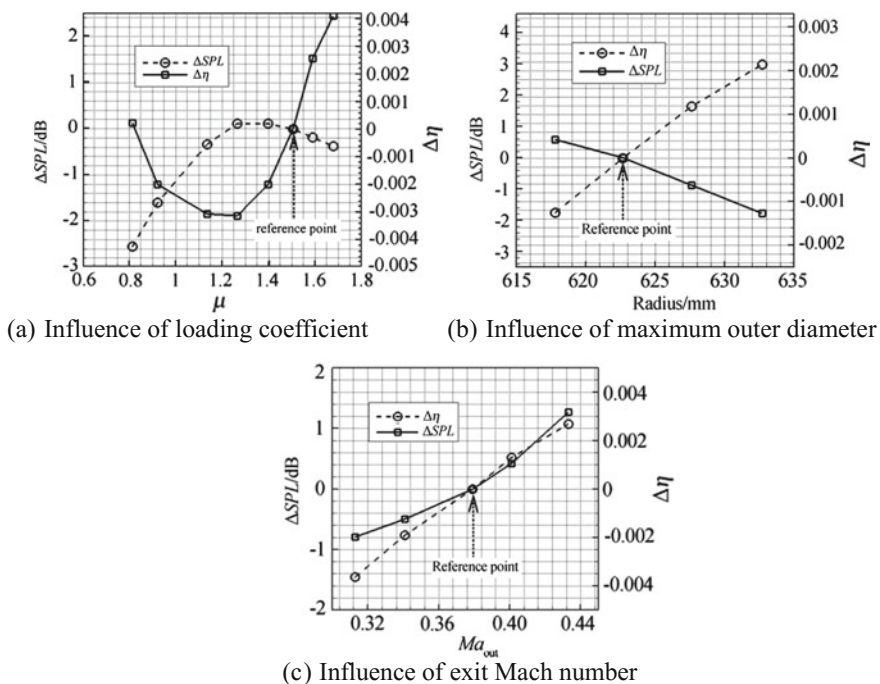


Fig. 8.14 Influence of key parameters of a civil LP turbine on aerodynamic performance and noise level [72]

of parameter selection and modeling, so as to achieve the improvement for both aerodynamic performance and noise level from the source.

8.3.2 *Noise Reduction in Low-Dimensional Aerodynamic Design*

Presently, a well design system has been established for aerodynamic design of low-pressure turbines. Therefore, it is an important aero-acoustic integrated design method that takes acoustic considerations and requirements into the present aerodynamic design system. According to spatial complexity, aerodynamic design of turbines can be divided into one-dimensional design, two-dimensional design, and three-dimensional design, which is the general steps of turbine aerodynamic design and then aero-acoustic conjugate design could be performed in any one of these three steps. As mentioned above, aero-thermodynamic characteristics of flows can be obtained more easily in low-dimensional (one dimension and two dimensions) aerodynamic design, so that one will get twofold results with half the effort. The same goes for acoustic problems.

Tyler and Sofrin modal the improvement method is the most important tool for analyzing noise reduction in one-dimensional aerodynamic design. As introduced by this method, selecting appropriate numbers of guide vanes and rotor blades can eliminate the discrete noise generated by the interaction between rotor and stator in a certain frequency range, thus reducing the noise influence on the outside. This principle has been successfully applied in aero-engine fan design and has become an important basis for determining number of fan blades [70]. Tyler and Sofrin indicated that, because of the limitation of the “pipeline” boundary conditions in turbomachines, noise generated by the interaction between unsteady inflows and blades can only exist in specific forms, named modes. The propagation mode is mainly determined by number of blades, rotating speed, and aerodynamic conditions (flow rate, temperature, etc.). As for a turbine stage consisting of B rotor blades and V stator blades, the circumferential modal number, m , of the sound modes generated by blade interaction can be obtained by the Tyler and Sofrin equation:

$$m = hB \pm sV \quad (8.1)$$

where, h is the number of blade passing frequency harmonic, s is an arbitrary integer, representing the space harmonics generated by the stator. The blade-tip circumferential Mach Number of the interfering rotating pressure modes in the above model can be written:

$$M_{a,m} = \frac{hB\omega R}{mc} \quad (8.2)$$

where, ω is the rotating speed, R is the blade tip radius, c is the sound velocity. The critical circumferential Mach Number can be obtained by the equation below:

$$M'_{a,m} = \frac{\alpha_{m,\mu}}{m} \quad (8.3)$$

where, $\alpha_{m,\mu}$ is the radial wave number, which depends on the inner and outer diameter of the turbine. Tyler and Sofrin indicates that when $M_{a,m} < M'_{a,m}$, the sound waves are eliminated and the amplitude would attenuate rapidly along the axial direction, as well as when $M_{a,m} > M'_{a,m}$, the sound waves show the outgoing characteristics. By eliminating discrete noise, the above method serves as a simple approach for determining the number of turbine blades. It is seen that the selection method of blade should conjugate with the design of turbine meridional channel [70]. A study has shown that the dominant sources of sound generated by turbine are the BPF (blade passing frequency) discrete noise rear turbine stage. Thus, the above blade number determination method is generally used for low-pressure turbine in the last one or two stages [71].

Integrating aerodynamic performance and noise assessment models with each other is of great significance for the design of low-pressure turbines in low-dimensional model. Tan, Qiao, et al. (from Northwestern Polytechnical University) introduced the Lowson discrete noise prediction model to the turbine aerodynamic design procedures, analyzing the influence of key parameters of a multi-stage low-pressure turbine on noise characteristics in a civil airplane. The results show that last-stage work distribution of the turbine has significant influence on aerodynamic noise. With the increase of last-stage work, noise level decreases first and then increases, while the aerodynamic efficiency of turbine components presents an opposite trend. Therefore, it is possible to obtain an optimal range of work distribution, in which both the aerodynamic performance and noise performance of turbine components could be satisfactory. In addition, both component efficiency and noise change monotonously with the outer diameter of the turbine. With the increase of outer diameter, both aerodynamic performance and noise level of the turbine are improved, in which the noise reduction mainly results from the reduction of relative velocity in rotor blade tip. Exit Mach Number is another important parameter in the design of low-pressure turbines. The flow field in the rotor of the last-stage turbine could be improved by growth of the exit Mach number and thus the aerodynamic performance may be improved as well. However, increase of exit Mach Number would lead to the increase of relative velocity of rotor blade tip, which is harmful to turbine noise control [72, 73].

8.3.3 Aero-acoustic Integrated Design Based on Fully 3D-Modeling

Both discrete noise and broadband noise are mainly caused by unsteady flows in turbines at different scales of space and time. In order to reduce the noise from the source, unsteady flows in turbines have to be organized effectively. All these works are closely related to three-dimensional models of turbines.

MTU and DLR in Germany are the earliest institutions studying turbine noise problems, which carried out a series of numerical and experimental studies on a high-speed three-stage low-pressure turbine test rig, and found that the interaction between the low-pressure turbine discrete noise mode and EGVs (Exit Guide Vane) has great influence on discrete noise characteristics [74], as well as the interaction between EGVs and some discrete noise may generate non-cut-off modes, thus going against turbine noise control [75]. To solve this problem, they discussed the method of reducing turbine noise by leaned EGVs (see Fig. 8.15) with the aim of changing the phase of the interaction between EGVs and upstream wakes as well as other unsteady flow structures by changing EGV, thus controlling the noise. Both numerical calculation and experimental results suggest that appropriate lean angle together with optimized number of EGVs can significantly reduce the noise caused by interaction between the low-pressure turbine and EGVs [76].

In fact, leaning and other 3D modeling methods could be used not only for EGVs, but also for guide vanes in the rear stages of the turbine to reduce noise. Zhao, Qiao, et al. studied a high-aspect-ratio low-pressure turbine and the results show that the reverse-lean guide vane design, in which the suction surface and the hub form an acute angle, can effectively reduce the noise of the turbine. However, this scheme may do harm to the aerodynamic performance of turbines. Thus, it is necessary to explore the feasibility and methods of reasonable leaned vane design in order to achieve improvement in both aerodynamic and noise performance [77, 78]. Besides Secondary flows in turbines could not only result in broadband noise, but also influence the interaction between rotor and stator in turbines, effecting the discrete noise. By taking the influence of leakage flows as an example, studies have shown that increased tip clearance would reduce the discrete noise caused by



Fig. 8.15 EGV layout schemes: conventional scheme (left), leaning scheme (right) [76]

interaction between the turbine rotor and upstream vanes, which is mainly because that the height of the blades that interact with upstream wakes decreases. However, larger clearance would also enhance leakage flows and thus may increase the noise caused by interaction between the leakage flows and downstream guide vanes [76]. Therefore, height of blade tip clearance needs to be considered in a multi-stage environment, even if only the noise problem is taken into consideration. Except rotor-stator interaction, clocking effects in multi-stage turbines are another important unsteady phenomenon, for which Blaszcak did an experimental study on the rotor-rotor and stator-stator clocking effects in a two-stage turbine, and suggest that clocking effects have significant influence on turbine noise, as well as reasonable use of clocking effects can effectively decrease turbine noise level [79]. Unfortunately, they observed opposite results in different experiments when exploring whether aerodynamic performance and noise level could be improved simultaneously. It is once again that confirms the complexity of the aero-acoustic conjugate problem, for which more systematic and comprehensive studies are needed to obtain its mechanism.

8.4 Multidisciplinary Design Optimization Technologies

As previously mentioned, in the process of turbine design, not only the aerodynamic performance should be taken into account, but also problems, including structure, strength, lifetime, heat transfer, noise, etc., should be considered. These problems are generally ascribed to the distribution of pressure, temperature, and other physical parameters in the fluid domain and solid domain of a turbine, which are interactively distributed and lead to a multidisciplinary conjugate design problem essentially. Generally, the multidisciplinary conjugate problem in the design of turbine would mainly include structure/strength/vibration problems, heat transfer problems, aerodynamic problems, noise problems, secondary air system, materials and processes, and so on. Although turbine design is a complicated systematic engineering with multidisciplinary conjugation due to the limitations of technologies and tools, it has always been done by an iteration process of design, verification, and modification, which are carried out in each discipline independently. This design process not only is difficult to achieve the best optimizations of turbine performance in all directions, but also prolongs the lead time of turbine components.

With the more strict requirements for lead time of turbine and comprehensive indexes (including performance, lifetime, reliability, cost of operating and manufacture, etc.), researchers have begun to consider the interaction among different subjects and studied the MDO technologies applicable for turbine design based on the previous study. MDO was first proposed by Sobieszczanski-Sobieski (later acted as the chairman of the technical committee of AIAA-MDO, NASA), which aims to fully study and understand the interaction between disciplines and subsystems by using computer and numerical simulation technologies, as well as obtain the optimal solution for the entire system and shorten design cycle, thus making the developed products more competitive at last. Because the MDO

technology has an obvious advantage in handling multidisciplinary conjugate problems, researchers have drawn universal attention from aviation industry and achieved great development in the recent 20 years. For example, NASA and Lockheed Martin Corporation (US) used the MDO technology in cooperative development of a aerospike engine for the X-33 aircraft. GE, PW, and other aero-engine companies also took the technology to their aero-engine design procedures so as to improve the performance of aero-engine, decrease lead time, and reduce life-cycle cost.

8.4.1 General Description of MDO Problem

Decomposing a complex system into several subsystems by disciplines or components is an effective method for analyzing the complex system. According to relations among subsystems, complex systems can be divided into two kinds: hierarchic systems and non-hierarchic systems. As for hierarchic system, information flows among subsystems are sequential and there are no coupling relations among subsystems, which are organized in a pyramidal pattern, where the upper layer makes requests to the lower layer and the lower layer retroaction its design results to the upper layer, thus developing a tree-like structure on the whole. Subsystems in a non-hierarchic system are not hierarchically organized, which means information between subsystems are conjugated together which means that iterative computations is required for problems among subsystems and the system presents a network structure in general, thus are also deemed as conjugate systems. Most complicated engineering systems in reality are non-hierarchic systems, in which the multidisciplinary conjugate problem in the design of gas turbine also belongs to the category of non-hierarchic systems.

The MDO problem mainly contains three basic elements including design variable, constraint condition, and objective function. Design variables are a group of mutually independent variables that are used to determine the system or design scheme, which should be determined in design and called independent variables or design parameters. If a system has n independent design variables (x_1, x_2, \dots, x_n) , then the design variables can be described with a vector or matrix:

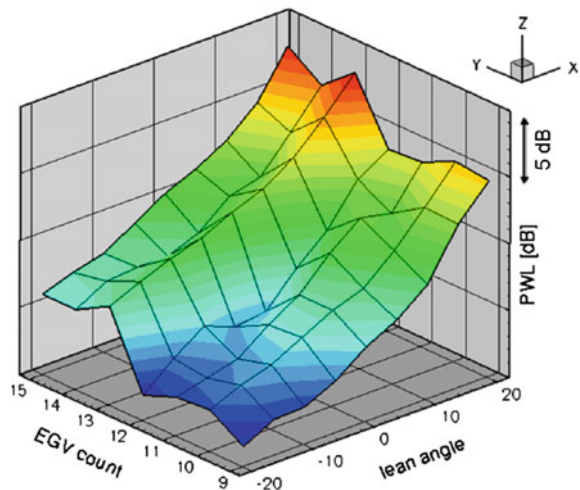
$$X = [x_1, x_2, \dots, x_n]^T \quad (8.4)$$

where, X is a vector in an n -dimensional space, namely a design scheme, of which projectional components on n mutually orthogonal coordinate axes are a group of design variables (x_1, x_2, \dots, x_n) of the design scheme, as well as the changes of the vector X in the n dimensional space is represent for the changes of these design variables. Mathematically, the range of variation of the design variables is unlimited in unconstrained optimization problems, however, in actual engineering problems, the exploration intervals (i.e. variable intervals) are typically set and given both the

upper and lower limits according to the problems actual situation as well as designers experience, so as to reduce the workload and reduce design time. In the orthogonal coordinate system consisting of design variables, the multi-dimensional exploration space formed by the upper and lower limits of the variable intervals is called a design space. If a problem contains n independent design variables, then its design space is a n -dimensional Euclidean space, denoted by E^n or R^n . The region is called a feasible region which is made up of all the points (x_1, x_2, \dots, x_n) meeting all constraint condition as well as the points X in the feasible region are called feasible design schemes or feasible solutions. In other words, a feasible design region in a variable space is the region which is limited by constraint conditions, and is a part of the variable space. In general, the optimization process of MDO and finally the optimal points should be only within the feasible region obtained. Otherwise, the obtained design parameters will lose their meaning since they do not meet the constraint conditions (see Fig. 8.16).

Constraint conditions are limiting conditions in design, which are generally functions of design variables and also called constraint functions. They are generally divided into performance constraints and boundary constraints. Performance constraints refer to technical indexes that need to be met in design, such as flow rate and power of turbine. In addition, Boundary constraints include the permitted ranges for the design, such as the size of turbine rotation speed, and weight as well. Constraint conditions can be typically divided into equality constraints and inequality constraints by their expression forms. The mathematical expressions of the two kinds of constraints can be written:

Fig. 8.16 Influence of EGV number and lean angle on turbine noise [76]



$$\begin{aligned} h_i(X) &= 0, & i &= 1, 2, \dots, l \\ g_j(X) &\leq 0, & j &= 1, 2, \dots, m \end{aligned} \quad (8.5)$$

where, l and m respectively represent the number of equality constraints and inequality constraints.

Objective function is also called target function, which is the criterion for assessing all the design schemes in the relevant space. In other words, objective function is mathematical description of design objectives and tasks. Generally, objective function is a function of independent design variables, $X = [x_1, x_2, \dots, x_n]^T$, which is described as $f(X)$:

$$f(X) = f(x_1, x_2, \dots, x_n) \quad (8.6)$$

In general, optimization problem is a process of obtaining the maximum or minimum value of the objective function.

For a design problem in which the variable space is E^n , the design variable is $X = [x_1, x_2, \dots, x_n]^T$ and the objective function is $f(X)$, as well as the equality constraint and inequality constraint are $h_i(X) = 0$ and $g_j(X) \leq 0$ respectively, then the design problem can be expressed as:

$$\begin{cases} \min & f(X) \\ \text{s.t.} & h_i(X) = 0, \quad i = 1, 2, \dots, l \\ & g_j(X) \leq 0, \quad j = 1, 2, \dots, m \\ & X \in E^n \end{cases} \quad (8.7)$$

8.4.2 Application of MDO Technology in Turbines

In design of turbine components, the most significant conjugate problems refer to the conjugate problems in the solid domain, including the structural strength and the heat transfer problems, as well as the problems in the fluid domain including aerodynamic and noise problem, as shown in Fig. 8.17. The conjugation between aerodynamic problem and other three problems respectively are discussed in the first three section of this chapter, but in fact, all the four problems are not independent. This is not only reflected in the above-discussed coupling mechanism between aerodynamic problem and the other three problems, but also because, technically, all physical problems are under the significant influence of factors in many aspects. For example, the distribution of stress field, displacement field, and other physical quantities in the solid domain, which are the concerns of the structural strength problem, is closely related to temperature field in the solid domain and pressure field in the fluid domain. Meanwhile, fluctuation pressure field in the fluid domain, which is the concern of the noise problem, is related to the

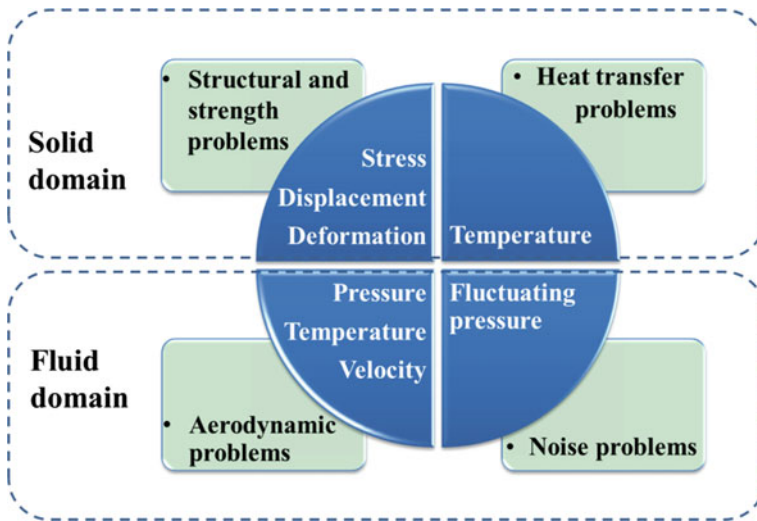


Fig. 8.17 Major multidisciplinary conjugate problems involved in turbine design

displacement field in the solid domain. Therefore, conjugate design optimization makes a great difference on the design of turbines.

Although there was no discussion and research on MDO for turbine components until 1990s, the MDO problem has got high attention from many research institutes and researchers, furthermore, considerable achievements have been made [81, 82]. Yue et al. (from Northwestern Polytechnical University) carried out a detailed study on MDO methods for turbine blades in an aero-engine. Figure 8.18 shows the procedures of fully 3D multidisciplinary feasible optimization design of turbine blades, which were established by them. By using modeling parameters of each section of the turbine blades as system design variables of the MDO, as well as using aerodynamic performance, natural vibration frequency, and blade equivalent stress of the turbine blades as optimization objectives and constraint conditions, this optimization system, in each optimization cycle, first conducts a multidisciplinary (aerodynamics, heat transfer, and structure) conjugate analysis and then carries out analysis and inspection from three disciplines including fatigue, vibration, and reliability.

A major factor limiting the wide application of the multidisciplinary tightly-coupled design optimization method is the huge computational cost in the process of repeated iterative optimization, which is enormous even if the global approximation equation for the tightly-coupled analysis is established by using test design method. The time consumption of single-discipline analysis of these sample points is acceptable, but the huge amount of test design points would make the time cost of the tightly-coupled analysis unacceptable. In order to improve both the precision of the multidisciplinary optimization design of turbine blades and the optimization efficiency so as to enhance the realizability of the multidisciplinary

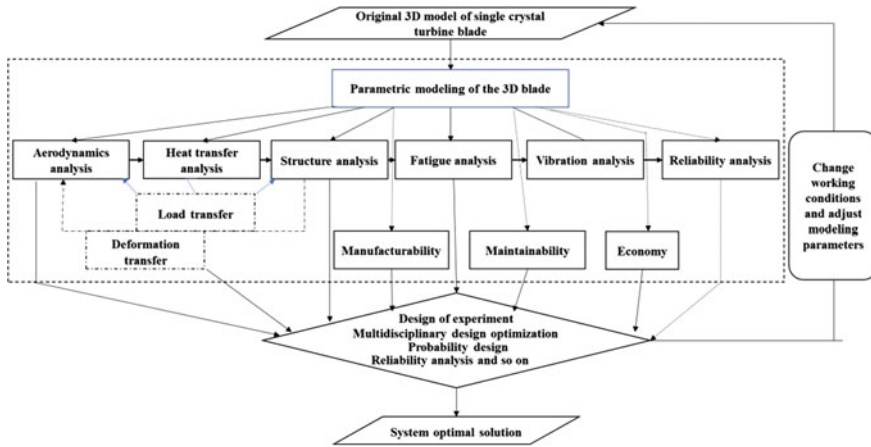


Fig. 8.18 Typical multidisciplinary design optimization procedures for turbine blades [80]

optimization design, Wang et al. established a set of multiple-precision analysis based multidisciplinary design optimization methods by introducing the VCM (Variable complexity modeling) method as well as combining the CO (Collaborative Optimization) strategy [83]. Figure 8.19 shows the multiple-precision analysis based CO strategy which is used in the multidisciplinary optimization design of turbine blades. The optimization strategy is designed to take the multiple-precision analysis model into the CO strategy by means of variable complexity modeling. Two subsdiscipline-level optimizers, which are respectively used to deal with structural strength optimization and aerodynamic optimization, are connected to the system-level optimizer, of which their operation modes are

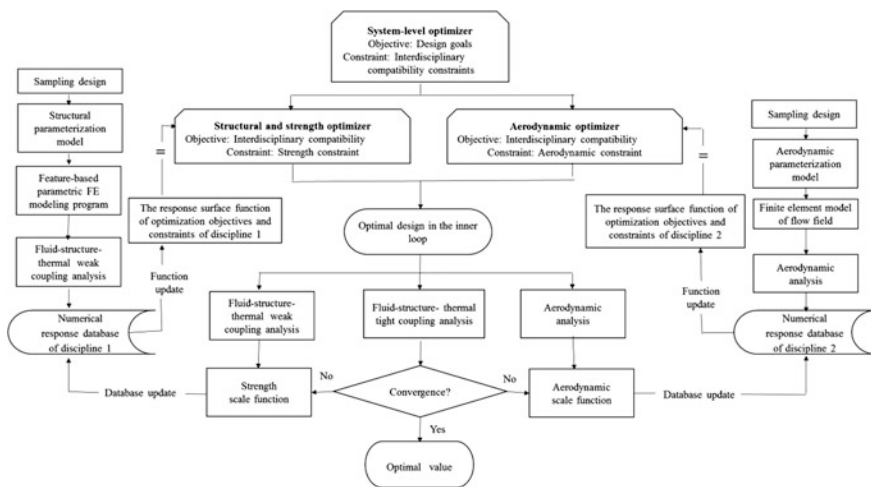


Fig. 8.19 Multiple-precision MDO analysis based CO strategy [83]

same as that of the CO strategy. The most important characteristic of this optimization strategy is the nesting of a CO cycle in the major cycle. Aerodynamic analysis, flow-structure loosely-coupled analysis, and flow-structure tightly-coupled analysis would be performed simultaneously for the optimal values obtained through CO, in which the former two kinds of analysis are medium-precision analysis, while the last analysis is high-precision analysis. Response data of the last analysis serves as scaling functions for the former two kinds of analysis. Results of an application of the multidisciplinary optimization method in blade design of a turbine show that, only 9 iterations of high-precision analysis were needed to ensure the precision of the optimized results by the optimization algorithm.

MDO methods are not yet perfect and there are some issues in practical engineering applications of the methods, but they have great advantages in improving design efficiency and success rate. With the development of research and computing technologies, MDO methods may become an integral part of advanced turbine design system in the near future.

References

1. Li, X. (2006). *Modern gas turbine technology*. Beijing: Aviation Industry Press.
2. Han, J. C., Duffa, S., & Ekkad, S. V. (2000). *Gas turbine heat transfer and cooling technology*. New York: Taylor & Francis.
3. Cao, Y., Tao, Z., & Xu, G. (2005). *Heat transfer in aero-engine*. Beijing: Beihang University Press.
4. Dixon, J. A., Valencia, A. G., Coren, D., et al. (2014). Main annulus gas path interactions—Turbine stator well heat transfer. *Journal of Turbomachinery*, 136, 21010.
5. Janke, E., & Wolf, T. (2010). *Aerothermal research for turbine components: an overview of the European AITEB-2 project*. ASME Paper GT2010-23511.
6. Han, J. C., & Rallabandi, A. (2010). Turbine blade film cooling using PSP technique. *Frontiers in Heat and Mass Transfer*, 1, 013001.
7. Monico, R. D., & Chew, J. W. (1993). Modelling thermal behaviour of turbomachinery discs and casings. *AGARD, Heat Transfer and Cooling in Gas Turbines*.
8. Dunn, M. G., Kim, J., Civinskas, K. C., et al. (1994). Time-averaged heat transfer and pressure measurements and comparison with prediction for a two-stage turbine. *Journal of Turbomachinery*, 116(1), 14–22.
9. Ameri, A. A., & Bunker, R. S. (2000). Heat transfer and flow on the first-stage blade tip of a power generation gas turbine: Part 2—Simulation results. *Journal of Turbomachinery*, 122(2), 272–277.
10. Saha, A. K., Acharya, S., Bunker, R., et al. (2006). Blade tip leakage flow and heat transfer with pressure-side winglet. *International Journal of Rotating Machinery*.
11. Roy, R. P., Xu, G., & Feng, J. (2001). A study of convective heat transfer in a model rotor-stator disk cavity. *Journal of Turbomachinery*, 123(3), 621–632.
12. Pasinato, H. D., Squires, K. D., & Roy, R. P. (2004). Measurements and modeling of the flow and heat transfer in a contoured vane-endwall passage. *International Journal of Heat and Mass Transfer*, 47(26), 5685–5702.
13. Simone, S., Montomoli, F., Martelli, F., et al. (2012). Analysis on the effect of a nonuniform inlet profile on heat transfer and fluid flow in turbine stages. *Journal of Turbomachinery*, 134, 11012.

14. Dunn, M. G. (2001). Convective heat transfer and aerodynamics in axial flow turbines. *Journal of Turbomachinery*, 123(4), 637–686.
15. Rigby, D. L., & Lepicovsky, J. (2001). *Conjugate heat transfer analysis of internally cooled configurations*. ASME Paper GT2001-0405.
16. Huang, H. (2002). *Numerical and experimental investigation on flow and heat fields in turbine cascade*. Beijing: Chinese Academy of Sciences.
17. Bohn, D., Becker, V., Kusterer, K., et al. (1999). *3-D internal flow and conjugate calculations of a convective cooled turbine blade with serpentine-shaped and ribbed channels*. ASME Paper 99-GT-220.
18. Li, Y. (2011). *A 3-D conjugate heat transfer solver and methodology research*. Beijing: Beihang University.
19. Wang, P., Li, Y., Zou, Z. P., et al. (2012). Improvement of turbulence model for conjugate heat transfer simulation. *Numerical Heat Transfer (Part A)*, 62(8), 624–638.
20. Li, H., Feng, G., Wang, S., et al. (2003). Numerical simulation method of aerodynamics-thermodynamics coupling in 3-D turbine cascade. *Beijing: Journal of Engineering Thermophysics*, 24(5), 770–772.
21. Zhang, H. (2013). *Investigation of numerical conjugate heat transfer method and coupling mechanism for hybrid porous/fluid/solid domains*. Beijing: Beihang University.
22. Zhang, H., Zou, Z., Li, Y., & Ye, J. (2011). Preconditioned density-based algorithm for conjugate porous/fluid/solid domains. *Numerical Heat Transfer (Part A)*, 60(2), 129–153.
23. Baoguo, Wang, Ge, Gao, Weiguang, Huang, et al. (2014). *Unsteady Aerodynamics*. Beijing: Beijing Institute of Technology Press.
24. Lucor, D., Xiu, D., & Su, C. H. (2003). Predictability and uncertainty in CFD. *International Journal for Numerical Methods in Fluids*, 43(5), 483–505.
25. Lehmann, K., Thomas, R., Hodson, H., et al. (2009). *Heat transfer and aerodynamics of over-shroud leakage flows in a high-pressure turbine*. ASME Paper GT2009-59531.
26. Chen, W., Kan, R., & Ren, J. (2010). Experimental investigation of heat transfer and pressure drop in a two-pass internal coolant passages of gas turbine airfoil. *Beijing: Journal of Aerospace Power*, 12, 2779–2786.
27. Arroyo, O. C., Gunnar, J. T., & Wallin, F. (2012). Experimental heat transfer investigation of an aggressive intermediate turbine duct. *Journal of Turbomachinery*, 134, 51026.
28. Serkan, Ö. (2004). Effect of heat transfer on stability and transition characteristics of boundary-layers. *International Journal of Heat and Mass Transfer*, 47(22), 4697–4712.
29. Wu, X., & Moin, P. (2010). Transitional and turbulent boundary layer with heat transfer. *Physics of Fluids*, 22(8), 1–8.
30. Shafi, H. S., Antonia, R. A., & Krogstad, P. A. (1997). Heat flux measurements in a turbulent boundary layer on a rough wall. *International Journal of Heat and Mass Transfer*, 40(12), 2989–2993.
31. Krogstad, P. A., Antonia, R. A., & Browne, L. W. B. (1992). Comparison between rough and smooth-wall turbulent boundary layers. *Journal of Fluid Mechanics*, 245, 599–617.
32. Han, J. C. (2013). Fundamental gas turbine heat transfer. *Journal of Thermal Science and Engineering Applications*, 5(2), 21007.
33. Giel, P. W., Fossen, G. J., Boyle, R. J., et al. (1999). *Blade heat transfer measurements and predictions in a transonic turbine cascade*. ASME Paper 99-GT-125.
34. Garg, V. K. (2002). Heat transfer research on gas turbine airfoils at NASA GRC. *International Journal of Heat and Fluid Flow*, 23(2), 109–136.
35. Mischo, B., Burdet, A., & Abhari, R. S. (2011). Influence of stator-rotor interaction on the aerothermal performance of recess blade tips. *Journal of Turbomachinery*, 133, 11023.
36. Maffulli, R., & He, L. (2013). *Wall temperature effects on heat transfer coefficient*. ASME Paper GT2013-94291.
37. Xing, J., Zhou, Sh., Cui, E. (1997). A survey on the fluid-solid interaction mechanics. *Beijing: Advances in Mechanics*, 27(1):19–30.
38. Sheng, Zhou, et al. (1989). *Turbomachinery aeroelasticity introduction*. Beijing: National Defense Industry Press.

39. Wilson, M. J., Imregun, M., & Sayma, A. I. (2006). *The effect of stagger variability in gas turbine fan assemblies*. ASME Paper GT2006-90434.
40. Fang, Ch. (2004). Prospective development of aeroengines. *Shenyang: Aeroengines*, 30(1), 1–5.
41. Marshall, J. G., & Imregun, M. (1996). A review of aeroelasticity methods with emphasis on turbomachinery applications. *Journal of Fluids and Structures*, 10(3), 237–267.
42. Meng, Y., Li, L., Li, Q. (2006). Transient analytical method of vane forcing response under stator-rotor wake influence. *Beijing: Journal of Beijing University of Aeronautics and Astronautics*, 32(6):671–674.
43. Meng, Y., Li, L., Li, Q. (2007). Investigation of force under asymmetry stator wake. *Beijing: Journal of Beijing University of Aeronautics and Astronautics*, 33(9):1005–1008.
44. Gong, S. (2008). *Research on unsteady flow and blade forced response in turbomachinery*. Beijing: Beihang University.
45. Gong, S., Zou, Z., Yang, Zh., et al. (2009). Numerical simulation of fluid-solid coupling of blades in the last stage of a steam turbine. *Beijing: Journal of Engineering for Thermal Energy and Power*, 24(1):31–36.
46. Whitehead, D. S. (1959). The vibration of cascade blades treated by actuator disk methods. *Proceedings of the Institution of Mechanical Engineers*, 173(1), 555–574.
47. Carta, F. O. (1967). Coupled blade-disc-shroud flutter instabilities in turbojet engine rotors. *ASME Journal of Engineering for Power*, 89(3), 419–426.
48. Carta, F. O., & St.Hilaire, A. O. (1980). Effect of interblade phase angle and incidence angle on cascade pitching stability. *ASME Journal of Engineering for Gas Turbines and Power*, 102(2), 391–396.
49. Ellenberger, K., Gallus, H. E. (1999). *Experimental investigations of stall flutter in a transonic cascade*. ASME Paper 99-GT-409.
50. He, L. (1996). *Unsteady flow in oscillating turbine cascade; Part 1: Linear cascade experiment*. ASME Paper 96-GT-374.
51. Bendiksen, O. O., & Friedmann, P. P. (1982). The effect of bending-torsion coupling on fan and compressor blade flutter. *ASME Journal of Engineering for Power*, 104(3), 617–623.
52. Nowinski, M., & Panovsky, J. (2000). Flutter mechanisms in low pressure turbine blades. *ASME Journal of Engineering for Gas Turbines and Power*, 122(1), 82–88.
53. Tchernycheva, O., Fransson, T. H., Kielb, R. E., et al. (2001). *Comparative analysis of blade mode shape influence on flutter of two-dimensional turbine blades*. ISABE Paper ISABE-2001-1243.
54. Yang, H., He, L., Wang, Y. (2008). Experimental Study on Aeroelasticity in Linear Oscillating Compressor Cascade. PartII: Tip-clearance Effect. *Beijing: Acta Aeronautica et Astronautica Sinca*, 29(4):804–810.
55. Wang, Y. (1999). *Researches on several problems of blade flutter in turbomachinery*. Beijing: Beihang University.
56. Zhang, X., & Wang, Y. (2010). Influence of interblade phase angle on the flutter of rotor blades. *Beijing: Journal of Aerospace Power*, 25(02), 412–416.
57. Xu, K., & Wang, Y. (2011). Application of time domain method in aeroelastic computations for compressor rotors. *Beijing: Journal of Aerospace Power*, 26(01), 191–198.
58. Zhang, X., Wang, Y., & Xu, K. (2011). Effects of parameters on blade flutter in turbomachinery. *Beijing: Journal of Aerospace Power*, 26(07), 1557–1562.
59. Zhang, Z. (2009). *Numerical simulation of flutter in turbomachinery*. Beijing: Beihang University.
60. Zhang, Z., Zou, Z., Wang, Y., et al. (2010). Flutter prediction method applied in turbomachinery design. *Beijing: Journal of Propulsion Technology*, 31(2), 174–180.
61. Zhang, Z., Zou, Z., Wang, Y., et al. (2010). Investigation of flutter prediction method for transonic fan. *Beijing: Journal of Aerospace Power*, 25(3), 537–548.

62. Huff, D. (2004). *Technologies for turbofan noise reduction*. NASA Glenn Research Center. Cleveland, Ohio, 10th AIAA/CEAS Aeroacoustics Conference Manchester, United Kingdom, 2004.
63. Qiao, W. (2010). *Aeroengine aeroacoustics*. Beijing: Beihang University Press.
64. Nesbitt, E. (2011). Towards a quieter low pressure turbine: Design characteristics and prediction needs. *International Journal of Aeroacoustics*, 10(1), 1–16.
65. Batard, H. (2005). *Development of the quiet aircraft—Industrial needs in terms of aircraft noise and main achievements in Europe*. Forum Acusticum 2005 International Conference, Budapest, Hungary.
66. Mathews, D. C., Nagel, R. T., & Kester, J. D. (1975). *Review of theory and methods for turbine noise prediction*. AIAA Paper 75-540.
67. Lavin, S. P., Ho, P. Y., & Chamberlin, R. (1984). *Measurements and predictions of energy efficient engine noise*. AIAA Paper 84-2284.
68. Sun, X., & Zhou, S. (1994). *Aeroacoustics*. Beijing: National Defense Industry Press.
69. Dai, X., Jing, X., & Sun, X. (2011). Nonlinear acoustic dissipation mechanism of a slit resonator. *Beijing: Journal of Aerospace Power*, 26(3), 530–536.
70. Tyler, J. M. & Sofrin, T. G. (1962). *Axial flow compressor noise studies*. SAE Technical Paper 620532.
71. Enghardt, L., Moreau, A., Tapken, U., et al. (2009). *Radial mode decomposition in the outlet of a LP turbine-estimation of the relative importance of broadband noise*. AIAA Paper 2009-3286.
72. Lowson, M. V. (1970). Theoretical analysis of compressor noise. *Journal of the Acoustical Society of America*, 47(1), 371–385.
73. Tan, H., Qiao, W., Zhao, L., et al. (2012). Aerodynamics/acoustics integration design method of low pressure turbine-overall parameters optimization. *Beijing: Journal of Propulsion Technology*, 33(4), 573–578.
74. Enghardt, L., Tapken, U., Neise, W., et al. (2001). *Turbine blade/vane interaction noise: Acoustic mode analysis using in-duct sensor rakes*. AIAA Paper 2001-2153.
75. Broszat, D., Korte, D., Tapken, U., et al. (2009). *Validation of turbine noise prediction tools with acoustic rig measurements*. AIAA Paper 2009-3283.
76. Broszat, D., Kennepohl, F., Tapken, U., et al. (2010). *Validation of an acoustically 3D designed turbine exit guide vane*. AIAA Paper 2010-3806.
77. Zhao, L., Qiao, W., Tan, H. (2013). Aerodynamic-acoustic Three-dimensional Numerical Optimization of Low Pressure Turbine: Lean Vane Strategy. *Beijing: Acta Aeronautica et Astronautica Sinica*, 34(2): 246–254.
78. Zhao, L. (2012). *Theory and method investigation of the aerodynamic-acoustics integration design in turbine*. Xi'an: Northwestern Polytechnical University.
79. Blaszcak, J. R. (2008). *Performance improvement and noise reduction through vane and blade indexing of a two-stage turbine*. AIAA Paper 2008–2941.
80. Yue, Z., Li, L., Yu, K., et al. (2007). *Multidisciplinary design optimization of aeroengine turbine blades*. Beijing: Science Press.
81. Talya, S. S., Chattopadhyay, A., & Rajadas, J. N. (2000). *Multidisciplinary analysis and design optimization procedure for cooled gas turbine blades*. AIAA Paper 2000-4877.
82. Chi, Z., Ren, J., & Jiang, H. (2013). Coupled aerothermodynamics optimization for the cooling system of a turbine vane. *Journal of Turbomachinery*, 136, 051008.
83. Wang, R., Jia, Z., Hu, D., et al. (2013). Multiple precision MDO strategy for turbine blade. *Beijing: Journal of Aerospace Power*, 28(5), 961–970.

Index

A

- Active clearance control, 73, 91
- Aero-acoustic conjugate, 542, 544, 545, 548
- Aerodynamic design considering unsteady effects, 433
- Aerodynamic design process, 364, 409
- Aerodynamic efficiency, 7, 27, 29, 42, 103, 187, 205, 208, 211, 212, 218, 221, 222, 240, 241, 322, 325, 336, 340, 341, 353, 384, 387, 432, 446, 465, 472, 488
- Aerodynamic jet, 485, 486, 493, 495, 503
- Ainley & Mathieson loss model, 282–287, 290
- AMDC loss model, 279, 288
- Area ratio, 80, 115, 118, 122, 124, 129, 131, 136, 137, 285, 304, 305, 327, 460
- Aspect ratio, 3, 16, 43, 62, 66, 67, 86, 99, 124, 144, 145, 223, 260, 261, 286, 287, 290, 298, 302, 303, 324, 325, 340, 488, 535
- Axial flow turbine, 126
- Axial velocity ratio, 7, 321, 322, 325, 327, 333, 334, 348–351, 353, 356–360, 364

B

- Blade-endwall integration design technology, 433, 438, 440
- Blade load, 25, 65–67, 69, 75, 78, 154, 244, 310, 311, 343, 400, 422, 469, 483
- Body force, 328, 330–332, 495

C

- Calmed effect, 148
- Circulation coefficient, 26, 27
- Clocking effect, 187–189, 465, 466
- Composite blade modeling, 429
- Conjugate heat transfer, 380, 381, 385, 387, 527–530
- Cooled turbine efficiency, 31
- Cooling flow mixing loss model, 313

- Coull & Hodson profile loss model, 310, 311, 313, 335
- Counter-rotating turbine, 349–351, 356–359
- Craig & Cox loss model, 297–304, 335

D

- Denton loss model, 306
- Deviation angle, 280, 281, 449
- Deviation angle model, 280

E

- Endwall, 3, 7, 15, 16, 62, 66, 67, 69–74, 100, 101, 105, 106, 118, 120, 126, 127, 134, 140, 147, 223–238, 241, 245, 246, 259, 284, 290, 306, 309, 320, 373, 387, 388, 415, 416, 420, 422–424, 427, 438, 440, 442, 455, 457, 469, 527, 528, 533
- Expansion ratio, 29, 31, 43, 240, 321, 346, 347, 363, 376, 379, 447, 451, 485, 513, 515
- Expansion wave, 21, 52, 54

F

- Fence, 498–500
- Fine flow organizing and design technologies, 433
- Fine organizing for shock wave systems, 447
- Fine organizing technology for rotor blade tip leakage flow, 440
- Flow coefficient, 7, 15, 43, 76, 78–80, 86, 87, 89, 144, 176, 182, 183, 321, 322, 325, 327, 333–335, 337, 340, 342, 344, 349, 351, 353, 355–359, 443
- Flow control, 2, 12, 16, 138, 140, 221, 222, 241, 260, 261, 265, 272–274, 428, 483, 484, 486–488, 492, 493, 495–497, 499, 500, 502, 504, 510
- Flow organizing, 278, 433, 442, 443, 446, 447, 455, 483

- Flow organizing considering the interaction between cooling flow and the main flow, 455
- Flow-structure interaction, 534, 537–539, 541
- Flutter, 206, 534, 535, 537, 539–541
- Forced response, 534, 535, 537, 538, 541
- G**
- Gas turbine, 1, 4, 68, 74, 126, 345, 349, 353, 391, 487, 488, 493, 495, 512, 540, 549
- Geometric control technology, 513
- H**
- Hanging structure, 261, 265
- Hot streak, 465–469
- I**
- Integrated design of structural vanes and splitter vanes in ITDs, 462
- Integrated design of strut and compact inter-turbine duct, 459
- Integration of inter-turbine duct struts and LP turbine guide vanes, 461
- Inter Turbine Duct (ITD), 115–120, 122–134, 136–138, 140
- K**
- Kacker & Okapuu loss model, 288, 289, 291, 343
- K-H instability, 152, 155, 159, 162, 164
- L**
- Leading-edge modeling, 410, 411
- Leakage flow, 17, 18, 24, 25, 68, 72, 73, 75–77, 81–89, 105, 107, 131, 133, 134, 144, 146, 196–199, 201–206, 208, 209, 211–215, 217, 219, 220, 222, 223, 296, 307, 308, 426, 440–446, 459, 467, 483, 503–505, 507, 509, 510, 512, 517, 533
- Loading coefficient, 7, 25, 43, 75, 81, 321, 322, 325, 327, 333–335, 337, 340, 341, 344, 348–350, 352, 356, 361, 428, 449
- Loss model, 22, 66, 76, 77, 79–82, 86, 282, 288, 290, 292, 307, 308, 313, 315–318, 325, 334, 335, 340, 347, 348, 364, 371
- Low-dimensional design space, 320, 322
- Low pressure turbine, 144, 163, 245, 353, 488, 490, 492, 495, 497, 521, 544
- Low Reynolds number, 144, 159, 223, 239–241, 244–246, 248, 263, 272, 339, 483, 488, 490, 492, 493, 497, 508
- M**
- Mid-span section assessing method, 322
- Mixing, 10, 17, 22–24, 31–33, 77, 79, 81, 82, 84–87, 91, 95, 99, 127, 131, 146, 198, 199, 204–206, 211, 217, 220, 234, 238, 248, 279, 280, 294, 296, 306–309, 313–316, 422, 438, 440, 443, 455, 465, 491, 502, 509, 527
- Multidimensional coupling, 213, 215
- Multidisciplinary design optimization, 131, 548, 553
- N**
- Nonaxisymmetric endwall modeling, 429, 433, 434, 436, 438, 460
- Numerical evaluation system of turbine aerodynamic performance, 364
- P**
- Parametric blade modeling, 403, 404, 408
- Plasma, 486, 495–497, 507
- Pneumatic control, 513, 517–519, 521
- Potential, 2, 13, 19, 20, 33, 47, 56, 57, 116, 147, 175, 184, 199, 202, 217, 266, 272, 273, 278, 279, 362, 389, 399, 535
- Pressure gradient, 11–13, 15, 16, 47–49, 58, 60–62, 64, 66, 69, 71, 99, 100, 116, 118, 120, 125, 126, 128, 129, 136, 146, 149, 153, 154, 159, 168, 172, 173, 181, 191, 194, 199, 223, 225, 226, 228, 229, 232, 239, 245, 262, 264, 268, 272–274, 279, 327, 375, 410, 414, 417–420, 422, 425, 427, 436, 438, 459, 488, 497, 501–503, 515, 527, 532
- Pressure surface, 14, 17, 19, 21, 25, 69–71, 76, 78, 100, 167, 192, 226–230, 232, 233, 235, 246, 268, 293, 306, 308, 310, 313, 401, 404, 409, 411, 415, 418, 419, 422, 440, 444, 467–469, 492, 497, 499, 501, 502, 504, 505, 517, 540
- Profile loss, 47–49, 75, 131, 138, 146, 149, 154, 162, 167, 171, 172, 176, 178, 181, 182, 190, 244, 245, 279, 282–285, 287–290, 292–294, 297, 298, 300–302, 304, 310, 311, 313, 317, 323, 335, 336, 371, 428
- R**
- Reaction degree, 8, 296, 327, 333, 334, 337, 340, 348, 349, 356, 361–364, 417, 424, 485, 512

Reverse jet, 152

S

Sealing, 2, 74, 103, 106, 107, 109, 111, 209, 222, 231, 455–459, 497, 519, 520, 531, 533

Secondary flow, 7, 8, 15–17, 22, 25, 62, 70, 86, 100, 101, 106, 117, 123, 145, 146, 189, 201, 202, 204, 213, 220, 223–227, 229, 234–236, 238, 241, 245, 246, 248, 424, 426, 434, 483, 497–499, 502, 503, 505, 521

Secondary flow loss, 37, 43, 62, 65–67, 72, 75, 81, 145, 146, 206, 223, 225, 226, 488, 501

Shock wave, 20, 21, 46–49, 51, 54, 57–60, 144, 424, 433, 448, 449, 533

Shroud, 17, 43, 45, 49, 86, 88, 89, 91, 146, 147, 196–200, 202–214, 217–222, 286, 287, 292, 397, 399, 441–443, 509, 510, 512

S&K chart, 136

Skewed blade, 415, 417, 418, 420, 423, 424

Smith chart, 321, 322, 325, 335, 336

S2 streamsurface calculation, 364

Stacking, 277, 278, 399, 410, 414–416, 430, 431, 452

Strouhal number, 164, 165, 176

Strut, 122–124, 129, 137, 138, 427, 459, 462

Suction surface, 13–15, 17–21, 25, 45–47, 55, 60, 63–65, 69–71, 73, 76–78, 80, 99, 100, 105, 158, 160, 163, 167, 168, 175, 176, 181, 183, 186, 192, 201, 223–226, 228, 230, 232, 233, 235, 239, 240, 242–244, 246, 268, 274, 293, 298, 301, 306, 308–311, 313, 327, 381, 401–404, 408–410, 414, 418–422, 439, 444, 466, 467, 486, 488, 490, 492, 495, 497, 499, 501–504, 507, 515, 517, 531, 533, 541, 547

Surface roughness, 12, 148, 151, 279, 292, 293, 300, 485, 490, 497

Surface trip wire, 488

Swept blade, 16, 428

T

Tip leakage loss, 8, 17, 18, 78, 86, 279, 280, 282, 286–288, 291, 292, 296, 297, 305–307, 323, 325, 415, 424

Transition, 10–12, 15, 59, 149, 151–159, 161–163, 165, 168, 169, 171, 173–175, 180, 186, 187, 189, 191–195, 209, 230–232, 235, 238, 239, 243–245, 263, 273, 309, 375, 378, 381, 384, 403, 410,

411, 414, 484, 489, 490, 493, 497, 499, 501, 527, 529, 531, 532

Traupel loss model, 293–297, 300, 335

Turbine, 1, 2, 4, 6–8, 12, 14, 15, 17–22, 25, 27, 29–34, 37, 39–41, 43–46, 49, 54, 60–62, 66, 68, 69, 73, 74, 76, 78, 81, 83, 86–88, 91–93, 95, 99, 100, 103–105, 107, 117, 118, 130, 131, 133, 136–138, 140, 143, 144, 146–149, 154, 157, 158, 160–163, 165, 166, 170–173, 175, 178, 182–192, 196, 198, 199, 202–208, 211, 212, 214, 216–218, 220–223, 225–232, 234–237, 239–246, 259, 261, 268, 272, 274, 277–280, 282, 284–286, 288, 291, 294, 297, 305, 307, 309, 310, 313, 320–328, 330–340, 343–347, 349–353, 355, 356, 358, 360–363, 375, 377–382, 384, 388, 398–400, 402, 404, 406, 408, 410, 412, 414–416, 422, 423, 426–434, 436, 437, 440, 441, 443, 446–452, 455, 459–463, 465, 466, 468, 471, 472, 483, 486, 487, 493, 495–499, 501, 503–505, 507–510, 512, 513, 515–519, 525–527, 529–535, 537–548, 550–553

Turbine rear frame, 137, 143, 144, 259

Turbulence intensity, 12, 14, 15, 62, 95, 103, 107, 118, 126, 159, 161–163, 176, 178, 185, 268, 270, 455

Turbulence model, 209, 263, 364, 375, 378, 381, 384, 389, 529

Turbulent spot, 11, 152, 162, 192, 194

V

Variable-speed power turbine, 345

Velocity triangle, 7, 144, 203–205, 291, 320, 322–324, 327, 330, 344, 345, 350, 351, 353, 358, 359, 362, 363

Versatile core-engine turbine, 345, 347

Vortex generator, 140, 461, 483–486, 491–493, 500–502, 507

VSPT program, 338, 343

W

Wake, 14, 22, 49, 56, 95–97, 123, 129, 144, 146, 157–159, 165–178, 180–185, 187–189, 192–194, 202, 215, 235–238, 244–247, 266, 270, 279, 294, 311, 465, 489, 497, 499, 535, 537, 538

Wake passing frequency, 168, 181, 193, 194, 237, 470, 471

Z

Zweifel coefficient, 25–27, 67, 340, 343, 437, 440